1985

Turbulent disruptions from the Strauss equations

Jill Potkalitsky Dahlburg
College of William & Mary - Arts & Sciences

INFORMATION TO USERS

This reproduction was made from a copy of a document sent to us for microfilming. While the most advanced technology has been used to photograph and reproduce this document, the quality of the reproduction is heavily dependent upon the quality of the material submitted.

The following explanation of techniques is provided to help clarify markings or notations which may appear on this reproduction.

1. The sign or "target" for pages apparently lacking from the document photographed is "Missing Page(s)". If it was possible to obtain the missing page(s) or section, they are spliced into the film along with adjacent pages. This may have necessitated cutting through an image and duplicating adjacent pages to assure complete continuity.

2. When an image on the film is obliterated with a round black mark, it is an indication of either blurred copy because of movement during exposure, duplicate copy, or copyrighted materials that should not have been filmed. For blurred pages, a good image of the page can be found in the adjacent frame. If copyrighted materials were deleted, a target note will appear listing the pages in the adjacent frame.

3. When a map, drawing or chart, etc., is part of the material being photographed, a definite method of "sectioning" the material has been followed. It is customary to begin filming at the upper left hand corner of a large sheet and to continue from left to right in equal sections with small overlaps. If necessary, sectioning is continued again — beginning below the first row and continuing on until complete.

4. For illustrations that cannot be satisfactorily reproduced by xerographic means, photographic prints can be purchased at additional cost and inserted into your xerographic copy. These prints are available upon request from the Dissertations Customer Services Department.

5. Some pages in any document may have indistinct print. In all cases the best available copy has been filmed.

University Microfilms International
300 N. Zeeb Road
Ann Arbor, MI 48106

Dahlburg, Jill Potkalitsky

TURBULENT DISRUPTIONS FROM THE STRAUSS EQUATIONS

The College of William and Mary in Virginia PH.D. 1985

PLEASE NOTE:

In all cases this material has been filmed in the best possible way from the available copy. Problems encountered with this document have been identified here with a check mark __✓__.

1. Glossy photographs or pages _____
2. Colored illustrations, paper or print _____
3. Photographs with dark background _____
4. Illustrations are poor copy _____
5. Pages with black marks, not original copy _____
6. Print shows through as there is text on both sides of page _____
7. Indistinct, broken or small print on several pages ✓
8. Print exceeds margin requirements _____
9. Tightly bound copy with print lost in spine _____
10. Computer printout pages with indistinct print _____
11. Page(s) _____ lacking when material received, and not available from school or author.
12. Page(s) _____ seem to be missing in numbering only as text follows.
13. Two pages numbered _____. Text follows.
14. Curling and wrinkled pages _____
15. Dissertation contains pages with print at a slant, filmed as received _____
16. Other _____

_____

_____

University
Microfilms
International

TURBULENT DISRUPTIONS

FROM

THE STRAUSS EQUATIONS

A Dissertation

Presented to

The Faculty of the Department of Physics

The College of William and Mary in Virginia

In Partial Fulfillment

Of the Requirements for the Degree of

Doctor of Philosophy

---

by

Jill Potkalitsky Dahlburg

1985

APPROVAL SHEET

This dissertation is submitted in partial fulfillment of

the requirements for the degree of

Doctor of Philosophy

Jill Potkalitsky Dahlburg

David C. Montgomery

George Vahala

Eugene Tracy

Roy L. Champion

George T. Rublein

TABLE OF CONTENTS

ACKNOWLEDGEMENTS

The suggestion of this work came from my thesis advisor, David Montgomery. Most of the detailed effort implicit here also arose as a consequence of his helpful guidance. The scalar version of the simulation code generated for this thesis could never have existed without the greatly appreciated instructions and suggestions of Thomas Zang. Major contributions by William Matthaeus in the generation of the vectorized version of the free decay code are noted with sincere appreciation. Conversations concerning this research effort, with Russell Dahlburg, Murshed Hossain and George Vahala, were at times extraordinarily useful. Thank you all. Additional, active participation in this project, on the part of Gary Doolen is also gratefully acknowledged.

ABSTRACT

The subject of this thesis is an analysis of results from pseudospectral simulation of the Strauss equations of reduced three-dimensional magnetohydrodynamics. We have solved these equations in a rigid cylinder of square cross section, a cylinder with perfectly conducting side walls, and periodic ends. We assume that the uniform-density magnetofluid which fills the cylinder is resistive, but inviscid. Situations which we are considering are in several essential ways similar to a tokamak-like plasma; an external magnetic field is imposed, and the plasma carries a net current which produces a poloidal magnetic field of sufficient strength to induce current disruptions. These disruptions are characterized by helical "m = 1, n = 1" current filaments which wrap themselves around the magnetic axis. An ordered, helical velocity field grows out of the broad-band, low amplitude noise with which we initialize the velocity field. Kinetic energy peaks near the time the helical current filament disappears, and the current column broadens and flattens itself out. We find that this is a nonlinear, turbulent phenomenon, in which many Fourier modes participate. By raising the Lundquist number used in the simulation, we are able to generate situations in which multiple disruptions are induced. When an external electric field is imposed on the plasma, the initial disruption, from a quiescent state, is found to be very similar to those observed in the undriven runs. After the lobed "m = 1, n = 1" stream function pattern develops, however, a quasi-steady state with flow is maintained for tens of Alfven transit times. If viscous damping is included in the driven problem, the steady state may be avoided, and additional disruptions produced in a time less than a large-scale resistive decay time.

TURBULENT DISRUPTIONS

FROM

THE STRAUSS EQUATIONS

I. TOKAMAK DISRUPTIONS

The tokamak is one of the most widely studied species of the genus "magnetic fusion confinement device." In essence, the tokamak is a torus-shaped magnetic bottle. Two basic confining magnetic fields are present in a tokamak, a toroidal field B_ϕ and a poloidal field B_θ; see Fig. 1a. The toroidal field is produced by an external toroidal solenoid. The toroidal plasma itself serves as the secondary of a transformer. A changing magnetic field in the primary produces an electric current in the toroidal direction of the plasma. This current Ohmically heats the plasma, and generates a poloidal magnetic field which assists the stronger externally imposed magnetic field in confining the plasma.

Although a tokamak is a good precursor for a confinement fusion device, it is far from a final state reactor. Two fundamental types of plasma confinement problems exist for a tokamak plasma, problems shared with other magnetic fusion confinement devices. The primary difficulty is that the plasma has a myriad of instabilities associated with it. Some of the most dangerous, disruptive instabilities, even lead to the termination of the discharge, and can seriously damage the device. A complementary problem is that fusion-oriented devices operate in a temperature range which makes internal diagnosis of the dynamics troublesome. Accurate (if any) experimental observations of many necessary quantities - ion densities, varying magnetic fields, fluid velocities, and current distributions, for example - are difficult to obtain. Thus, in order to generate the μῦθος πλαστός (likely story) for what happens when these instabilities take place, it is necessary to augment experimental observations with extrapolative theoretical modelling. For problems of interest, it is in general important to implement computational methods, to generate as much in-

formation as possible on the dynamics of the plasma.

One of the most central questions in the whole subject of tokamak confinement has been "what happens in the disruptive instability?" (Bickerton (1977); Rutherford (1980); Robinson (1982)). Only when the disruptive process is reasonably well understood, and controlled, may the tokamak evolve into a practical fusion reactor. It is a class of idealized plasma problems related to disruption which we explore in the body of this work.

Following a brief introduction to the tokamak, and its present experimental status, experimental observations of the disruptive instabilities are considered, with particular emphasis on internal disruptions. After a survey of the various emergent interpretations and models of these observations, this approach to the problem of current disruptions in a bounded magnetofluid is described.

A. The Tokamak.

Figure 2, after Robinson (1982), shows a standard arrangement for a traditional tokamak. Table 1, produced by Bickerton (1977), is a list of representative tokamak devices. Note that some devices no longer have an iron core but rather an air core. Also, for some devices, vertical coils with feedback have replaced the copper stabilizing shell. A feed-back arrangement becomes necessary when shaped cross-sections, with better stability properties, are used. This arrangement is also more convenient (Bickerton (1977); Robinson (1982)).

1. Diagnostics.

According to Bickerton (1977), it is "astonishing" that we still have no direct way to measure the poloidal magnetic field, or equivalently, the radial variation of the current density. It is calculated by assuming that the tor-

oidal current density $j_\varphi(r)$ varies as the electron temperature, T_e, to the 3/2 power, and that the effective charge of the plasma ions is uniform across the plasma.

The electron density and temperature, and the ion temperature, all can be measured by Thomson scattering, the scattering of laser light by electrons. In a review article, Magar (1981) explains that an electron placed in the field of a laser beam will be accelerated and hence emit radiation. Irregularities in the density distribution give rise to net scattering. Random nonuniformities produce "incoherent scattering"; the resultant scattered power is proportional to the electron density. Since electrons form a polarizing shield around ions, scattering off these coherent clouds allows the observer to determine the phase velocity of the density fluctuations, and hence of the ion temperature. Analogously, by scattering off individual electrons, one can infer electron temperatures. These measurements have been made practical by the advent of the high power pulsed laser. The pulsing is a drawback; only a few measurements may be taken per discharge.

Although less accurate than Thomson scattering, analysis of x-ray emission yields the electron temperature as a continuous function of time. Bickerton (1977) describes this as a chordal line of sight measurement which requires some unravelling to give $T_e(r,t)$; it yields the highest temperature in a sight line. Gill (1981) discusses x-ray diagnostics in depth. He gives formulae that allow one to convert the measured radiation in a plasma into information about the electron temperature, assuming the plasma is Maxwellian, and that no discrete emission lines are present. He also describes the x-ray pinhole technique, which has been used (von Goeler, et al (1974)) to study the magnetohydrodynamic activity of the hottest part, the central region, of a tokamak plasma. By com-

paring signal phases at various positions in the plasma, the periodicity of the disturbance may be inferred.

Another diagnostic tool is the external magnetic pick-up coil, which allows one to detect small magnetic fluctuations outside the plasma. These fluctuations can be measured at several locations around the plasma, analysed into their Fourier components, and interpreted in terms of magnetohydrodynamic (MHD) modes (Wesson (1981)).

Norton (1976), and Hutchinson (1976) carefully inserted magnetic probes to follow the development of internal magnetic field structures in the tokamak LT-3. Hutchinson deduces the toroidal current density from these measurments by assuming cylindrical symmetry.

Bickerton (1977) mentions that ion temperatures may also be measured by analysis of the fast neutral atoms leaving the plasma. Further, although the measurement of current and loop voltage are relatively straightforward, he warns that even in deriving the resistive part of the voltage, difficulties may ensue. In short, he suggests that a good general principle is to measure everything with two methods, and "to treat all results with initial disbelief".

2. Parameters, Timescales.

Bickerton (1977) states that the basic question about tokamaks is whether or not they can be made to contain a plasma which will satisfy the reactor criterion first set forth by Lawson in 1958. The reactor criterion is a statement about what is necessary in the way of plasma confinement, to achieve fusion. The plasma must be dense enough, and stay in the machine long enough, with enough thermal energy to overcome the Coulomb repulsion between nuclei, for a useful amount of energy to be produced. If a mixture of deuterium and tritium is used in the tokamak, the ballpark "enoughs" are that the temperature of the

plasma be on the order of 5 to 10 keV, and the product of the particle density, n, and energy confinement time, τ_E, be at least 10^{14} cm^{-3} sec (Bateman (1978)). It is estimated that the next generation machines, JET in particular, will approach this criterion (Rutherford (1980)).

It is also necessary to monitor other, less dramatic figures, on the way to the goal of fusion. Observation and theory must be comparable, for any use to be made of their coexistence. For these comparisons to take place, the language of theory must agree with that of experiment at some level. The most basic bridge between theory and experiment is that built by dimensionless numbers and general timescales. For instance, the value of a single dimensionless number, the Reynolds number R = ((characteristic velocity) * (characteristic length) / (kinematic viscosity)) allows an estimate of whether a flow is laminar or turbulent, and consequently which sort of theory may apply.

In order to obtain a straightforward view of the plasmas under investigation, we calculate similar numbers for some existing fusion devices, using formulae from Braginskii (1965), and typical plasma parameters of the current generation fusion devices from Bickerton (1977). Results of these calculations are in Table 2. The constants, in cgs units, used to create this table are those given by Book (1980). Where the bracketed numbers refer to formula numbers in Braginskii's article, symbols used are:

[2.7] $\sigma_\perp$ = perpendicular electron conductivity.

[2.23] η_{i1} = ion dynamic viscosity coefficient.

[2.24] η_{i3} = ion dynamic viscosity coefficient.

[6.32] D_M = magnetic diffusivity, $f(\sigma_\perp)$.

[7.18] ρ = mass density.

[8.19] V_A = Alfven speed, $f(B_\varphi)$.

From these coefficients are calculated:

τ_R = resistive decay time = (minor radius)^2 / D_M.

τ_A = Alfvén transit time = (major radius) / V_A.

S = Lundquist number = $\tau_R / \tau_A = 1/\eta$.

P_{m_1} = magnetic Prandtl number = $[\eta_\perp / \rho] / D_M$.

P_{m_2} = magnetic Prandtl number = $[\eta_\parallel / \rho] / D_M$.

Note that for all numbers calculated, we: assume that z, the charge state, is unity; use the Spitzer logarithm (Spitzer (1962)); designate the directions $\perp$ / $\parallel$ to mean perpendicular / parallel to the external magnetic field.

2. General Macroscopic Difficulties.

The struggle to create a productive fusion reactor has spanned decades, and is still continuing. A major difficulty is an engineering one, associated with the operation of the machine. Another, more serious difficulty is the following. Even present generation machines cannot be run in possible regimes of large current with arbitrarily shaped current density profiles and large number densities. Physical instabilities restrict the operation of tokamaks, to the point that the devices will only work in isolated windows of parameter space.

A very important tokamak number is the "safety factor", q. This parameter is a measure of the relative field strengths toroidally to poloidally, or the number of times a field line wraps the long way around the torus divided by the number of times it wraps poloidally, in the limit of an infinite number of windings. From the geometry of field lines, when the surfaces on which the field lines lie have circular cross section, $q(r) = (r B_\varphi) / (R B_\theta)$. It is found that the most dangerous unstable modes tend to be those in which the helicity of the perturbation is the same as that of the tokamak's magnetic field, since a perturbation with this shape involves the least bending of ex-

isting magnetic field lines. This perturbation can be written in terms of f(r) * exp [i (m θ - n ϕ)]; when q = m / n, the perturbation helix matches that of the field, and the possibility of simple, linear instability arises (e.g., Manheimer et al (1984)). These ideas will be treated in more detail in Chapter 3, with n ϕ = k z / R, R -> 1.

At this point, using this terminology, we can briefly categorize the five macroscopic tokamak instabilities, according to Bateman (1978).

First seen was what is often termed the sausage, or m = 0 instability. The instability has no poloidal dependence. It is suggestively called the sausage instability, since the plasma column tends to pinch itself into a form resembling links, when subject to this instability.

When a moderate longitudinal magnetic field was imposed on the plasma column to stabilize the m = 0 instability, another highly macroscopic instability appeared, the m = 1. This instability is also known as the kink instability, because when this mode is active in the plasma, the plasma column itself may distort and wrap itself helically about the magnetic axis. The safety factor "q" is useful in determining the linear onset of this instability. For q(r = plasma edge) = $q_{edge} < 1$, is may be shown that a plasma column which does not touch the confining wall is unstable to a helical "m = 1, n = 1" perturbation, even in a straight cylinder. If $q_{edge} > 1$, the plasma is not subject to this instability. The criterion $q_{edge} > 1$ is called the Kruskal-Shafranov stability criterion (Kruskal, et al (1958); Shafranov (1970); Bateman (1978)).

Mirnov oscillations were observed soon after the m = 1 instability was seen. These oscillations were detected as small perturbations in the magnetic field at the edge of the plasma column. Fourier decomposition of the signals yielded information about their "m's" and "n's", their poloidal and toroidal

wave numbers; m running from 6 down through 2, with n = 1, is common early in a discharge.

Found next were sawtooth oscillations. In 1974, von Goeler, Stodiek and Sauthoff observed reproducible oscillations in soft x-rays emitted from the hotter central region of the plasma. These indications of disruptive activity within the plasma are so named because the x-rays which produce them generate a sawtooth pattern on the oscilloscope screen.

Throughout the history of tokamak operation, the disruptive instability would frequently appear. This is a generic name for a wide class of unexplained, abrupt transitions of tokamak plasmas, which often occur without warning. The disruptive process is frequently characterized by expansion of the plasma column, and a large, negative voltage spike kicking back against the transformer. The understanding of disruptive behavior is of paramount importance in the tokamak fusion effort. We turn now to a closer look at some experimental studies of large scale disruptive activity in tokamak plasmas.

B. Focus on Disruptive Activity.

Rapid, explosive-like tokamak disruptions range from internal disruptions that occur at regular intervals deep within the plasma, with no visible effect on global discharge parameters, to major disruptions that may lead to termination of the discharge in a single burst of activity (Biskamp (1979)). Radomtsev (1984) categorizes an abrupt flattening of the electron temperature, or equivalently, a power of the toroidal current density profile, as a function of radius, an internal disruption. He classes non-internal, or external, disruptions as varying in degree from minor to major. A plasma with current will survive a minor disruption, but not a major one.

External disruptions have been seen since the earliest times of tokamak

operation. Major disruptions are observed as catastrophic interruptions of plasma current density and electron temperature (Sauthoff, et al (1978)). Thorough documentation comes about far less easily than observation. Only a few agreed-upon features mark the existence of a generic external disruption. According to Kadomtsev (1975, 1984), the plasma column itself expands along the minor radius at the onset of the disruption, followed by a redistribution of the current density, a negative spike on the measured loop voltage, and an abrupt decrease in the major radius of the plasma column.

The external disruption, then, can not be classed as a phenomenon which is either independent of the plasma free surface, or its toroidicity. Numerical simulation of such a series of events is entirely beyond the present capabilities of available computers. Nonetheless, attempts have been made to model aspects of the external disruption (Waddell, et al (1978), (1979); Hicks, et al (1981), (1982); Diamond, et al (1984)). We will not pursue that course here.

Instead, the focus in this work will be on the internal disruption. Since this subclass of disruptive instabilities occurs deep within the plasma, it may readily be argued that particular edge effects play a less crucial role. We embark on a study of the internal disruptive instability with the hope that exploration of it will lead to a clearer vision of the underlying causes of disruptive activity in a wide variety of situations.

1. Experimental Observations of Internal Disruptions.

According to Bateman (1978), a breakthrough in the field of diagnostics came when von Goeler, et al (1974) first used sensitive, moveable soft x-ray detectors to observe continuous, reproducible oscillations at the center of the ST tokamak. This x-ray emission with sawtooth structure was also observed in other tokamak discharges (Jahns, et al (1978)). Kadomtsev (1984) considers the

observations of von Goeler, Stodick and Sauthoff to be even more than a major technical advance; he conjectures that results of their work may hold the key to understanding disruptive processes.

In 1974, von Goeler, et al (1974) obtained "images" of the ST tokamak plasma column by means of a slot aperture. The x-ray emission from different regions of the plasma, filtered through 1- and 3- mil Be foils, was measured with silicon surface barrier detectors, moveable in the image plane. Their mobility allows an observer to sample different chords of the plasma cross section. Radiation intensity is said to be a function of the electron density, n_e, and temperature T_e , and of the impurity concentration, while the fluctuations in the radiation are predominantly caused by fluctuations in T_e . The oscilloscope traces of these fluctuations show a "sawtooth-like" pattern, with slow rise and fast drop near the center of the column. Scanning slightly further out in plasma radius yields an "inverted" sawtooth, with a fast rise and slow, exponential drop. By assuming a stationary discharge and a constant value of impurity concentration across the current column, they calculate the safety factor, q(r), derived from Thomson scattering, to find that q(r = 0) = 0.8, and q(r = 2 cm.) = 1.0. They measure relative sawtooth amplitude as a function of radial chords, and find that the sawtooth amplitude has a node at the q = 1 point. It is outside that point that the sawtooth is inverted. By simultaneously measuring the sawtooth at different locations poloidally and toroidally, they observe that the sudden break of the sawtooth occurs at the same time everywhere. They conjecture that this indicates independence of variation in θ and φ, i.e. the sawtooth behaves like and m = 0, n = 0 mode, an "internal disruption". They report that, inside the q = 1 surface, T_e sharpens until the sawtooth breaks,then flattens, causing a decrease of T_e inside, and increase just outside the q = 1 surface. The outer increase dies off exponen-

tially during the reheating of the central part.

Each internal disruption, or abrupt flattening of the T_e profile, is preceded by a growing sinusoidal "kink mode" oscillation, with "m = 1, n = 1" (θ, ϕ) dependence. Von Goeler and coworkers (1974) infer the poloidal mode number m and toroidal mode number n of the disturbance by comparing phase relationships among x-ray traces taken at a variety of chords.

Jahns, et al (1978) describe the evolution of sawtooth oscillations in ORMAK, and give examples of the soft x-ray signals taken from the hot, central plasma of that tokamak. From many particular cases, they see that, in ORMAK, sawteeth are generally characterized by a repetition time of 0.5 to 2.5 milliseconds, and a disruption, or fall time, of about one tenth of that. The observed m = 1 oscillation has a frequency in the neighborhood of one cycle in a tenth of a millisecond. Beyond some radius, the sawtooth signals are "inverted", with a fast rise coincident with the disruptive fall of the "inside" sawteeth. The inversion radius, or q = 1 surface, ranges from 3 to 8 cm. Recalling from Table 1 that ORMAK's minor radius is 23 cm., it is clear that the inner region of the sawtooth activity is separated from the wall of the device.

Bateman (1978) also refers to ORMAK data in his description of the scenario. He adds to the description given by Jahns, et al (1978), when he states that the amplitude of the m = 1 oscillation, strongest in the neighborhood of the q = 1 surface, does not seem to be directly correlated with the strength of the sawtooth oscillation. In general, however, it is observed that the m = 1 oscillation grows during the rise time of the interior sawtooth, and vanishes just after the disruption. Bateman (1978) also notes that in 1976 the TFR group established that the x-ray sawtooth is primarily due to changes in T_e, and not due to density variations.

Bauthoff and co-workers, (1979), describe internal disruptive instabilities in PLT. Apparently, the mass of data acquired in PLT (with and without neutral beam injection) is not as straightforward as that obtained from ORMAK. They present information about the evolution of m = 1 modes, bursts of which can either be correlated to internal disruptions or decay without a disruptive event. Their signals of line-integrated emissivity display m = 1 oscillations at a fundamental rotation frequency ω visible on traces whose signals originate from the center, out through chords ± 8 cm. from the center. They note that the central trace exhibits 2ω behavior, since the hot spot passes within view twice per revolution. (According to Bateman (1978), the rotation frequency of the m = 1, n = 1 helical structure is not understood; it may be due to diamagnetic effects, or to rotation of the torus as a whole.)

Bauthoff, and coworkers, (1979), report that an inward spiral trajectory of the peak after disruption is also seen, better observed in a relatively small sawtooth. The peak emissivity may be seen to first spiral out to r ≈ 6 cm. A burst of x-ray activity is observed even in radii beyond 12 cm., which suggested that the peak region creates a localized protrusion into the previous concentric circular structures. After this "disruption", the peak emissivity region then spirals back toward the center. Bauthoff, et al (1979), conjecture that the two different outcomes of bursts of m = 1 activity may be related to the extent of the radial excursion of the magnetic axis; the closer the axis approaches the q = 1 surface, the more energy is lost from the center.

A new system of fast data acquisition and high performance amplifiers used on the TFR soft x-ray arrays of surface barrier detectors added new information to the observations of sawteeth in tokamak devices. Dubois, et al (1983) describe the observed sawtooth phenomena in TFR as being characterized by a regeneration part, during which the temperature, and hence the x-ray emissivity

profile, becomes peaked. An oscillation of m = 1 parity begins to grow. The central signal abruptly drops as the electron temperature profile flattens, indicating that an internal disruption has occurred. In some cases, however, the disruption itself generates complicated signals, sharp spikes in the emissivity near the time of maximum disruption. Dubois, et al (1983) report that these features seem to be present in all internal disruptions, and were not detected previously because their amplitude relative to the m = 1 mode and to the total temperature variation was much less; more delicate time resolution than previously employed was necessary to observe them.

The basic, repetitive story of internal disruptions, then, is that summarized by Kadomtsev (1975). He ignored the plasma rotation and described, from the work of von Goeler, et al (1974), that a slow m = 1, n = 1 instability occurs in the plasma, and grows to an order of about 10 % of the total radiation. This instability then gives way to an abrupt disruption, corresponding to a rapid symmetric cooling of the central region, and heating of the peripheral region. He interprets these results in terms of a cylindrical, helical flux function, where θ is replaced by z. The curl of this flux function generates an auxiliary magnetic field $\underset{\sim}{B}_* = \underset{\sim}{B}_\perp - (r B_z / R)\,\hat{e}_\theta$. The auxiliary field vanishes at the q = 1 surface, creating a situation which is unstable to perturbations. Because of finite resistivity, he conjectures that the lines of $\underset{\sim}{B}_*$ break and "reclose" at an x-point located on the q = 1 surface. This reclosing becomes progressively more rapid, and cannot stop until the entire internal region is reclosed with lines of the external field, and $\underset{\sim}{B}_*$ has acquired one sign throughout the plasma, i.e., the safety factor q has become greater than unity everywhere. Heating of the plasma column occurs, causing $\underset{\sim}{B}_*$ to again develop a singular surface, and the scenario to repeat. These ideas will

be discussed in further detail in Chapter 3.

2. Numerical Experiments.

Kadomtsev's scenario led Waddell and co-workers (1976) to perform a single helicity ($f(r, \Upsilon = m\theta + kz)$, only) numerical calculation to test the above hypothesis. They describe this hypothesis as one in which the $m = 1$ mode resistively allows the plasma to evolve from a state in which helical flux contours are circular, to a lower energy state in which helical flux contours are again circular, thereby flattening the current density and increasing q at the origin.

They solved a pair of equations for the fluid vorticity and magnetic helical flux function in a straight cylinder geometry, in which $B_\theta >> B_z$ (self-consistent) and $q \sim 1$; the plasma was assumed to be an incompressible magnetofluid. By allowing the plasma to completely fill the cylinder, the boundary condition on the magnetic field at the edge of the plasma was the same as the one at the edge of the computational domain. They chose the condition that the time derivative of the flux function at the wall ($r = a$) was constant. An initially peaked-on-axis model for the unperturbed toroidal current density was employed, with resistivity modelled to vary as the inverse of the initial current profile. A Lundquist number of $S = 5 \times 10^4$ was chosen, where $S = \tau_R / \tau_A$, for $\tau_R = a^2 / \bar{\eta}$, $\tau_A = (\rho)^{1/2} a / (kB_z)$, with $\bar{\eta}$ = characteristic value of the resistivity. The spatial resolution was not reported. The initial perturbation to the system was an $m = 1$ mode.

By monitoring the kinetic energy of the system, they followed the evolution of the dynamics. They found that by the time kinetic energy was a maximum, the toroidal current had flattened inside the $q = 1$ surface, with a skin current at the x-point, and $q(r = 0) \sim 1$. As the kinetic energy decreased slowly, the contours of helical flux evolved, but remained complex, strictly differing from

Kadomtsev's conjecture that they would return to a circular state. The flux function was fairly uniform across the center, however. Flow patterns remained essentially unchanged as the instability progressed, except that the velocity at the plasma center was noted to increase relative to that at the singular layer, as the instability developed. They reported no additional bursts of activity.

In 1976, Sykes and Wesson (1976) reported results from a three-dimensional, hydromagnetic simulation. Resistivity, viscosity, Ohmic heating and an energy loss were included in the equations solved, with the resistivity varying as $T_e^{-3/2}$, a varying function of position and time. They chose $\underset{\sim}{v} \cdot \hat{n} = 0$ for the velocity field boundary condition, where $\hat{n}$ is the unit normal vector to the surface and $\underset{\sim}{v}$ is the plasma velocity, and for magnetic field conditions they supplied an appropriate electric field at the wall to maintain constant current. Although their computational grid was only 14 * 14 * 18, they qualitatively observed a relaxation oscillation in the central value of the pressure, similar to experimentally observed sawteeth. This oscillation they attributed to the Ohmic heating of the plasma and consequent channeling of the current. After some computational time, they found that for the calculations reported, the oscillations decayed away and the instability finally took the form of a stationary helix. In order to better understand the magnetic field structure, they "unwound" the magnetic field, transforming to a coordinate system in which $B_r^* = B_r$, and $B_\theta^* = B_\theta - 2\pi r B_z / (\text{cylinder length})$. In this frame, they observed that at t = 0, q > 1 throughout the magnetofluid. Subsequent concentration of current led to q < 1 in an inner region. An instability arose, in which the original magnetic axis moved to one side, and a new one appeared on the opposite side of the plasma where a magnetic "island" had formed around the q = 1 surface. The new island then displaced the old, with another axisymmetric configuration

formed, the value of q now greater than unity. Subsequent cycles behaved differently from the first. A new magnetic island was formed on the surface of minimum q, when q fell below unity. This island did not remove the original island, but was itself expelled by a resurgence of the original island having q > 1. In summary, they saw features similar to experiment, and results supportive of Kadomtsev's interpretation.

Also in 1976, Strauss (1976) published his equations of reduced three dimensional MHD, which may be further reduced to the single helicity set used by Waddell, et al (1976), but do not a priori impose a single fixed helicity on the system. These equations are probably the simplest possible MHD description that retains some three-dimensionality of MHD turbulence in a current-carrying bounded magnetofluid. Though inadequate in situations in which the currents are strong enough to generate internal magnetic fields as strong as the externally-imposed dc magnetic fields, they appear as the logical first step in acquiring computational experience with realistic geometries. We shall discuss these equations at more length in Chapter 2.

Strauss (1976) reported results of numerical simulation of these equations in rectangular geometry, at unspecified, non-zero values of viscosity and resistivity, with boundary conditions such that $\hat{n} \cdot \underset{\sim}{B}_{wall} = \hat{n} \cdot \underset{\sim}{v}_{wall} = 0$, i.e. boundary conditions appropriate for rigid, free-slip, perfectly conducting walls. The viscosity and resistivity were necessary to damp the highest harmonics. His numerical solutions of the equations confirmed the existence of fast growing fixed-boundary kink modes in non-circular tokamaks.

These equations were later used by Waddell, Carreras, Hicks and Holmes (1979) (and Hicks, et al (1981)), and Biskamp and Welter (1982) to study situations in which many modes nonlinearly interact, in circular cylinder geometry.

Waddell, et al (1979) concentrated on situations perhaps appropriate to the major disruptive situation, seeking to observe interactions of the m = 2, n = 1 and m = 3, n = 2 modes, by selecting q profiles initially flat in the plasma core and high values of S ($\sim 10^5$). Biskamp and Welter (1982) chose very large values for S ($\sim 5 \times 10^5$), and imposed boundary conditions corresponding to constant current. The consequent time-dependent behavior of the imposed electric field at the wall can model the behavior of the loop voltage in a major disruption. Their simulations admittedly suffered from the inability to resolve the small spatial scales which are generated by the nonlinear terms. When they ran their simulations for long times, however, they reported observation of explosive simultaneous growth in both small-scale Alfven turbulence, and large scale modes; in this poorly resolved regime, they observed that as the energy of the dominant modes peaked, the applied electric field went negative. These simulations, although seminal, may be dangerously ill-resolved.

Dnestrovskii, et al (1977) used different sets of equations to piece together a full simulation of internal disruptive activity. They described three stages: in stage (1), the plasma heated and q(axis) decreased; the energy balance and current diffusion equations were simulated in this stage. The rapid disruption stage, (2), employed equations which followed from the MHD theory of reconnection of magnetic surfaces. In stage (3), they resumed the integration of equations employed in stage (1), and q(r = 0) again decreased. A cyclic procedure was thus envisaged.

Simulations of other systems have also begun to be performed in investigation of these resistive internal modes in tokamak plasmas, modes which depend on a third dimension for their existence. Some go to higher orders in inverse aspect ratio expansion, (for example, Izzo, et al (1983)), while others allow for fully three-dimensional motion of the magnetofluid (Bateman, et al (1974);

Schnack, et al (1983); Aydemir and Barnes (1984)). Aydemir and Barnes (1984) report the absence of total reconnection, and the observation of multiple changes in sign of the m = 1 vorticity pattern, when they choose an inverse aspect ratio of 1/3.

Other fusion devices are also simulated. It is interesting to note that Wakatani, et al (1983) observe that results they obtained from simulation of internal disruptions in HELIOTRON E, as well as those recently obtained for reversed field pinches (Caramana, et al (1983)) seem to suggest that the picture of internal disruption based on the Kadomtsev (1975) reconnection model may apply to all magnetic confinement systems unstable to m = 1 modes. It is even more important, therefore, to discover all we can about these internal disruptions.

3. Theoretical Studies.

Although Kadomtsev's model appears in essence to agree with both experimental and simulation results, many difficulties remain. Jahns, et al (1978), (Waddell, et al (1978)) expanded on the basic idea by developing a model for the time evolution of the electron temperature and the shear at the magnetic surface, to obtain a value for the repetition time of ORMAK's sawteeth which agrees moderately well with experiments. They conclude that resistive instabilities and magnetic reconnection, in conjunction with resistive heating, are responsible for sawteeth oscillations in tokamaks.

Dubois, et al (1983), however, cite the experimental results which point to "incomplete reconnection" (Bauthoff, et al (1979)) as evidence that the total reconnection model is inadequate. They suggest that the agreement between experiment and theory in the model of Jahns and co-workers (1978) is not sufficiently convincing, because line-of-sight integration, and a realistic x-ray

emissivity function were not taken into account. They demonstrate that a kinematic model in which turbulence, starting in the region of the q = 1 surface and propagating toward the core of the plasma, gives a better description of the behavior of internal disruptions.

Lichtenberg (1984) suggests intrinsic stochasticity, generated by nonlinear interactions of the m = 1, n = 1 mode with a mode arising from the toroidal equilibrium, as the mechanism for the disruptive phase of the m = 1 oscillation. He, too, objects to the concept of the magnetic island growing to fill the entire region within the q = 1 surface, pointing to experimental results in which the island persists after disruption. He suggests that growth of the "m = 1, n = 1" island could be countered by an increase in the thickness of the stochastic layer from the more rapid growth of second order islands.

An altogether different hypothesis, ostensibly generated to explain major disruptions, is the idea of Montgomery (1982). He conjectures that an alternative explanation to "tearing mode" theory is one expressed in terms of inverse magnetic helicity cascades, where magnetic helicity is defined as the integral (volume averaged) over space of the magnetic field dotted into its vector potential. He demonstrates that the inverse cascade behavior, generated from a variety of possible sources of small scale turbulence, would appear as an attempt of the current to flatten itself. That the onset of major disruptive activity is unpredictable is noted to be suggestive of the appearance of an inverse helicity cascade, also.

It is clear that additional, accurate information about disruptive MHD activity resulting from various current disruptions would be welcome.

C. Our Approach.

In this work, we consider a situation which is tokamak-like in the following ways. Imagine cutting the tokamak torus, and straightening it into a cylinder, one with periodic ends. For computational convenience, consider this to be a cylinder with rectangular cross section, where "poloidal" translates into a function of x and y, while "toroidal" is replaced by z; see Fig. 1b. The large toroidal magnetic field, then, becomes a field which is externally imposed in the z-direction, and the current induced in the plasma also points in z. The rigid metal walls of the device are assumed to be perfectly conducting, with free-slip boundary conditions imposed.

With the Strauss equations (Strauss (1976); Montgomery (1982)) of reduced three-dimensional MHD as our model, we address the general problem of MHD disruptive instabilities. Considering quiescent initial conditions - smooth current profiles and low amplitude random noise in the velocity field - we perform numerical simulations to discover what sorts of turbulent behavior such laminar conditions can generate.

We numerically solve the Strauss equations by means of a FORTRAN code written for the problem. The algorithm is fully pseudospectral in space, with an explicit form of time-stepping. All possible Fourier modes have been kept in the simulation. Dissipation is sufficient to resolve any generated small scale spatial structure. The results are thus numerical solutions of the full physical model.

This thesis demonstrates the value of realistic computer simulations as a useful diagnostic tool. The Strauss equations are time-advanced in a periodic, rectangular box, and current disruptions are accurately observed.

The equations and notation are introduced in the second chapter. Kadomtsev's model will be considered in more detail, in the third chapter, the

last of the introductory chapters. In the fourth chapter, our simulation machine will be described, and how the "knobs" γ_f and B_o may be adjusted. We will discuss free-decay code results, for various parameters, in the fifth chapter. A low-order model of the Strauss equations will be derived in the sixth chapter; this model contains some features of the free-decay simulation results, and may be used to generate predictions for the driven simulation results. In the seventh chapter are results from simulations in which a constant external electric field is imposed for all time. The eighth chapter contains a summary, and suggestions for further work.

II. THE NOTATION AND EQUATIONS USED

A. Single fluid, three-dimensional, incompressible MHD.

The equations of continuity and motion which describe flows of an incompressible, conducting fluid are:

$$\nabla \cdot \underset{\sim}{v} = 0 \tag{1}$$

$$\rho \left(\frac{\partial \underset{\sim}{v}}{\partial t} + \underset{\sim}{v} \cdot \nabla \underset{\sim}{v} \right) = -\nabla p + \rho \nu \nabla^2 \underset{\sim}{v} + \frac{\underset{\sim}{j}}{c} \times \underset{\sim}{B} \tag{2'}$$

together with a phenomenological Ohm's law,

$$\sigma \left(\underset{\sim}{E} + \frac{\underset{\sim}{v}}{c} \times \underset{\sim}{B} \right) = \underset{\sim}{j}$$

and the relevant Maxwell's equations,

$$\nabla \cdot \underset{\sim}{B} = 0$$

$$\nabla \times \underset{\sim}{B} = \frac{4\pi}{c} \underset{\sim}{j} + \frac{1}{c} \frac{\partial \underset{\sim}{E}}{\partial t} \tag{3'}$$

$$\frac{\partial \underset{\sim}{B}}{\partial t} = -c \nabla \times \underset{\sim}{E}$$

These are a set of equations which may be taken to govern the behavior of an incompressible magnetofluid, where $\underset{\sim}{v}(x,y,z,t)$ = velocity field of the fluid; $\underset{\sim}{\omega} = \nabla \times \underset{\sim}{v}$ = fluid vorticity; ρ = density, here assumed uniform and constant; ν = kinematic viscosity; $\underset{\sim}{B}(x,y,z,t)$ = magnetic field; $\underset{\sim}{j} = \nabla \times \underset{\sim}{B}$ =

current density; σ = conductivity; c = speed of light in vacuo; and $\underset{\sim}{E}$ = electric field.

The equations of MHD, and the approximations necessary to generate them, are discussed at length in a variety of places (e.g. Alfvén (1962); Braginskii (1965); Chen (1974); Bateman (1978); Montgomery (1983)). The essential measures of applicability are set forth by Braginskii (1965). His derivation of transport equations from kinetic equations is valid under the assumptions that the average quantities in a plasma (number of particles per unit volume, mean velocity of these particles, and kinetic temperature) change much more slowly in time and space than the time and distance it takes for the distribution functions, which characterize each particle component, to relax to local Maxwellians. He also assumes that the effect of the magnetic field on the collision itself may be ignored, or the Larmor radius is large compared with the Debye radius, i.e. $B^2 << 8\pi c^2$ [mass density of a species]. Although these measures are frequently unjustified, the equations apparently are valuable in a wide variety of situations. This simpler model, the MHD model, is generally applied to the study of large scale plasma phenomena, in situations where more sophisticated models are too complicated to be of value. We will use the single fluid (e.g. Braginskii (1965)) MHD model here.

An additional approximation is that of incompressibility. Montgomery (1983) applied an argument similar to the one which establishes the incompressibility of a non-conducting fluid to a magnetofluid. He showed that so long as we consider a "high beta" plasma, basically one in which the Alfvén speed is less than the speed of sound, the approximation is valid. That is, since $\beta = p / (B^2 / 8\pi)$, and the speed of sound in a fluid is the thermal speed, $\beta \equiv$ (speed of sound)^2/ (Alfvén speed)^2, where we have represented the pressure p as [number density] * [Boltzmann's constant] * [temperature], an Alfvén speed =

$B / (4\pi\rho)^{1/2}$ and where we take a thermal speed to be $(2p/\rho)^{1/2}$. He notes that the addition of an external magnetic field B_o to the dynamics of the system relaxes this constraint somewhat, for the case in which B_o is large compared to the fluctuating $\underset{\sim}{B}$. Then, if the ratio of B to B_o is much less than $\beta(B_o)$, incompressibility of the fluid is a good approximation. Tokamak plasmas have very large external fields imposed on them, which somewhat justifies the incompressibility assumption. This assumption is also very convenient. No equation of state, nor one for internal energy is necessary; instead, the pressure may be computed from a Poisson equation which is immediately derivable from the momentum equation. Further, the diffusivities of both fields will be approximated as time-independent scalars.

Ignoring high-frequency effects in Faraday's law, an equation may be obtained for the time-advancement of the magnetic field from Ampere's law,

$$\frac{\partial \underset{\sim}{B}}{\partial t} + \underset{\sim}{v}\cdot\nabla\underset{\sim}{B} = \underset{\sim}{B}\cdot\nabla\underset{\sim}{v} + \eta\nabla^2\underset{\sim}{B} \qquad (4')$$

where a scalar magnetic diffusivity, $\eta = c^2/(4\pi\sigma)$, is introduced through Ohm's law. If an initial magnetic field is properly solenoidal, it will remain that way as a function of time.

B. Dimensionless Units.

We follow Fyfe and Montgomery (1976) in the way the equations are made dimensionless. Let U_o be some characteristic velocity of the fluid, L_o a characteristic length, and ρ_o a characteristic density which we will choose to be $(4\pi)^{-1}$. The other variables are defined in terms of these. A dimensionless, eddy turnover time is created by means of a dimensionless distance divided by a dimensionless velocity, while, for instance, pressure is measured in units of $\rho_o U_o^2$, and the magnetic field in units of $(4\pi\rho_o U_o^2)^{1/2}$.

When these dimensionless variables are introduced in to the primed equations of the previous section, the following set is obtained:

$$\frac{\partial \underline{v}}{\partial t} + \underline{v}\cdot\nabla\underline{v} = -\nabla p + \underline{j}\times\underline{B} + \nu\nabla^2\underline{v} \qquad (2)$$

$$\nabla\times\underline{B} = \underline{j} \qquad (3)$$

$$\frac{\partial \underline{B}}{\partial t} + \underline{v}\cdot\nabla\underline{B} = \underline{B}\cdot\nabla\underline{v} + \eta\nabla^2\underline{B} \qquad (4)$$

Now ν is the inverse of the Reynolds number based on U_0, and η is the inverse of a similar Reynolds number, with kinematic viscosity replaced by laboratory magnetic diffusivity. It can be either a magnetic Reynolds number (when U_0 is a flow speed) or a Lundquist number (when U_0 is an Alfvén speed).

For quiescent initial conditions, ones in which the magnetic energy, $E_E = \frac{1}{2V_{Vol}}\int d^3x\, B^2$ is much greater than the fluid's kinetic energy, $E_v = \frac{1}{2V_{Vol}}\int d^3x\, v^2$, it is most convenient to scale the equations by a characteristic quantity other than the flow speed. The scaling we choose is the Alfven speed, $V_A = B / (4\pi\rho_0)^{1/2}$. Times are thus measured in terms of Alfven transit times: a distance of one unit is traversed in one unit of time, when $V_A = 1$. The inverse of η becomes the Lundquist number, $S = L_0 V_A$ / [laboratory magnetic diffusivity], while the fluid Reynolds number becomes $L_0 V_A$ / [kinematic viscosity]. It is this situation which is considered here.

C. Tokamak Ordering.

The magnetic field in a tokamak plasma is most simply comprised of two types

of field. The poloidal field arises self-consistently from the Ohmic current, while the toroidal field is largely generated by external coils. This toroidal field is at least an order of magnitude greater than the self-consistent poloidal field. Numerical studies by Shebalin, Matthaeus and Montgomery (1983) demonstrate that spectral transfer in incompressible MHD turbulence is inhibited in the direction parallel to a strong, externally imposed magnetic field. These results imply that more spectral transfer ought to be expected to occur in the poloidal plane, perpendicular to the external field, and less in the direction parallel to that field. Good use can be made of this inhibition of excitation in what is here the z-direction; any turbulence in the magnetofluid may be expected to be anisotropic, and mostly occurring poloidally. It is natural, then, to conjecture that derivatives which consider poloidal wave numbers will be larger generally than those which are taken with respect to z.

Following Montgomery (1982), we generate a series of equations (Strauss (1976)) from the full three-dimensional set, from order of magnitude considerations alone, by means of an expansion parameter ϵ . This parameter may be interpreted as an inverse aspect ratio; typical values of the inverse aspect ratio for current generation machines are listed in Table 2.

Let the large external magnetic field be represented as B_0/ϵ everywhere in the system. Upon expanding the self-consistent fields in powers of this parameter, the following series are obtained:

$$\underline{B} = \underline{B}^{(0)} + \epsilon \underline{B}^{(1)} + \epsilon^2 \underline{B}^{(2)} + \cdots$$

$$\underset{\sim}{V} = \underset{\sim}{V}^{(0)} + \epsilon \underset{\sim}{V}^{(1)} + \epsilon^2 \underset{\sim}{V}^{(2)} + \cdots$$

Inserting these series into the equations, the results are considered order by order. At each order, it is demanded that $\nabla \cdot \underset{\sim}{v}^{(n)} = 0$, $\nabla \quad B^{(n)} = 0$, $n \geq 0$. An order of magnitude must be assigned to the time derivative; no zeroth order population of Alfven waves is allowed to exist, which means that the time derivative is O(1).

By considering $O(\epsilon^{-1})$, $\underset{\sim}{B}^{(0)}$ and $\underset{\sim}{v}^{(0)}$ are seen to be at most functions of ϵz. $\nabla \cdot \underset{\sim}{B}^{(0)} = 0$, and $\nabla \cdot \underset{\sim}{v}^{(0)} = 0$, are used, to obtain $B_\perp^{(0)} = \nabla_\perp \times A(x,y,\epsilon z,t)\,\hat{e}_z$ and $\underset{\sim}{v}_\perp^{(0)} = \nabla \times \psi(x,y,\epsilon z,t)\,\hat{e}_z$, where A is the magnetic vector potential and ψ is the velocity stream function.

At the next order, O(1), the fast spatial variation of $\underset{\sim}{B}_\perp^{(1)}$ and $\underset{\sim}{v}_\perp^{(1)}$ is averaged over, leaving the gentler ϵz dependence unaltered. At this order, the formal parameter, ϵ, is then set equal to unity.

D. The Strauss Equations.

The very plausible and convenient set of equations which results at first order are the Strauss equations of reduced three-dimensional MHD (Strauss (1976); Montgomery (1982)).

$$\frac{\partial \underset{\sim}{v}_\perp}{\partial t} + \underset{\sim}{v}_\perp \cdot \nabla_\perp \underset{\sim}{v}_\perp = -\nabla_\perp p + \underset{\sim}{B}_\perp \cdot \nabla_\perp \underset{\sim}{B}_\perp + B_0 \frac{\partial \underset{\sim}{B}_\perp}{\partial z} + \nu \nabla_\perp^2 \underset{\sim}{v}_\perp \tag{5}$$

$$\frac{\partial \underset{\sim}{B}_\perp}{\partial t} + \underset{\sim}{v}_\perp \cdot \nabla_\perp \underset{\sim}{B}_\perp = \underset{\sim}{B}_\perp \cdot \nabla_\perp \underset{\sim}{v}_\perp + B_0 \frac{\partial \underset{\sim}{v}_\perp}{\partial z} + \eta \nabla_\perp^2 \underset{\sim}{B}_\perp \tag{6}$$

where $$\underset{\sim}{B}_\perp = (B_x, B_y, 0) = \nabla_\perp \times A(x,y,z,t)\,\hat{e}_z$$

$$\underset{\sim}{v}_\perp = (u, v, 0) = \nabla_\perp \times \psi(x, y, z, t)\, \hat{e}_z$$

and

$$j \hat{e}_z = -\nabla_\perp^2 A \hat{e}_z = \nabla_\perp \times \underset{\sim}{B}_\perp$$

$$\omega \hat{e}_z = -\nabla_\perp^2 \psi \hat{e}_z = \nabla_\perp \times \underset{\sim}{v}_\perp$$

These equations are quite similar to the equations of two-dimensional MHD. The only z-derivatives that appear in the system are those which are multiplied by the large toroidal field $B_0 \hat{e}_z$. All other derivatives are taken with respect to x or y.

It is a consequence of this ordering that the velocity and magnetic fields in the z-direction are passive scalars at this order.

$$\left(\frac{\partial}{\partial t} + \underset{\sim}{v}_\perp \cdot \nabla_\perp\right) v_z = \underset{\sim}{B}_\perp \cdot \nabla_\perp v_z + B_0 \frac{\partial}{\partial z} B_z + \nu \nabla_\perp^2 v_z \qquad (7)$$

$$\left(\frac{\partial}{\partial t} + \underset{\sim}{v}_\perp \cdot \nabla_\perp\right) B_z = \underset{\sim}{B}_\perp \cdot \nabla_\perp B_z + B_0 \frac{\partial}{\partial z} v_z + \eta \nabla_\perp^2 B_z \qquad (8)$$

If they are initially zero, they will remain so. They are initialized to zero in the simulations described in this work.

Thus, we are left with a system of four equations to solve, rather than six. This system may be reduced further, by taking the curl of the momentum equation, and removing the curl from the magnetic field equation, to obtain

$$\frac{\partial \omega}{\partial t} = \nabla_\perp \cdot (\underline{v}_\perp \omega + \underline{B}_\perp j) + B_0 \frac{\partial j}{\partial z} + \nu \nabla_\perp^2 \omega \qquad (9)$$

$$\frac{\partial A}{\partial t} = \hat{e}_z \cdot (\underline{v}_\perp \times \underline{B}_\perp) + B_0 \frac{\partial \psi}{\partial z} + \eta \nabla_\perp^2 A + E_0 \qquad (10)$$

This is a system of two equations to time-advance, one for the vorticity, $\omega(x,y,z,t)$, and another for the vector potential, $A(x,y,z,t)$. The additional term which appears in (10), E_0, may at most be the gradient of a scalar.

The quadratic constants of the motion for the Strauss equations are the same as those for the full three-dimensional set: the total energy, $E = \frac{1}{2V_{vol}} \int d^3x (v^2 + B^2)$; the cross helicity $H_C = \frac{1}{2V_{vol}} \int \underline{v} \cdot \underline{B}\, d^3x$; and, formally, the magnetic helicity, $H_M = \frac{1}{2V_{vol}} B_0 \int A\, d^3x$. As will be seen later, efficient pseudospectral simulation of these equations is possible when conservation of energy is pseudospectrally enforced.

II. Boundary Conditions.

The boundary conditions imposed on the system are those appropriate to a periodic cylinder with rigid, free-slip, perfectly conducting side walls. For infinitely conducting walls, the normal component of the magnetic field must go to zero at the wall. This will result if the vector potential is constant, at the wall at any instant of time; this constant is here set to zero. In this current version of the Strauss code, the boundary condition imposed on the velocity field at the wall is that only the normal component of the velocity field go to zero at the wall, or $\underline{v} \cdot \hat{n} = 0$, where $\hat{n}$ is a unit vector normal to the wall. In analogy with the magnetic quantities, this condition is met if

the velocity stream function is a constant at the wall, a constant which may be set to zero. Finite conductivity within the fluid gives the condition that the tangential component of the current must go to zero at the wall.

$$\underset{\sim}{j} = \sigma(\underset{\sim}{E} + \underset{\sim}{v} \times \underset{\sim}{B}) \quad \text{, from Ohm's law}$$

$$j|_{tan} = \sigma E|_{tan} + \sigma(uB_y - vB_x)|_{tan}$$

becomes $j|_{wall} = 0$, since the tangential component of the electric field is continuous, and must be zero inside a perfect conductor.

If the stream function and the vector potential are expanded in half-range Fourier sine series in x and y, and full complex Fourier series in z, all these conditions are automatically met. Hence, this is the choice of expansion functions made for our simulation code (hereafter, the "sine-Strauss code).

III. CYLINDRICAL MODELLING

A difficulty arises when attempting analytical arguments in a geometry with two non-ignorable coordinates. In order to gain some comprehension of the situation later treated numerically, polar coordinates are here employed to summarize some existing approaches which are beginnings to satisfactory analytical treatments of the problem.

A. The Internal m = 1 Mode, in a Circular Cylinder.

Following Manheimer *et al* (1984), instabilities are sought in the linearized Strauss equations in polar coordinates. If (x,y) -> (r,θ), only z-independent equilibria without flow are allowed, and perturbations of the form f(r) * exp(imθ - ikz) are assumed, equation (9) becomes

$$\frac{\partial \omega^{(1)}}{\partial t} = \underline{B}_\perp^{(1)} \cdot \nabla_\perp j^{(0)} + \underline{B}_\perp^{(0)} \cdot \nabla_\perp j^{(1)} + B_0 \frac{\partial j^{(1)}}{\partial z}$$

$$= B_r^{(1)} \frac{\partial}{\partial r} j^{(0)} + B_\theta^{(0)} \frac{im}{r} j^{(1)} - B_0 (ik j^{(1)})$$

$$= i \left[B_\theta^{(0)} \frac{m}{r} - k B_0 \right] j^{(1)} + B_r \frac{\partial}{\partial r} j^{(0)}$$

where $F = m B_\theta^{(0)} / r - k B_0$, and perturbations are assumed to vary as $\exp(\gamma t)$, the following may be obtained

$$\gamma \omega^{(1)} = i F j^{(1)} + B_r^{(1)} \frac{\partial}{\partial r} j^{(0)} \qquad (11)$$

From $$\nabla \times \underset{\sim}{B})_z = \frac{1}{r}\frac{\partial}{\partial r}(r B_\theta) - \frac{1}{r}\frac{\partial}{\partial \theta} B_r$$

$$j^{(1)} = \frac{1}{r}\frac{\partial}{\partial r}(r B_\theta^{(1)}) - \frac{im}{r} B_r^{(1)}$$

with $$j^{(0)} = \frac{1}{r}\frac{\partial}{\partial r}(r B_\theta^{(0)})$$

$$= \frac{1}{r m}\frac{\partial}{\partial r}(r^2 F),$$

and (11) may be written

$$\gamma \omega^{(1)} = iF\left\{\frac{1}{r}\frac{\partial}{\partial r}(r B_\theta^{(1)}) - \frac{im}{r} B_r^{(1)}\right\} + \frac{B_r^{(1)}}{m}\left[3\frac{\partial F}{\partial r} + r\frac{\partial^2 F}{\partial r^2}\right] \qquad (12)$$

Since $\nabla \cdot \underset{\sim}{v} = 0$, and $\nabla \cdot \underset{\sim}{B} = 0$,

$$v_\theta^{(1)} = \frac{i}{m}\frac{\partial}{\partial r} r v_r^{(1)}$$

and $$B_\theta^{(1)} = \frac{i}{m}\frac{\partial}{\partial r} r B_r^{(1)}$$

Also, $$\omega^{(1)} = \nabla \times \underset{\sim}{v})_z = \frac{1}{r}\frac{\partial}{\partial r} r v_\theta^{(1)} - \frac{im}{r} v_r^{(1)}$$

These equalities allow the re-expression of (12), where the superscript (1) is dropped.

$$\gamma\left[\frac{1}{r}\frac{\partial}{\partial r}\left(r\frac{i}{m}\frac{\partial}{\partial r}(r v_r)\right) - \frac{im}{r} v_r\right] = iF\left[\frac{1}{r}\frac{\partial}{\partial r}\left(\frac{ir}{m}\frac{\partial}{\partial r}(r B_r)\right) - \frac{im}{r} B_r\right] + \frac{B_r}{m}\left[3\frac{\partial F}{\partial r} + r\frac{\partial^2 F}{\partial r^2}\right] \qquad (13)$$

At this point, a way to express B_r in terms of v_r is needed, if possible. Turning to equation (6), and employing the same perturbations as were used for (9), (6) yields:

$$\gamma \underset{\sim}{B})_r = \nabla \times (\underset{\sim}{v} \times \underset{\sim}{B}))_r - \eta \nabla \times (\nabla \times \underset{\sim}{B}))_r$$

$$= -\underset{\sim}{v}_\perp \cdot \nabla_\perp \underset{\sim}{B}^{(0)} + \underset{\sim}{B}_\perp^{(0)} \cdot \nabla_\perp \underset{\sim}{v}_\perp + B_0 \frac{\partial v_r}{\partial z} + \eta \nabla_\perp^2 \underset{\sim}{B})_r$$

If η is small enough to be neglected,

$$\gamma B_r = -\left[-\frac{v_\theta}{r} B_\theta^{(0)}\right] + \left[\frac{B_\theta^{(0)}}{r} \frac{\partial v_r}{\partial \theta} - \frac{v_\theta B_\theta^{(0)}}{r}\right] - B_0 i k v_r$$

$$= (-ik B_0 + \frac{im}{r} B_\theta^{(0)}) v_r$$

$$B_r = -\frac{iF v_r}{\gamma} \tag{14}$$

Inserting (14) into (13) yields

$$\gamma^2 \left\{ \frac{\partial}{\partial r} \left(r \frac{\partial}{\partial r} (r v_r) \right) - m^2 v_r \right\}$$

$$= F \left[-\frac{\partial}{\partial r} \left[r \left\{ \frac{\partial}{\partial r} (r F v_r) \right\} \right] + m^2 v_r F \right]$$

$$+ m r v_r F \left[\frac{1}{m} \left(3 \frac{\partial F}{\partial r} + r \frac{\partial^2 F}{\partial r^2} \right) \right]$$

$$= F^2 \left[-v_r - 3r \frac{\partial v_r}{\partial r} - r^2 \frac{\partial^2 v_r}{\partial r^2} + m^2 v_r \right]$$

$$- 2F r^2 \frac{\partial v_r}{\partial r} \frac{\partial F}{\partial r}$$

And since $\quad \frac{1}{r} \frac{\partial}{\partial r} \left(r^3 \frac{\partial}{\partial r} v_r \right) = \frac{1}{r} \left(3r^2 \frac{\partial}{\partial r} v_r + r^3 \frac{\partial^2}{\partial r^2} v_r \right),$

$$(\gamma^2 + F^2)\left[\frac{1}{r}\frac{\partial}{\partial r} r^3 \frac{\partial}{\partial r} V_r\right] = (m^2-1) V_r (\gamma^2+F^2) - 2F r^2 \frac{\partial V_r}{\partial r} \frac{\partial F}{\partial r} \quad (15)$$

or

$$\frac{1}{r}\frac{\partial}{\partial r}\left[r^3(F^2+\gamma^2)\right]\frac{\partial}{\partial r} V_r = (m^2-1)(\gamma^2+F^2) V_r \quad (16)$$

White (1983) remarks of (16) that when $r^3\gamma^2$ is neglected with respect to $r^3 F^2$, the equation may be observed to exhibit a singular nature in the neighborhood of $F = 0$. Since $F = B_\theta^{(r)} m / r - k B_z = \frac{B_\theta^{(r)}}{r}[m - r n B_z / (B_\theta R)]$, $F = 0$ when $q = m / n$, i.e. when $r = m B_\theta^{(r)} / (k B_z)$. This radius is defined to be the singular radius, r_s.

Manheimer examines the behavior of (16) in the neighborhood of $r = 0$. From (15), when $r \sim 0$, $2F r^3 \frac{\partial V_r}{\partial r} \frac{\partial F}{\partial r} \to 0$. That leaves

$$\frac{\partial}{\partial r} r^3 \frac{\partial}{\partial r} V_r = -r(1-m^2) V_r \quad (17)$$

Solutions to (17) are of the form $v_r = \beta r^n$, or $v_{r_a} = \beta r^{m-1}$, $v_{r_b} = \beta r^{-1-m}$. v_{r_b} must be discarded because it is not well-behaved in the neighborhood of the origin, and $v_r = \beta r^{m-1}$ remains.

This solution yields the information that for $m > 1$, $v_r(r \sim 0) = 0$, or the plasma center does not move. If $m = 1$, however, $v_r = \beta$. Hence, near the origin, (Manheimer[1,4](1983)),

$$v_r \; \mathrm{Re}\left[\beta(\cos\theta + i\sin\theta)(\cos kz - i\sin kz)\right]$$

$$= \beta\left[\cos\theta\cos kz + \sin\theta\sin kz\right]$$

At $z = 0$,

$$v_r = \beta \cos\theta$$
$$= \underset{\sim}{v} \cdot \hat{e}_r$$
$$= \underset{\sim}{v} \cdot [\hat{e}_x \cos\theta + \hat{e}_y \sin\theta]$$
$$\Rightarrow \quad \underset{\sim}{v} = \beta \hat{e}_x$$

At $z = \frac{\pi}{2k}$, $\quad \underset{\sim}{v} = \beta \hat{e}_y$

Similarly, $\quad B_r = \alpha [-\sin\theta \cos kz + \cos\theta \sin kz]$

$$= -\alpha \hat{e}_y, \quad \text{at} \quad z = 0.$$
$$= \alpha \hat{e}_x, \quad \text{at} \quad z = \frac{\pi}{2k}.$$

That is, the solution is seen to be one in which the velocity field locally points towards increasing vector potential, A.

A helical perturbation is observed in both fields. It is apparent, then, that the m = 1 linear instability may be of use in modelling internal disruptive activity. It is the only m considered in the remainder of this chapter.

Since the solution found is constant near r = 0, and $\underset{\sim}{v} \cdot \hat{n})_{wall} = 0$, only $v_r = 0$ could satisfy the boundary condition. For interesting behavior to be found in a cylinder with circular cross section, other terms in the equations must be allowed, e.g. a nonzero value of the resistivity. Note that this situation does not hold necessarily for cylinders with non-circular cross-section. In 1976, Edery, Laval, Pellat and Soule showed that the stability of the m = 1

ideal mode, the internal kink mode, is very sensitive to small distortions of a circular cylindrical equilibrium.

Even though it is found to be necessary at this order, resistivity may not be important everywhere in the plasma. Manheimer et al (1984) argues that if the time for a mode to grow is much greater than the time it would take for Alfven waves to establish a pressure balance, away from the singular region, then pressure balance can be maintained almost everywhere. Outside a narrow layer, it is conceivable that constant solutions can exist.

Inside the layer, near $r = 0$, (14) is no longer the appropriate governing equation. Resistivity cannot be neglected, or

$$B_r = \left(\frac{F v_r}{\gamma} + \frac{\eta}{\gamma} \nabla^2 \underline{B} \right)_r \qquad (18)$$

In this case, (15) cannot be obtained from (13), but possible growth rates must be calculated from the coupled (13) and (18). Coppi, Pellat, Rosenbluth and Rutherford (1977) have calculated such rates for the general case, where B_z may also be a function of radius.

B. Kadomtsev's Scenario for an Internal Disruption.

This complicated route is not necessary in order to understand a process that may explain an internal disruption. The process whereby the plasma may first develop an internal helical perturbation, then flatten, was described in a single helicity framework by Kadomtsev in 1975.

1. Single Helicity.

Strauss (1976) showed that for a perturbation of the form $\exp[\, i(m\theta + kz)\,]$, $\frac{\partial}{\partial z} = \frac{k}{m} \frac{\partial}{\partial \theta}$, and for $\eta = B_0 = 0$, equation (10) may be rewritten:

$$\frac{\partial A}{\partial t} + \underline{v}_\perp \cdot \nabla_\perp A = B_0 \frac{k}{m} \frac{\partial \psi}{\partial \theta}$$

$$= B_0 \frac{k}{m} \left[\frac{1}{2r} \frac{\partial \psi}{\partial \theta} \hat{r} \cdot \nabla r^2 \right]$$

$$= B_0 \frac{k}{2m} \underline{v} \cdot \nabla r^2$$

or $$\frac{\partial A}{\partial t} + \underline{v}_\perp \cdot \nabla_\perp \varphi = 0$$

where $\varphi = A_z - \frac{B_0 k r^2}{2m} = A_z - \frac{kr}{m} A_\theta$, for $A_\theta = \frac{rB_z}{2}$. Since $\frac{kr}{m} A$ is time-independent,

$$\frac{\partial \varphi}{\partial t} + \underline{v}_\perp \cdot \nabla_\perp \varphi = 0 \qquad (19)$$

It may be shown that φ is flux through a helical ribbon at radius r and pitch defined by $\tau = kz + m\theta$, by integrating A along a path tangent to $\hat{e}_z - \frac{kr}{m} \hat{e}_\theta$ (White (1963)). That is, $\int \underline{B} \cdot d\underline{S} = \int \nabla \times \underline{A} \cdot d\underline{S} = \int \underline{A} \cdot d\underline{\ell}$; the helical flux, φ, is flux through a helical ribbon, or the line integral of $\underline{A}$ around that ribbon.

Similarly, if a perturbation of exp(i(mθ - kz)) is employed, a helical flux function $\varphi = A_z + \frac{kr}{m} A_\theta$ is obtained. In this case, $\nabla \times \varphi \hat{e}_z = \underline{B}_\perp - \frac{k}{m} r B_0 \hat{e}_\theta$, i.e. Kadomtsev's field, $\underline{B}_* = \underline{B}_\perp - \frac{r}{m} \frac{r}{R} B_0 \hat{e}_\theta$, for $k = n / R$; recall that B_0 is the externally imposed B_z.

2. The Description.

From the observations of an internal disruption in von Goeler, et al (1974), Kadomtsev (1975) conjectured that since the q = 1 surface was reported to lie in the plasma, the unstable mode was of a form m = 1. He thus specified his choice of helicity to m / n = 1, or $\underline{B}_* = \underline{B}_\perp - \frac{r}{R} B_0 \hat{e}_\theta$.

Note that $\underset{\sim}{B}_{*} = 0$ when $\underset{\sim}{B}_{\perp} = \frac{r}{R} B_{\phi}\hat{e}_{\theta}$, or equivalently when $q = 1$. $\underset{\sim}{B}_{*}$ is greater than zero, or has counterclockwise orientation, for $q < 1$. Also, it is less than zero, with clockwise orientation, for $B_{\theta} < \frac{r}{R} B_{\phi}$ or for $q > 1$. A potentially dynamic configuration thus exists, one highly analogous to the familiar sheet pinch geometry (Dahlburg, Montgomery, Zang and Hussaini (1983)). Small amounts of resistivity added to the MHD description will serve to make reconnection of the magnetic field lines possible. Random nonuniformities then may trigger the instability in the region of a nascent x-point. Reconnection will begin to take place. Kadomtsev suggested that the reclosing of the field with itself will intensify the field in a region opposite to the reclosing region, generating a force that will squeeze the internal column toward the opposing field. The process will become thus progressively more rapid, and not be able to stop until the field $\underset{\sim}{B}_{*}$ acquires the same sign throughout the column ($q > 1$), and the current has become redistributed.

Incompressibility of the fluid, solenoidality of the magnetic field, and negligible resistivity in regions away from the singular surface lead to the idea that flux is distributed to a definite radius r_{δ} beyond the radius r_{s} of the $q = 1$ singular surface. The disturbance starts in the neighborhood of r_{δ}, and works its way out from r_{δ}, and toward the origin. By the completion of the reconnection process, the inner flux has reclosed with an equal amount of outer flux of opposite sign. Beyond r_{0}, the helical flux function remains unperturbed. It is generally possible, then, for a discontinuity to arise in the first derivative of the helical flux function with respect to radius; that is, a sheet current may be observed at $r = r_{0}$, with sign opposite to that of the inner current column.

Kadomtsev (1975) gives a simple example, to demonstrate these features, in which $\psi(t = 0) = \propto \frac{r^2}{2}(r_{s}^{2} - r^{2}/2)$. He finds that the energy in $\underset{\sim}{B}_{*}$ after reclosing would be about 93% less than it was at $t = 0$.

This energetically favorable mechanism is one which plausably explains a single sawtooth. If the flux function returns to a helically unperturbed state at the end of the reclosing, as he conjectures, and the velocity field goes away, external heating can once again drive the current to a smoothly steepened profile, with a $q = 1$ surface again in the plasma. The single helicity disruption can then repeat.

Although this reasonable single helicity scenario cannot be expected to hold exactly in a three-dimensional plasma with a cross-section that is other than circular, it may provide an approximate description of the events which take place in a quiescent plasma which has a $q = 1$ singular surface embedded in the large-scale vector potential. We proceed, now, to a nonlinear, multiple helicity calculation of these conditions, a numerical simulation of the Strauss equations in rectangular geometry.

IV. THE SIMULATION CODE

We turn to a discussion of the method we use to gain information from the Strauss equations.

A. Algorithm for the Sine-Strauss Code.

1. Focus on the Two-Dimensional Square.

It is easier to first consider the two-dimensional, bounded poloidal cross-section of our calculation. Let the stream function and the vector potential be expanded in the sine series in x and y. We now have two spaces we can think about, a physical (x, y) space, and a wavenumber (k_x, k_y) space. The sine series are global and orthogonal,

$$\sum_{n=1}^{N-1} \sin\left(\frac{\pi j n}{N}\right) \sin\left(\frac{\pi k n}{N}\right) = \frac{N}{2}\,\delta_{jk}$$

Hence, if we are given values of the velocity stream function and the magnetic vector potential everywhere on the bounded x,y grid, their real Fourier coefficients, their counterparts on the bounded wavenumber k_x,k_y grid, may be obtained. For instance, if we assign values to the stream function which correspond to sin(x)*sin(y) at all grid points x_j and y_k , the Fourier space would have one non-zero point, $k_x = 1$, $k_y = 1$. We would efficiently (Gottlieb & Orszag, 1977) obtain this information, numerically, by using some version of Cooley and Tukey's (1965) fast Fourier transforms (FFTs). Here we use Temperton's FFTs (1981), a vectorized version of earlier scalar FFTs.

2. The Full Expansions.

It is natural to expand the variables in full, complex Fourier series in the periodic "toroidal" direction. The full, three-dimensional expansions, then,

are sine series in x, sine series in y, and complex exponentials in z. Since the equations are nonlinear, care must be taken to normalize the sums "on the way to Fourier space", to avoid inserting unconsidered factors of N in the time step size.

For example, the vector potential is expanded

$$A(x_j, y_k, z_\ell) = \sum_{m,n=1}^{N-1} \sum_{p=-M/2}^{M/2-1} \tilde{A}_{mnp} \sin(mx_j) * \sin(ny_k) \exp[ipz_\ell]$$

$$x_j = \pi j/N, \quad y_k = \pi k/N, \quad z_\ell = 2\pi \ell/M$$

$$j,k = 1, \ldots, N-1, \quad \ell = 0, \ldots, M-1$$

with transformation

$$\tilde{A}_{mnp} = \left(\frac{2}{N}\right)^2 \frac{1}{M} \sum_{j,k=1}^{N-1} \sum_{\ell=0}^{M-1} A_{jk\ell} \sin(mx_j) * \sin(ny_k) \exp[-ipz_\ell]$$

$$m,n = 1, \ldots, N-1, \quad p = -\frac{M}{2}, \ldots \frac{M}{2}-1$$

Values of the stream function and the vector potential at every grid point, then, are all that is needed to generate any of the other MHD variables required, at a given time.

3. Time Advancement.

We are not considering static solutions, however. The equations have partial derivatives with respect to time, which also must be treated. For convenience, an explicit, weakly unstable method, the second order Runge-Kutta scheme, is chosen. For $u = \omega$ or A, and f = the right hand side of equa-

tion (9) or (10), $\frac{\partial u}{\partial t} = f$ is discretized with second order Runge-Kutta:

$$u^{n+1/2} = u^n + \frac{\Delta t}{2} f^n$$

$$u^{n+1} = u^n + \Delta t f^{n+1/2}$$

where Δt is the timestep and n is the time index.

Our time step is small enough that accuracy is linearly assured for approximately nine hundred Alfvén transit times, (Dahlburg, et al (1985)) even without dissipation. It is possible to demonstrate that the method may be stablized, in a model linear problem, by a suitable choice of diffusivity. The convenience, then, is not outweighed by any errors generated by this method, and we find it to be a satisfactory one.

The nonlinear terms in the Strauss equations also present a source of potential numerical difficulties. A standard way to treat these terms is to remove all aliasing errors generated by them, at each time step (Orszag (1971)). This dealiasing process can at worst slow a code down by about a factor of two for each dimension. We would consequently prefer to solve the equations in a much more efficient form than the dealiased Galerkin form.

A good candidate for an efficient form is that of collocation, where by collocation is meant that the equations themselves are enforced at each grid point. The nonlinear terms would then be evaluated in the actual physical space of the problem, at each grid point, and no further manipulation would be performed on them.

Collocation, combined with a spectral evaluation of the derivatives, was termed "pseudospectral" by Orszag (1971). In two papers, (Orszag (1972); Fox

and Orszag (1973)), he reported that the pseudospectral method generates solutions which are nearly identical to the more careful spectral, or dealiased, method, when an amount of viscosity sufficient to remove unresolvable small spatial structure is introduced. These results were obtained for the two-dimensional Navier-Stokes equation, in its vorticity formulation. They further reported that more accurate solutions were generated by the code when the equations were written in a form which pseudospectrally conserved kinetic energy.

We performed a series of numerical experiments on the two-dimensional MHD equations. Our results were in basic agreement with the findings from the Navier-Stokes equation, with a single exception. We observed intense numerical instability, unless the equations were written in a form which pseudospectrally conserves total energy. So, we choose to time advance the equations in a form which would semi-conserve total energy in the absence of any dissipation. By running a two-dimensional version of the code, we find that indeed the energy is conserved to within a few percent, for many Alfvén transit times. Including dissipation in the problem yields the necessary result that spectral and pseudospectral results agree remarkably well for long times. These findings are discussed at greater length in Appendix A of this thesis.

4. Algorithm.

Given vorticity, $\omega(k_x,k_y,z)$, and vector potential, $A(k_x,k_y,z)$, everywhere on the (k_x,k_y,z) grid at the n-th time step, we solve for the vorticity and vector potential at the (n + first) step, and so on. Because the code is pseudospectral, time advancement can be performed in the most convenient space.

We wish to run this code on a vector computer, a CRAY-1, and consequently we must consider its small core memory. If we wanted to write the code with a completely straightforward algorithm, about fourteen three dimensional arrays would

be needed; arrays like "U" and "BX", and so forth, could then be used, where the array name would directly correspond with the information the array contained. This algorithm would have the disadvantage of not fitting in the machine for any realistic grid size. Hence, we perform the entire calculation in just six arrays, a constraint which makes an intricate algorithm necessary.

The key features of the algorithm are the following. All nonlinear product terms are formed in the actual physical space of the system. Derivatives are taken in the suitable Fourier space. The Strauss approximation is such that the only z-derivatives ever needed are on the stream function, and the current. Only these two arrays, then, are ever transformed to the full, complex Fourier space in z. This efficient feature of the code comes about because we are using a pseudospectral scheme, rather than a spectral one. In other words, the pseudospectral code is even more efficient than the earlier estimate given would indicate. Again, for convenience, the actual time-advancement is performed in a hybrid (k_x,k_y, z) space. With this fully-vectorized algorithm, we find that the 32 * 32 * 16 grid code takes about 0.7 sec/timestep on a CRAY-1 supercomputer.

8. Choices of the small parameter, η.

Before we actually begin reporting physical computations, one more question must be resolved: how much dissipation is necessary to keep all nonlinearly generated spatial scales within the available computational limits? The answer to this can only be estimated, a priori. A rule of thumb for finite difference codes is that there is about a one to one correspondence between number of grid points in any one dimension, and the value of the Reynolds number. This would mean, for example, that a grid of 1000 * 1000 * 1000 points would be necessary to properly resolve a simulation with a Reynold's number of 1000.

Additional factors of four, or so, may alter the estimate by suggesting that in general a spectral code needs about one fourth the resolution a comparable finite difference code would require, for the same degree of accuracy. This leaves us with only crude estimates; we must turn to empirical tests.

We find that much small scale spatial structure is generated in the simulation near the time of a kinetic energy peak. By examining plots of our total spectral energies at these times, we may determine whether or not the simulation was a numerical success. We find that on a 32 * 32 * 16 grid, with a Lundquist number, $1/\eta$, of 100, we indeed have enough resolution to believe the results. This may be easily read off a contour plot of modal energy. The axis is K-perp = sqrt(k_x*k_x + k_y*k_y), while the ordinate is K-par = k_z. This contour plot, then, gives a good idea of what is happening to the total modal energy in the full Fourier space available to the calculation. The lowest value of modal energy plotted is $1 * 10^{-7}$. It is evident that this simulation evolved with a sufficient amount of resolution; see Fig. 3a.

If the Lundquist number is raised by only a factor of five, while leaving the grid size unchanged, the simulation is not so successful. A plot of total modal spectral energy, scaled identically to the one above it, shows that the resolution has been severely exceeded, as displayed in Fig. 3b. In this case, the numerical results are deemed untrustworthy.

We are able to run at Lundquist numbers > 100, however. We find that it is necessary to increase the grid size, in order to do so. The last plot of spectral energy, again scaled as above, shows the total modal spectral energy for our most ambitious run, one with $k_{x\ max}$ = 64, $k_{y\ max}$ = 64, and $k_{z\ max}$ = 16, and a Lundquist number of 400. Again we observe basically sufficient resolution to generally accept our simulation's results, as shown in Fig. 3c.

Because the boundary conditions imposed on the velocity field are the free-

slip conditions, the majority of zine-Strauss simulations are run with no viscosity whatever. A consequence of the Alfvén effect is that at high wavenumbers, kinetic and magnetic energies approach equipartition. By virtue of this, if one field's Fourier coefficients are being dissipated in the high wavenumber portion of phase space, so also will the other field's Fourier coefficients be diminished. Therefore, only one diffusivity, here the inverse Lundquist number, is necessary to drain off small scale structure in both fields (cf Kraichnan (1965); Pyfe, Montgomery and Joyce (1977)).

V. SIMULATION RESULTS, DECAY.

We now embark on a discussion of the numerical simulation results generated by the Sine-Strauss code.

A. Choices of the large parameter, B_0.

A crucial large parameter must be set in the calculations. This parameter is the field strength of the externally imposed magnetic field, B_0. For $B_0 \gg 1$, we expect, from the work of Shabalin, et al (1983), that the spectral transfer would be reduced to near two-dimensionality. For B_0 too small, the Strauss approximation would break down. We find that for a middle range of values of B_0, we are able to induce current disruptions, processes which thrive on spectral transfer in all three Fourier dimensions. Recall from the derivation of the Strauss equations in the second chapter that the small formal expansion parameter (interpretable as the ratio of minor radius to major radius) multiplies both B_0 and z everywhere; that is, $\epsilon B_0 \frac{\partial}{\partial(\epsilon z)} = B_0 \frac{\partial}{\partial z}$.

We will now exhibit results from a trio of simulations. All three are initial value problems, with the same initial current profile:

$$j(x,y,z) = 30 \sin x \sin y \exp\left[-5(x-\pi/2)^2 - 5(y-\pi/2)^2\right]$$

For each of the three runs, the velocity field is initialized with broad-band, low order random noise:

$$\tilde{\omega}_{\underline{k}} \sim G(in^{-2}) \quad \text{for} \quad k_x, k_y \in [4,8], \; k_z \in [1,4]$$

The difference between the first and the second simulation is that we choose

$B_0 = 8$ for CASE 1, and $B_0 = 4.3$ for CASE 2. Both of these runs were performed on grids with $k_{x\,max} = k_{y\,max} = 32$, and $k_{z\,max} = 8$, with Lundquist number = 100. It is in values of Lundquist number, the grid size, and particular values of $\tilde{v}_x(t = 0)$ that the second and the third runs differ. CASE 3 was run on a doubled, 64 * 64 * 32 grid, with a Lundquist number of 400.

B. $B_0 = 8$, $\eta = 0.01$.

CASE 1, the run with the large value of B_0, is an inhibited simulation. After a brief burst of activity, we find that the modal transfer quickly becomes almost exclusively two-dimensional.

1. Geometry.

The simulations themselves are performed in a three-dimensional box in physical space, with a box of identical magnitude in Fourier space. We find it most useful to focus on a few slices in the cylinder, when displaying our solutions. In particular, the ones shown here will be the $(x,y,z=\pi)$ slice, a "poloidal cut", and the $(x,z,y=\pi/2)$ slice, a "toroidal cut"; see Fig. 4. It is convenient to remember that the initial magnetic axis is a dot in the middle of the poloidal cut, at $(x = \frac{\pi}{2}, y = \frac{\pi}{2})$, and is a line up the center of the toroidal cut, at $(x = \pi/2)$.

2. Initial Conditions.

We use these slices to display contours of the initial conditions, in Fig. 5. The cross-sections are the poloidal $(x,y,z=\pi)$ slices, while the series of parallel lines are the $(x,z,y=\pi/2)$ slices. The externally imposed magnetic field points along these contours. Note that the contours of initial vector potential, and of current, are very smooth and unperturbed. A poloidal cut of the stream function suggests a velocity field which is random, and of not much

strength.

The initial omnidirectional energy spectra are displayed in two ways, in Fig. 6. To the left are "mountaintop plots", where the contour values are chosen at equally spaced intervals. To the right are "powers of 2" plots: contour values chosen here are separated by powers of two. Also, this column of plots are all contoured with the same values, a feature which enables us to see equal levels of small scale spatial structure in the kinetic energy, the magnetic energy, and in the combined, total energy.

This type of diagnostic is useful for two reasons. One is that by examining the spectral plots we can immediately detect where most of the magnetofluid energy is centered in the computation's Fourier space. The other, less physical reason, is that by frequently observing these plots, we are able to see the magnitude of small scale spatial structure generated in the simulation, and consequently determine if numerical resolution is grossly exceeded.

3. Global diagnostics.

We also find it useful to consider the global quantities, as a function of time. For instance, we find the kinetic energy to be the most valuable herald of interesting activity; see Fig. 7a. Magnetic energy is less sensitive; the overall decay of the mean current is the dominant feature of this quantity, as may be observed in Fig. 7b. A ratio of kinetic to magnetic energy will often highlight the relative amounts of activity in the two fields, plotted in Fig. 7c. By monitoring the net, volume averaged current, Fig. 7d, we can see that the integrated current in the cylinder does not decay much at all during this simulation. The change of magnetic energy with respect to time varies as the square of the current; this quantity shows us, in Fig. 7e, that magnetic energy wears away smoothly, and without any periods of enhanced dissipation.

We consider this run to be a non-disruptive one, since no disturbance is able to rise up out of the initial, very low-level noise in the velocity field, and grow to dominate. The current column kinks a small amount, but only that. The major activity in the simulation, long before we terminated it, was the unrelieved Ohmic decay of the magnetic field.

4. Calculating Q.

Another diagnostic, one which might possibly explain why this run is so uneventful, is the safety factor "Q". Q has a formula in a right circular cylinder. In a cylinder of square cross section, however, it must be obtained numerically.

The standard definition for the safety factor, Q, in a fusion device is the number of times a magnetic field line winds toroidally divided by the number of times the field line winds poloidally, in the limit of an infinite number of windings (cf Bateman 1978). We apply that definition here to a cross-section in which neither of the coordinates (x,y) is ignorable. The key feature of our algorithm is that we use the equation for a magnetic field line to obtain the ratio of toroidal (z) distance traversed to a single transit poloidally.

At any instant t, the sine-Strauss code produces a vector potential $A(k_x,k_y,z,t)$ for all Fourier coefficients k_x, $k_y = 0, \ldots, N$; $z = 0, \ldots, 2\pi(N-1)/N$. We transform this array to the full, complex Fourier space in k_x, k_y and k_z, and read off the real two-dimensional array $A(k_x,k_y,k_z=0,t)$, to obtain a vector potential which has been toroidally averaged. We use this array to form z-averaged values for $B_x(k_x,k_y)$ and $B_y(k_x,k_y)$. Interpolated values for $B_x(x,y)$ and $B_y(x,y)$ may be obtained from these Fourier coefficients. For instance:

$$B_x(x,y) = \sum_{m,n=1}^{N-1} \tilde{B}_{x\,m,n} \sin(mx) \cos(ny)$$

where x and y are not necessarily the grid points.

Adding a constant small increment dz to z, and generally starting at a grid point ($x_j = \pi j/N$, $y = 16\pi/32$, $z = 0$), $j \in (N/2, N-1)$, we step along a magnetic field line by means of the equation

$$\frac{dx}{B_x} = \frac{dy}{B_y} = \frac{dz}{B_z} \qquad (20)$$

After one loop poloidally, we find ourselves back within the computational (x,y) elemental grid square from which we began the circuit. We then calculate, for one trip around the center of the square,

$$Q = \text{(z distance stepped)/(length of the square cylinder)}.$$

For moderate distances off the center of the square at $(\pi/2, \pi/2)$, this Q-value is nearly equal to that given by the formula for the q-value over a length L of of a straight circular cylinder,

$$q = \frac{2\pi r}{L}\frac{B_z(r)}{B_\theta(r)}$$

where $B_z = B_0$, $r = (\pi/2 - x)$ and $B_\theta = B_y(x, y = \pi/2)$. Typically, we plot Q vs. x for the region of interest.

Upon calculating "Q" profiles for this run, we find that they are smoothly increasing functions of distance from the magnetic axis. Initially, the "Q = 1" surface is within the plasma, in Fig. 8a, but by t = 8.82 the surface has left the plasma, never to return, as displayed in Fig. 8b.

5. Quiescent results; t = 8.82.

Contours, Fig. 9, at t = 8.82 show a largely unperturbed state.

Spectra at this time, Fig. 10, yield the information that most of the

energy is located in the $k_z = 0$ modes, the two-dimensional ones. This result substantiates the two-dimensional work of Shebalin, et al (1983), in this geometry.

C. $B_o = 4.3$, $\eta = 0.01$.

This simulation begins with all the same parameters and conditions as the one just presented, except that here $B_o = 4.3$, instead of 0.0. Here, after only a few Alfvén transit times, an unstable "m=1", "n=1" mode rises dramatically out of the noise, and comes to dominate the velocity field. Current filaments form, and helically wrap themselves around the magnetic axis. The filaments contract towards the outer rim of the disturbance.

Near the time of the first peak in kinetic energy, the current profile abruptly becomes flat, with much small scale spatial structure visible in the shell of the current column.

The kinetic energy decreases, then, and current filaments again form, to once more wrap themselves about the axis. The helical sense is still counterclockwise, the helicity of the initial unperturbed field. The dissipation has brought about a decrease in the amplitudes of higher order Fourier modes, however. This time, the run soon becomes quiescent, with the disruptive behavior a feature of the past.

1. Q-Profile at t = 0.

Again we compute an initial "Q" profile, to find that "Q" dips well below unity on axis. This is perhaps unrealistic for a tokamak. We feel that this choice is justified for two reasons. The first is that, since this is a freely decaying run, the initial current must be quite peaked for us to observe any disruptive behavior before Ohmic dissipation becomes overwhelming.

Next, note the value of "Q" near the wall of the cylinder, in Fig. 11. This value is not so unrealistic, nor unreported. We may allow, then, that this "Q"

profile exists within the realm of the possible, for a tokamak plasma.

2. Global Quantities.

The global quantities of this run suggest a much different history from the dynamics of the previous run. We observe dramatic growth in the kinetic energy, energy which rises orders of magnitude above its initial value, in Fig. 12a.

We find this quantity points to times of disruptive activity in the magnetofluid. In the following sections, we examine contours and spectra during the periods of enhanced motion, to explore this activity.

Again, we note that the integrated current, Fig. 12b, does not vary much through the run, although steady Ohmic decay of the mean profile is occuring, as may be seen in Fig. 12g.

3. A Time History of the Run.

t = 4.44.

We follow the development of this eruption. Contours at t = 4.44, Fig. 13, show that the current has begun to kink about the axis. Characteristic lobes of the "m=1", "n=1" pattern have grown out of the noise in the stream function, a poloidal cross section of which is shown. Note that the vector potential contours are hardly distorted from their initial state.

If we take a closer look at the poloidal cut of current density, by means of a three-dimensional perspective plot, Fig. 14a, we find that the current profile has developed a flatter region, in the side opposite to the current maximum.

We are also able to examine the behavior of the three-dimensional magnetic field lines, by means of a field line tracing code. The code, written for this problem, employs a third order Lagrange interpolating polynomial to obtain values of the magnetic field between computational grid points. We follow the

line by means of equation (28), storing x,y values each time the followed field line spirals through the $z = \pi$ plane. Results from this code are plotted in Fig. 14 b,c. In Fig. 14b we see a closed, crescent-shaped figure emerging, while Fig. 14c displays another shape, that of an oval, centered on a different x,y point. The crescent corresponds to the flattened region in the current perspective plot, and the oval surrounds the current maximum.

The "mountaintop plot" of the kinetic energy spectrum shows that the perturbation is predominantly in the $k_z = 1$ band of wavenumbers, and that a variety of perpendicular wavenumbers combine to form the "m=1" lobes.

t = 6.6.

At this later time, contours of constant current are seen to trace an even greater disturbance, as shown in Fig. 16. Again, the vector potential contours are only slightly rearranged. We observe that the stream function amplitude is increasing, consistent with the time history of the kinetic energy.

t = 7.8.

The stream function lobes have grown in amplitude, as may be observed in Fig. 17, as has the velocity field they imply. In the $(x,y,z=\pi)$ plane, this field points in the direction of the current maximum.

We see that the current filament has begun to tighten up, the helical filament pulling toward the periphery of the disturbance.

Again, the contours of constant vector potential are only slightly disturbed.

By spectral plots, Fig. 18, we see that the "m = 1, n = 1" mode is growing in strength, with more and more Fourier coefficients nonzero.

It is quite apparent that the vector potential is very unperturbed, when we look at the "blow-up" of the toroidal cross section, in Fig. 19a. At this same time, the current cross-section, plotted in Fig. 19b, is quite perturbed. The

current is the negative Laplacian of the vector potential, and as such, displays the activity of the smaller scales more clearly. We see here that there is much small scale spatial activity, particularly in the neighborhood of the current maximum.

Poloidal cuts augment the view cited above. Contours of constant vector potential, plotted in Fig. 20a, are very smooth and nearly unperturbed. No hint of a magnetic island can be found. As above, we see a distorted current, Fig. 20b, with the maximum drawing itself towards the outer edges of the perturbed region.

Poincare traces through the x, y, z $=\pi$ plane, at this time, display the information that lines of the magnetic field lie on surfaces much more closely paralleling surfaces of constant current than constant vector potential. Three separate traces are plotted in Fig. 21. Only the smallest, closed oval, forms in a clockwise sense, indicating a safety factor q $<$ 1 in that region.

t = 8.76.

At this time, a little after the kinetic energy peak, the current has become quite broad and widely flat, in Fig. 22. Only a vestige of the helix remains. This flattening of the current we find to be a nonlinear process, and one in which many Fourier coefficients participate. Even at this Lundquist number, of 100, we see (well-resolved) small scale turbulence, particularly in the neighborhood of the vestigal current maximum.

t = 8.82.

It is interesting to note that current density perspective plots, at t = 8.82, Fig. 23, depict flattened profiles, with only a small positive blip in the vicinity of where the current maximum had been. To the outside of this steepened current is a current "dip", a well-like region where the current nearly

jets negative.

t = 16.98.

We can see in Fig. 24 that the maximum velocity field is now pointing in a direction oppositely to the way it had pointed previously. The current filament, as well, is kinking up everywhere opposite to its previously perturbed state. Kadomtsev's (1975) conjecture of saturation followed by a long period of quiescence is apparently not borne out, in this geometry.

t = 17.52.

The stream function lobes now exhibit a shell-like pattern, in Fig. 25, with the newest "m = 1" pair at the center. Very little is happening in the current, and even less in the vector potential. The contour plot of the vector potential $(x,y,z=\pi)$ at t = 17.52 shows that the simulation is in a near equilibrium state. At this same time, the current $(x,y,z=\pi)$ depicts an only slightly perturbed current. This is the final solution of the run.

It is interesting to note that as the poloidal magnetic field strength decreases and the effective toroidal field strength increases, the small scale motion becomes more and more two-dimensional; see Fig. 26. Again, this is what we would expect from the work of Shebalin, et al (1983). These spectra may also be viewed as evidence that the Strauss approximation is valid, for the conditions.

4. Additional Diagnostics.

Something of the run's history can be seen in a time series of plots of "Q" versus radius, in Fig. 27. "Q" near the axis at $x = \pi/2$ increases until after

the first kinetic energy peak. At this time, the Q = 1 surface can no longer be found in the magnetofluid. Then, "Q" dips slightly, for a short time. After this, it resumes its resistive rise.

Another way to obtain a global view of the run is to consider the energies in various k_z's, in Fig. 28. Kinetic energy is plotted with a dashed line, while magnetic energy is plotted with the solid line. The "m=1", "n=1" mode grows up in $k_z = 1$, as all the spectral plots have suggested. That most of the kinetic energy is located in this wavenumber may also be seen in Fig. 28a. The magnetic energy of $k_z = 1$ and the kinetic energy of $k_z = 1$ are just about exactly out of phase with one another.

Enhanced excitation near the time of the disruption may also be found in the energies with $k_z = 2$ and $k_z = 3$. While the $k_z = 2$ energies peak at slightly different times, the modes in the $k_z = 3$ band are excited simultaneously, as may be seen in Figs. 28 b,c.

Although the energy scales down by a factor of ten in each plot, it is clear that this phenomenom is a nonlinear one, in which many modes participate. In order to discover how nonlinear this disruptive process can be, at Lundquist numbers of only 100, it is necessary to consider the linearized Strauss equations. Results from simulating the linearized Strauss equations, using these CASE 2 parameters, are discussed in Appendix II. A comparison among linear and nonlinear solutions is set forth there.

D. $B_c = 4.3$, $\eta = 0.0025$.

We move on now to results from a large grid run, CASE 3. The initial conditions are virtually identical to the previous nonlinear run discussed above. Here, however, we choose a Lundquist number of 400, on the grid of size 64 * 64 * 32.

1. Global Quantities.

An immediate difference from CASE 2 is seen in the plot of kinetic energy versus time, in Fig. 29. Instead of only one kinetic energy peak, more than one was attained. The plot of j*j versus time is also qualitatively different: the j*j peak points to a time of enhanced dissipation of magnetic energy. This enhanced dissipation is even visible on a plot of magnetic energy versus time. Finally, it is interesting to note that the net current does not change much at all throughout the run.

2. A Time History of CASE 3.

t = 10 32.

Like in the Lundquist number 100 run, the current develops helical filaments, which wrap themselves about the magnetic axis, as may be seen in Fig. 30. A negative filament has formed, to the outside of the inner, very positive one.

A three-dimensional plot of the current(x,y,z=π), Fig. 31a, clearly shows a rippled current profile, whose maximum is no longer at the geometric center of the cylinder. The developing negative jet is also visible. As in CASE 2, we observe the suggesion of a variety of closed regions in the z = π plane Poincaré plots of magnetic field lines, Fig 31b. Here, too, a crescent shaped figure corresponds to a pronounced current shelf.

t = 13.26

In Fig. 32, we display close-up plots of current (32a), velocity field (32b), and poloidal magnetic field lines (32c). From Fig. 32a we see that the negative current sheath lies very close to the most positive part of the current. A small disturbance is set up in the fluid to the outside of this sheath, with a velocity field pointing toward the current jet, in Fig. 32b. Poloidal magnetic field lines, in Fig. 32c, are strongest in the neighborhood of this

sheath.

t = 14.52.

As in the Lundquist number 100 run, the helical filament of current has nearly removed itself from the current column, at this time, a time near the first large kinetic energy peak, Fig. 33. Much small scale spatial structure has developed, with a shallow negative current "moat" encircling a positive current sheath. Within this region, the current is relatively flattened.

At this point it is necessary to add a warning about the resolution of this Lundquist number (S) = 400 simulation. It is clear from Figs. 33e and f that modal energy spectra are very well-behaved even at this time. The simulation is fully trustworthy, in all its particulars, through t ~ 12. Beyond this time, much small-scale spatial structure is generated, and the current density displays an increasing tendency to 'jet' more and more, both positively and negatively.

Since the energies remain fully well-behaved, however, it is highly likely that this run may be trusted throughout, as far as gross suggestive behavior is concerned.

The question of why the simulation slightly exceeded its allotment of resolution may be raised. Most probably, S = 400 is somewhat too large for a grid of 64 * 64 * 32. A narrower internal layer than could be resolved attempted to evolve. Increasing the grid (to an impossibly expensive size), with this value of S, would cure the difficulty.

A three-dimensional plot of the current contours of the previous contours show the intensity of the negative jet, as well as an abundance of small-scale spatial structure. Random nonuniformities are particularly observable to the outside of the current column.

t = 16.26.

Near the local kinetic energy minimum, the current profile once again displays much internal structure in Fig. 35. The column is in the process of kinking up in a way opposite to its previous helical deformation, as even the toroidal cut of vector potential indicates.

The sharp, forming current cliff is visible in a perspective plot of current density, Fig. 36a, as well as the overall asymmetry in the channel itself. Notice the "hole" near $x = \pi$, $y = 0$; this demonstrates the overall distortion of the current column. Fig. 36b shows crescent shaped Poincaré plots of magnetic field line traces in the $z = \pi$ plane.

t = 17.46.

Finally, we consider solutions near the second kinetic energy peak, in Fig. 37. Again, most of the current variation is located in the outer regions of the column; within this shell, the current is once again quite flat.

We can imagine this oscillatory process, perhaps reminiscent of the incomplete disruptions observed by Sauthoff, et al (1979), continuing for longer periods of time at higher values of the Lundquist number.

VI. LOW ORDER MODEL

In the disruptive results from free decay simulations, reported in the fifth chapter, an "m = 1, n = 1" large-scale mode is seen to grow and eventually dominate the dynamics, in conjunction with much small-scale turbulent structure. For a clearer understanding of the process, the isolated interaction among the largest scales in the evolution of the disruptive behavior can be studied, by means of a low-order truncation model of the Strauss equations. In this chapter, we derive such a model. We then add a forcing term to the vector potential equation, and a viscous term to the stream function equation, and discuss consequences these new terms might imply. Analogous studies of the possible transition to disorder in the Benard convection problem have been performed by Lorenz (1963), and most recently continued by Curry, et al (1984).

A. Implication from Code Results.

Nearly all contour plots of the velocity stream function generate the suggestion that the dominant $k_z = 1$ mode is of the form sin(x)*sin(2y). This suggestion may be substantiated by the examination of numerical values of these modes. Although the largest mode is not always $\psi_{r_{ij}}(k_x = 1, k_y = 2, k_z = 1)$ or $\psi_{r_{ij}}(k_x = 2, k_y = 1, k_z = 1)$, a linear combination of this pair may generally be found to contribute more to the mean square stream function than any other single modal element. The same is observed to be true of the vector potential. Hence, we approximate the "m = 1, n = 1" disturbance as sin(x) * sin(2y) * exp[$\pm$ iz] and sin(2x) * sin(y) * exp[$\pm$iz].

The largest mode in the $k_z = 0$ band of wavenumbers is $A_y(k_x = 1, k_y = 1, k_z = 0)$. An examination of the $k_z = 0$ part of stream function solutions shows

that only very low order noise exists in this wavenumber. We thus take $A_r(k_x = 1, k_y = 1, k_z = 0)$ to be the only mode retained in the $k_z = 0$ band.

B. Truncation Model.

We begin with the Strauss equations (9) and (10). Writing each term explicitly,

$$\frac{\partial \omega}{\partial t} = -u\frac{\partial \omega}{\partial x} - v\frac{\partial \omega}{\partial y} + B_x\frac{\partial j}{\partial x} + B_y\frac{\partial j}{\partial y} + B_0\frac{\partial j}{\partial z} + \nu\nabla_\perp^2\omega \quad (21)$$

$$\frac{\partial A}{\partial t} = uB_y - vB_x + B_0\frac{\partial \psi}{\partial z} + \eta\nabla_\perp^2 A + E_0 \quad (22)$$

For now, we set $\nu = E_0 = 0$.

Let

$$A(k_z = 0) = A^\circ = a \sin x \sin y$$
$$= a\,h$$

with

$$B_x^\circ = \lambda\frac{\partial h}{\partial y} = a \sin x \cos y$$

$$B_y^\circ = -\lambda\frac{\partial h}{\partial x} = -a \cos x \sin y$$

and

$$j^\circ = 2a\,h$$

Although we will show that more general combinations are allowed, let the pair of counterclockwise helical perturbations be the following:

$$A(k_z = 1) = A' = \alpha\,[\sin 2x \sin y \cos z + \sin x \sin 2y \sin z]$$
$$= \alpha\,f$$

$$\psi(k_z=1) \equiv \psi' = \beta\left[\sin x \sin 2y \cos z - \sin 2x \sin y \sin z\right]$$
$$\equiv \beta g$$

$\Rightarrow$

$$B_x' = \alpha \frac{\partial f}{\partial y} = \alpha\left[\sin 2x \cos y \cos z + 2 \sin x \cos 2y \sin z\right]$$

$$B_y' = -\alpha \frac{\partial f}{\partial x} = -\alpha\left[2 \cos 2x \sin y \cos z + \cos x \sin 2y \sin z\right]$$

$$u' = \beta \frac{\partial g}{\partial y} = \beta\left[2 \sin x \cos 2y \cos z - \sin 2x \cos y \sin z\right]$$

$$v' = -\beta \frac{\partial g}{\partial x} = -\beta\left[\cos x \sin 2y \cos z - 2 \cos 2x \sin y \sin z\right]$$

These yield

$$\omega = \omega(k_z=1) \equiv \omega' = 5\beta g$$

$$j = j(k_z=0) + j(k_z=1) \equiv j^0 + j' = 2A^0 + 5A' = A(h + 5f$$

We find that only the $k_z = 1$ dependence survives in equation (21), since

$$B_x \frac{\partial j}{\partial x} = [B_x][\frac{\partial j^0}{\partial x} + \frac{\partial j'}{\partial x}] = [B_x^0 + B_x'][-2B_y^0 - 5B_y']$$

$$+ B_y \frac{\partial j}{\partial y} = [B_y][\frac{\partial j^0}{\partial y} + \frac{\partial j'}{\partial y}] = [B_y^0 + B_y'][2B_x^0 - 5B_x']$$

$$B_x \frac{\partial j}{\partial x} + B_y \frac{\partial j}{\partial y} = 3\left[B_x' B_y^0 - B_x^0 B_y'\right],$$

and $$-u \frac{\partial \omega}{\partial x} - v \frac{\partial \omega}{\partial y} = -5\beta^2\left[\frac{\partial g}{\partial y}\frac{\partial g}{\partial x} - \frac{\partial g}{\partial x}\frac{\partial g}{\partial y}\right] = 0$$

Further, since $\frac{\partial f}{\partial z} = 5\alpha g$, **(21) becomes**

$$\frac{\partial w'}{\partial t} = 3\left[B_x' E_y^\circ - B_x^\circ B_y'\right] + 5 B_z \alpha g \tag{23}$$

The nonlinear terms in (23) may be rewritten.

$$B_x' E_y^\circ = -(\alpha \frac{\partial f}{\partial y})(\lambda \frac{\partial h}{\partial x})$$

$$= -\alpha\lambda\left[(\sin\bar{\alpha}\,\cos\bar{\alpha})(\cos y \sin y)\right]\cos z$$
$$-2\alpha\lambda\left[\sin^2\bar{\alpha}\,(\cos^2 y - \sin^2 y)\right]\sin z$$

$$= \alpha\lambda F$$

$$B_x^\circ B_y' = -(\lambda \frac{\partial h}{\partial y})(\alpha \frac{\partial f}{\partial x})$$

$$= -\lambda\alpha\left[(\sin^2\bar{\alpha}\,\cos\bar{\alpha})(\cos y \sin 2y)\right]\sin z$$
$$-2\lambda\alpha\left[(\sin^2\bar{\alpha}\,\cos\bar{\alpha})(\cos^2 y \sin y)\right]\cos z$$

$$= \lambda\alpha G$$

By means of trigonometric identities F and G may be re-expressed:

$$\frac{\partial w'}{\partial t} = 3\left[B_x' B_y^\circ - B_x^\circ B_y'\right] + 5 B_0 a j \tag{23}$$

The nonlinear terms in (23) may be rewritten.

$$B_x' B_y^\circ = \left(\alpha \frac{\partial f}{\partial y}\right)\left(\lambda \frac{\partial h}{\partial x}\right)$$

$$= -\alpha\lambda\left[(\sin\tilde{\alpha}x \cos x)(\cos y \sin y)\right]\cos z$$
$$-\tilde{\alpha}\alpha\lambda\left[(\sin x \cos x)(\cos\tilde{\alpha} z \sin y)\right]\sin z$$

$$= \alpha\lambda F$$

$$B_x^\circ B_y' = -\left(\lambda \frac{\partial h}{\partial y}\right)\left(\alpha \frac{\partial f}{\partial x}\right)$$

$$= -2\lambda\alpha\left[(\sin x \cos x)(\cos y \sin 2y)\right]\sin z$$
$$-2\lambda\alpha\left[(\sin x \cos\tilde{\alpha} x)(\cos z \sin y)\right]\cos z$$

$$\equiv \lambda\alpha G$$

By means of trigonometric identities F and G may be re-expressed:

$$F = -\frac{1}{4}\left[(\sin 3x + \sin x)\sin 2y\right]\cos z - \frac{3}{4}\left[\sin 2x(\sin 3y - \sin y)\right]\sin z$$

$$\alpha\lambda F = a\lambda\left[-\frac{1}{4}(\sin 3x \sin 2y + \sin x \sin 2y)\cos z - \frac{1}{2}(\sin 2x \sin 3y - \sin 2x \sin y)\sin z\right]$$

$$G = -\frac{1}{4}\left[\sin 2x(\sin 3y + \sin y)\right]\sin z - \frac{1}{2}\left[(\sin 3x - \sin x)\sin 2y\right]\cos z$$

$$a\lambda G = a\alpha\left[-\frac{1}{4}(\sin 2x \sin 3y + \sin 2x \sin y)\sin z - \frac{1}{2}(\sin 3x \sin 2y - \sin x \sin 2y)\cos z\right]$$

Thus,

$$\alpha\lambda(F-G) = -\frac{3}{4}a\alpha g + \frac{\lambda\alpha}{4}\left[\sin 3x \sin 2y \cos z - \sin 2x \sin 3y \sin z\right]$$

Neglecting terms with k_x, $k_y > 2$, we have

$$\frac{\partial w'}{\partial t} = \left[5B_0\alpha - \frac{9\lambda\alpha}{4}\right]g \qquad (23')$$

$$= 5g\frac{\partial\theta}{\partial t}$$

Now, consider (22):

$$\frac{\partial A^0}{\partial t} + \frac{\partial A'}{\partial t} = u'B_y' - v'B_x' + u'B_y^0 - v'B_x^0 + B_0\frac{\partial v'}{\partial z} + \eta\nabla_1^2 A^0 + \eta\nabla_1^2 A'$$

This separates into an equation for the $k_z = 1$ component of A:

$$\frac{\partial A'}{\partial t} = u' B_y^\circ - v' B_x^\circ + B_0 \frac{\partial \psi'}{\partial z} - \eta j' \qquad (24)$$

and an equation for the $k_z = 0$ component of A:

$$\frac{\partial A^\circ}{\partial t} = u' B_y' - v' B_x' - \eta j^\circ \qquad (25)$$

As above, we compute terms of (24):

$$u' B_y^\circ = -\left(\beta \frac{\partial g}{\partial y}\right)\left(\alpha \frac{\partial h}{\partial x}\right)$$

$$= -\beta\alpha\left[2(\sin x \cos x)(\cos 2y \sin y)\right]\cos z + \beta\alpha\left[(\sin 2x \cos x)(\cos 2y \sin y)\right]\sin z$$

$$= \beta\alpha H$$

$$v' B_x^\circ = -\left(\beta \frac{\partial g}{\partial x}\right)\left(\alpha \frac{\partial h}{\partial y}\right)$$

$$= -\beta\alpha\left[(\cos x \sin x)(\sin 2y \cos y)\right]\cos z + \beta\alpha\left[(\sin 2x \sin x)(\cos 2y \cos y - \sin 2y \sin y)\right]\sin z$$

$$= \beta\alpha I$$

Using trigonometric identities, we find that

$$H = -\tfrac{1}{2}\left[\sin 2x (\sin 3y - \sin y)\right]\cos z + \tfrac{1}{4}\left[(\sin 3x + \sin x)\sin 2y\right]\sin z$$

$$I = -\tfrac{1}{4}\left[\sin 2x (\sin 3y + \sin y)\right]\cos z + \tfrac{1}{2}\left[(\sin 3x - \sin x)\sin 2y\right]\sin z$$

$$\Rightarrow \quad G_{\alpha\beta}(H-I) = \frac{3}{4} G_{\alpha\beta} f + \frac{G_{\alpha\beta}}{4} \left[\sin 2x \sin 3y \cos z + \sin 3x \sin 2y \sin z \right]$$

Again, neglecting terms with k_x, $k_y > 2$.

$$\lambda' B_y^{\,o} - \nu' B_x^{\,o} = \frac{3}{4} \lambda_{\alpha\beta} f$$

Since $\frac{\partial \psi}{\partial z} = -\beta f$, (24) becomes

$$\frac{\partial A'}{\partial t} = \left[\frac{3}{4} \lambda_{\alpha\beta} f - B_\alpha \beta - 5 \eta_\alpha \right] f \qquad (24')$$

$$= f \frac{\partial \alpha}{\partial t}$$

Terms of (25) may be rewritten:

$$\lambda' B_y' = \left(\beta \frac{\partial g}{\partial y} \right)\left(\alpha \frac{\partial f}{\partial x} \right)$$

$$= +\alpha\beta \left[-4 (\sin x \cos 2x)(\cos 2y \sin y)(\cos z)^2 + (\sin 2x \cos x)(\cos y \sin 2y)(\sin z)^2 \right]$$

$$\nu' B_x' = \alpha\beta \left[-4 (\cos 2x \sin x)(\sin y \cos 2y)(\sin z)^2 + (\cos x \sin 2x)(\sin 2y \cos y)(\cos z)^2 \right]$$

or

$$\lambda' B_y' - \nu' B_x' = \alpha\beta \left[-\frac{\partial f}{\partial x}\frac{\partial g}{\partial y} + \frac{\partial g}{\partial x}\frac{\partial f}{\partial y} \right]$$

$$= \alpha_\lambda \beta \left[-8 ((\sin 3x - \sin x)(\sin 3y - \sin y)) + 2 ((\sin 3x + \sin x)(\sin 3y - \sin y)) \right]$$

$$= -\frac{3}{4} \alpha\beta \sin x \sin y,$$

where we neglect terms with k_x, $k_y > 2$, $k_z > 1$.

Equation (25) becomes

$$\frac{\partial A^0}{\partial t} = -\frac{3}{4}\alpha\beta h - 2\eta a h = h\frac{\partial a}{\partial t} \qquad (25')$$

Or, (23'), (24') and (25') are:

$$\frac{d\beta}{dt} = \left[B_0 - \frac{9}{20}a\right]\alpha \qquad (26)$$

$$\frac{d\alpha}{dt} = \left[\frac{3}{4}a - B_0\right]\beta - 5\eta\alpha \qquad (27)$$

$$\frac{da}{dt} = -\frac{3}{4}\alpha\beta - 4\eta a \qquad (28)$$

1. More General Perturbations.

In order for (26) - (28) to be useful, the perturbations nonlinearly generated by the large grid code must be compatible with the form assumed by the equations. Although the form $A' = \alpha f$, $\psi' = \beta g$ is assumed in the derivation, more general perturbations are also allowed.

Numerical values for the dominant modes with $k_x, k_y < 3$, $k_z < 2$, in CASE 2, are listed in Table 3. Other cases exhibit exactly similar behavior. From that table it is apparent that $k_x, k_y < 3$, $k_z < 2$ perturbations are basically of the form

$$A' = \alpha\left[-\delta f + \epsilon g\right] \qquad (29)$$

$$\psi' = \beta\left[-\epsilon f - \delta g\right] \qquad (30)$$

where, as before, $f = \sin 2x \sin y \cos z + \sin x \sin 2y \sin z$

and $g = \sin x \sin 2y \cos z - \sin 2x \sin y \sin z.$

2. Demonstration of Applicability.

Using (29) and (30), we recompute terms that form equations (23'), (24') and (25'). Starting with (23'), where

$$B_x' = \alpha \left[-\delta \frac{\partial f}{\partial y} + \epsilon \frac{\partial g}{\partial y} \right]$$

$$B_y' = -\alpha \left[-\delta \frac{\partial f}{\partial x} + \epsilon \frac{\partial g}{\partial x} \right]$$

$$u' = \beta \left[-\delta \frac{\partial g}{\partial y} - \epsilon \frac{\partial f}{\partial y} \right]$$

$$v' = -\beta \left[-\delta \frac{\partial g}{\partial x} - \epsilon \frac{\partial f}{\partial x} \right]$$

the nonlinear terms become

$$B_x' B_y^\circ = -\alpha \left[-\delta \frac{\partial f}{\partial y} + \epsilon \frac{\partial g}{\partial y} \right] \lambda \frac{\partial h}{\partial x}$$

$$= +\alpha\lambda\delta \left[\frac{\partial f}{\partial y} \frac{\partial h}{\partial x} \right] - \alpha\lambda\epsilon \left[\frac{\partial g}{\partial y} \frac{\partial h}{\partial x} \right]$$

$$= \alpha\lambda \left[-\delta F + \epsilon H \right]$$

and $B_x^\circ B_y' = \alpha\lambda \left[\delta \frac{\partial h}{\partial y} \frac{\partial f}{\partial x} - \epsilon \frac{\partial h}{\partial y} \frac{\partial g}{\partial x} \right] = \alpha\lambda \left[\delta I - \epsilon G \right]$

Thus, $B_x' B_y^\circ - B_x^\circ B_y' = -\alpha\lambda\delta \left[F - G \right] + \alpha\lambda\epsilon \left[H - I \right]$

$$= \frac{3}{4}\alpha\lambda\delta g + \frac{3}{4}\alpha\lambda\epsilon f$$

$$= -\frac{3}{4}\alpha\lambda \left[-\delta g - \epsilon f \right]$$

where as before we neglect terms with $k_x, k_y > 2$.

Also, $\frac{\partial \psi'}{\partial z} = S\frac{\partial}{\partial z}(\alpha[-\delta f + \epsilon g]) = -S\alpha(\delta g + \epsilon f)$. Thus, the form of (23'), or equivalently (26), is unchanged.

The more general perturbations also generate eqation (24'), as may be seen by considering

$$u'B_y^{\,0} = \beta\lambda\{+\delta\frac{\partial g}{\partial y}\frac{\partial h}{\partial x} + \epsilon\frac{\partial f}{\partial y}\frac{\partial h}{\partial x}\} \equiv \beta\alpha\{-\epsilon F - \delta H\}$$

and

$$v'B_x^{\,0} = \beta\alpha\{+\delta\frac{\partial g}{\partial x}\frac{\partial h}{\partial y} + \epsilon\frac{\partial f}{\partial x}\frac{\partial h}{\partial y}\} \equiv \beta\alpha\{-\epsilon G - \delta I\}$$

That is,

$$u'B_y^{\,0} - v'B_x^{\,0} = \beta\lambda[-\epsilon F + \epsilon G - \delta H + \delta I]$$
$$= \beta\lambda[-\epsilon(-\delta f + \epsilon g) - \delta(h - I)]$$
$$= \beta\lambda[\epsilon^2 g - \delta h + \delta I]$$

where again we neglect terms with $k_x, k_y > 2$. Further, since $\frac{\partial \psi'}{\partial z} = -\beta[-\delta f + \epsilon g]$, the form of (24'), or equivalently (27) is still valid.

Finally, we consider (25'). The nonlinear term, $u'B_y' - v'B_x'$, must be re-evaluated. Using the notation of above,

$$u'B_y' - v'B_x' = -[\beta(-\delta\frac{\partial g}{\partial y} - \epsilon\frac{\partial f}{\partial y})][\alpha(-\delta\frac{\partial f}{\partial x} + \epsilon\frac{\partial g}{\partial x})]$$
$$+ [\beta(-\delta\frac{\partial g}{\partial x} + \epsilon\frac{\partial f}{\partial x})][\alpha(-\delta\frac{\partial f}{\partial y} + \epsilon\frac{\partial g}{\partial y})]$$
$$= \alpha\beta[\delta^2 + \epsilon^2][\frac{\partial g}{\partial x}\frac{\partial f}{\partial y} - \frac{\partial g}{\partial y}\frac{\partial f}{\partial x}]$$
$$= \alpha\beta[\delta^2 + \epsilon^2][-\frac{3}{4}h]$$

where we neglect terms with $k_x, k_y > 2$, $k_z > 1$. As long as we impose the

constraint that $[\delta^2+\epsilon^2] = 1$, a restriction that we are free to demand, the form of (25'), or (28), is also unaltered. Thus the form of perturbations generated from nonlinear simulation are not incompatible with the form used in the derivation of the low-order truncation model, equations (26), (27) and (28).

For the particular CASE 2, δ and ϵ are greater than zero. If they were of opposing sign the same results would be obtained, as may be seen by setting $+\delta$ to $-\delta$ everywhere in the above demonstration.

C Results from the Model, $B_o = 0$.

In the inviscid decay problem, only one critical point exists, where by critical point is meant solution to the time-independent equations (26) - (28). The critical point is $(\beta, \alpha, \lambda) = (0, 0, 0)$, as may be seen from the following:

$$\text{Equation (26)} \Rightarrow \quad 0 = B_o\alpha - \frac{9\lambda}{20}\alpha \quad \text{or} \quad \lambda = \frac{20B_o}{9}.$$

$$\text{Equation (27)} \Rightarrow \quad 0 = -5\eta\alpha - B_o\beta + \frac{3\lambda\beta}{4} \quad \text{or} \quad \alpha = \frac{2}{15\eta}B_o\beta.$$

$$\text{Equation (28)} \Rightarrow \quad 0 = -\frac{3}{4}\alpha\beta - 2\eta\lambda \quad \text{or} \quad \beta^2 = -\frac{20\eta^2\lambda}{B_o}$$

For simulated (positive) λ and B_o, β would have to be imaginary, which is not allowed.

1. Linear.

In order to obtain information about the behavior of solutions to the low-order model, we first examine a linearized version of them. Since is the amplitude of the equilibrium, h(sin(x)*sin(y)), it is reasonable to treat as a parameter. Equation (26) and (27) become a pair of linear, coupled ordinary differential equations, and their solution is:

$$\begin{pmatrix}\beta\\ \alpha\end{pmatrix} = d_1\begin{pmatrix}b+\sqrt{b^2+4ac}\\ 2c\end{pmatrix}e^{\lambda_1 t} + d_2\begin{pmatrix}b-\sqrt{b^2+4ac}\\ 2c\end{pmatrix}e^{\lambda_2 t} \qquad (29)$$

for $\lambda_{\pm} = -\frac{5}{2}\eta \pm \frac{1}{2}\sqrt{25\eta^2 + 4(B_0 - \frac{9}{20}\alpha)(\frac{3}{4}\alpha - B_0)}$

where $a = B_0 - \frac{9}{20}\alpha$, $b = 5\eta$ and $c = \frac{3}{4}\alpha - B_0$

To understand what this solution does as a function of the parameter α, first note that, generally, the only critical point of (26) and (27) is ($\beta = 0$, $\alpha = 0$). The behavior of (29) can be determined locally in the neighborhood of ($\beta = 0$, $\alpha = 0$) by considering the eigenvalues $\lambda_{\pm}$.

From Bender and Orszag (1979), we know that:

IF $\lambda_{\pm}$ ARE	TRAJECTORIES	($\beta = 0$, $\alpha = 0$) IS
both real, both < 0.	all go to ($\beta = 0, \alpha = 0$) as a function of time.	a stable node.
both real, $\lambda_+ > 0$, $\lambda_- < 0$.	go to ($\beta = 0$, $\alpha = 0$) in the direction of $\underline{v}_-$, and leave in the direction of $\underline{v}_+$.	a saddle point.
complex conjugates, with real part < 0.	spiral to ($\beta = 0$, $\alpha = 0$) as a function of time.	a stable spiral.

where $\underline{v}_+$ is the vector which corresponds to λ_+, while $\underline{v}_-$ is the vector that corresponds to λ_-.

For $\alpha > 20\ B_0 / 9$, an unrealistically large value, $\lambda_{\pm}$ suggest that ($\beta = 0$, $\alpha = 0$) is a stable spiral. By setting η to zero, $\frac{d\beta}{dt}$ is seen to be a positive function of β, or the spiral is counterclockwise, as may be observed in numerical solution of (26) and (27), where we have used the second-order Runge-Kutta scheme on the time derivative.

When $\alpha \geq 20\ B_0 / 9$, with $\eta > 5\eta^2 + 4(B_0 - \frac{9}{20}\alpha)(\frac{3}{4}\alpha - B_0)$, ($\beta = 0$, $\alpha = 0$) becomes a stable node.

For $\alpha = 20\ B_0 / 9$, β = constant, with $\alpha(t \to \infty) \to 2\ B_0 / (15\ \eta)$.

In the region $4 B_0 / 3 < \lambda < 2\pi B_0 / 9$, ($\beta = 0$, $\alpha = 0$) is a saddle point. Trajectories enter the region of ($\beta = 0$, $\alpha = 0$) in the ($\mp\beta, \pm\alpha$) quadrants, with a limiting slope of

$$\frac{\alpha}{\beta} = \frac{2\left[\frac{3}{4}\lambda - B_0\right]}{5\eta - \sqrt{25\eta^2 + 4\left(\frac{3}{4}\lambda - B_0\right)\left(B_0 - \frac{9}{2\pi}\lambda\right)}}$$

and leave the neighborhood of ($\beta = 0, \alpha = 0$) in the ($+\beta, +\alpha$) quadrants, with a limiting slope of

$$\frac{\alpha}{\beta} = \frac{2\left[\frac{3}{4}\lambda - B_0\right]}{5\eta + \sqrt{25\eta^2 + 4\left(\frac{3}{4}\lambda - B_0\right)\left(B_0 - \frac{9}{2\pi}\lambda\right)}}$$

This behavior may be seen by numerical solution of (26) and (27), depicted in Fig. 41.

When $\lambda = 4 B_0 / 3$, β = arbitrary constant, while $\alpha(t \to \infty) \to 0$.

For $\lambda < 4 B_0 / 3$, the other root of $25\eta^2 + 4\left(B_0 - \frac{2\pi}{9}\lambda\right)\left(\frac{3}{4}\lambda - B_0\right) > 0$ turns the critical point ($\beta = 0$, $\alpha = 0$) into a stable node.

If $\lambda \leq 4 B_0 / 3$, ($\beta = 0$, $\alpha = 0$) is once again a stable spiral; from $\alpha = 0$, $\frac{d\alpha}{dt} < 0$, the solution may be seen to spiral in a clockwise sense, as may be observed in another numerical solution of (26) and (27), shown in Fig. 42.

2. Nonlinear.

When equation (28) is solved simultaneously with (26) and (27), the behavior of α and β in the neighborhood of ($\beta = 0$, $\alpha = 0$) still must vary as a function of λ. For instance, as λ decays from an initial value greater than $4 B_0 / 3$, but less than $2\pi B_0 / 9$, the solutions α and β first behave in the neighborhood of ($\beta = 0$, $\alpha = 0$) as if that point was a saddle point, then as if it was a stable spiral. If α and β are not very small, they measurably modulate the decay of $\lambda(t)$. These behaviors may be seen for a few initial conditions and parameters, in Fig. 43.

D. Comparison with Code Results.

In order to compare the behavior of the nonlinear full-grid simulation results with results from the low-order model, we obtain "β" and "α" from the full-grid stored solutions, as indicated in Table 3. The "β", "α" and "α" from CASE 2 are plotted in Fig. 44. Solutions of (26) - (28), from conditions and parameters of CASE 2 are plotted in Fig. 45. Although the agreement is only qualitative, it is noteworthy that even in a model based only on the very large scales, quasicyclic behavior of the solutions is observed, behavior in which both magnetic field and velocity field perturbations participate. However, subsequent bursts of the quasi-cyclic activity are unlike the first; β and α both grow together only in the first event of the series.

We must turn to driven simulations in order to observe repeated, simultaneous growth of β and α.

E. neous growth of β and α . Term, the External Electric Field E_0.

If we add a forcing term to the Strauss equations, by setting E_0 to a positive constant, the mean field cannot decay to zero. It is physically meaningful for E_0 to be non-zero; an electric field is imposed at the walls of most fusion devices, to maintain the current. When added to the Strauss model, the driving mechanism can be responsible for repeated periods of joint growth of β and α, for suitable choices of parameters E_0, B_0 and η. In this section, we will explore the behavior of the driven, inviscid, low-order model.

1. The Equations.

The dominant sinusoidal mode in any positive constant would be of the form sin(x)*sin(y), $k_z = 0$. The driving term is added to equation (28), then. We choose $E_0 \sim 2\eta\alpha_0$, and (28) becomes

$$\frac{d\alpha}{dt} = -\frac{3}{4}\alpha\beta + 2\eta(\alpha_0 - \alpha) \qquad (30)$$

(26) and (27) are unaltered.

No critical point exists for (26), (27) and (30) at ($\beta = 0$, $\alpha = 0$, $\lambda = 0$). This point, by inspection, is replaced with ($\beta = 0$, $\alpha = 0$, $\lambda = \lambda_0$). A multitude of additional time-independent solutions exist: the line β = constant, with $\lambda = \lambda_0 = 4\ B_0 / 3$, and $\alpha = 0$ contains the ($\beta = 0$, $\alpha \neq 0$) critical point as a special case.

Two additional critical points, ($\beta = \beta_+$, $\alpha = \alpha_+$, $\lambda = 20\ B_0 / 9$), and ($\beta = \beta_-$, $\alpha = \alpha_-$, $\lambda = 20\ B_0 / 9$), also may be identified, where

$$\alpha_\pm = \pm \frac{4}{3}\sqrt{\frac{B_0}{5}\left(\lambda_0 - \frac{20}{9}B_0\right)} \quad , \quad \beta_\pm = \pm 10\eta\sqrt{\frac{1}{5E_0}\left(\lambda_0 - \frac{20}{9}B_0\right)}$$

These points exist in the presence of substantial forcing, when $\lambda_0 > 20\ B_0 / 9$.

3. Solutions.

Samples of the dynamical systems behavior which may be generated by this driven, dissipative system are shown in Figs. 46 - 52. Table 4 is a chart of the parameters and initial conditions used to generate the solutions shown in these figures, along with brief descriptions of the observed behavior.

3. The Addition of Viscosity.

If we add a dissipation term to the equation for the amplitude of the stream function perturbation, we have

$$\frac{\partial\beta}{\partial t} = \left[B_0 - \frac{9}{20}\lambda\right]\alpha - 5\nu\beta \qquad (31)$$

where ν = (kinematic viscosity) / ($V_A\ L_0$), as defined in the second chapter.

One critical point of the system (31), (27) and (30) is still ($\beta = 0$, $\alpha = 0$, $\lambda = \lambda_0$). Interestingly, the line β = constant, $\alpha = 0$, and $\lambda = \lambda_0 = 4\ B_0 / 3$ no longer solves the time-independent system. In its place are two critical

points ($\beta = \beta_1(\alpha_1)$, $\alpha = \alpha_1(\alpha_1)$, $\lambda = \lambda_+$); two more, ($\beta = \beta_1(\lambda_-)$, $\alpha = \alpha_1(\lambda_-)$, $\lambda = \lambda_-$) may also be found, where

$$\lambda_\pm = \frac{16}{9} B_0 \pm \frac{4}{9} \sqrt{B_0^2 - 375 \nu \eta}$$

$$\alpha_\pm = \pm \sqrt{\frac{7}{15} (\alpha_0 - \lambda) \left(\frac{3}{4} \alpha \cdot B_0\right)}$$

and

$$\beta_\pm = \pm 10 \eta \sqrt{\frac{2 (\alpha_0 - \lambda)}{15 \left(\frac{3}{4} \lambda \cdot B_0\right)}}$$

The latter pair of solutions, functions of λ_1, reduce to the two non-trivial critical points of the driven inviscid model described in section (1) above.

This altered system, (31), (27) and (30), is explored in Figs. 53 - 55; Table 4 again accompanies the figures. Figure 55 is of particular interest; exhibited there is a solution with features very similar to those found in the Lorenz (1963) model, for certain classes of conditions. Note that the low order model presented here differs significantly from the Lorenz model in that quadratic nonlinear terms made up of the other two amplitudes appear in each of the three amplitude equations (31), (27) and (30), while in the Lorenz model such terms only appear in two of the three equations of that model.

Sustainment of nonlinear behavior is observed in both the driven, inviscid model, (26), (27) and (30), and the driven, viscous model, (31), (27) and (30). This sustainment ought to be a feature of the time-dependent solutions of the driven Strauss equations, as well; results from full grid simulation of these equations is the subject of the next chapter.

VII. SIMULATION RESULTS, DRIVEN

Of the simulations appropriate to internal disruption, which were discussed in the first chapter, most were performed in the presence of some form of external forcing and variable resistivity. These terms were employed to inhibit the resistive decay of the current profile. Two combinations were dominant, both of which imposed a resistivity profile which varied as the inverse of the initial current density. Of the simulations considered, only Sykes and Wesson (1976) then allowed the resitivity profile to evolve. In addition to the use of variable resistivity, some simulations were performed in the presence of an electric field which maintained a constant current (e.g. Biskamp and Welter (1983)). Others (e.g. Waddell, et al (1976)) imposed an equilibrium toroidal electric field, E_o , at the wall, which initially set $\eta j = E_o$, or prohibited the resitive decay of the initial current density. Although convenience is a primary reason for keeping the variable resistivity fixed in time, Waddell, et al (1976) noted that since the important modes grow up on time scales which are faster than resistive decay times, results should not qualitatively depend on the specific resistivity profile chosen.

In the simulations described in this chapter, the resistive decay of the initial current profile is countered. A resistivity profile which varies in space as the inverse of the initial current profile, approaching values of O(1) at the walls, is chosen. Since the vector potential is poloidally expanded in sine functions, the value of this quantity is automatically zero in the very resistive region at the wall. Hence, in order to prevent the resistive decay of the initial current profile, E_o is chosen to be a small positive constant which balances $-\eta j(t = 0)$ at all the internal grid points. The simulation results

reported in this chapter are fundamentally different from those discussed in the fifth chapter, in that both a non-zero value of the external electric field E_o is chosen for all runs, and a variable resistivity is employed. Since the resistivity is now a function of x and y, the ηj term in equation (10) may not be generated in sine-Fourier space, but rather in physical space, with the other nonlinear terms of equations (9) and (10).

Three sets of conditions, CASE 4, CASE 5, and CASE 6 are considered. Both CASE 4 and CASE 5 are simulated on a 32 * 32 * 16 grid, with resistivity profiles $\eta(x,y) = [\ 200 * \exp\{ -1.2\ (x - \pi/2)^2 -1.2\ (y - \pi/2)^2\ \}\ ]^{-1}$. CASE 4 and CASE 5 differ only in the initial amplitudes of the current density profiles, and the values of the external fields, B_o and E_o. While CASE 4 has

$$j(t=0) = 10 \exp[-1.2(x-\pi/2)^2 - 1.2(y-\pi/2)^2], \quad B_o = 3 \text{ and } E_o = 1/200,$$

CASE 5 is run with

$$j(t=0) = 8 \exp[-1.2(x-\pi/2)^2 - 1.2(y-\pi/2)^2], \quad B_o = 2.4 \text{ and } E_o = 1/200.$$

Although the disruptive events occur at slightly different computational times in the two cases, the features of the events are very similar. CASE 6, run on a 64 * 64 * 32 grid, is initialized with

$$j(t=0) = 8 \exp[-(x-\pi/2)^2 (y-\pi/2)^2], \quad \eta = \frac{1}{350}, \quad B_o = 2.4, \quad E_o = \frac{1}{350}$$

In all three cases, the vorticity Fourier coefficients are initialized with random noise of $O(10^{-2})$ in a broad band of wave numbers, k_x, $k_y \in [4, 8]$, $k_z \in [1, 4]$.

In order to address the effects generated by the altered current profile, and the variable resistivity, we performed an unforced, inviscid simulation with CASE 4 parameters and conditions. This run, discussed in the third appendix, displays features similar to the constant resistivity decay runs of the fifth chapter, in that magnetic and velocity field perturbations first grow to-

gether, then apparently attempt to oscillate in sign as the solutions rapidly damp to zero in the very resistive fluid. This quasi-cyclic behavior is not observed in the inviscid, driven simulations.

Disruptive behavior is observed after only a few Alfvén transit times in the inviscid driven runs of CASE 4, CASE 5, and CASE 6, followed by a nearly steady situation with sustained, finite flow, which can be maintained for tens of Alfvén transit times. This state is reminiscent of that suggested by the low order model for the driven, inviscid case; solutions with constant equilibrium amplitude λ, constant, arbitrary stream function amplitude β, and a zero value for the vector potential perturbation amplitude α, do exist.

CASES 4 and 5 are repeated with non-zero values of fluid viscosity. It is assumed that neglect of the no-slip boundary condition does not invalidate the results, since the relevant modes grow up far in the interior of the computational cylinder. Further, note that although a viscosity, or "smoothing" term is frequently added to the velocity field equation solved in many simulations, (e.g. Sykes and Wesson (1976); Strauss (1976); Aydemir, Barnes, Caramana, Mirin, Nebel, Schnack and Sgro (1984)), the condition generally imposed on the velocity field is that appropriate for free-slip, rigid side walls (Sykes and Wesson (1976); Strauss (1976); Schnack, Baxter and Caramana (1983); Aydemir and Barnes (1984)). Upon the inclusion of a viscous term, a disturbance which is repetitive is here observed, with a period that is far longer than the periodicity of the free-decay bursts. In these driven, disruptive bursts, the velocity field does not change sign; rather, a single-signed perturbation repeatedly grows and decays. Once again the qualitative behavior of the low-order model may be correlated with that of the large-grid simulation; no sustained, steady-state velocity field is observed in the viscous, large-grid simulations, while the addition of a viscous term to the low-order model removes a possible

solution with λ = constant, β = constant > 0, and α = 0.

We turn to specific results from these simulations, CASES 4, 5 and 6, which support the above description.

A. $B_0 = 3.0$, $\eta(x,y) = [\ 200 * \exp\{ -1.2(x - \pi/2)^2 - 1.2(y - \pi/2)^2 \}\ ]^{-1}$.

Here we consider simulations for which the initial poloidal magnetic energy only varies by a few percent from that quantity in CASES 1, 2 and 3. The external magnetic field B_z is chosen so that the safety factor $Q(x = \pi/2, y = \pi/2, t = 0) \doteq 0.6 = 2\ B_0 / j(x = \pi/2, y = \pi/2, t = 0)$. An external electric field, constant in space and time, is imposed. This driving term, E_0, exactly balances the $\eta(x,y) * j(x,y,t = 0)$ term with an amplitude of 0.05. Contour plots of the initial conditions are displayed in Fig. 56.

1. $\nu = 0.0$.

We first consider the inviscid CASE 4 simulation. Out of the broad-band, low order vorticity perturbation, "m = 1, n = 1" helical structures emerge to dominate the spectra of both perturbed fields. The growth of these structures may be traced in time histories of global quantities, shown in Fig. 57; of primary interest is a plot of kinetic energy, E_z, versus time.

As the kinetic energy grows, a helical current filament wraps itself around the line ($x = \pi/2$, $y = \pi/2$, z), while bean-shaped counter-rotating stream function lobes generate a velocity field which points across the poloidal cut toward the region of maximum current density, as may be seen in Fig. 58, t = 16.56. With behavior similar to that observed in the undriven simulations described in the fifth chapter, the current filament intensified in regions toward the edge of the disturbance, while the velocity field grows stronger; see Fig. 59, t = 20.64. By t = 26.40, the current column approaches a flattened state. This state is virtually achieved by t = 36.24, as may be seen in Fig. 61. Through-

out this time, although the kinetic energy peaks again, near t = 32, the "m = 1, n = 1" stream function pattern is observed to remain unaltered in sign, only varying in amplitude.

The velocity field perturbation continues to exist for tens of Alfvén transit times, almost in a steady state, as may be seen at a sample time of 42, in Fig. 62. An unusual horseshoe-shaped current filament, hollow to the center of the poloidal cut, has developed, which co-exists with the long-lived velocity field. By comparing Figs. 62b with 62d, it is clear that the velocity field points across the center of the poloidal cut, away from the region of lesser current density and toward the "base" of the horseshoe-shaped current filament. Apparently, this filamentary structure is not paralleled in surfaces upon which magnetic field lines lie; no "horseshoe-shaped islands" can be detected in Poincare traces of magnetic field lines in the $z = \pi$ plane, at t = 42; see Fig. 63.

After tens of Alfvén transit times, when sufficient resolution must seriously become suspect, the velocity field has decayed to a local minimum, at t = 101.84. After this time, another burst of kinetic activity is observed, with features very similar to the first. At t = 109.44, near the time of the second kinetic energy maximum, a helical filament once again has formed, in the same physical location where the t $\doteq$ 16 filament had been; see Fig. 64. This filament behaves like the one near t $\doteq$ 16 did: it nearly disappears into the edge of the disturbance as the current profile broadly flattens. Through this time, the velocity field perturbation has grown in amplitude, with unchanged sign.

Following this burst of activity, a horseshoe-shaped current filament once again develops, while the velocity field settles into a nearly constant-amplitude steady state flow pattern, as may be seen in Fig. 65.

As indicated above, this second burst of disruptive activity occurs under

conditions of uncertain resolution. Plots of modal kinetic energy spectra during this time, Fig. 66, are encouraging: the perturbation at low wavenumbers wholly dominates. Amounts of excitation, of $O(10^{-5}, 10^{-6})$ do exist in the highest wavenumbers through this time, however, and must generate considerable aliasing error.

An identical run performed on a 16 * 16 * 16 grid was able to track the same solution through $t \sim 65$. The coarser grid run's solutions then diverged from the 32 * 32 * 16 grid run's solutions, as may be seen in Fig. 67. It is conjectured that aliasing error sustained the coarser grid run's perturbation, prohibiting a second disruptive event from taking place. Although this auxiliary run established the numerical validity of the first event, the validity of the second event is somewhat questionable.

2. $\nu = 0.01$.

Multiple events of disruptive activity may be accurately generated, however. Inclusion of a viscous damping term, which can cause the sustained velocity field perturbation to be diminished, leads to a time history depicted in Fig. 68. There it may be observed that, about 25 Alfvén transit times after the first burst of kinetic energy and net current, another similar burst occurs.

Because a second disruptive event was observed in the inviscid CASE 4 simulation (under conditions of some numerical error), it is not possible to say that the multiplicity of events only occurs through the action of viscous damping of a sustained velocity field perturbation. It is clear, however, that development of the fluid flow depends strongly on whether a viscous term is added to the equation of motion. Inclusion of viscosity tends to damp the flow, and leads to pronounced subsequent bounces.

We proceed to a study of a similar set of simulations, CASE 5, to establish that this behavior occurs over a range of parameters.

B. $B_o = 2.4$, $\eta(x,y) = [\ 200 * \exp\{ -1.2(x - \pi/2)\ \ -1.2(y - \pi/2)\}\ ]^{-1}$.

As in the CASE 4 simulations, $Q(x = \pi/2,\ y = \pi/2,\ t = 0) \doteq 0.6$ in the CASE 5 simulations, described in this section. The values of $j(x = \pi/2,\ y = \pi/2,\ t = 0)$ [= 0.0] and B_o [= 2.4] are set to achieve this. To balance $\eta(x,y) * j(x,y,t = 0)$, $E_o = 0 / 200$, for all time, at all interior grid points.

1. $\nu = 0.0$.

This simulation is quite similar to the CASE 4 inviscid, driven run, as may be seen in time histories of some global quantities, Fig. 69. Following the typical burst of disruptive activity, the current density develops a horseshoe-shaped filament, while the velocity field again points toward the base of the horseshoe. These features are depicted in Fig. 70. A current cross-sectional slice at $x = \pi / 2$, y, $z = \pi$ clearly exhibits the hollow center of the current density, the amplitude of which drops from approximately 25% of the off-center maximum, to a value $j(x = \pi/2,\ y = \pi/2,\ z = \pi) \doteq 4.3$. Contours at a later time, 35.04, show that the horseshoe filament is filling in, while the stream function perturbation remains nearly steady, and unchanging in sign; see Fig. 71. No additional bursts of activity were observed to occur in this simulation, through a computational time of 52.

2. $\nu = 0.01$.

Upon the inclusion of a viscous damping term in the equation of motion, however, a multitude of disruptive bursts of activity were generated. Globals from the viscous, forced CASE 5 simulation, Fig. 72, point to bursts of activity taking place regularly, after an initial disruption at t = 32.1. A second burst occurs at t = 56.28, while a third happens at t = 80.86.

Each event is characterized by the formation, then disappearance, of an "m = 1, n = 1" helical current filament, and the diminishing, then growth, of a

single-signed helical stream function pattern. Prior to the first flattening of the current density, both a well-formed filament and a large-amplitude velocity field perturbation may be seen, at t = 29.28, in Fig. 73. Following the first kinetic energy peak, the current column has become broadly flat, with much small-scale spatial structure present toward the column edges. Though diminished in amplitude, the same stream-function perturbation exists at t = 39.36 as had been visible at t = 29.28; see Fig. 74.

A few Alfvén transit times before the second kinetic energy peak, a helical filament clearly has formed once again, in the same region as the t = 29.28 filament had been. The stream function perturbation, unchanged in sign, has grown in amplitude; these features are apparent at t = 54.72, Fig. 75.

The disruptive process described in this section is a repetitive one, with each subsequent burst of activity qualitatively much like the first. The enveloping amplitude of the perturbed field weakens as the simulation proceeds, however. It is likely that highly regular and uniform "sawtooth" bursts of disruptive activity may require plasma processes not included in the Strauss approximation.

C. $B_o = 2.4$, $\eta(x,y) = [\ 350 * \exp\{\ -(x - \pi/2)^2 - (y - \pi/2)^2\}\ ]^{-1}$.

In the simulations, CASES 4 and 5, only a small central region of the magnetofluid is exposed to a resistivity of O(0.01) or less. In order to establish that the small central region of variable resistivity in CASES 4 and 5 is not a stabilizing factor which enforces the long period of nearly steady-state solutions with flow, in the inviscid CASES 4 and 5, we perform an additional driven, inviscid simulation, on a 64 * 64 * 32 grid, with $\eta_{max} = 1 / 350$, and $\bar{\eta}(\text{center}) = \frac{4}{N^2} \sum_{x,y=\frac{N}{4}+1}^{\frac{3N}{4}} \eta(x,y) = 0.00447$. As in CASES 4 and 5, we take the safety factor $Q(x = \pi/2,\ y = \pi/2,\ t = 0) \doteq 0.6 = 2\ B_o / j(x = \pi/2,\ y = \pi/2,\ t = 0)$; we choose $B_o = 2.4$, and $j(t = 0) = 8 \exp\{\ -(x - \pi/2)^2 - (y - \pi/2)^2\}$.

The driving term E_o balances $\eta(x,y) * j(x,y,t = 0)$ at all internal points, with a value of 8 / 350.

Selected globals for this simulation, CASE 6, are shown in Fig. 76. These globals indicate that, following an initial burst of disruptive activity at about t = 30, a quasi steady-state with flow, similar to the states attained by the driven, inviscid CASES 4 and 5, is achieved. Contours at t = 39.24, Fig. 77, display the dominant velocity field pattern. At this time, the current density is peaked along the center line of the stream function perturbation. Only one magnetic axis may be inferred from Poincaré traces of magnetic field lines in the $z = \pi$ plane; samples of traces at t = 39.24 are shown in Fig. 78.

The stream function perturbation apparent near t = 39 continues to dominate the $k_z = 1$ spectrum. The largest stream function modes in the $k_z = 1$ band, averaged over a period of time from t = 57.48 to t = 60.06 are found to be

$$\psi(k_z = 1) = -5.6\times10^{-2}\,[\sin 2x \sin y \cos z + \sin x \sin 2y \sin z] + 3.2\times10^{-2}\,[\sin x \sin 2y \cos z - \sin 2x \sin y \sin z]$$

Similarly, the largest vector potential modes in the $k_z = 1$ band, likewise averaged over a period of computational time from t = 57.48 to t = 60.06 are:

$$A(k_z = 1) = 6.2\times10^{-2}\,[\sin 2x \sin y \cos z + \sin x \sin 2y \sin z] + 1.1\times10^{-2}\,[\sin x \sin 2y \cos z - \sin 2x \sin y \sin z]$$

Employing the notation used in the sixth chapter, these perturbations may be re-written:

$$\psi' = \beta\,[-\epsilon f - \delta g]$$
$$A' = \alpha\,[-\delta f + \epsilon g]$$

for $\delta(4)/\epsilon(4) = -0.57143$ and $\delta(A)/\epsilon(A) = -0.56364$. The δ/ϵ ratios average to $\delta/\epsilon = -0.567$. Further, $-\beta\epsilon = -0.056$, or $\beta(\epsilon) = 0.0644$, while $-\beta\delta = 0.032$, or $\beta(\delta) = 0.0649$; the experimental values for β differ by only about 0.8%. Similarly, $-\alpha\delta = 0.0062$, which yields $\alpha(\delta) = 0.0126$, and $\alpha\epsilon = 0.011$, which also gives $\alpha(\epsilon) = \alpha(\delta) = 0.0126$. These perturbations are thus of a type for which the low order model is applicable.

From the simulation described in this section, it is clear that the combination of an increased grid size and a consequent smaller $\bar{\tau}_1$ does not alter the basic driven, inviscid scenario observed in CASES 4 and 5.

VIII. DISCUSSION

Much effort has been devoted to the experimental and numerical study of disruptive activity in current-carrying magnetofluids. Results from relevant experiments, and from earlier computations, are summarized in the first chapter. In this chapter, after a brief comparison of the results reported in this work with results from prior numerical studies, the applicability of our results to experimental observation is addressed. Possible future directions will then be suggested.

A. Summary.

Almost every previous work considered employed some form of external driving. Surprisingly, not only our driven results, reported in the seventh chapter, but also our free decay results, reported in the fifth chapter, agree somewhat with the driven, single helicity calculations of Waddell, et al (1976) and the driven three-dimensional results of Sykes and Wesson (1976). In all three simulations, "m = 1, n = 1" disturbances are observed to grow. Waddell, et al (1976), only follow one flattening of the current, while the simulation of Sykes and Wesson (1976) generates repetitive expulsions of the q = 1 surface from the plasma. In our simulations, we also observe quasi-cyclic repetition of the activity; in the free-decay, constant resistivity simulations, the activity repeats on nearly Alfvénic timescales, while in the driven, variable resistivity simulations, the period of the disturbance is in general much longer.

Although Waddell, et al (1979) also perform simulations with the Strauss equations, their choice of a flat, initial q-profile, as opposed to the strongly-varying ones employed here, makes their computations apparently incom-

mensurable with ours. The electric-field dependent results of Bishamp and Welter's (1963) simulations are not exactly comparable with ours, since our reported simulations employ no "constant current" driving mechanism. Finally, it is difficult to correlate results from these simulations with simulations in which different aspect ratio expansions are emphasized.

One major difference which separates this work from previous simulations is the values here chosen for the Lundquist number. We employ no "radial smoothing", nor do we use any "mode selection" for numerical stability or reasonable temporal evolution of spatial profiles. The Strauss equations are simulated by means of an undistorted, three dimensional grid in Fourier space, in which all modes dynamically accessible are available to the time-dependent solutions, and many are active. Except where clearly indicated, our results are well-converged numerical solutions to the posed problem, with unrestricted initial conditions.

In summary, we find that qualitative features of disrupting, bounded, current-carrying magnetofluids can be studied by efficient (0.7 sec./timestep on the CRAY1 at 32 * 32 * 16 resolution) pseudospectral computation, in the presence of resistive, free-slip boundary conditions. Appropriate initial conditions are thought to be current and magnetic field profiles which have current maxima in the center of the channel (but which are not analytic equilibria) plus small amounts of random noise broadly distributed in Fourier space. From such conditions, which relax quickly toward nearly quiescent equilibria, a single disruptive event can develop and complete its evolution in relatively few Alfvén transit times and in far less than large-scale resistive decay times. These events are characterized by helical concentrations of "m = 1, n = 1" current and vorticity. Even in the unforced problem, the disruptive process is

observed to be cyclic, on an Alfvén timescale, with repeated bounces of the kinetic energy as a function of time. Results from the linearized Strauss equations, reported in the second appendix, agree with the nonlinear ones for a few Alfvén transit times, then diverge significantly from the disruptive, nonlinear results. A low order truncation model of the Strauss equations, described in the sixth chapter, is found to contain some of the quasi-cyclic and steady features the large-scale simulations exhibit, but much of the interesting dynamical systems behavior of this model is apparently unparalleled in the large-grid results. The inclusion of an external electric field and variable resistivity in the inviscid, large-grid simulations give rise to an initial disruptive event which is much like the ones observed in the undriven simulations, followed by a nearly steady-state situation with flow, which survives for tens of Alfvén transit times. The addition of a viscous damping term to the equation of motion leaves the initial event basically unaltered. Viscosity tends to damp the generated flow, and, following the initial burst of disruptive activity, pronounced subsequent bounces in global quantities as a function of time occur in driven, viscous simulations.

A quantitative comparison of these results with the experimental observations of disruptive activity is unrewarding. One reason for this is that our simulations represent idealized situations, without features which may affect observed time scales and signal size, such as compressibility, toroidicity, a vacuum region surrounding the plasma, uneven walls, limiters, with which the plasma interacts chemically, and gas puffing. Another reason is that while values of Lundquist number were chosen to insure numerically accurate solutions to the Strauss model as a function of time, they are far less than those represented in Table 1, for current generation fusion devices; the enhanced values of diffusion used here may lead to a less pronounced separation of large-scale

resistive decay and Alfvén transit timescales than exists experimentally. Qualitative comparison, however, is instructive.

The free-decay, quasi-cyclic oscillations occur in the absence of forcing, and with a marked generation of small-scale turbulent structure at the periphery of the current column. Several workers, notably DuBois, et al (1983), and Lichtenberg (1984), have suggested that turbulence in the neighborhood of the reconnection region is responsible for incomplete reconnection of the m = 1 evolution. Our simulation results agree with the hypothesis that turbulence is generated in the neighborhood of the separatrix. Also, the quasi-cyclic nature of the disruptive activity in the decay simulations indicate that helical "m = 1, n = 1" structures exist throughout the event, i.e. Kadomtsev's (1975) suggestion of a symmetric state evolving after a single disruptive bounce, is not realized in our simulations. It is possible, then, that the quasi-cyclic activity observed in the free decay simulations is similar in nature to the post-disruptive "m = 1, n = 1" activity reported by Sauthoff, et al (1979), from experimental PLT data.

Further, the inclusion of strong driving in the simulations can generate repeated bounces on timescales which are not incompatible with the timescales of repetitive sawteeth (von Goeler, et al (1974)); in both situations, the timescales are longer than Alfvenic timescales but shorter than the large-scale resistive times. Our driving mechanism is imposed at every grid point, rather than only being allowed to resistively diffuse inward. We thus neglect many effects the turbulence might have on the driving mechanism. The addition of a viscous damping term also reduces the level of generated small-scale spatial structure. Here, although a small post-bounce is generally observed in the inviscid, driven simulations, only isolated events are seen in the viscous,

driven runs. Our driven simulations thus could simulate disruptive activity in a less turbulent magnetofluid, one in which repeated, quasi-cyclic attempts at reconnection are not dominant.

B. Directions for Further Work.

In order to observe dynamic cascade behavior of simulated equations, turbulence researchers have added small, external forcing terms to the solved equations (for example, Fyfe, et al (1977), Bossain, et al (1983)), to overcome the strongly damping effects of necessarily large diffusion coefficients. Attempts to include such forcing terms in the sine-Strauss code have met with failure. No damping exists in the z-direction, in the Strauss equations. Instead, the action of the strong external field $b_0 \hat{e}_z$ is depended upon to restrict nonlinear development in that direction. We have found that banded small scale forcing terms generate much nonlinear development in all three allowed directions, and resolution is quickly lost in the z-direction. Hence, to observe important dynamical behavior of the MHD equations in Strauss-like geometry, with current generation computers, it will be necessary to solve the full 3-d MHD equations, with Strauss-like conditions and natural dissipation in all three directions. Small-scale random forcing terms may then be added, with simulation resolution not exceeded.

A parallel study using a low order model like the one proposed in the sixth chapter, would be appropriate for sufficiently Strauss-like three-dimensional conditions. A small-scale, random driving term added to the equation for the stream function perturbation could simulate the poloidal small-scale structure with $k_z = 1$ dependence that is generated in the neighborhood of the reconnection region, and would lead to a means of exploring what effects very small scales could have on the largest modes available to the system.

The clearest extension of the large-grid simulations reported in this work to full three-dimensionality would be to perform simulations with a code which employs a set of expansion functions that reduce to the ones used here. Such a set has been proposed by Turner (1984). Upon the generation of this code, the question of how an inverse cascade of the magnetic helicity may effect disruptive behavior (Montgomery (1982)) could be accurately explored.

APPENDIX A

TWO-DIMENSIONAL NUMERICAL EXPERIMENTS:

SPECTRAL VERSUS PSEUDOSPECTRAL SIMULATION

A. Introduction to the Simulation Problem.

When turning to a digital computer as an aid in the understanding of a physical process, it is necessary to select a numerical method of solution of the modelling equations as carefully as the equations themselves were chosen. Spurious results may otherwise be obtained, or even no results at all.

Several factors are generally considered when creating a numerical algorithm, among them efficiency, accuracy and stability. Although accuracy is the most crucial of the three, stability, or the lack thereof, is possibly the first one approached when trying out a new method. If the correctly programmed numerical method is totally and explosively unstable, no reliable physical insights can ever be obtained from a simulation which employs this algorithm.

The consequences of simulating the two-dimensional MHD equations, both spectrally and pseudospectrally, is the subject of this appendix. A further categorization, that of representing the nonlinear terms in two numerically different ways, is introduced. By means of simulation, it will be found that when the equations are pseudospectrally solved in a form which does not conserve energy, the simulation is a spectacularly numerically unstable one. However, when the equations are again solved in their fully aliased, or pseudospectral representation, in a way which numerically conserves the total energy of the system, the solutions are quite well-behaved. It is further de-

monstrated that when a suitable amount of dissipation is introduced into the the system, the conservation-form pseudospectral method again yields stable results. These results are found to agree well with those generated by a code which is fully spectral, a code in which all aliasing errors have been removed.

B. The System of Equations Used to Demonstrate the Problem.

As an illustration of the influence the algorithm chosen has on a simulation, consider the numerical solution of the two dimensional MHD equations for vorticity and vector potential, computationally time advanced in the following form (A-1).

$$\text{(a)} \quad \frac{\partial \omega}{\partial t} = \nabla \cdot (-\underline{v}\omega + \underline{B} j) + \nu \nabla^2 \omega$$

(A-1)

$$\text{(b)} \quad \frac{\partial A}{\partial t} = \nabla \cdot (-\underline{v} A) + \eta \nabla^2 A$$

These equations are a special case of the Strauss equations, discussed in Chapter II. They may be obtained from the Strauss equations by setting the external magnetic field, B_0 to zero, and allowing no z-variation in ω or A. For convenience, the definitions of the now two-dimensional variables used are repeated here. Let the vorticity ω be given by $\omega \hat{e}_z = \nabla \times \underline{v} = \nabla^2 \psi \hat{e}_z$, for $\underline{v}$, the solenoidal velocity field, and $\psi = \psi(x, y, t)$, the scalar stream function. Also, let $A = A(x, y, t)$ be the vector potential, from which the solenoidal, self-consistent magnetic field, $\underline{B} = \nabla \times A \hat{e}_z$, and the current density, $j \hat{e}_z = \nabla \times \underline{B} = \nabla^2 A \hat{e}_z$, may be obtained. The same set of dimensionless units as were used in the body of the work are used here.

The geometry of these simulations will be any horizontal plane of the full three-dimensional domain described in chapter 2. As there, walls bound the fluid in x and in y. For the runs described in this appendix, the strictly

two-dimensional magnetofluid is confined to a square in the x,y plane with sides of length π. The boundary conditions imposed are those appropriate for rigid, free-slip, perfectly conducting walls, namely, the vector potential and stream function vanish at the walls, as does the current density. Three quadratic constants of the motion exist for the two-dimensional MHD equations (A-1): total energy, $E = \frac{1}{2V_{ol}} \int d^2x \, (v^2 + B^2)$; mean square vector potential, $\mathcal{A} = \frac{1}{2V_{ol}} \int d^2x \, A^2$; and cross helicity, $P = \frac{1}{2V_{ol}} \int d^2x \, \underline{v} \cdot \underline{B}$ (Fyfe and Montgomery, 1976). In the following, focus will be on the total energy as a useful diagnostic.

C. Particulars of the Method Employed.

The spatial and temporal dimensions are essentially different in nature. A boundary value problem is posed in space, while in time, the conditions are those of an initial value problem. The derivatives in these dimensions are thus treated differently. First, consider the time derivatives.

The time-stepping chosen is identical to that used in the main simulation code, described in Chapter IV. Let $\frac{\partial u}{\partial t} = f$, where u would be either or A, and and f(u) then would represent the right hand sides of (A-1) (a) or (b). The second order Runge-Kutta, or Heun, method employed is

$$u^{n+1/2} = u^n + \frac{\Delta t}{2} f(u^n)$$

$$u^{n+1} = u^n + \Delta t \, f(u^{n+1/2})$$

where n is the time index, and Δt is the timestep. This method is numerically unstable when applied to a linear advection equation, as can be seen by performing von Neumann analysis on the model linear equation

$$\frac{\partial u}{\partial t} = U_0 \frac{\partial u}{\partial x} + \eta \frac{\partial^2 u}{\partial x^2}$$

with η set to zero (Hossain, 1983). The weak instability can be removed by a suitable choice of η (Dahlburg, Montgomery and Matthaeus, 1985). This is a time stepping method which has previously been successfully employed even for absolute equilibrium studies of equations (A-1), Galerkin simulations in which both diffusivities are set to zero (Pyfe, Joyce and Montgomery, 1977).

Basis functions are used for the spatial dimensions of the simulation, real Fourier sine series in both the x and y directions. The velocity stream function and the magnetic vector potential are expanded in these half-range Fourier series in both x and y. This corresponds to imposing the desired free slip, rigid wall boundary conditions on the velocity field, and perfectly conducting boundary conditions on the magnetic field. Spatial derivatives are taken spectrally, in the sine-Fourier space. Specifically, a physical-space quantity is transformed to the sine-Fourier space. Its coefficients are then multiplied by the appropriate power of wave number, and the result is returned to physical space by means of a half-range cosine series for a first derivative, and a half-range sine series when two derivatives are taken.

For instance, in one dimension, let

$$\psi(x_j) = \sum_{k=1}^{N-1} \tilde{\psi}_k \sin(kx_j), \qquad x_j = \pi j/N, \quad j = 1, \ldots, N-1$$

may be represented on $(0, 2\pi)$ by means of a full complex Fourier series:

$$\Psi(x_j) = \sum_{k=-N/2}^{N/2-1} \tilde{\Psi}_k \exp[ikx_j] \qquad x_j = \frac{2\pi j}{N}, \quad j = 0, \ldots, N-1$$

$$(x_j = \pi \text{ for } j = N/2)$$

The sine series representation for Ψ is recovered if the real part of $\tilde{\Psi}$ is zero, $\tilde{\Psi}_r(-k) = -\frac{1}{2}\tilde{\Psi}_k$, and the reality condition is imposed, so that $\tilde{\Psi}_r(-k) = +\frac{1}{2}\tilde{\Psi}_k$.

A derivative of the full complex series is taken in the following way:

$$\frac{\partial \psi(x_j)}{\partial x_j} = \sum_{k=-M/2}^{M/2-1} ik\, \Psi_k \left[\cos(kx_j) + i \sin(kx_j)\right]$$

For the Ψ previously defined, $\Psi_{ik} \neq 0$, $\Psi_{rk} = 0$, it is seen that the reality condition implies that only the cosine series survives

$$\frac{\partial \psi(x_j)}{\partial x_j} = -\sum_{k=M/2}^{M/2-1} k\, \Psi_k \cos(kx_j)$$

or, using the equivalence between Ψ and $\tilde{\Psi}$ set forth above,

$$\frac{\partial \psi(x_j)}{\partial x_j} = \sum_{k=1}^{N-1} k\, \tilde{\Psi}_k \cos(kx_j)$$

Similarly, one can obtain

$$\frac{\partial^2 \psi(x_j)}{\partial x_j^2} = -\sum_{k=1}^{N-1} k^2\, \tilde{\Psi}_k \sin(kx_j)$$

Product terms may also be considered.

$$\psi(x_j)\,\xi(x_j) = \sum_{k=1}^{N-1} \tilde{\Psi}_k \sin(kx_j) \sum_{\ell=1}^{N-1} \tilde{\xi}_\ell \sin(\ell x_j)$$

$$= \sum_m \phi_m \cos(mx_j)$$

implies $\dfrac{\partial}{\partial x_j}(\psi\xi) = -\sum_{k=1}^{N-1} k\, \phi_k \sin(kx_j)$

Let

$$\psi(x_j) = \sum_{k=-M/2}^{M/2-1} \Psi_k\, e^{ikx_j}, \quad \xi(x_j) = \sum_{\ell=-M/2}^{M/2-1} \xi_\ell\, e^{i\ell x_j}$$

where again only the imaginary parts of the Fourier coefficients are nonzero.

A fully aliased sum is obtained for $\sum_{k\ell} \tilde{\Psi}_k \tilde{\xi}_\ell \sin(kx_j) \sin(\ell x_j)$

$$\longrightarrow \quad \sum_{k,\ell} \Psi_k e^{ikx_j} \xi e^{i\ell x_j} = \sum_{k,\ell} \Psi_k \xi_\ell e^{ix_j(k+\ell)}$$

$$= \sum_{k,\ell} (i\Psi_k)(i\xi_\ell) e^{ix_j(k+\ell)}$$

$$= -\sum_{k,\ell} \Psi_{ik} \xi_{i\ell} (\cos[(k+\ell)x_j] + i \sin[(k+\ell)x_j])$$

$$= -\sum_{k,\ell} \Psi_{ik} \xi_{i\ell} \cos[(k+\ell)x_j]$$

implies an aliased sum $\sum_m \varphi_m \cos mx_j$.

That is, for the reality condition to be met, only the cosine part of the full complex series survives. The derivative of this product will bring down an "ik" from the exponential argument; again a sine series is obtained, by the reality condition.

A parallel argument demonstrates that

$$V\xi = \sum_k \tilde{v}_k \cos(kx_j) \sum_\ell \tilde{\xi}_\ell \sin(\ell x_j)$$

$$= \sum_{m=1}^{N-1} \varphi_m \sin(mx_j)$$

where the complex Fourier series coefficient for V would be real, only, with $V_r(k) = +V_r(-k)$.

For later reference, we note here that dealiasing the product terms is a simple matter: pad the complex Fourier coefficients with zeroes from -M/2-1 to -M and M/2 to M-1 when transforming an array to physical space to make a product (Orszag, 1971). From the conversion previously shown, it is clear that padding the sine coefficients with zeroes from N to 2N implies that the equivalent exponential coefficients are suitably padded with zeroes, and that a

dealiased sum will result.

D. Illustrative Numerical Experiment Runs Performed.

1. Without Dissipation; Diffusivities = 0.

The method chosen, the proposed series of numerical experiments is now embarked upon, beginning with what should be a simple numerical exercise. For this first simulation, RUN A1, the fully aliased sums are used, and the the equations are advanced with the spatial parts written in the form (A-1). With $\nu = \eta = 0$, $\Delta t = 1/250$, and the arbitrary initial conditions, the sine-Fourier coefficients

$$\tilde{A}_{3,1} = -0.4, \qquad \tilde{A}_{2,2} = 0.5, \qquad \tilde{A}_{3,5} = 4/34$$

and

$$\tilde{\omega}_{2,3} = \tilde{\omega}_{1,1} = -\tilde{\omega}_{7,8} = -\tilde{\omega}_{4,2} = 4,$$

all other sine-Fourier coefficients zero. The code is set into motion. Within only about 40 timesteps, a catastrophic instability, of the numerical variety, has forced the simulation to halt, by generating numbers too large for a computer to deal with. This explosion is demonstrated in a plot of total energy versus time, in Figure A1. It is apparent from this plot alone that no use can be made of any results which come from the equations numerically solved in this fashion.

Cures for this blow-up of energy do exist. One cure is to dealias the nonlinear product terms which appear in equations (A-1). Dealiasing is effected, as described above, by padding the Fourier coefficients with zeroes from $k_x, k_y = N$ to $2N$ when transferring the arrays to physical space to make the product terms, and then time advancing the returned products in the $k_x, k_y = 1, \ldots, N-1$ sine-Fourier space. A dealiased run, RUN A2, which starts

with the same initial conditions and parameters as were used in the fully aliased RUN 1, yield startlingly different results. Figure A2a shows a plot of the very well-behaved total energy versus time, while Figures A2b and A2c show plots of the kinetic energy ($E_V = \frac{1}{2V_0} \int d^2x\, v^2$) versus time, and the magnetic energy ($E_B = \frac{1}{2V_0} \int d^2x\, B^2$) versus time, respectively. Figures A2b and A2c establish that variation does exist in quantities other than the total energy. The solutions change much as a function of time, as Figures A2d through A2g show. Figure A2d is a Fourier space contour plot of $\tilde{\omega}_2(t=0)$, and A2e is a Fourier space contour plot of $\tilde{A}_2(t=0)$. Figures A2f and A2g are Fourier space contour plots of $\tilde{\omega}_2(t=8.76)$, and $\tilde{A}_2(8.76)$ respectively; these Fourier coefficients have evolved from those depicted in Figures A2d and A2e.

Results exactly identical to RUN A2 may be obtained by solving the equations (A-1) in the form

$$\text{(a)} \quad \frac{\partial \omega}{\partial t} = \nabla \cdot (-\underline{v}\,\omega + \underline{B}\,j) + \nu \nabla^2 \omega$$

(A-2)

$$\text{(b)} \quad \frac{\partial A}{\partial t} = \underline{v} \times \underline{B} \cdot \hat{e}_z + \eta \nabla^2 A$$

with the product terms dealiased as they were in RUN A2. That the time evolution of the Fourier coefficients of this run, RUN A3, is identical is most easily visualized by comparing Figure A3a, of $\tilde{\omega}_3(t=8.76)$, with Figure A2f, and Figure A3b, of $\tilde{A}_3(t=8.76)$, with Figure A2g, to observe that the evolving Fourier coefficients are indistinguishable.

When the appended zeroes are removed, however, and the same parameters and initial conditions are used, for RUN A4, the explosive aliasing instability (Phillips, 1959) is found to be absent. Instead, the solutions are very well-behaved, as is demonstrated by plots of total energy versus time, (Fig. A4a), kinetic energy versus time, (Fig. A4b), and magnetic energy versus time (Fig.

A4c). The instability observed in RUN A1 was thus removed by writing the time-advanced equations in a form (Zang, 1982) which semi-conserves total energy pseudospectrally. That is, ignoring any discretization errors, form (A-2) enforces numerical conservation of energy. The solutions are thus bounded as a function of time, and the simulation may be run for tens of units of time.

2. Dissipative; Diffusivities = 1/50.

It is of more physical interest to study a dissipative system. The simulations described above are now repeated, with finite amounts of viscosity and resistivity.

Repeating RUN A1 in RUN A5, where now $\nu = \eta = 0.02$, but all else is the same as above, it is seen that a reasonable amount of diffusion is insufficient to stabilize the aliasing instability. Plots of total energy versus time, (Fig. A5a), kinetic energy versus time, (Fig. A5b), and magnetic energy versus time, (Fig. A5c), demonstrate the solutions' lack of circumspection; the coefficients can only be time-advanced for a uselessly short interval.

As before, dealiasing effects the cure. RUN A6 is the same as RUN A2, except that $\nu = \eta = 0.02$. Here the solution behaves well as a function of time, as may be seen in Figures A6a, A6b, and A6c, which are plots of total energy versus time, magnetic energy versus time, and kinetic energy versus time, respectively. Figures A6d and A6e are physical space contour plots of the initial conditions for ω and A used throughout, while Figure A6f is a physical space contour plot of $\omega_6(t=0.76)$, and Figure A6g is a physical space contour plot of $A_6(t=0.76)$.

Repeating RUN A3 with $\nu = \eta = 0.02$, in RUN A7, establishes the fact that the equations may be dissipatively solved in either form (A-1) or in form (A-2). Identical results are obtained so long as the product terms are solved for on

the grid expanded for dealiasing. This may be easily observed by comparing the solutions $\omega_7(x,y,t=8.76)$ in Figure A7a with ω_6 of Figure A6f, and $A_7(x,y,t=8.76)$ in Figure A7b with A_6 of Figure A6g.

Expensive dealiasing may be avoided altogether, and the simulation still retain integrity, as RUN A8 demonstrates. RUN A8 is the repeated RUN A4, with $\nu = \eta = 0.02$. Plots of total energy versus time, (Fig. A8a), kinetic energy versus time, (Fig. A8b), and magnetic energy versus time, (Fig. A8c), compare well with the globals plotted in Figures A6a, A6b, and A6c. The solutions $\omega_8(t=8.76)$, (Fig. A8d), and $A_8(t=8.76)$, (Fig. A8e), are also physically similar, as can be observed by comparing Figures A6f and A6g with Figures A8d and A8e. The slight differences are less than a cell size in dimension; such plotting discrepancies may be expected.

This agreement allows the conclusion that the more economical pseudospectral method is a valid, and valuable technique for simulating the MHD equations. When the equations are numerically time-advanced in the form which conserves energy pseudospectrally, form (A-2), the nonlinear, or aliasing instability is removed. Ignoring time discretization errors, the solutions then remain bounded. Adding a sufficient amount of dissipation to the problem generates the additional result that the solutions produced by the conservation form pseudospectral scheme are seen to agree quite well with truly spectral solutions. Similar agreement was found in simulations of the two-dimensional Navier-Stokes equation (Orszag, 1972; Fox & Orszag, 1973).

APPENDIX B

SIMULATION OF THE LINEARIZED STRAUSS EQUATIONS WITH CASE 2 PARAMETERS

If we linearize equations (9) and (10) about a zeroth order state $A^{(0)}$, $\underset{\sim}{B}_{\perp}^{(0)}$ and $j^{(0)}$ (with finite values of $\Psi^{(0)}$, $\underset{\sim}{v}_{\perp}^{(0)}$ and $\omega^{(0)}$ allowed) the results for the perturbation fields is

(a) $$\frac{\partial \omega^{(1)}}{\partial t} = \nabla_{\perp} \cdot \left(\underset{\sim}{B}_{\perp}^{(0)} j^{(1)} + \underset{\sim}{B}_{\perp}^{(1)} j^{(0)} - \underset{\sim}{v}_{\perp}^{(0)} \omega^{(1)} - \underset{\sim}{v}_{\perp}^{(1)} \omega^{(0)} \right) + B_0 \frac{\partial j^{(1)}}{\partial z}$$

(B - 1)

(b) $$\frac{\partial A^{(1)}}{\partial t} = - \underset{\sim}{v}_{\perp}^{(1)} \cdot \nabla_{\perp} A^{(0)} - \underset{\sim}{v}_{\perp}^{(0)} \cdot \nabla_{\perp} A^{(1)} + B_0 \frac{\partial \Psi^{(1)}}{\partial z} + \eta \nabla_{\perp}^2 A^{(1)}$$

The zeroth order state $A^{(0)}$, $\underset{\sim}{B}_{\perp}^{(0)}$, $j^{(0)}$, with $\Psi^{(0)}$, $\underset{\sim}{v}_{\perp}^{(0)}$ and $\omega^{(0)}$, may either be allowed to participate in the dynamics according to

(a) $$\frac{\partial \omega^{(0)}}{\partial t} = \nabla_{\perp} \cdot \left(\underset{\sim}{B}_{\perp}^{(0)} j^{(0)} - \underset{\sim}{v}_{\perp}^{(0)} \omega^{(0)} \right)$$

(B - 2)

(b) $$\frac{\partial A^{(0)}}{\partial t} = - v_{\perp}^{(0)} \cdot \nabla_{\perp} A^{(0)} + \eta_0 \nabla_{\perp}^2 A^{(0)}$$

or may be approximated by setting η_0 to zero. In the latter case we shall refer to the zeroth order state $j^{(0)}$, $A^{(0)}$, $\underset{\sim}{B}_{\perp}^{(0)}$, $\Psi^{(0)}$, $\omega^{(0)}$ and $\underset{\sim}{v}_{\perp}^{(0)}$ as being "frozen", and in the former case, we shall say the zeroth order state is "thawed".

Only the frozen problem, because of the time-dependent zeroth-order coefficients in equations (B - 1)a,b for the thawed case, leads to a sharply defined linear eigenvalue problem with a well-defined temporal growth rate. For very high values of S (low η), the decay predicted by equation (B - 2)b will be sufficiently slow that the distinction between the frozen and thawed linearized

problems should be unimportant. But for the situation simulated, we find that our values of S are low enough that $A^{(0)}$, $\underset{\sim}{B}_{\perp}^{(0)}$, $j^{(0)}$, $\psi^{(0)}$, $\underset{\sim}{v}_{\perp}^{(0)}$ and $\omega^{(0)}$ alter significantly during the times of interest. Thus there are two more-or-less relevant linearized problems.

Since we wish to initialize the linear simulations with conditions from the nonlinear run CASE 2, we must first determine the extent to which the magnetofluid has relaxed to something that can reasonably be called an "equilibrium" state by, say, t = 1.74. This offers the most natural candidates for $A^{(0)}$, $\underset{\sim}{B}_{\perp}^{(0)}$, and $j^{(0)}$ and we form them from the total contributions from the $k_{\neq} = 0$ components only of magnetic quantities at t = 1.74. Zeroth order parts of $\psi^{(0)}$, $\underset{\sim}{v}_{\perp}^{(0)}$ and $\omega^{(0)}$ are initialized in this way, also, by, for instance, setting the almost negligible $\omega(t = 1.74, k_{\neq} = 0)$ equal to $\omega^{(0)}$. The extent to which these conditions represent an equilibrium is tested in the following manner.

We return to the primitive MHD variables, solve the Poisson equation for the pressure p, obtain the velocities, and compute the individual terms in the equation of motion. The question becomes the extent to which the remaining terms compare in magnitude from point to point with the magnitudes of those in the approximate equilibrium relation $\nabla_{\perp} p - \underset{\sim}{j} \times B_{\perp} \simeq 0$. The departure from equilibrium is systematically estimated by volume averaging the absolute values of each term in the zeroth order equation of motion. We find that $\nabla_{\perp} p$ and $\underset{\sim}{j} \times \underset{\sim}{B}_{\perp}$ typically have magnitudes of O(1) separately, and the other terms in the equation of motion typically have magnitudes of $O(10^{-4})$ at t = 1.74, a time near the first minimum of the kinetic energy. Thus we conclude that to a satisfactory approximation, the plasma has relaxed to an equilibrium state by this time.

The zeroth order initial conditions now determined, we choose the first or-

der quantities to parallel further the dynamics of the nonlinear run as closely as possible. We initialize the perturbation fields $\psi^{(0)}$, $v_\perp{}^{(0)}$, $\omega^{(0)}$, $A^{(0)}$, $\underset{\sim}{B}_\perp{}^{(0)}$ and $j^{(0)}$ from $k_z = 1$ components of their nonlinear counterparts at $t = 1.74$. Constant parameters agree with those of the nonlinear run CASE 2, also: $B_0 = 4.3$, $\eta = 0.01$, and $k_{y_{max}} = k_{x_{max}} = 32$. Both frozen and thawed runs share these conditions. In addition, for the thawed run, $\eta_0 = 0.01$, while for the frozen run, $\eta = 0.0$.

Upon time-advancing these conditions, we find that the linear perturbation energies follow the nonlinear $k_z = 1$ component of the energies for only a few Alfvén transit times, as may be seen in Fig. B1. Fig. B1a shows the $k_z = 1$ component of the kinetic energy for the frozen, thawed and nonlinear runs, while Fig. B1b displays the $k_z = 1$ component of the magnetic energy for all three cases. In both a and b, the frozen run's perturbation energies are represented by short dashed lines, the thawed linear run's perturbation energies are drawn with unbroken lines, and the nonlinear $k_z = 1$ components of the energies are traced with long dashed lines. The linear frozen run diverges from the nonlinear one first. Each perturbation energy of the frozen run grows exponentially, settling into a constant growth rate of 0.7, where we approximate a instantaneous growth rate γ from the relation energy$(t + \Delta t)$ = energy$(t) * \exp[2\gamma \Delta t]$, for each perturbed field. The thawed linear run follows its nonlinear counterpart for a somewhat longer time. As the disruptive activity strengthens, the results of the linear, thawed and nonlinear runs conclusively part company.

Figures B2 and B3 show contours from the three runs at the same time, t(nonlinear) = 8.82; each of Figs. B2 and B3 contains contour plots from all three runs. These contours clearly show the extent to which the linear runs' solutions are no longer comparable to those of the nonlinear case. For both linear

runs, plotted are the zeroth order quantities to which their full perturbations have been added.

Slices in the $z = \pi$ planes of vector potential A are shown for the nonlinear run in Fig. B2a; for the linear frozen run in B2c; and for the linear thawed run in B2e. Though the linear frozen vector potential is somewhat more askew than the vector potential contours of the other two cases, all three are similar. Since the vector potential depends most strongly on the larger scales present in the simulation, reflected in the similarity is the agreement of all three runs at the largest spatial scales. More differences may be seen by comparing modal magnetic energy spectra, plotted to the same scale, in Fig. B2 b, d and e.

Figures B3 a and b are current contours in the $z = \pi$ and $y = \pi / 2$ planes from the nonlinear run; Figs. B3 c and d are identical current slices at the same time from the linear frozen run; and Figs. B3 e and f are the same current cross-sections from the linear thawed run. Multiplying this additional factor of $k_\perp$ to the compared quantities affords us an even better glimpse at the differences among the three simulations. As might be expected, the linear frozen run's current is totally unlike that of the other two runs, with large regions of negative current growing near the center of the channel. Though the current of the linear thawed run is free of such large negative bubbles, it, too is quite kinked, and peaked off axis. The nonlinear run's current, at this same time, has flattened and broadened into a wide channel in which many Fourier modes are present. We thus draw the conclusion that it is only the presence of many nonlinearly active Fourier coefficients of higher wave numbers which generate the full scenario of the disruptive activity.

APPENDIX C

RESULTS FROM AN UNDRIVEN SIMULATION WITH CASE 4 PARAMETERS

The conditions and parameters of the simulations described in this appendix are those of CASE 4: the safety factor $Q(x = \pi/2,\ y = \pi/2,\ t = 0) \simeq 0.6 \approx 2\ B_0\ /\ j(\pi/2,\ \pi/2,\ t = 0)$, and a 32 * 32 * 16 grid is used. The current profile varies as the inverse of the resistivity profile, so that $\eta(x,y) * j(x,y,t = 0) =$ constant for all interior points. Both the external electric field and the viscous damping are ignored here; hence, the dominant features ought to agree with those observed in CASES 1, 2 and 3.

For purposes of numerical accuracy, it is crucial that the average value of the resistivity in regions of magnetofluid activity not be much less than $(4 * k_{y_{max}})^{-1}$, as was discussed in the fourth chapter. On the other hand, numerical stability of the 2nd order Runge-Kutta time-stepping as applied to the diffusion term of equation (10) demands that η approach O(1) as a maximum value, for a time-step of about 1/500 of an Alfvén transit time. This dual requirement on the value of η constrains the profiles considered for $1/\eta$, and consequently for j; current density profiles with fairly gentle slopes must be chosen, in order to allow η to vary as $1/j(t = 0)$ over most of the computational box. This requirement implies that the high wavenumber magnetic modes are less excited, initially, than they were in CASES 1, 2 and 3.

Since the time derivative of the vorticity varies as $\underset{\sim}{B}_\perp \cdot \nabla j$, a more gently sloped current profile can lead to a slower temporal variation of ω. The initial value of the poloidal magnetic energy is nearly the same here as it is for the fifth chapter's CASES 1, 2 and 3, with identical velocity field initializa-

tion, and $\frac{4}{N^2}\sum_{i,j=N/4+1}^{3N/4}\eta(x_i,y_j)=0.00867$. However, the disruptive activity in this run tion, and $\frac{4}{N^2}\sum_{i,j=N/4+1}^{3N/4}\eta(x_i,y_j)=0.00867$. However, the disruptive activity in this time for CASE 2 of about 6.9. Recall that the simulation of CASE 2 was stopped at a computational time of 17.52, because a near-equilibrium situation was attained. The energy in this simulation, by t ~ 20, is also much reduced. Hence, it is difficult to compare post-disruptive activity between CASE 2 and this run. Although not much quasi-cyclic behavior is observed in this run after the initial burst of activity, indications that the general features of this simulation agree with those observed in CASES 2 and 3 may be found.

This run differs considerably from the forced CASE 4 run, discussed in the seventh chapter, as may be seen in Fig. C1. Fig. C1a is a comparison plot of the total magnetic energy in the two inviscid CASE 4 runs. While the total magnetic energy in the unforced run decays by more than 60%, the total magnetic energy in the inviscid driven CASE 4 only decays by about 10% during the same period. The first burst of disruptive activity also takes place at different times, as may be inferred from a time history of kinetic energy, in Fig. C1b.

However, as the contour plots in Fig. C2 show, the initial burst of activity is much like its counterparts in all the cases discussed. This burst is characterized by the appearance of a helical current filament which wraps itself about the line ($x = \pi/2$, $y = \pi/2$, z). This magnetic activity is accompanied by the formation of a counter-rotating pair of bean-shaped stream function lobes which generate a velocity field that points across the center of the poloidal cut, toward the region of maximum current density. Near the time of the kinetic energy maximum, the current filament has virtually disappeared, with the current cross section becoming broad and flat, as may be seen in the contours at t = 20.64, Fig. C3.

Following this burst, the velocity field apparently attempts to reverse

itself, as may be seen at t = 23.52, in Fig. C4.

Contours at t = 40.00, Fig. C5, display current cuts which indicate excitation of oppositely signed magnetic perturbations; the regions of maximum current are everywhere opposite to where they were at t = 28.64. An extremely low amplitude stream function pattern indicates that regions with reversed flow likewise exist.

In conclusion, then, the general features of disruptive activity observed in this simulation are compatible with those of CASES 1, 2 and 3.

BIBLIOGRAPHY

Alfven, H. and Falthammar, C., "Cosmical Electrodynamics." Oxford University Press (1965).

Aydemir, A. Y., Barnes, D. C., Caramana, E., Mirin, A., Nebel, R., Schnack, D. and Sgro, A., LANL Preprint 84-3050 (1984).

Aydemir, A. Y. and Barnes, D. C., J. Comp. Phys., Vol 53, 100, and references therein (1984).

Bateman, G., Schneider, W. and Grossmann, W., Nucl. Fusion, Vol 14, 669 (1974).

Bateman, G., "MHD Instabilities." Cambridge, MIT Press (1978).

Bender, C. M. and Orszag, S. A., "Advanced Mathematical Methods for Scientists and Engineers." McGraw-Hill, New York (1978).

Bickerton, R. J., in "Theory of Magnetically Confined Plasmas, 1977." (eds. Coppi, B., Stringer, T., Pozzoli, R., Sindoni, E., Carnihan, J. P., Leotta, G. G.) Pergammon Press, New York (1979).

Biskamp, D., in "Physics of Plasmas Close to Thermonuclear Conditions, 1979." Vol 1, (eds. Coppi, B., Leotta, G. G., Pfirsch, D., Pozzoli, R. and Sindoni, E.) Pergammon Press, New York (1981).

Biskamp, D. and Welter, H., in "Plasma Physics and Controlled Nuclear Fusion Research 1982." (IAEA, Vienna), Vol 3, 373 (1983).

Book, D. L., "NRL Plasma Formulary." Naval Research Laboratory, Washington, D.C. (1980).

Braginskii, S. I., in "Reviews of Plasma Physics." Vol 1, (ed. Leontovich, M. A.) Consultants' Bureau, New York, 205 (1965).

Caramana, E. J., Nebel, R. A. and Schnack, D. D., Phys. Fluids, Vol 26, 1305 (1983).

Carreras, B. A., Hicks, H. R., Holmes, J. A. & Waddell, B. V., Phys. Fluids, Vol 23, 1811 (1980).

Carreras, B. A., Hicks, H. R. & Lee, D. K., Phys. Fluids, Vol 24, 66 (1981).

Chen, F. F., "Introduction to Plasma Physics." Plenum Press, New York (1974).

Cooley, J. W., Lewis, P. A. & Welch, P. D., J. Sound Vib., Vol 12, 315 (1970).

Cooley, J. W. and Tukey, J. W., Math. Comp., Vol 19 297 (1965).

Coppi, B., Galvao, R., Pellat, R., Rosenbluth, M., and Rutherford, P., Fiz. Plazmy, Vol 2, 961 (1976).

Curry, J. H., Herring, J. R., Loncaric, J. and Orszag, S., J. Fluid Mech., Vol. 147, 1 (1984).

Dahlburg, J. P., Montgomery, D. and Matthaeus, W. H., to appear in J. Plasma Physics (1985).

Dahlburg, R. B., Zang, T. A., Montgomery, D. and Hussaini, M. Y., Proc. Natl. Acad. Sci. USA, Vol 80, 5790 (1983).

Dahlquist, G., Bjorck, A. & Anderson, N., "Numerical Methods." Prentice-Hall, Englewood Cliffs, NJ (1974).

Diamond, P. H., Hazeltine, R. D., An, Z. G., Carreras, B., and Hicks, H. R. Phys. Fluids, Vol 27, 1449 (1984).

Dnestrovskii, Y. N., Lysenko, S. E. & Smith, R., Sov. J. Plasma Phys., Vol 3, 9 (1977).

Dubois, M. A., Pecquet, A. L. and Reverdin, C., Nucl. Fusion, Vol 23, 147 (1983).

Edery, D., Laval, G., Pellat, R. and Soule, J. L., Phys. Fluids Vol 19, 268 (1976).

Fyfe, D. & Montgomery, D. J. Plasma Phys., Vol 16, 181 (1976).

Fyfe, D., Montgomery, D. & Joyce, G. J. Plasma Phys., Vol 17, 369 (1977).

Fox, D. A. & Orszag S. A., J. Comp. Phys., Vol 11, 612 (1973).

Gill, R. D., in "Plasma Physics and Nuclear Fusion Research." (ed. Gill, R. D.) Academic Press, New York, 551 (1981).

Gottlieb, D. & Orszag, S. A., " Numerical Analysis of Spectral Methods: Theory and Applications." Society for Industrial and Applied Mathematics, 170 pages, Philadelphia (1977).

Hicks, H. R., Carreras, B., Holmes, J. A., Lee, D. K. and Waddell, B. V., J. Comp. Phys., Vol 44, 46 (1981).

Hicks, H. R., Carreras, B., Holmes, J. A., Lynch, V. E., Nucl. Fusion, Vol 22, 117 (1982).

Hicks, H. R., Carreras, B. A., Garcia, L. & Holmes, J. A., "The Reliability of Initial Value MHD Calculations of Tokamak Disruptions," Oak Ridge Nat'l Lab. preprint ORNL/TM-9127 (1984).

Hossain, M., Ph.D. dissertation, William and Mary (1983).

Hossain, M., Matthaeus, W. H. and Montgomery, D., J. Plasma Phys., Vol 30, 479 (1983).

Hussaini, M. Y., Streett, C. L. & Zang, T. A., ICASE NASA Contractor Report 172248, 61 pages (1983).

Hutchinson, I. H., Phys. Rev. Lett., Vol. 37, 338 (1976).

Izzo, R., Monticello, D. A., Strauss, H. R., Park, W., Manickam, J., Grimm, R. C. and DeLucia, J., Phys. Fluids, Vol 26, 3066 (1983).

Jahns, G. L., Soler, M., Waddell, B. V., Callen, J. D., and Hicks, H. R., Nucl. Fusion, Vol 18, 609 (1978).

Kadomtsev, B. B., Sov. J. Plasma Phys., Vol 1, 389 (1975).

Kadomtsev, B. B., in "Plasma Physics and Controlled Fusion." Vol 26, 217 (1984).

Kraichnan, R. H., Phys. Fluids, Vol 8, 1385 (1965).

Kruskal, M. D., Johnson, J. L., Gottlieb, M. B. and Goldman, L. M., Phys. Fluids, Vol 1, 421 (1958).

Lichtenberg, A. J., Nucl. Fusion, Vol 24, 1277 (1984).

Lorenz, E. N., J. Atmos. Sci., Vol 20, 130 (1963).

Magar, G., in "Plasma Physics and Nuclear Fusion Research." (ed. Gill, R. D.) Academic Press, New York, 539 (1981).

Manheimer, W. M. and Lashmore-Davies, C., "MHD Instabilities in Simple Plasma Configuration." Naval Research Laboratory, Washington, D.C. (1984).

Montgomery, D., in "Proc. U.S.-Japan Workshop on 3-d MHD Studies for Toroidal Devices." (B. A. Carreras, Ed.) Oak Ridge National Lab. Report CONF-811010, Oak Ridge TN. pp. 32-50 (1981).

Montgomery, D., Physica Scripta T2/1, 83 (1982).

Montgomery, D., in "Solar Wind Five." (ed. Neugenbauer, M.) NASA Conference Publication 2280, 107 (1983).

Morton, A. H., Nucl. Fusion, Vol 16, 571 (1976).

Orszag, S. A., Stud. Appl. Math, Vol 51, 253 (1972).

Phillips, N. A., in "The Atmosphere and the Sea in Motion."

Rockerfeller Institute Press, New York, pp 581-584, (1959).

Robinson, D. C., invited lecture at the Latin-American Workshop on Plasma Physics and Controlled Nuclear Fusion, Cambuqira, Minas Gerais, Brazil (1982).

Rutherford, P., Nucl. Fusion, Vol 20, 1086 (1980).

Sauthoff, N. R., von Goeler, S., Eames, D. R. and Stodiek, W. in "Symposium on Current Disruptions in Toroidal Devices." (eds. Lackner, K. and Zehrfeld, H. P.) Proc. IAEA, Garching (1979).

Schnack, D. D., Baxter, D. C., & Caramana, E. J., "A pseudo-spectral algorithm for three-dimensional magnetohydrodynamic simulation," Science Applications, Inc., report SAI#2383-477LJ/APPAT-14; submitted to J. Comp. Phys (1983).

Shafranov, V. D., Sov. Phys-Tech. Phys., Vol 15, 175 (1970).

Shebalin, J. V., Matthaeus, W. H. and Montgomery, D., J. Plasma Physics, Vol 29, 525 (1983).

Spitzer, L. "Physics of Fully Ionized Gasses." Interscience Publishers, New York (1962).

Strauss, H. R., Phys. Fluids, Vol 19, 134 (1976).

Sykes, A. and Wesson, J. A., Phys. Rev. Letters, Vol 37, 140 (1976).

Temperton, C., J.Comp.Phys., Vol 52, 1 (1983).

Turner, L., private communication (1984).

von Goeler, S., Stodiek, W. and Sauthoff, N., Phys. Rev. Lett., Vol. 33, 1201 (1974).

Waddell, B. V., Rosenbluth, M. N., Monticello, D. A. and White, R. B., Nucl. Fusion, Vol 16, 528 (1976).

Waddell, B. V., Carreras, B., Hicks, H. R., Holmes, J. A. and Lee, D. K., Phys. Rev. Lett., Vol 41, 1386 (1978).

Waddell, B. V., Carreras, B., Hicks, H. R. and Holmes, J. A., Phys. Fluids, Vol 22, 896 (1979).

Wakatani, M., Shirai, S., Tsushi, H., Kaneko, H., Motojima, O., Obiki, T., Iiyoshi, A., Uo, K., Nucl. Fusion, Vol 23 1669 (1983).

Wesson, J. A., in "Plasma Physics and Nuclear Fusion Research." (ed. Gill, R. D.) Academic Press, New York, 191 (1981).

White, R. B., in "Handbook of Plasma Physics." (Vol 1, eds. Galeev, A. N. and Sudan, R. N.) North-Holland Publishing Company (1983).

Zang, T. A., private communication (1982).

Table 1. Representative Tokamaks; from Bickerton (1977)

REPRESENTATIVE TOKAMAKS

DEVICE	COUNTRY	R_0 (cm)	a(cm)	B_ϕ(KG)	Ip (kA)	q	Air or Iron Core	Stabilising Shell Yes or No
T-3	USSR	100	17	25	100	4	Iron	Yes
T-4	USSR	100	17	50	200	4	Iron	Yes
ORMAK	USA	80	23	18	200	2.9	Iron	Yes
ST	USA	109	13	40	130	2.4	Iron	Yes
ATC	USA	66-35	17-11	20-50	80-200	4.1	Air	No
TFR	FRANCE	98	20	50	300	4.1	Iron	Yes
PULSATOR	FRG	70	17	28	80	3.6	Iron	Yes
ALCATOR	USA	54	9.5	75	100	6	Air	Yes
DITE	UK	112	23	28	200		Iron	No
PLT	USA	130	40	35(46)	600	3.6	Air	No
T-10	USSR	150	37	35(50)	400		Iron	Yes
DOUBLET IIA	USA	66	35x100	8	140	6.5	Air	No
TOSCA	UK	30	10		25		Air	No
JFT-2	JAPAN		25	18	150			Yes
DIVA	JAPAN				15		Iron	Yes
FT	ITALY	83	21	100	1000		Air	Yes
PDX	USA	140	45	50	500		Air?	No
ASDEX	FRG	154	40	30	500		Air	No
DOUBLET III	USA	140	45x150	26(42)	3500(5000)		Air	No
JET	EUROPE	296	125x210	27	2800		Iron	No
TFTR	USA	248	85	52	7500		Air	No
JT60	JAPAN	300	100	50	3000		Air	No
T-20	USSR	500	200	30	5000		Iron	Yes

Table 2. Parameters and Timescales for Representative Tokamaks

MACHINE	ST	ORM	PULS	TFR	ALC	ATC	PLT
minor radius / major radius	1.1×10^{-1}	2.9×10^{-1}	1.6×10^{-1}	2.0×10^{-1}	1.8×10^{-1}	1.9×10^{-1}	3.1×10^{-1}
toroidal magnetic field (gauss)	3.5×10^{4}	1.8×10^{4}	2.7×10^{4}	4×10^{4}	5.5×10^{4}	1.5×10^{4}	3.5×10^{4}
safety factor, q(edge)	5.3	3.7	4.7	4 1	8.7	3.2	3 6
number density, n_e	6.5×10^{12}	2×10^{13}	7×10^{13}	2.4×10^{13}	4.7×10^{13}	2.1×10^{13}	2.6×10^{13}
electron temperature	8.7×10^{2}	1.2×10^{3}	7.5×10^{2}	1.9×10^{3}	6×10^{2}	7×10^{2}	1.3×10^{3}
ion temperature (ev)	2×10^{2}	3.4×10^{2}	3×10^{2}	8.2×10^{2}	3.2×10^{2}	2×10^{2}	1.2×10^{3}
energy confinement time τ_E (sec)	2.6×10^{-3}	9×10^{-3}	6.5×10^{-3}	8.1×10^{-3}	1.4×10^{-2}	1.1×10^{-2}	4×10^{-2}
IN CGS UNITS:							
σ_1, electron conductivity	1.3×10^{17}	2.1×10^{17}	1.1×10^{17}	4.1×10^{17}	8×10^{16}	9.5×10^{16}	4.2×10^{17}
η_{i1}, ion viscosity$_1$	1×10^{-11}	2.7×10^{-10}	1.6×10^{-9}	5.5×10^{-11}	1.8×10^{-10}	5.7×10^{-9}	6.0×10^{-11}
η_{i3}, ion viscosity$_3$	3.1×10^{-6}	2.6×10^{-5}	6.5×10^{-5}	4.1×10^{-5}	2.4×10^{-6}	2.3×10^{-5}	9.9×10^{-5}
D_m, magnetic diffusion	5.5×10^{2}	3.4×10^{2}	6.4×10^{2}	1.7×10^{2}	8.4×10^{2}	7.3×10^{2}	1.7×10^{2}
ρ, mass density	1.1×10^{-11}	2.3×10^{-11}	1.2×10^{-10}	4.9×10^{-11}	8.7×10^{-11}	3.5×10^{-11}	4.2×10^{-11}
V_A, Alfven speed	6.2×10^{7}	6.8×10^{7}	2.4×10^{7}	8.7×10^{7}	3.5×10^{7}	4.3×10^{7}	1.5×10^{8}
τ_R, resistive decay time	2.6×10^{-1}	1.6	1.9×10^{-1}	2 3	1×10^{-1}	3.9×10^{-1}	1 3
τ_A, Alfven transit time	1.8×10^{-6}	1.2×10^{-6}	2.9×10^{-6}	1×10^{-6}	1.5×10^{-6}	2.0×10^{-6}	1×10^{-6}
S, Lundquist number	1.5×10^{5}	1.3×10^{6}	6.5×10^{4}	2.1×10^{6}	6.5×10^{4}	1.9×10^{5}	1.3×10^{6}
P_{m1}, $[\eta_{i1}/\rho]$ / D_m	1.8×10^{-3}	2.3×10^{-2}	2.1×10^{-2}	7.9×10^{-3}	7.4×10^{-3}	2.2×10^{-2}	8×10^{-2}
P_{m3}, $[\eta_{i3}/\rho]$ / D_m	5.2×10^{2}	3.2×10^{3}	8.7×10^{2}	5.9×10^{3}	3.3×10^{2}	9×10^{2}	1.3×10^{4}

Table 3. Largest k = 1 Mode Coefficients, CASE 2

POR	t	τ	υ	φ	χ	ϵ/δ	% dif. from avg.
ψ'	6.6	-2.43×10^{-3}	-7.27×10^{-3}	-7.28×10^{-3}	2.55×10^{-3}	2.92	3.8
A'		5.25×10^{-3}	-2.01×10^{-3}	-1.82×10^{-2}	-5.28×10^{-3}	2.76	1.9
ψ'	7.8	-5.43×10^{-3}	-9.46×10^{-3}	-9.46×10^{-3}	3.55×10^{-3}	2.71	3.7
A'		3.07×10^{-3}	-1.12×10^{-3}	-1.02×10^{-3}	-3.09×10^{-3}	2.88	2.4
ψ'	8.82	-3.11×10^{-3}	-8.9×10^{-3}	-8.92×10^{-3}	3.14×10^{-3}	2.85	1.3
A'		-1.93×10^{-3}	5.97×10^{-4}	7.42×10^{-4}	1.91×10^{-3}	2.90	3.1
ψ'	10.98	1.48×10^{-3}	3.74×10^{-3}	3.91×10^{-3}	-1.53×10^{-3}	2.95	5.3
A'		-2.20×10^{-3}	7.32×10^{-4}	8.09×10^{-4}	2.21×10^{-3}	2.57	2.0
ψ'	12.90	-1.31×10^{-4}	4.72×10^{-4}	-4.67×10^{-4}	1.31×10^{-4}	3.41*	
A'		1.67×10^{-3}	-5.45×10^{-4}	-6.21×10^{-4}	[illegible]	2.75	1.2

Avg 2.81$\bar{3}$

where $4\left(\frac{\epsilon}{\delta}\right)_\psi = \frac{2\varphi_\psi}{2\tau_\psi} - \frac{2\varphi_\psi}{2\chi_\psi} + \frac{2\upsilon_\psi}{2\tau_\psi} - \frac{2\upsilon_\psi}{2\chi_\psi} = \frac{-\beta\epsilon}{-\beta\delta} - \frac{-\beta\epsilon}{+\beta\delta} + \frac{-\beta\epsilon}{-\beta\epsilon} - \frac{-\beta\epsilon}{+\beta\epsilon}$

$4\left(\frac{\epsilon}{\delta}\right)_A = -\frac{2\tau_A}{2\varphi_A} + \frac{2\chi_A}{2\varphi_A} - \frac{2\tau_A}{2\upsilon_A} + \frac{2\chi_A}{2\upsilon_A} = \frac{\alpha\epsilon}{-\alpha\delta} + \frac{-\alpha\epsilon}{-\alpha\delta} - \frac{\alpha\epsilon}{\alpha\epsilon} + \frac{-\alpha\epsilon}{-\alpha\delta}$

for
$2\tau(t)$ = coefficient of sin(x) sin(2y) cos(z)
$2\upsilon(t)$ = coefficient of sin(2x) sin(y) cos(z)
$2\varphi(t)$ = coefficient of sin(x) sin(2y) sin(z)
$2\chi(t)$ = coefficient of sin(2x) sin(y) sin(z)

* separate values almost zero, since near local minimum in E_ψ; ignore this one.

Table 4. Chart of Sample Low-order Model Runs

Fig.	B_0	Q_0	a	η	α	β	ν	
46	3	7.66̄	6.66̄	.01	1.0327456	2.5819889	0	Solution spirals away from initial (critical) point.
47	3	1.66̄	6.66̄	.001	1.0327456	2.5819887 $\times 10^{-3}$	0	Solution spirals away from initial (critical) point.
48	3	7.66̄	6.66̄	1×10^{-5}	1.0327456	2.5819889 $\times 10^{-5}$	0	A cycle is traced; note that the IC's (and $-\alpha$, $-\beta$) are critical points.
49	3	7.99̄	6.66̄	1×10^{-5}	1.0327456	2.5819887 $\times 10^{-5}$	0	Increased forcing, with all other conditions like 48, generate a cycle.
50	3	7.99̄	5.55̄	1×10^{-5}	1.0327456	2.5819887 $\times 10^{-5}$	0	Lowering both forcing and $Q(t=0)$ from 5# => cycle.
51	3	7.99̄	6.6	1×10^{-5}	1.0327456	2.5819887 $\times 10^{-5}$	0	Raising both the forcing and $Q(t=0)$ makes cycle like 48.
52	3	4	4	.01	0.01	1	0	Note approach to the point β = constant = 1, α = #, a critical point.
53	3	4	4	.01	0.01	1	.01	Adding viscosity to IC's of 53 change the critical point: β = #
54	3	5	4.0027857	.01	1.2635701	0.7984706	.01	Solution spirals away from initial (critical) point.
55	4	6	5	.01	4.472136 $\times 10^{-2}$	4.472136 $\times 10^{-2}$	.05	Behavior indicating presence of Lorenz-like attractor is seen.

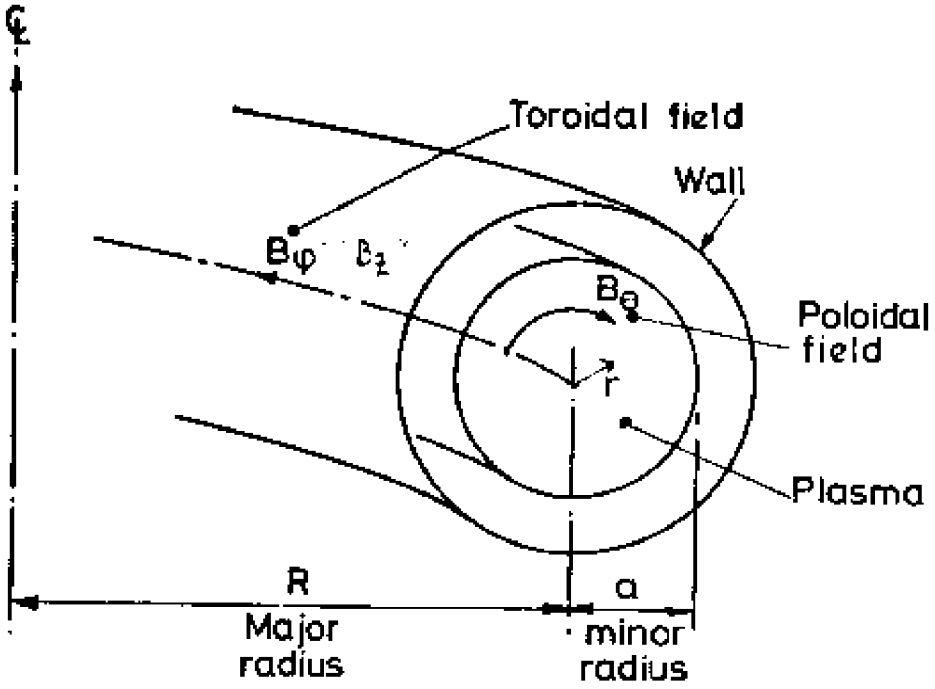

Fig. 1a. Fields and co-ordinates used to define a toroidal pinch.

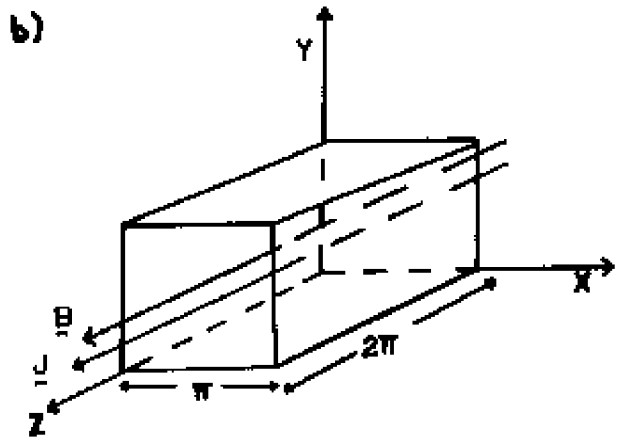

Figure 1. - Geometry: (a) fields and co-ordinates used to define a toroidal pinch; from Robinson (1982), and (b) simulation geometry.

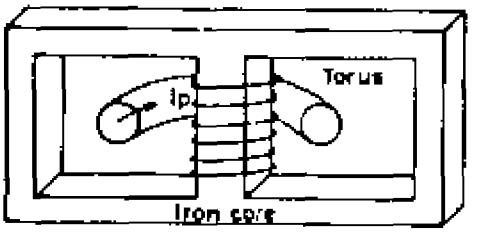

(a) General arrangment

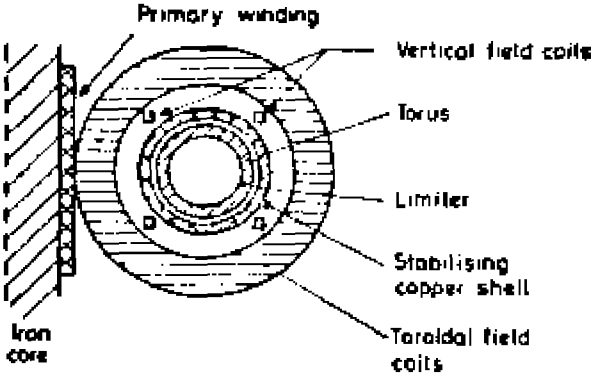

(b) Meridional cross-section

Figure 2. - Standard disposition of coils and vacuum vessel for a toroidal pinch: (a) general arrangement, and (b) meridional cross-section; from Robinson (1982).

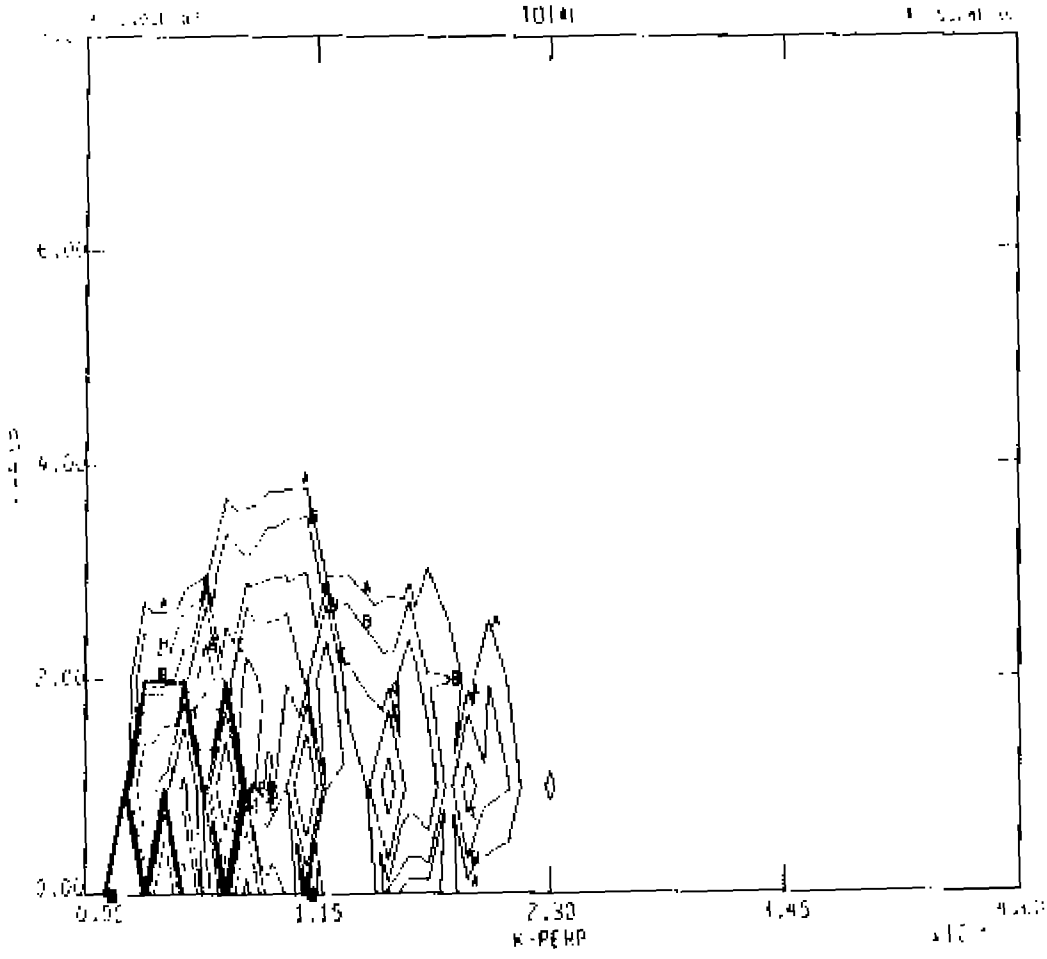

Figure 3. - Contour plot of total modal energy for: (a) CASE 2,

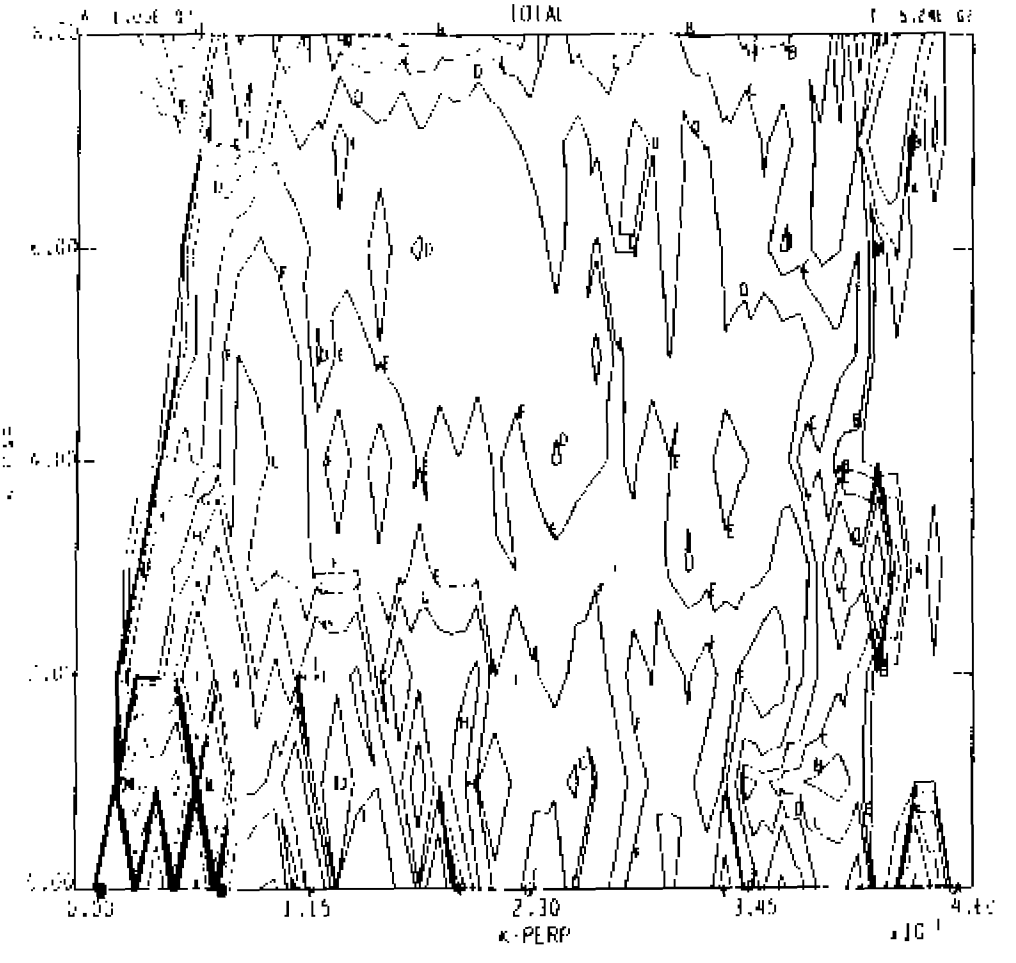

3 (b) discarded run.

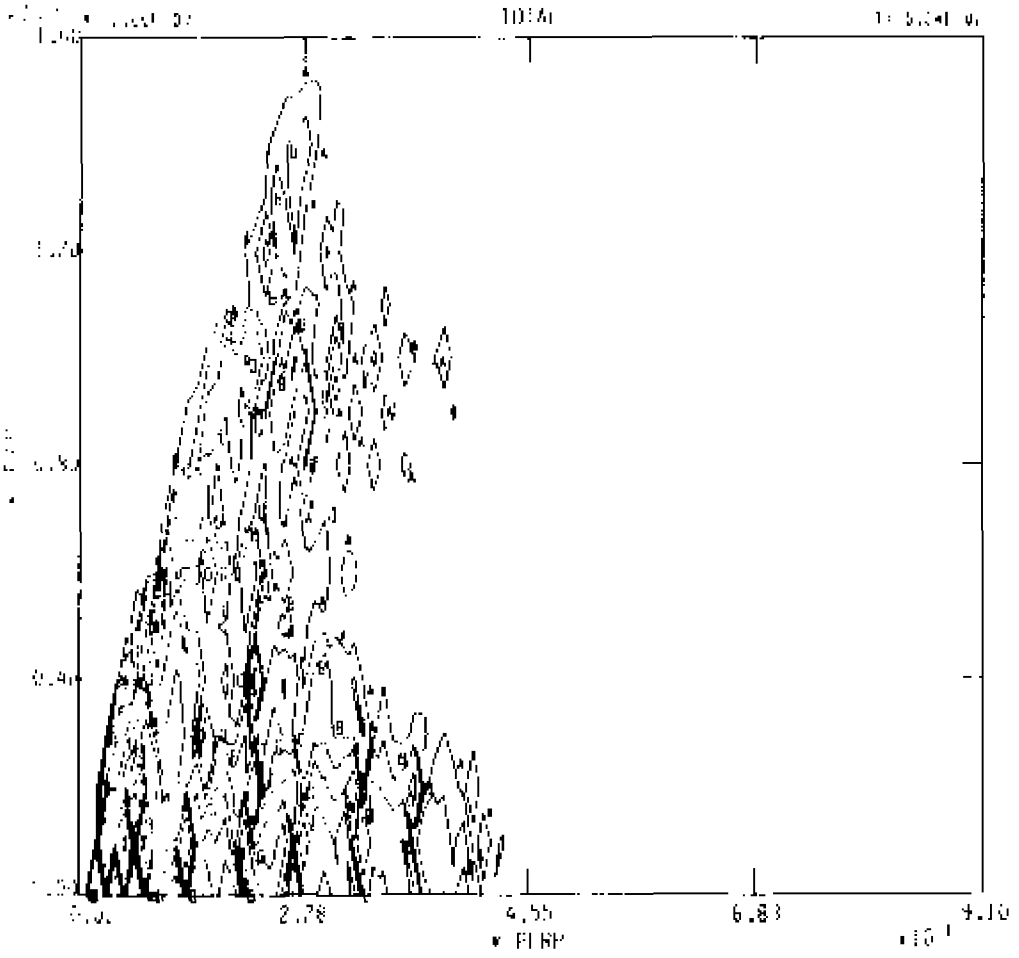

and 3 (c) CASE 3, where

	(a)	(b)	(c)
k_x	32	32	64
k_y	32	32	64
k_z	8	8	16
η	0.01	0.002	0.0025
t_{max}	8.52	13.14	14.76

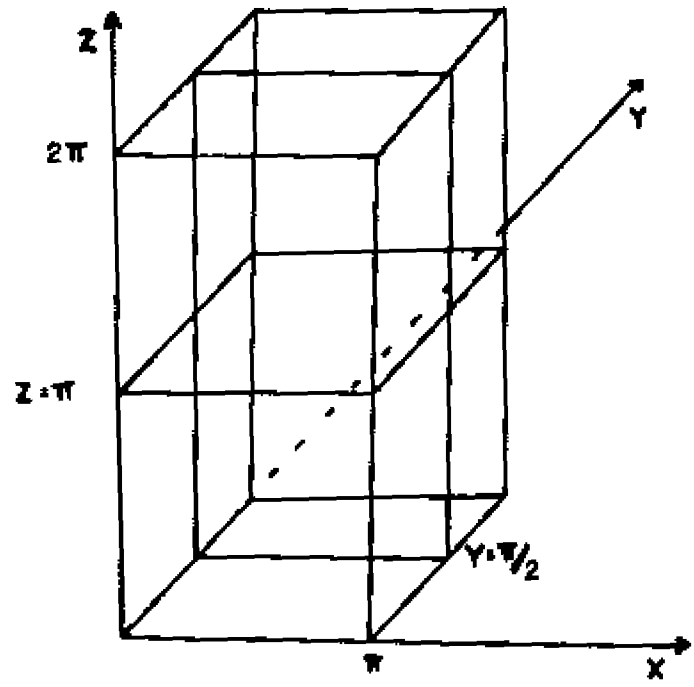

Figure 4. - Poloidal and toroidal "cuts" in the computational box. The poloidal cut is taken at $z = \pi$, and the toroidal cut is a slice at $y = \pi/2$.

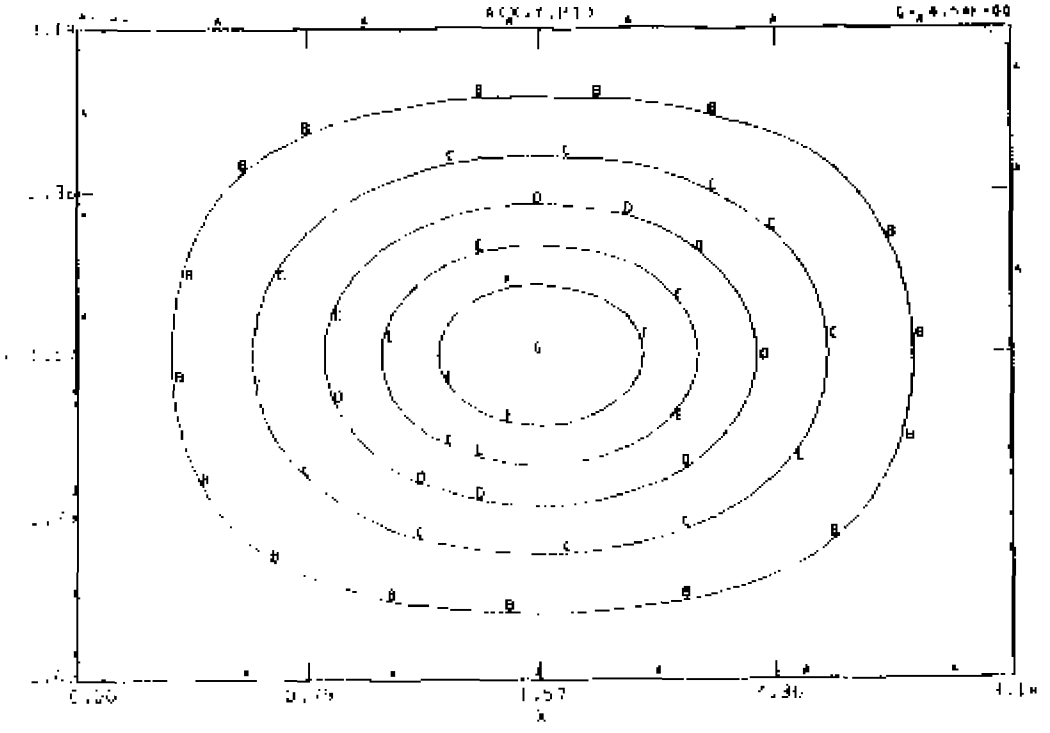

Figure 5. - Contour plots at t = 0 of initial conditions for the decay runs.
5 (a): contours of A = constant, poloidal cut.

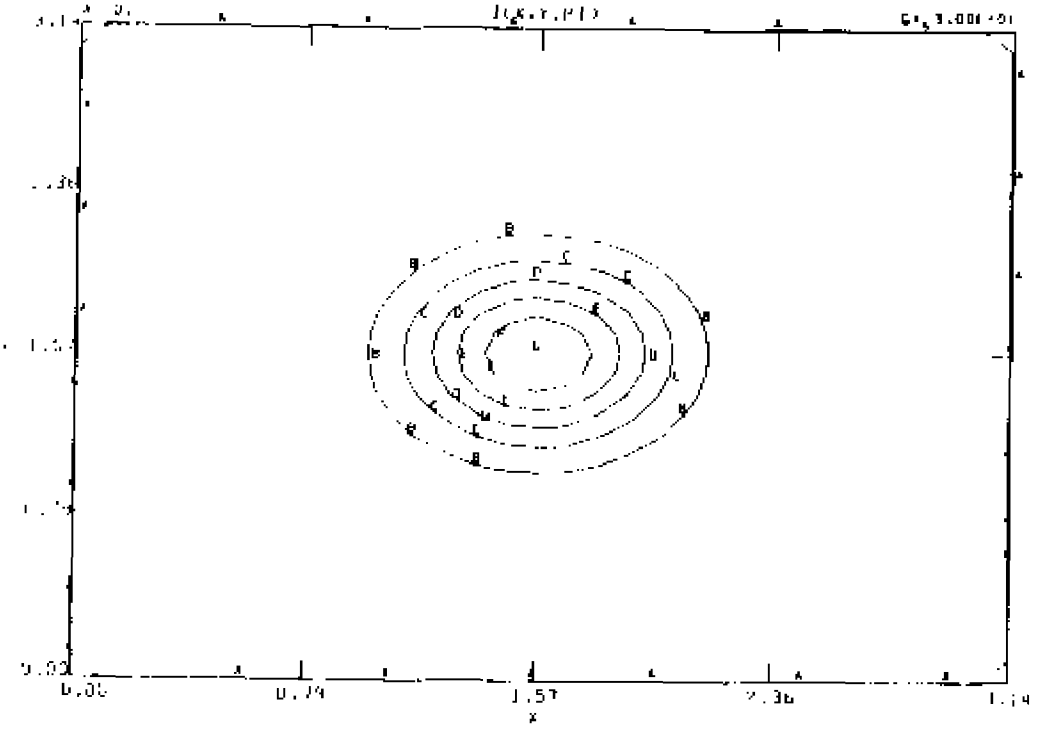

5 (b): contours of j = constant, poloidal cut.

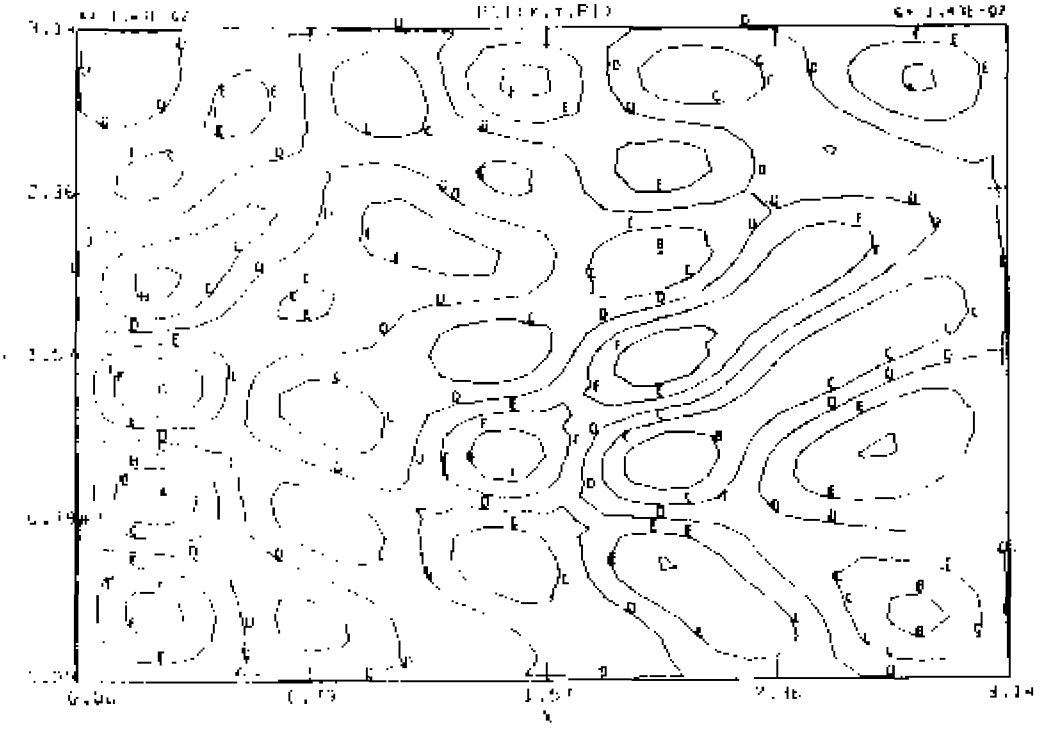

5 (c): contours of Ψ = constant, poloidal cut.

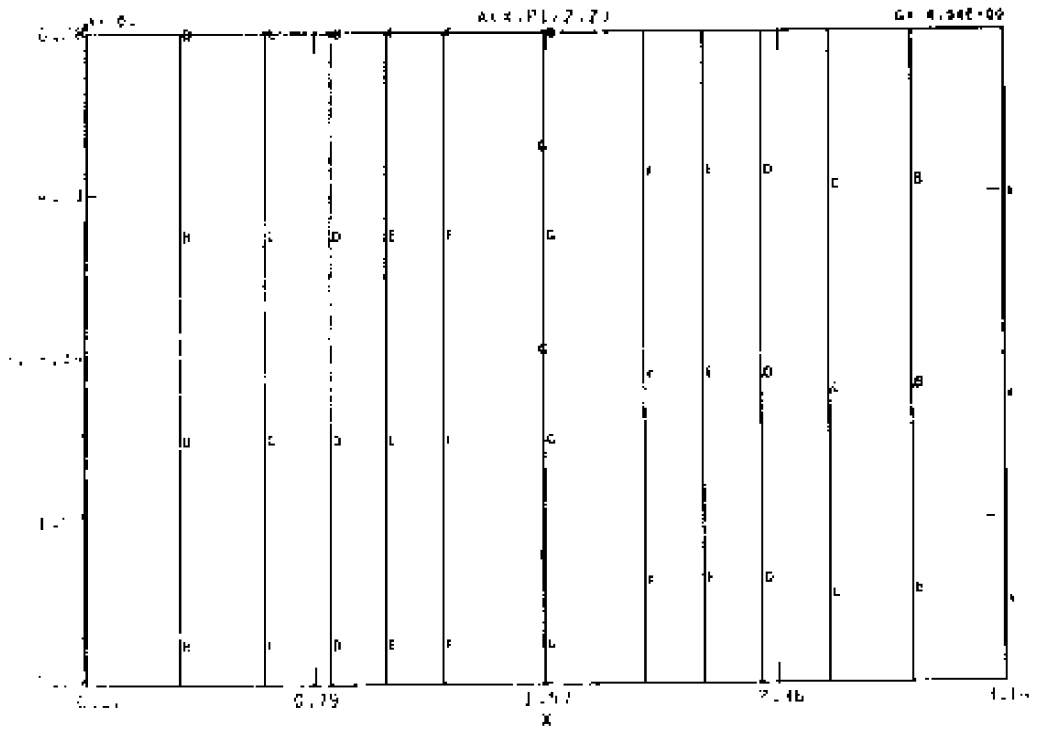

5 (d): contours of A = constant, toroidal cut.

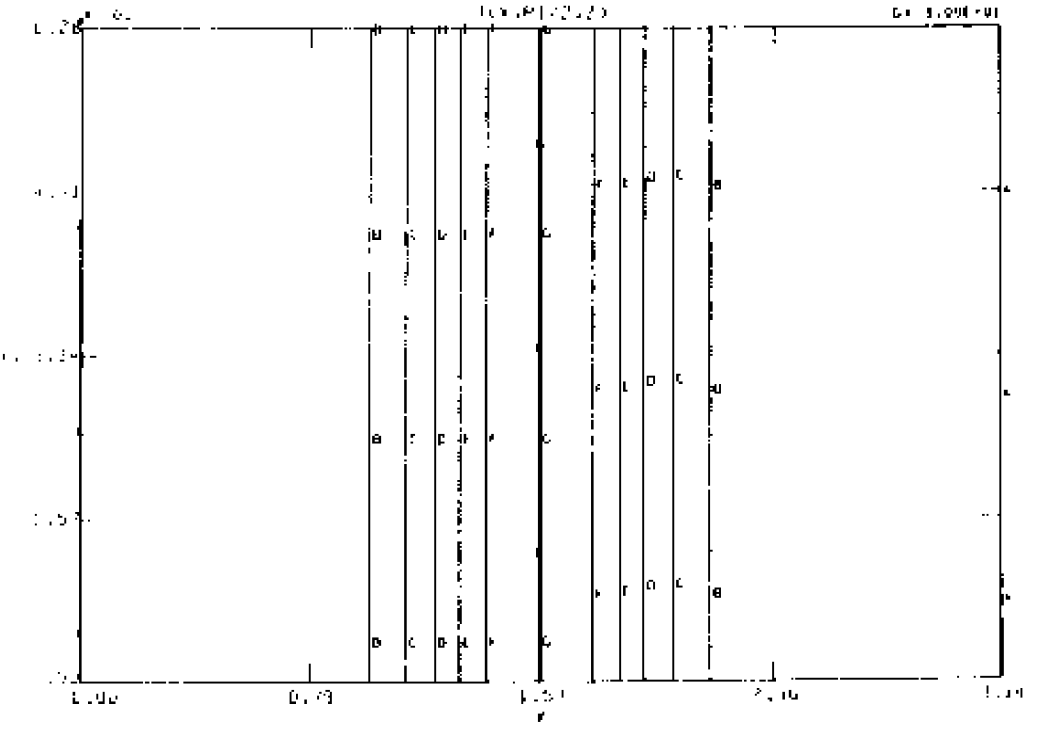

5 (e): contours of j = constant, toroidal cut.

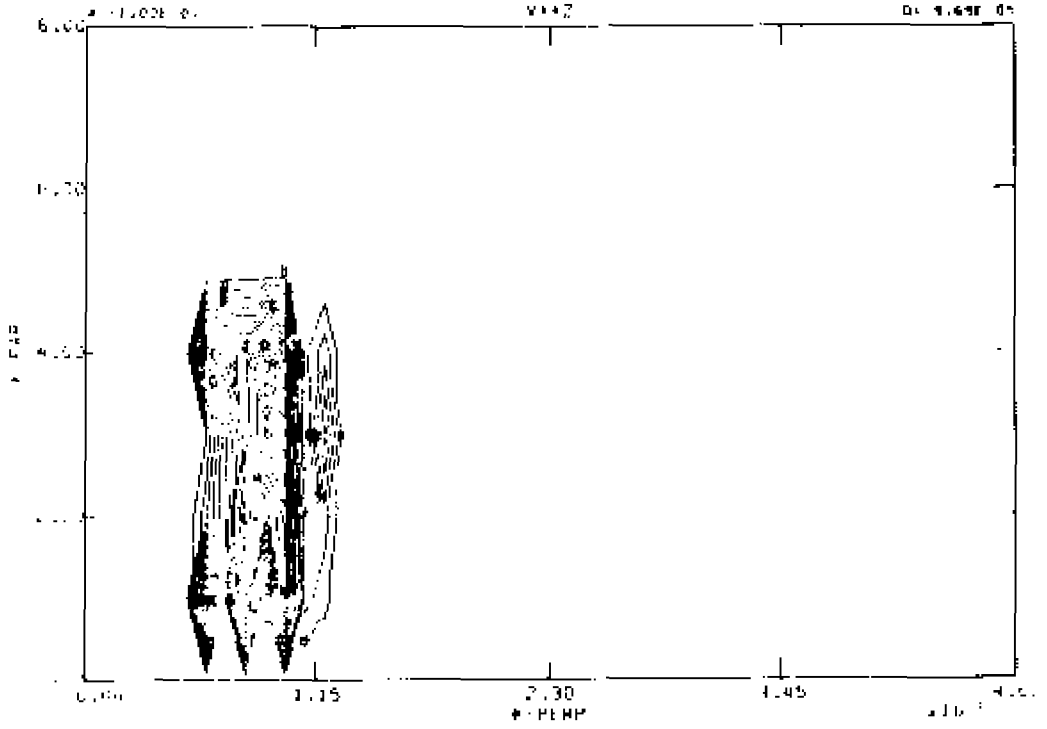

Figure 6. - Contours of energy in Fourier space at t = 8.8:
6 (a): equally spaced contours of constant kinetic energy.

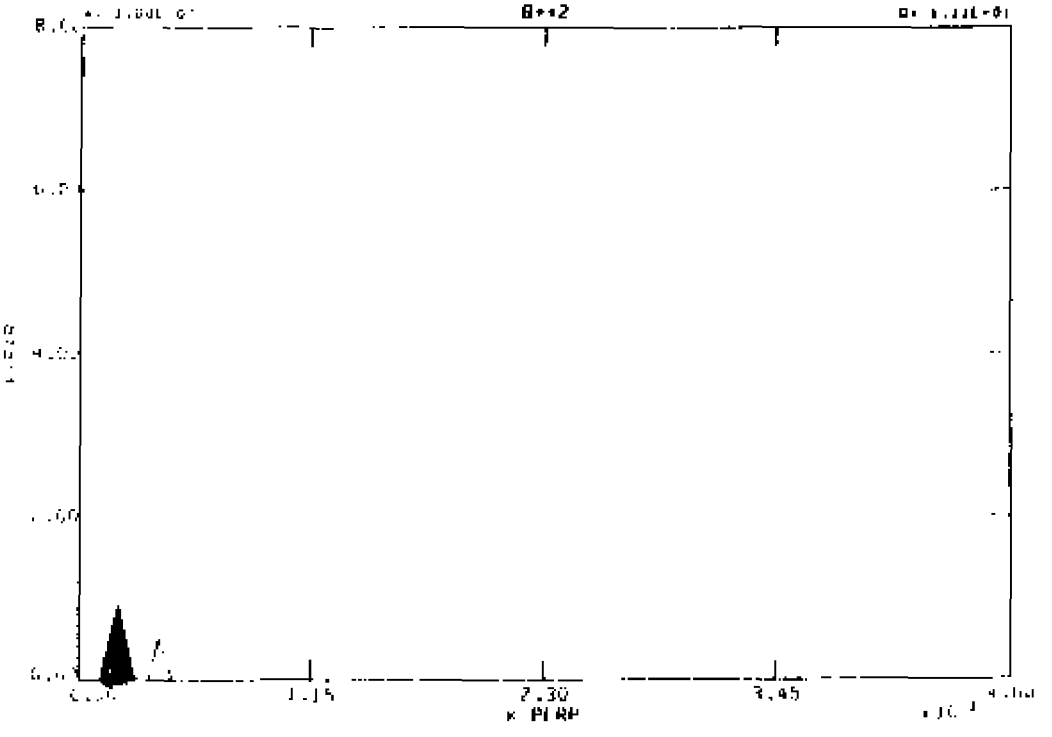

6 (b): equally spaced contours of constant magnetic energy.

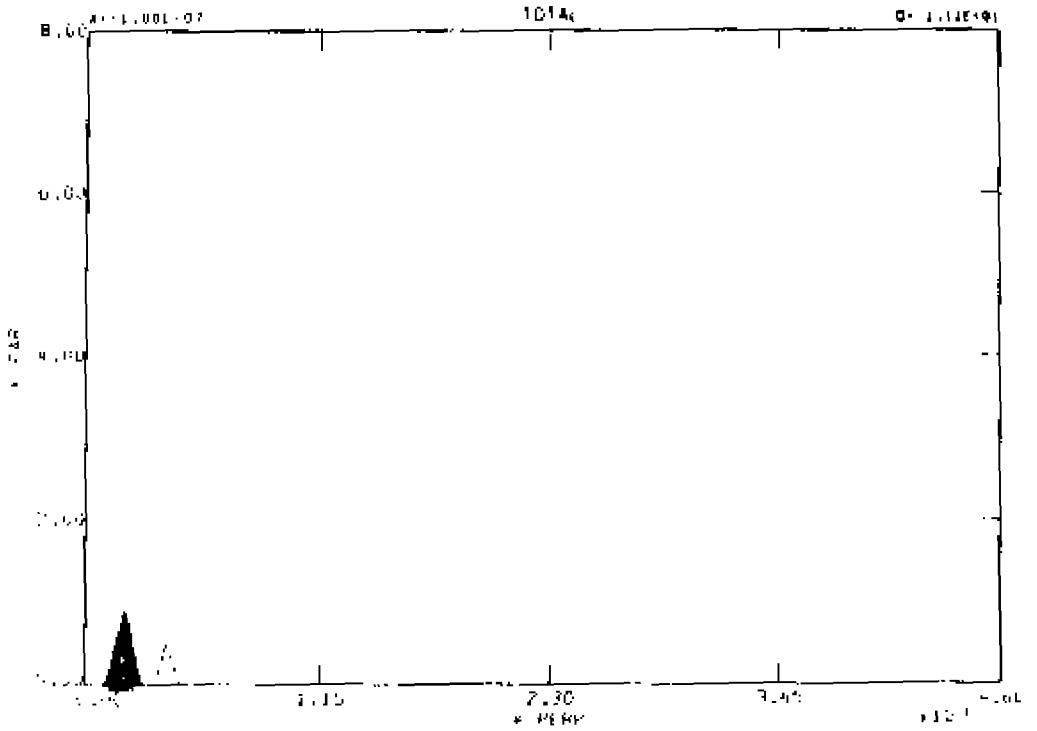

6 (c): equally spaced contours of constant total energy.

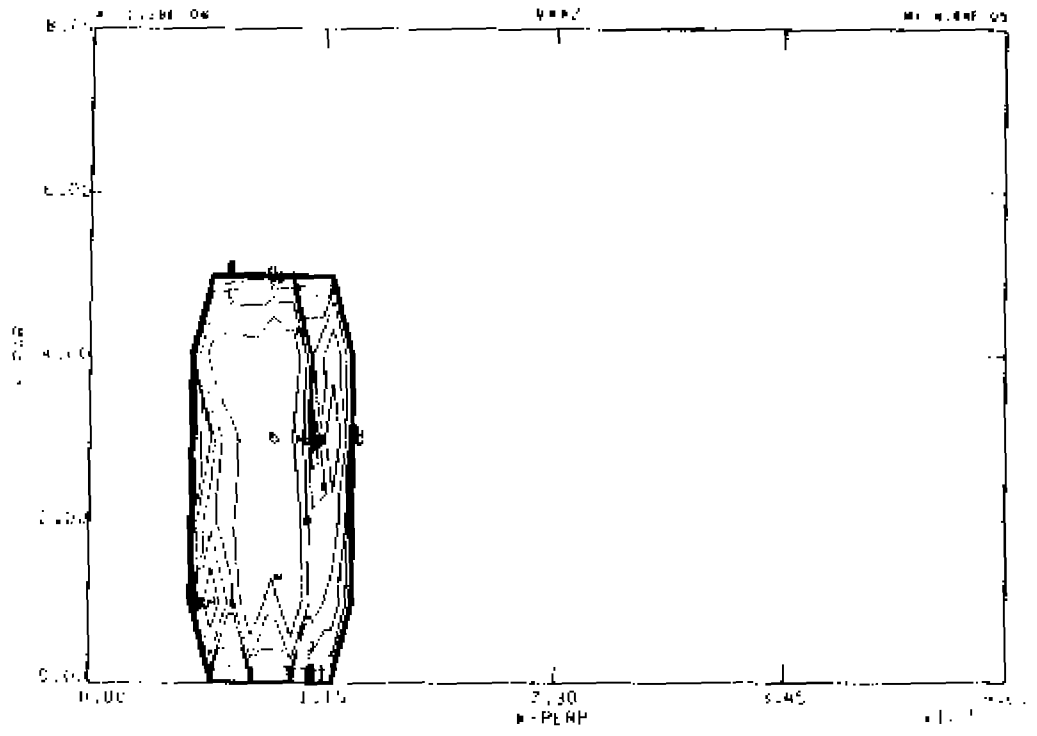

6 (d): contours separated by powers of two of constant kinetic energy

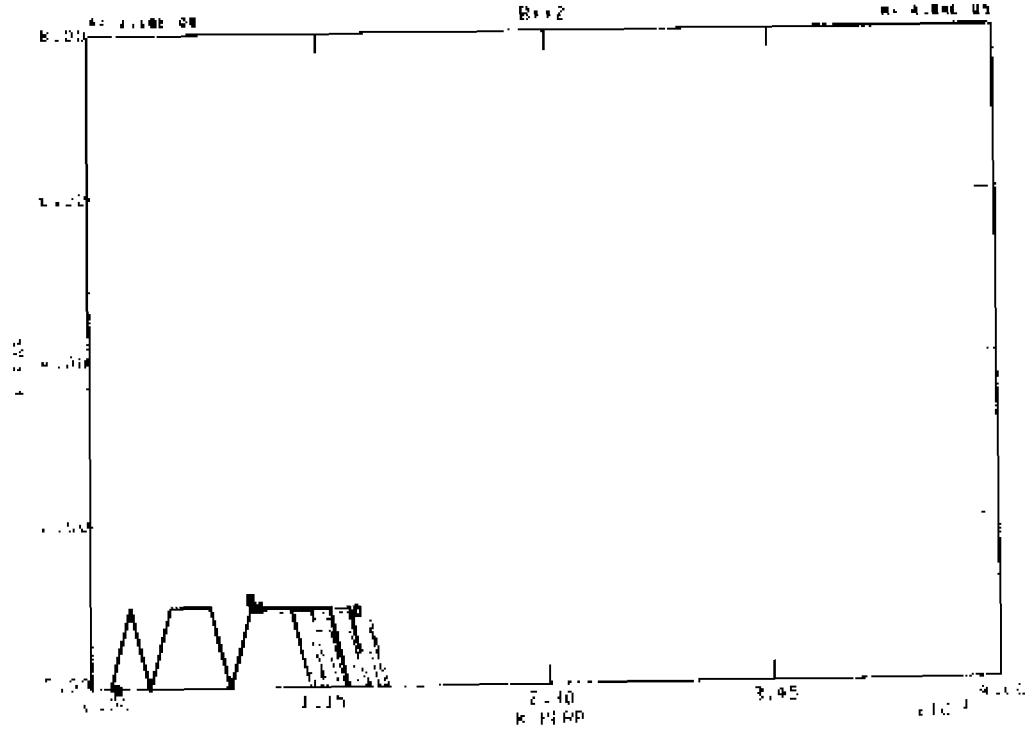

6 (e): contours separated by powers of two of constant magnetic energy.

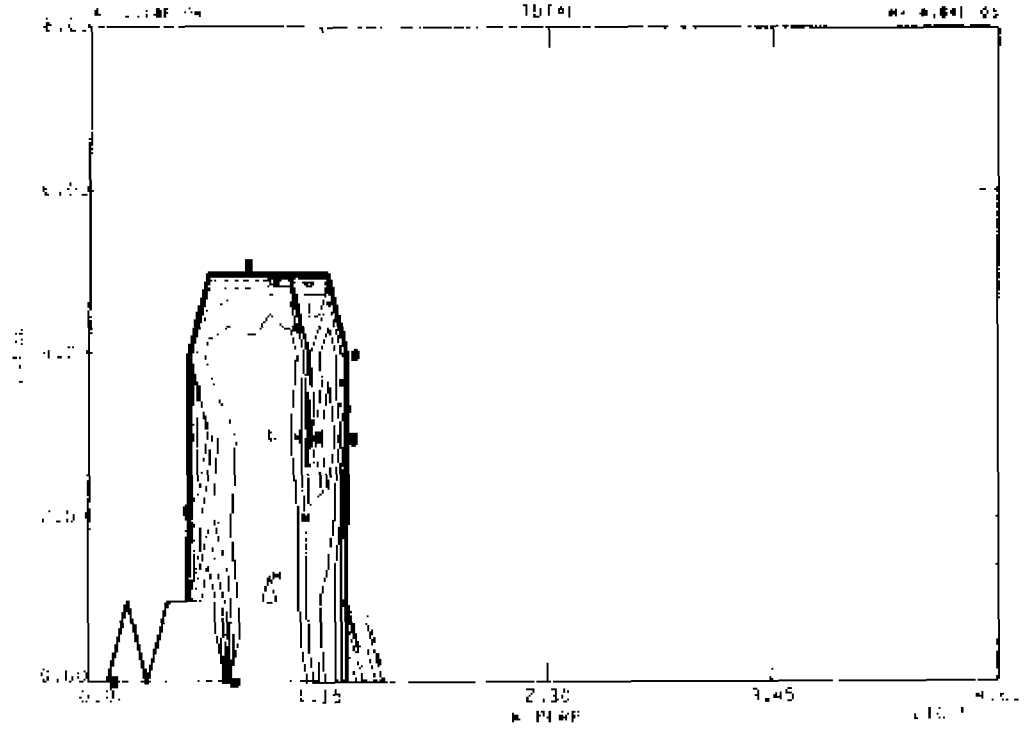

6 (f): contours separated by powers of two of constant total energy.

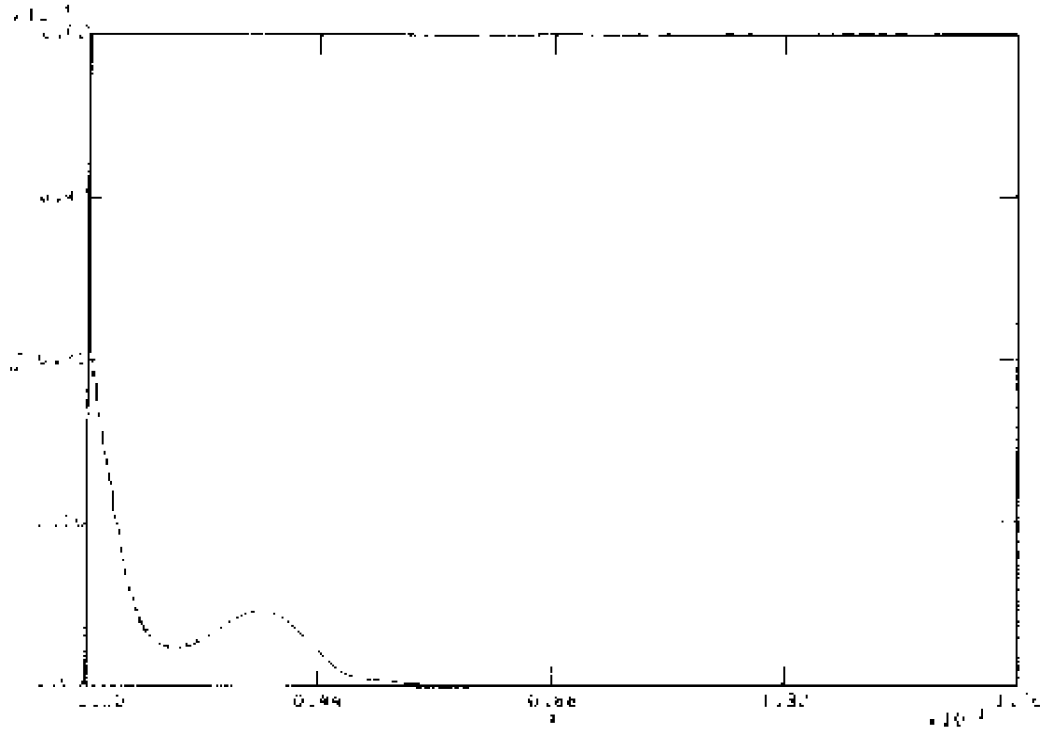

Figure 7. - Globals as a function of time for CASE 1;
7(a): total kinetic energy [E_v] as a function of time.

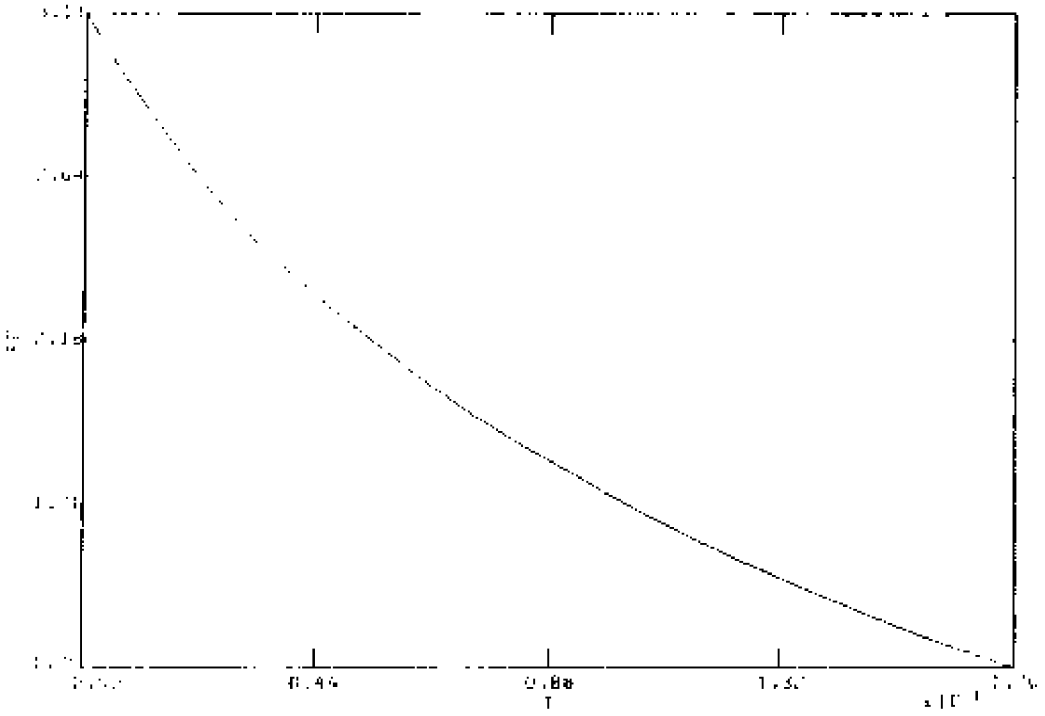

7(b): total magnetic energy [E_B] as a function of time.

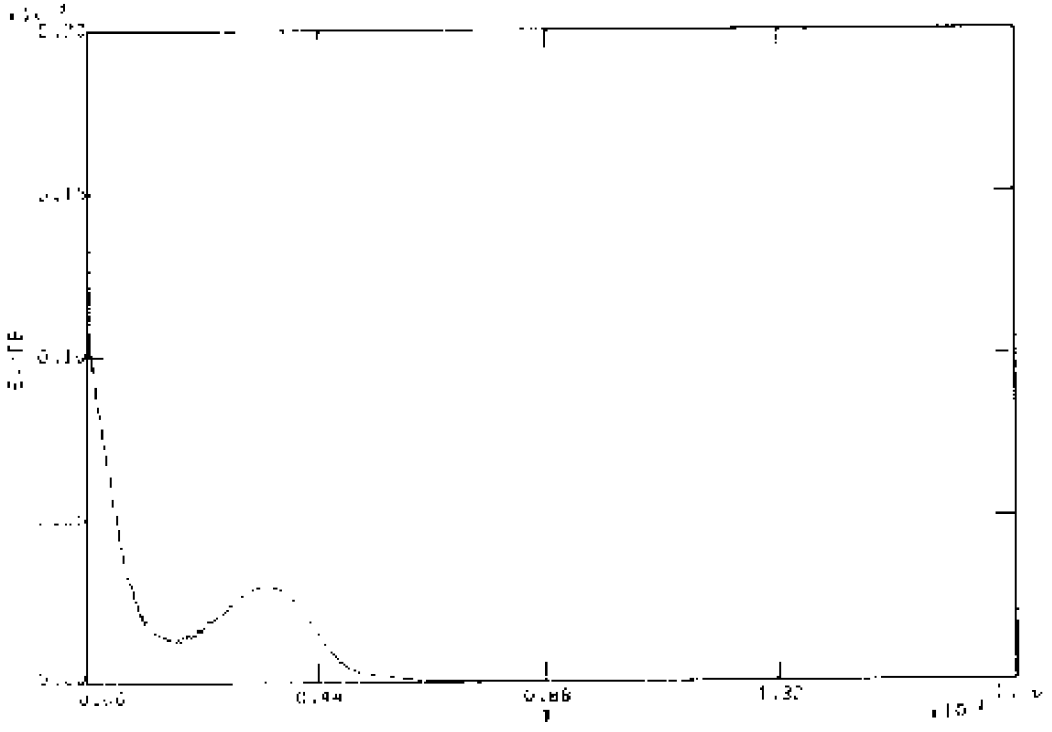

7(c): E_y / E_0 as a function of time.

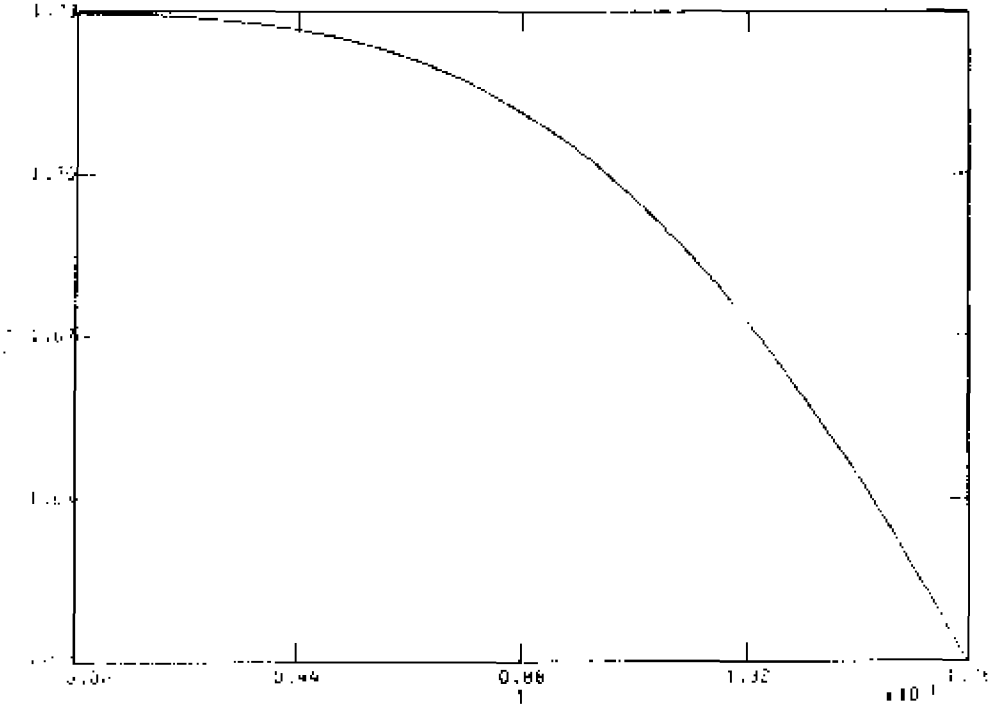

7(d): total integrated toroidal current as a function of time, and

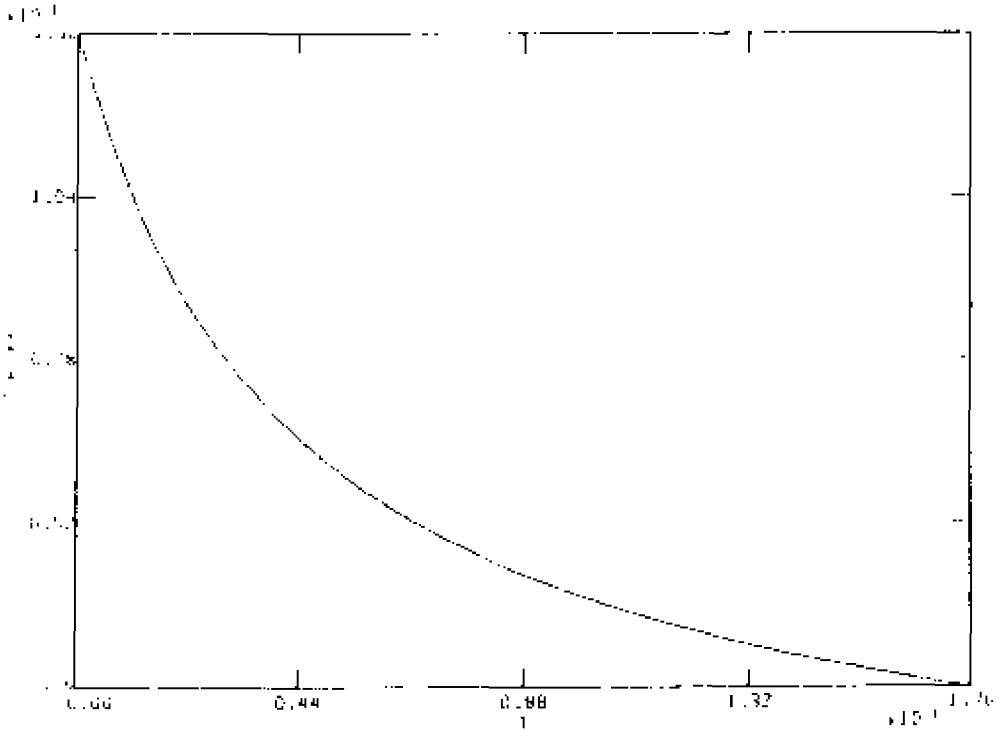

7(e): half the mean square current denstiy as a function of time.

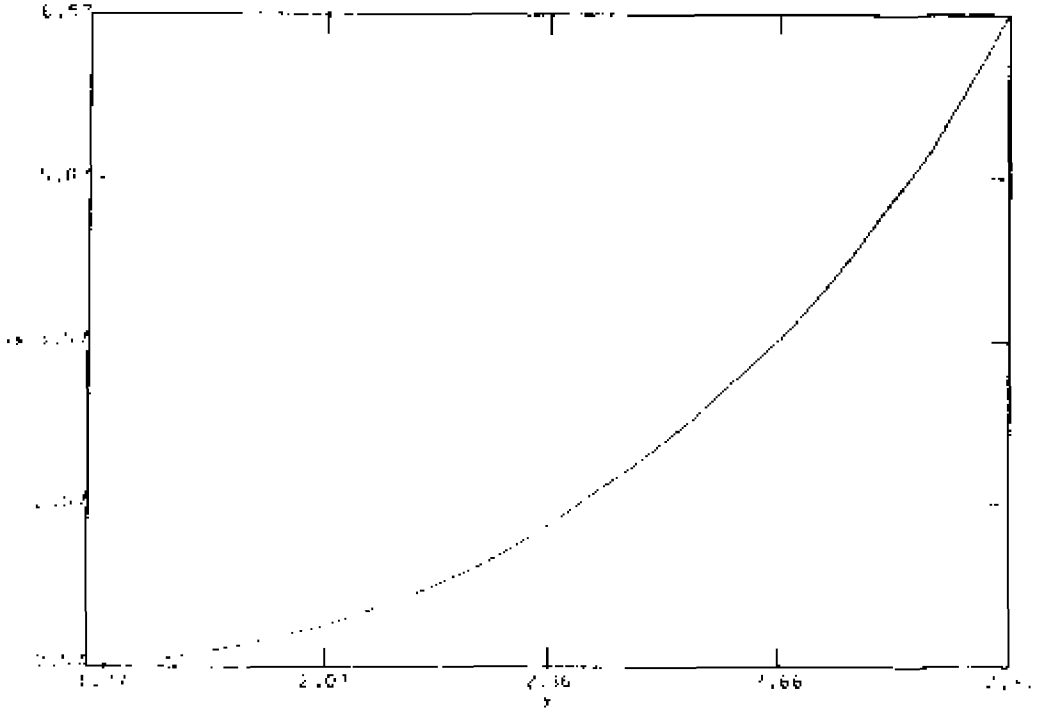

Figure 8. - Q-profiles for CASE 1: (a) t = 0,

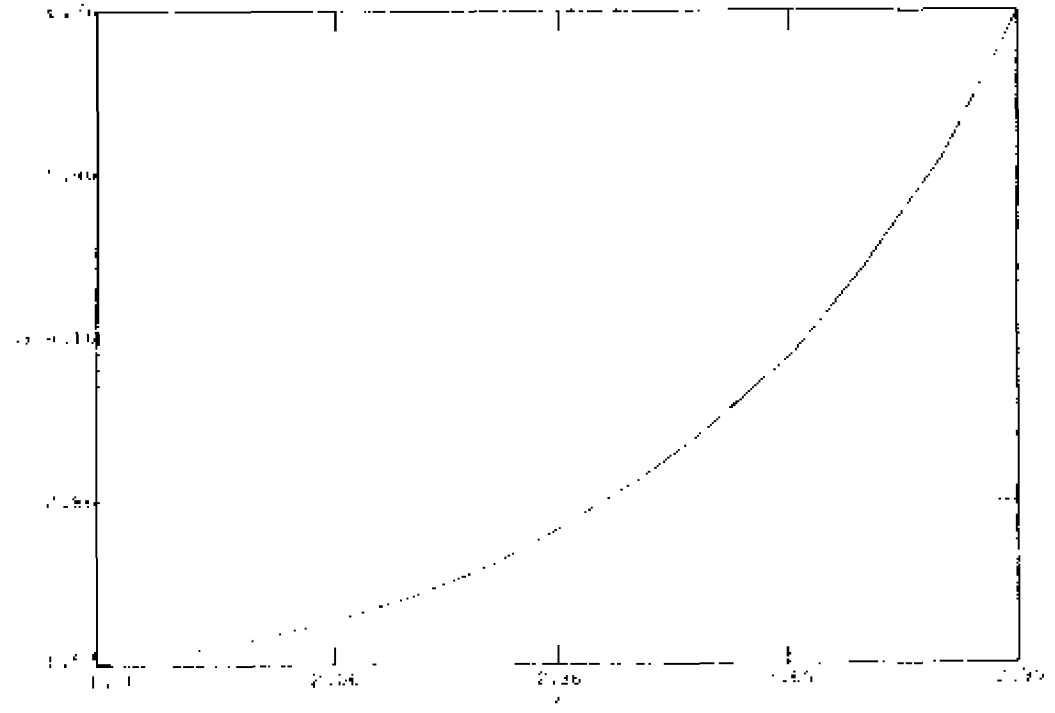

and 8 (b) t = 0.82.

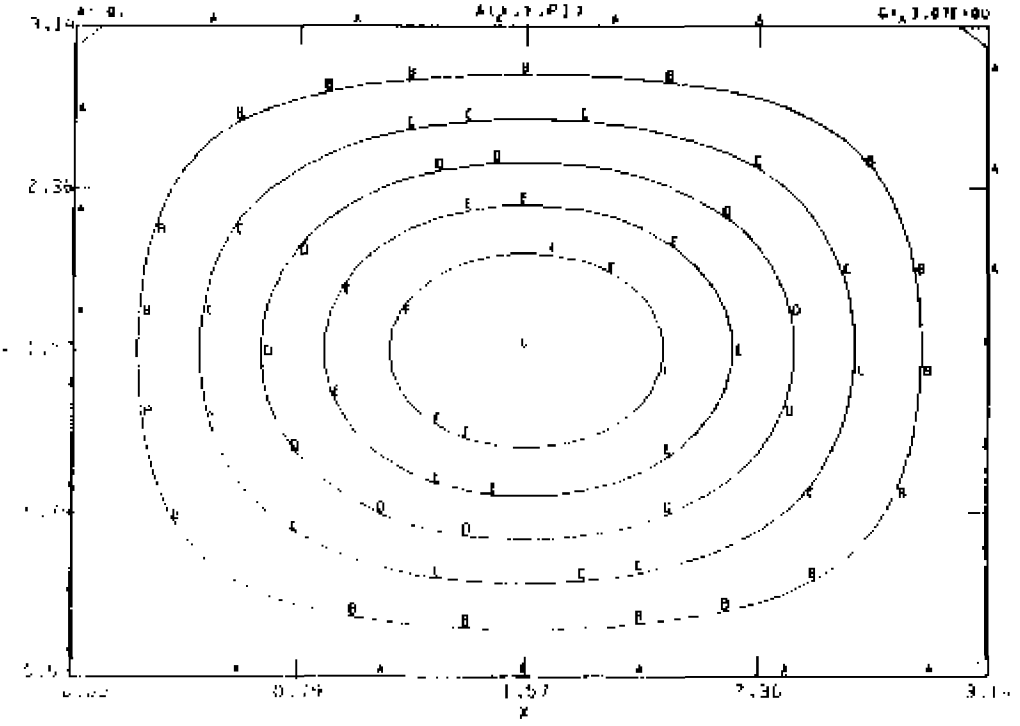

Figure 9. - Contour plots at t = 0.02 from CASE 1:
9 (a): contours of A = constant, poloidal cut,

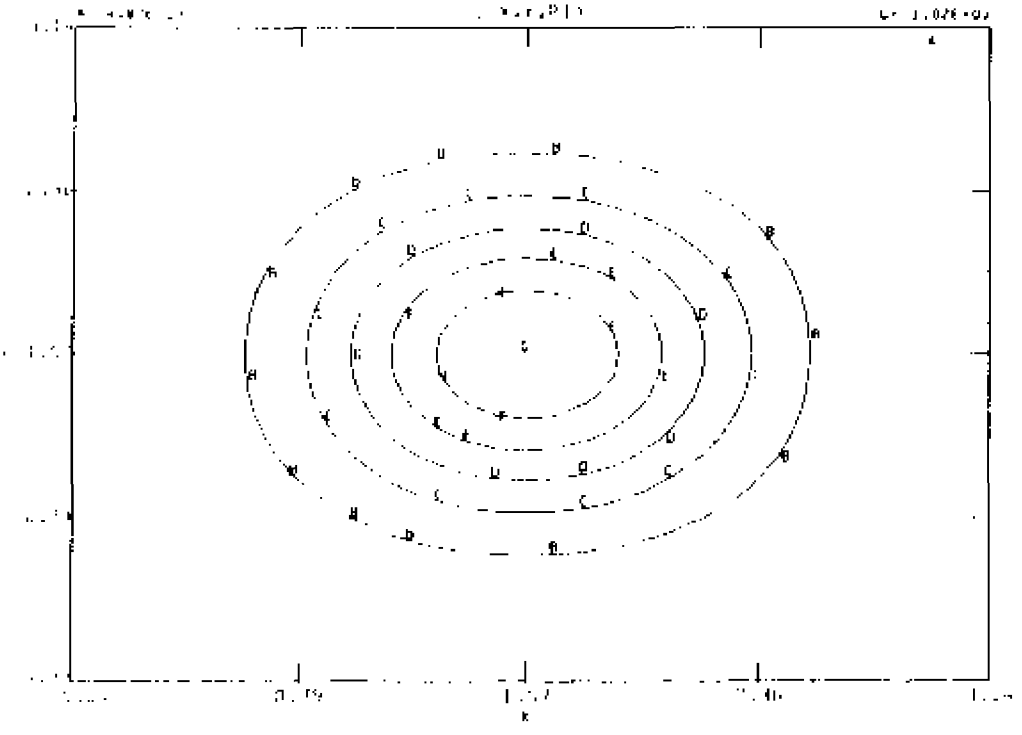

9 (b): contours of j = constant, poloidal cut,

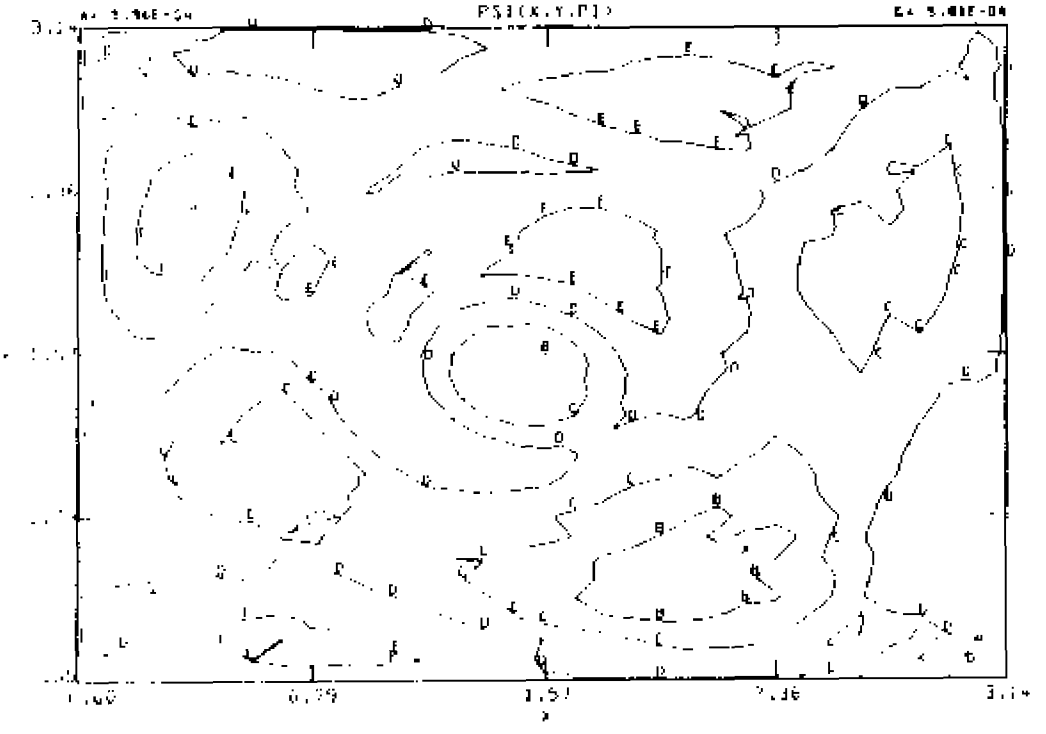

9 (c): contours of Ψ = constant, poloidal cut.

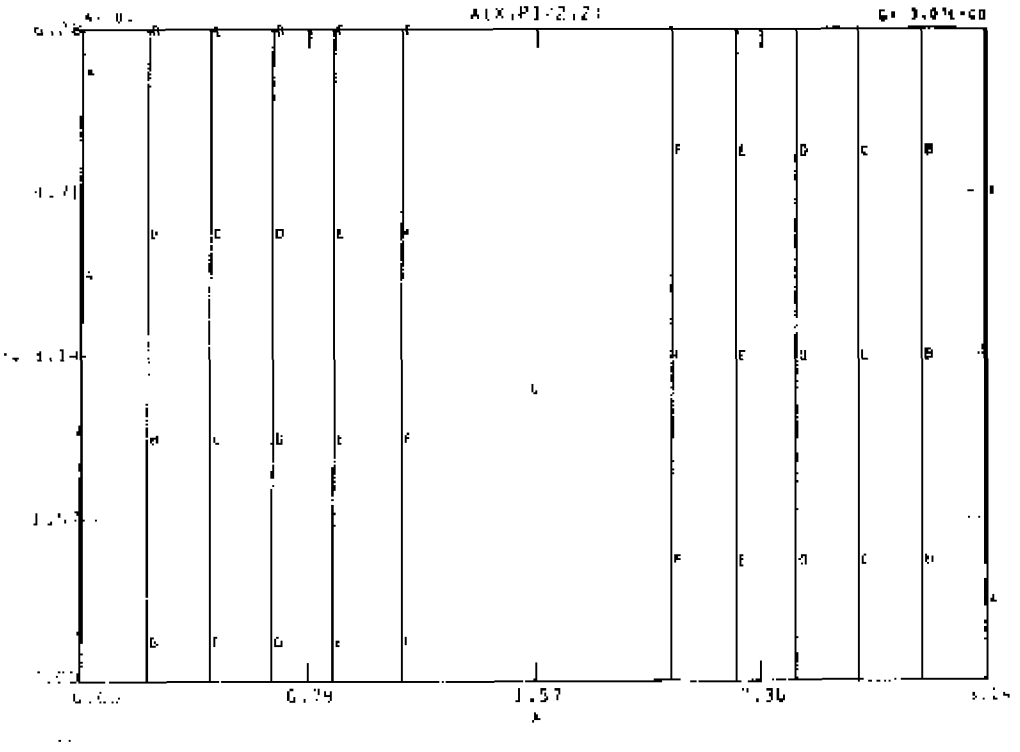

9 (d): contours of A = constant, toroidal cut.

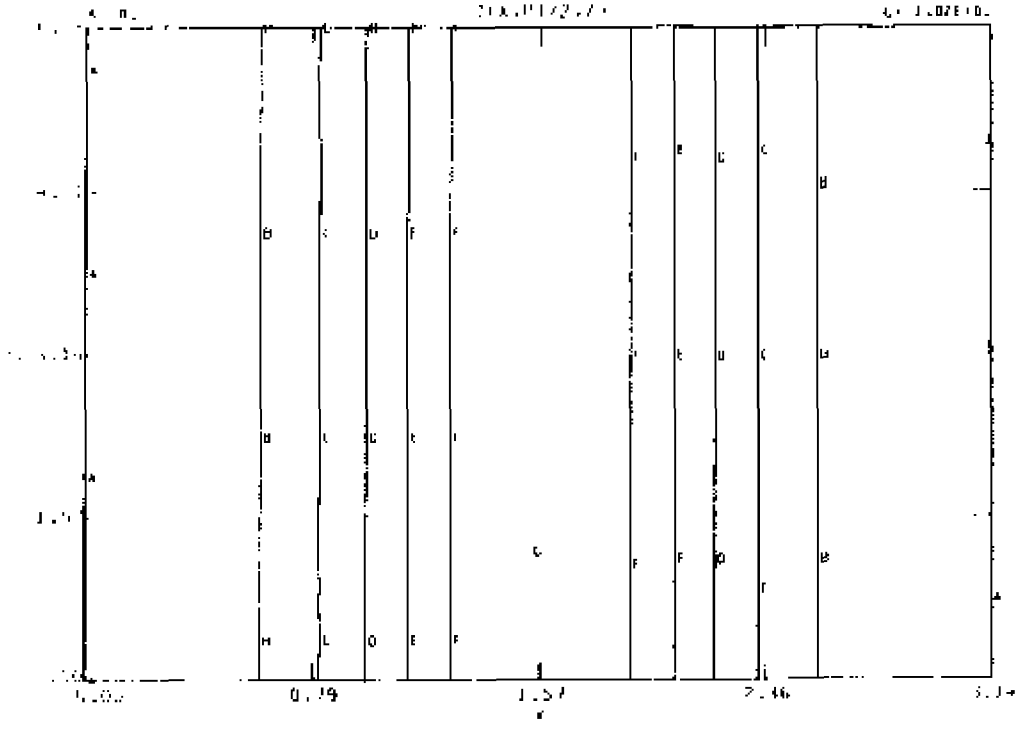

9 (e): contours of j = constant, toroidal cut.

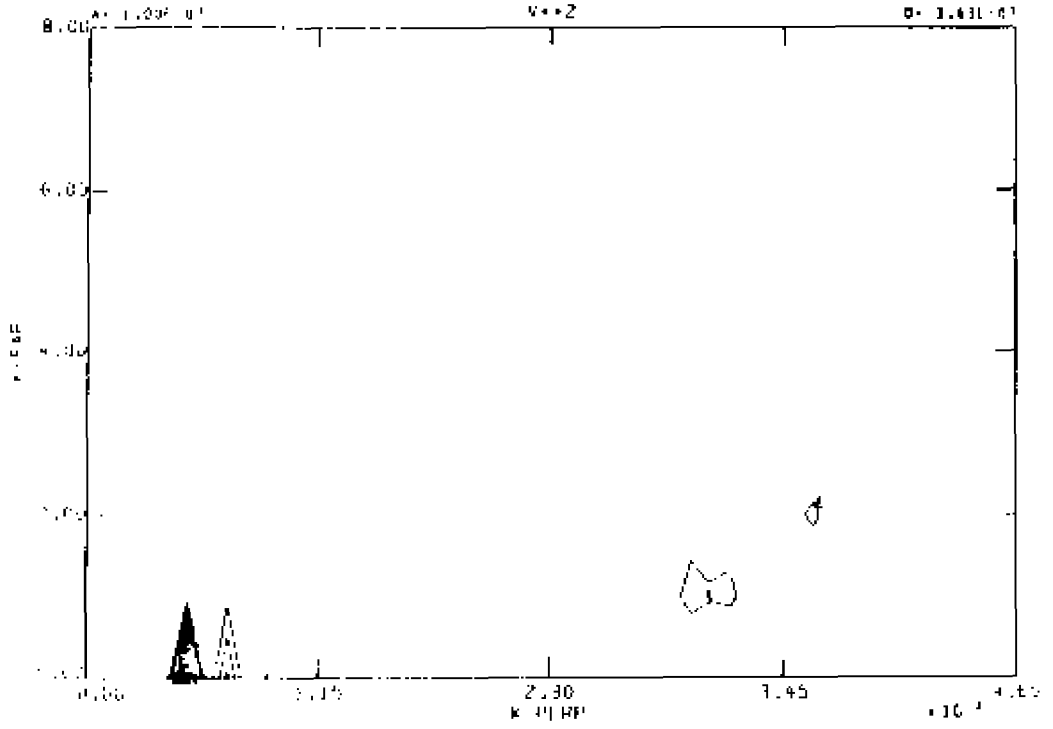

Figure 10. - Contours of energy in Fourier space at t = 0.02, CASE 1:
10 (a): equally spaced contours of constant kinetic energy.

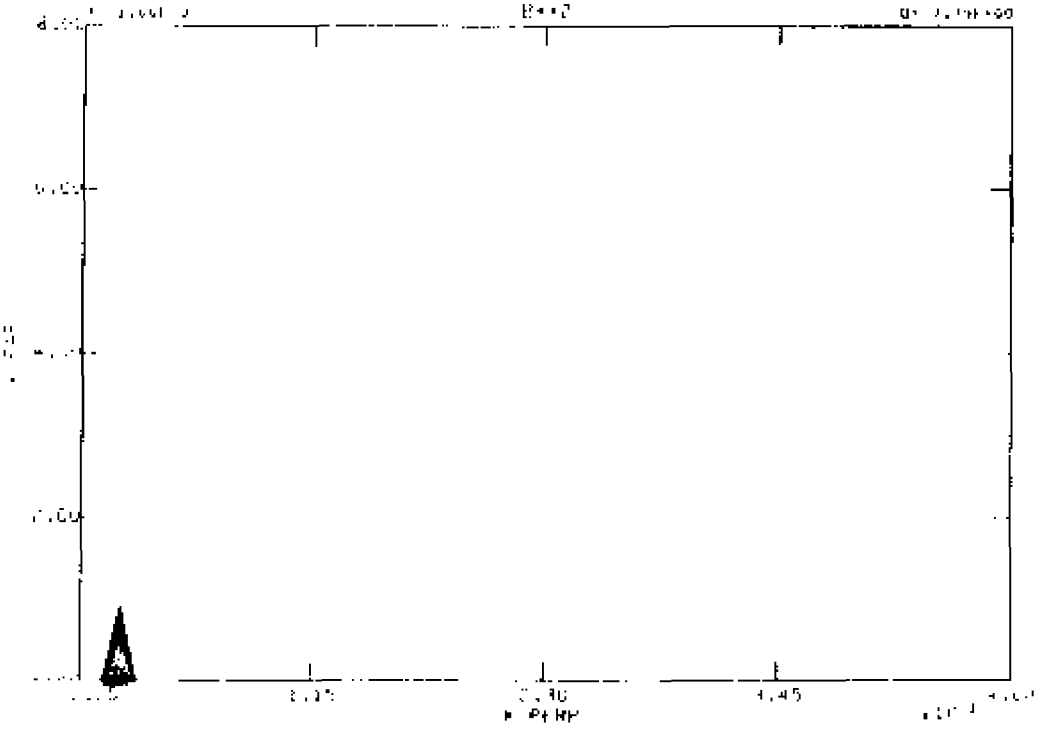

10 (b): equally spaced contours of constant magnetic energy.

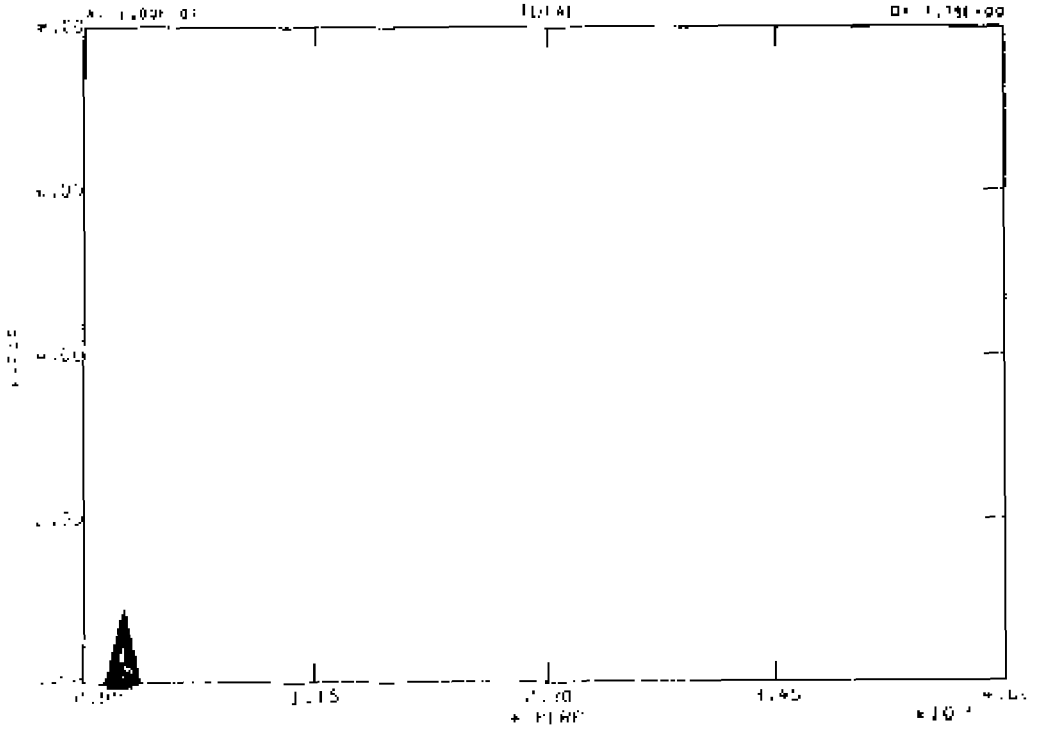

10 (c): equally spaced contours of constant total energy.

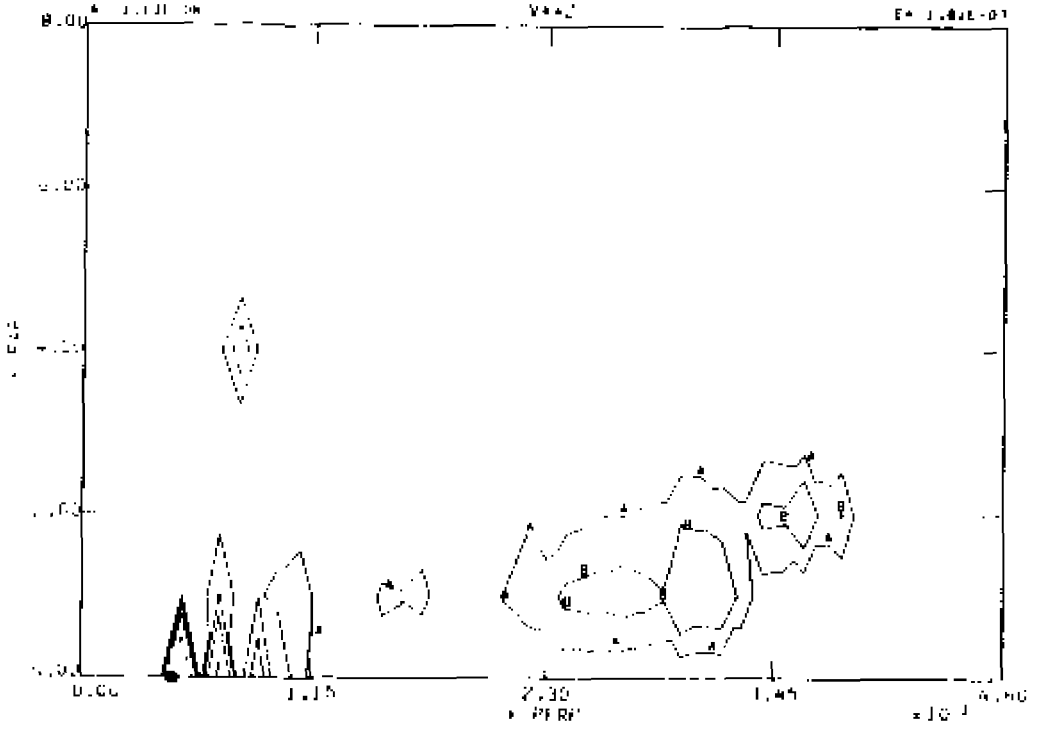

10 (d): contours separated by powers of two of constant kinetic energy.

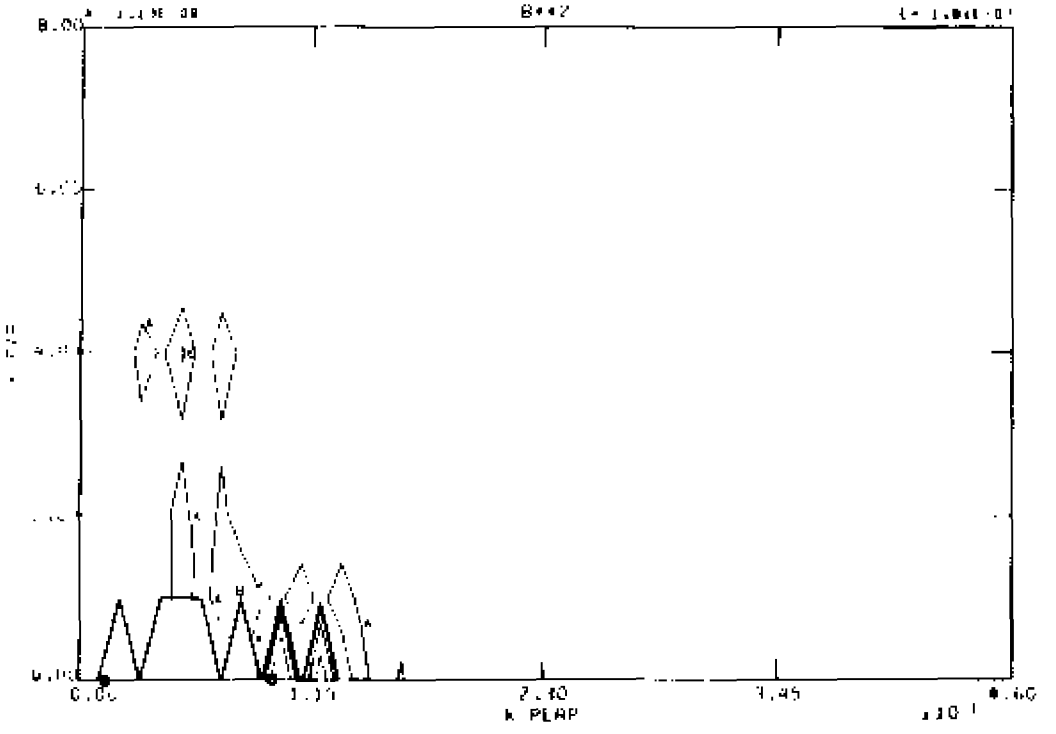

18 (e): contours separated by powers of two of constant magnetic energy.

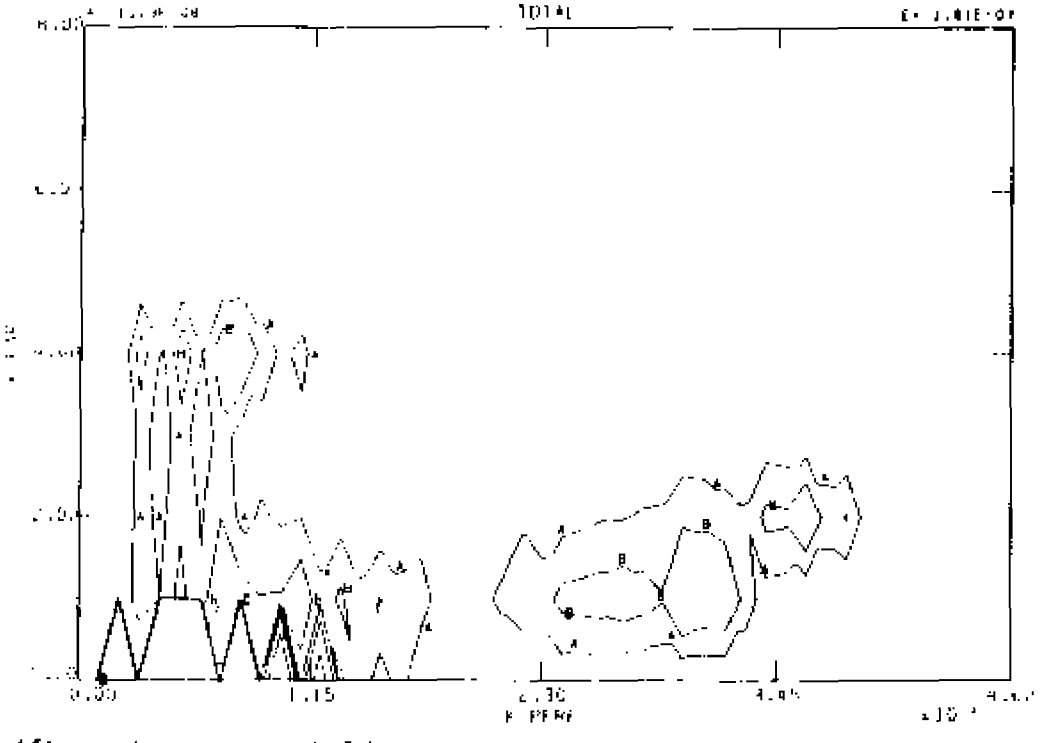

18 (f): contours separated by powers of two of constant total energy

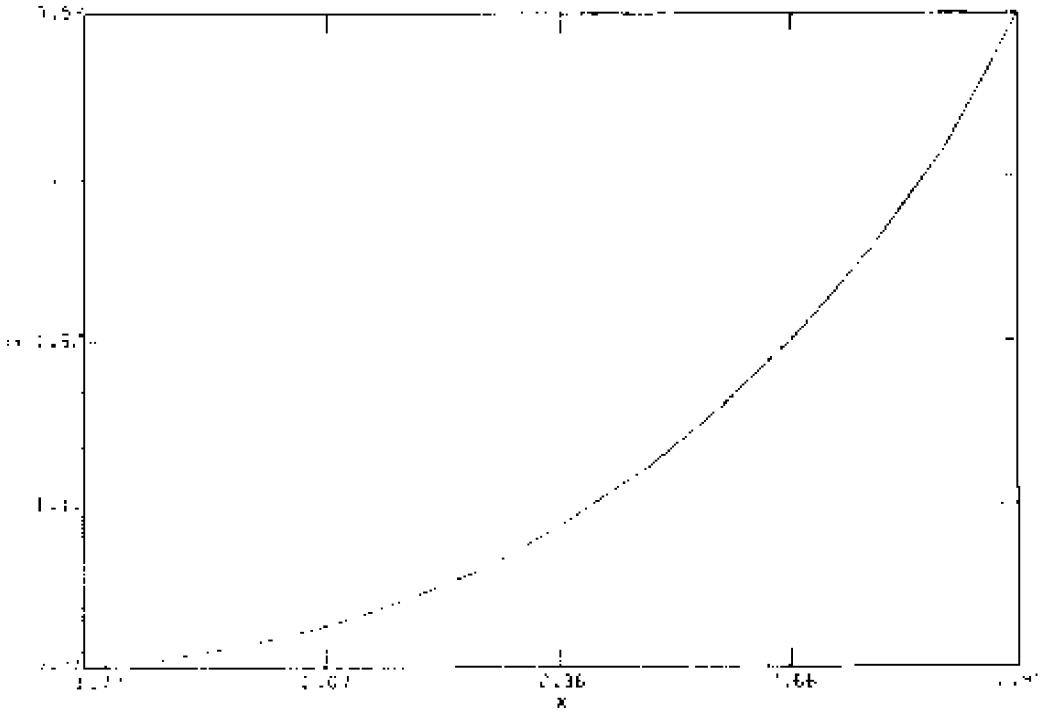

Figure 11. - Q-profile at t = 0.0 for CASES 2 and 3.

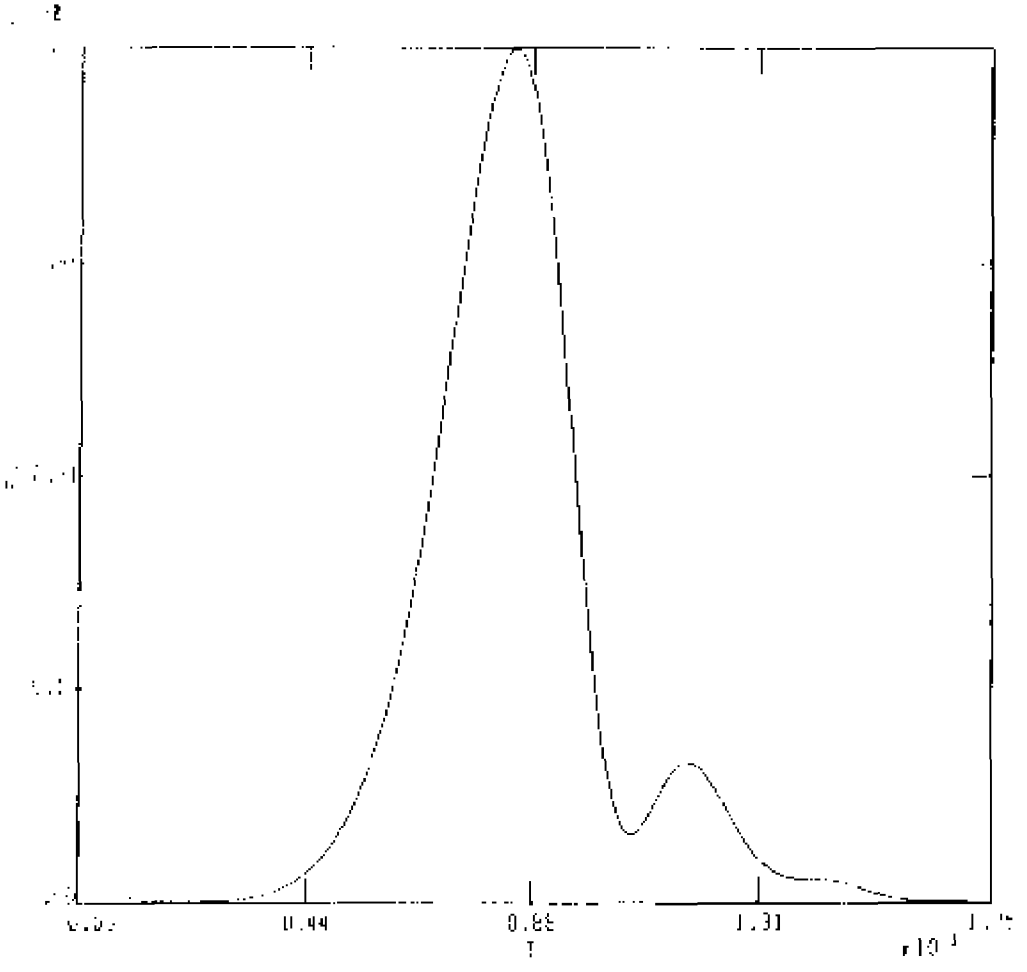

Figure 12. - Globals for CASE 2, ($\mathcal{R}_L$ = 0.01):
12(a): kinetic energy as a function of time.

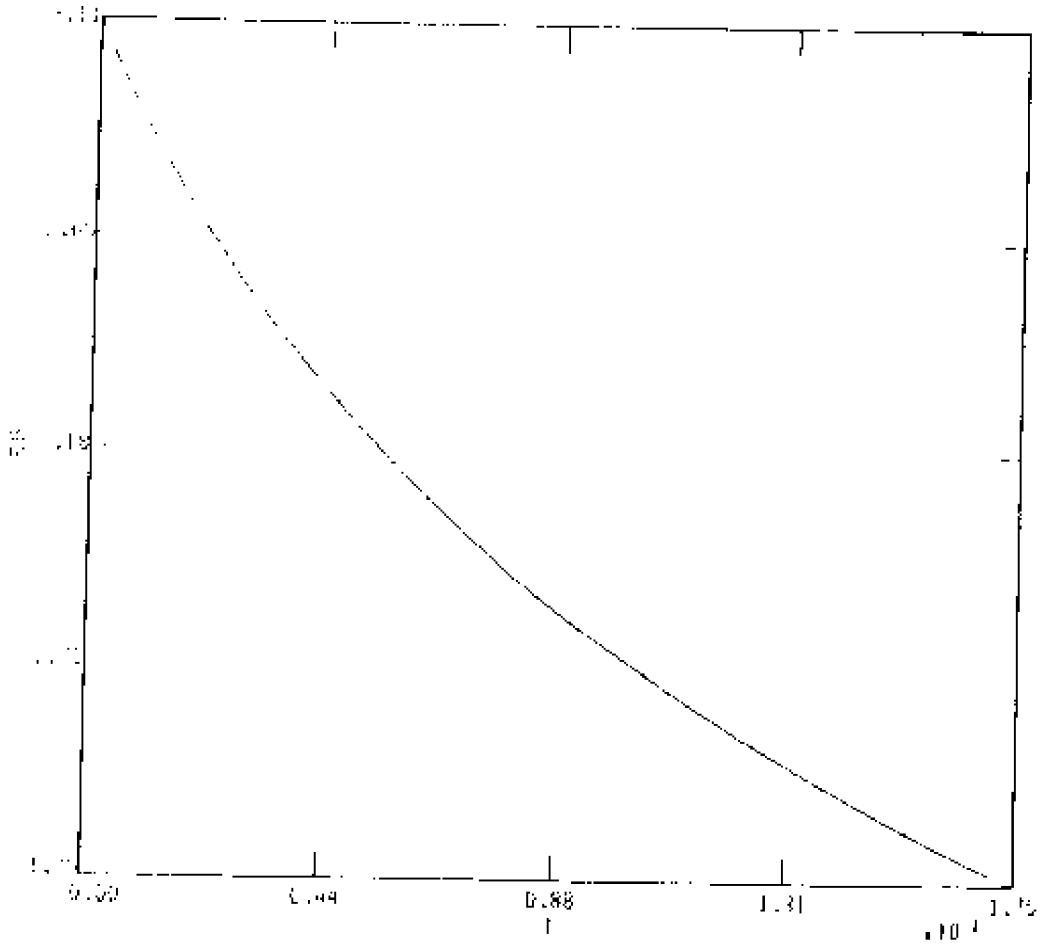

12(b): Magnetic energy as a function of time.

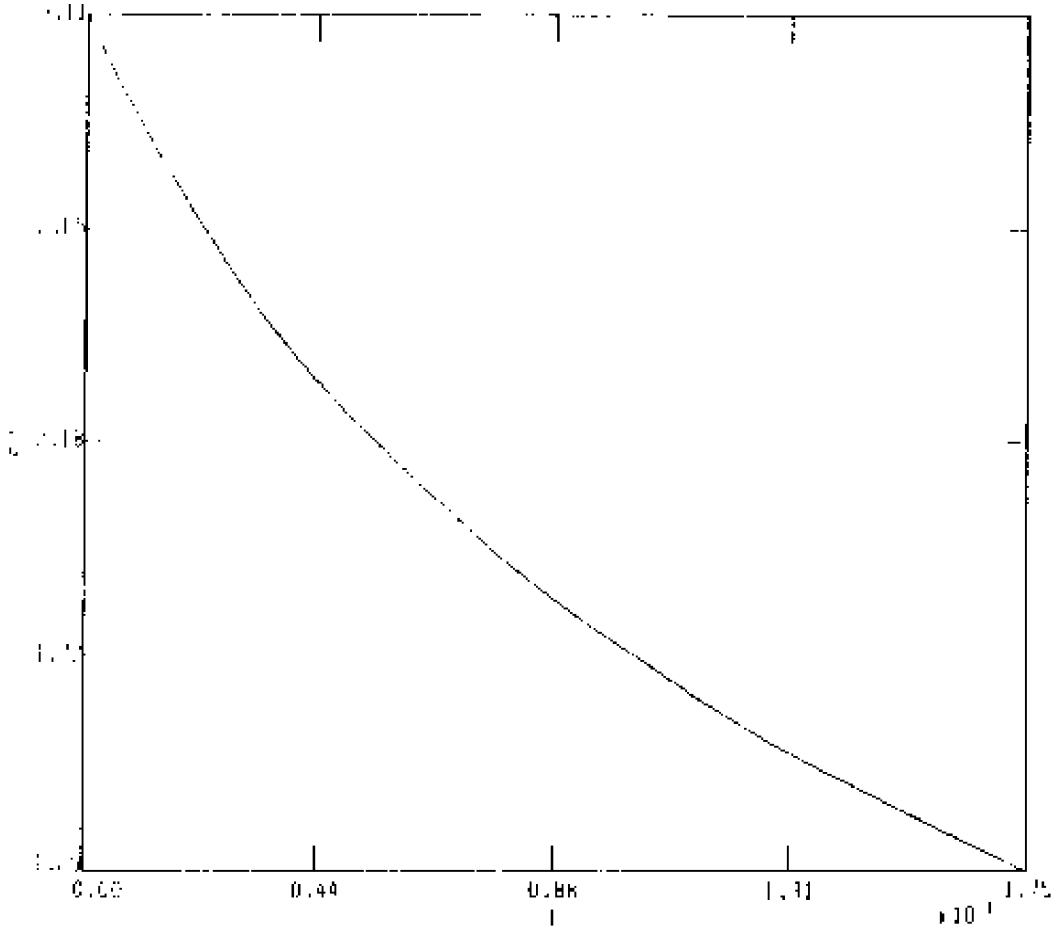

12(c): total energy as a function of time.

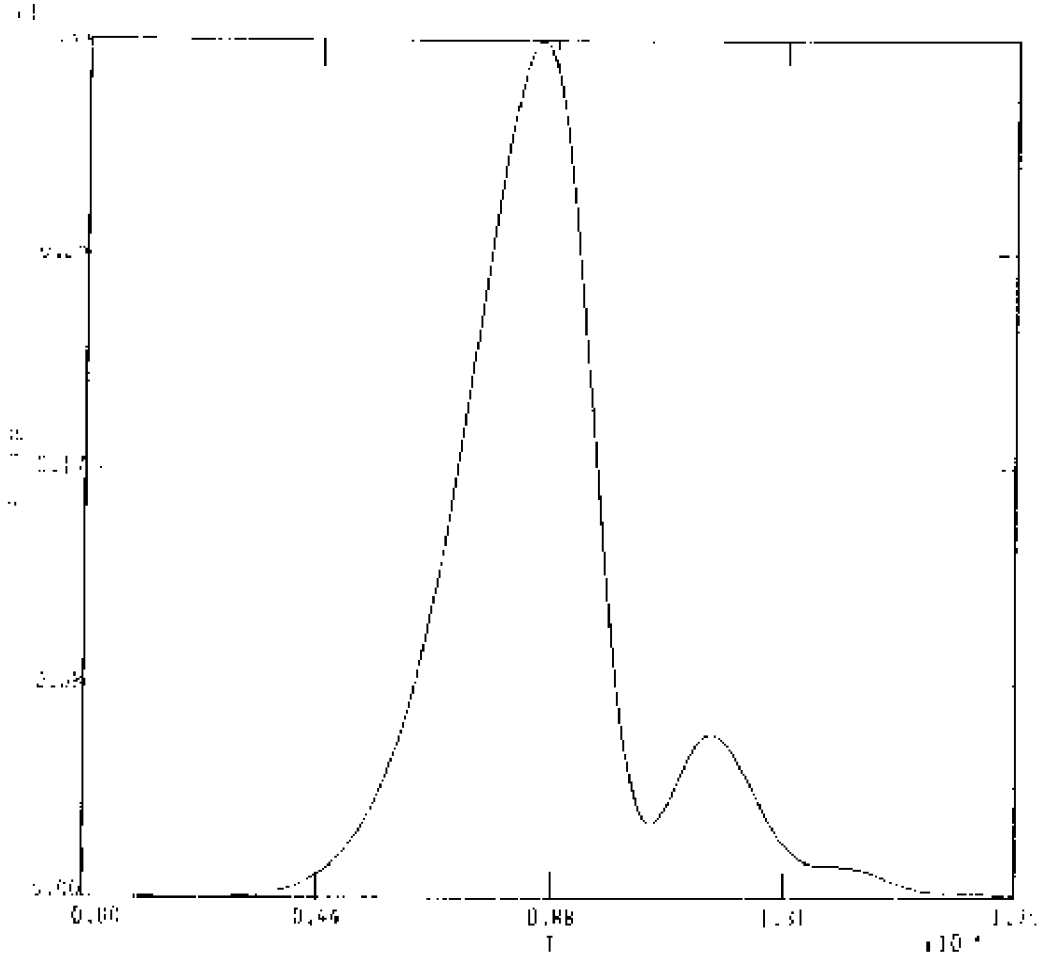

12(d): ratio of kinetic to magnetic energy as a function of time.

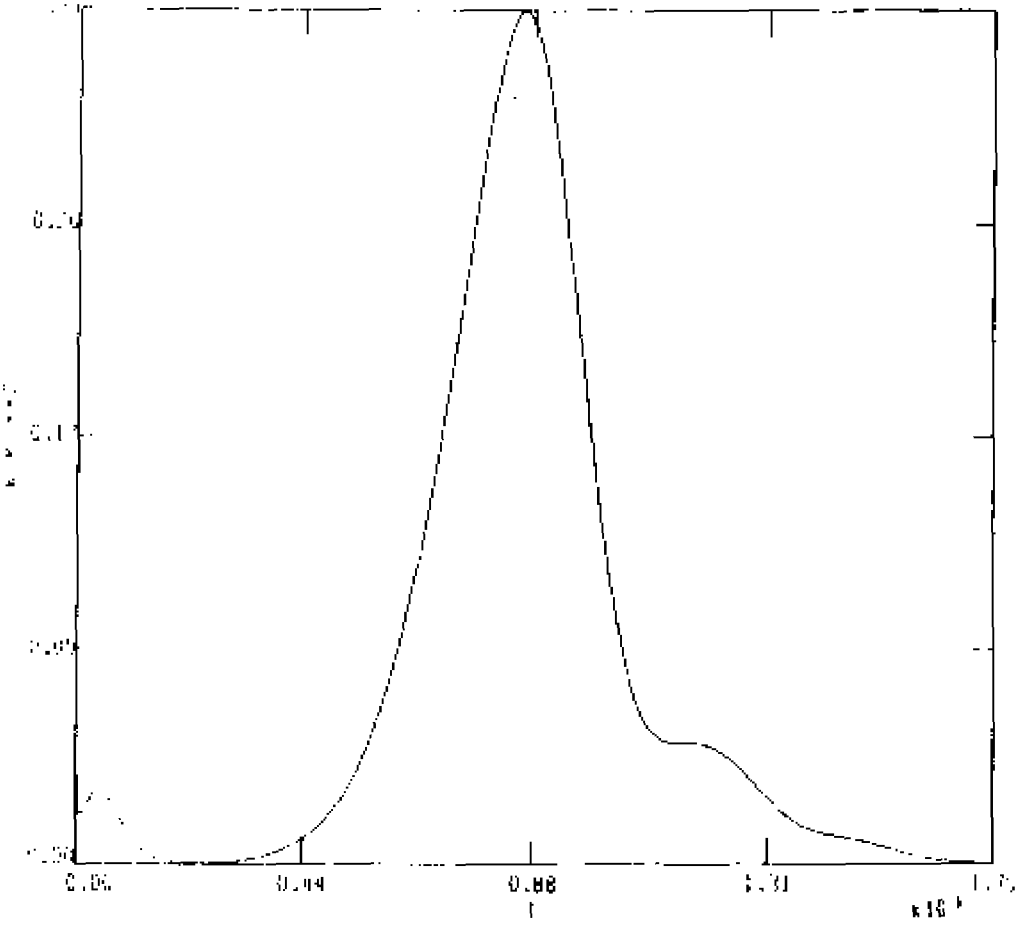

12(e): half the mean square vorticity as a function of time.

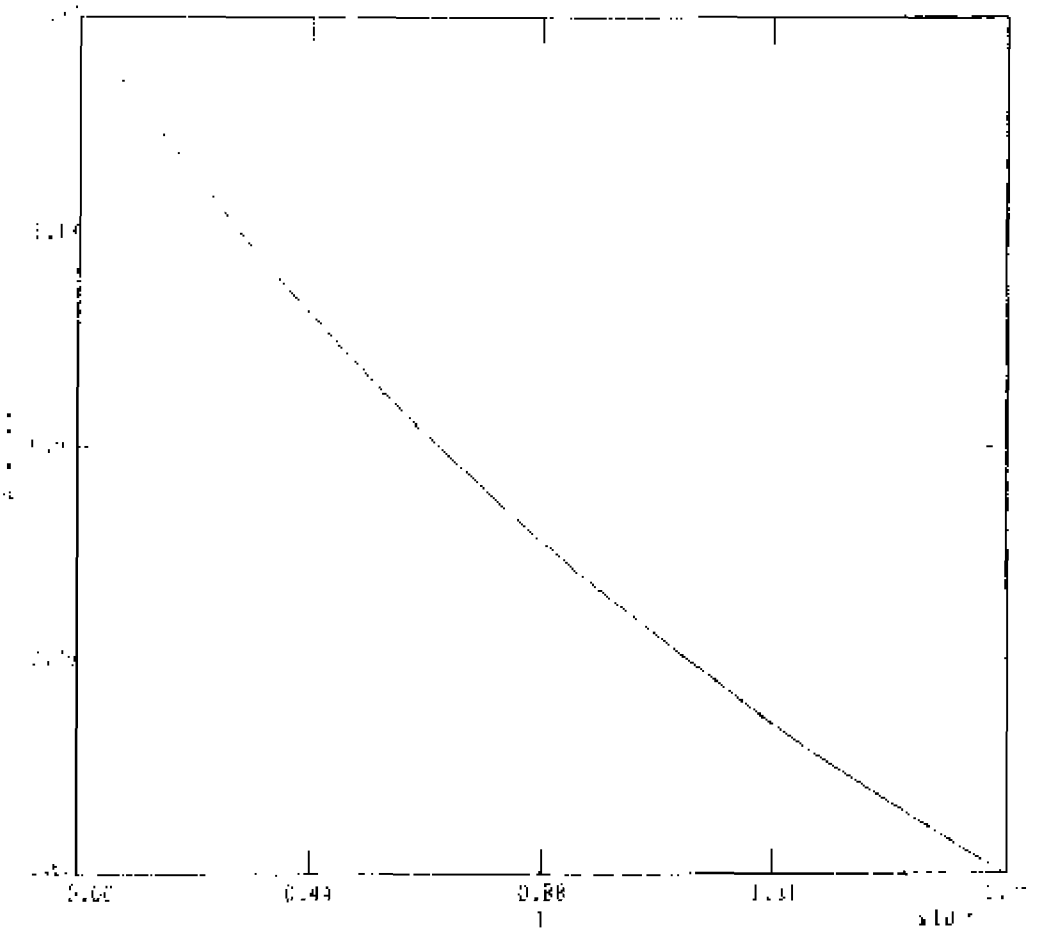

12(f): half the mean square vector potential as a function of time.

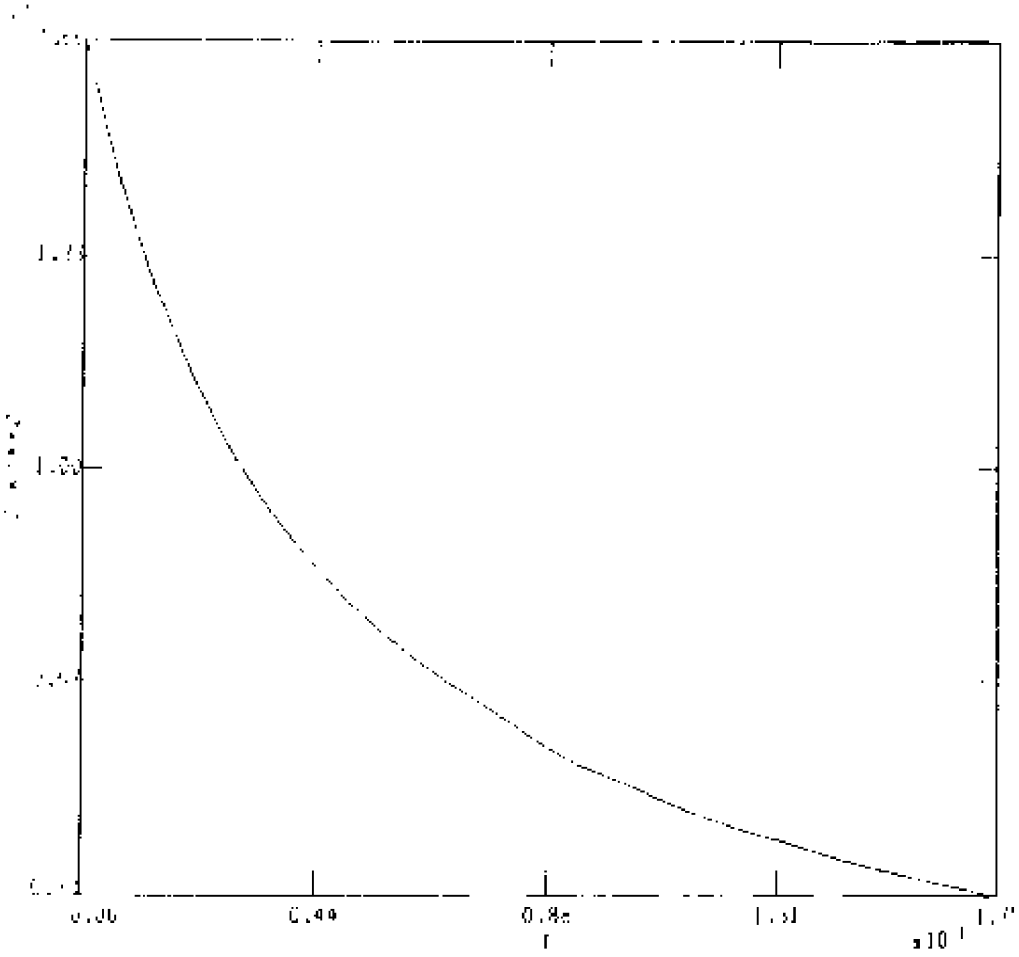

12(g): half the mean square current as a function of time, and

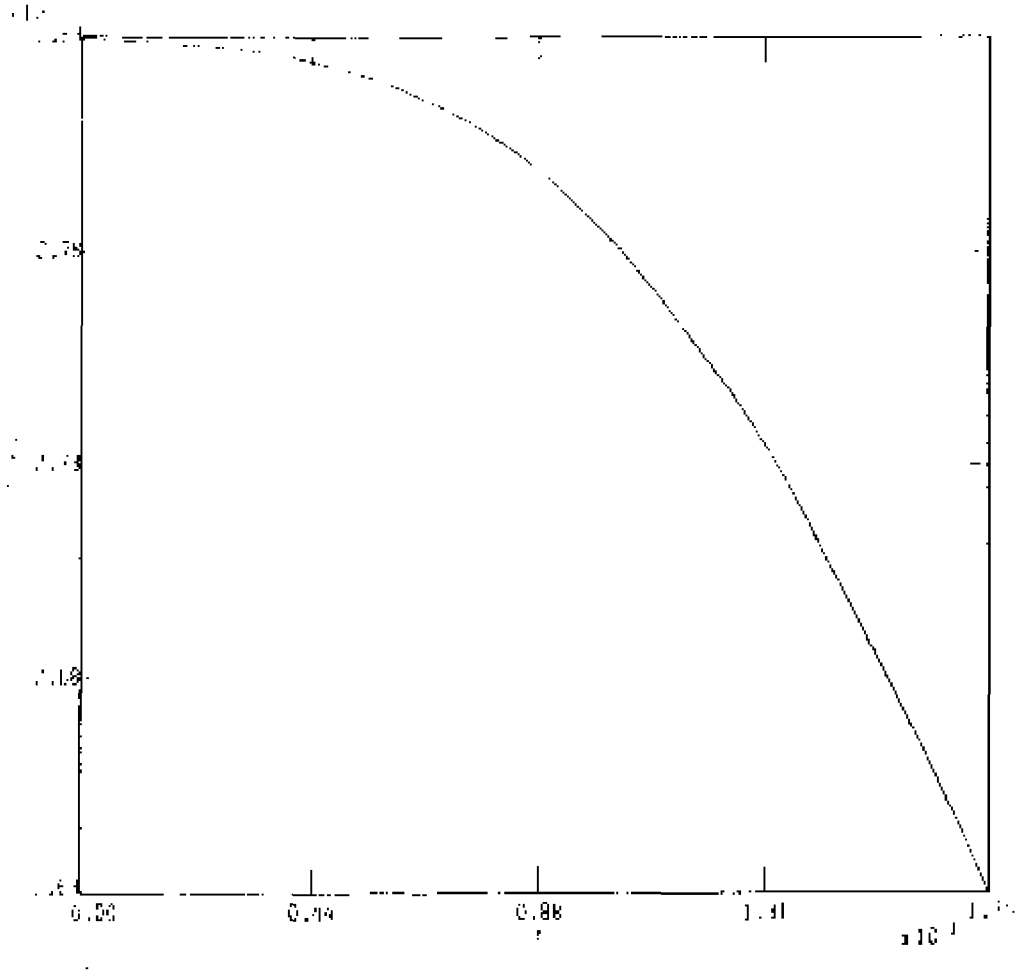

12(h): total integrated current density as a function of time.

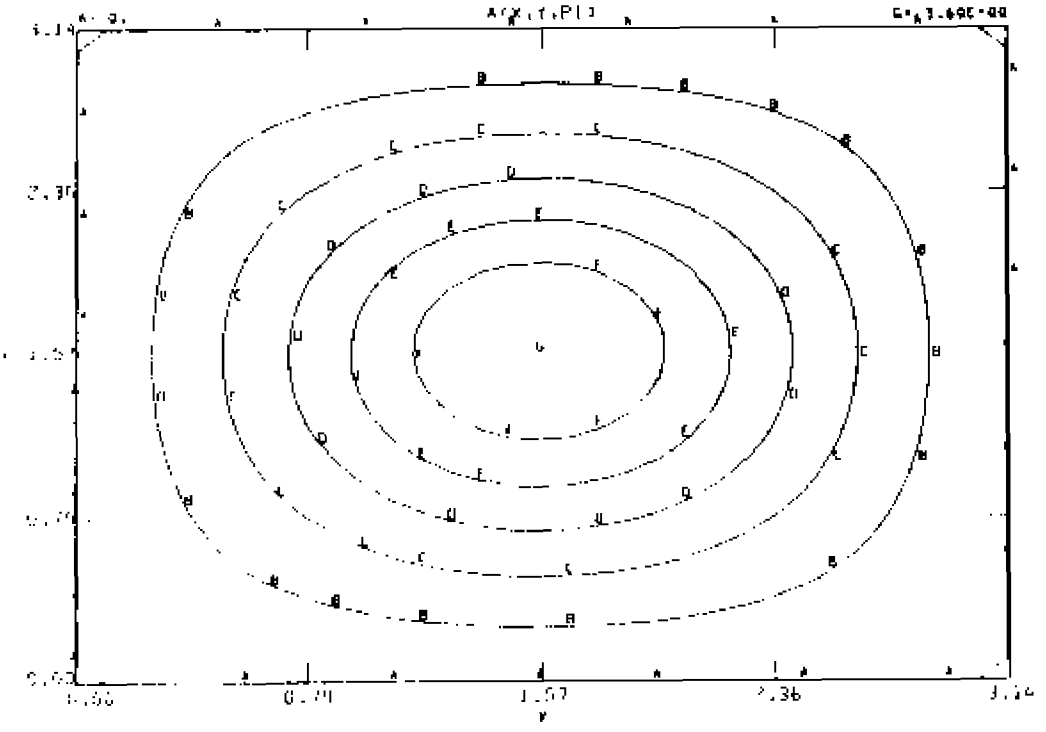

Figure 13. - Contour plots at t = 4.44 from CASE 2:
13 (a): contours of A = constant, poloidal cut,

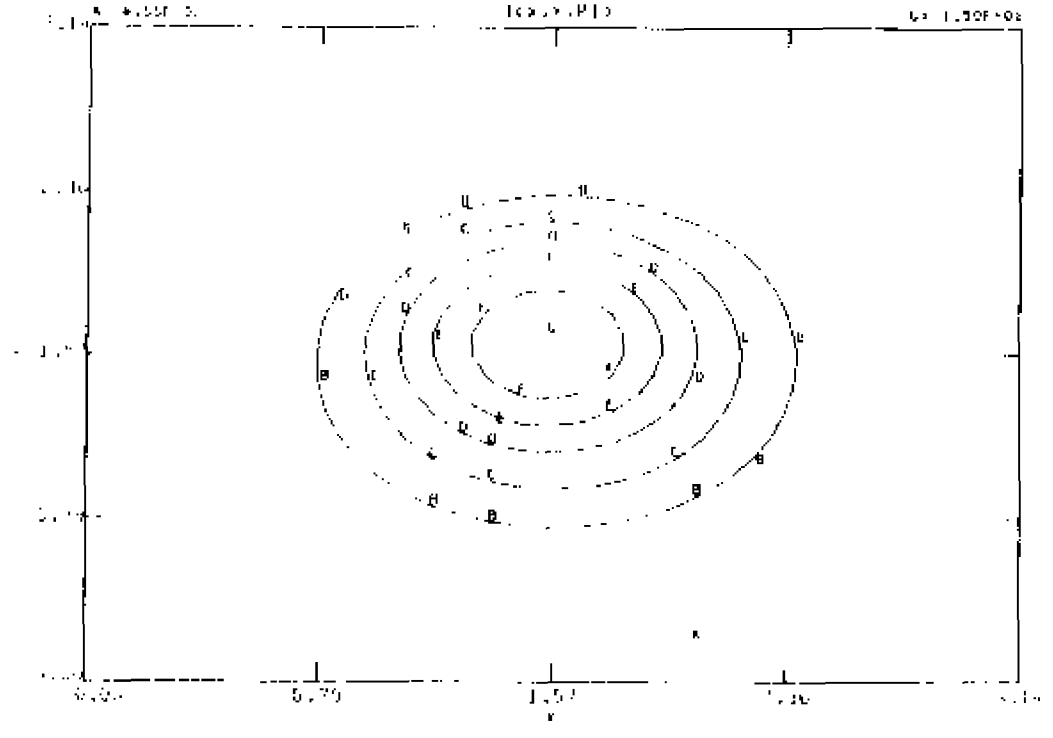

13 (b): contours of j = constant, poloidal cut,

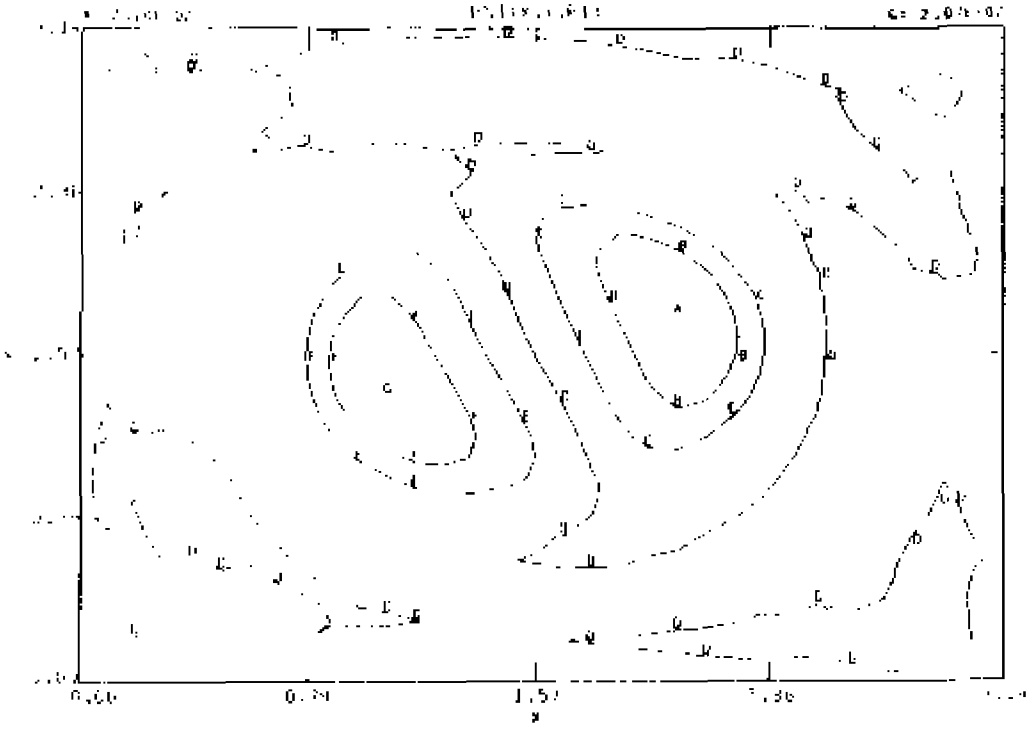

13 (c): contours of Ψ = constant, poloidal cut.

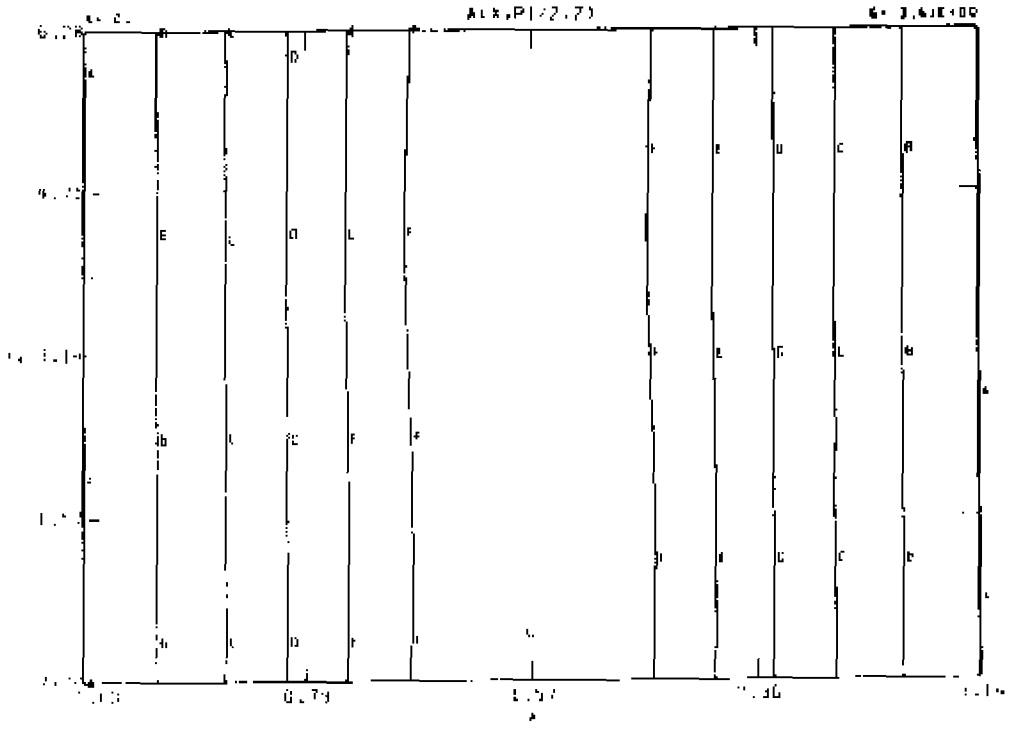

13 (d): contours of A = constant, toroidal cut.

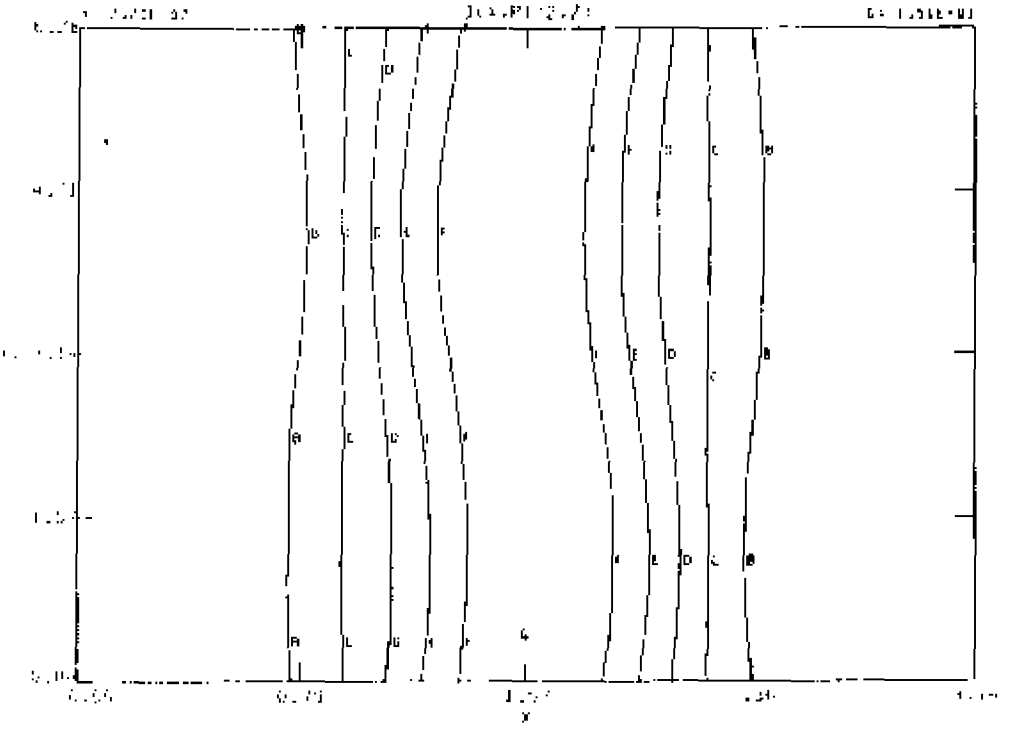

13 (e): contours of j = constant, toroidal cut.

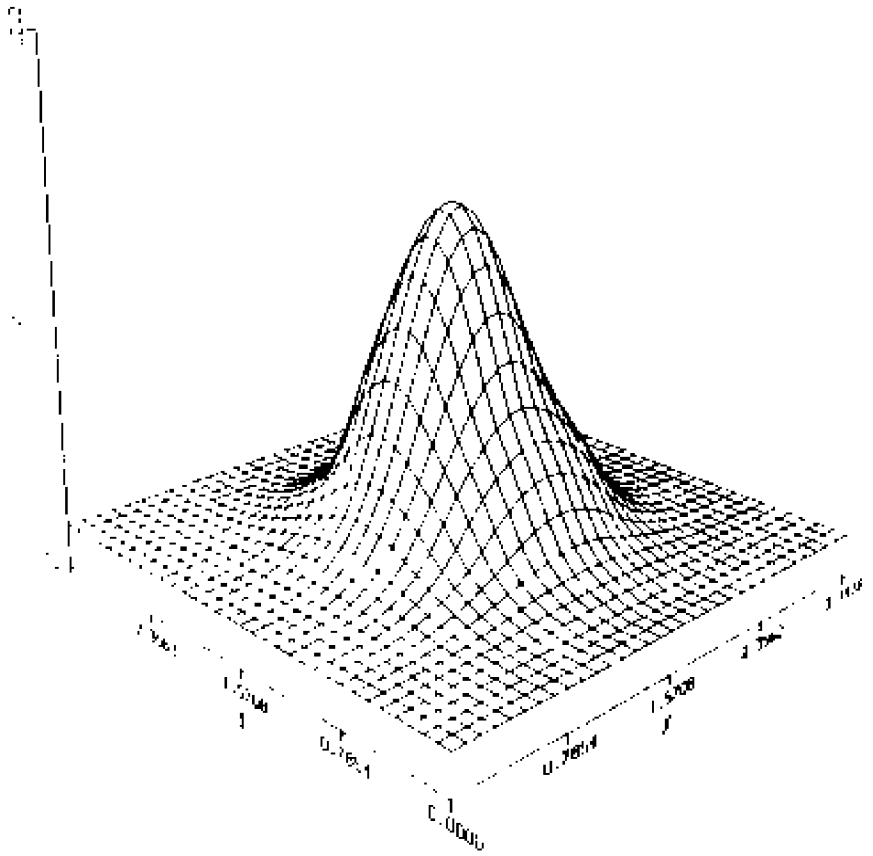

Figure 14. - At t = 4.44, CASE 2:
14 (a): a 3-d perspective plot of j, poloidal cut, at t = 4.44.

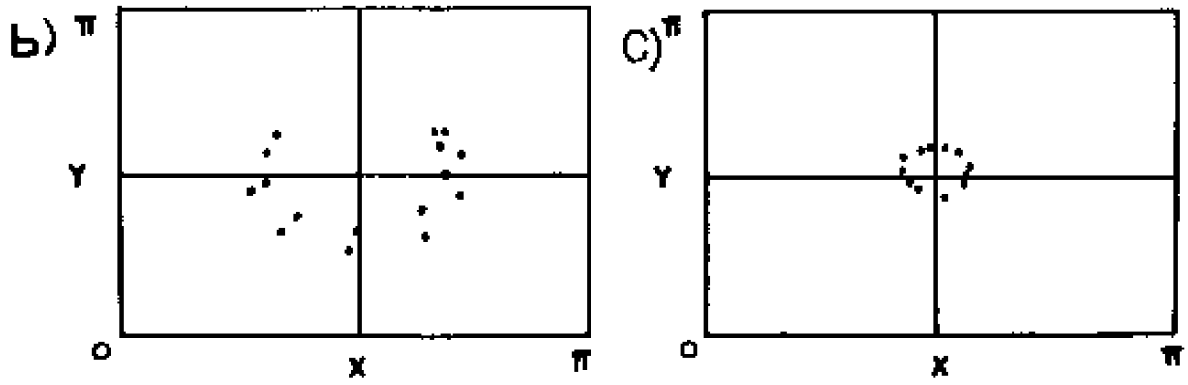

14 (b), 14 (c): Poincare plots of magnetic field line traces in the z =π plane.

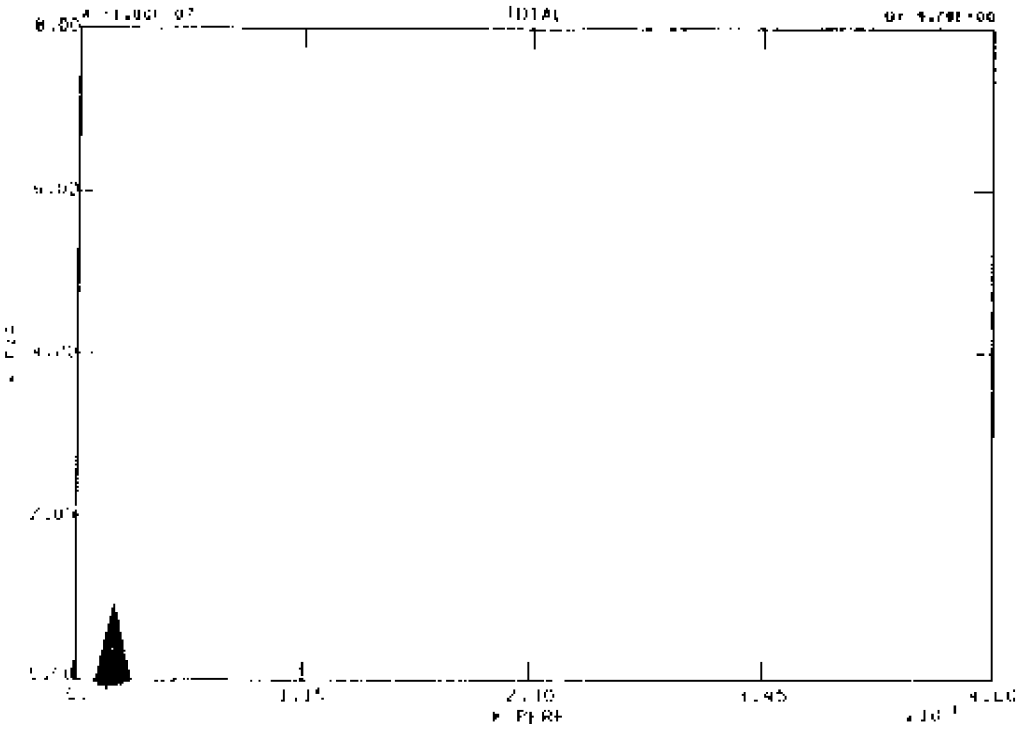

15 (c): equally spaced contours of constant total energy.

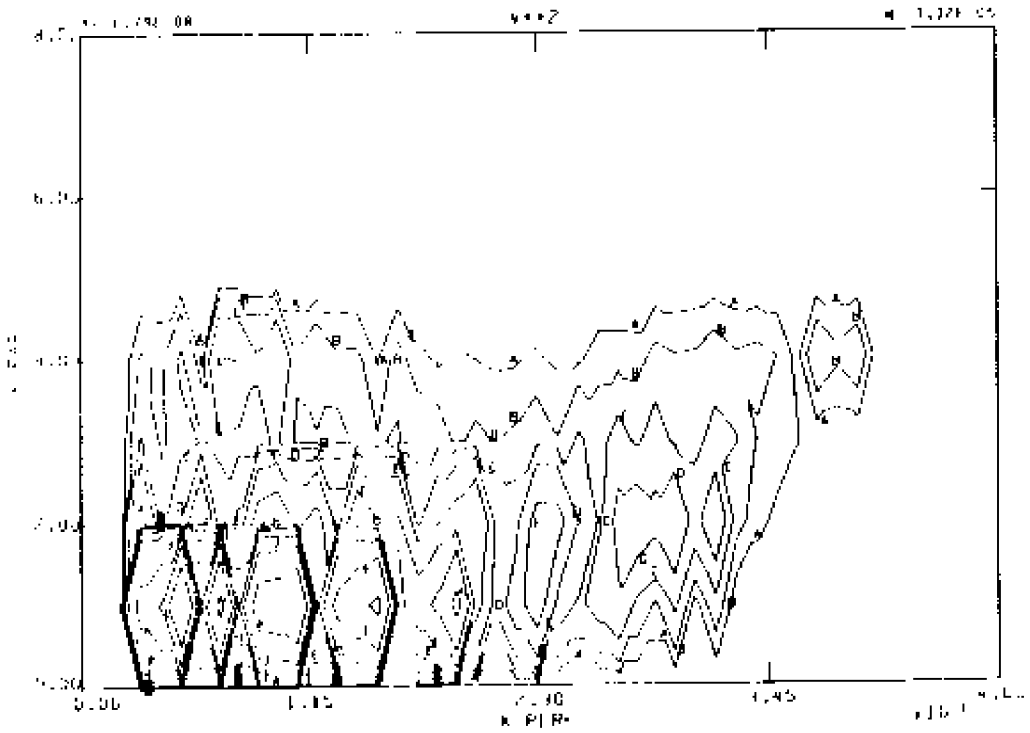

15 (d): contours separated by powers of two of constant kinetic energy

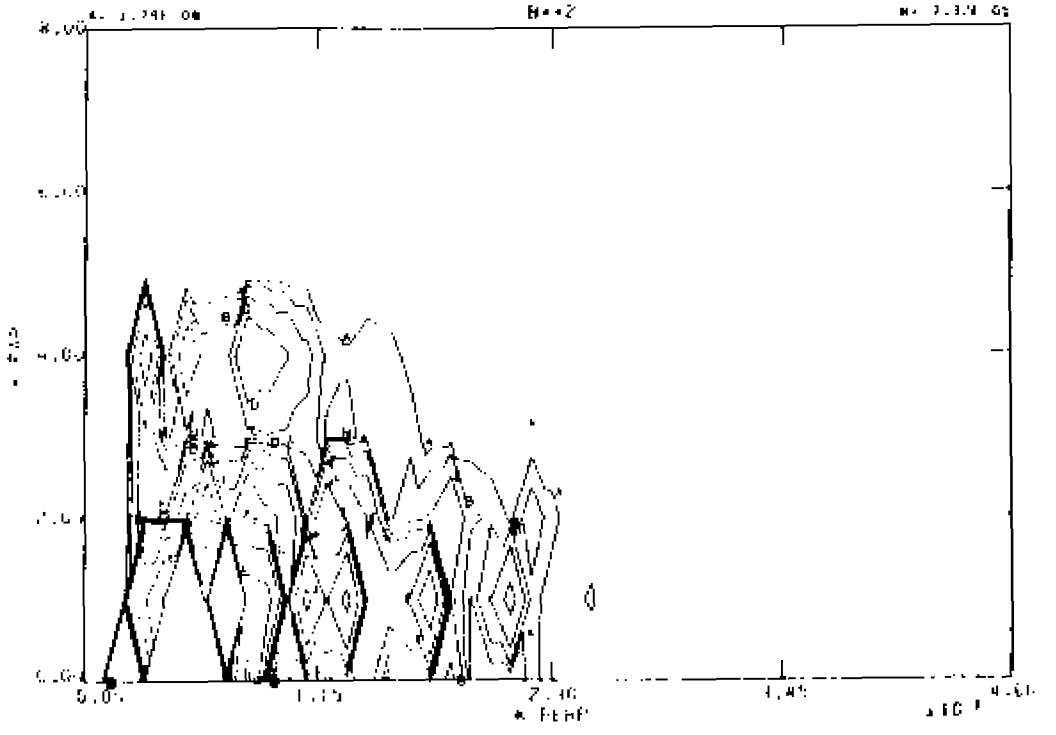

15 (e): contours separated by powers of two of constant magnetic energy

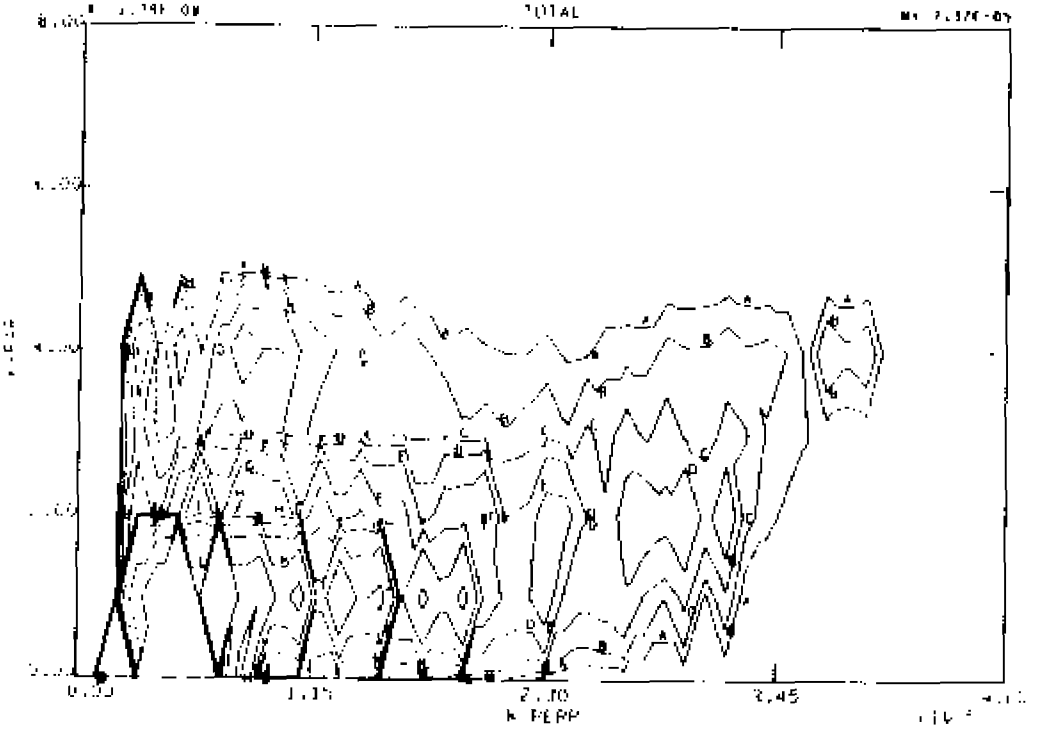

15 (f): contours separated by powers of two of constant total energy

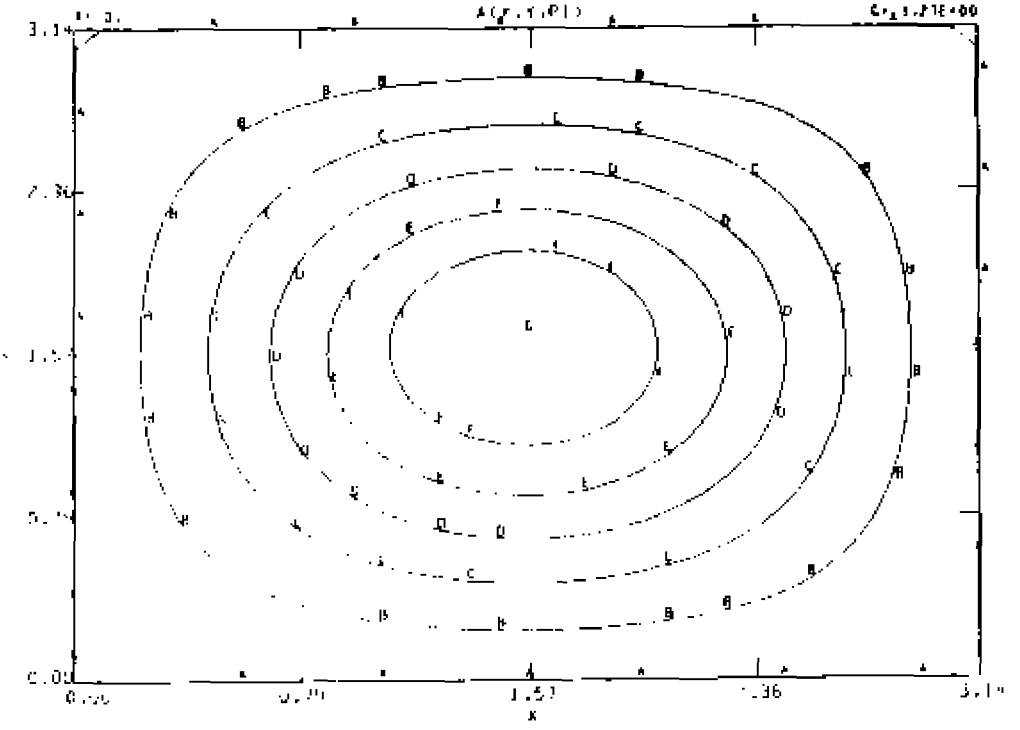

Figure 16. - Contour plots at t = 6.68 from CASE 2:
16 (a): contours of A = constant, poloidal cut,

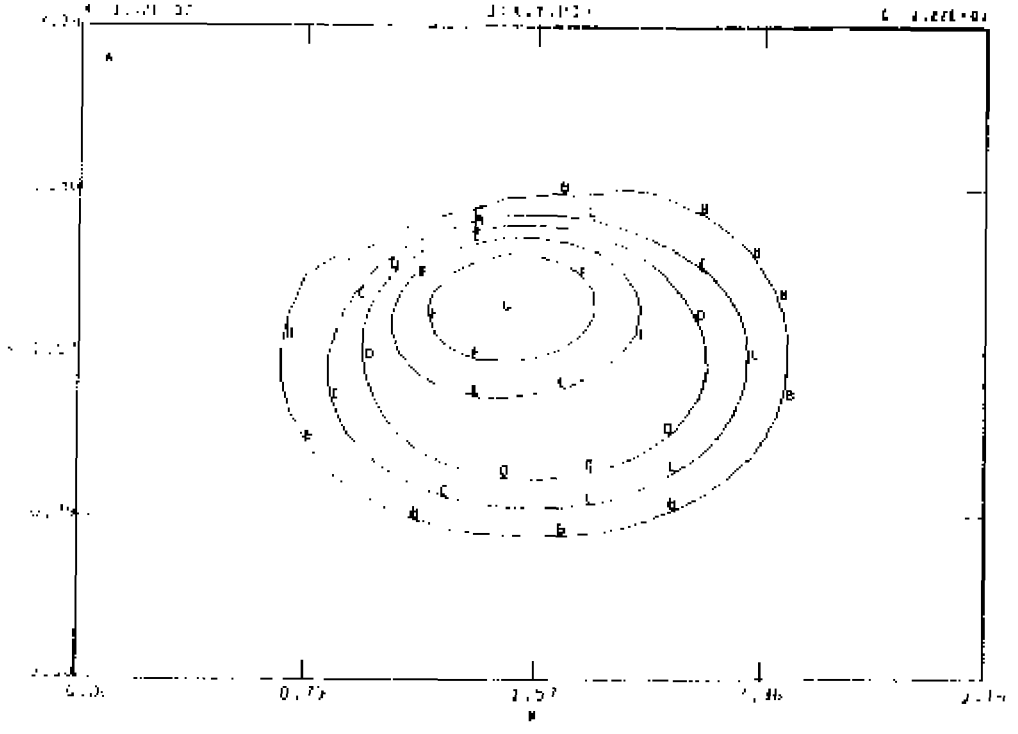

16 (b): contours of j = constant, poloidal cut.

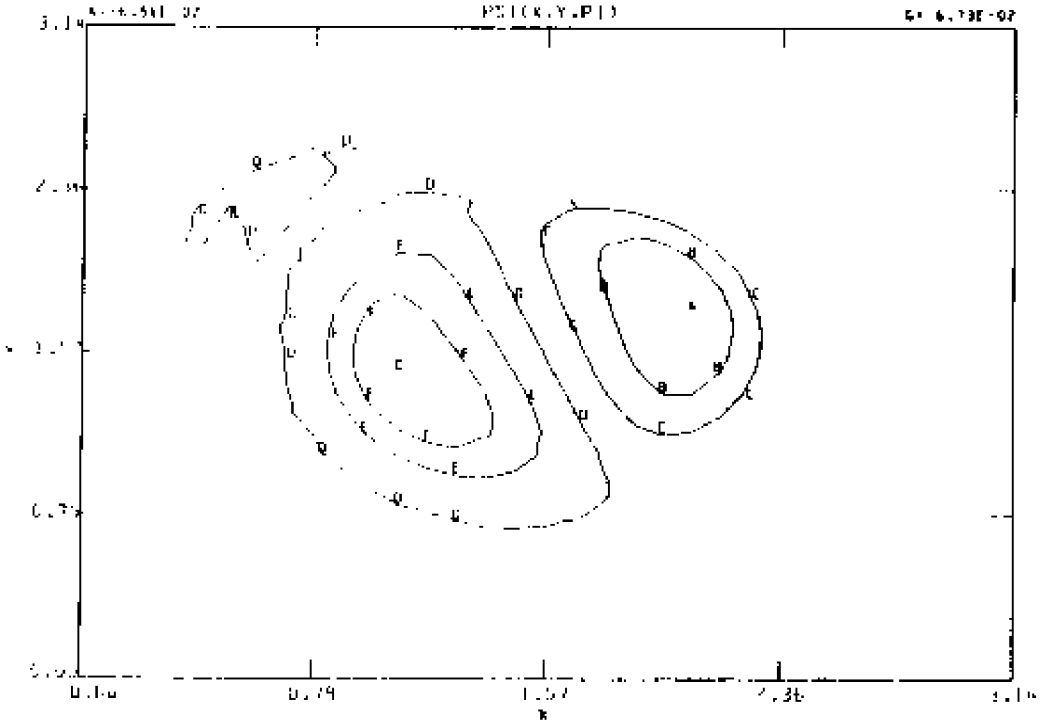

16 (c): contours of Ψ= constant, poloidal cut.

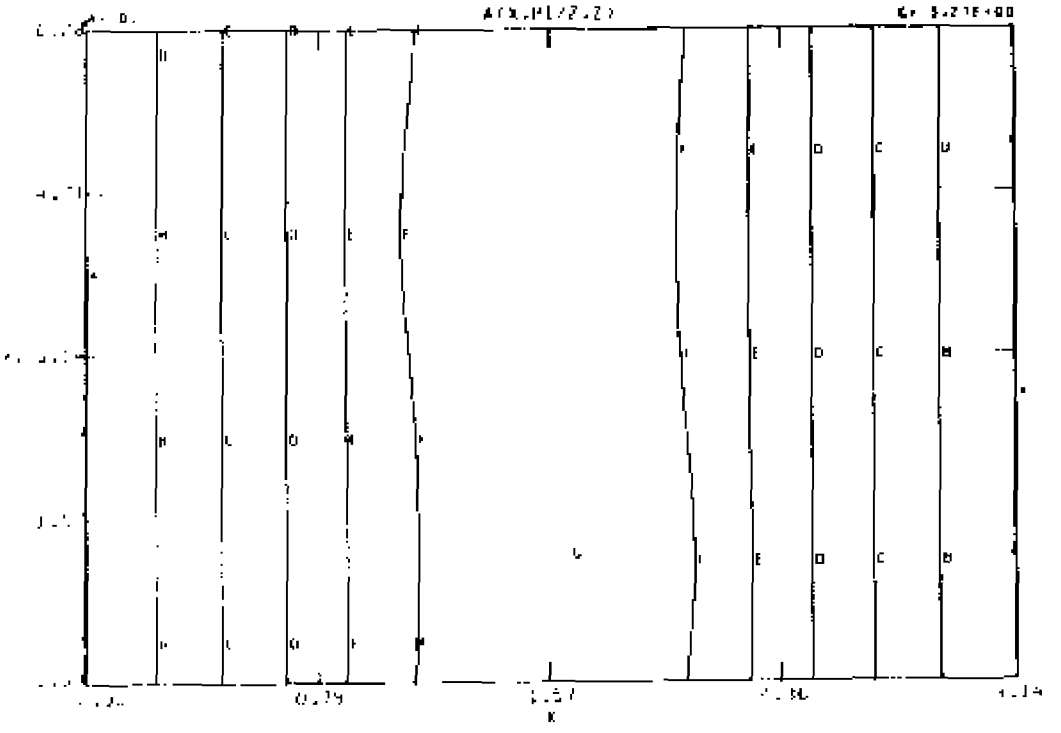

16 (d): contours of A = constant, toroidal cut.

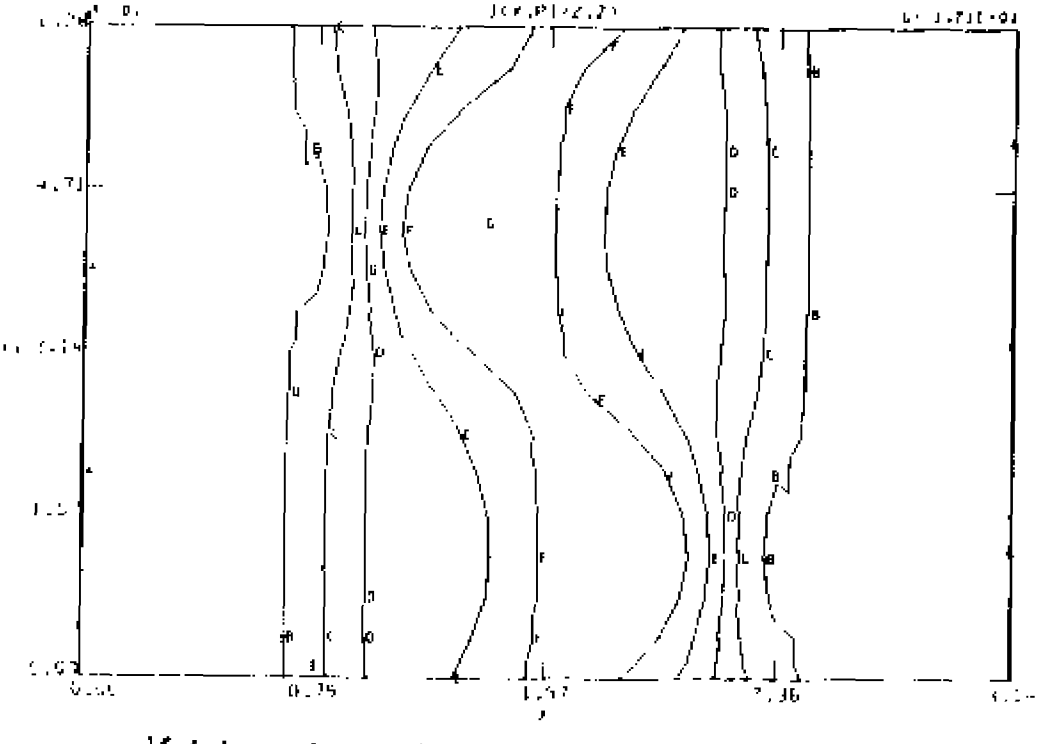

16 (e): contours of j = constant, toroidal cut.

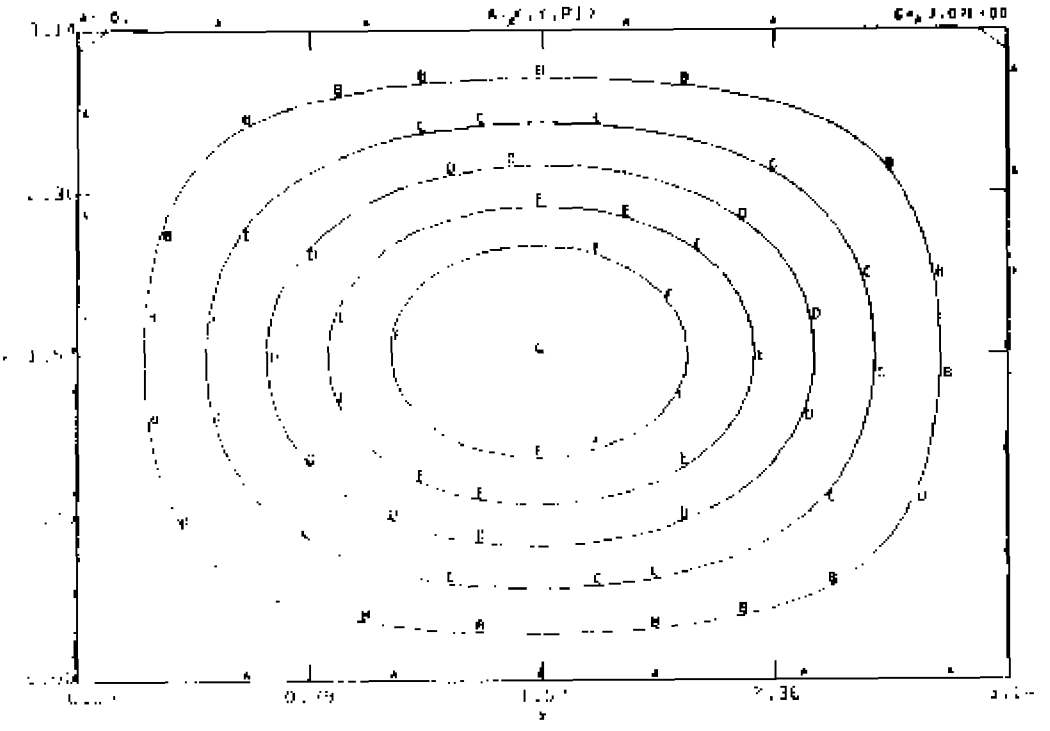

Figure 17. - Contour plots at t = 7.80 from CASE 2:
17 (a): contours of A = constant, poloidal cut,

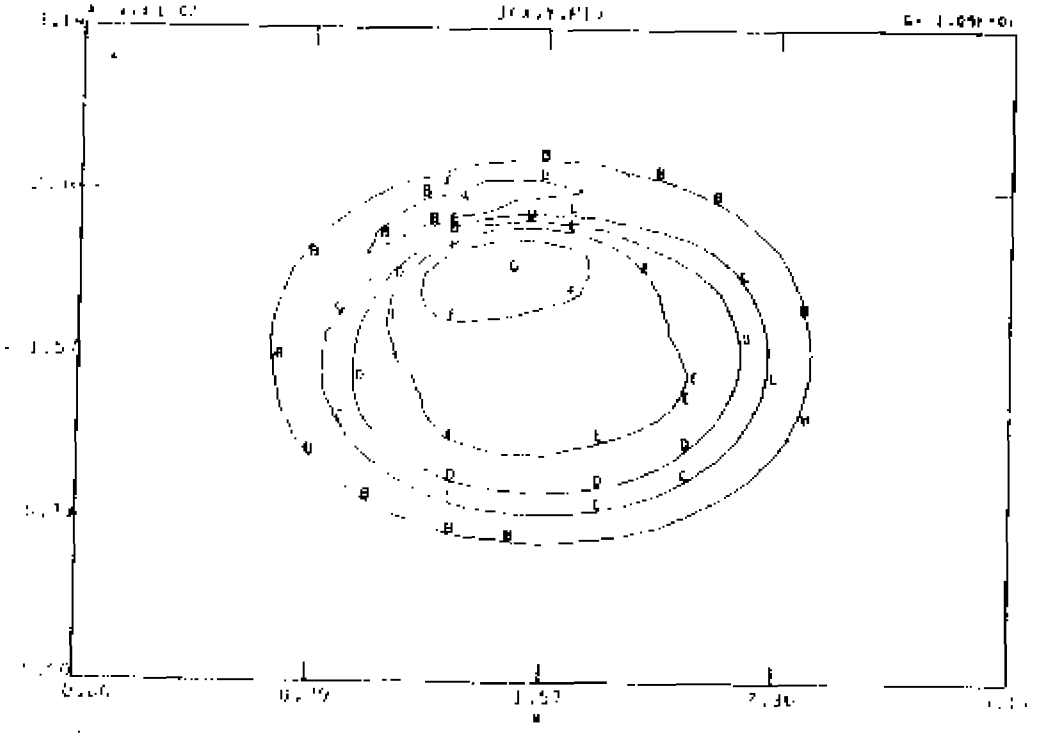

17 (b): contours of j = constant, poloidal cut.

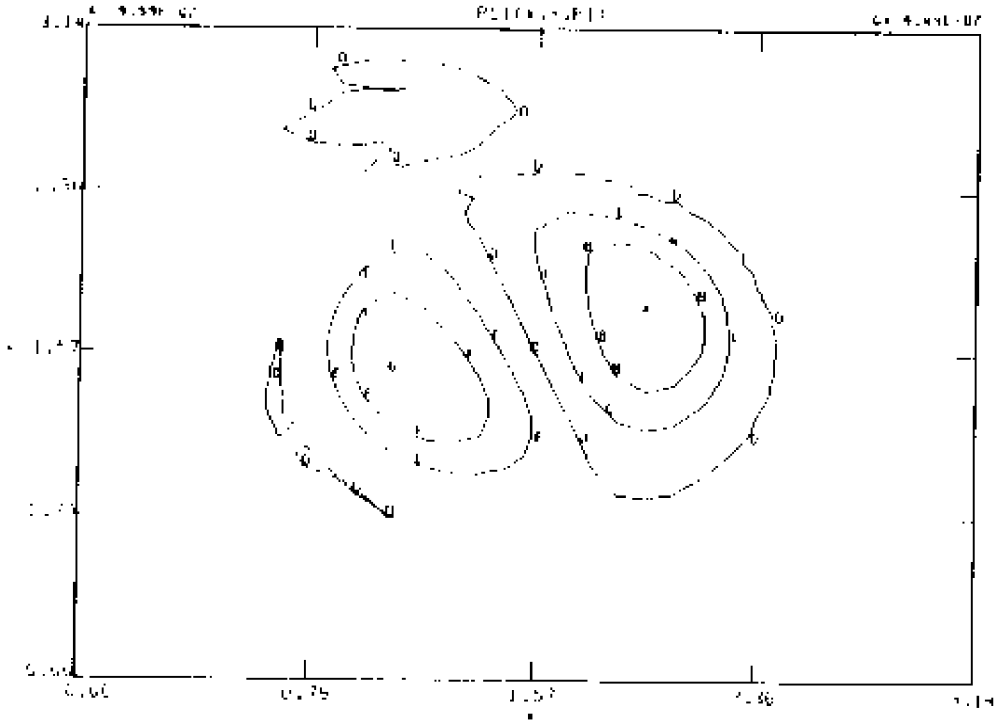

17 (c): contours of Ψ= constant, poloidal cut.

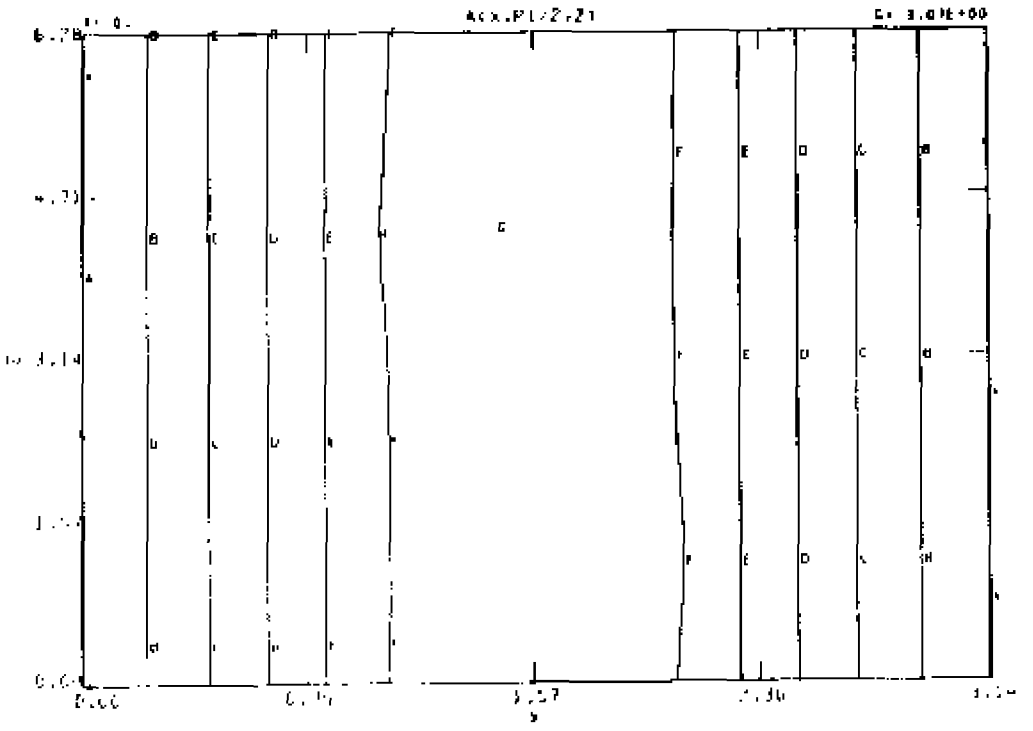

17 (d): contours of A = constant, toroidal cut.

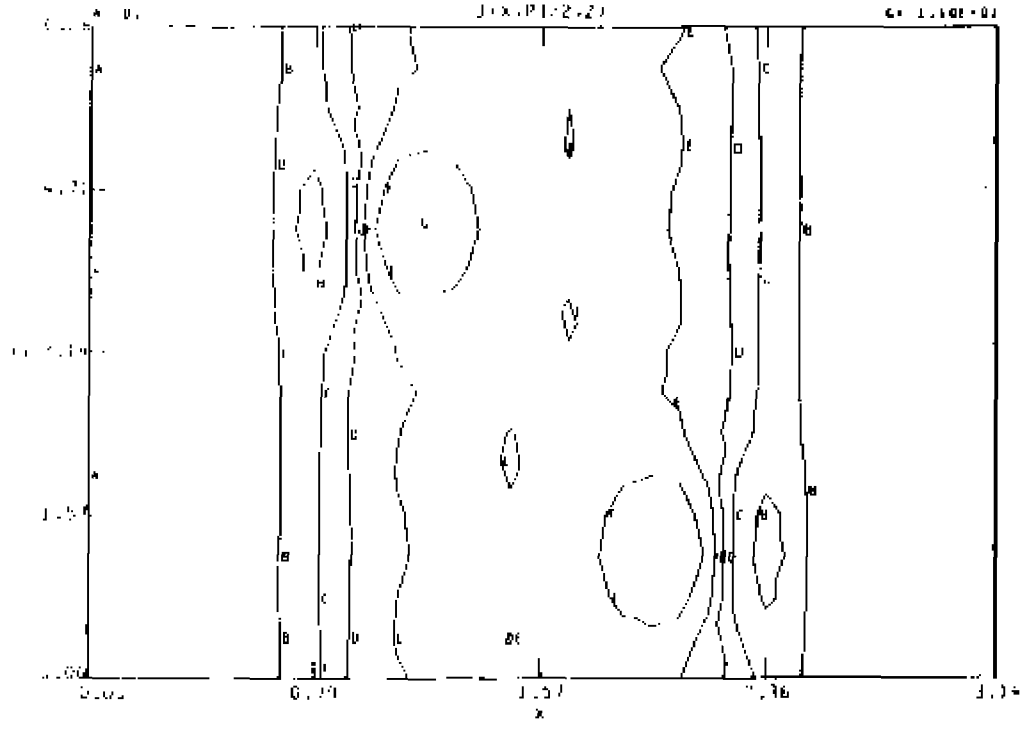

17 (e): contours of j = constant, toroidal cut.

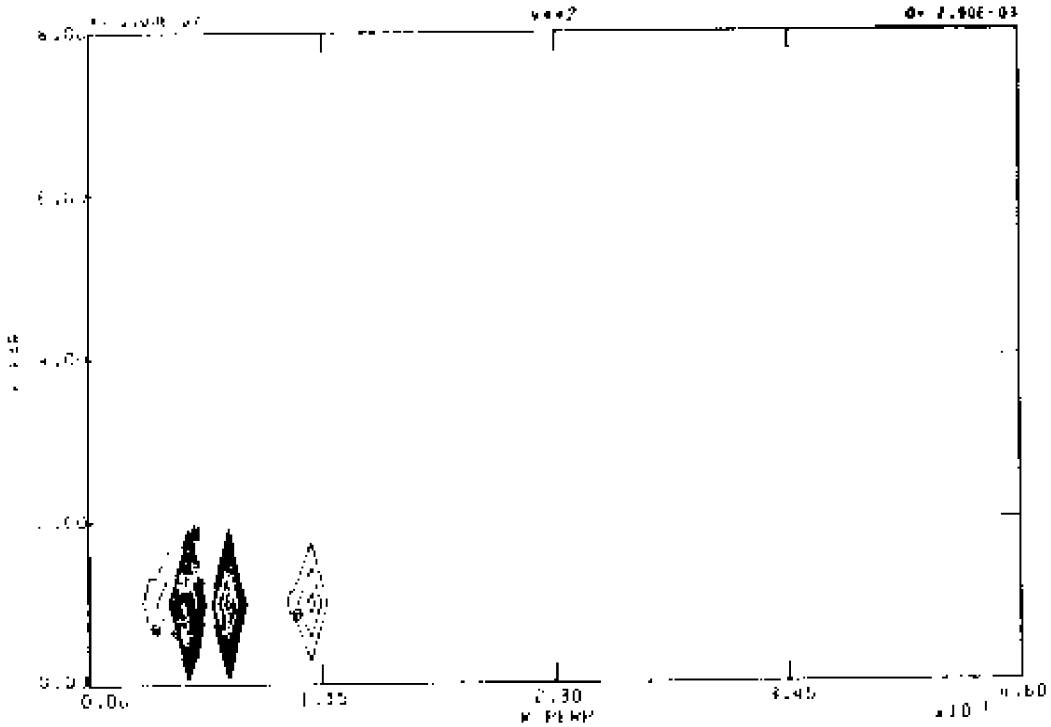

Figure 18. - Contours of energy in Fourier space at t = 7.80, CASE 2:
18 (a): equally spaced contours of constant kinetic energy.

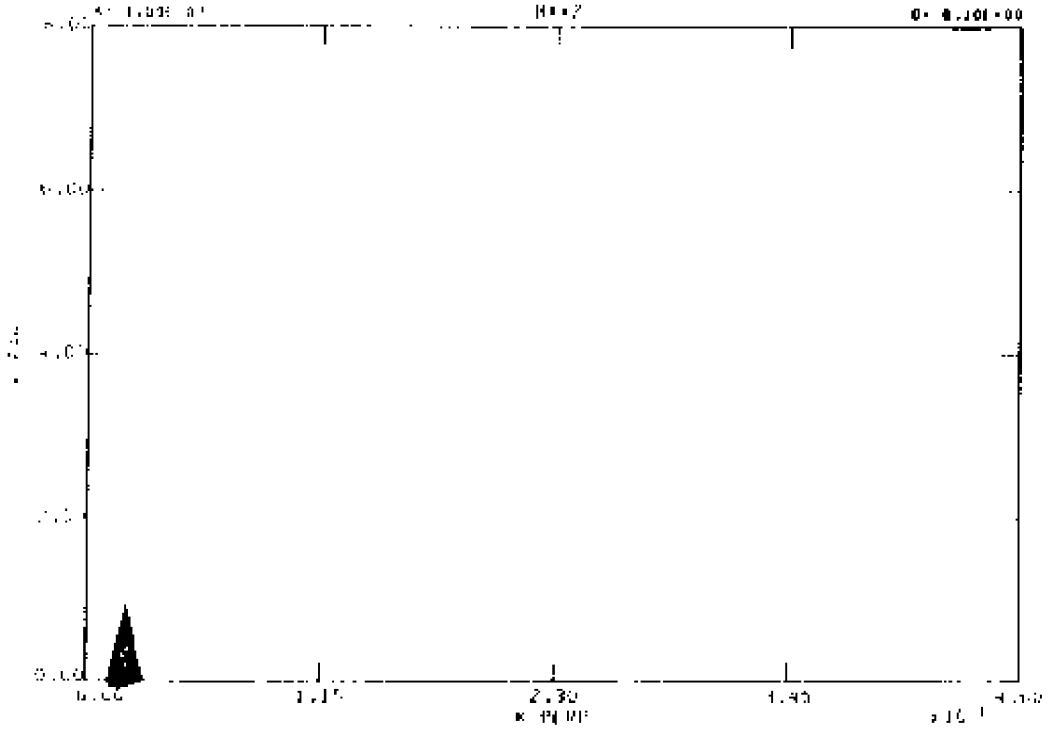

18 (b): equally spaced contours of constant magnetic energy.

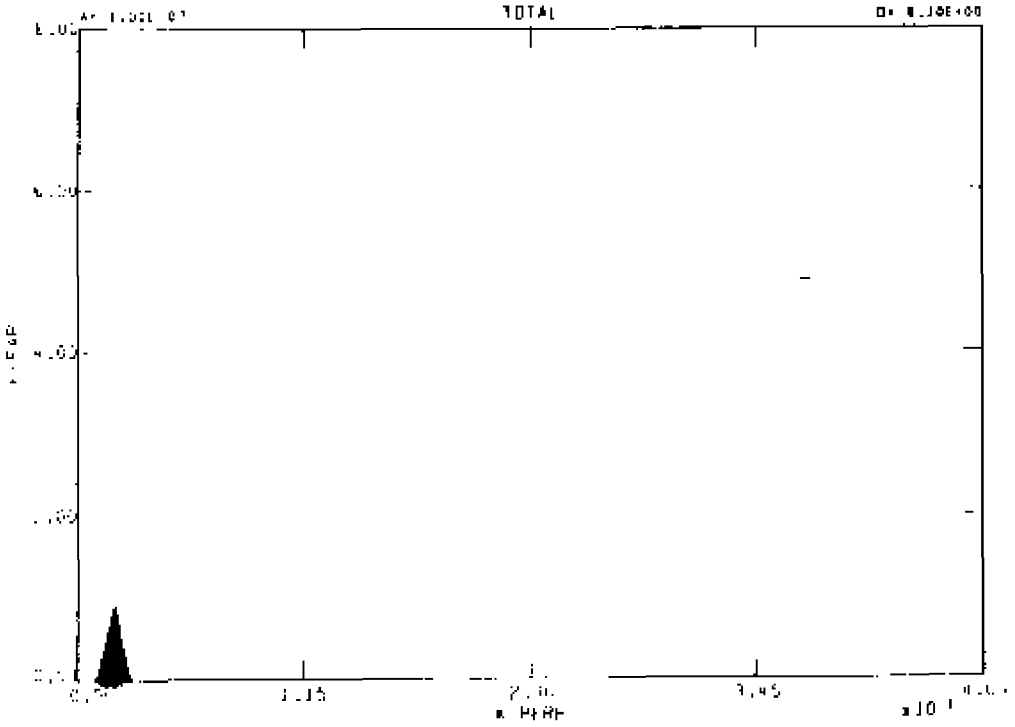

18 (c): equally spaced contours of constant total energy.

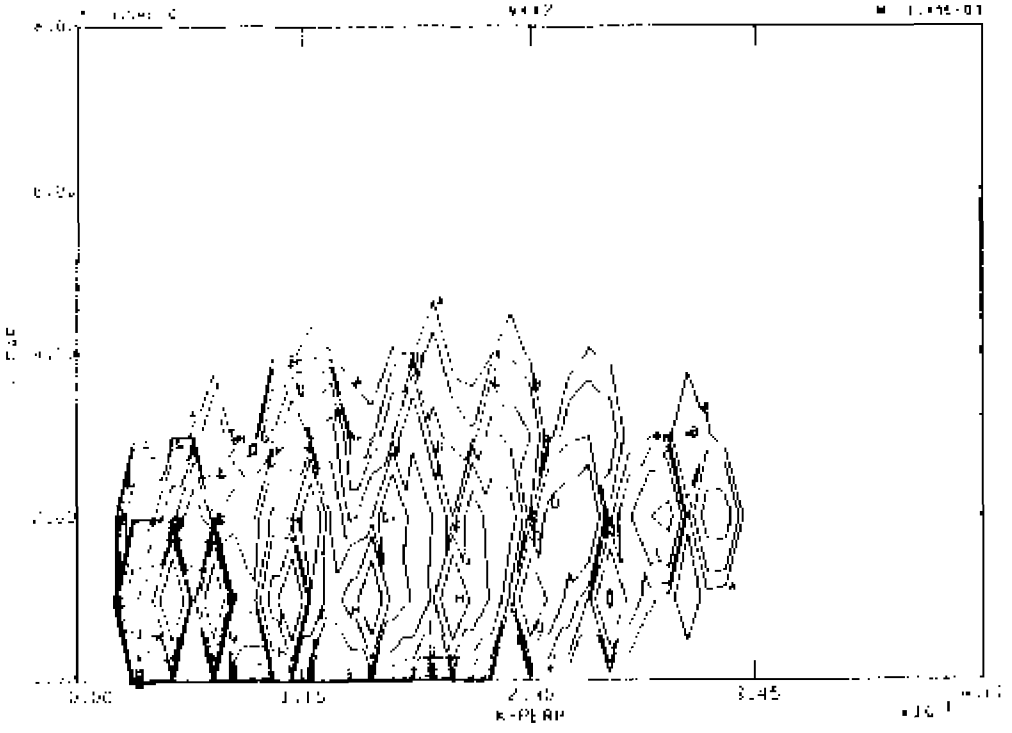

18 (d): contours separated by powers of two of constant kinetic energy.

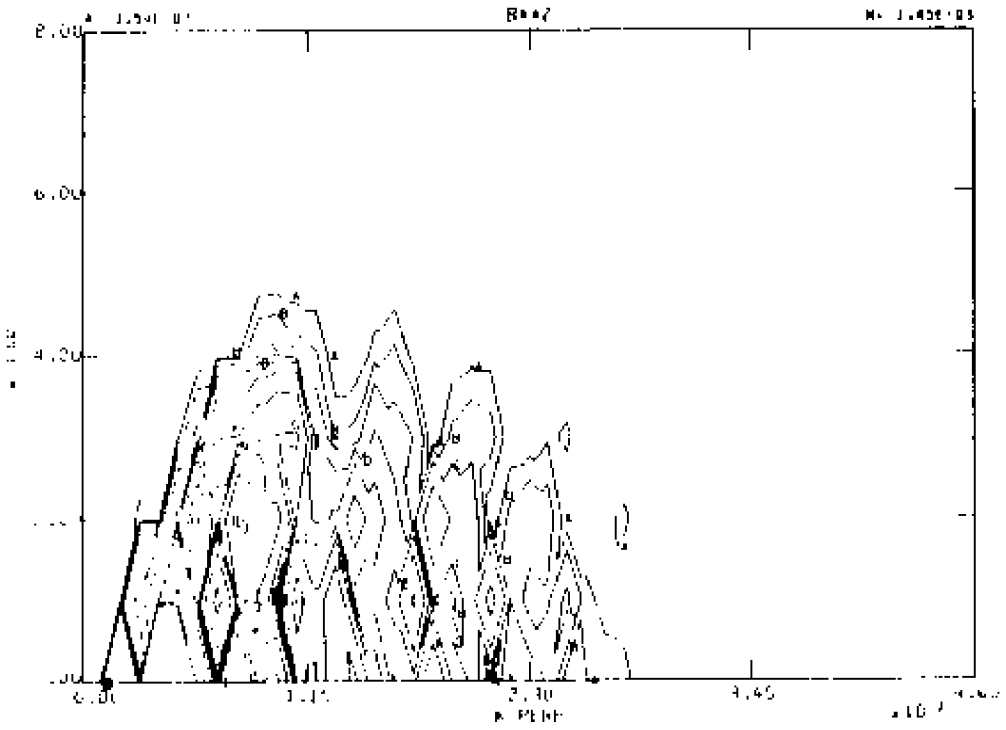

18 (e): contours separated by powers of two of constant magnetic energy.

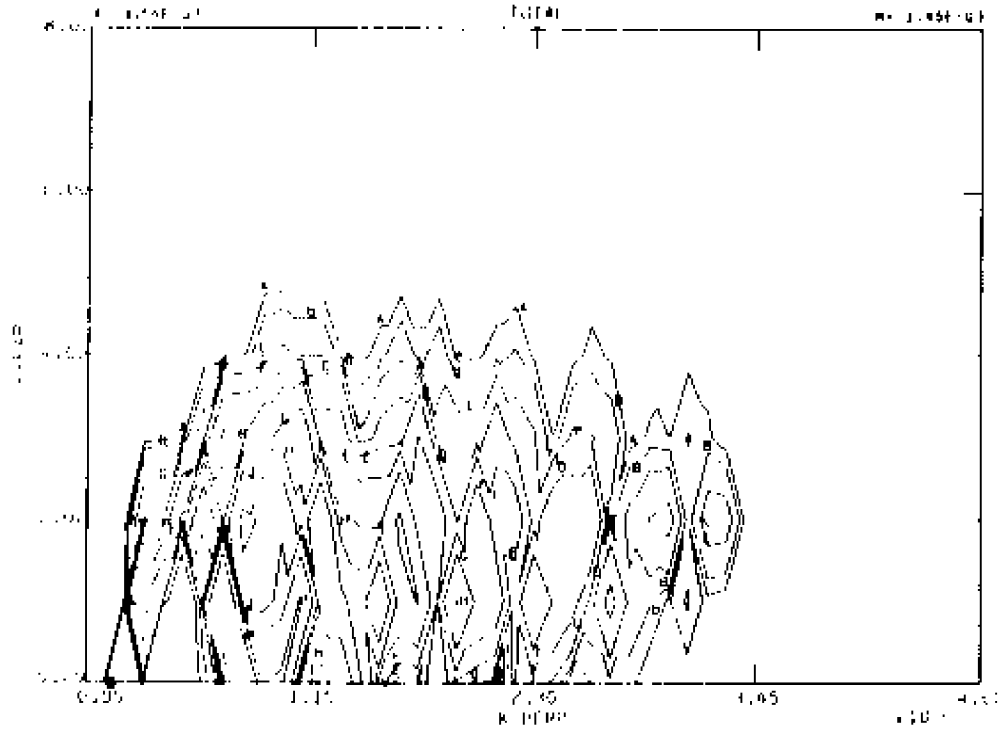

18 (f): contours separated by powers of two of constant total energy

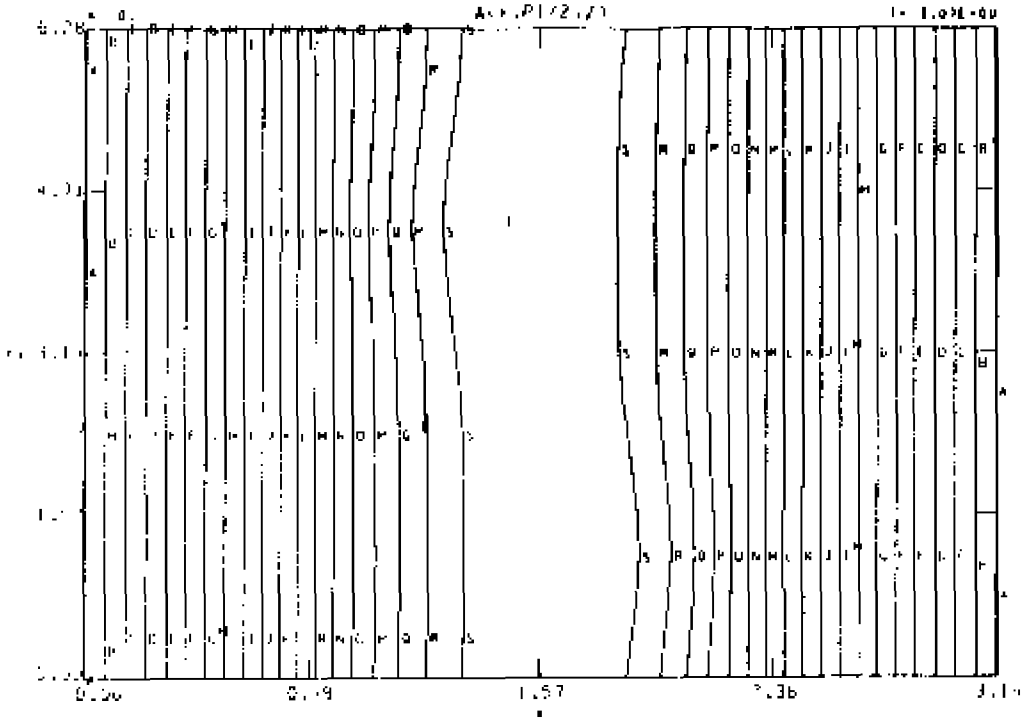

Figure 19. - At t = 7.88, CASE 2, enlarged toroidal cuts of:
19(a) vector potential, A, and

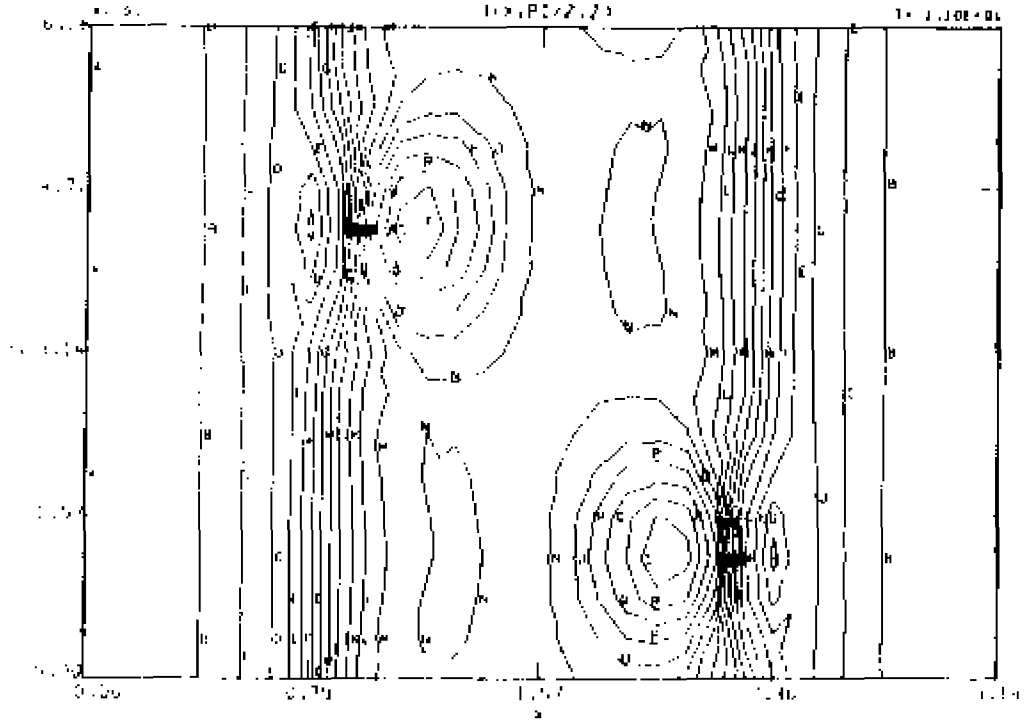

19(b) current density, j.

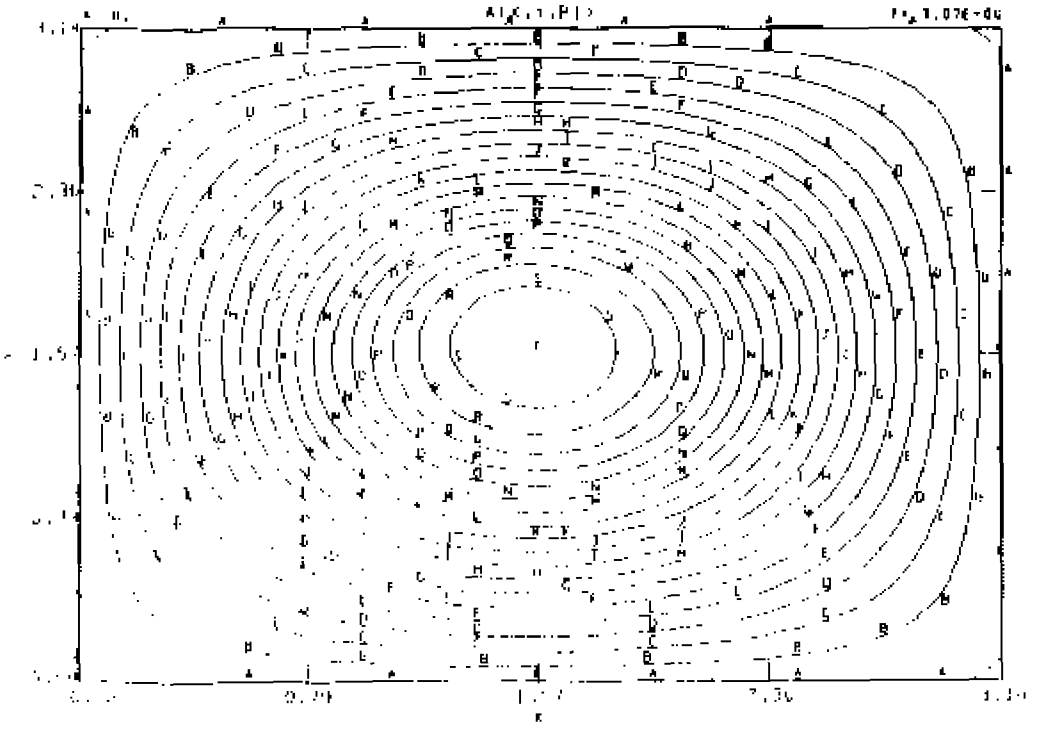

Figure 20. - At t = 7.00, CASE 2, enlarged poloidal cuts of:
20(a) vector potential, A, and

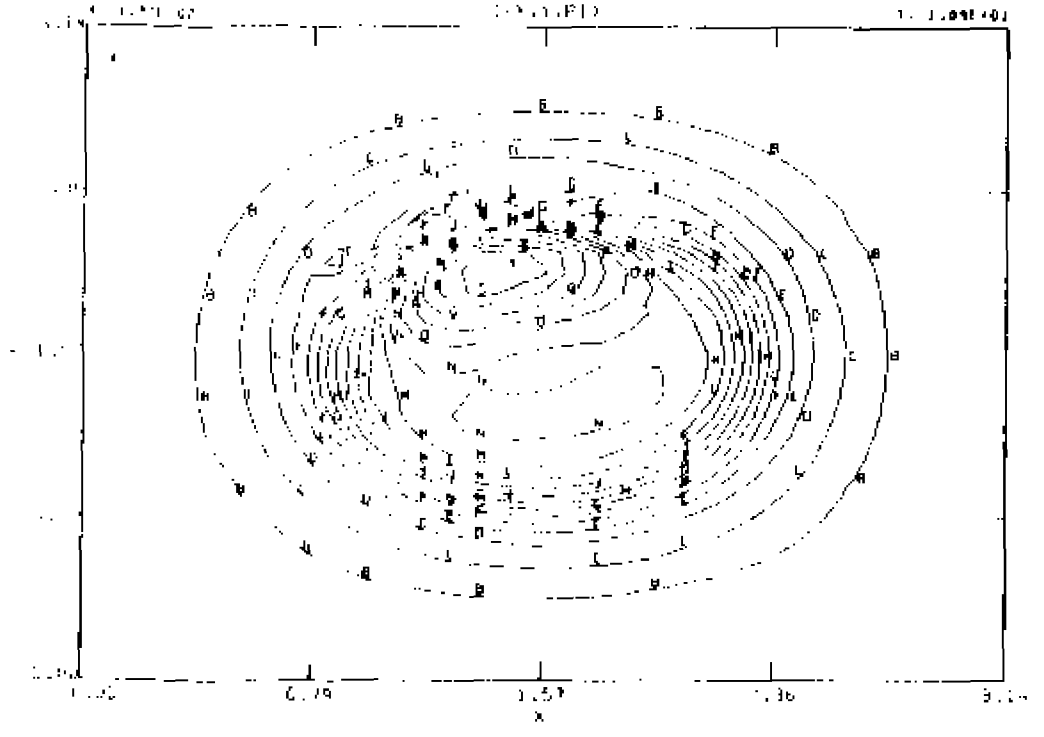

20(b) current density, j.

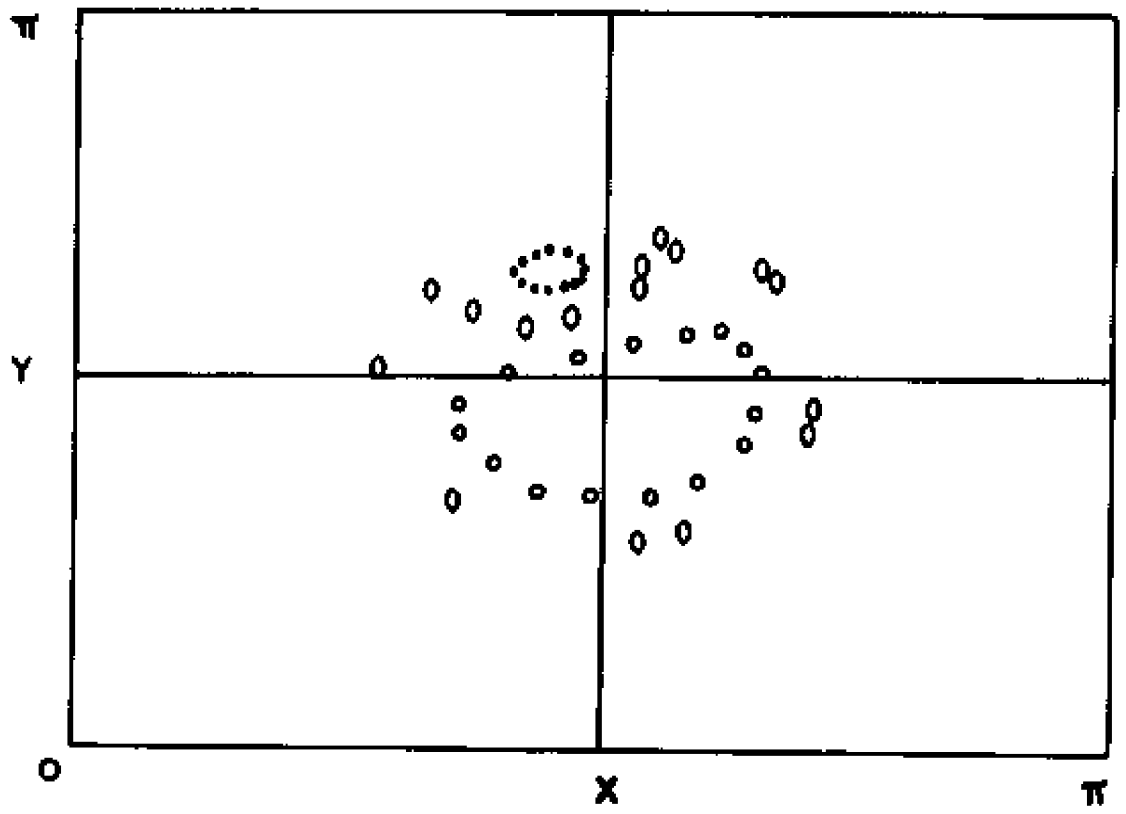

Figure 21. - Poincaré traces at t = 7.80 of magnetic field lines in the z = π plane, CASE 2.

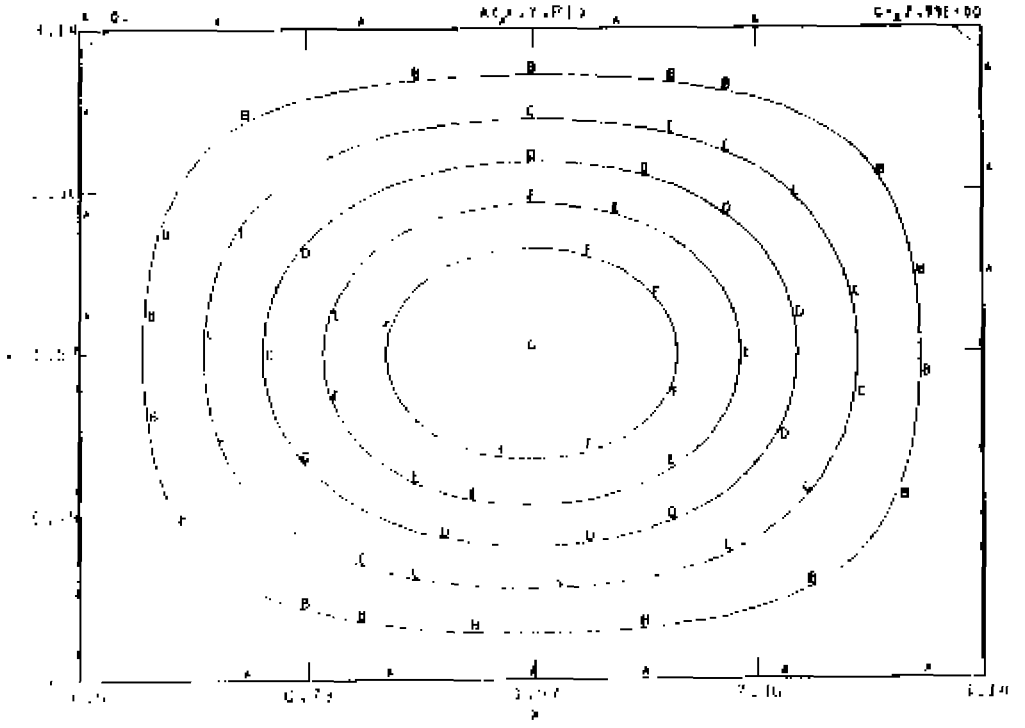

Figure 22. - Contour plots at t = 0.76 from CASE 2:
22 (a): contours of A = constant, poloidal cut,

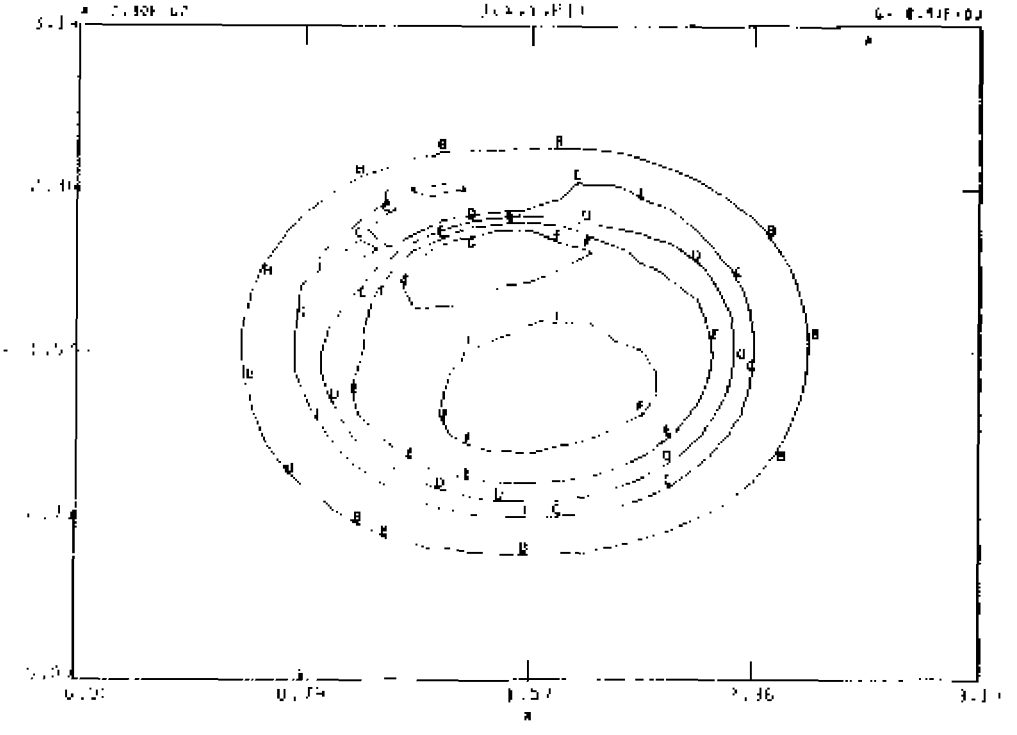

22 (b): contours of } = constant, poloidal cut,

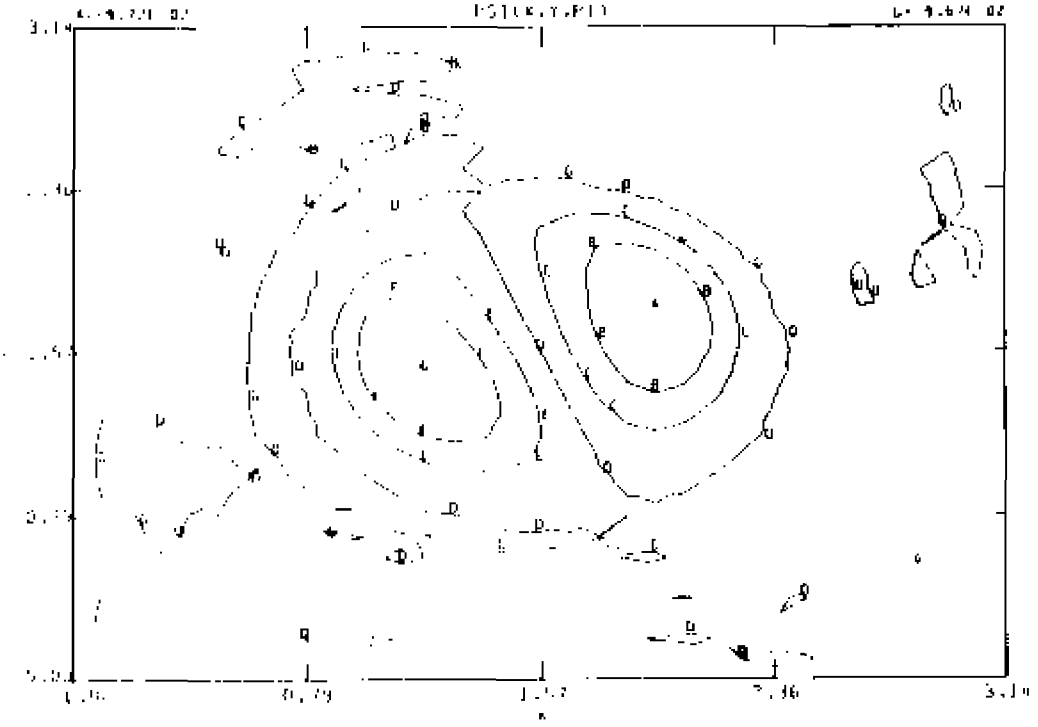

22 (c): contours of Ψ= constant, poloidal cut.

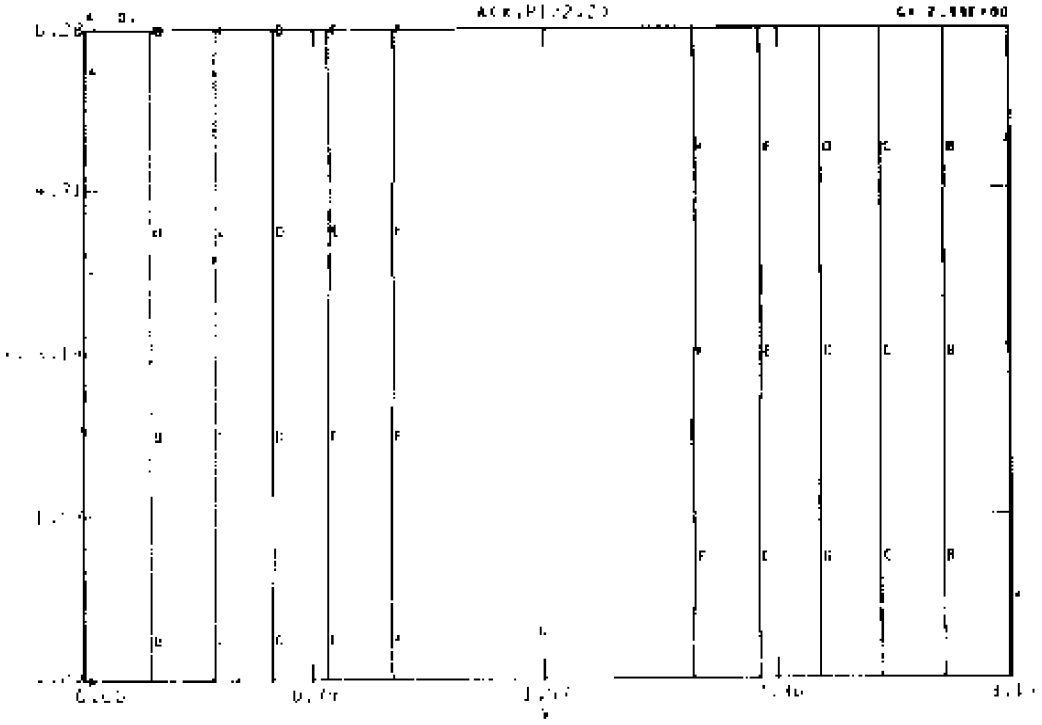

22 (d): contours of A = constant, toroidal cut.

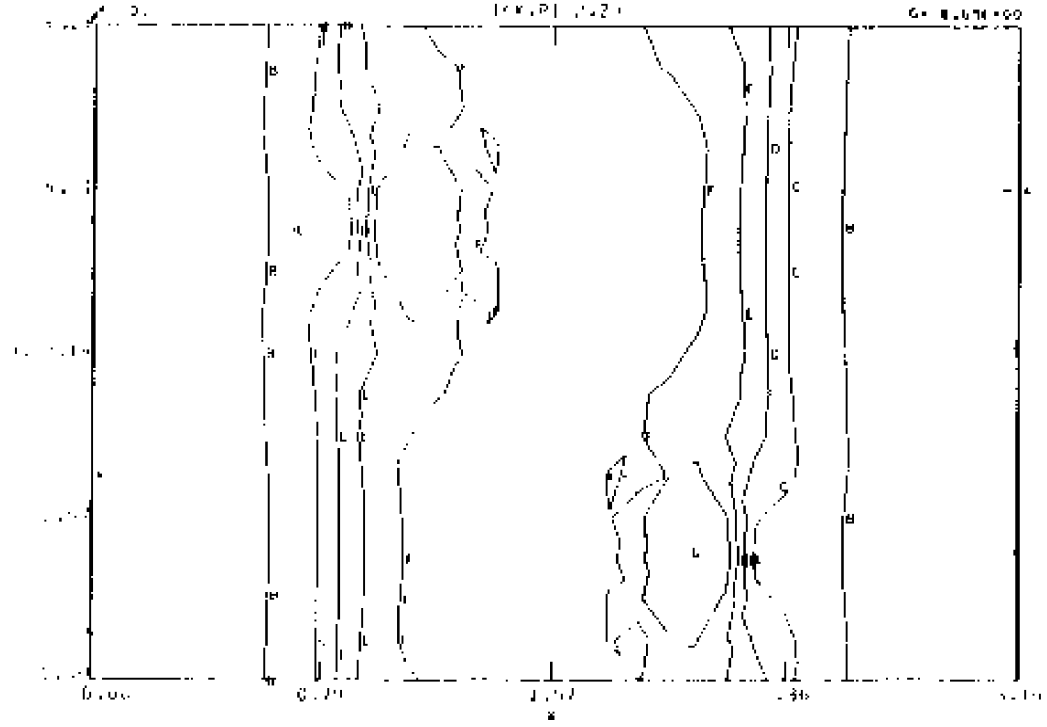

22 (e): contours of j = constant, toroidal cut.

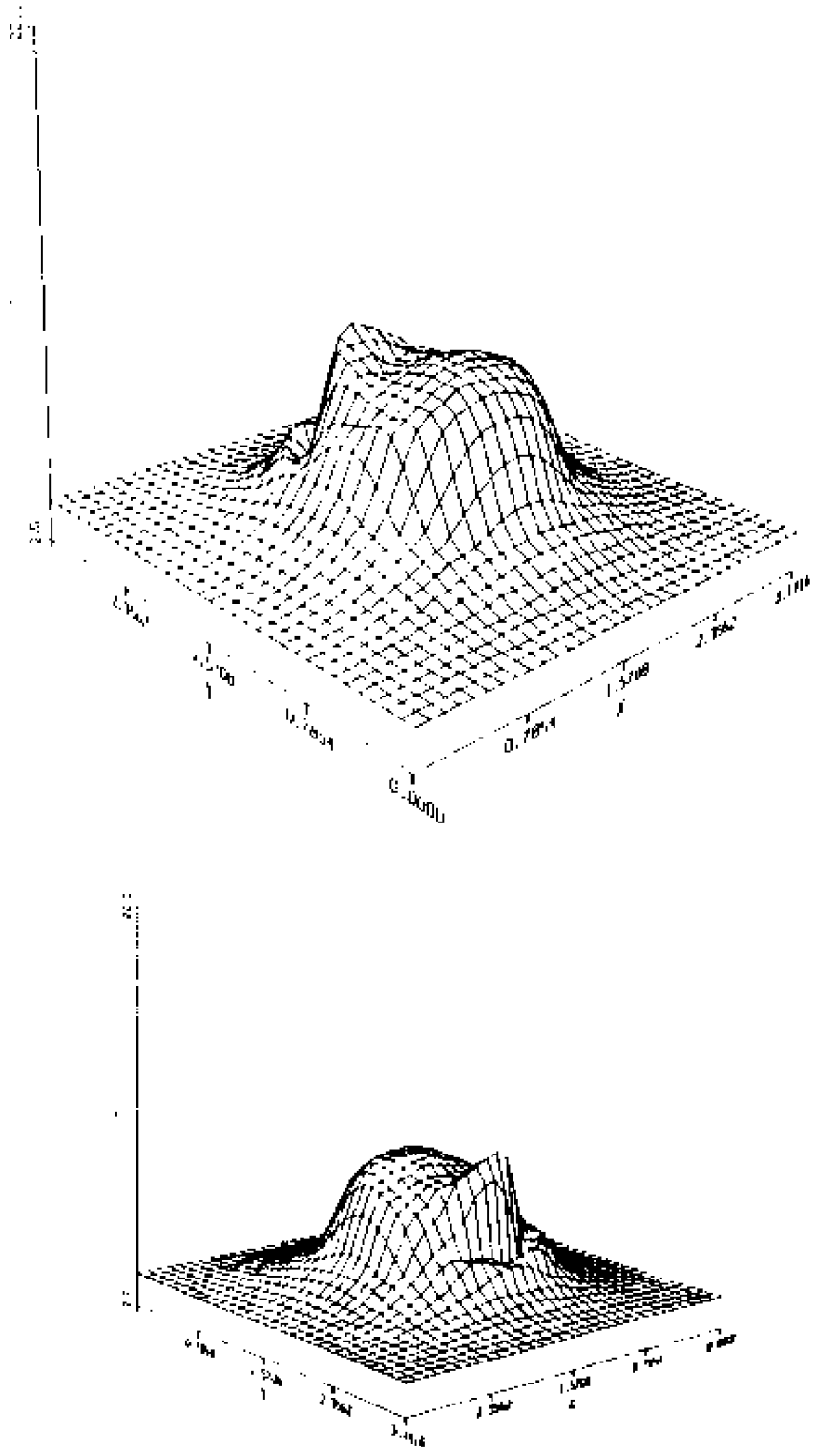

Figure 23. - Perspective plots of j(t = 8.82) in the z = π , plane, CASE 2.

Note: See Fig. 8(3e) for contour plots of the same quantity.

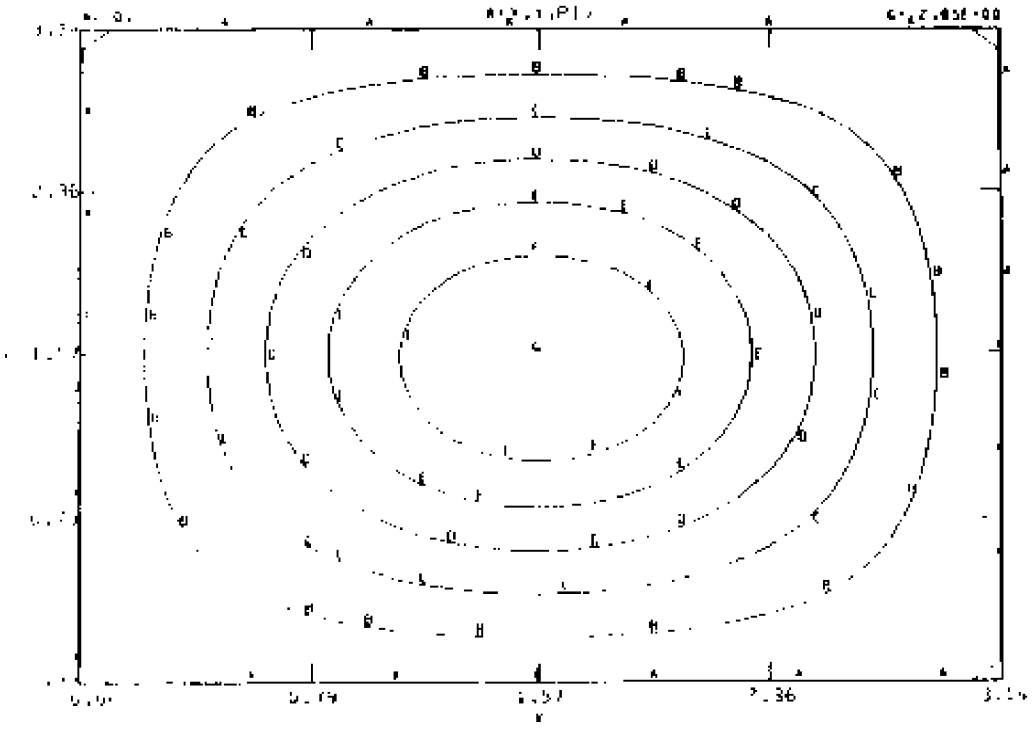

Figure 24. - Contour plots at t = 10.90 from CASE 2:
24 (a): contours of A = constant, poloidal cut,

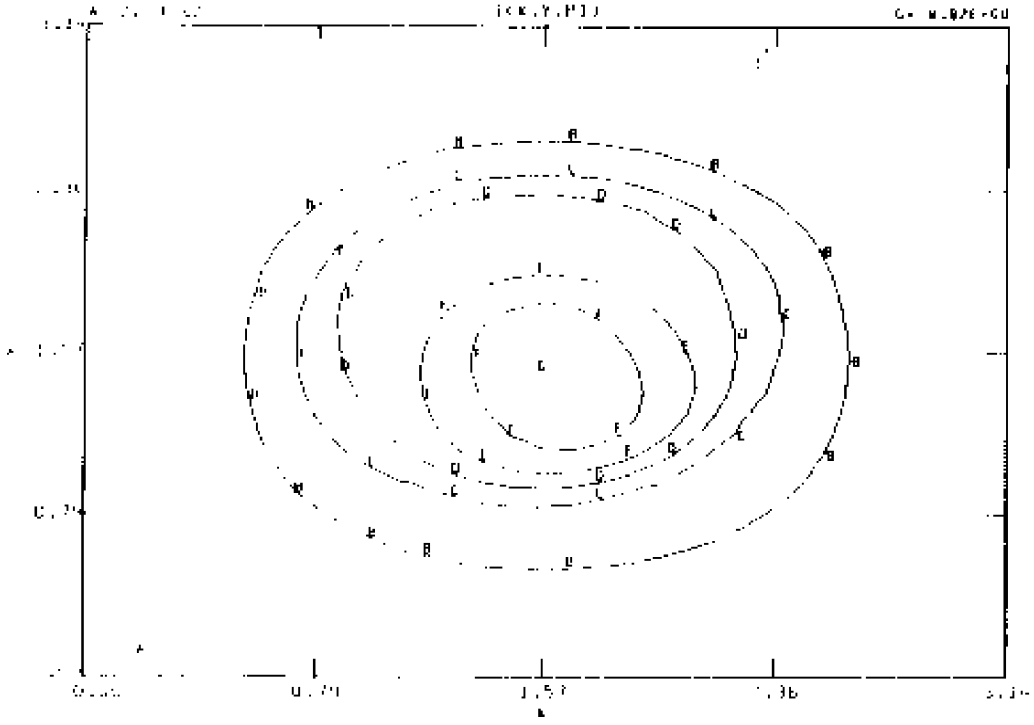

24 (b): contours of j = constant, poloidal cut,

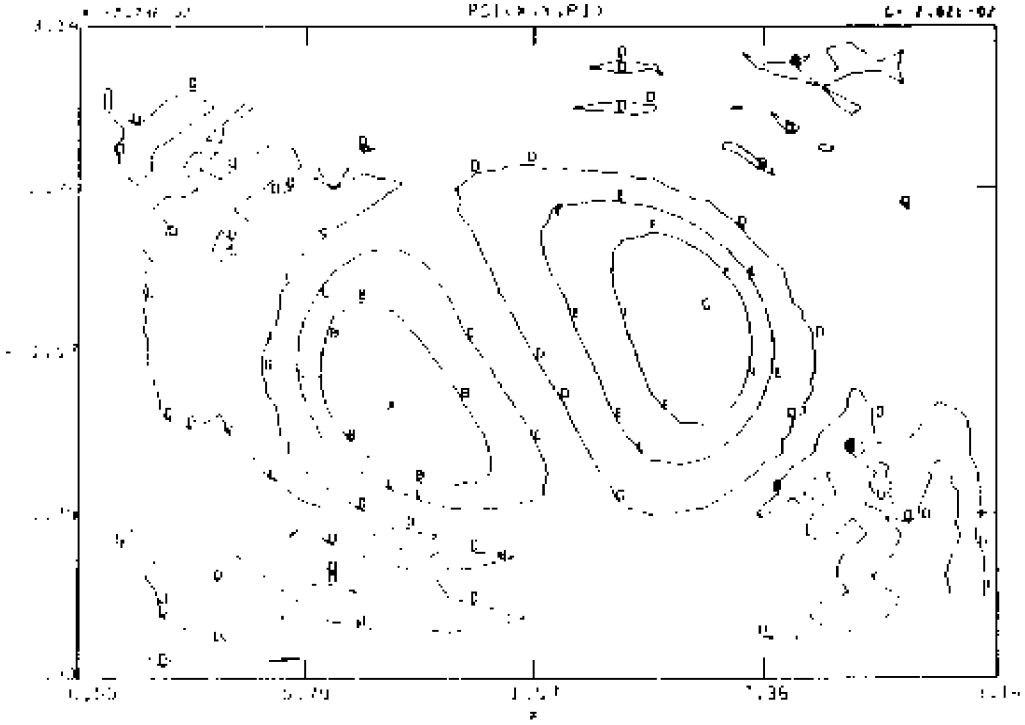

24 (c): contours of ψ= constant, poloidal cut.

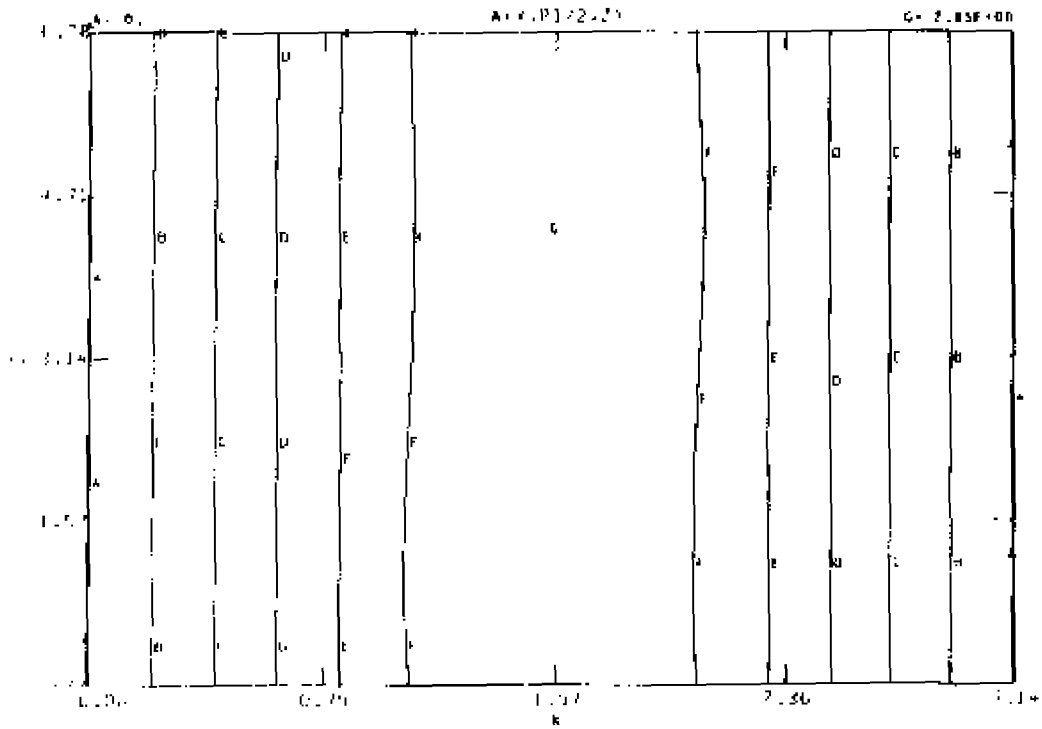

24 (d): contours of A = constant, toroidal cut.

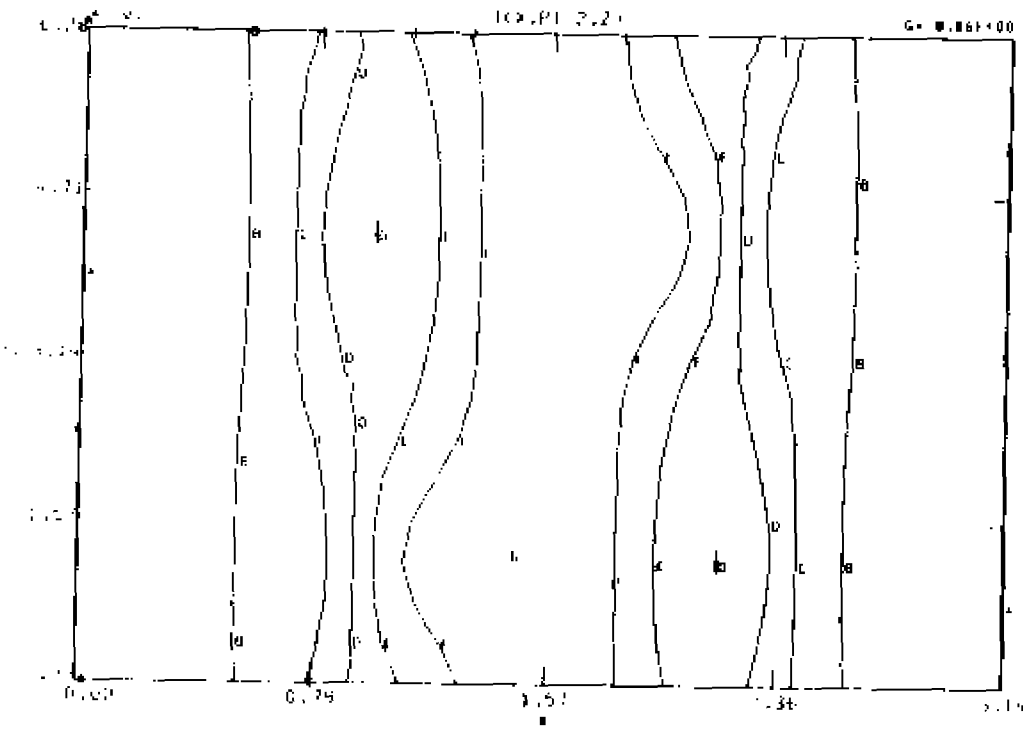

24 (e): contours of j = constant, toroidal cut.

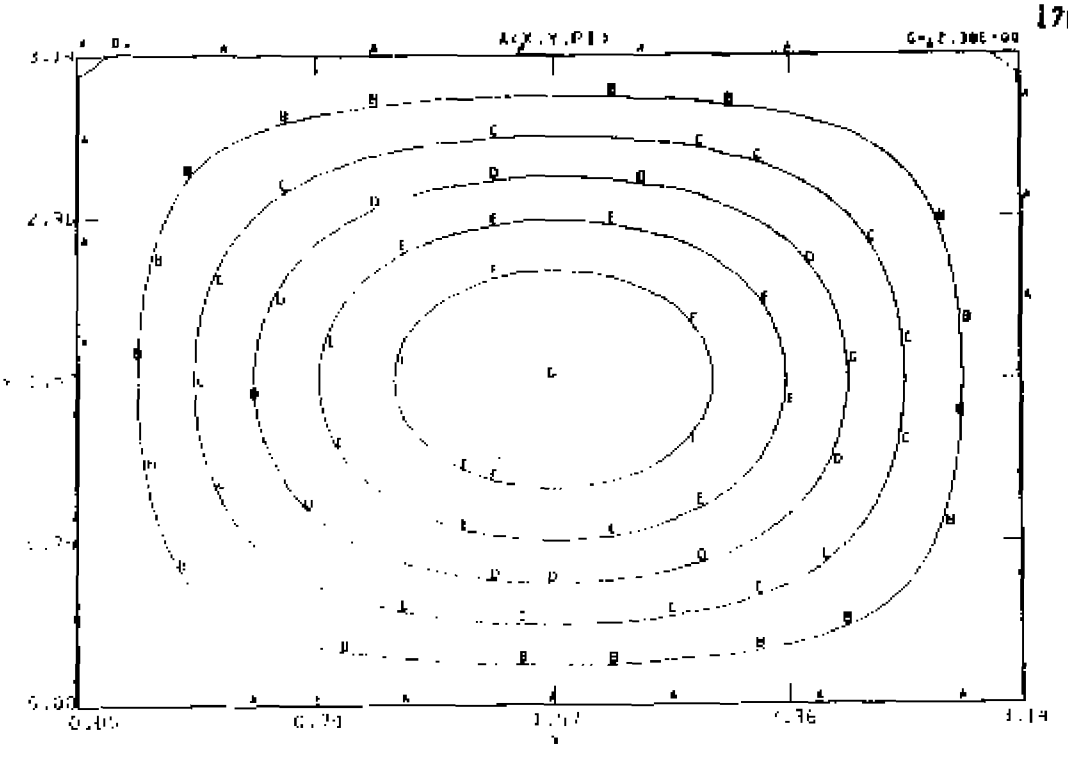

Figure 25. - Contour plots at t = 17.52 from CASE 2:
25 (a): contours of A = constant, poloidal cut.

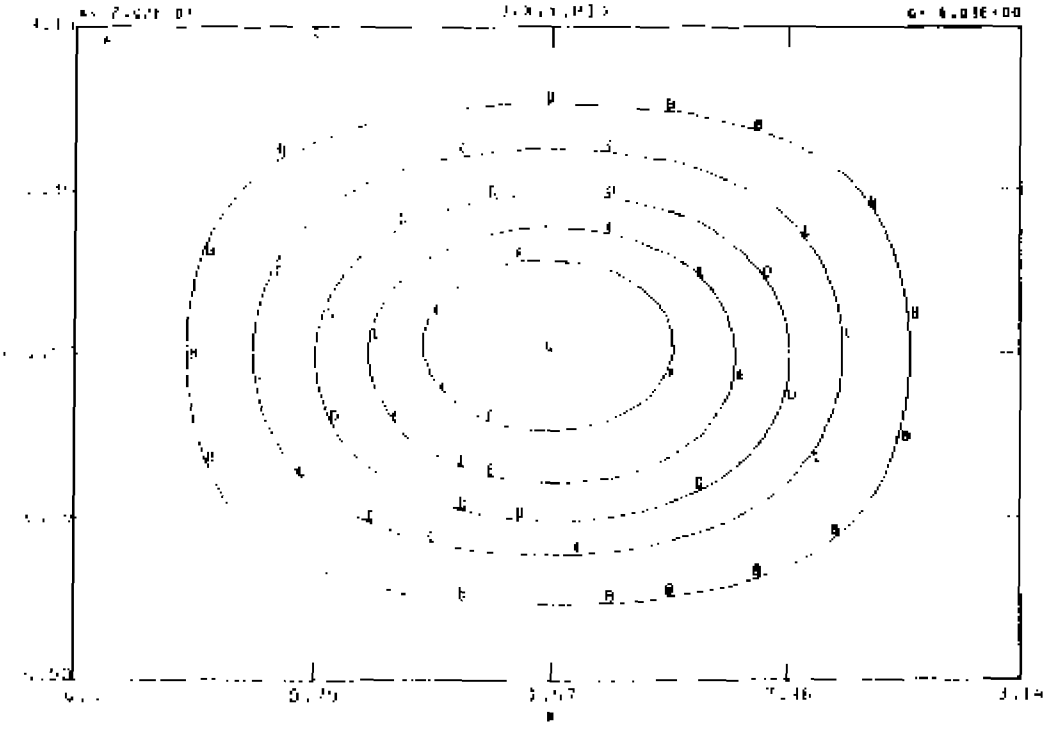

25 (b): contours of j = constant, poloidal cut.

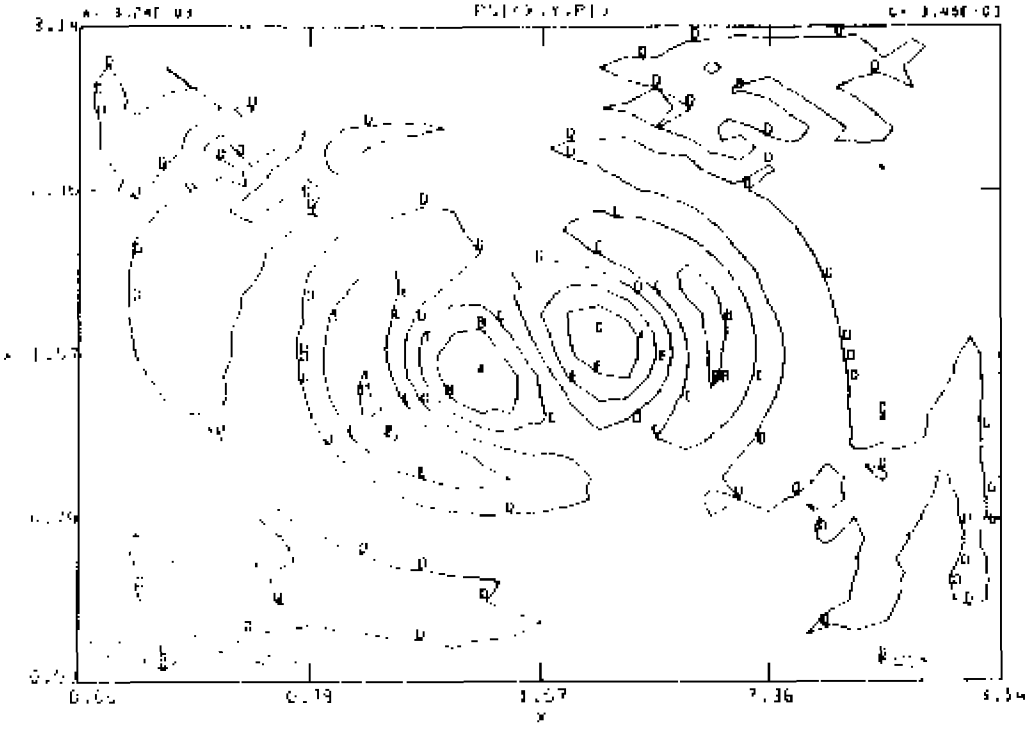

25 (c): contours of Ψ= constant, poloidal cut.

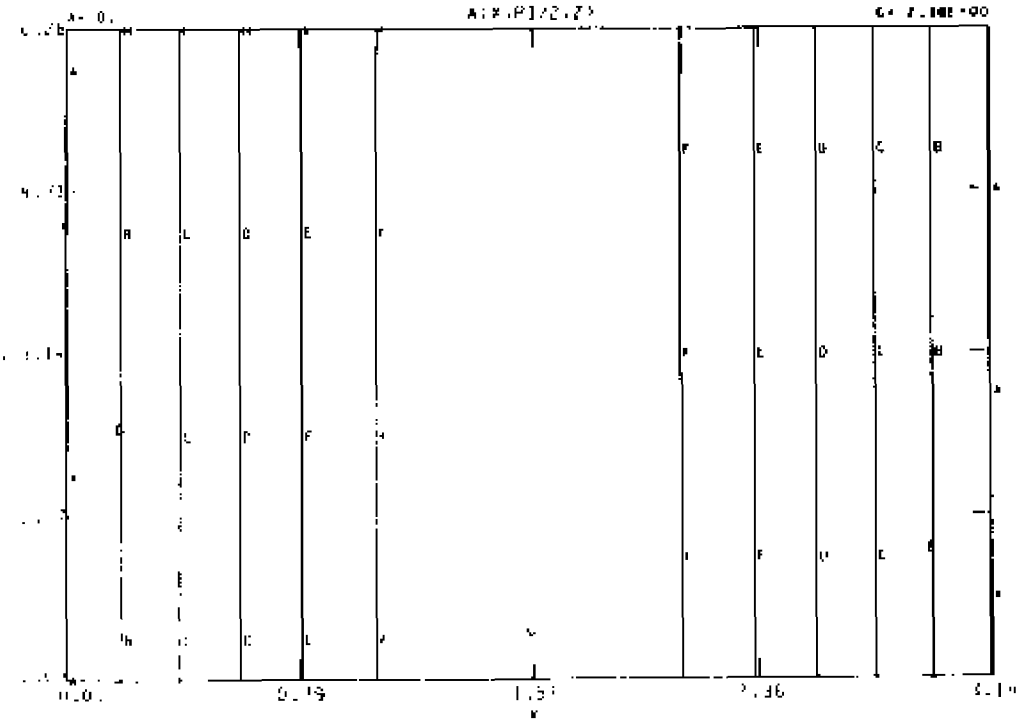

25 (d): contours of A = constant, toroidal cut.

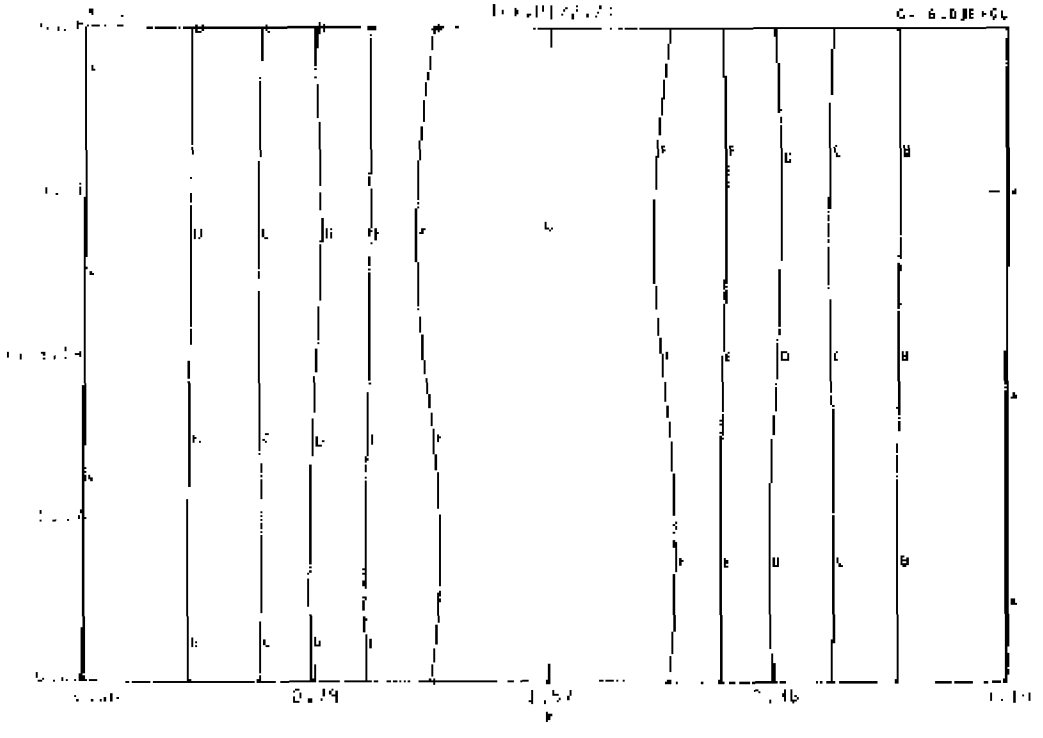

25 (e): contours of j = constant, toroidal cut.

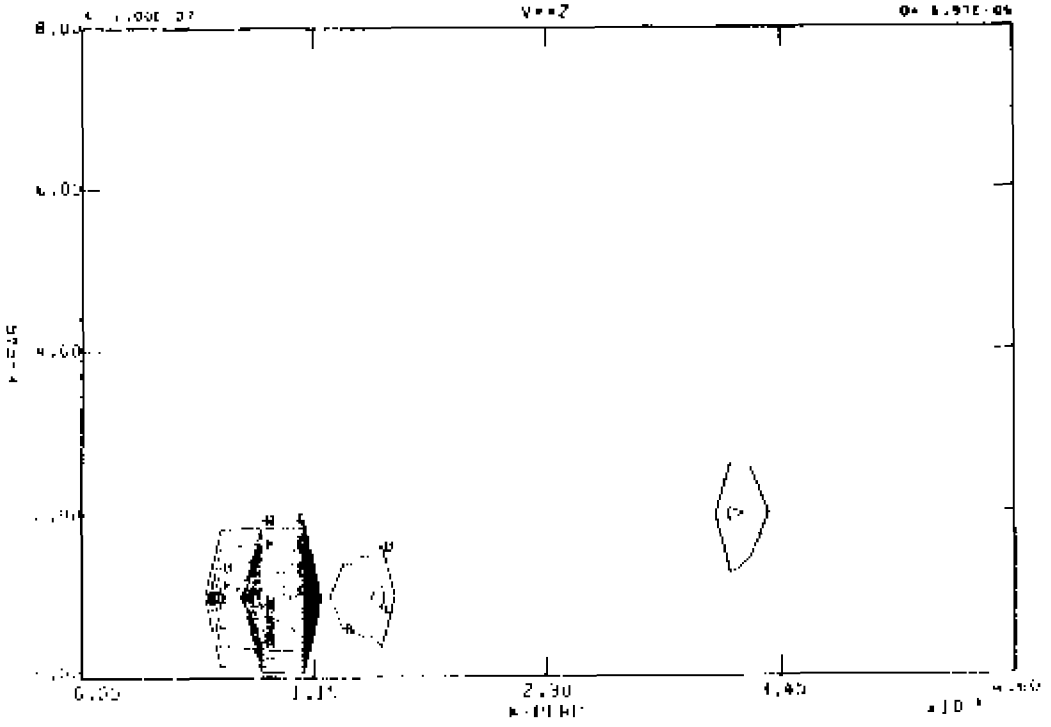

Figure 26. - Contours of energy in Fourier space at t = 17.52, CASE 2:
26 (a): equally spaced contours of constant kinetic energy.

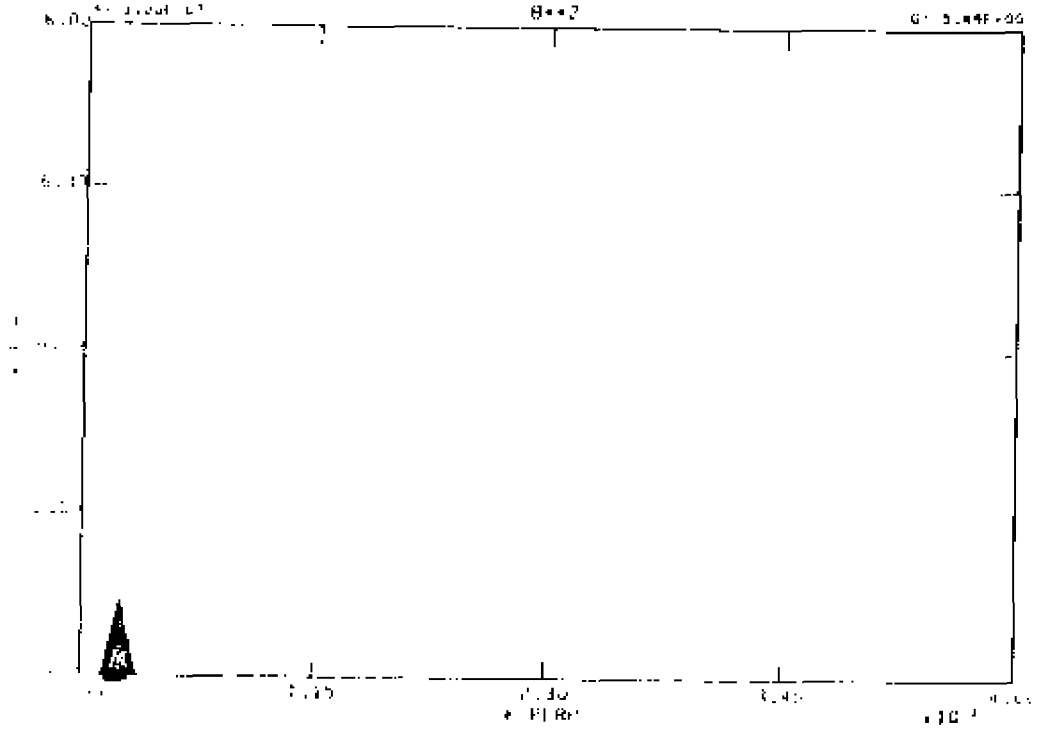

26 (b): equally spaced contours of constant magnetic energy.

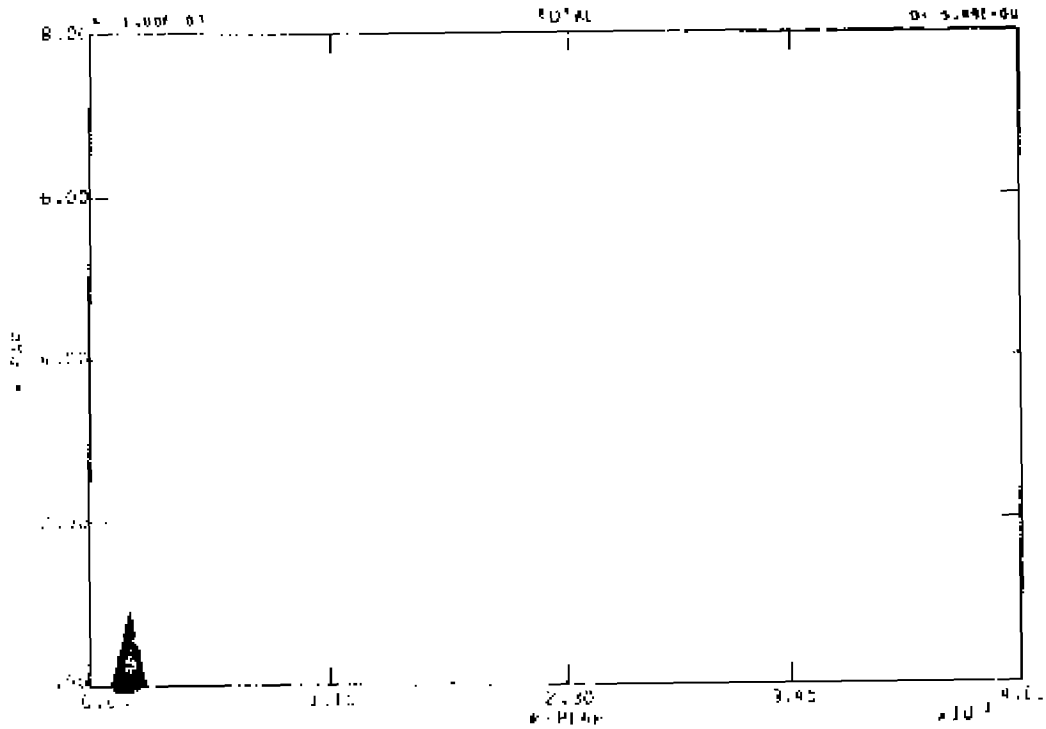

26 (c): equally spaced contours of constant total energy.

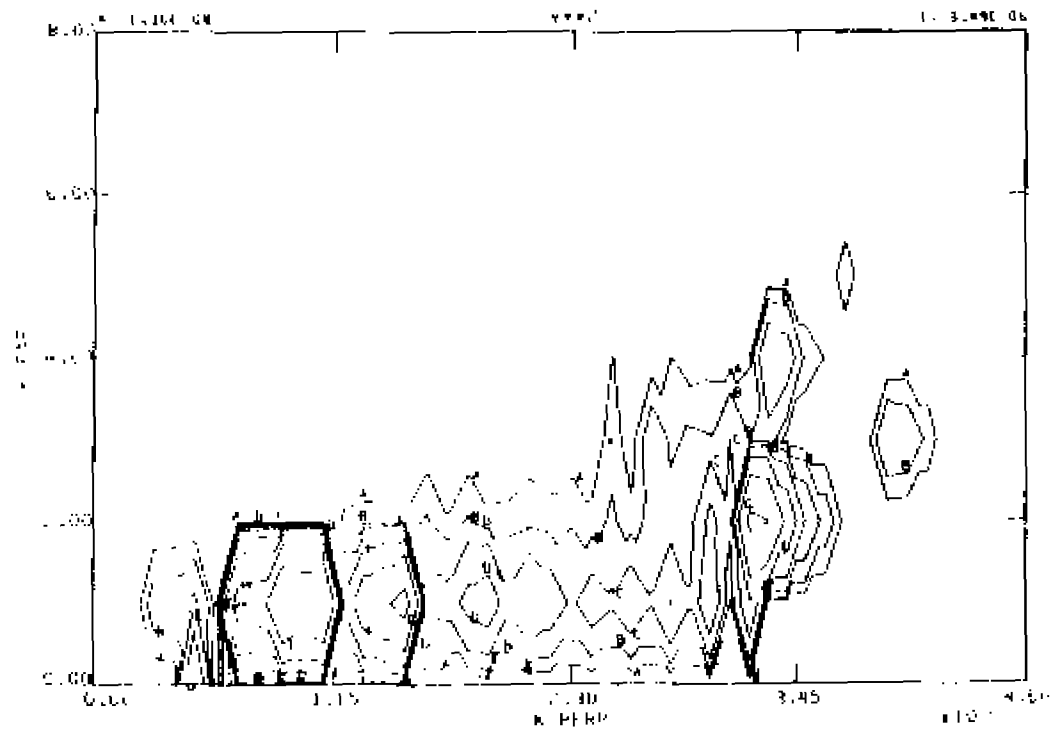

26 (d): contours separated by powers of two of constant kinetic energy.

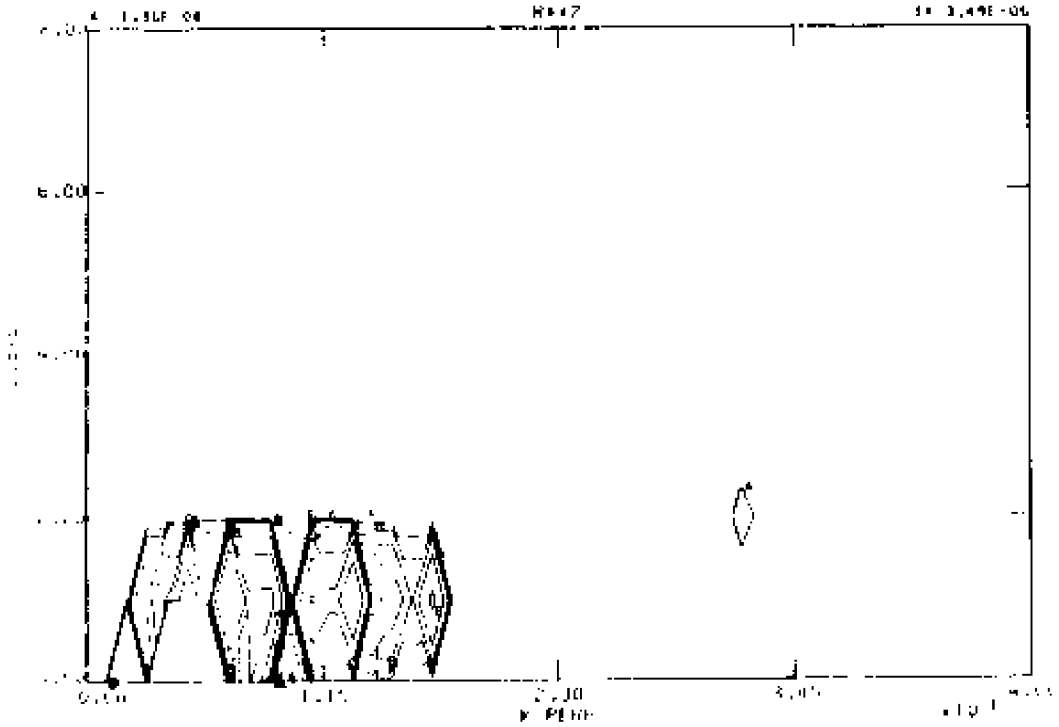

26 (e): contours separated by powers of two of constant magnetic energy.

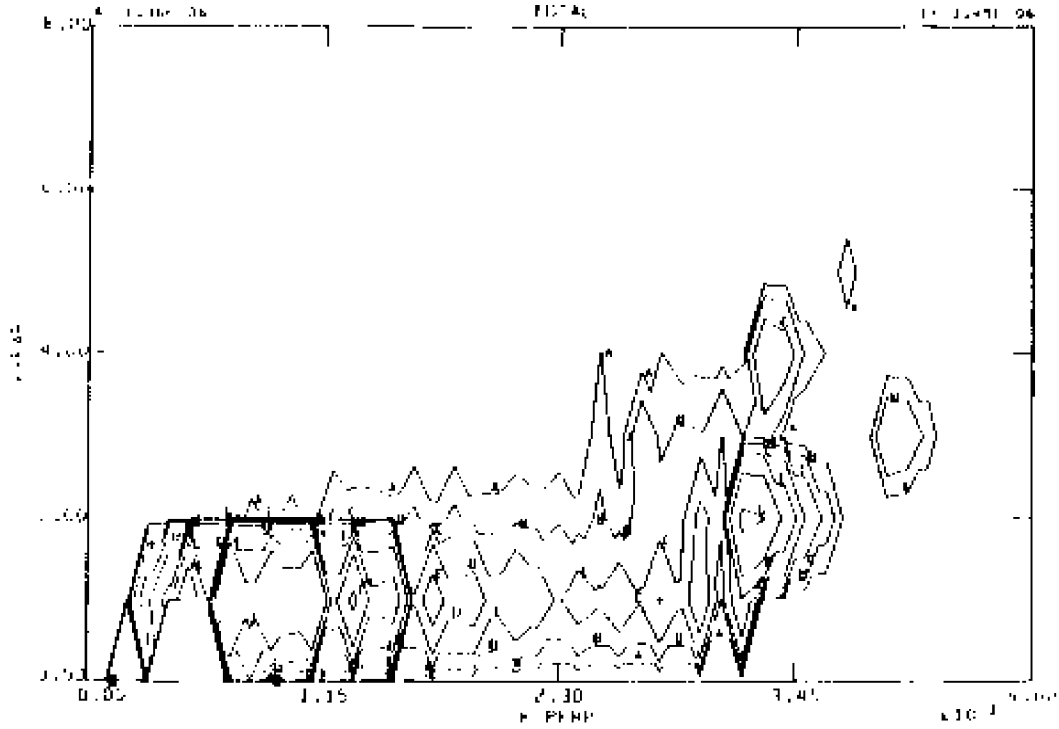

26 (f): contours separated by powers of two of constant total energy.

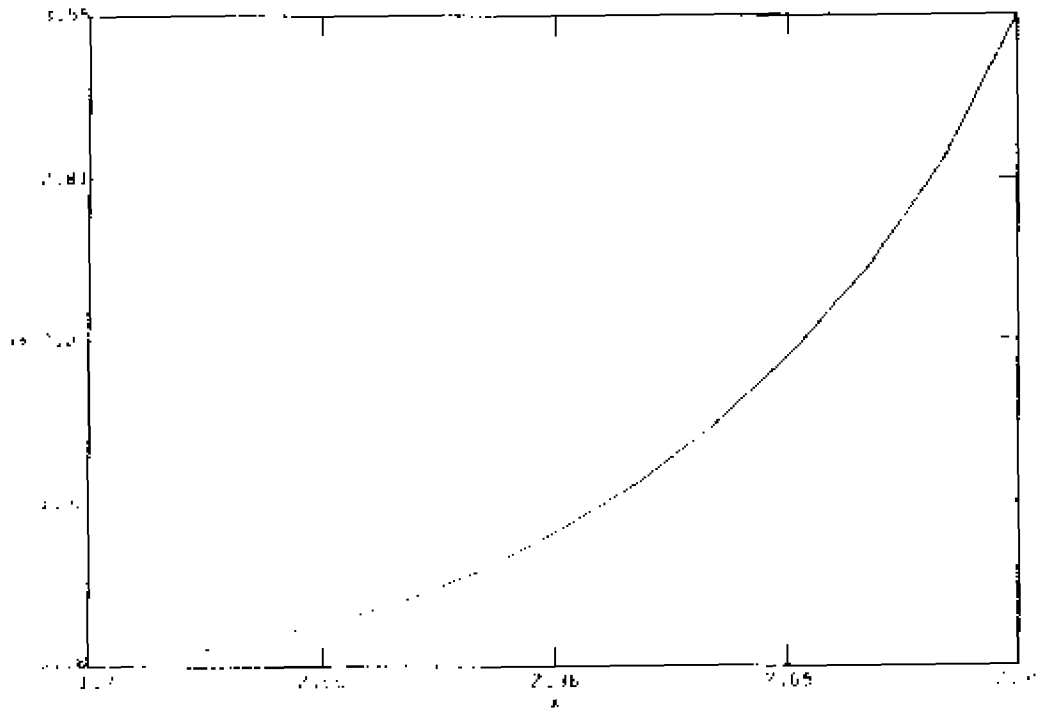

Figure 27. - Q-profiles at:
27(a): t = 4.44

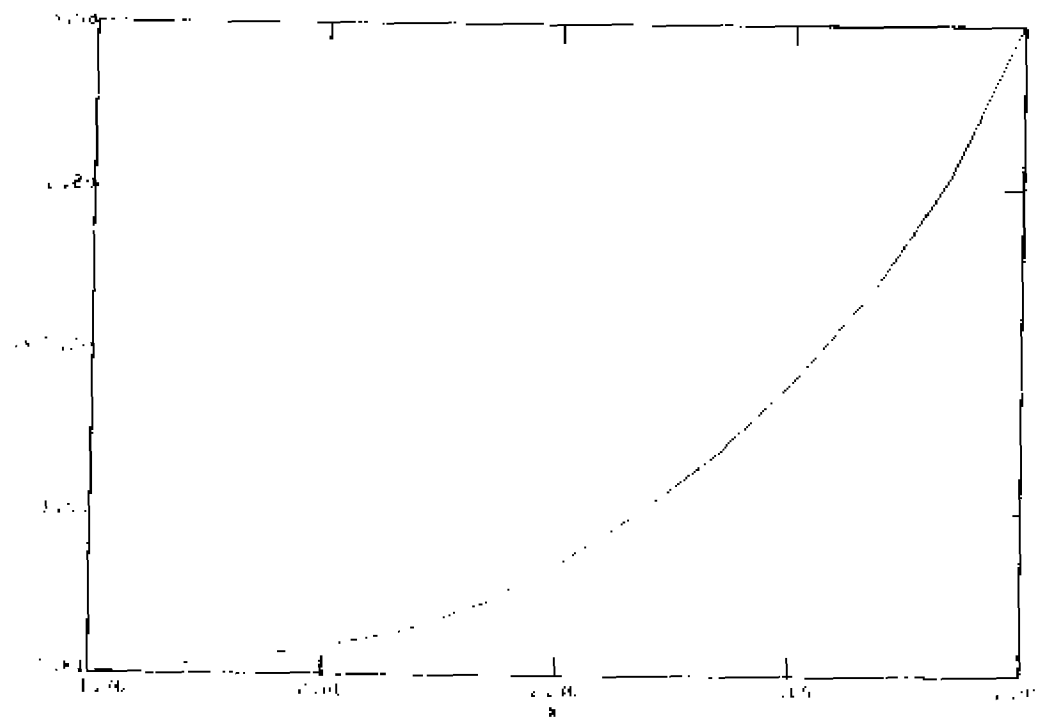

27(b): t = 6.60

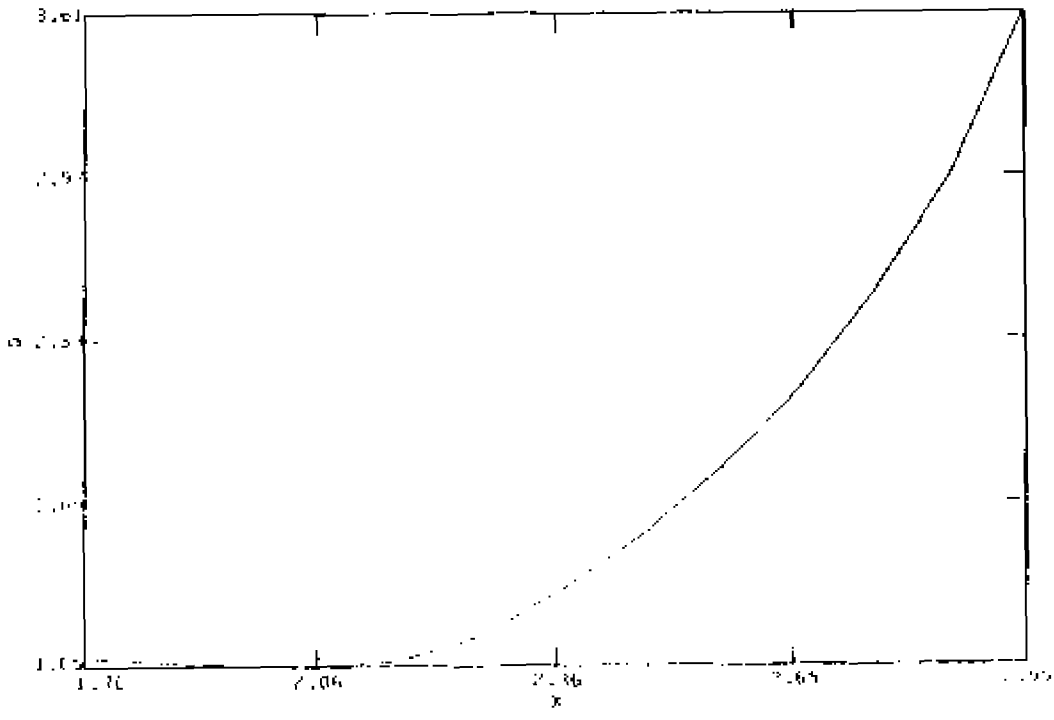

27(c): t = 7.80

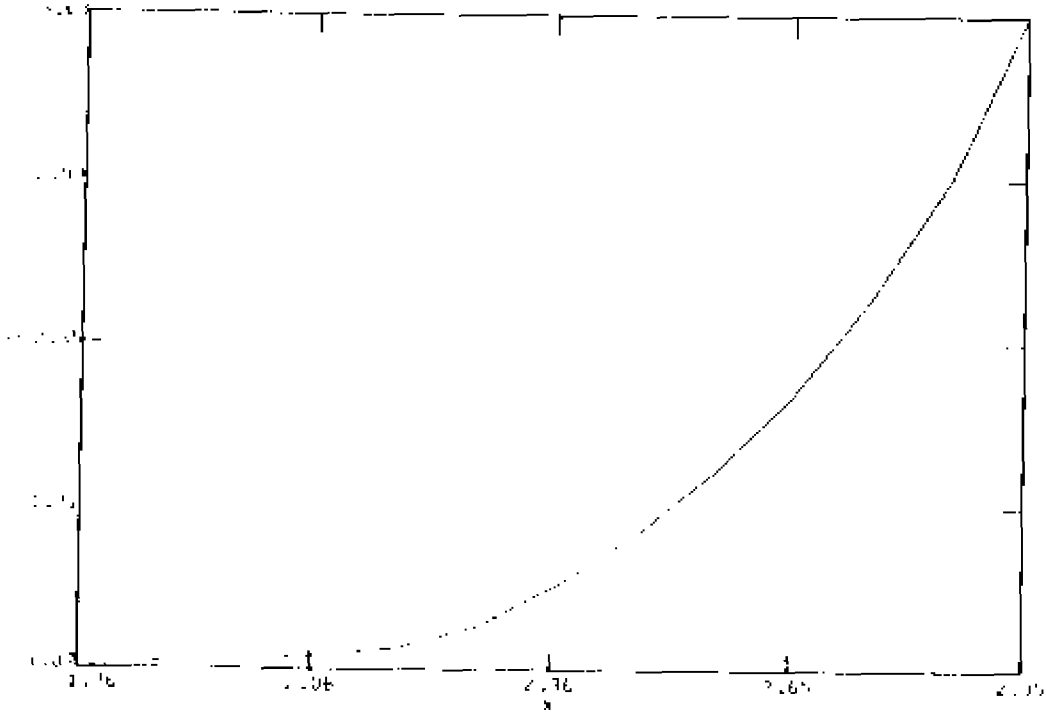

27(d): t = 8.76

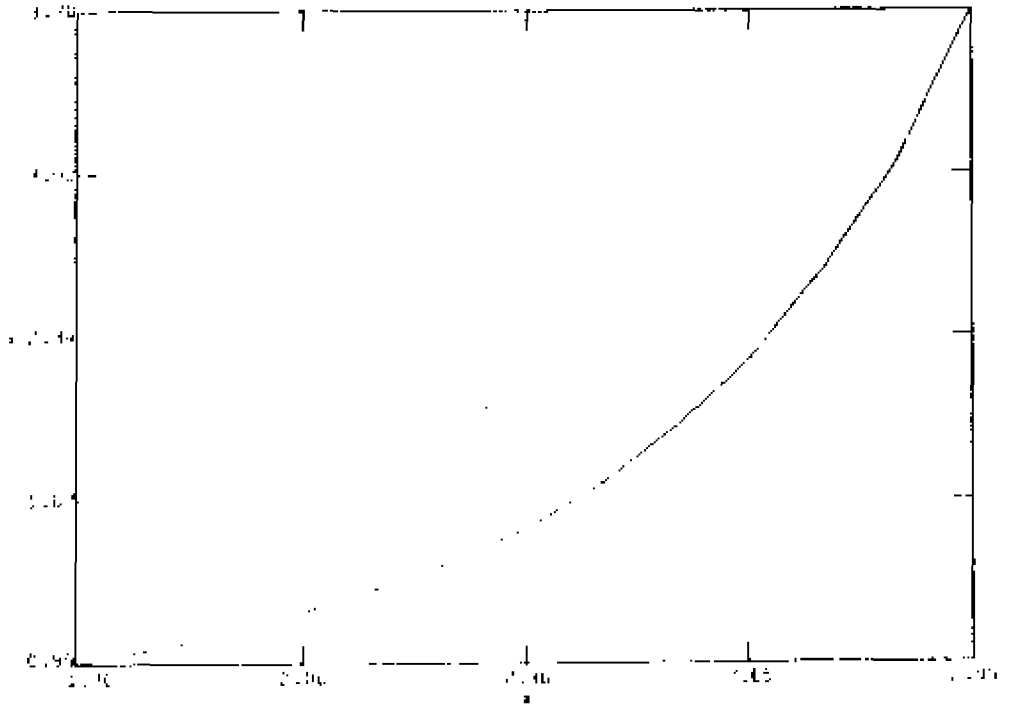

27(e): t = 10.98

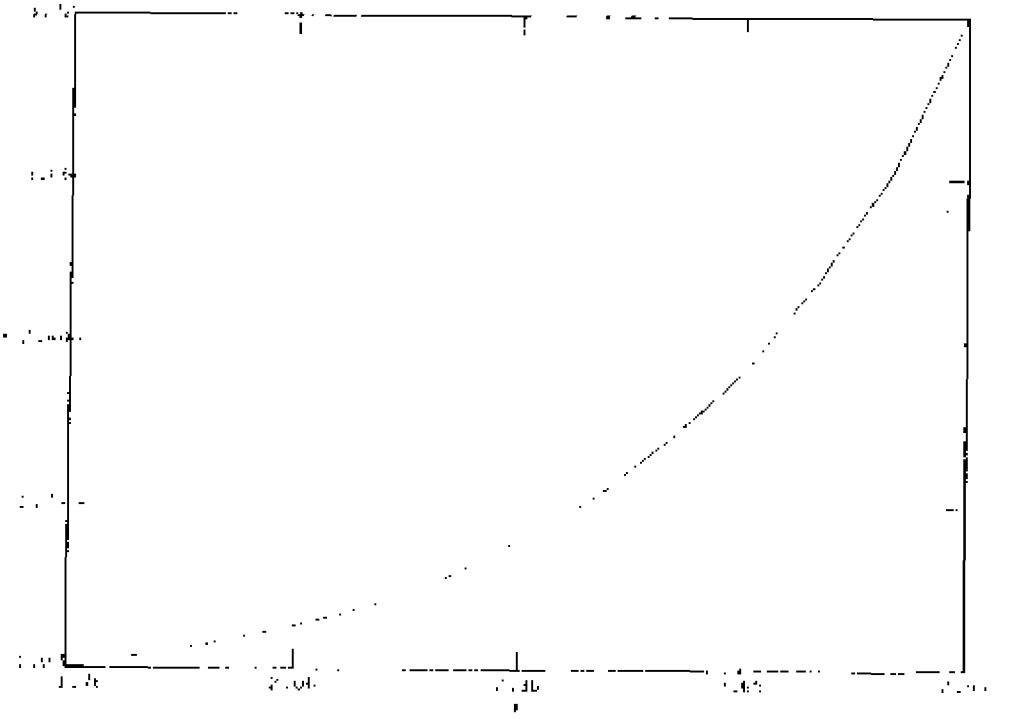

27(f): t = 11.70

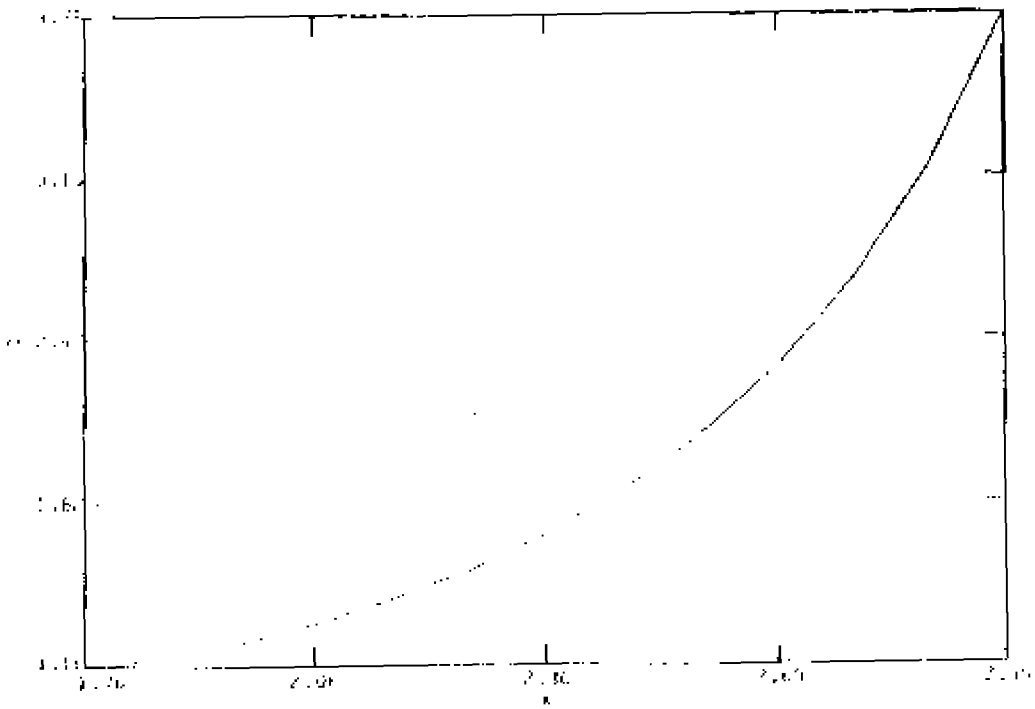

27(g): t = 13.14

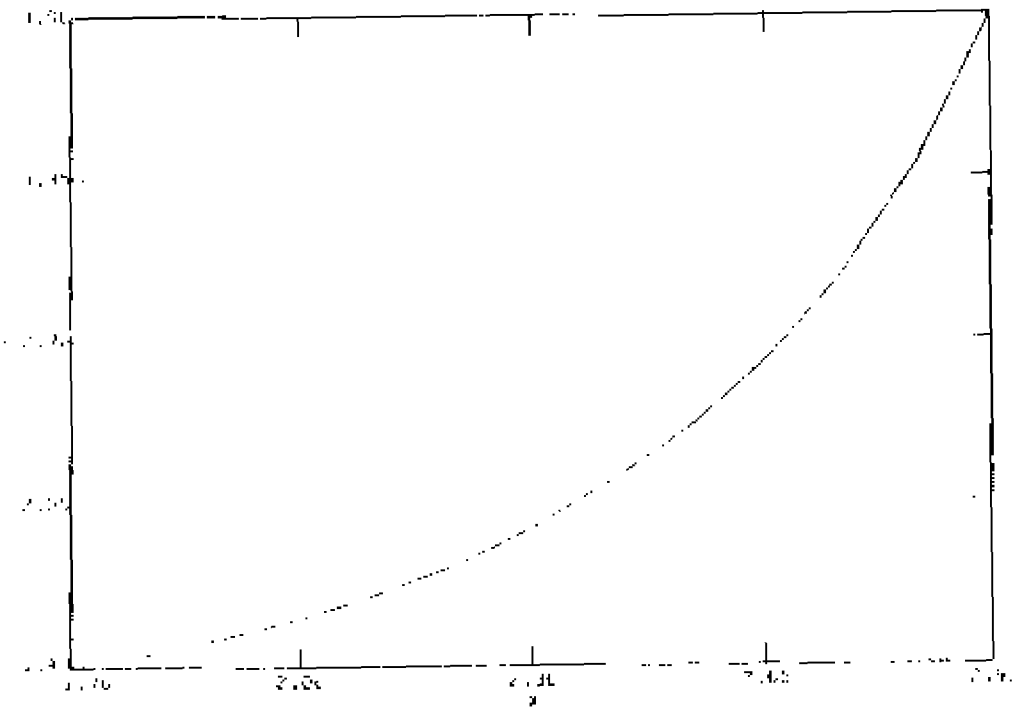

27(h). t = 17.52

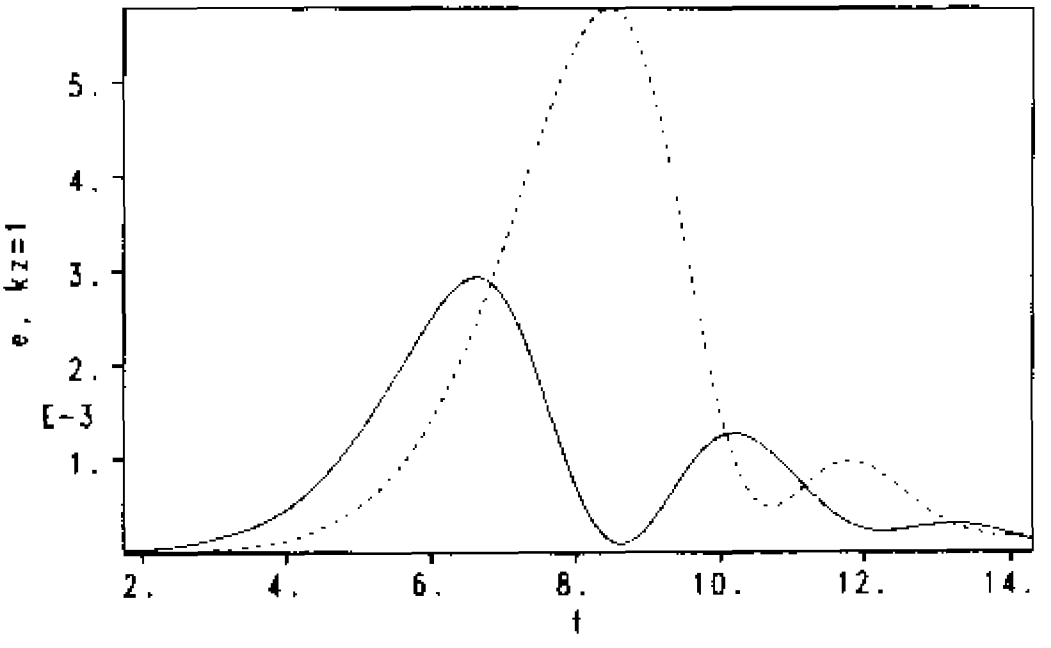

Figure 28. - CASE 2, energies(k_z) as a function of time, with dashed line for kinetic energy, and solid line for magnetic energy: 28(a): $k_z = 1$.

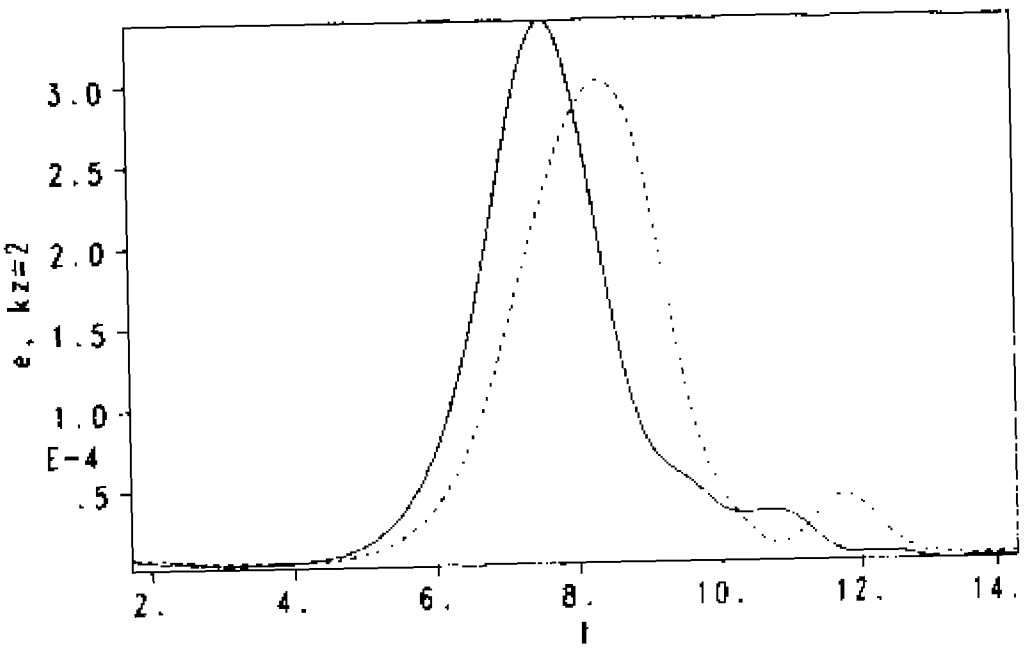

28(b): k_z = 2, and

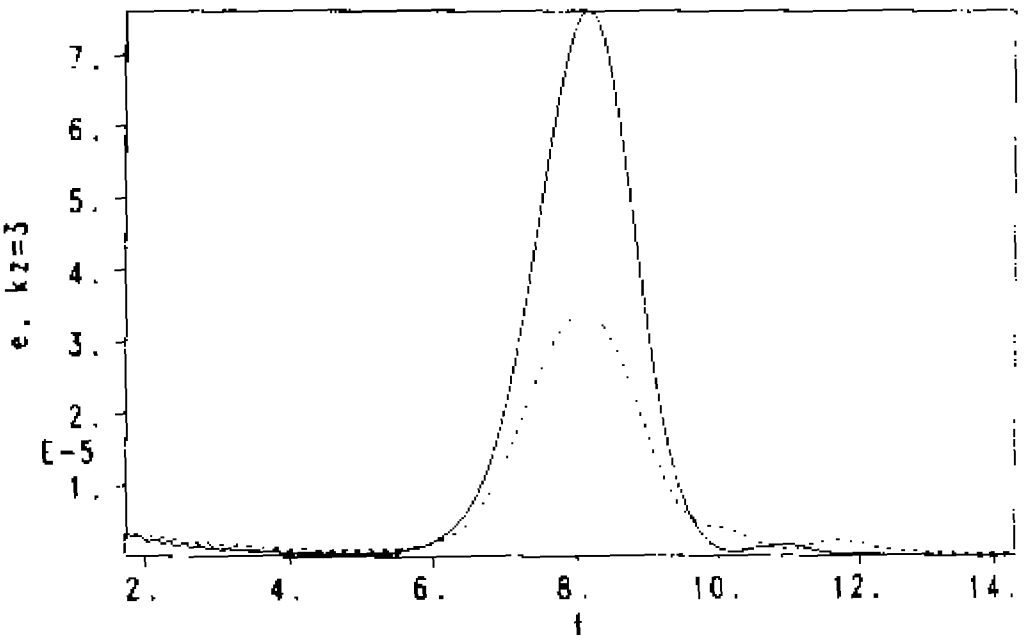

28(c): k_z = 3.

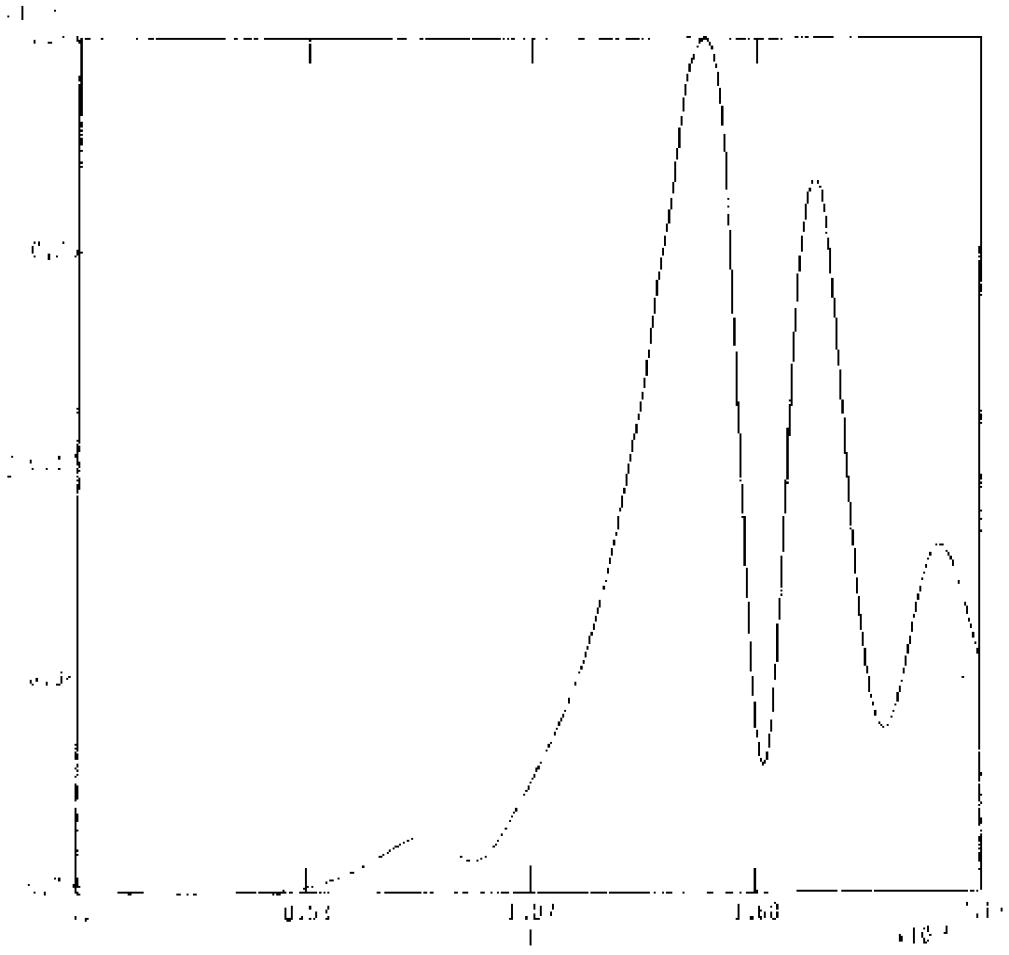

Figure 29. - Globals for CASE 3, (ν= 0.0025):
29(a): kinetic energy as a function of time.

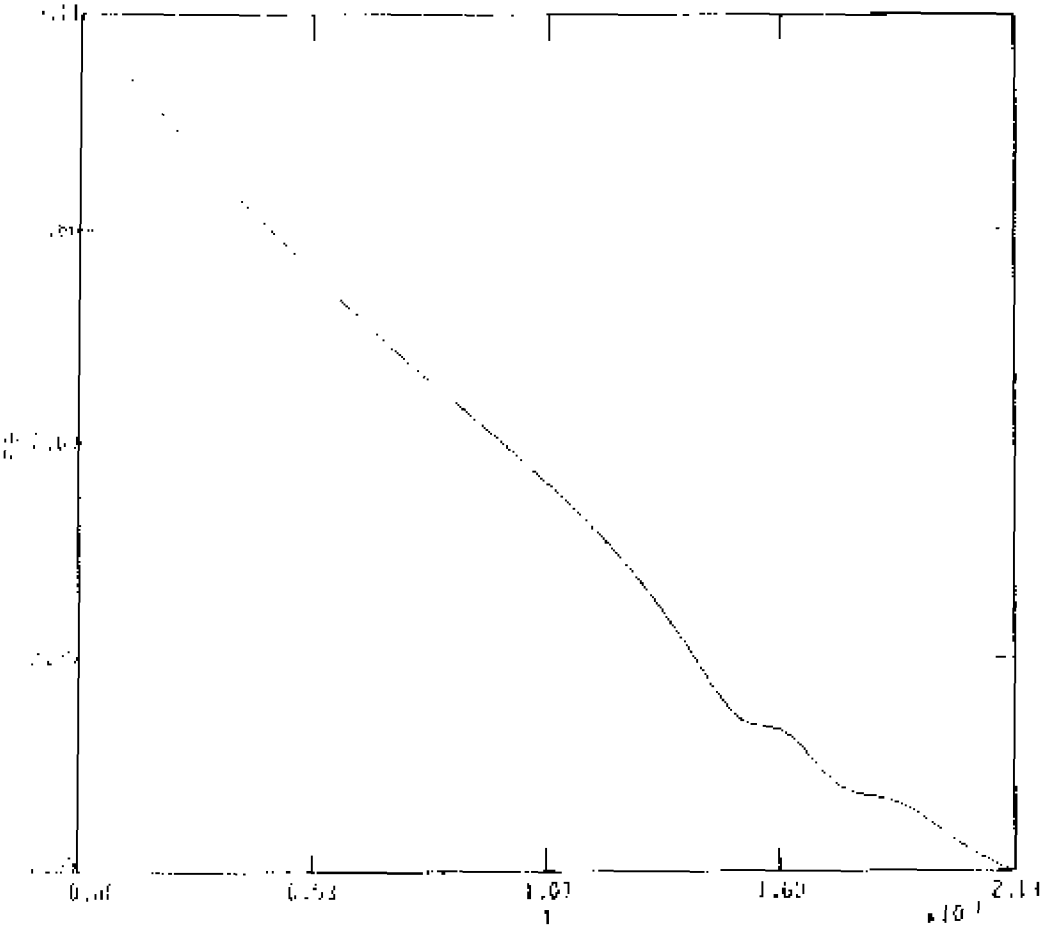

29(b): magnetic energy as a function of time.

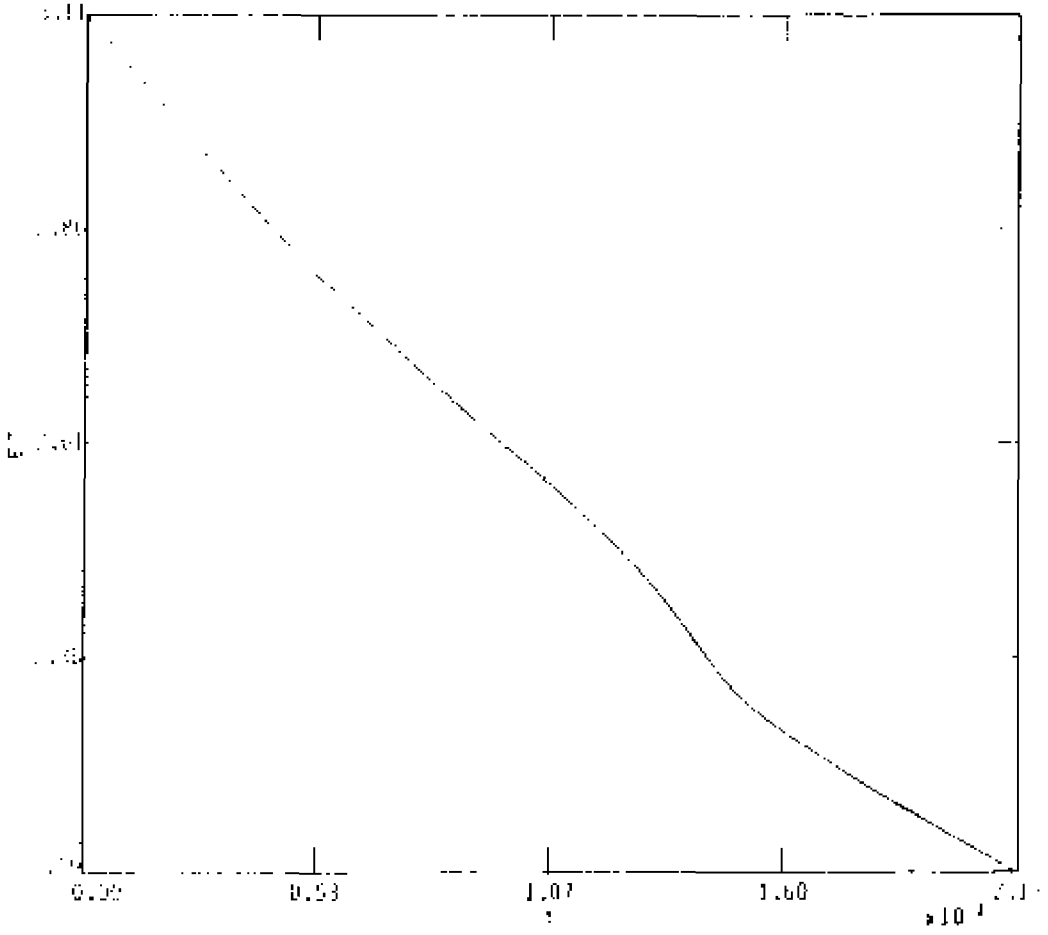

29(c): total energy as a function of time.

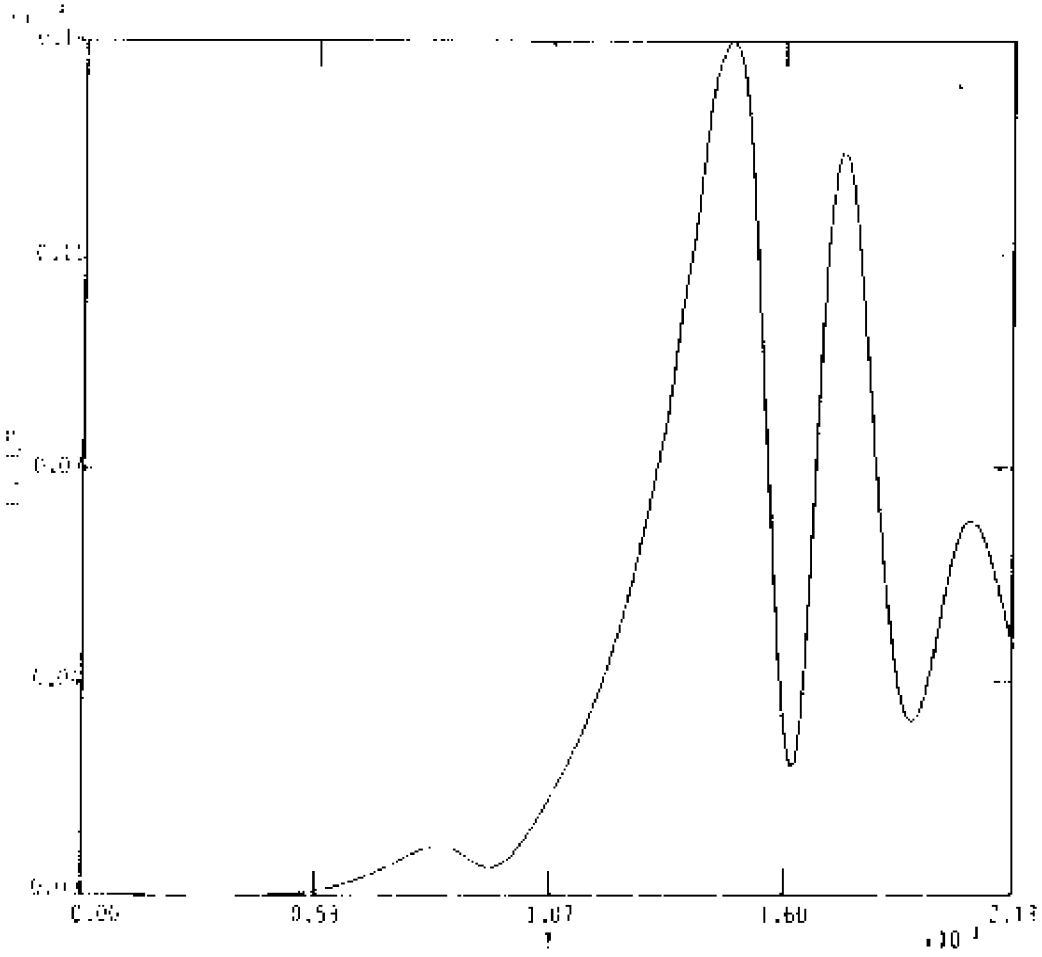

29(d): ratio of kinetic to magnetic energy as a function of time.

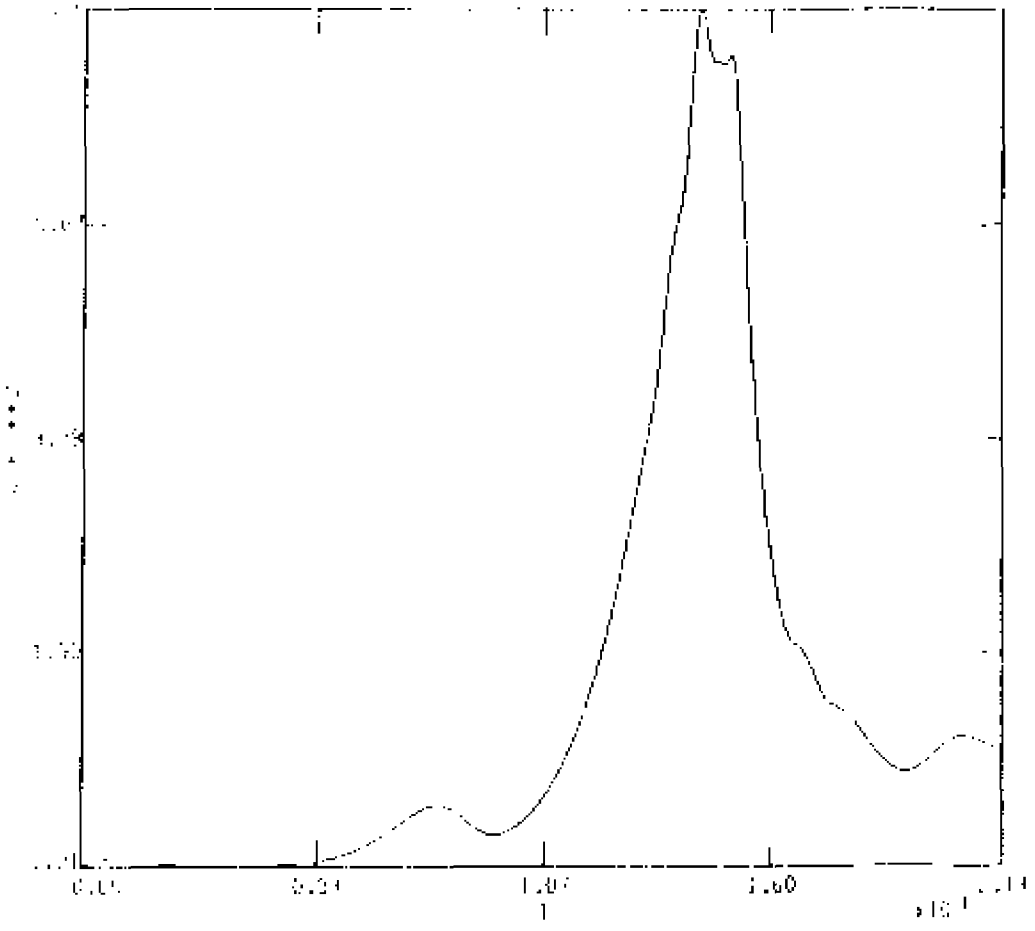

29(e): half the mean square vorticity as a function of time.

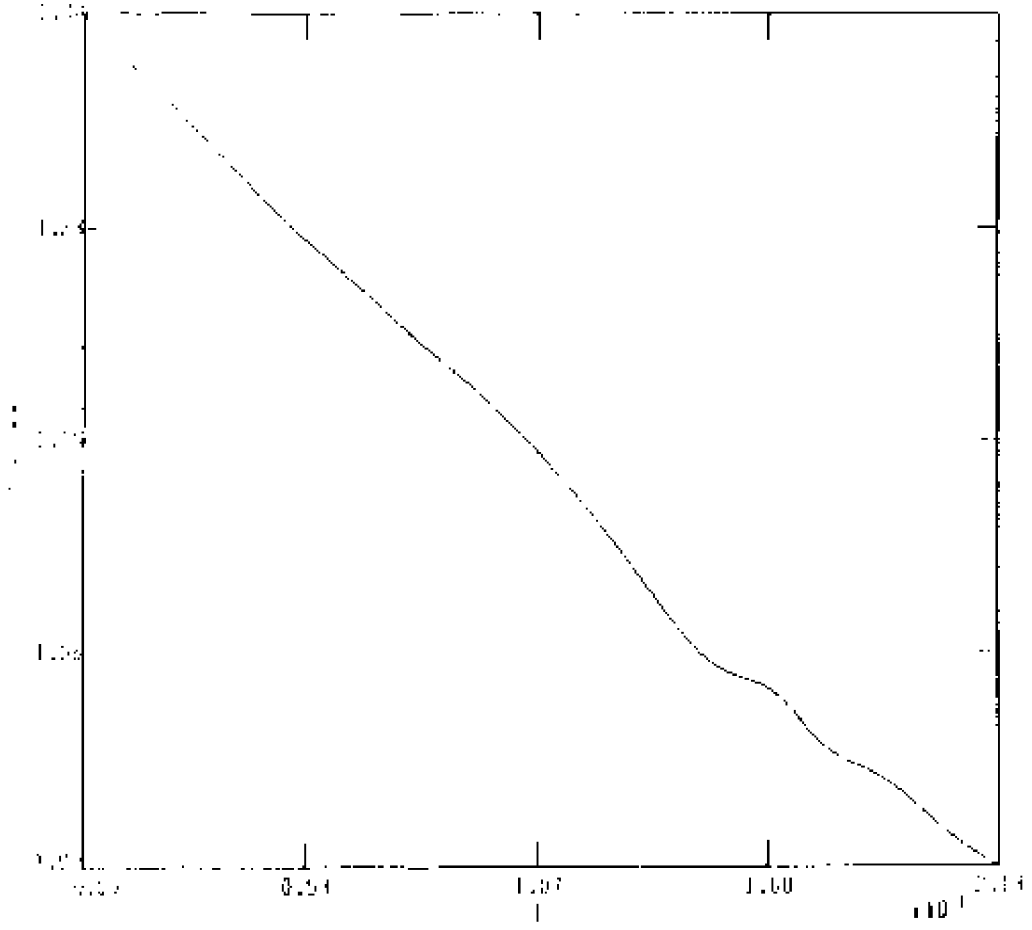

29(f): half the mean square vector potential as a function of time.

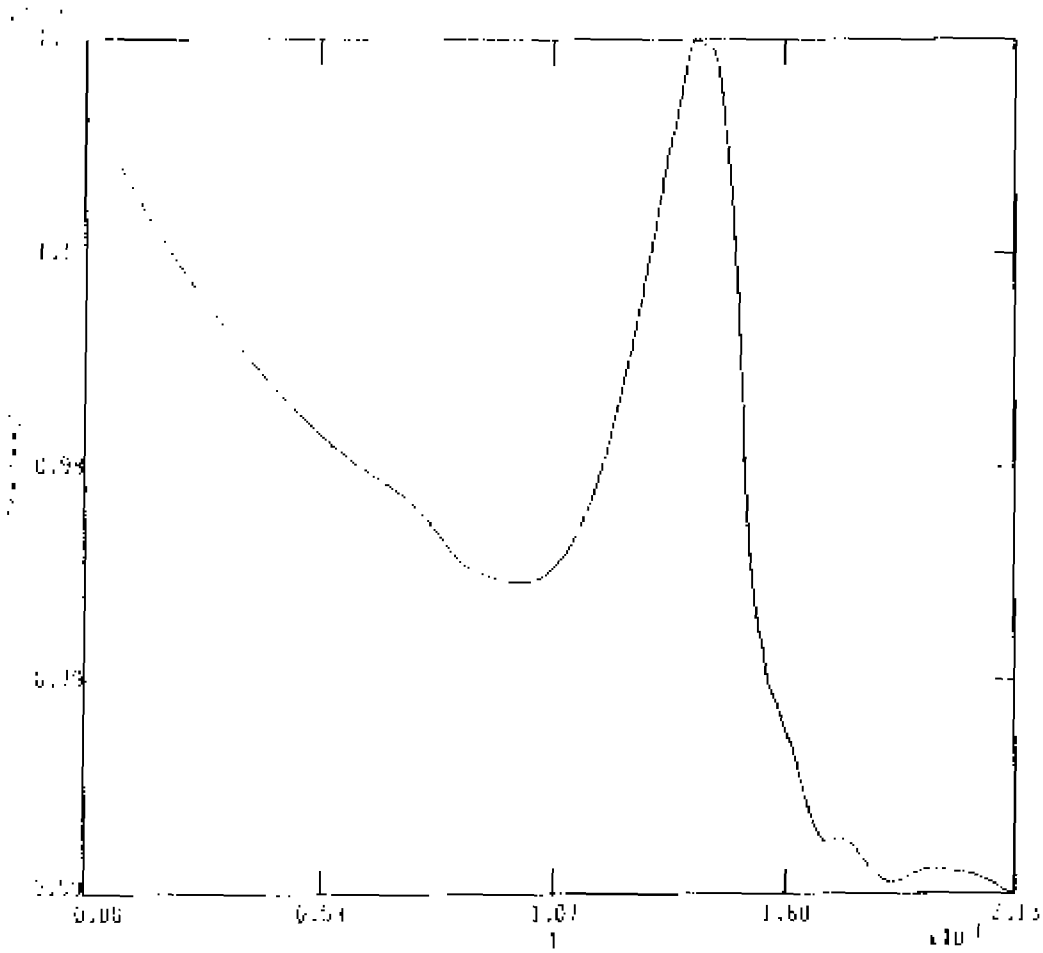

29(g): half the mean square current as a function of time, and

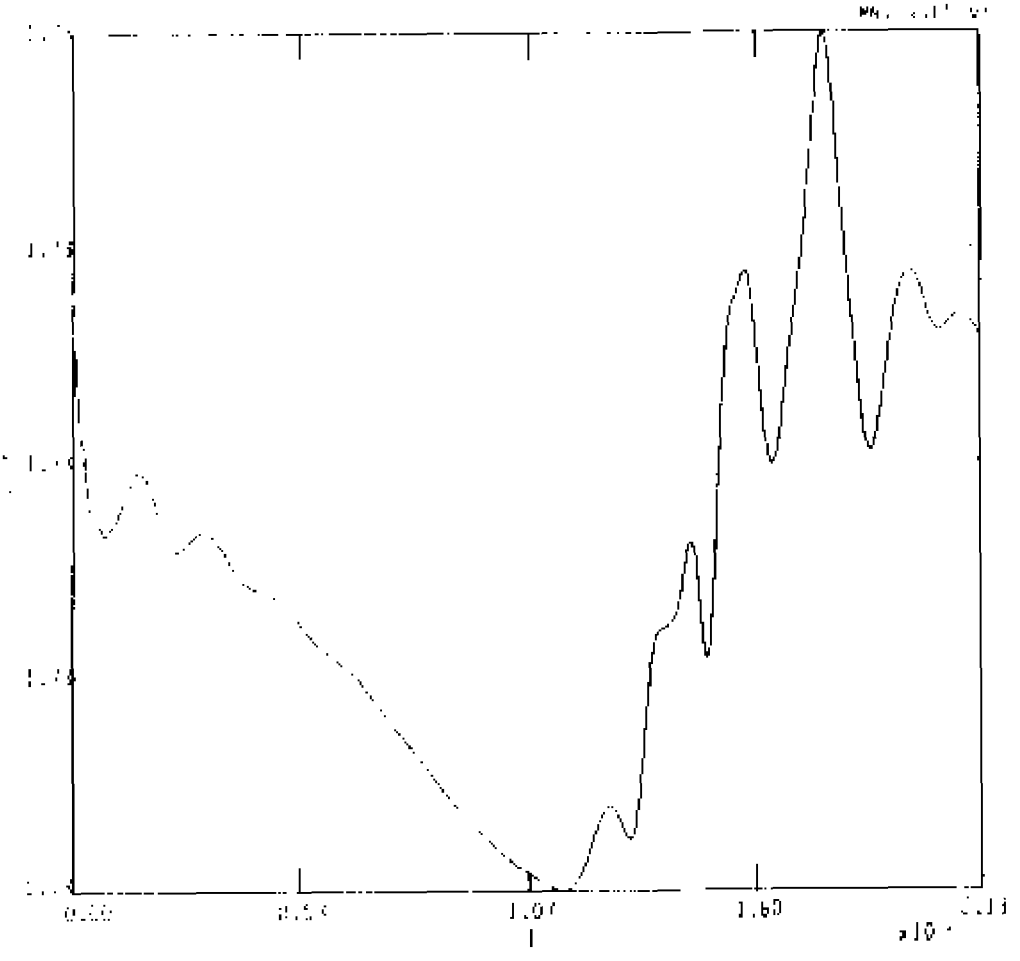

29(h): total integrated current density as a function of time.

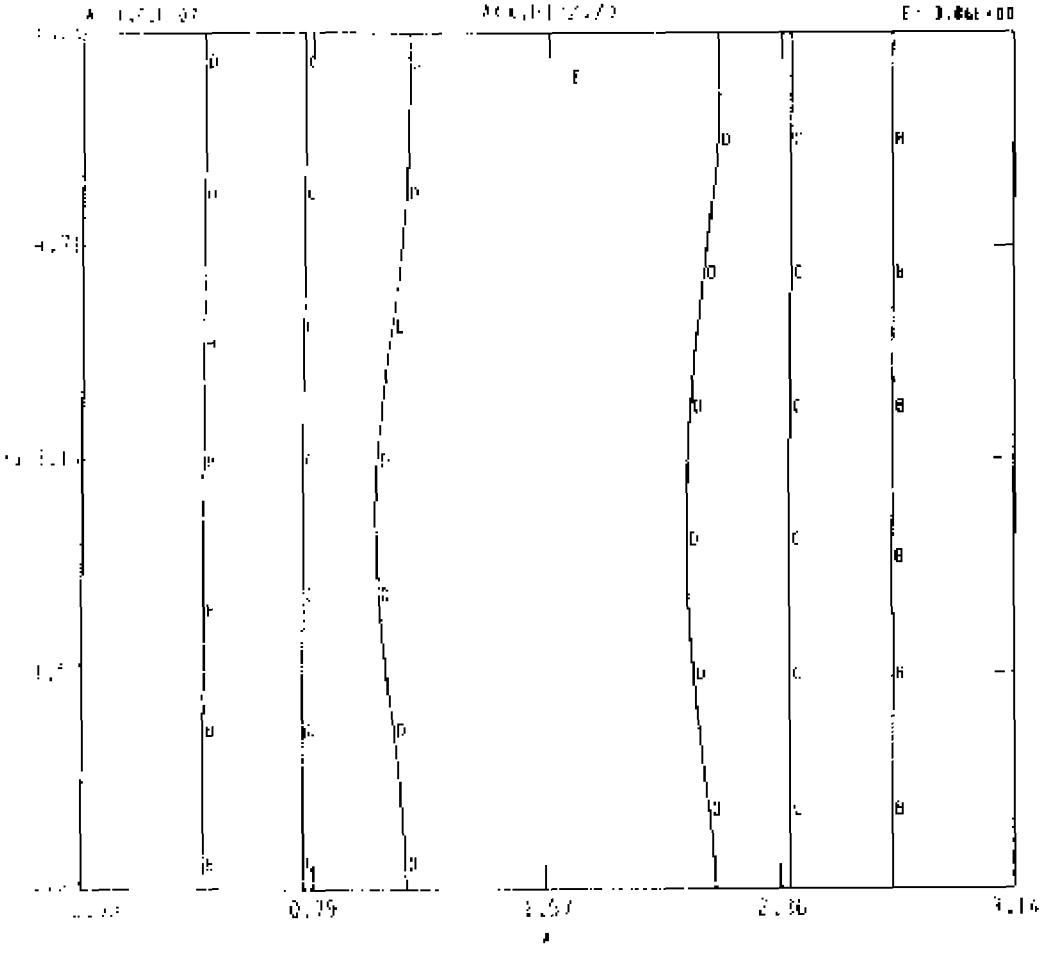

Figure 30. - Contours at t = 10.32, CASE 3:
30 (a): Contours of constant A, toroidal cut.

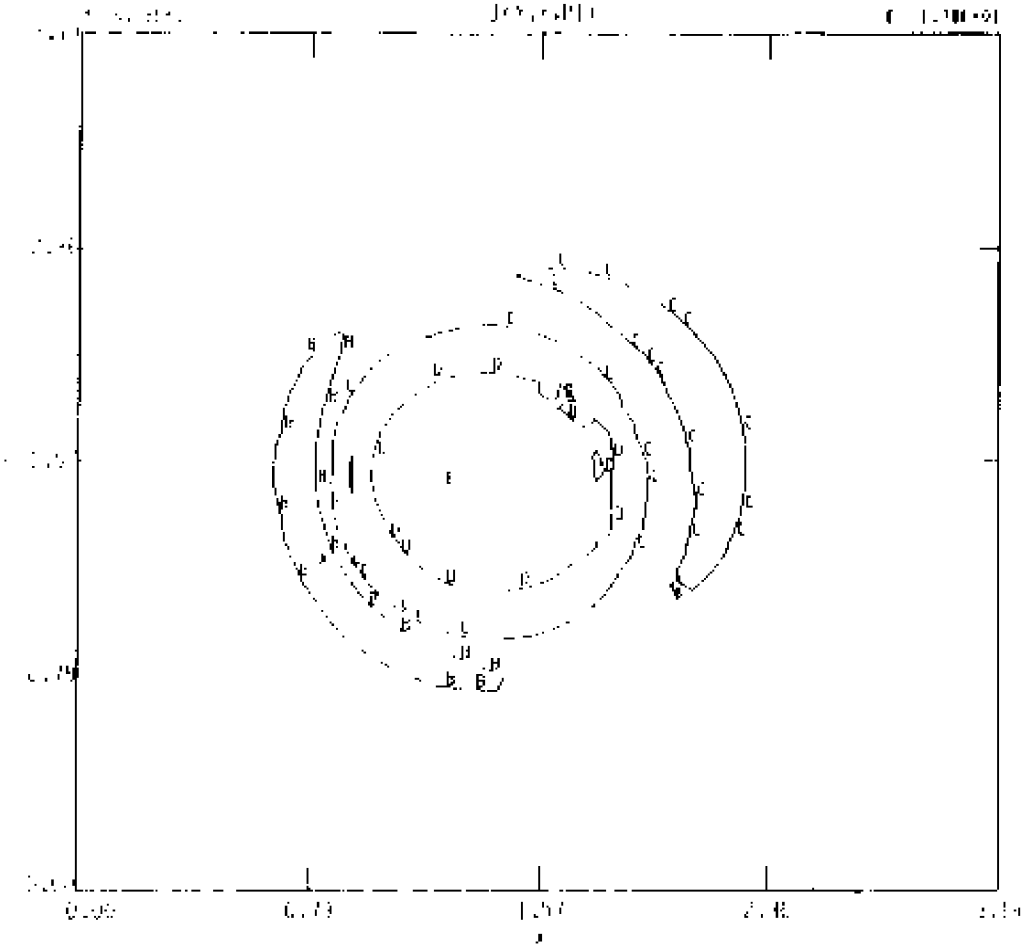

30 (b): Contours of constant j, poloidal cut.

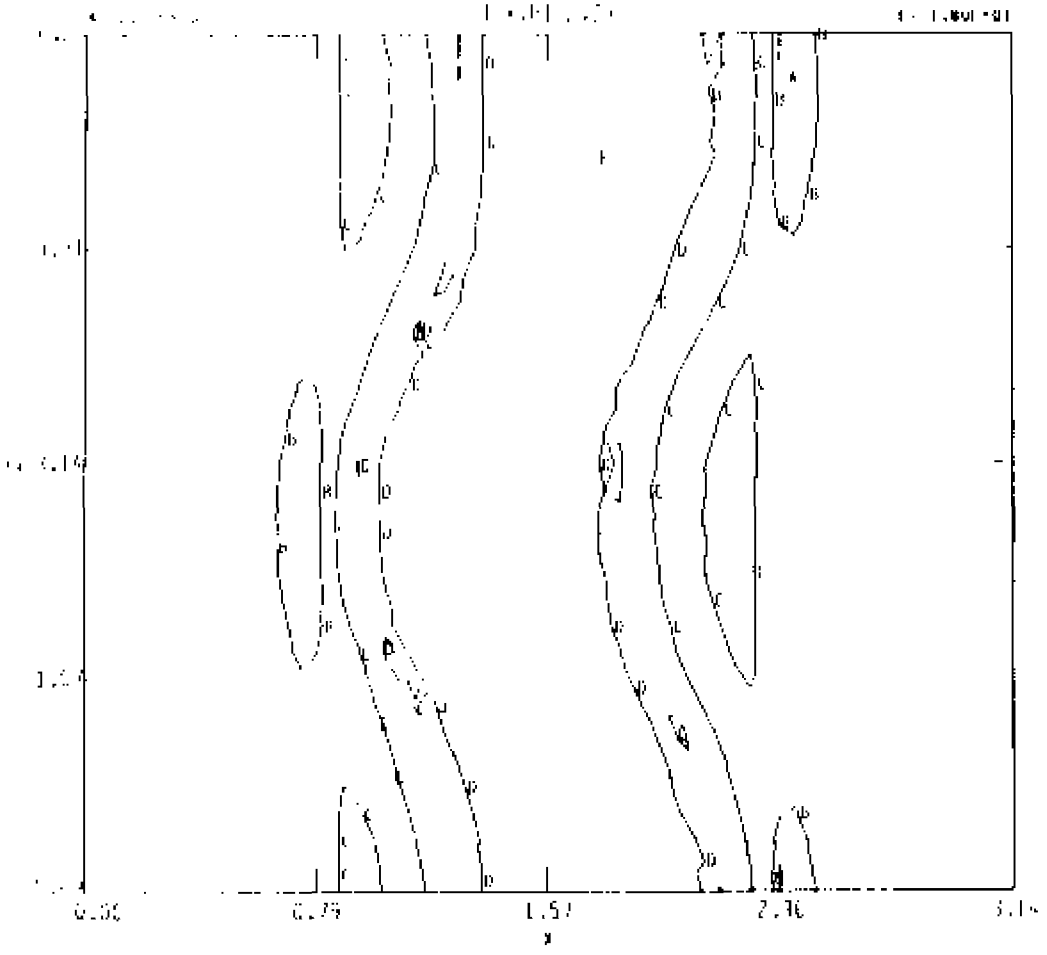

30 (c): Contours of constant j, toroidal cut.

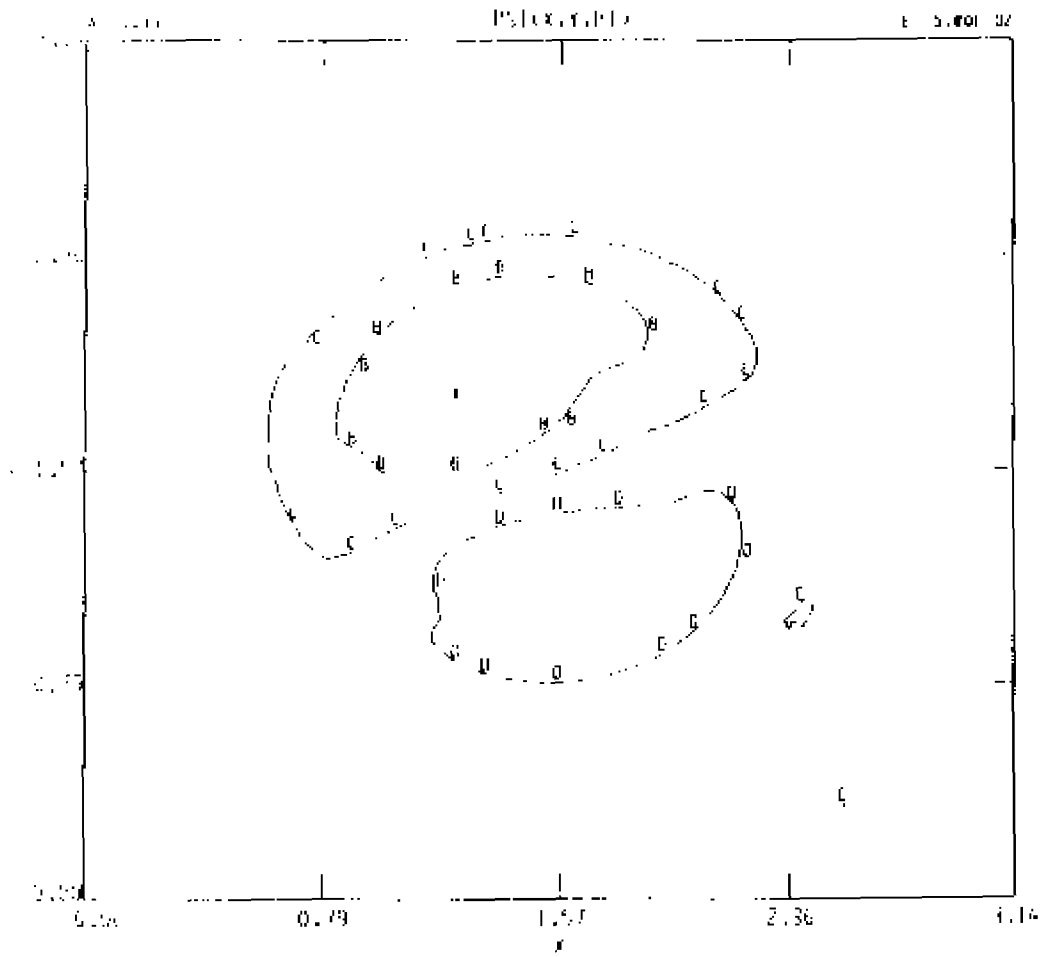

30 (d): Contours of constant Ψ, poloidal cut.

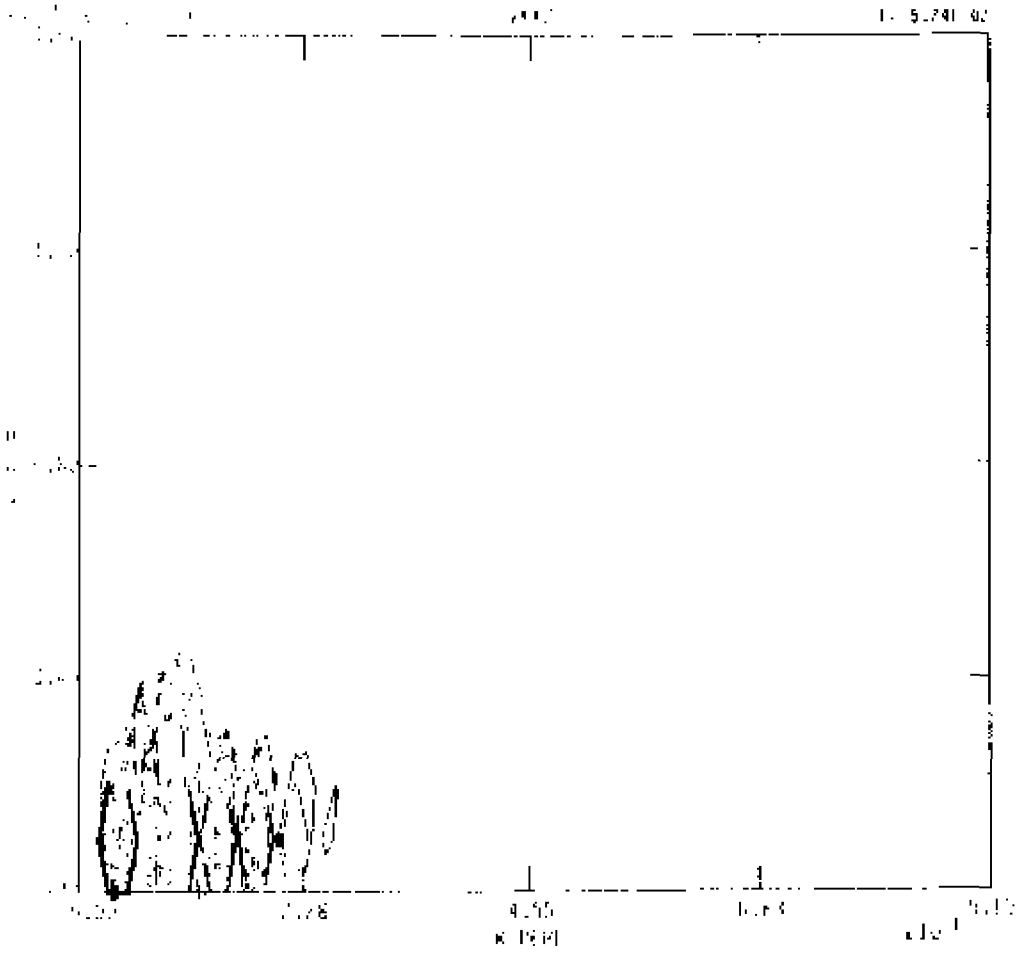

30 (e): Contours of modal kinetic energy, spaced by powers of two,

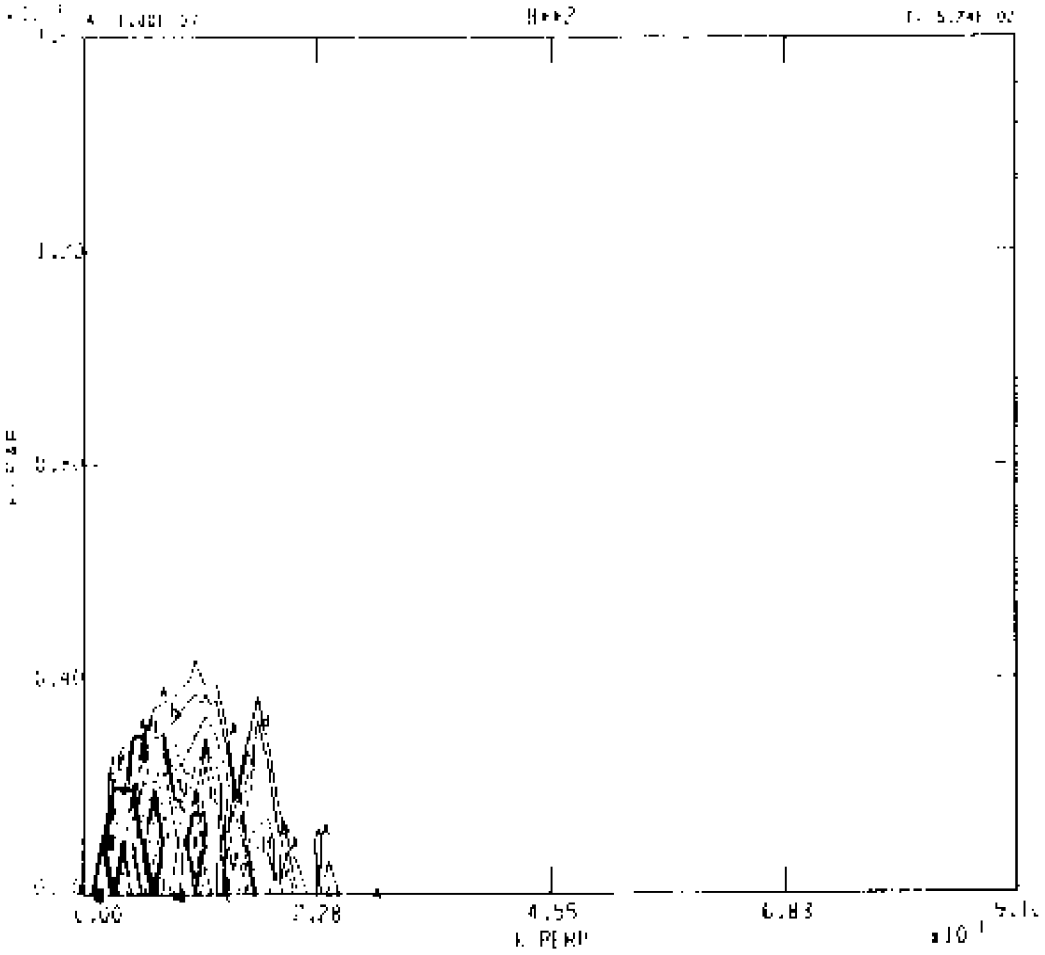

and 3# (f): Contours of modal magnetic energy, spaced by powers of two.

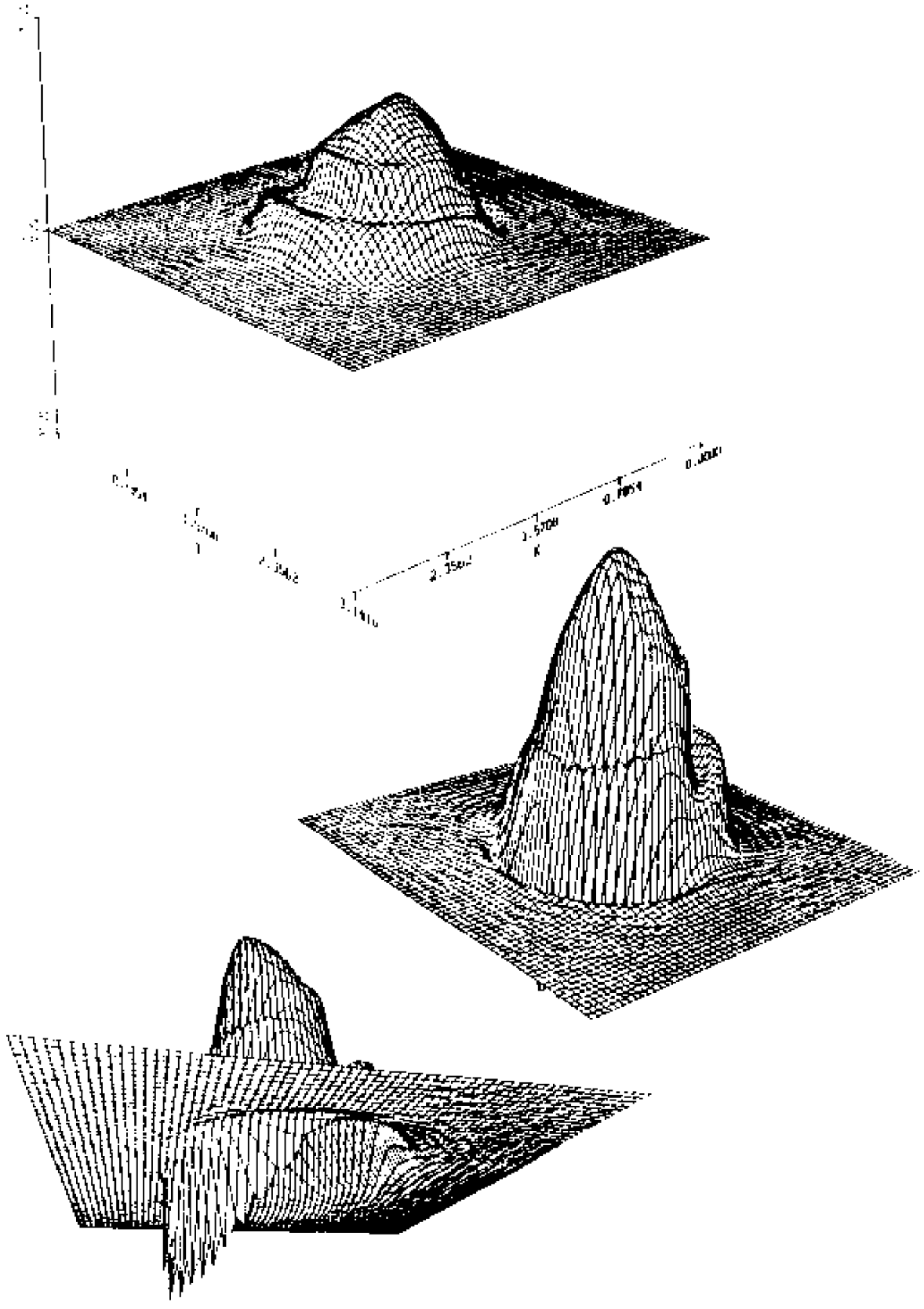

Figure 31. - CASE 3, t = 10.32:
31(a): Perspective plots of current in the z = π plane, and

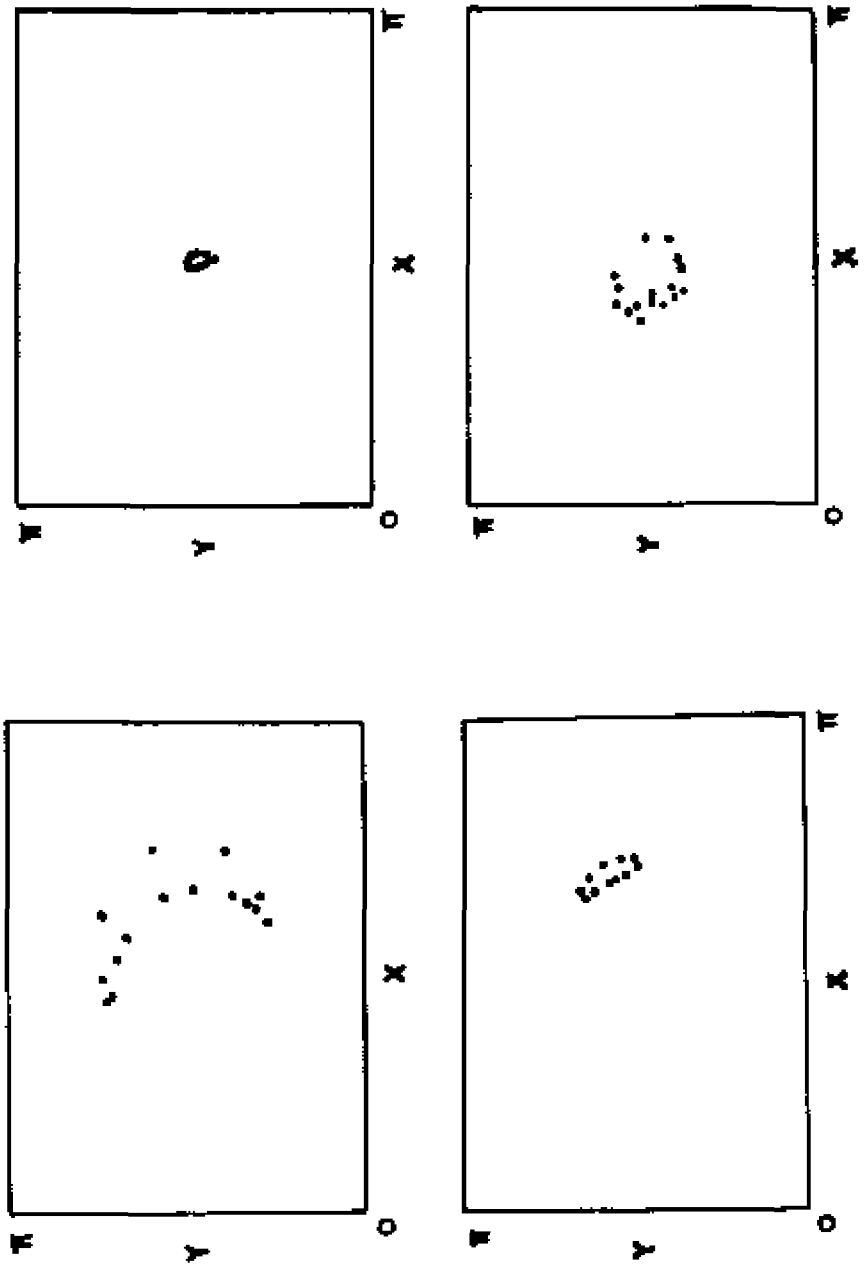

31(b): Poincare plots of magnetic field line traces in the z = π plane.

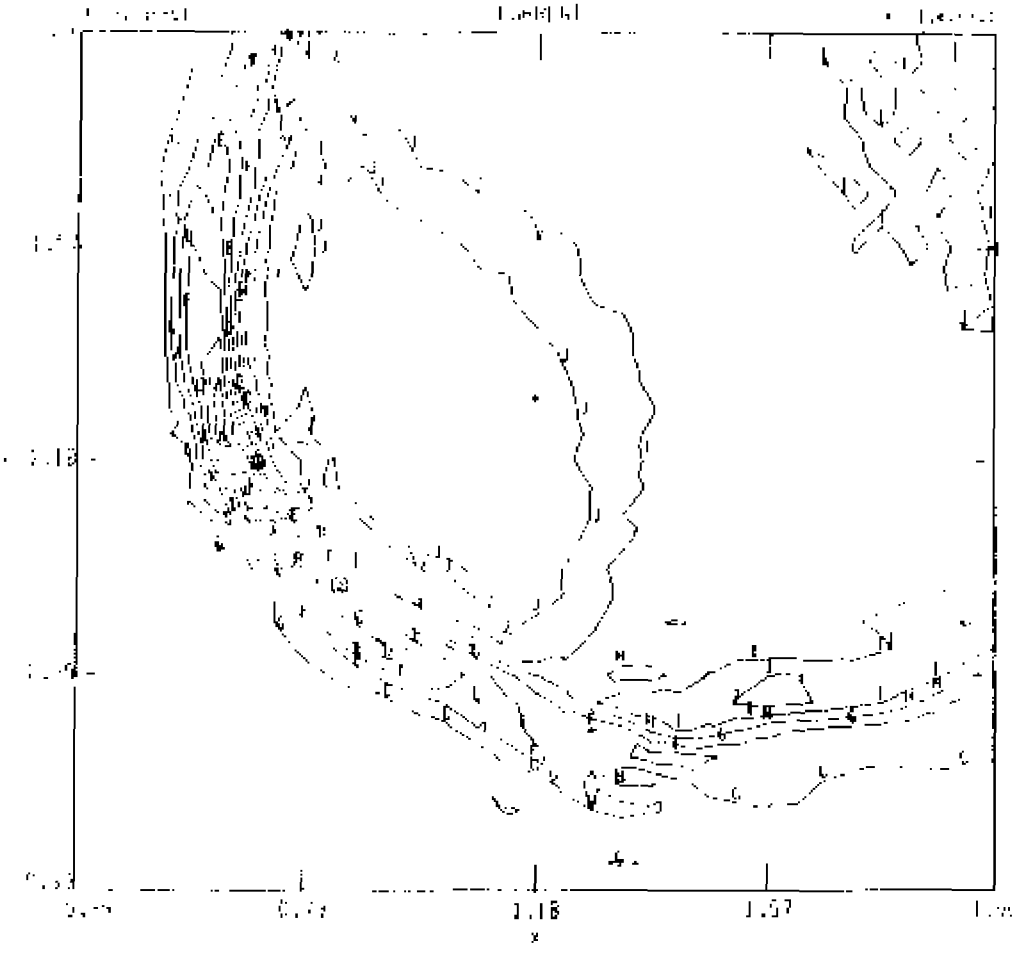

Figure 32. - CASE 3, t = 13.26:
32(a): close-up of j, poloidal cut.

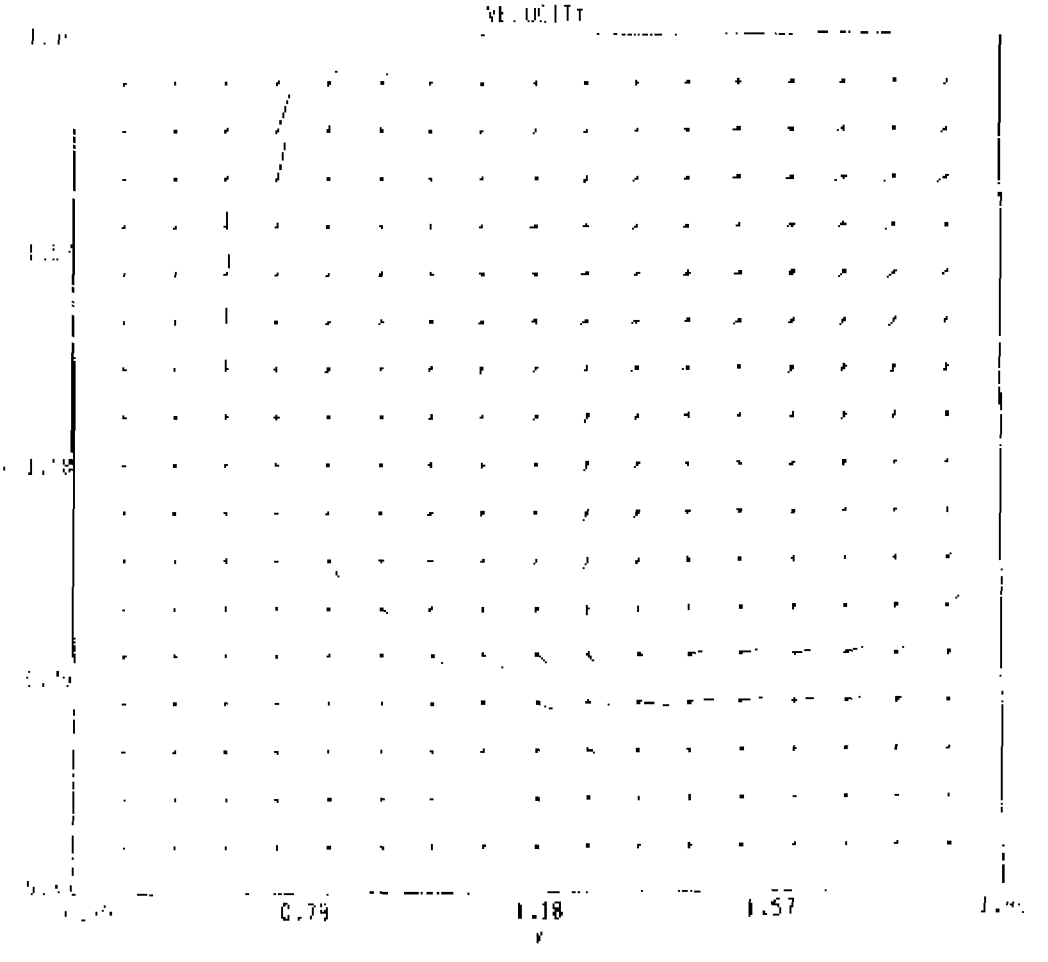

32(b): close-up of the velocity field, poloidal cut, and

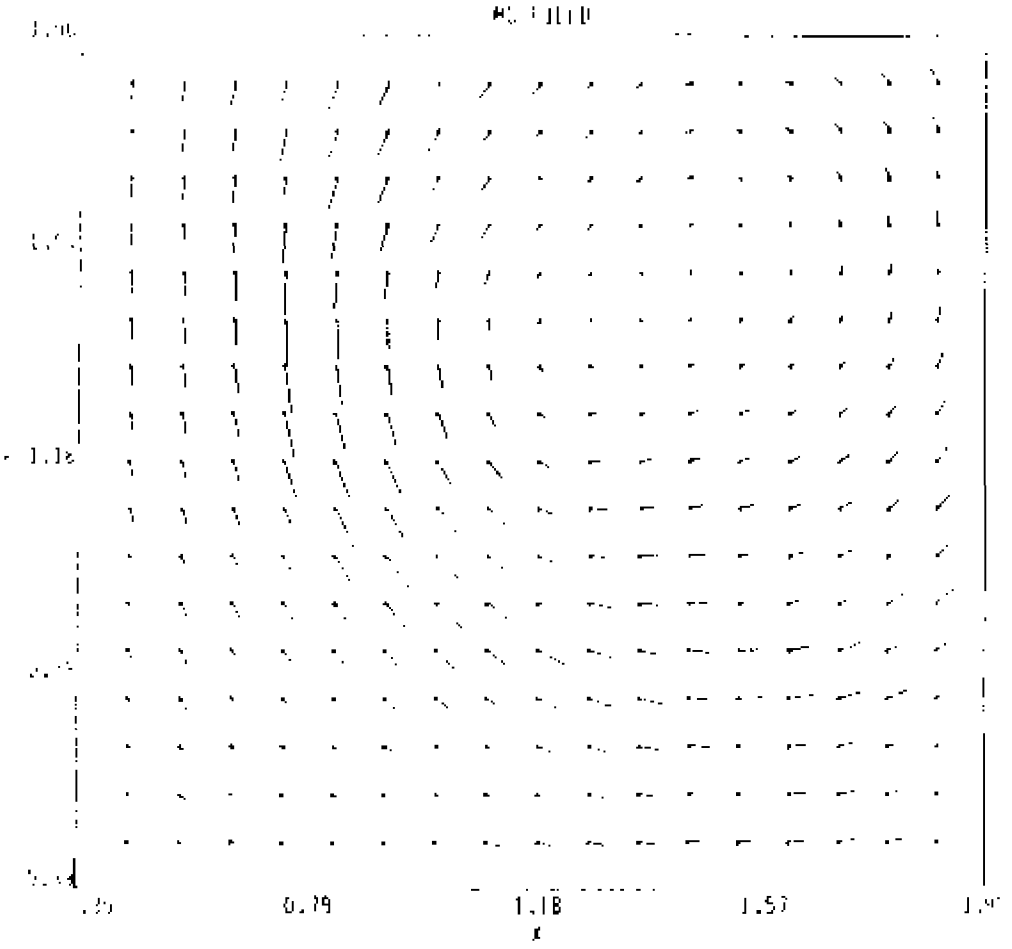

32(c): close-up of the poloidal magnetic field, poloidal cut.

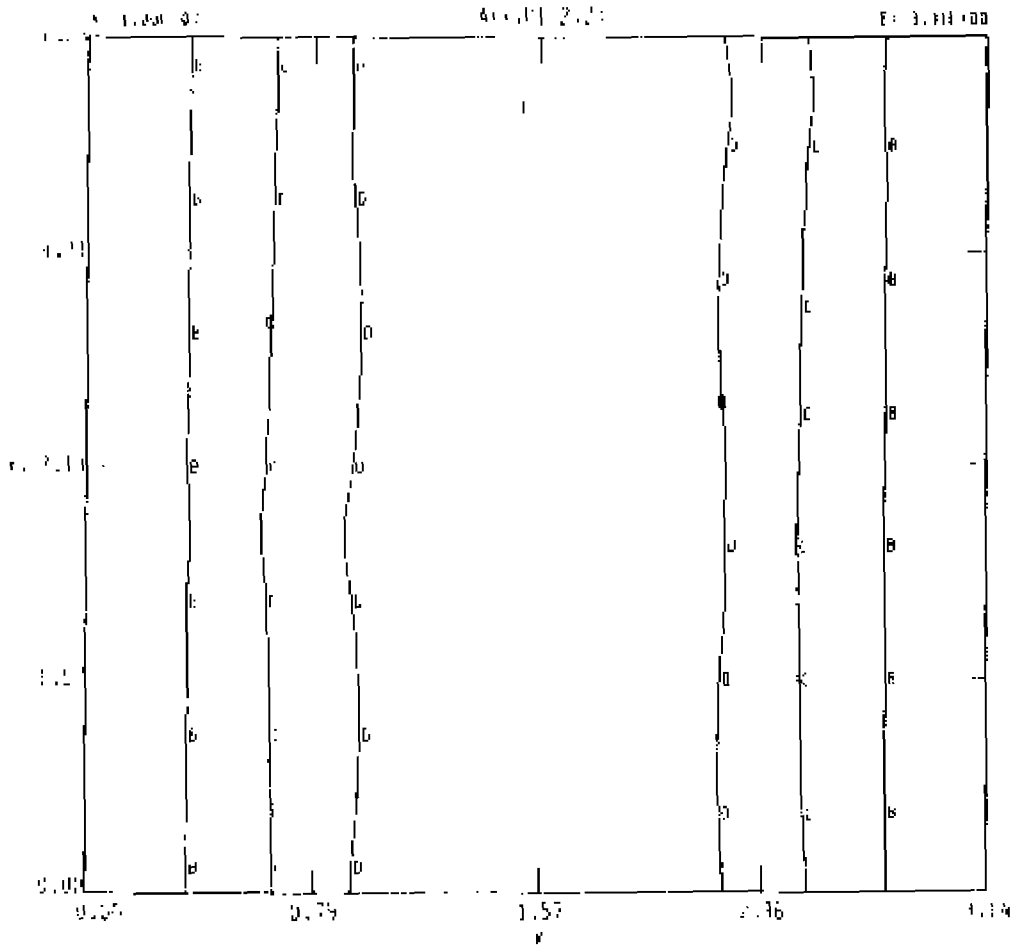

Figure 33. - Contours at t = 14.52, CASE 3:
33 (a): Contours of constant A, toroidal cut.

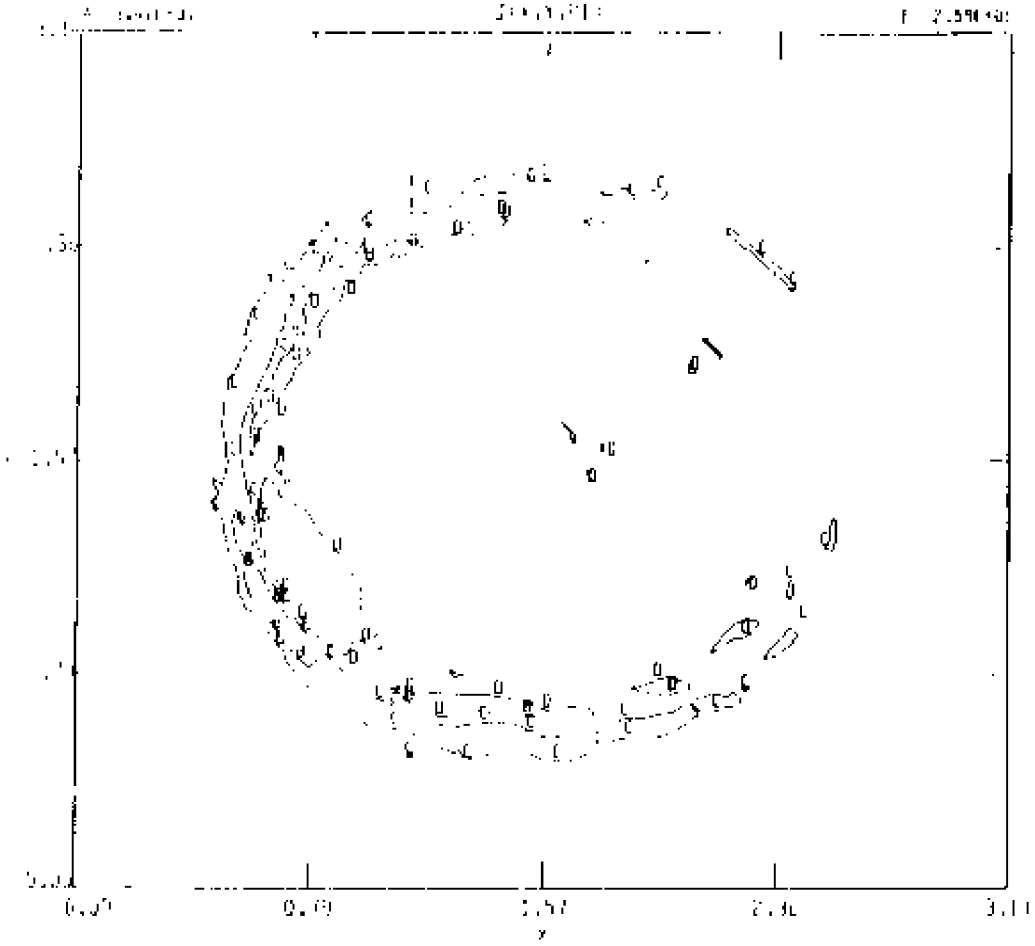

33 (b): Contours of constant j, poloidal cut.

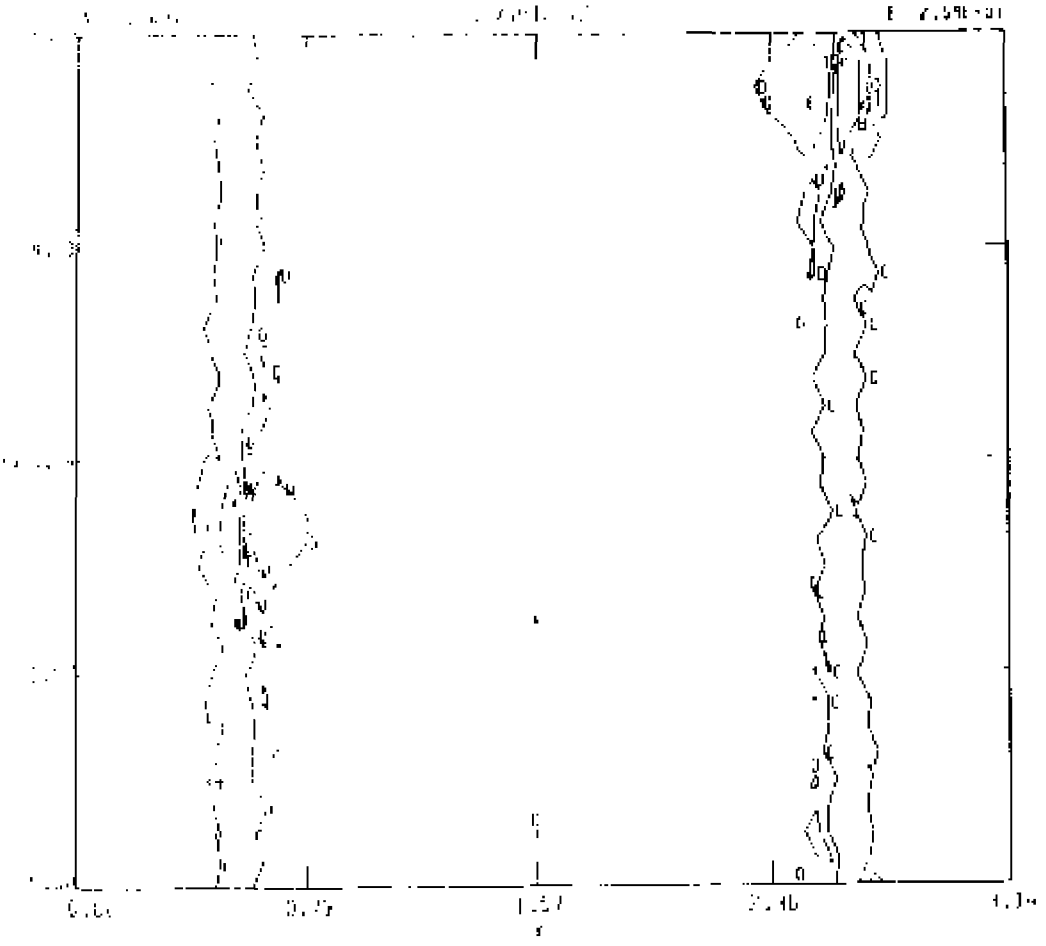

33 (c): Contours of constant j, toroidal cut.

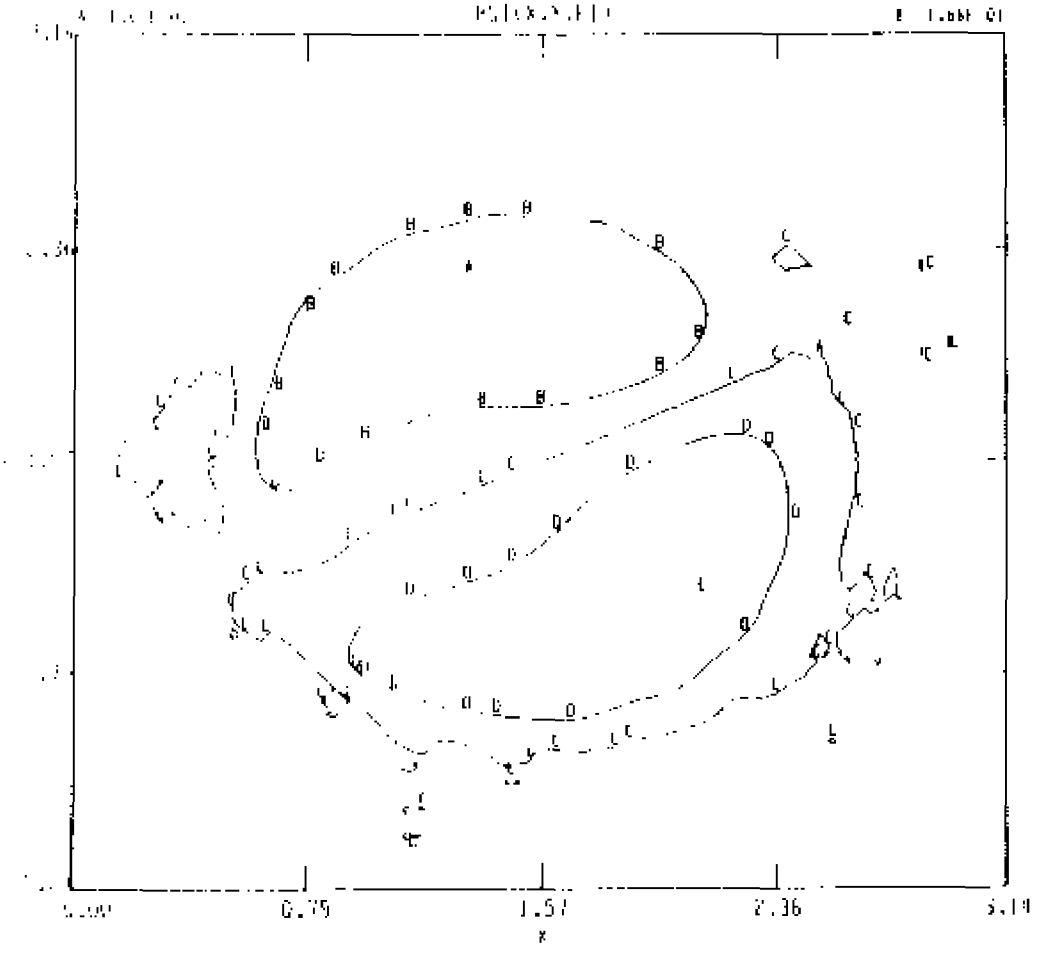

33 (d): Contours of constant Ψ, poloidal cut.

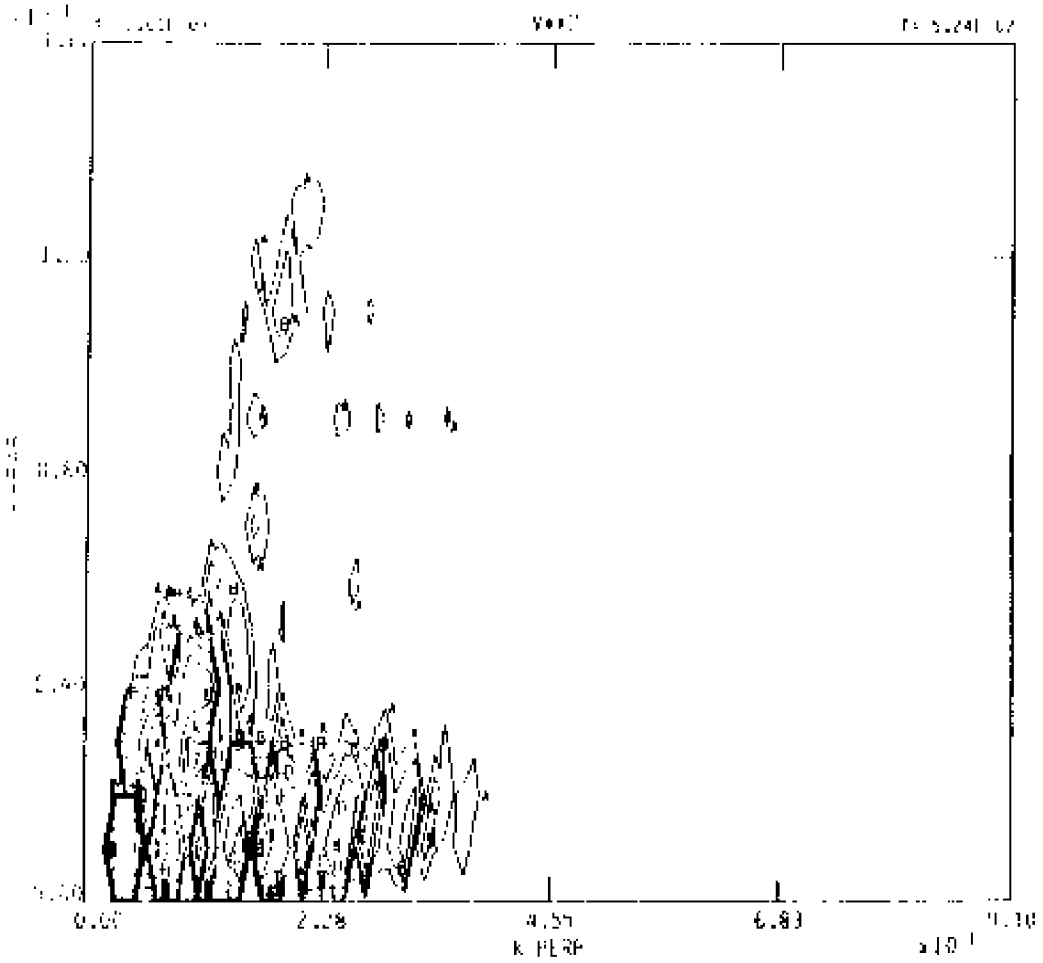

33 (e): Contours of modal kinetic energy, spaced by powers of two,

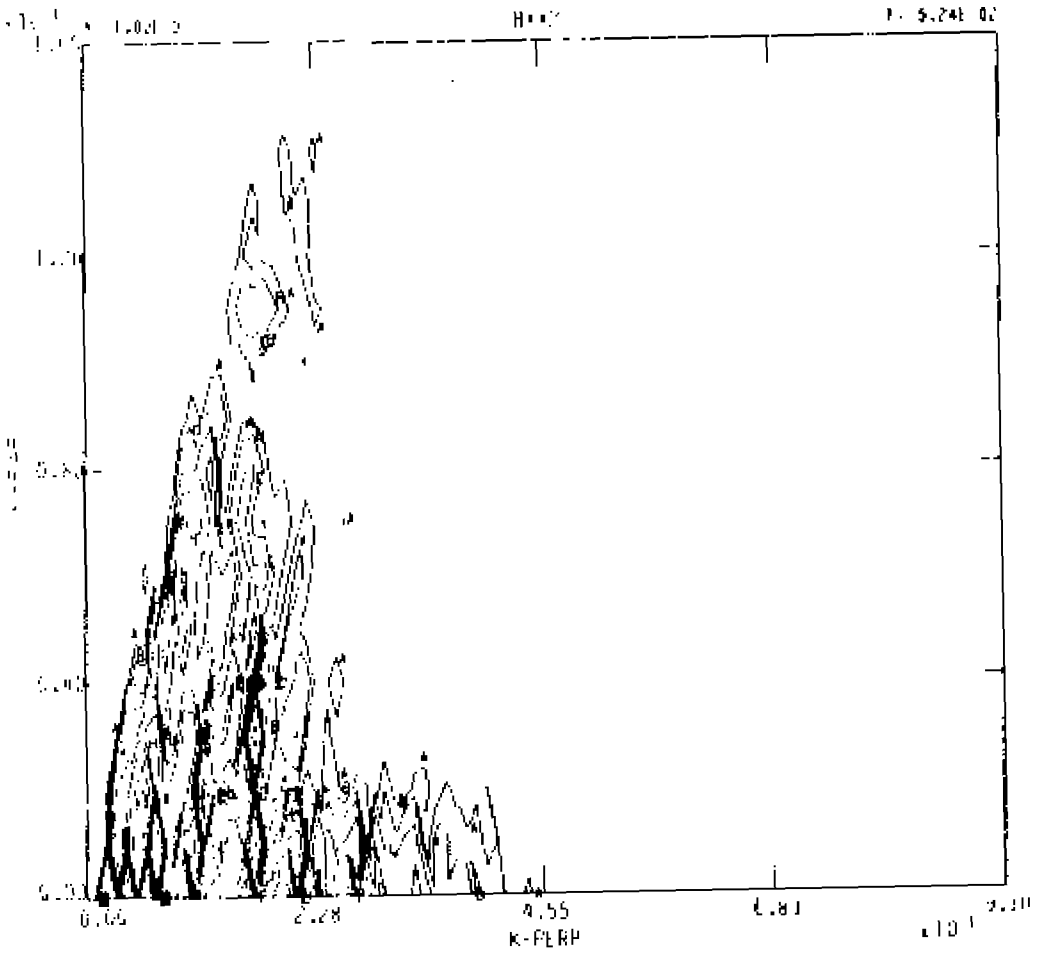

and 33 (f). Contours of modal magnetic energy, spaced by powers of two.

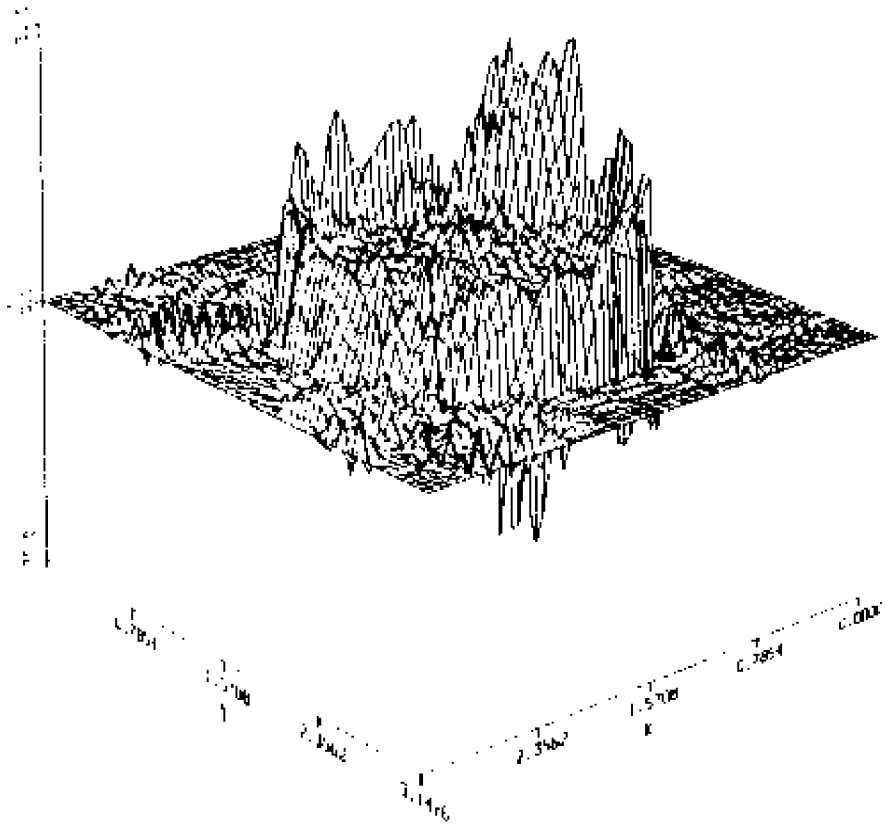

Figure 34: - Perspective plot of $j(x,y,z = \frac{\pi}{4}, t = 14.52)$, CASE 3.

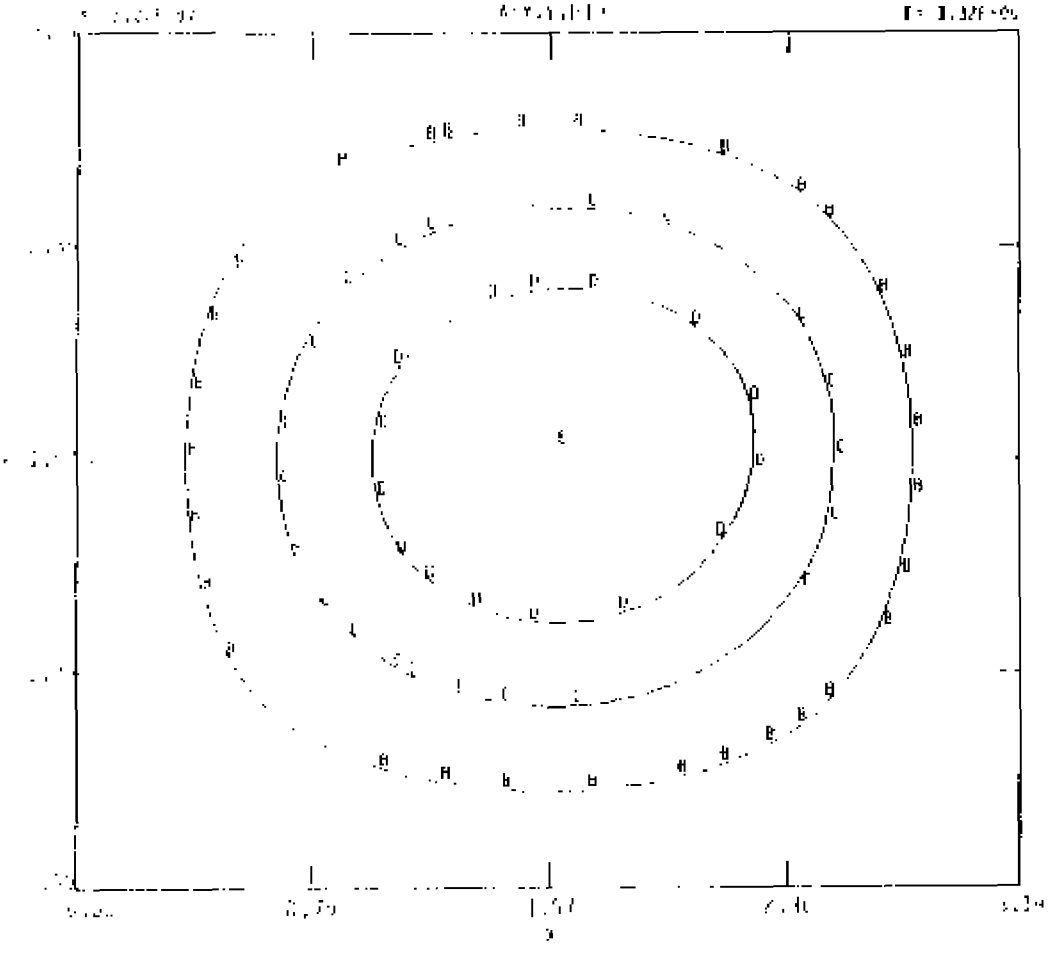

Figure 35. - CASE 3, t * 16.26:
35 (a): contours of A = constant, poloidal cut.

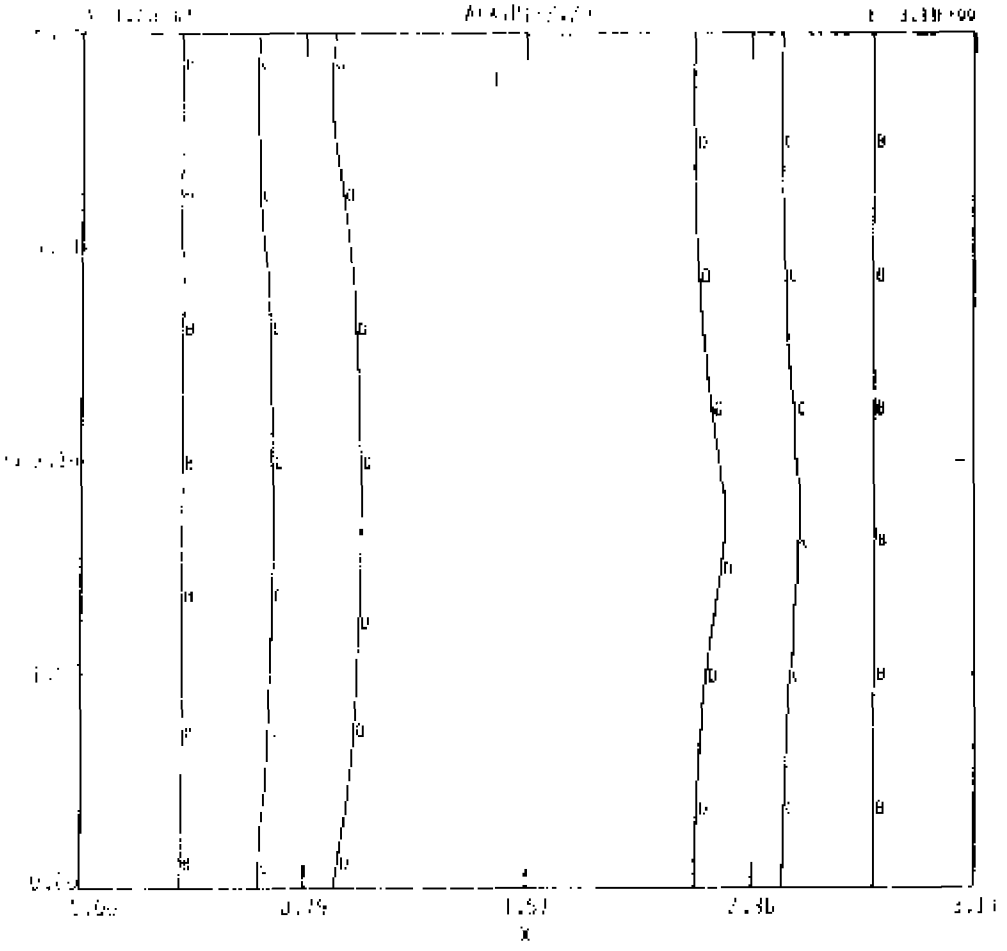

35 (b): contours of A * constant, toroidal cut.

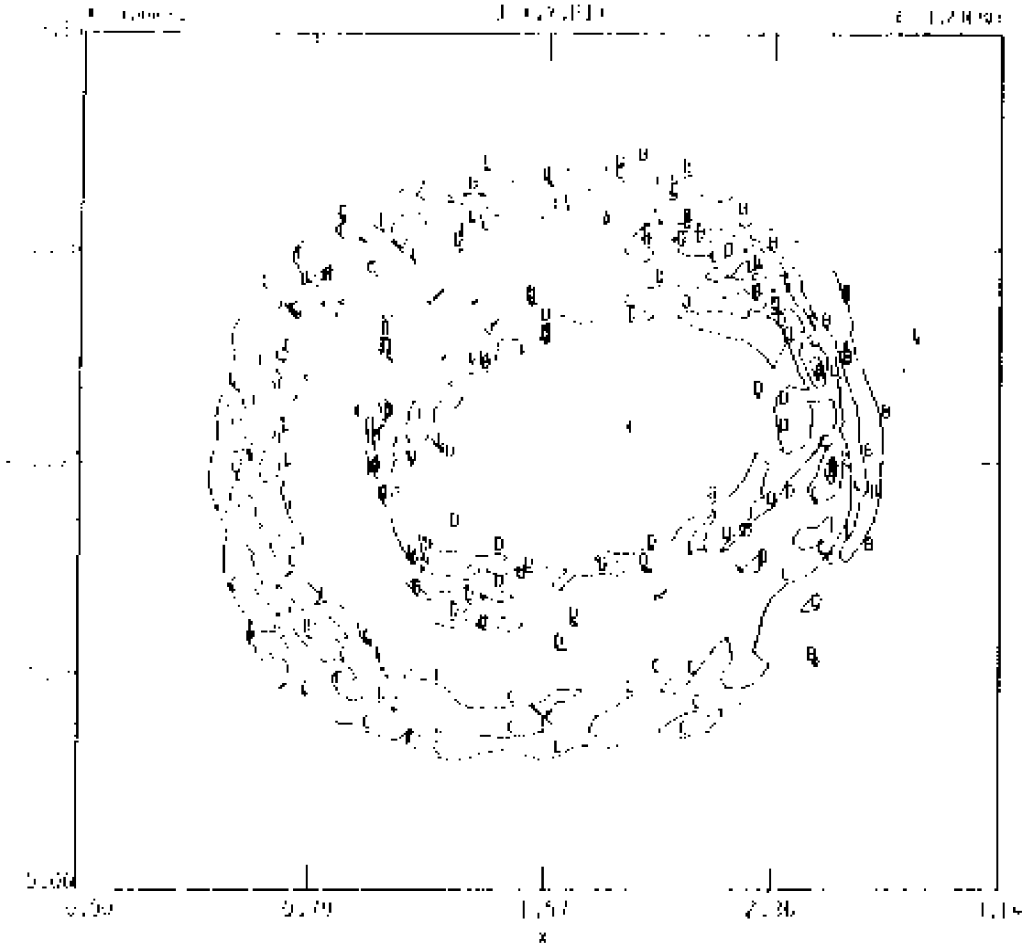

35 (c): contours of j = constant, poloidal cut.

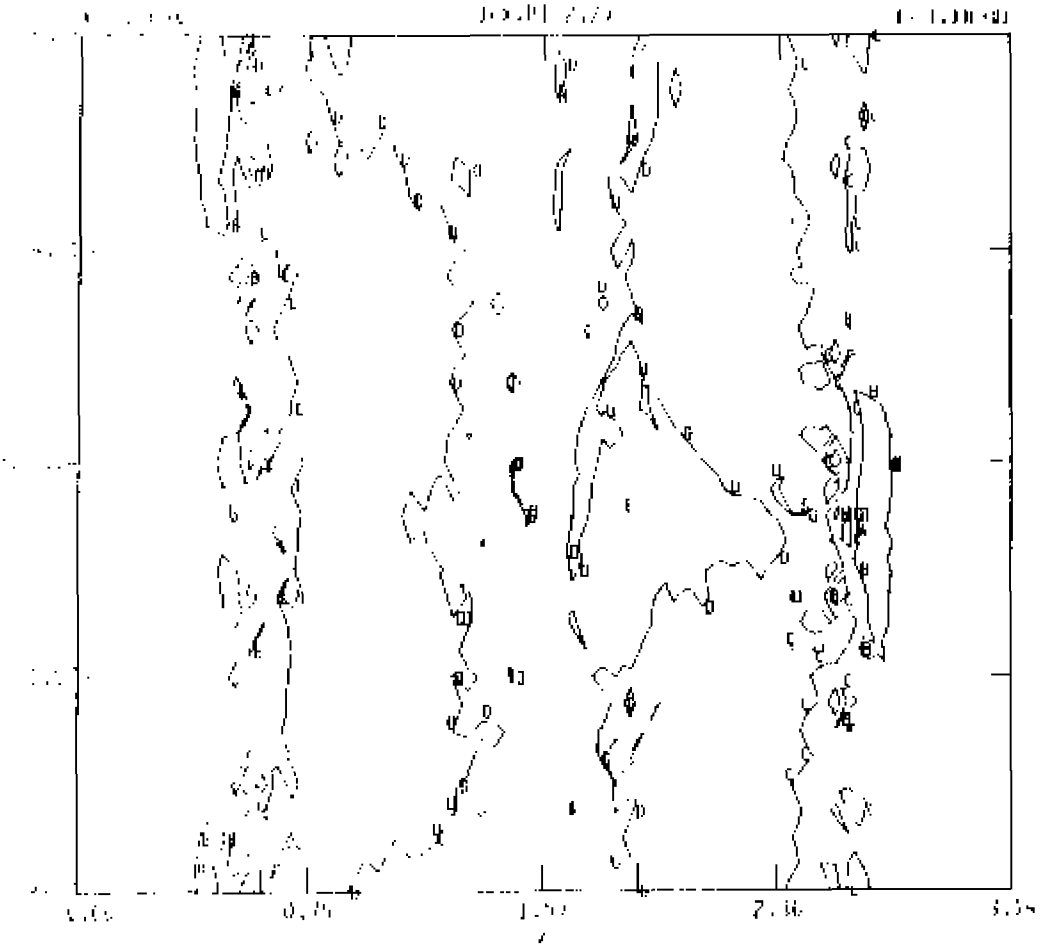

35 (d): contours of j = constant, toroidal cut.

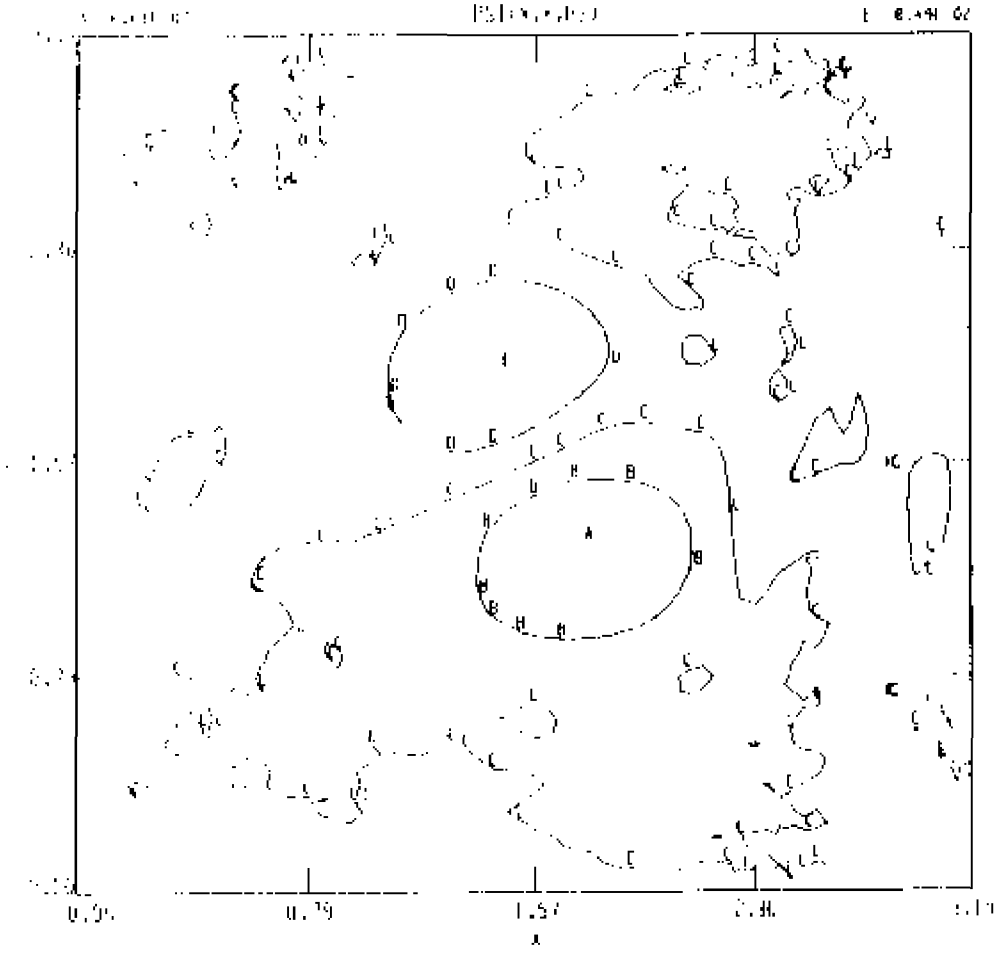

35 (e): contours of Ψ = constant, poloidal cut, and

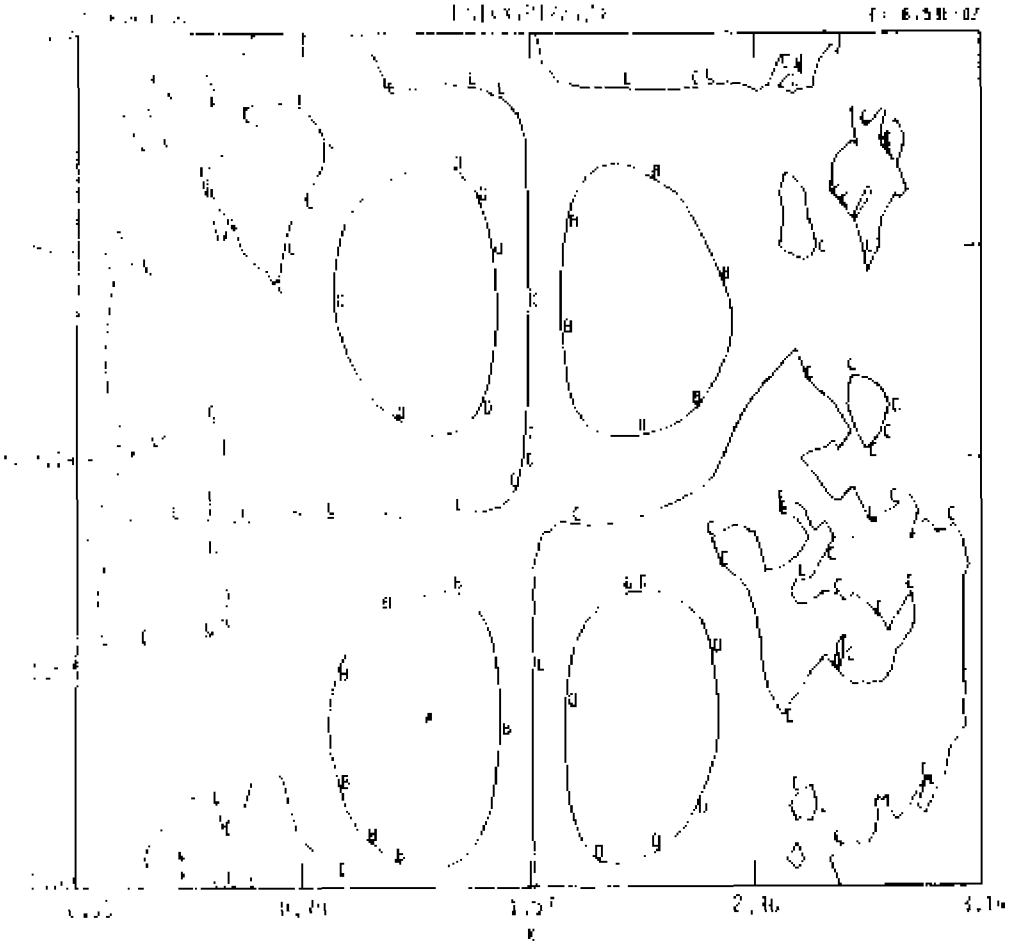

35 (f): contours of Ψ= constant, toroidal cut.

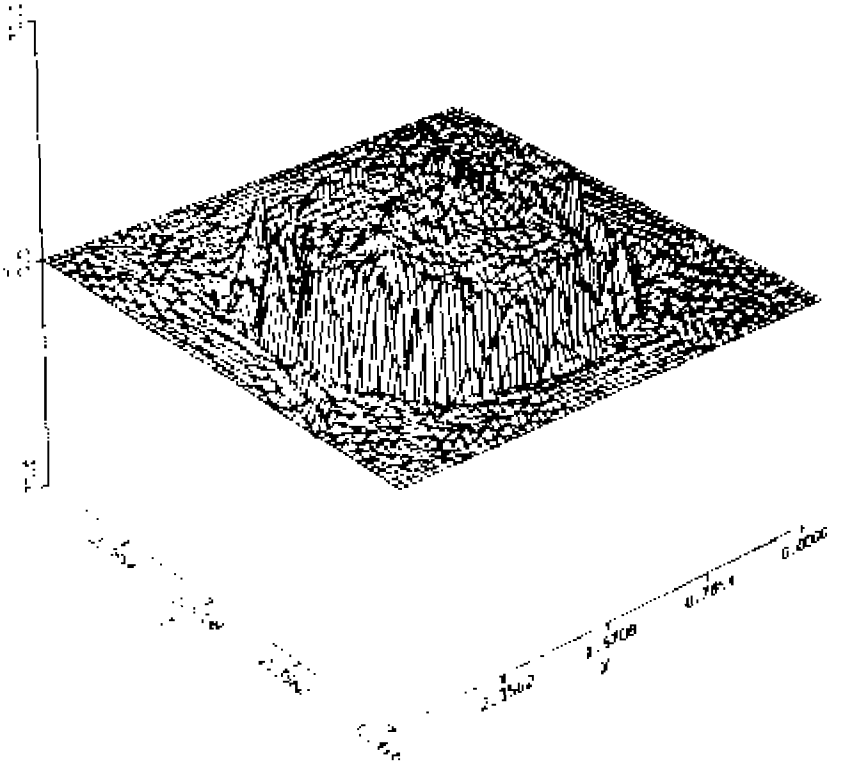

Figure 36. - CASE 3, t = 16.26:
36(a): Perspective plot of current in the z = π plane, and

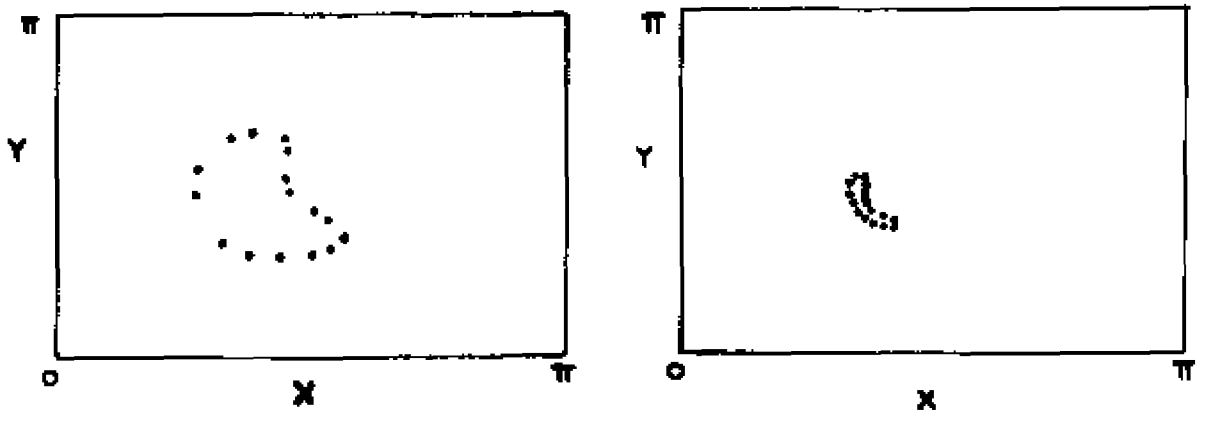

36(b): Poincaré plots of magnetic field line traces in the z =π plane.

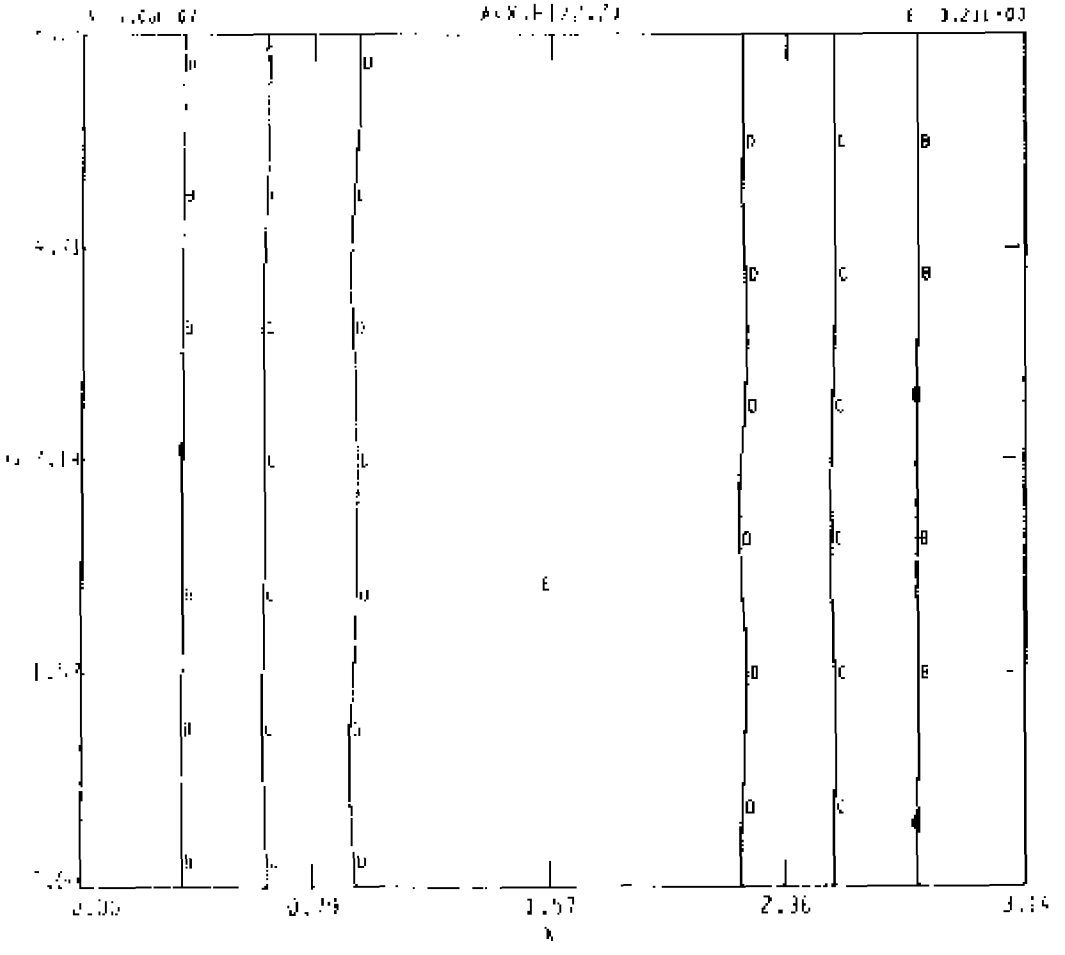

Figure 37. - Contours at t = 17.46, CASE 3:
37 (a): Contours of constant A, toroidal cut.

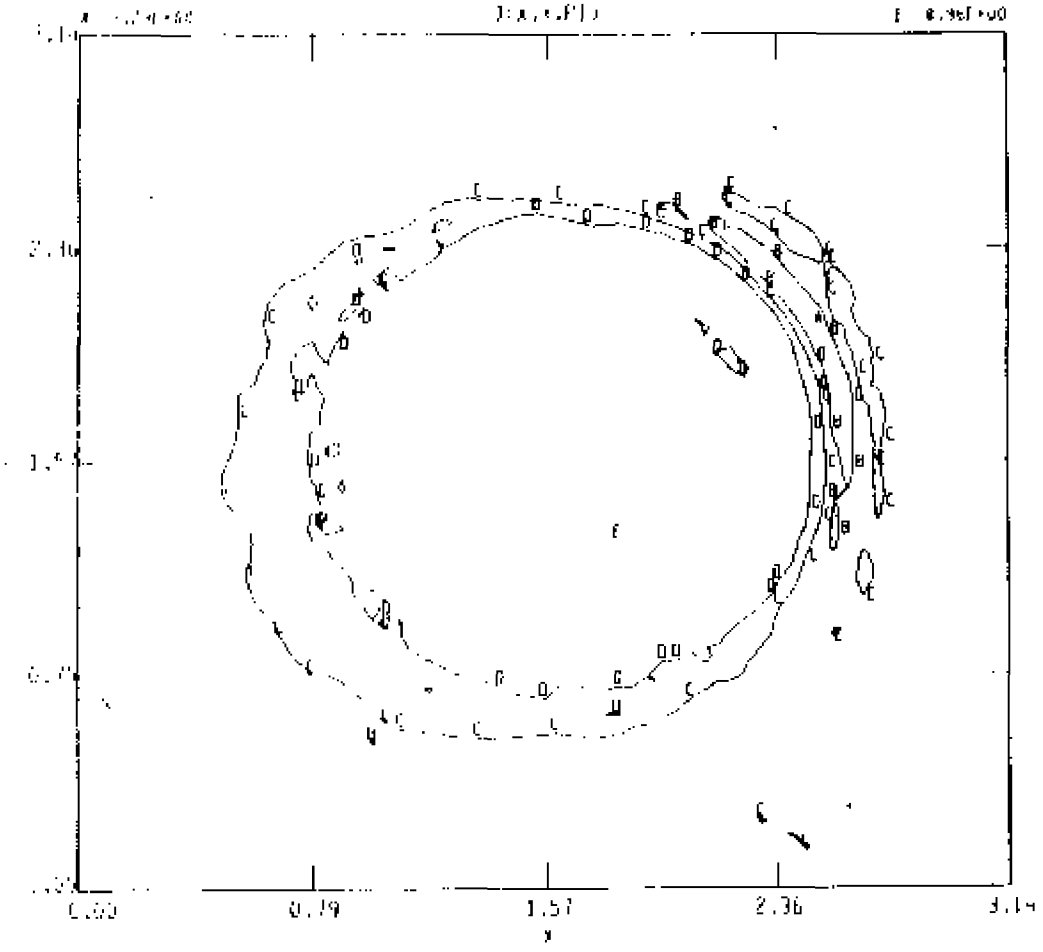

37 (b): Contours of constant j, poloidal cut.

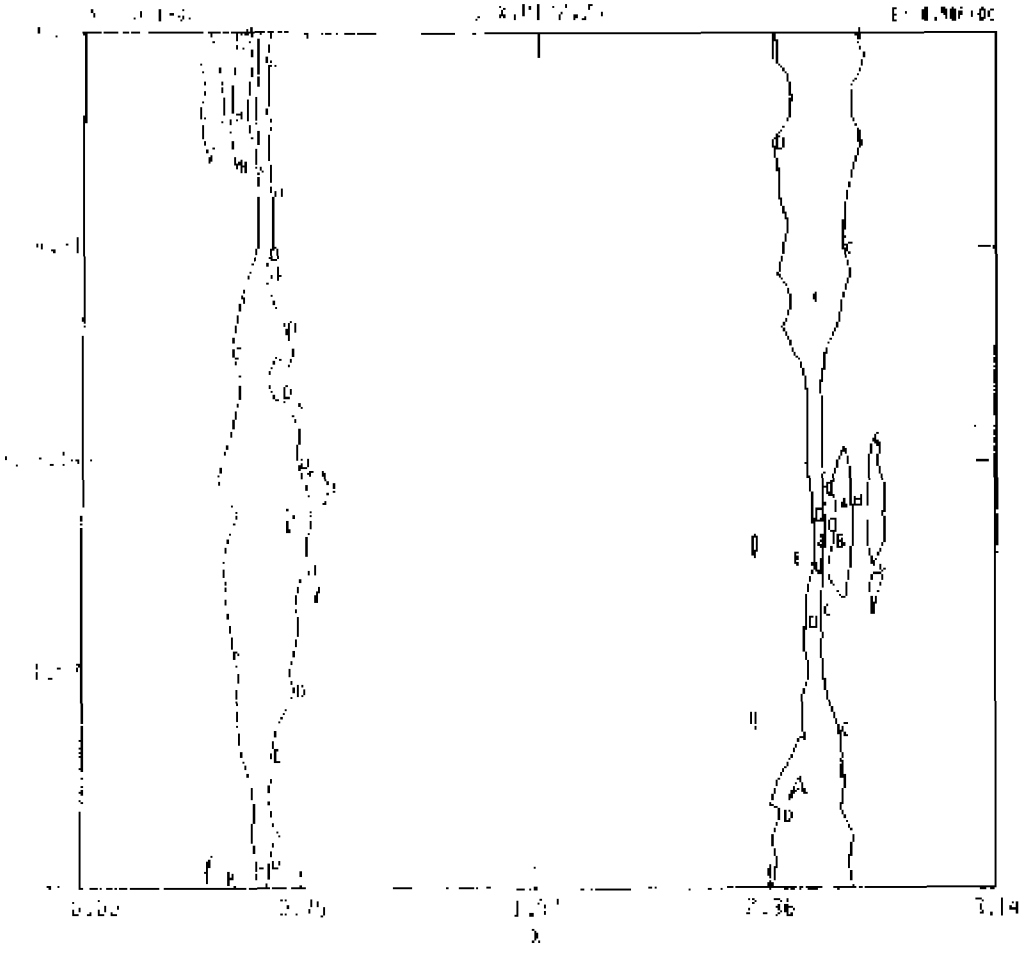

37 (c): Contours of constant j, toroidal cut.

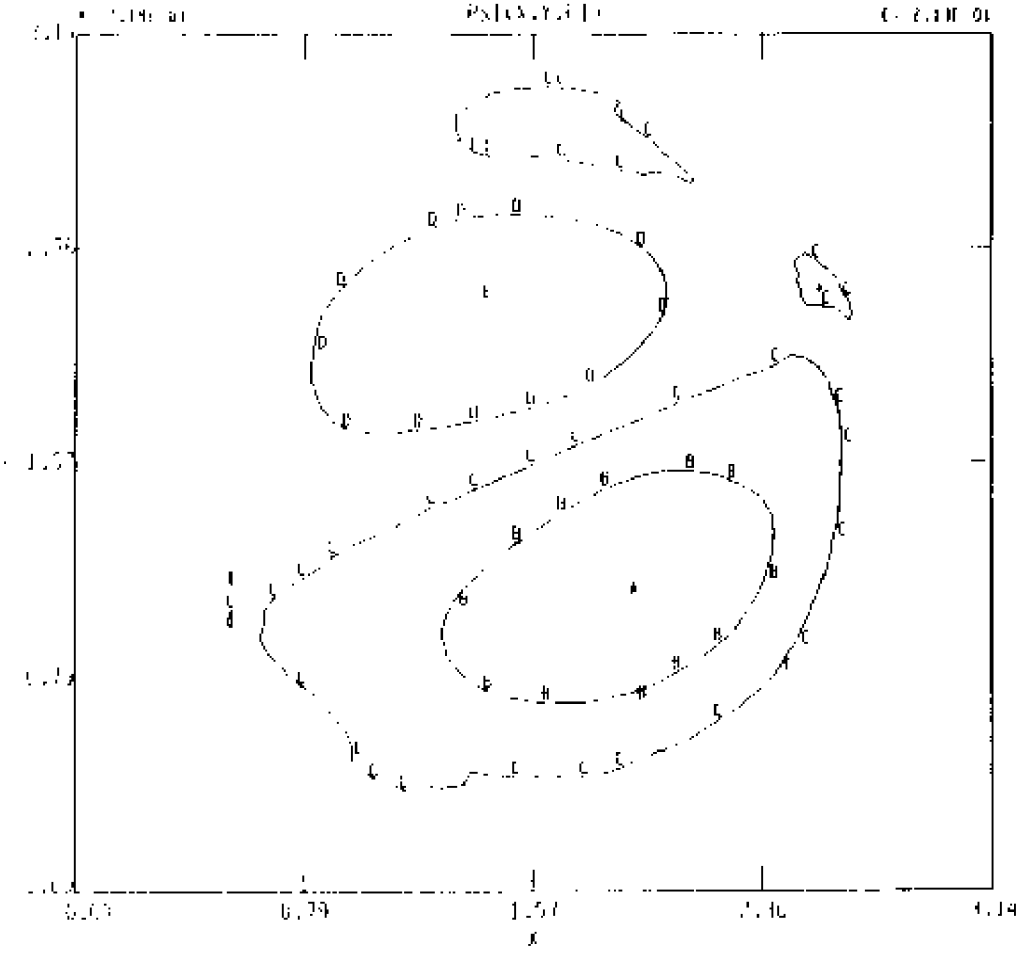

37 (d): Contours of constant Ψ, poloidal cut,

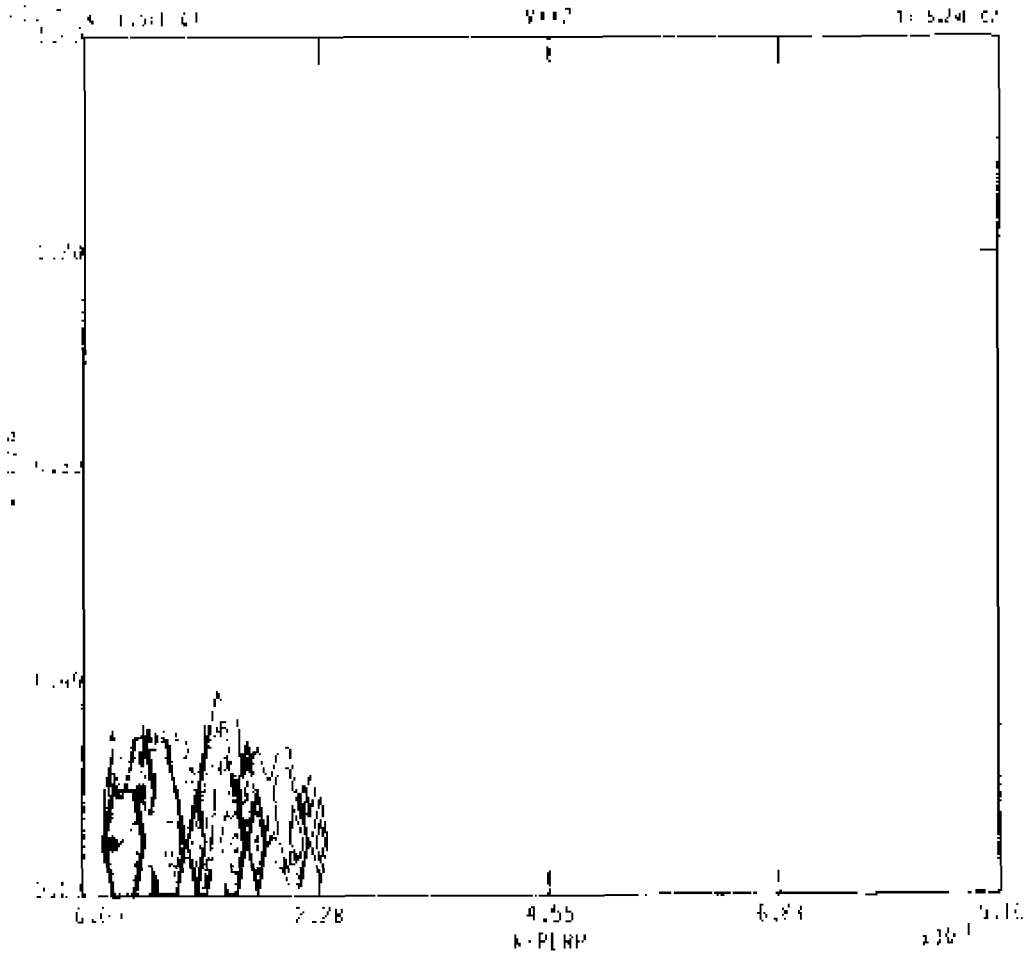

37 (e): Contours of modal kinetic energy, spaced by powers of two,

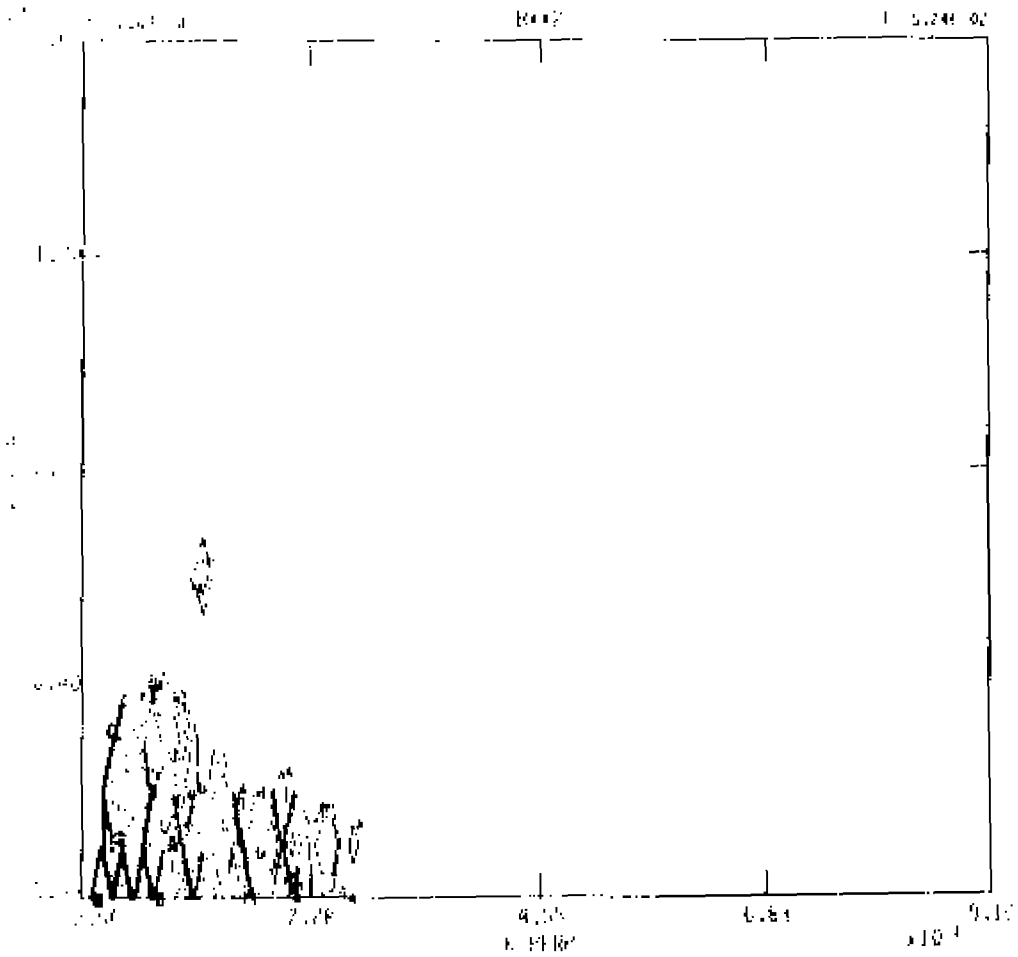

and 37 (f). Contours of modal magnetic energy, spaced by powers of two.

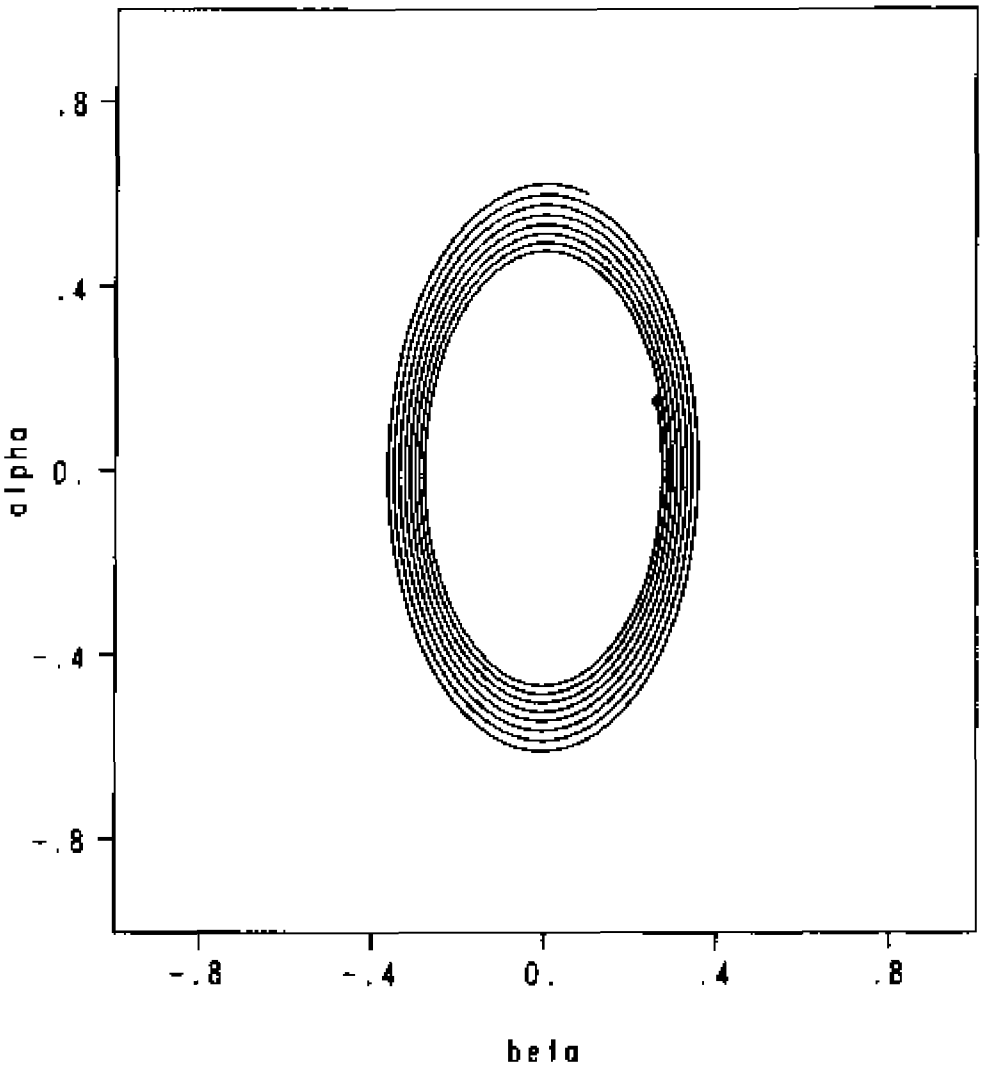

Figure 40. - Numerical solution of equations (26) and (27), with $\alpha = 15$, $B_0 = 4.3$, and $\eta = 0.01$.

Note: $\alpha > 20\, B_0 / 9$.

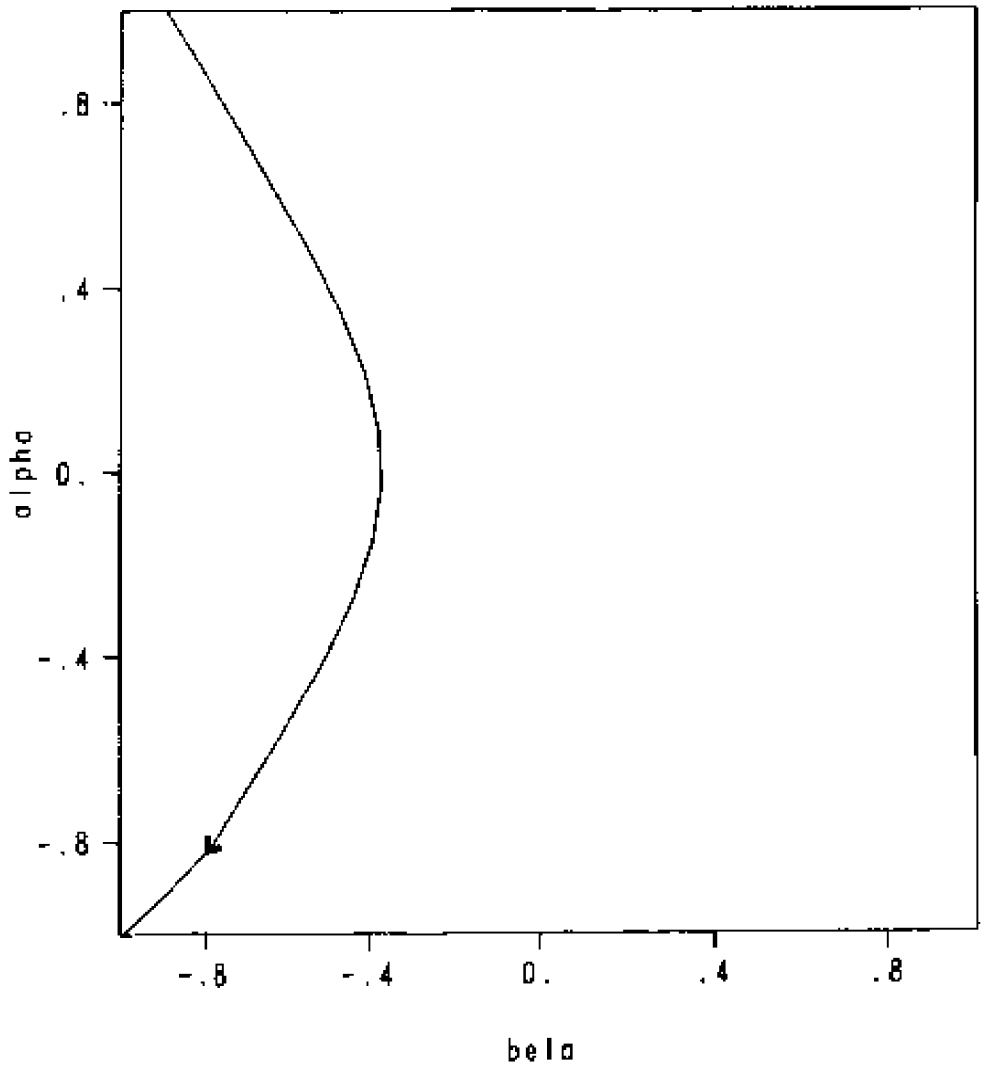

Figure 41. - Numerical solution of equations (26) and (27), with $\mu = 7.5$, $B_0 = 4.3$, and $\eta = 0.01$

Note: $4 B_0 / 3 < \alpha < 20 B_0 / 9$.

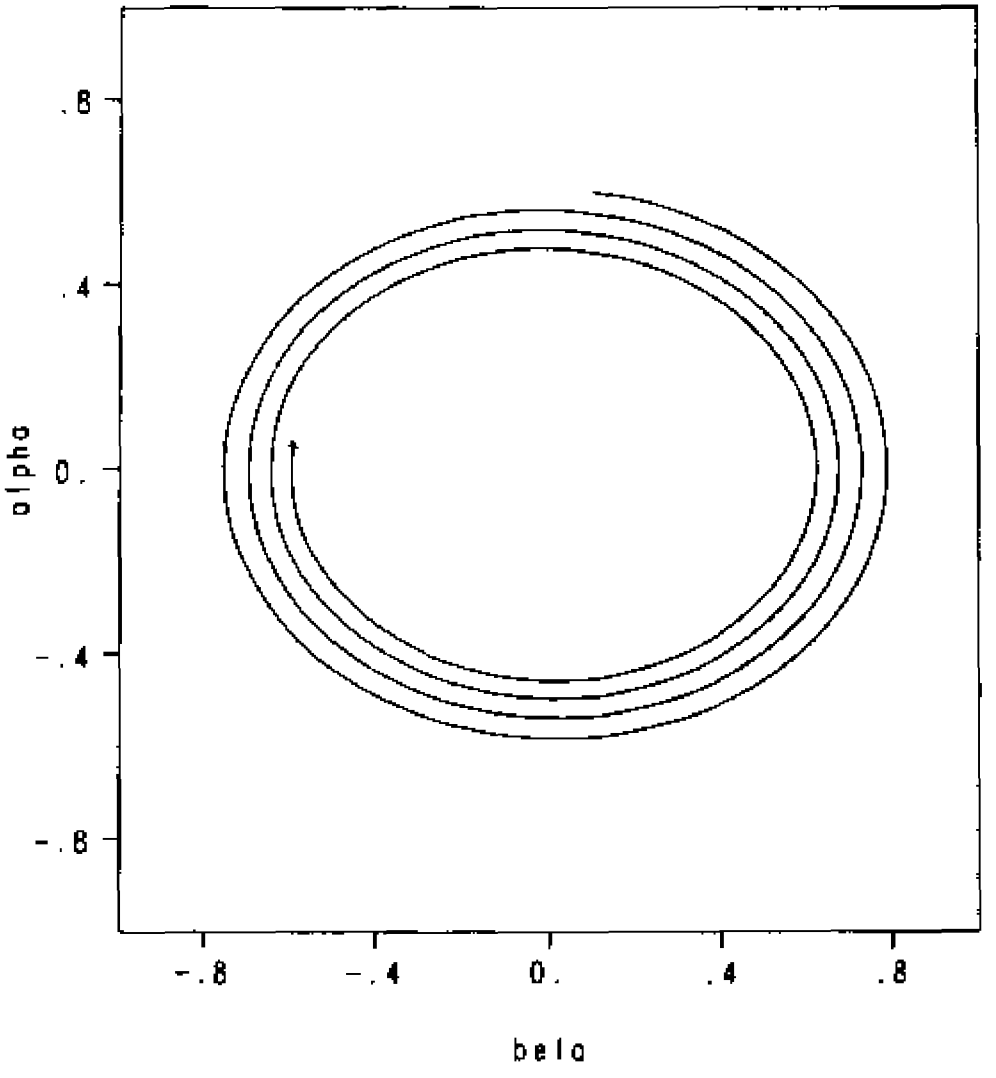

Figure 42. - Numerical solution of equations (26) and (27), with $\Omega = 3.75$, $B_0 = 4.3$, and $\eta = 0.01$.

Note: $\Omega < 4\,B_0 / 3$.

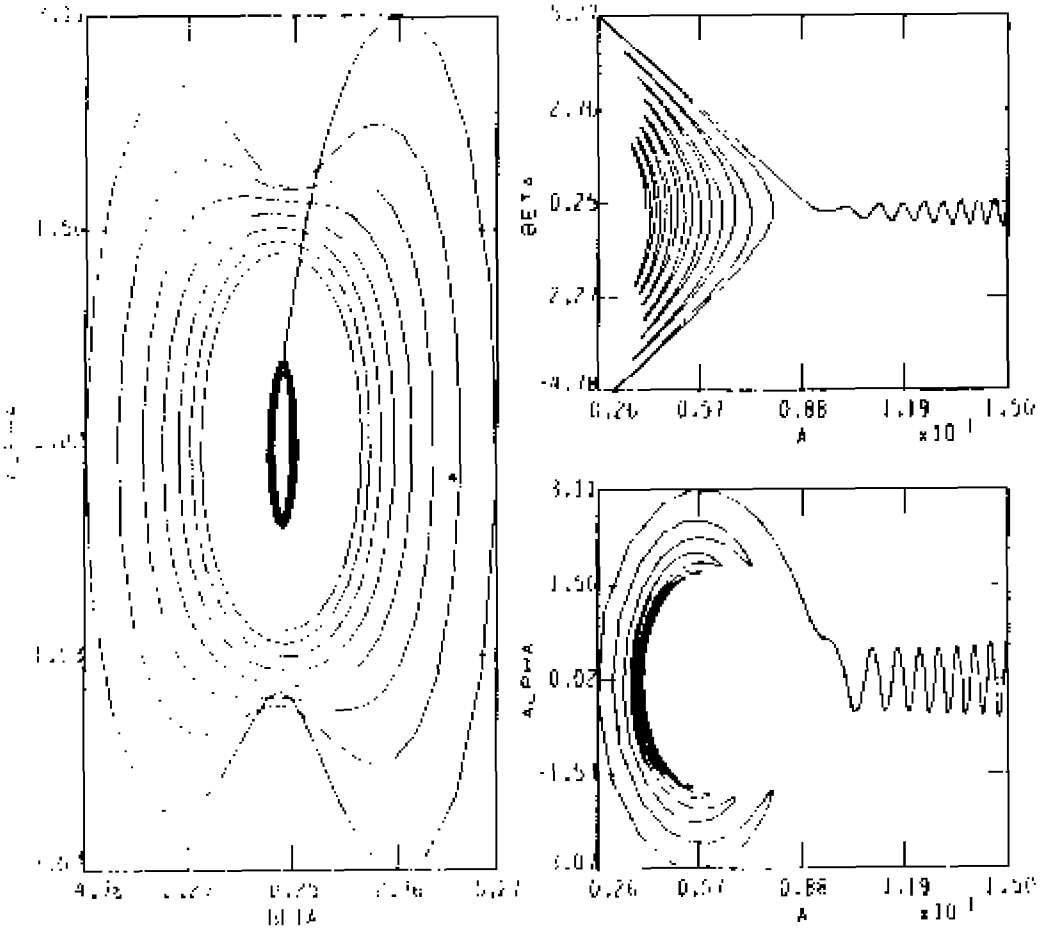

Figure 43. - Solutions of the nonlinear, undriven low-order model, equations (26), (27), and (30): 43(a): $b_0 = 4.3$, $\eta = 0.0100$, $\beta = 0.1$, $\alpha = 0.6$, $\hat{\mu} = 15.00$,

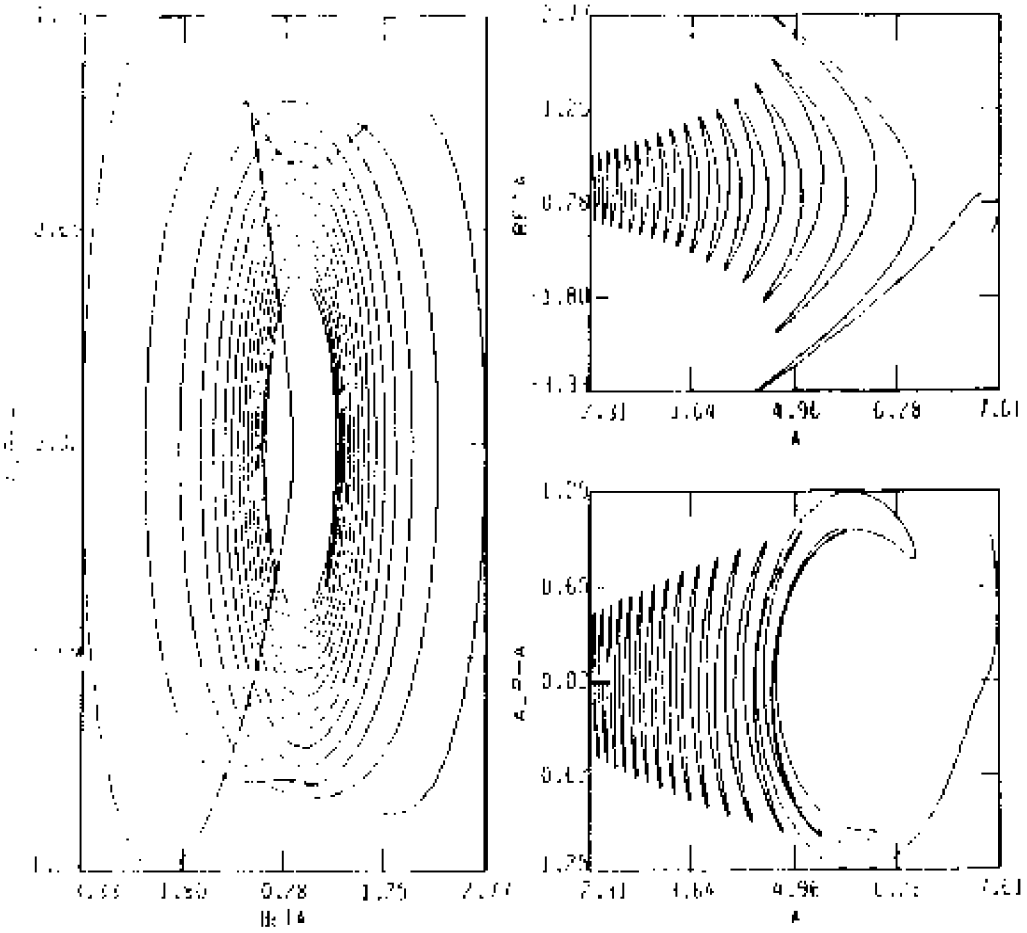

43(b): $B_0 = 4.3$, $\eta = 0.0100$, $\beta = -0.0$, $\alpha = 1.0$, $a = 7.50$,

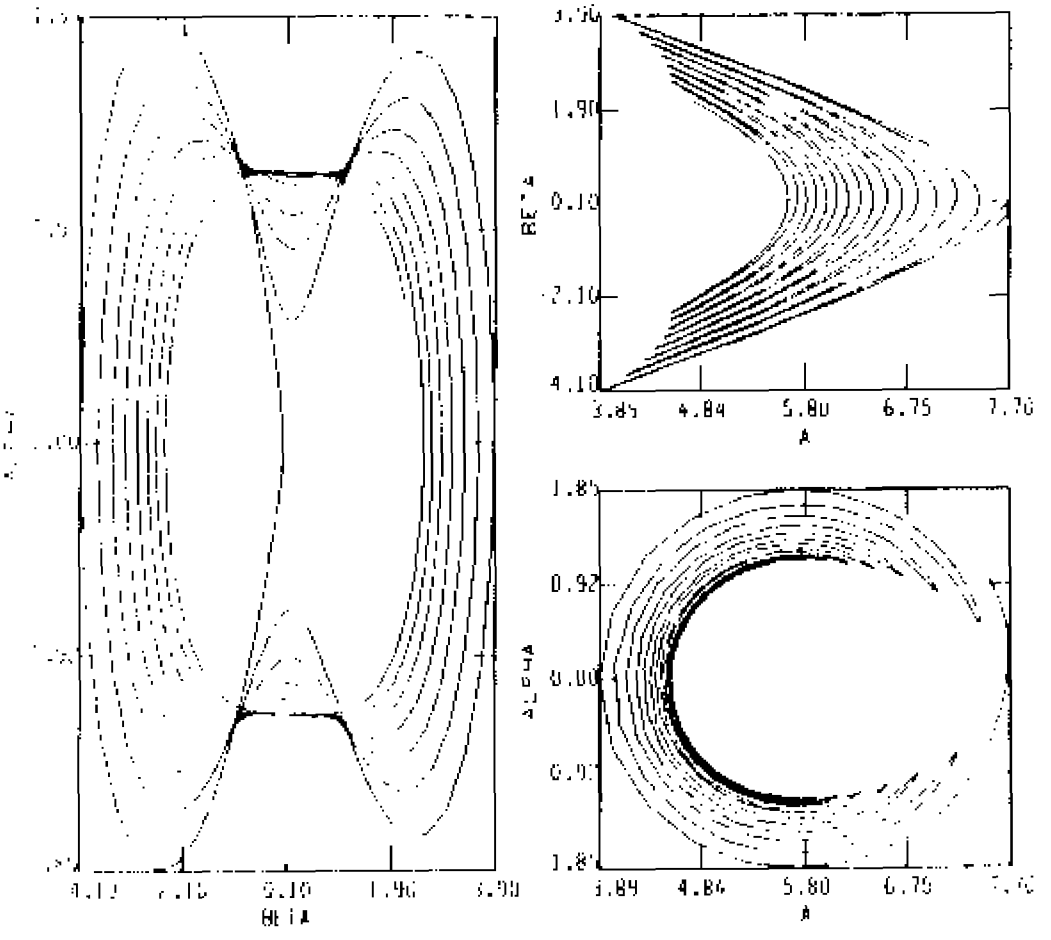

43(c): B_o = 4.3, η = 0.0025, β = -0.8, α = 1.0, λ = 7.50.

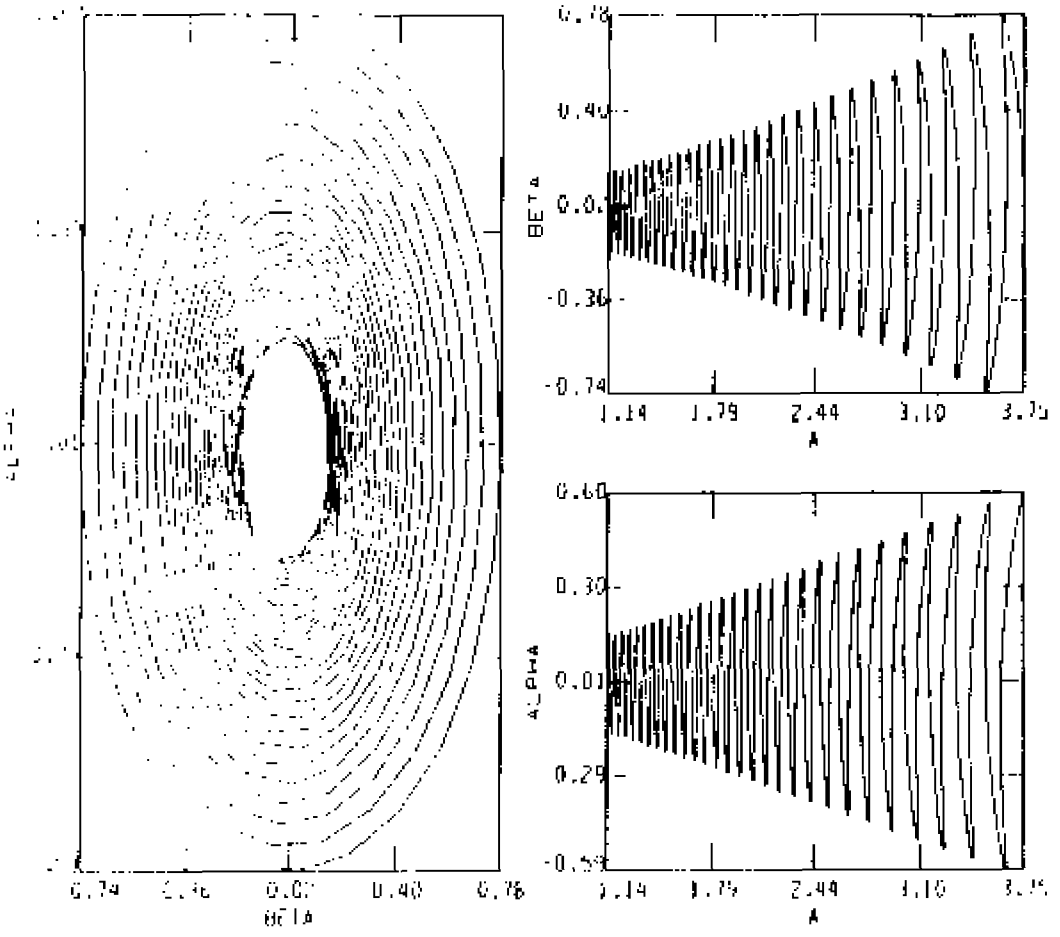

43(d): B_o = 4.3, η = 0.0100, β = 0.1, α = 0.6, a = 3.75,

Note: t_{min} = 0.0, and t_{max} = 59.88.

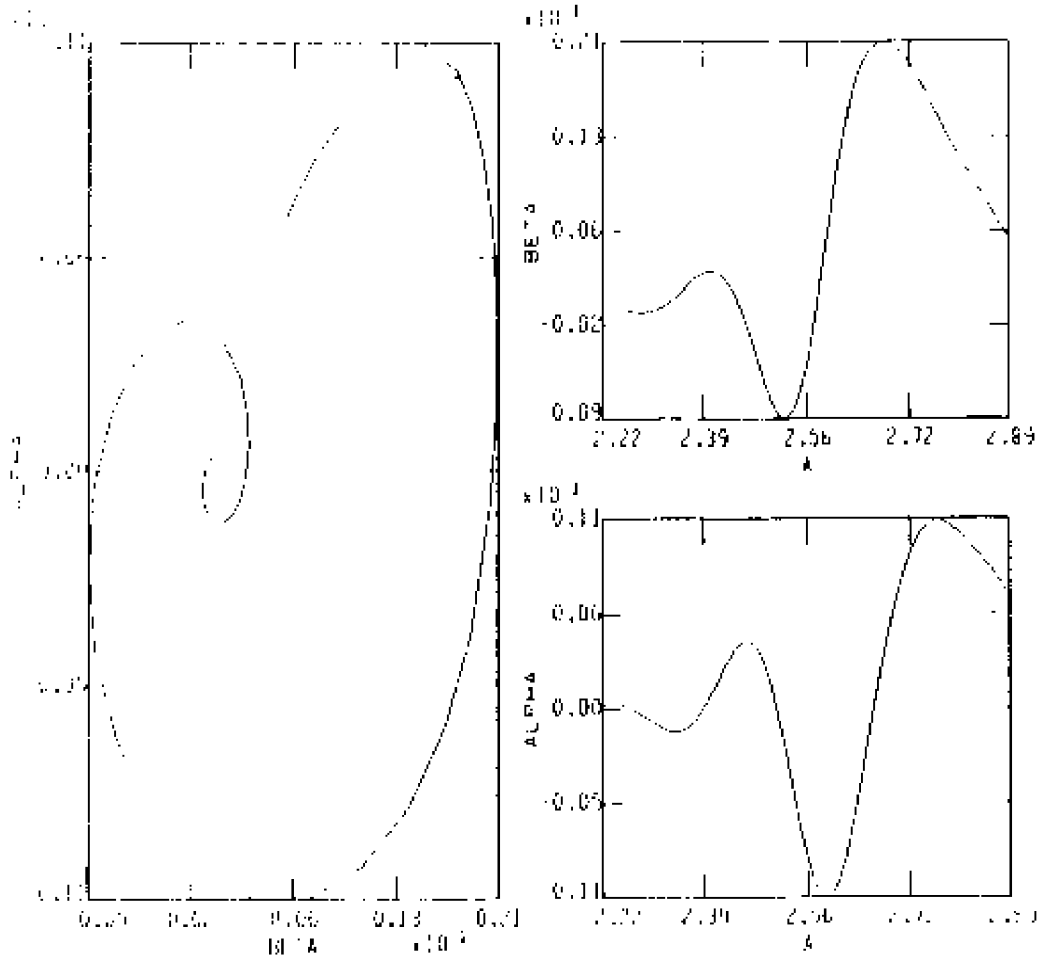

Figure 44. - CASE 2 full-grid simulation experimental values for β, α and λ with t_{min} = 4.44 and t_{max} = 17.52.

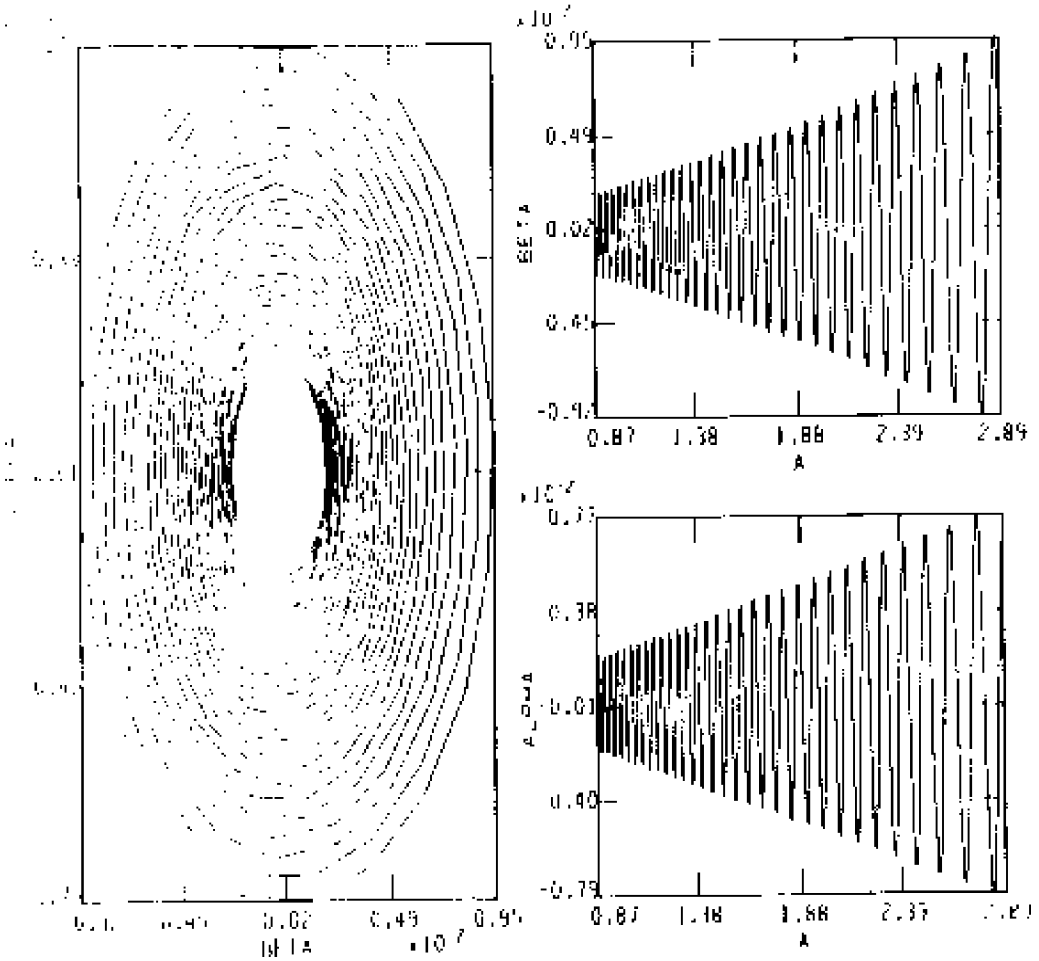

Figure 45. - Solution of equations (26), (27) and (28)
with parameters and conditions as for Fig 44,
(B_0 = 4.3, η = 0.01, α = 0.0067724, β = 0.0053),
45(a): with Ω = amplitude of sin(x)*sin(y) at 4.44 = 2.89, and

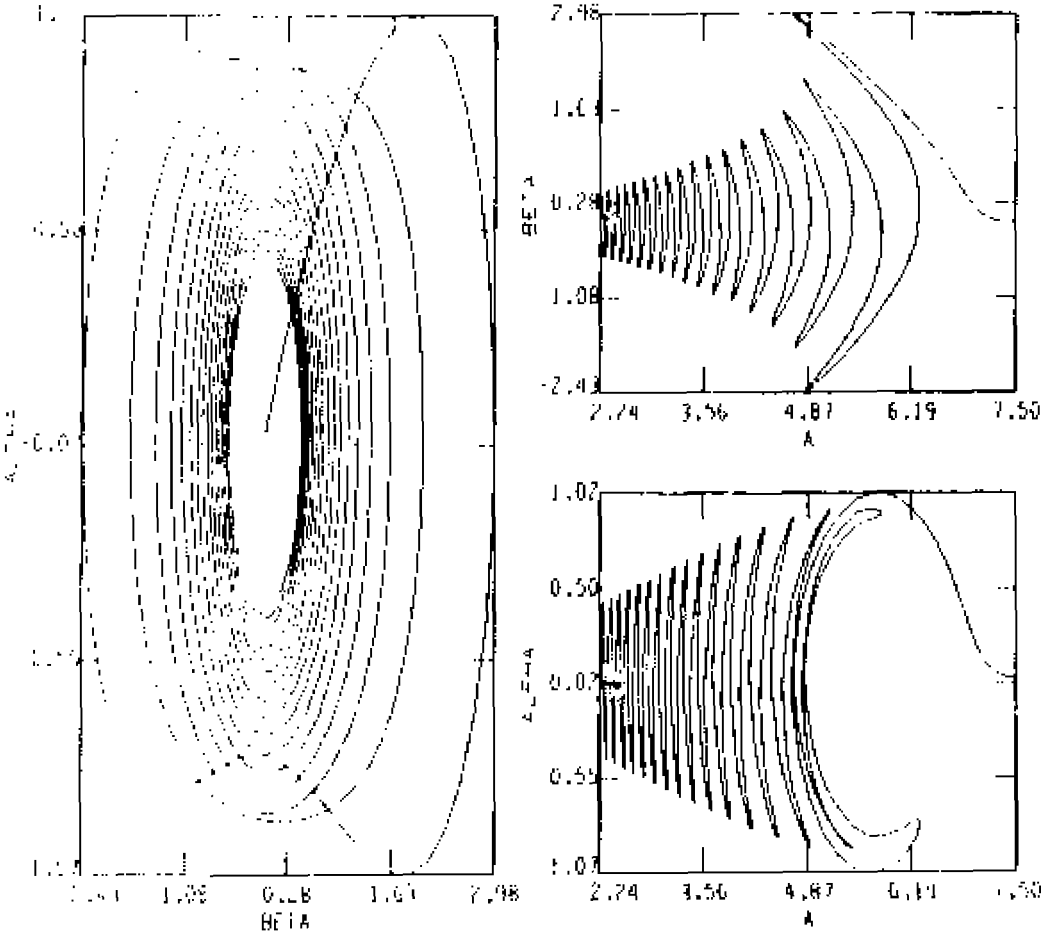

45(b): with $\alpha = j_{max}(t = 4.44) / 2 = 7.5$.

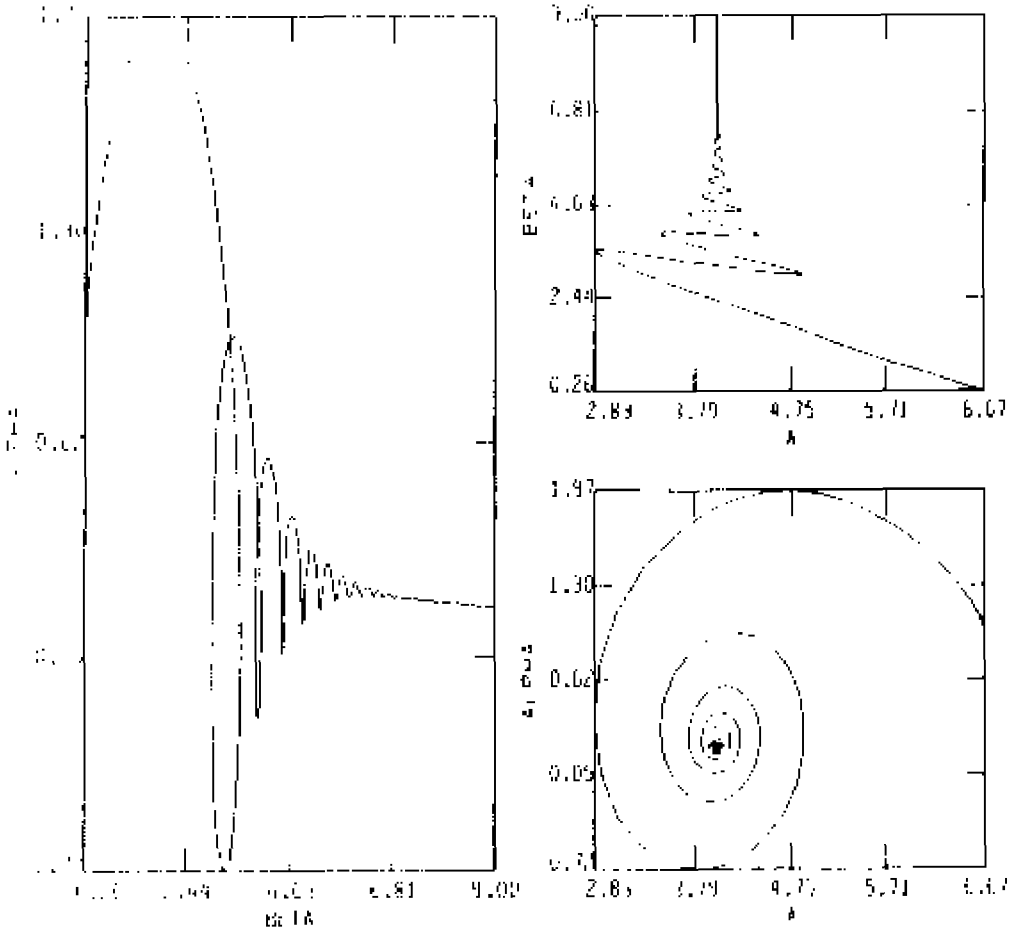

Figure 46. - Solution of (26), (27) and (30) for an initial critical point:
B_0 = 3.000000, Ω_0 = 7.6666666, α = 6.6666666,
η = 0.100000, α = 1.0327956, β = 0.25819889,
ν = 0.000000,
with t_{min} = 0.0, and t_{max} = 59.80.

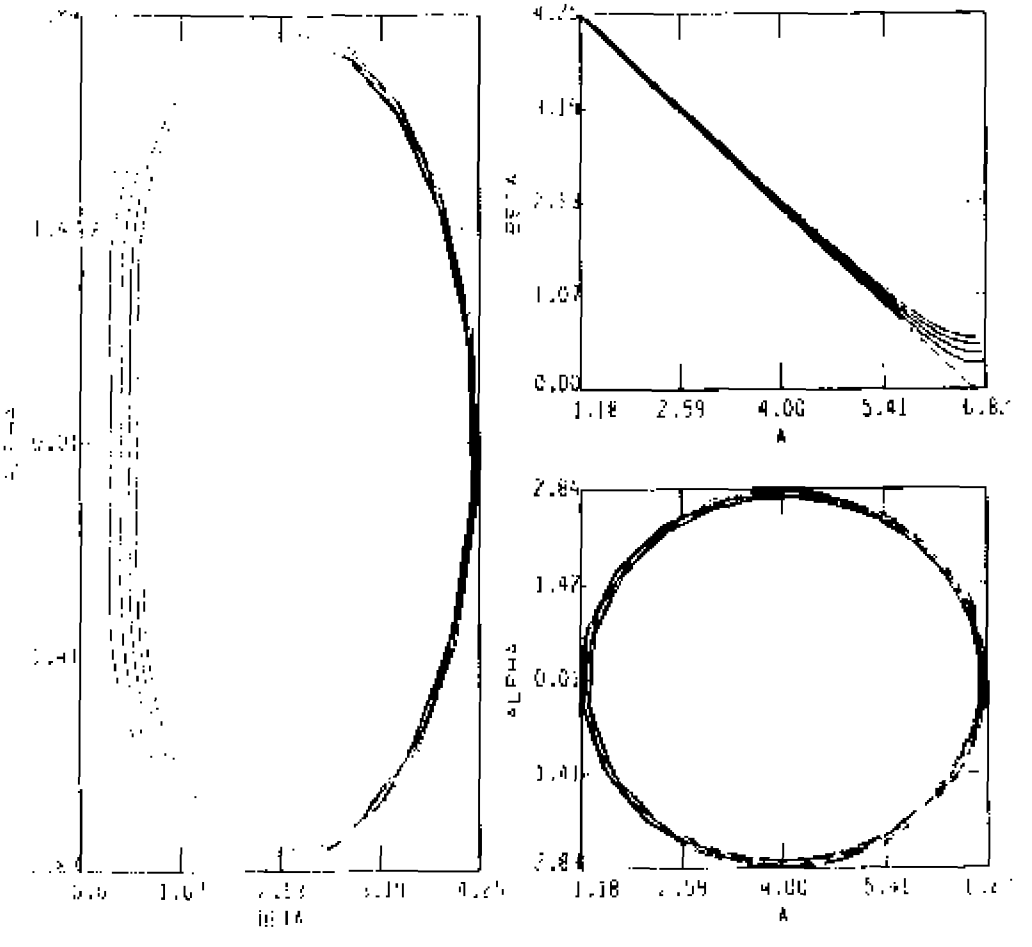

Figure 47 - Solution of (26), (27) and (39) for an initial critical point:
B_2 = 3.000000, θ_0 = 7.6666666, α = 6.6666666,
γ = 0.001000, α = 1.0327956, β = 0.0025819889,
ν = 0.000000,
with t_{min} = 0.0, and t_{max} = 59.00.

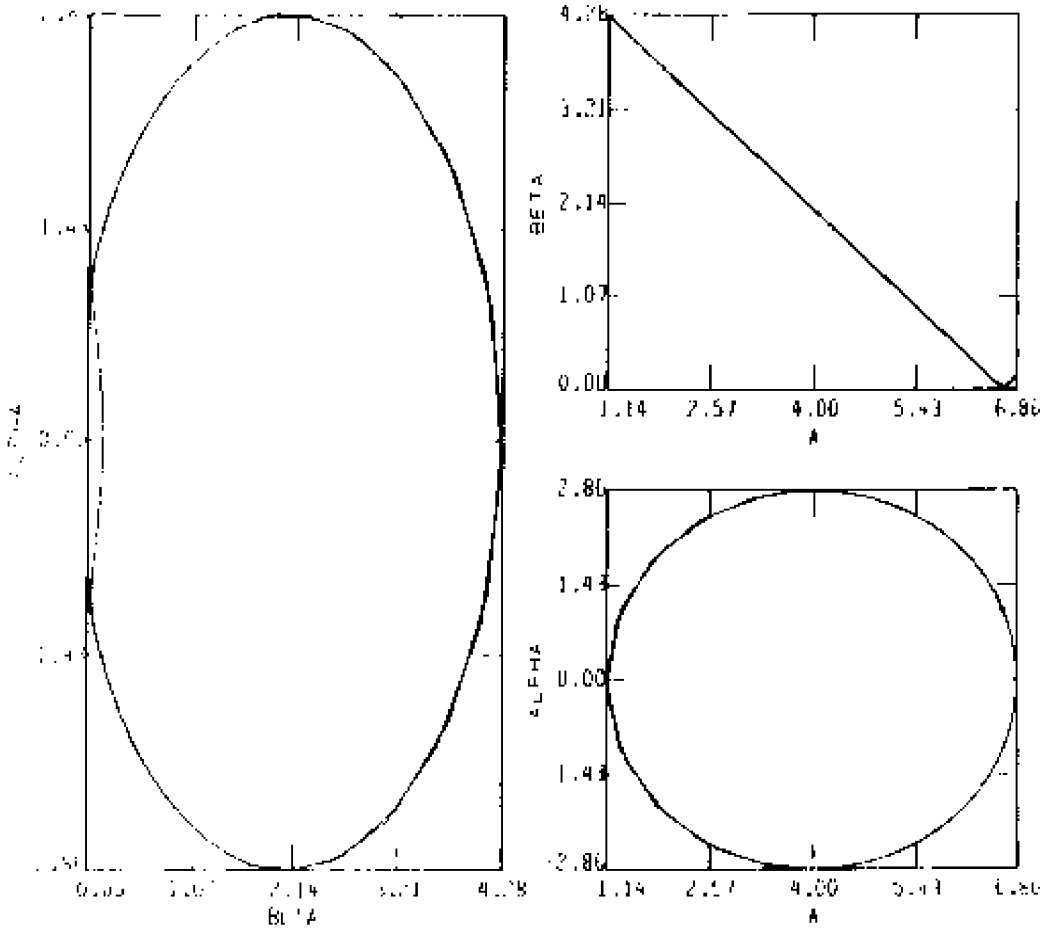

Figure 48. - Solution of (26), (27) and (30) for an initial critical point:
B_0 = 3.000000, α_0 = 7.6666666, α = 6.6666666,
η = 0.000010, σ = 1.0327956, β = 0.000025819889,
υ = 0.000000,
with t_{min} = 0.0, and t_{max} = 59.00.

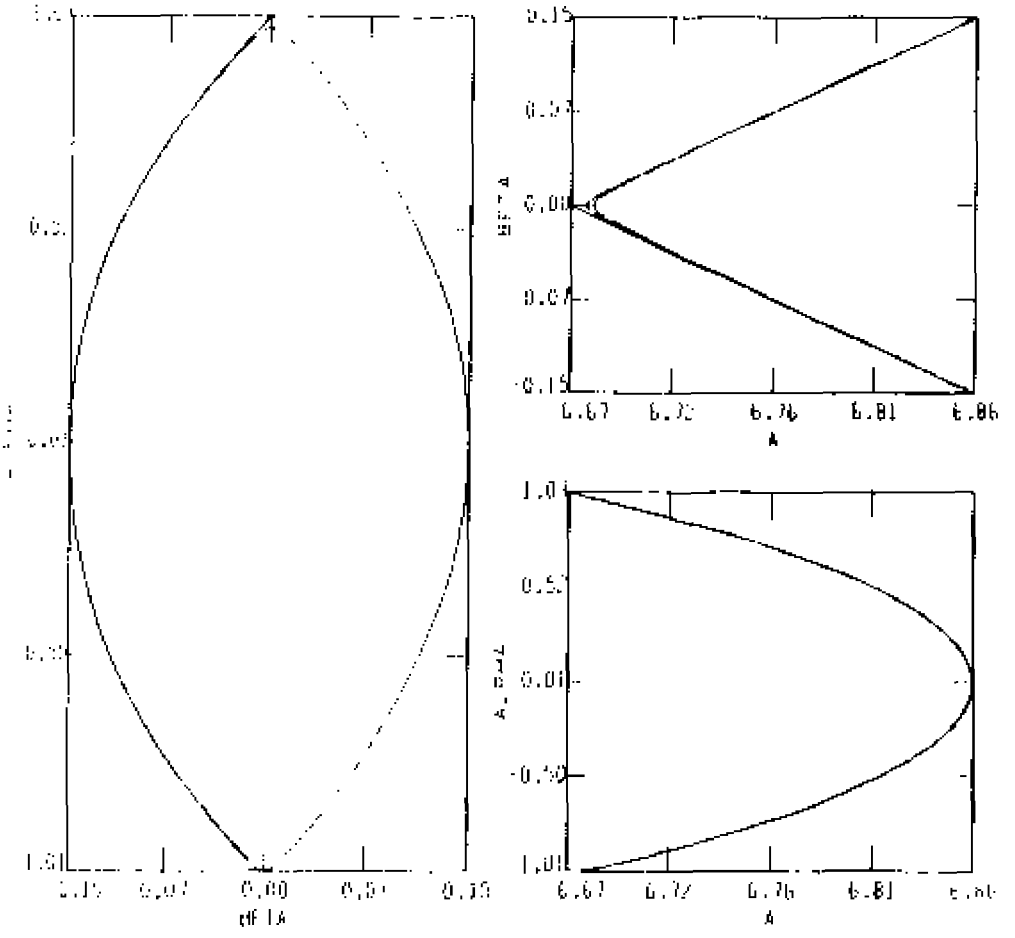

Figure 49. - Solution of (26), (27) and (30) for an initial point:
B_0 = 3.000000, α_0 = 7.9999999, λ = 6.6666666,
η = 0.000010, α = 1.0327956, β = 0.00025819889,
ν = 0.000000,
with t_{min} = 0.0, and t_{max} = 59.00.

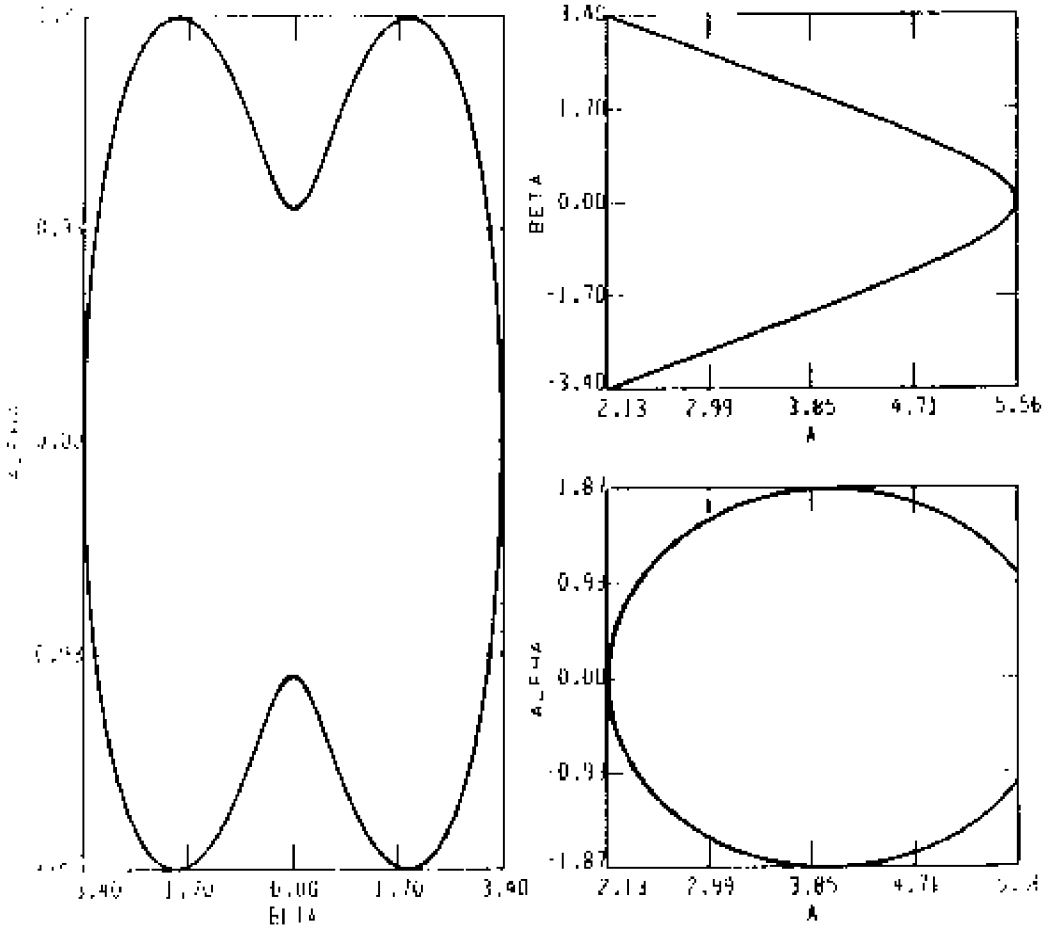

Figure 50. - Solution of (26), (27) and (30) for an initial point:
B_0 = 3.000000, $\mathcal{A}_0$ = 7.9999999, $\mathcal{A}$ = 5.5555555,
η = 0.000010, α = 1.0327956, β = 0.000025019089,
ν = 0.000000,
with t_{min} = 0.0, and t_{max} = 59.80.

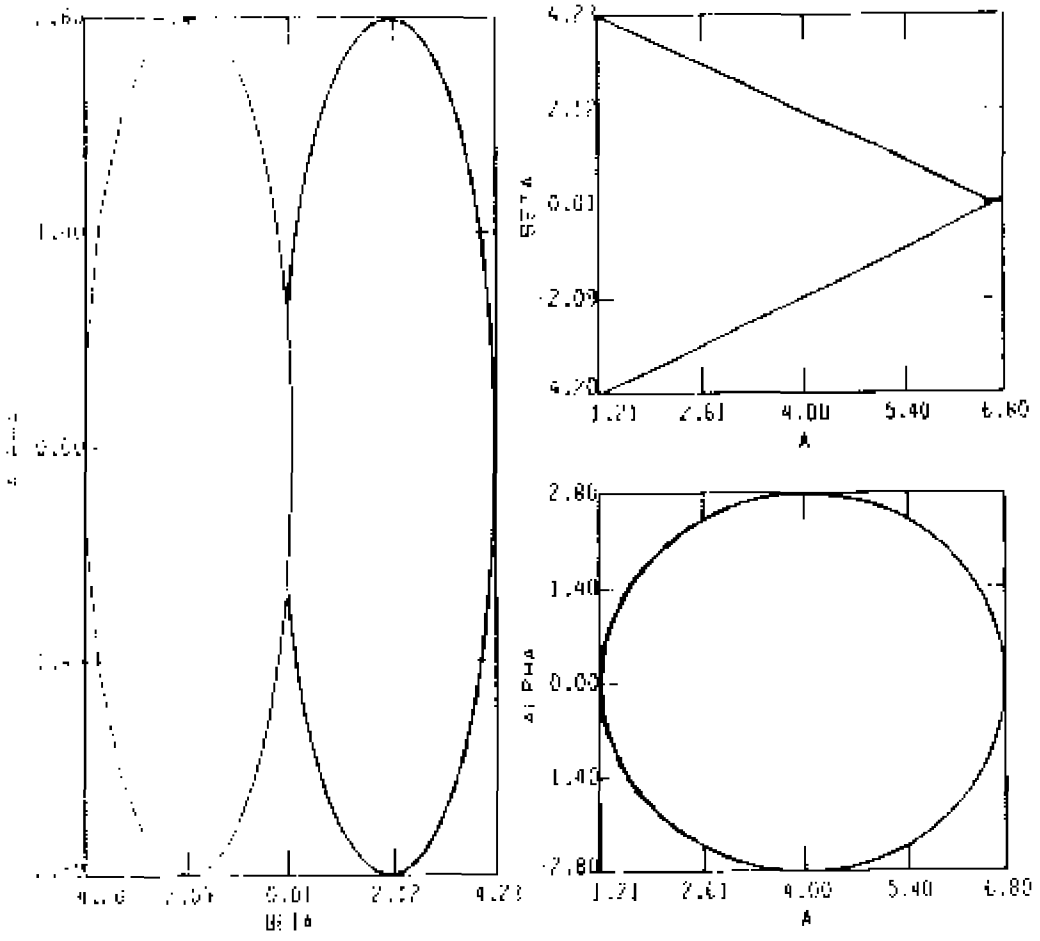

Figure 51. - Solution of (26), (27) and (30) for an initial point:
B_0 = 3.000000, β_0 = 9.9999999, α = 6.6000000,
η = 0.000010, α = 1.0327956, β = 0.000025819889,
ν = 0.000000,
With t_{min} = 0.0, and t_{max} = 59.00.

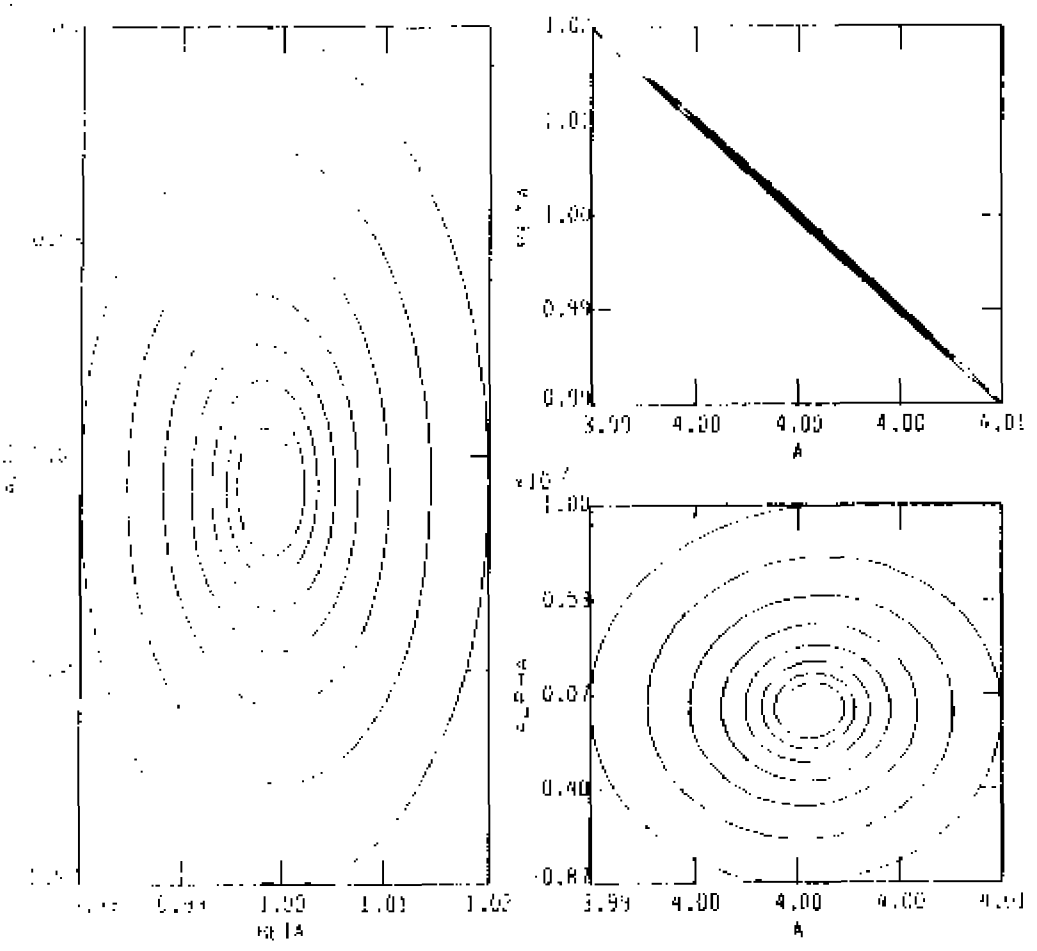

Figure 52. - Solution of (26), (27) and (30) for an initial point:
B_0 = 3.000000, A_0 = 4.0000000, a = 4.0000000,
η = 0.010000, α = 0.0100000, β = 1.0000000,
ω = 0.000000,
with t_{MIN} = 0.0, and t_{MAX} = 59.80.

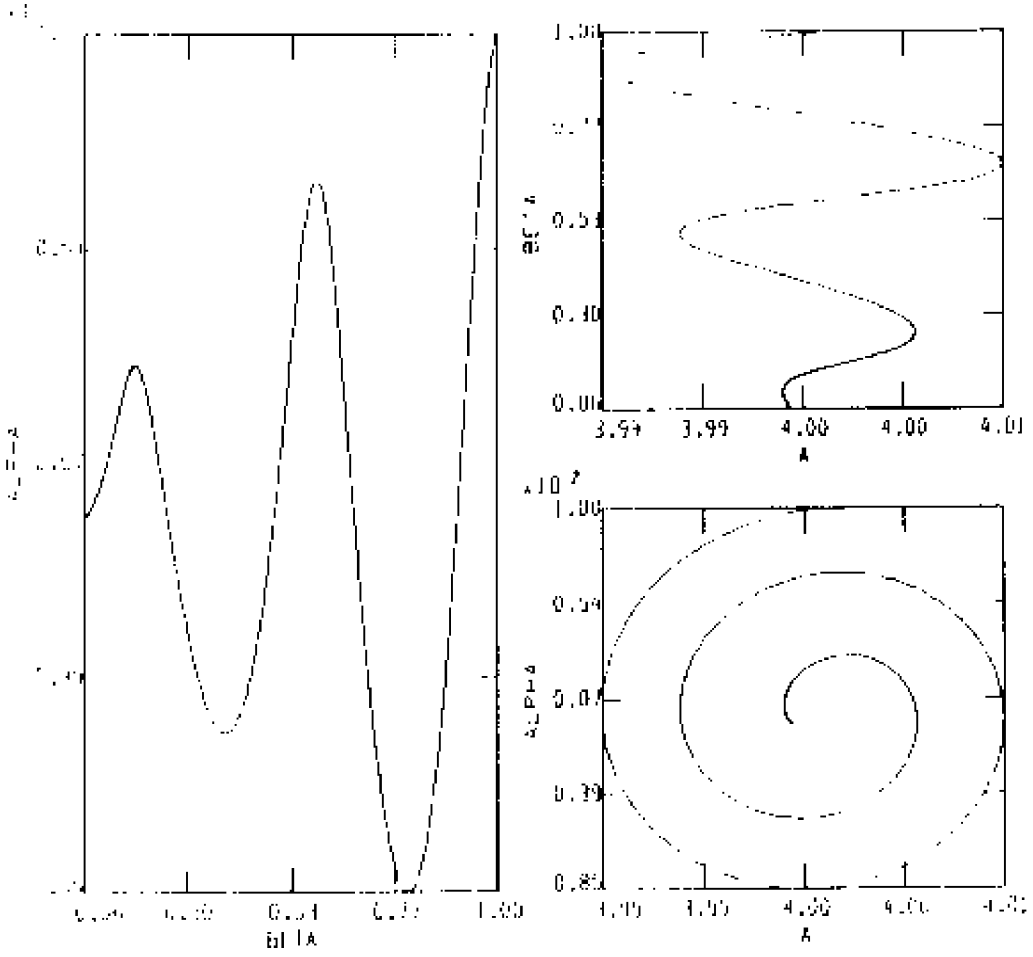

Figure 53. - Solution of (31), (27) and (30) for an initial point:
B_0 = 3.000000, A_0 = 4.0000000, a = 4.0000000,
γ = 0.010000, α = 0.0100000, β = 1.0000000,
ν = 0.010000,
with t_{min} = 0.0, and t_{max} = 59.88.

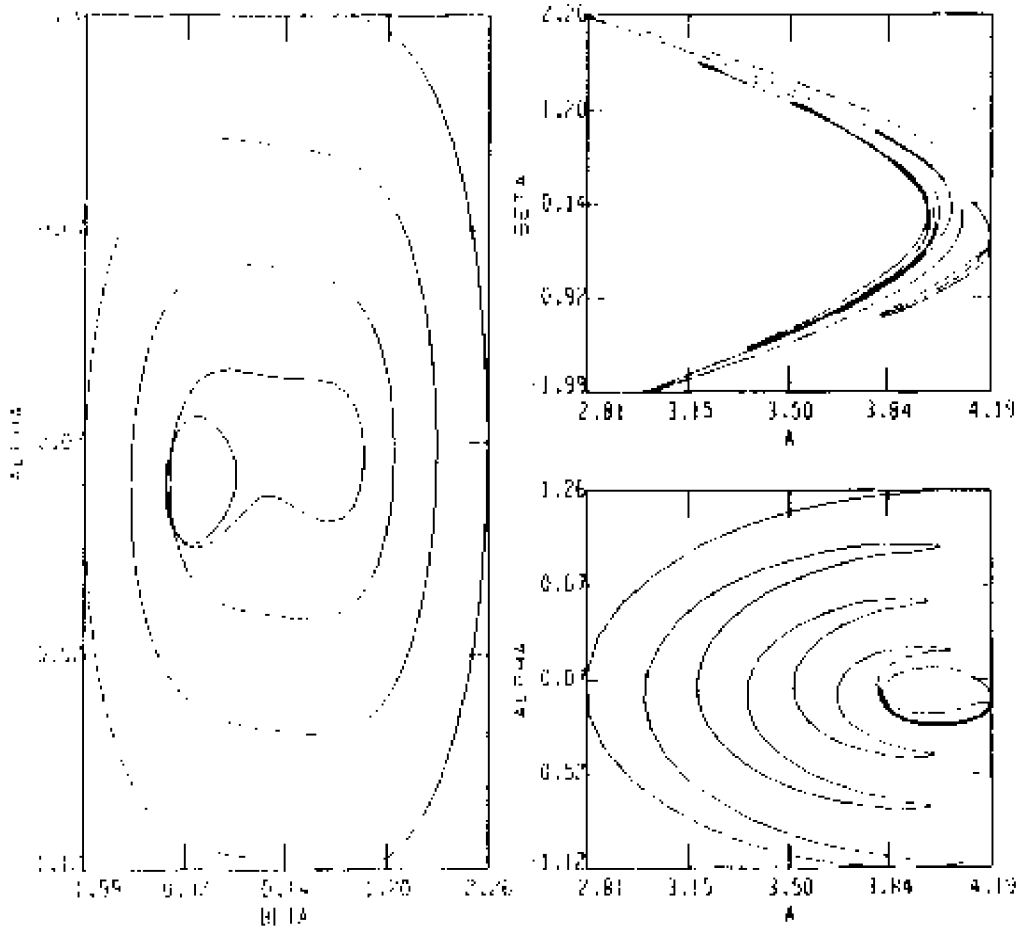

Figure 54. - Solution of (31), (27) and (30) for an initial critical point:
B_o = 3.000000, α_o = 5.0000000, α = 4.0027007,
η = 0.010000, α = 1.2635901, β = 0.79846706,
ν = 0.010000,
with t_{min} = 0.0, and t_{max} = 59.88.

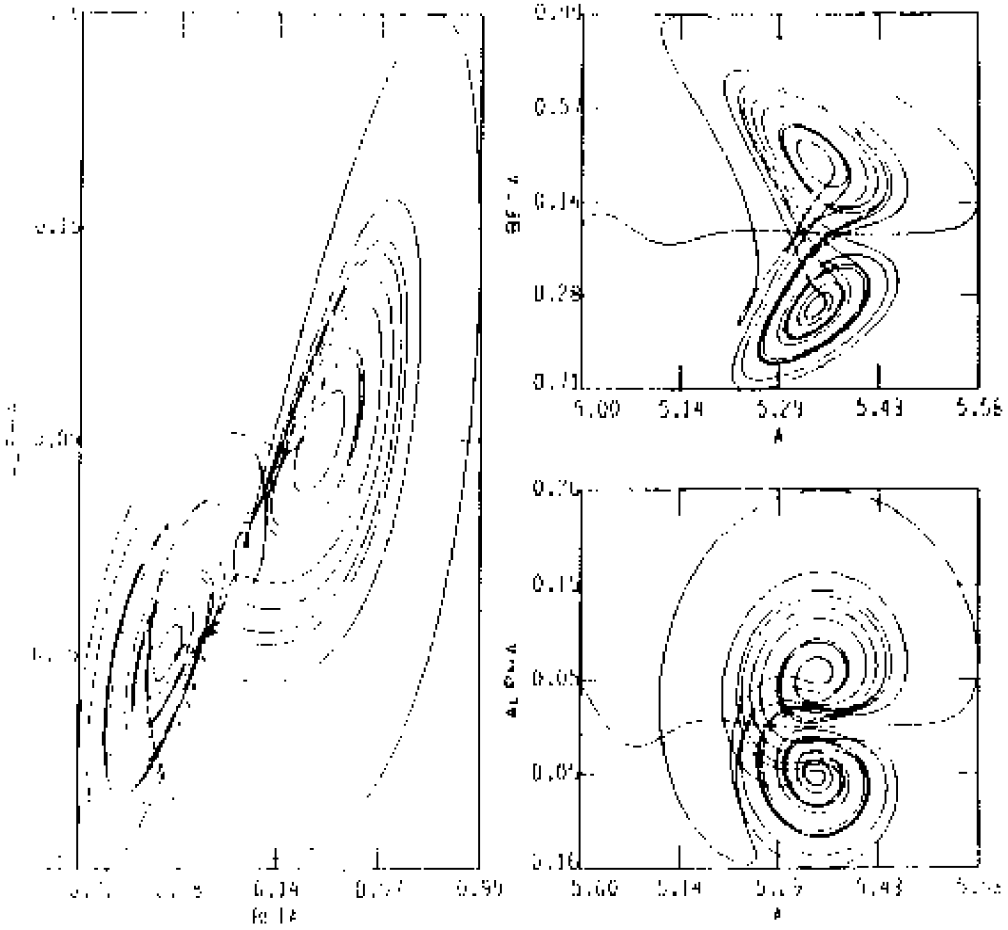

Figure 55. - Solution of (31), (27) and (30) for an initial point:
B_o = 4.000000, Ω_o= 6.0000000, α = 5.0000000,
η = 0.010000, α = 0.04472136, β = 0.04472136,
υ = 0.050000,
with t_{min} = 0.0, and t_{max} = 500.00.

Note: non-trivial critical points are ($\beta_\pm$, $\alpha_\pm$, Ω), where
Ω = 5.343000, $\alpha_\pm$ = ±0.0524146, $\beta_\pm$ = ± 0.33385098.

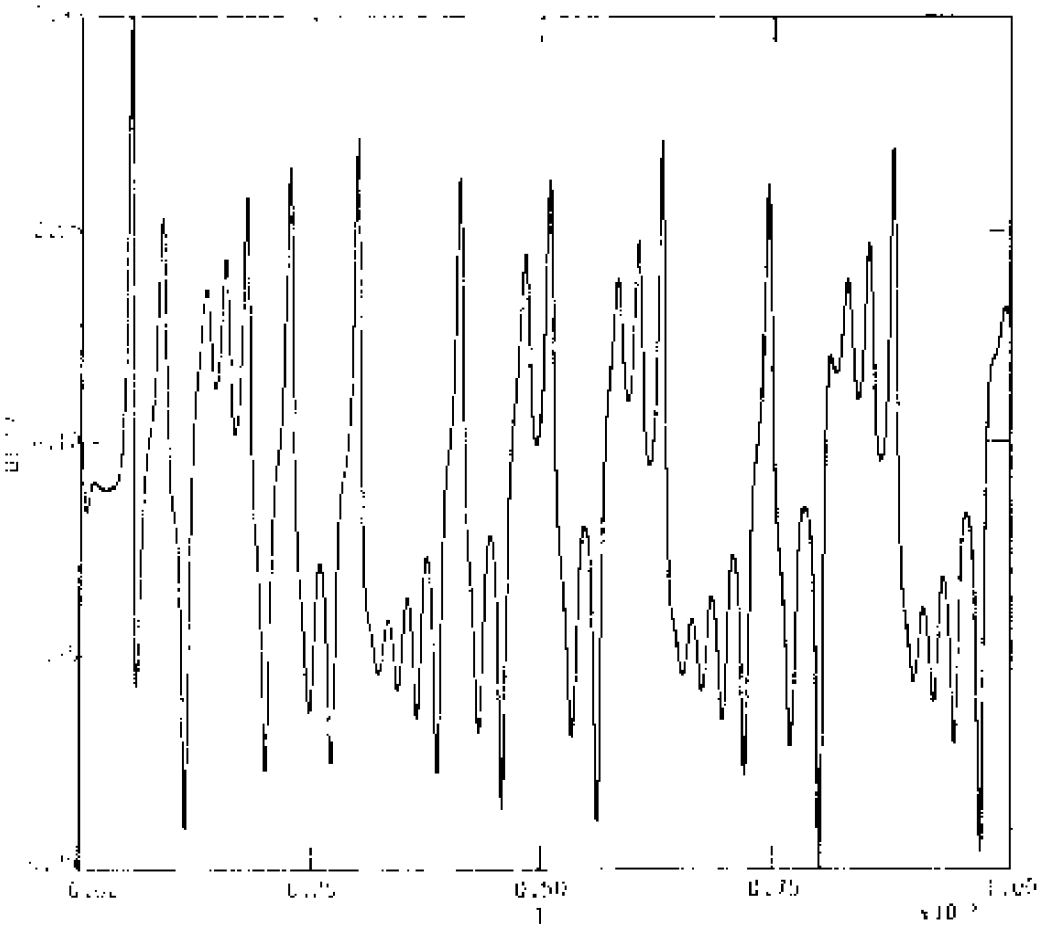

Figure 55 - (continued)

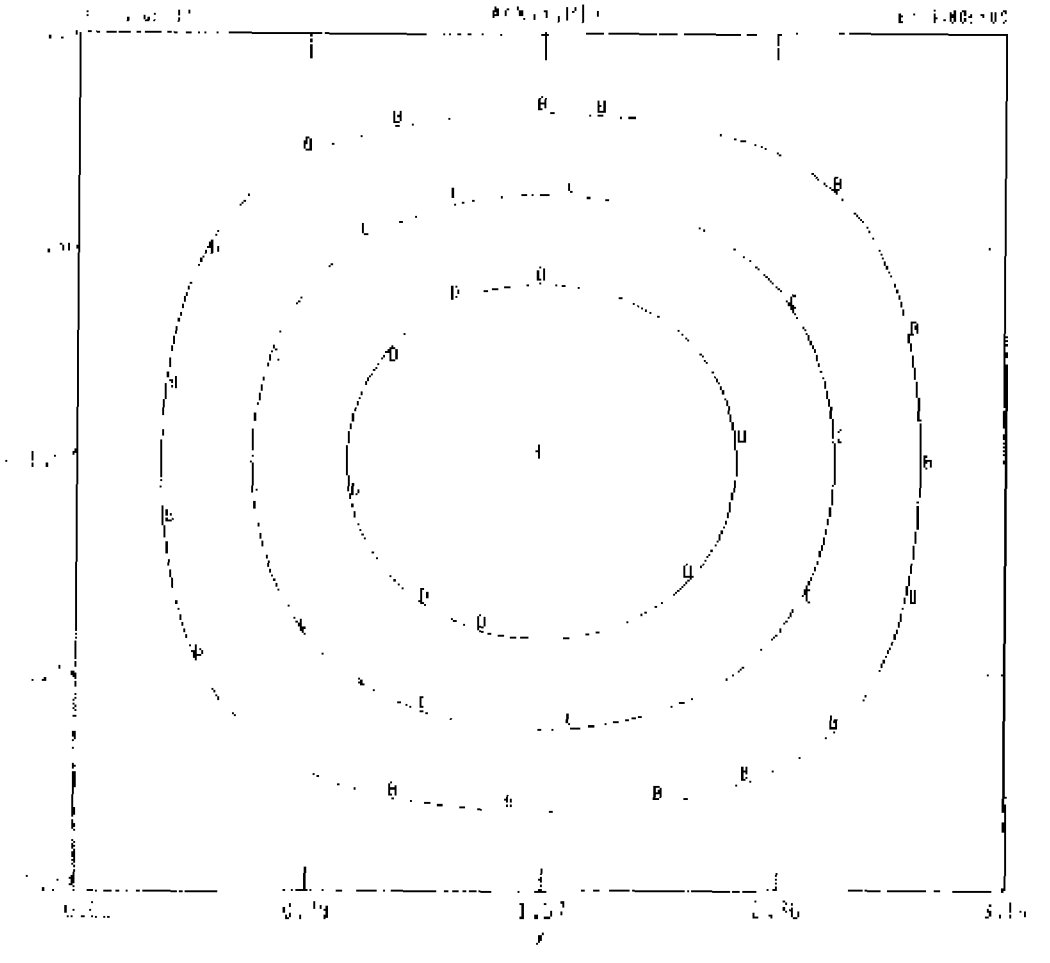

Figure 56. - Contours at t = 0.0, for CASE 4.
56 (a): contours of A = constant, poloidal cut.

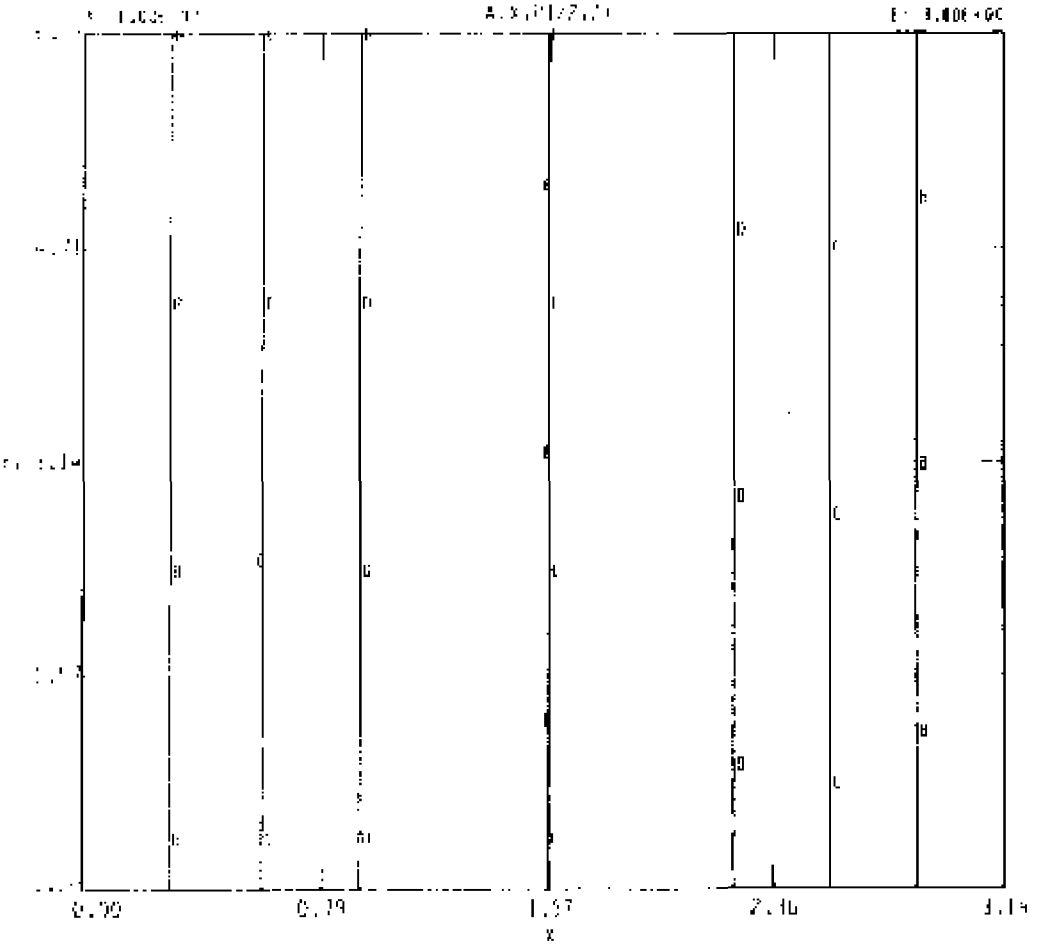

56 (b): contours of A = constant, toroidal cut,

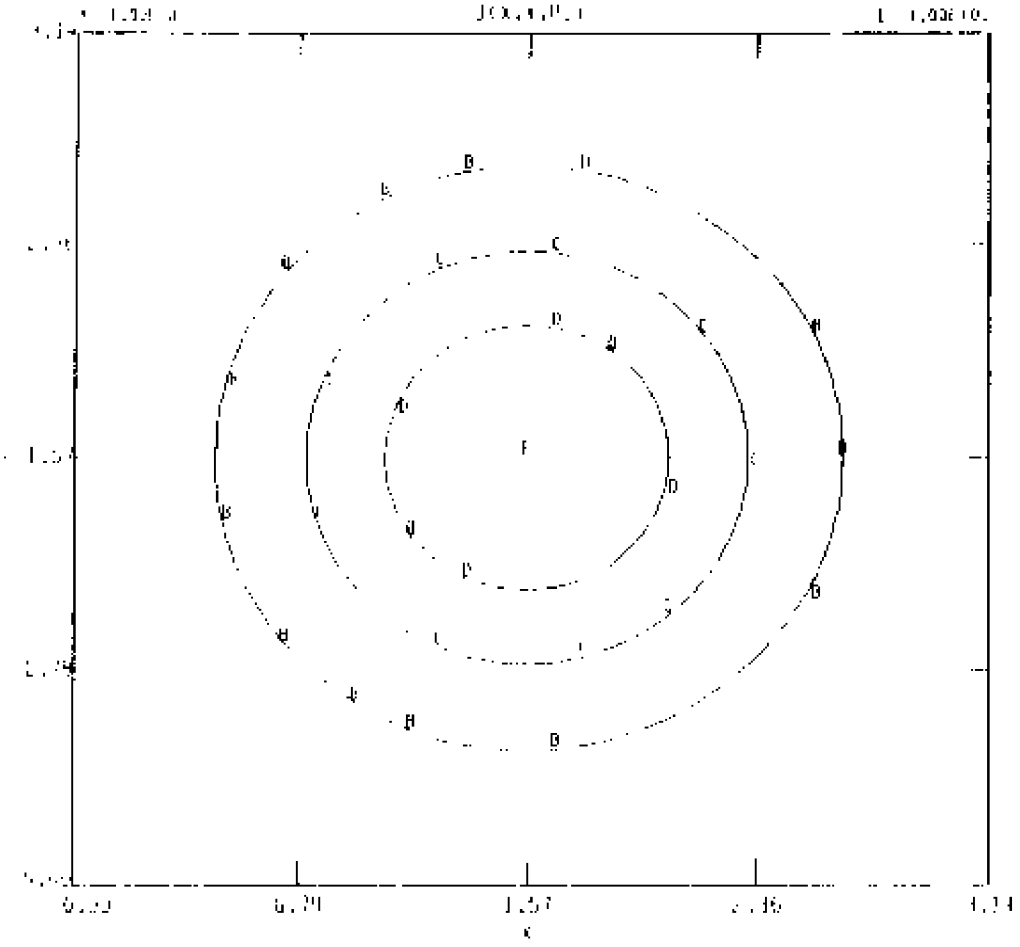

56 (c): contours of j = constant, poloidal cut.

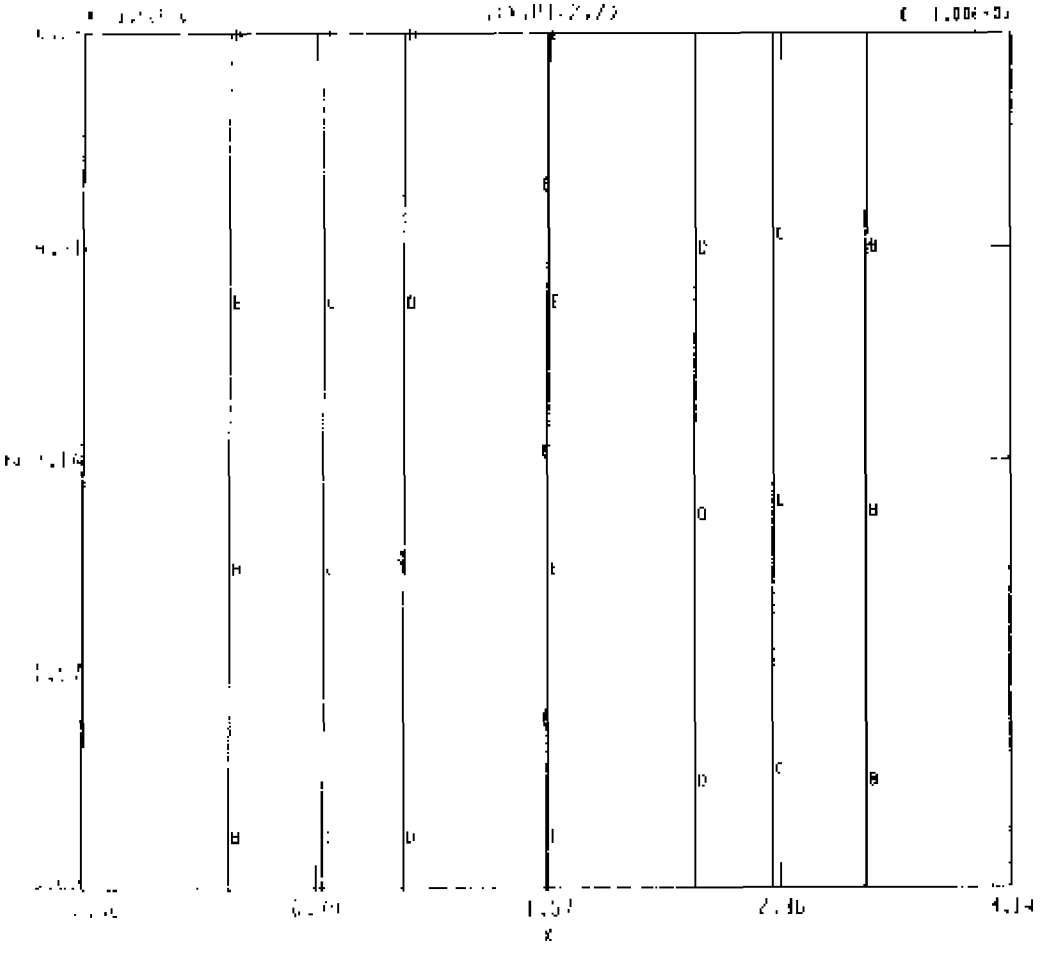

56 (d): contours of j = constant, toroidal cut.

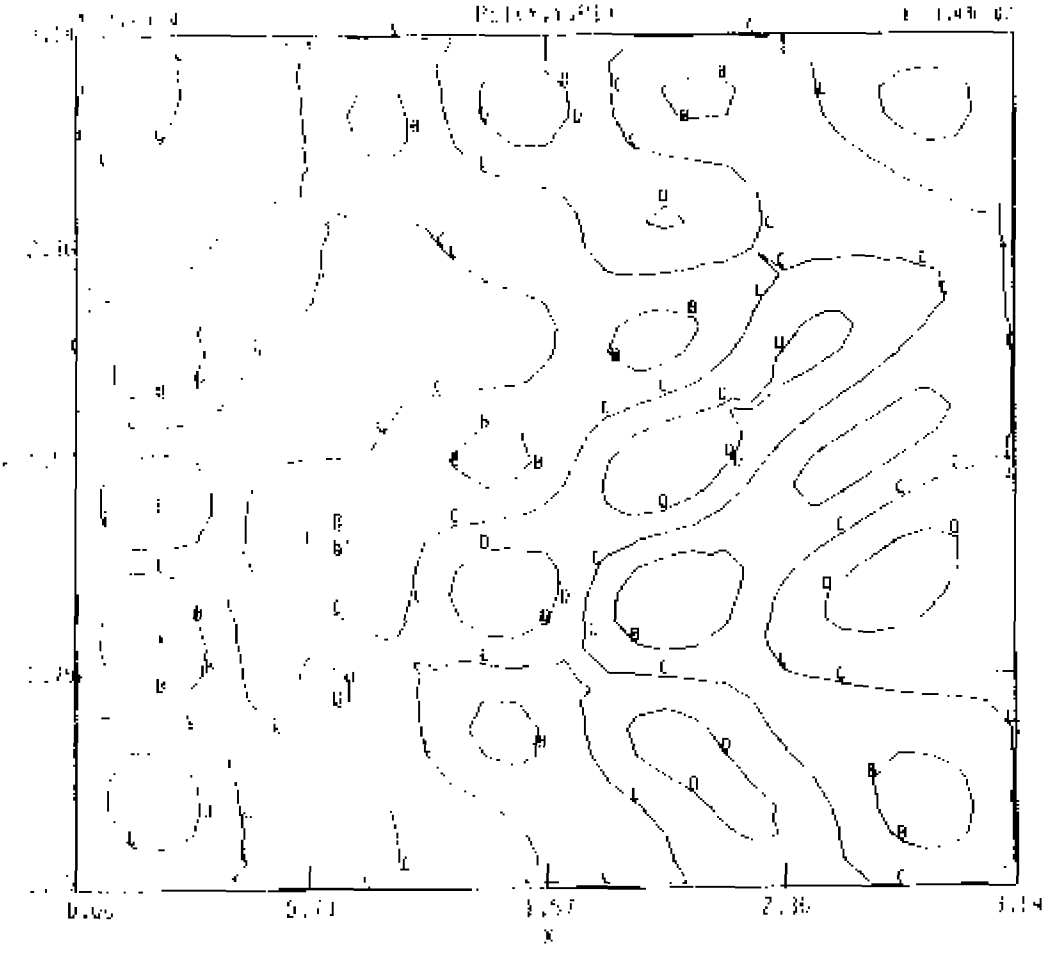

56 (e): contours of Ψ = constant, poloidal cut, and

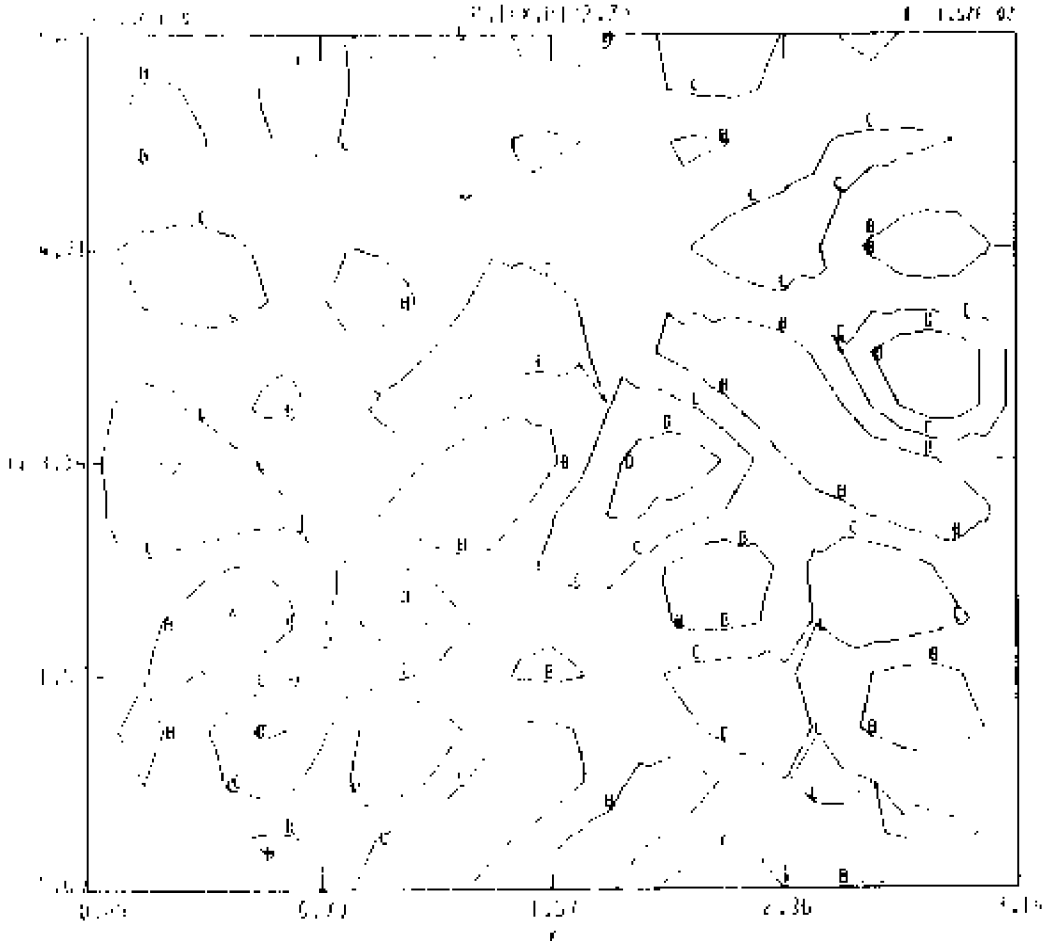

56 (f): contours of Ψ= constant, toroidal cut.

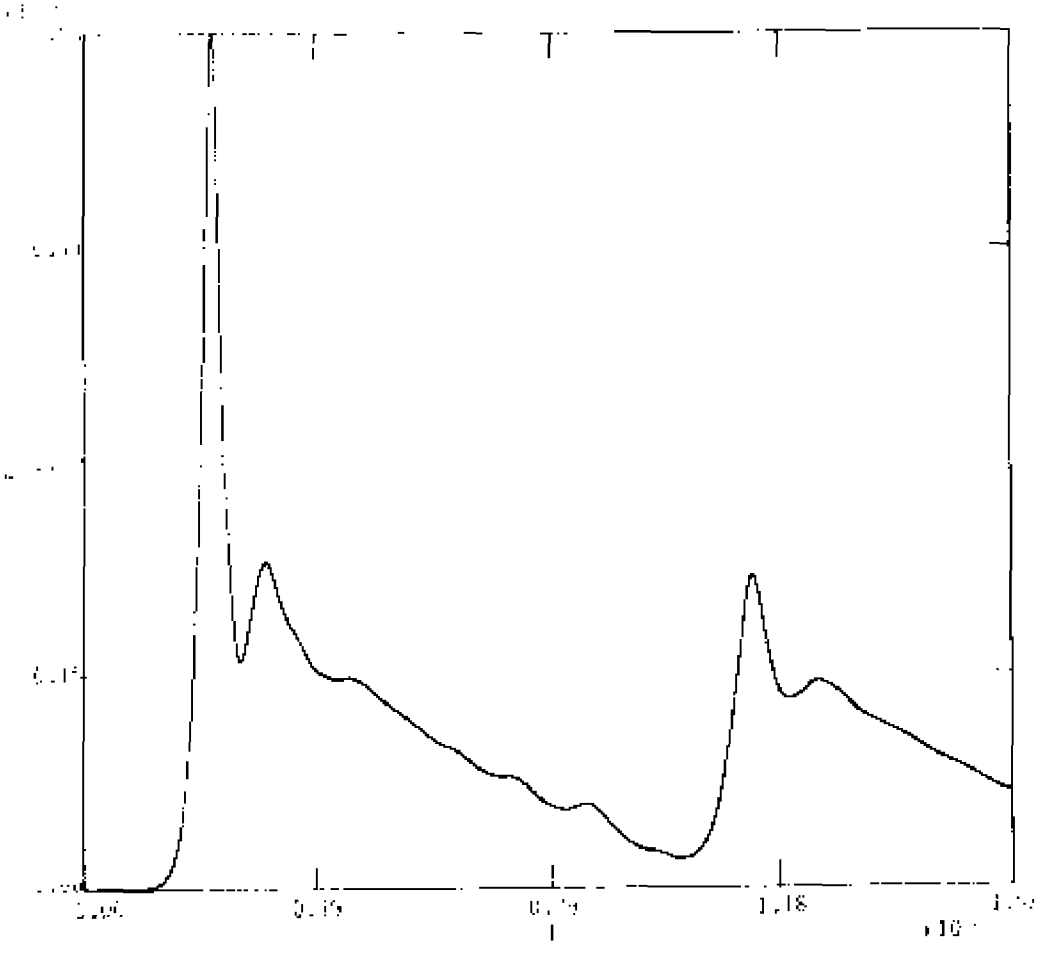

Figure 57. - Globals, CASE 4, with E_o = 10/200, υ = 0.8, 57(a): kinetic energy as a function of time,

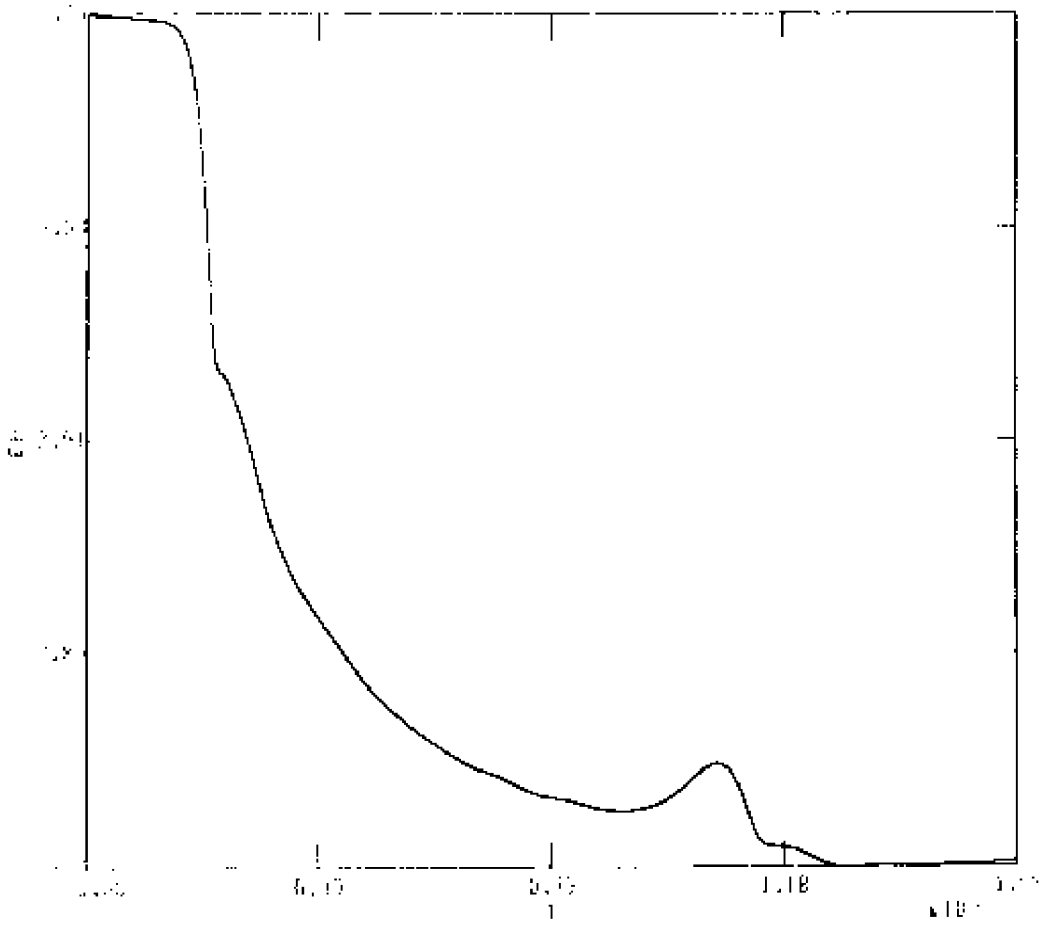

57(b): Magnetic energy as a function of time.

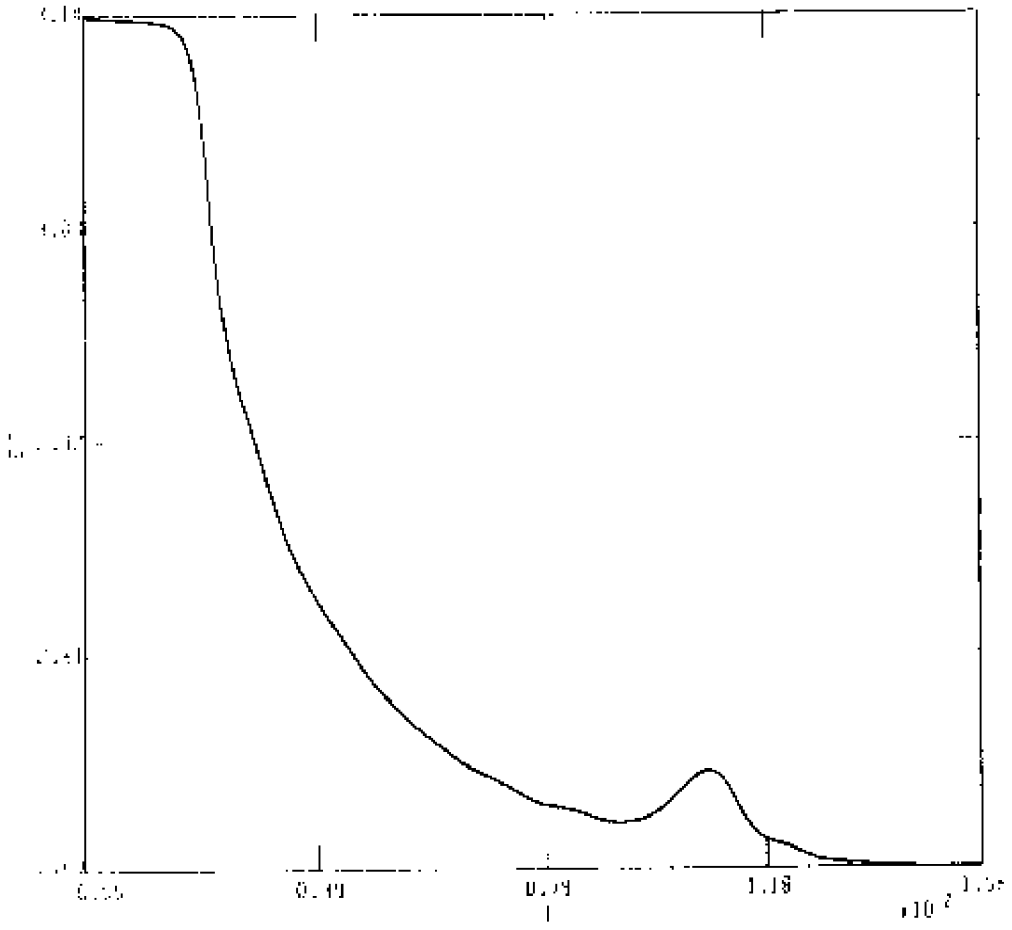

57(c): total energy as a function of time.

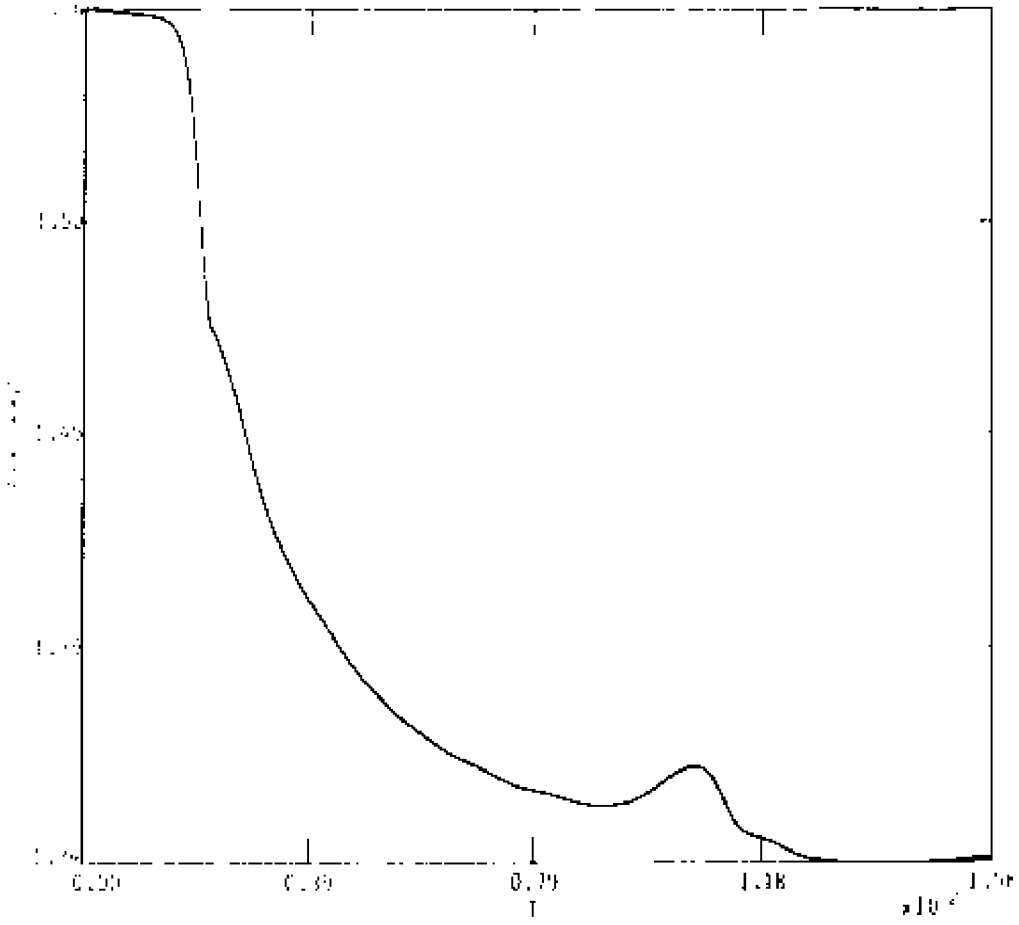

57(d): half the mean square vector potential as a function of time.

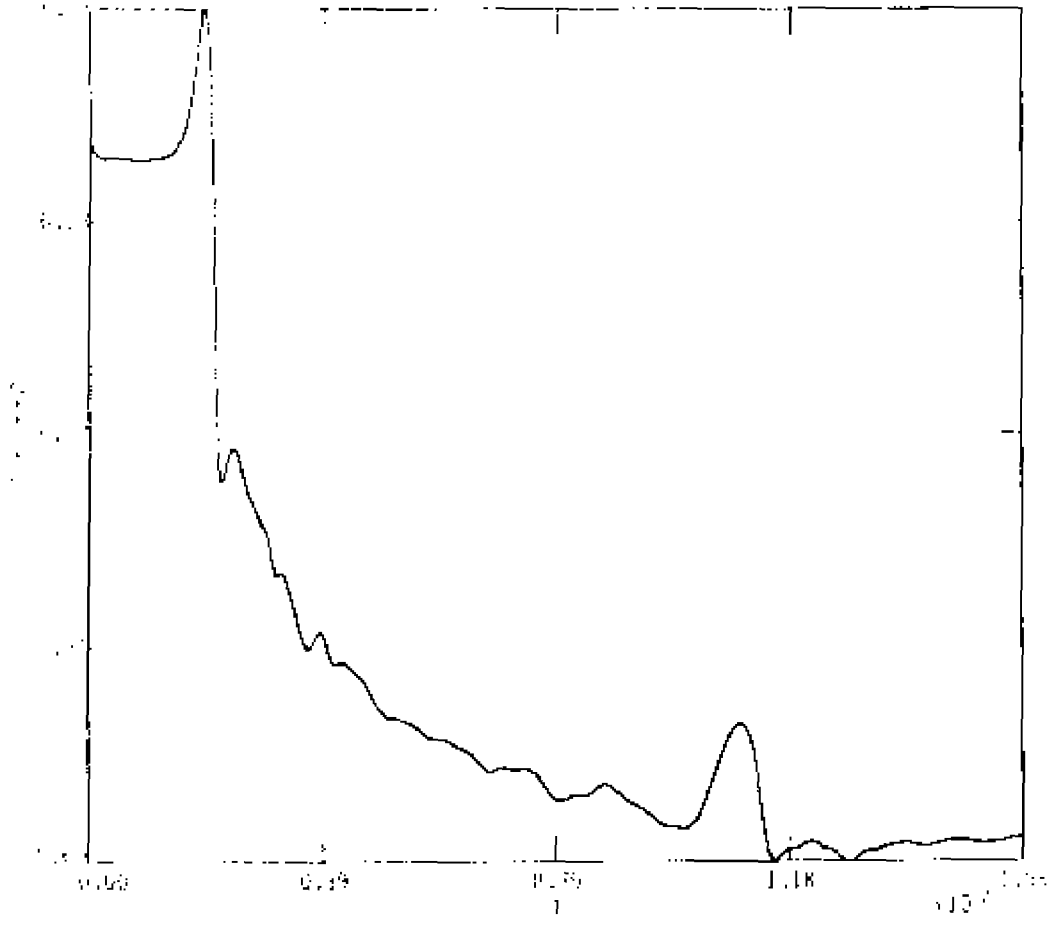

57(e): half the mean square current as a function of time.

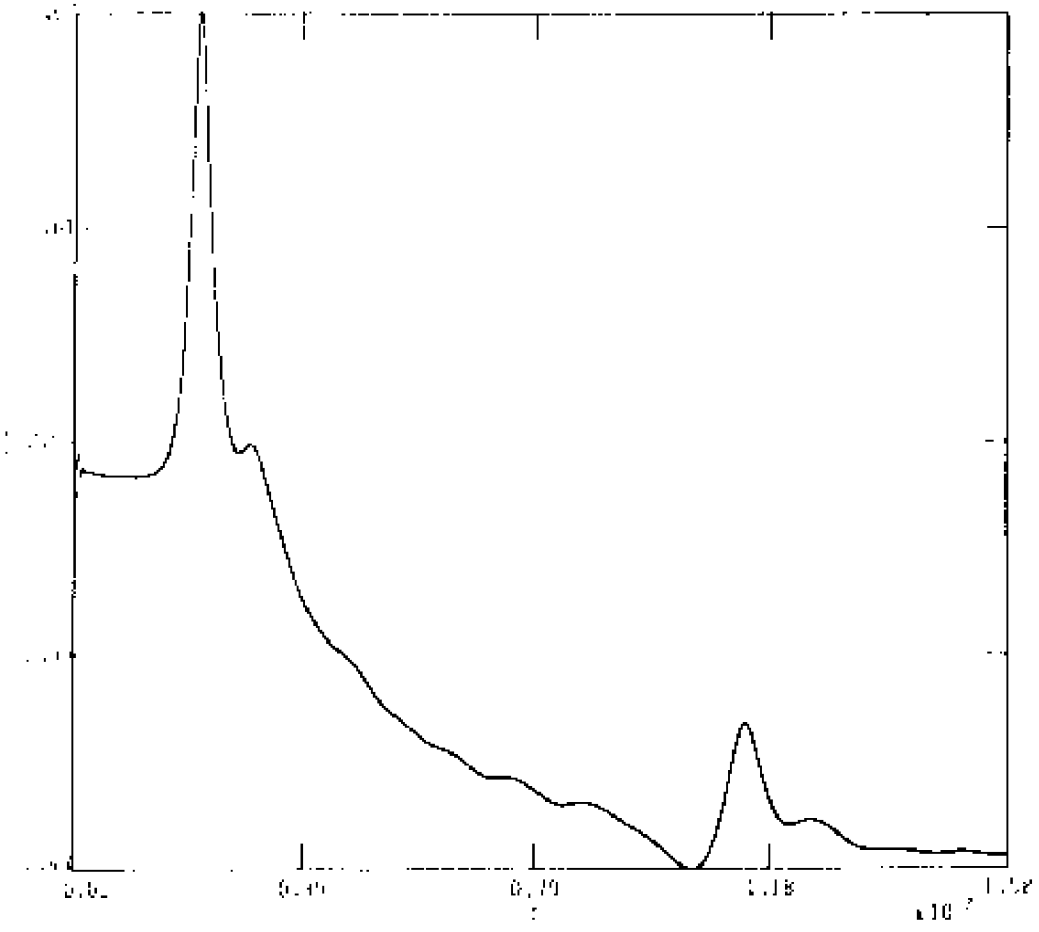

57(f): total integrated current as a function of time.

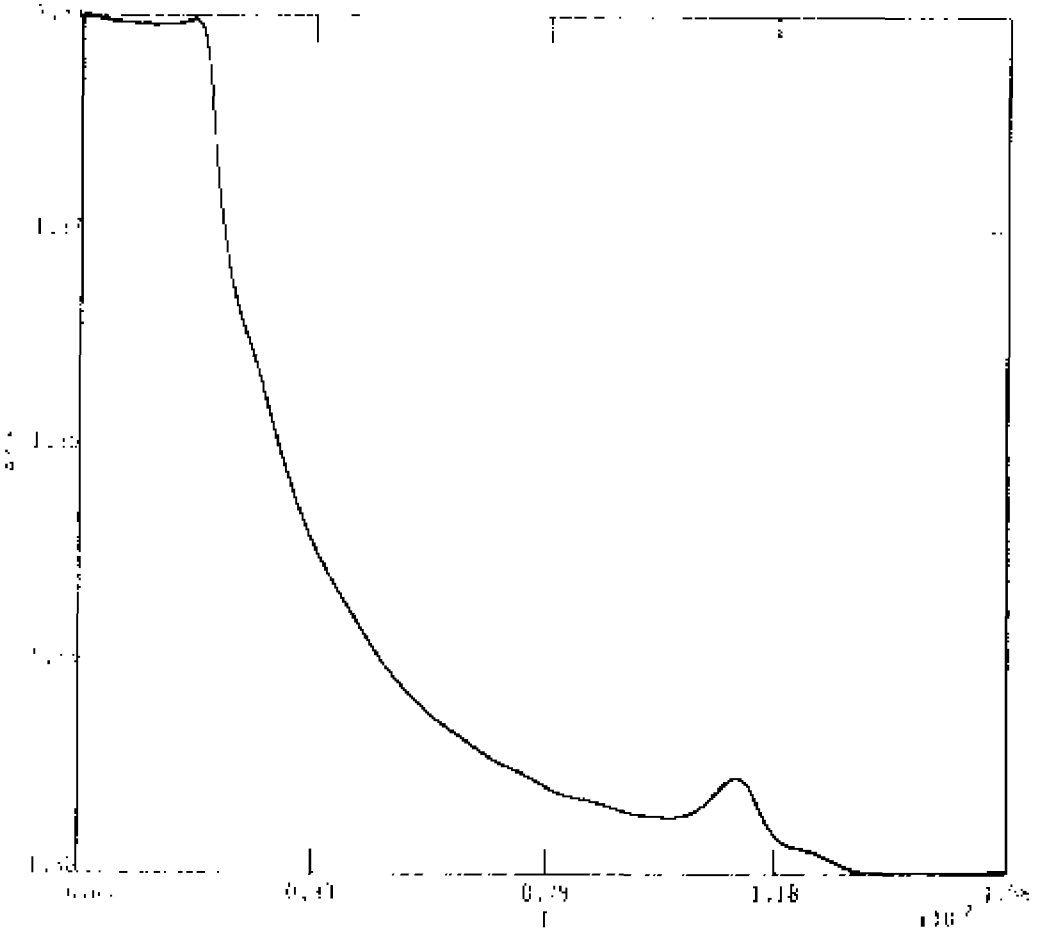

57(g): total integrated vector potential as a function of time.

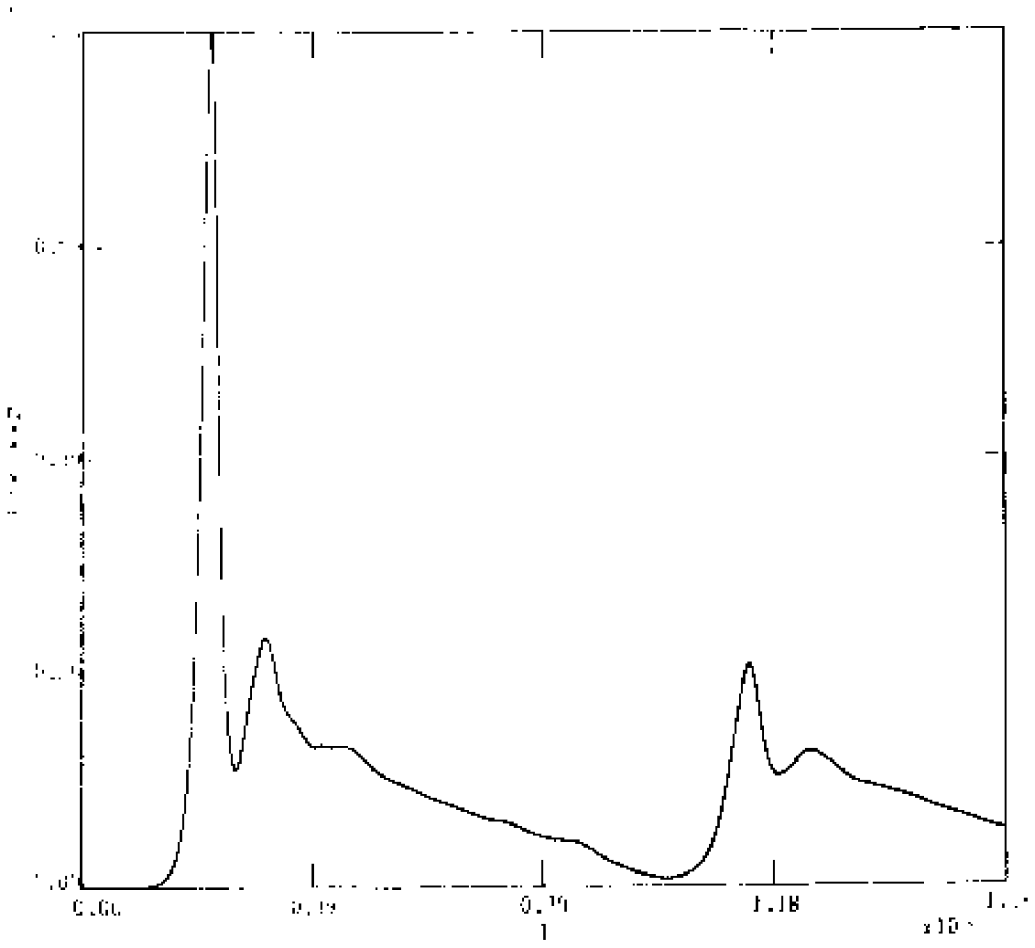

57(h): half the mean square stream function as a function of time, and

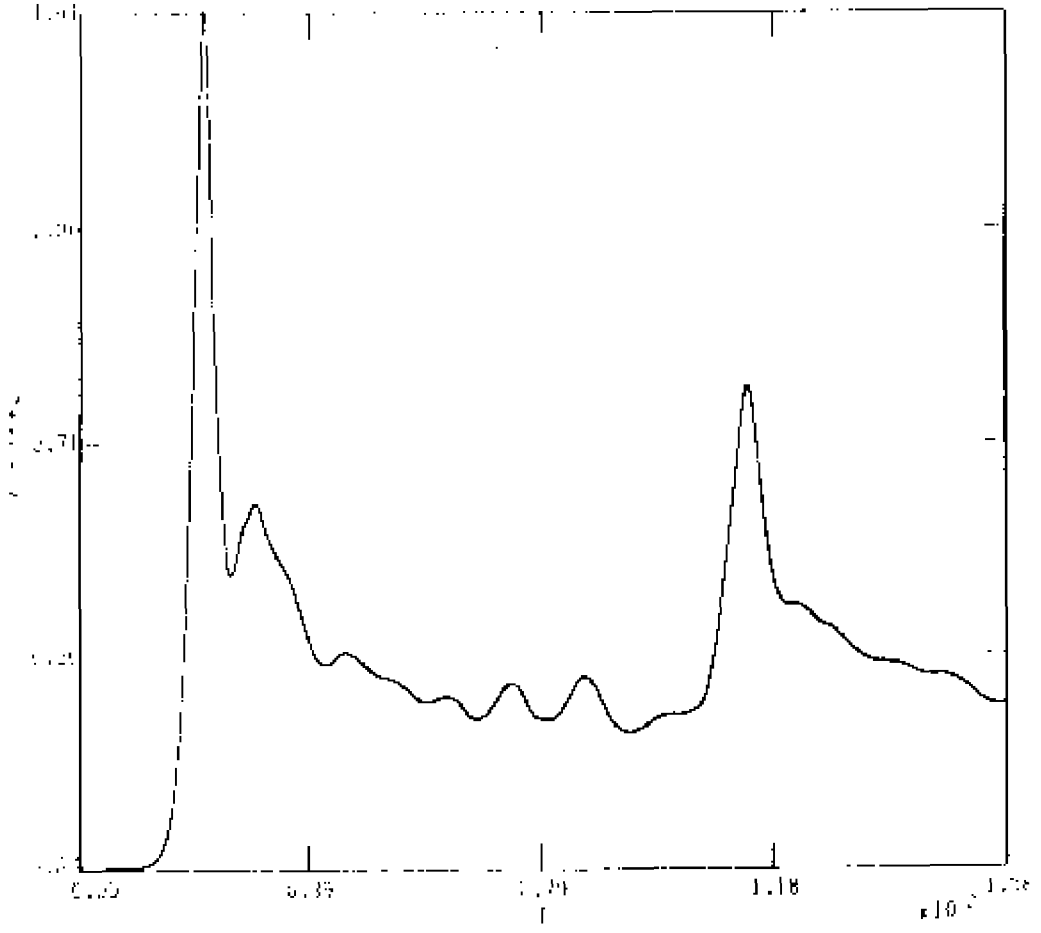

57(1): half the mean square vorticity as a function of time.

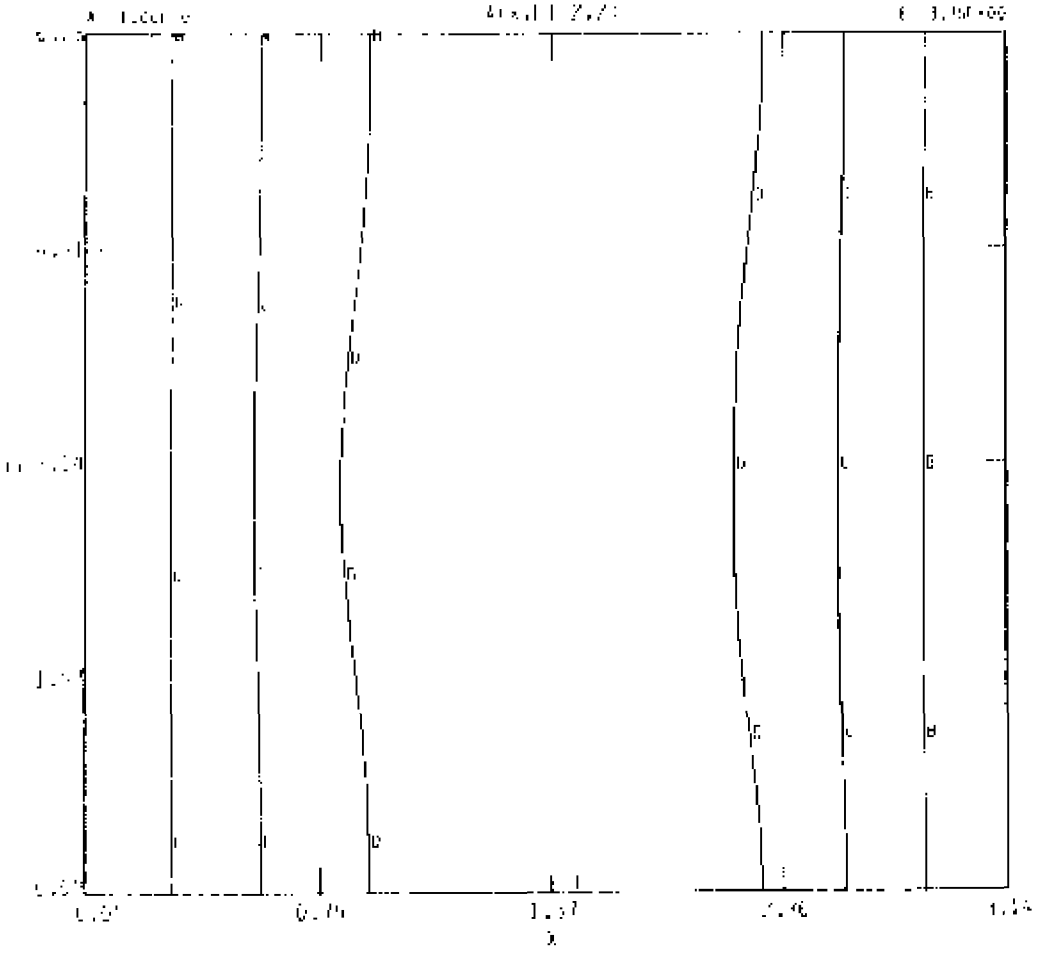

Figure 58. - Contours at t = 16.56, for CASE 4, E_o = 0.05, ν = 0.0:
58 (a) : contours of A = constant, toroidal cut.

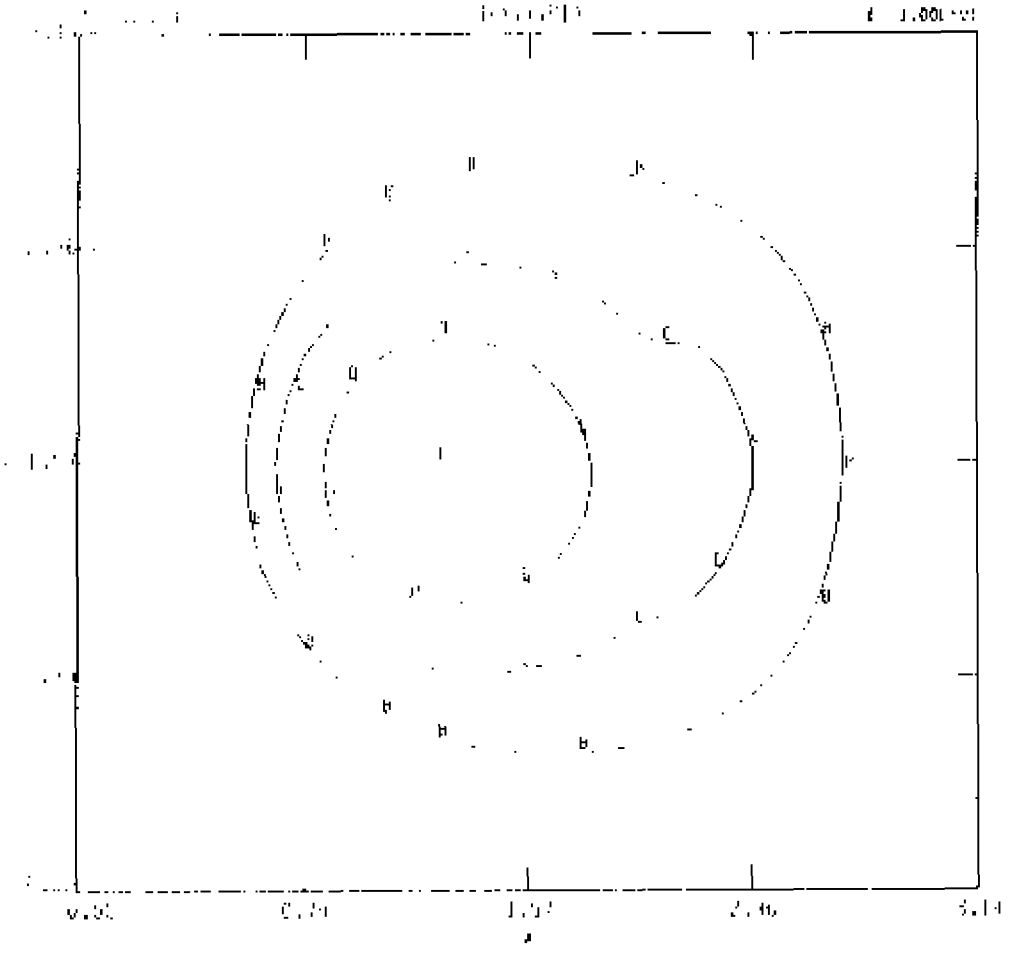

5θ (b): contours of j = constant, poloidal cut.

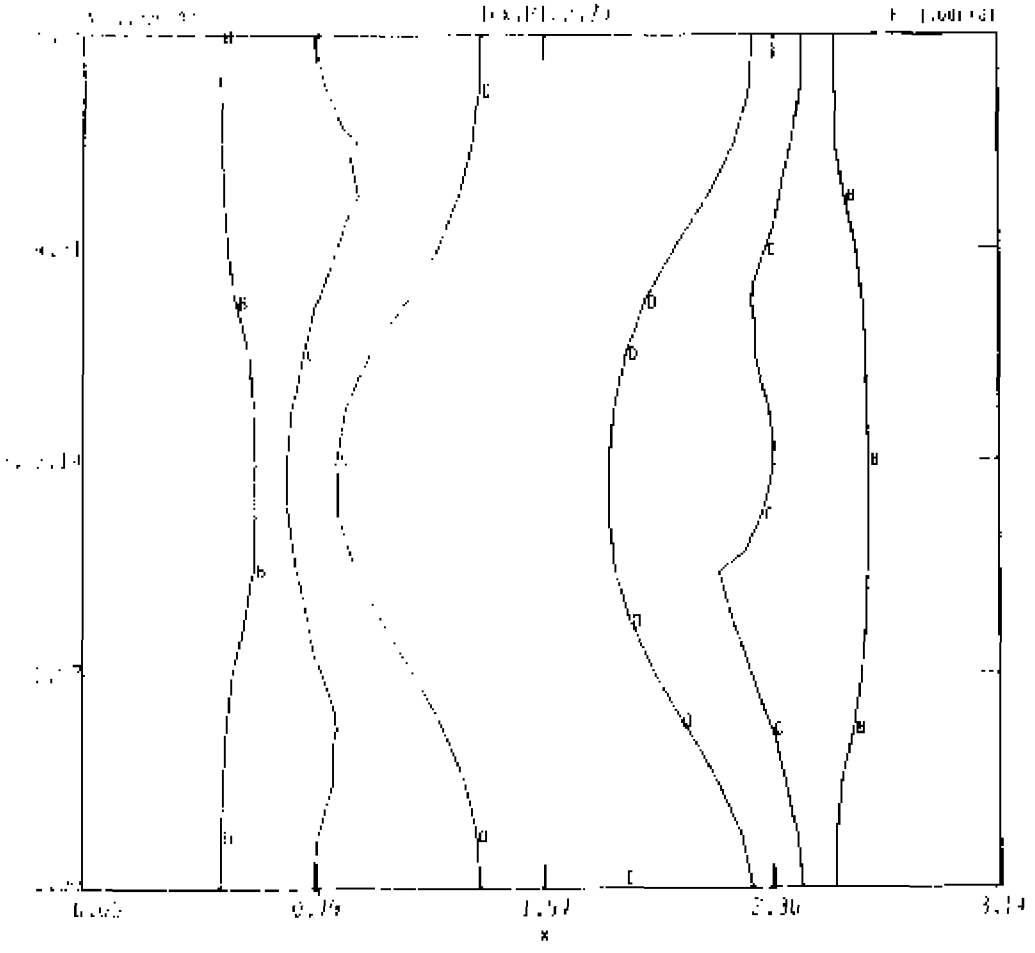

58 (c): contours of j = constant, toroidal cut.

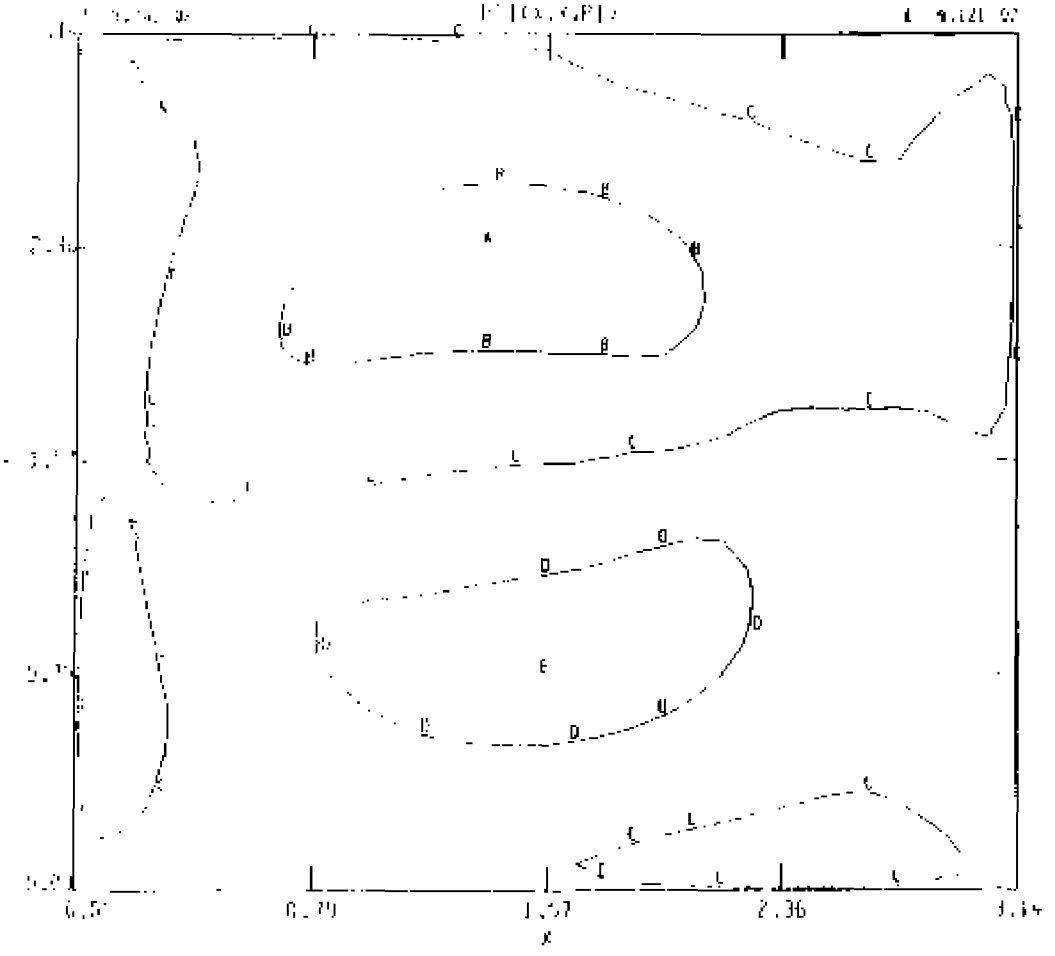

and 58 (d): contours of Ψ = constant, poloidal cut.

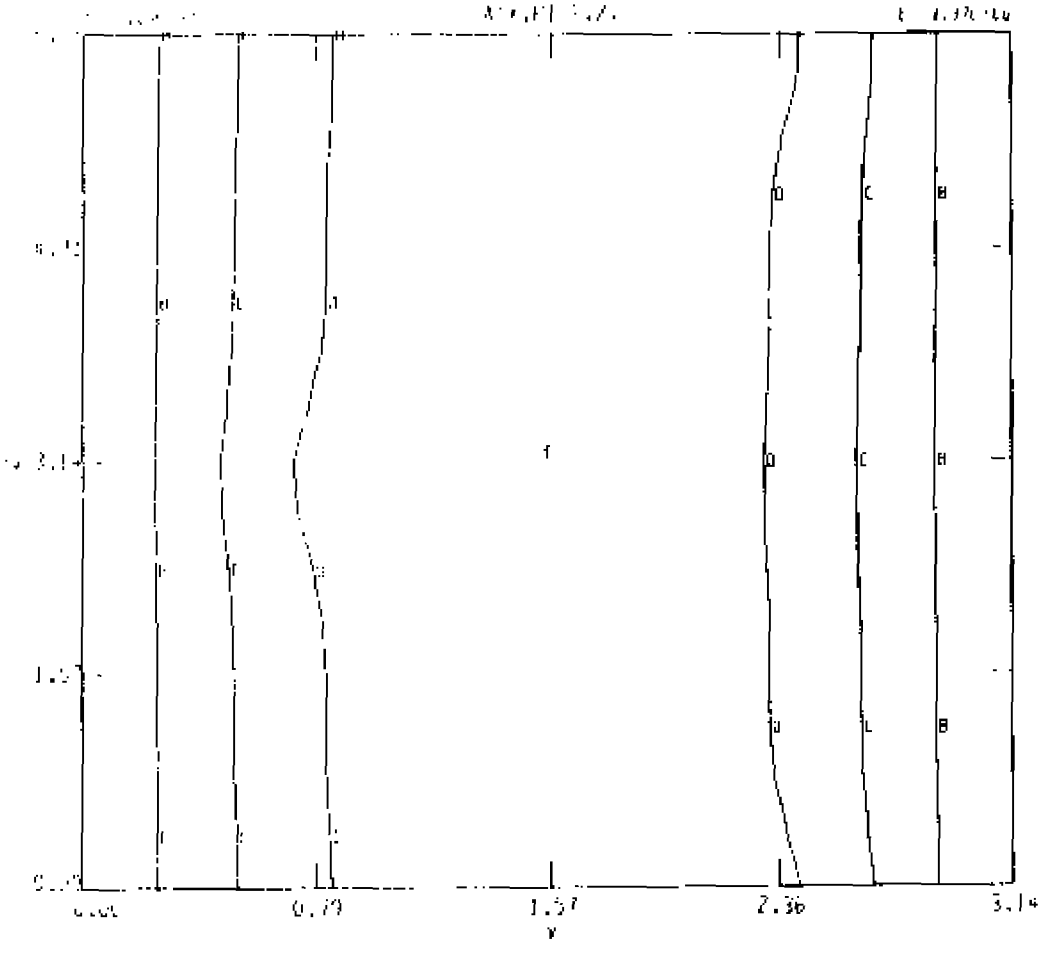

Figure 59. - Contours at t = 20.64, for CASE 4, E_o = 0.05, υ = 0.0;
59 (a) : contours of A = constant, toroidal cut.

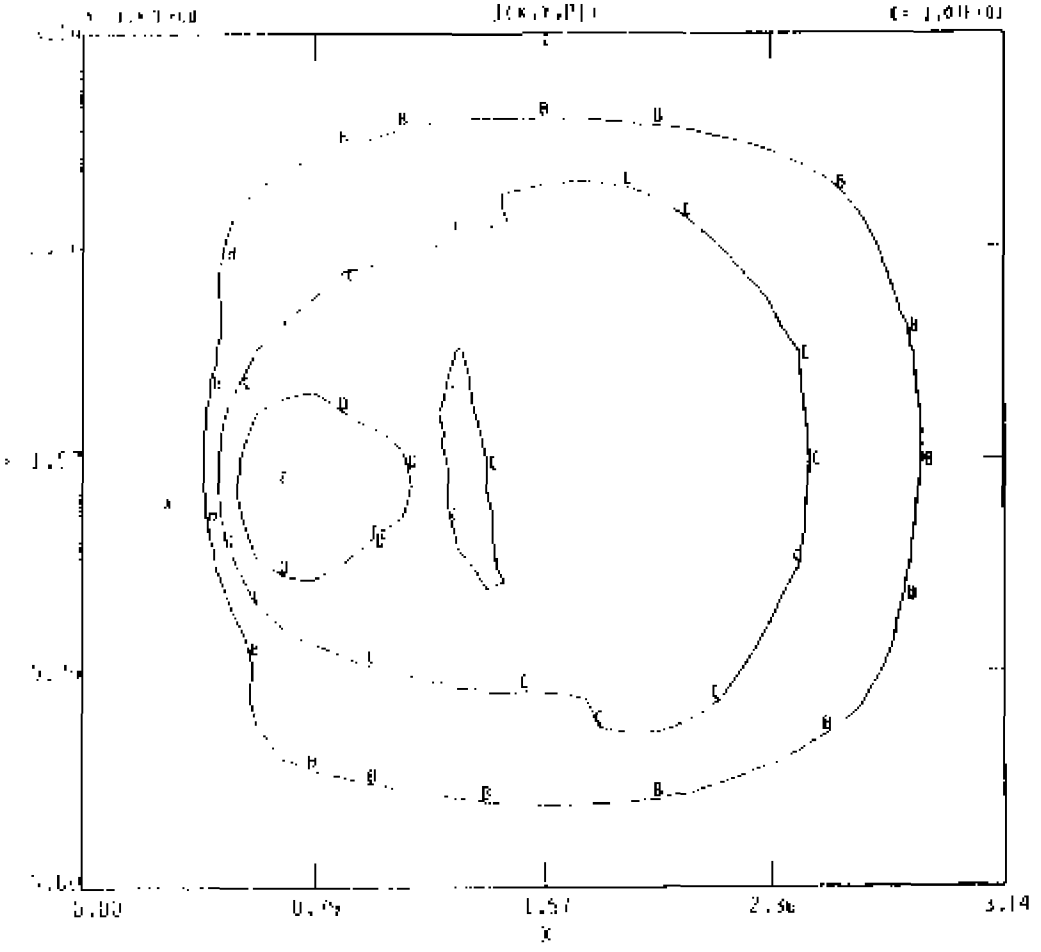

59 (b): contours of j = constant, poloidal cut.

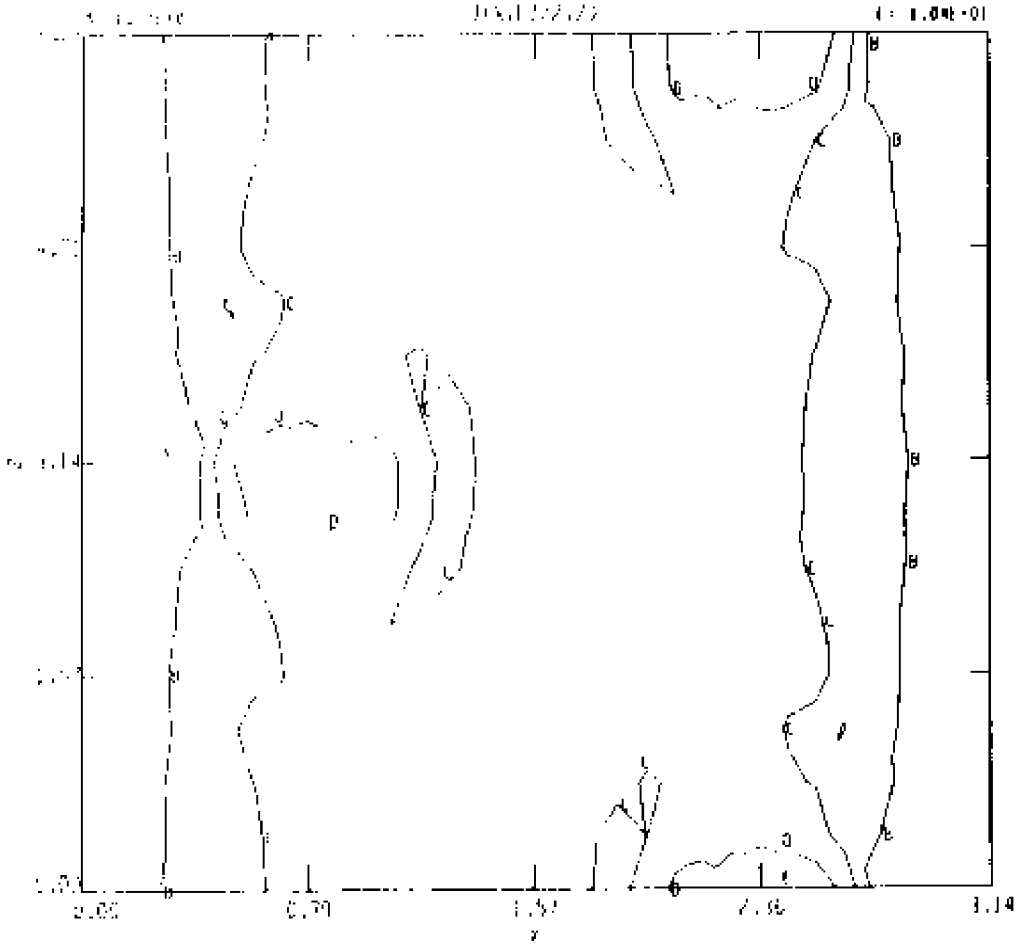

59 (c): contours of j = constant, toroidal cut.

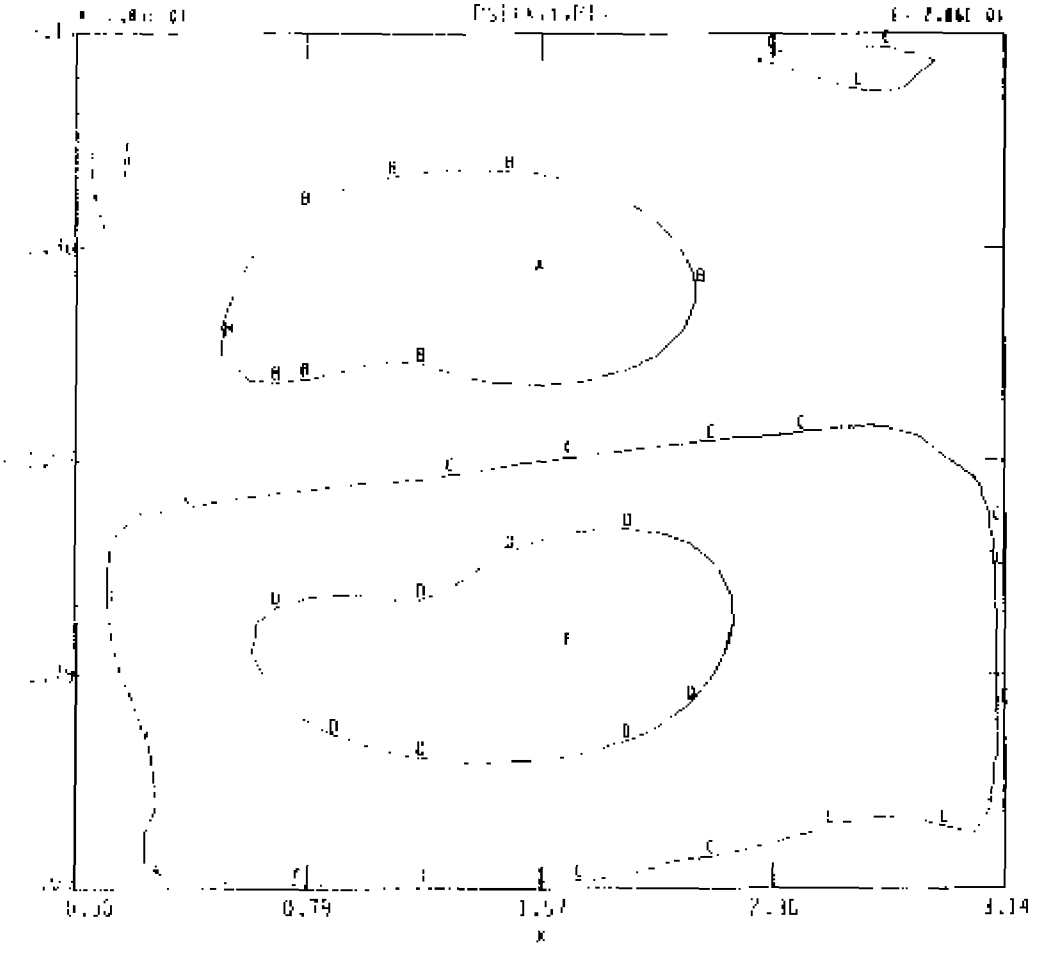

and 59 (d) : contours of Ψ* constant, poloidal cut.

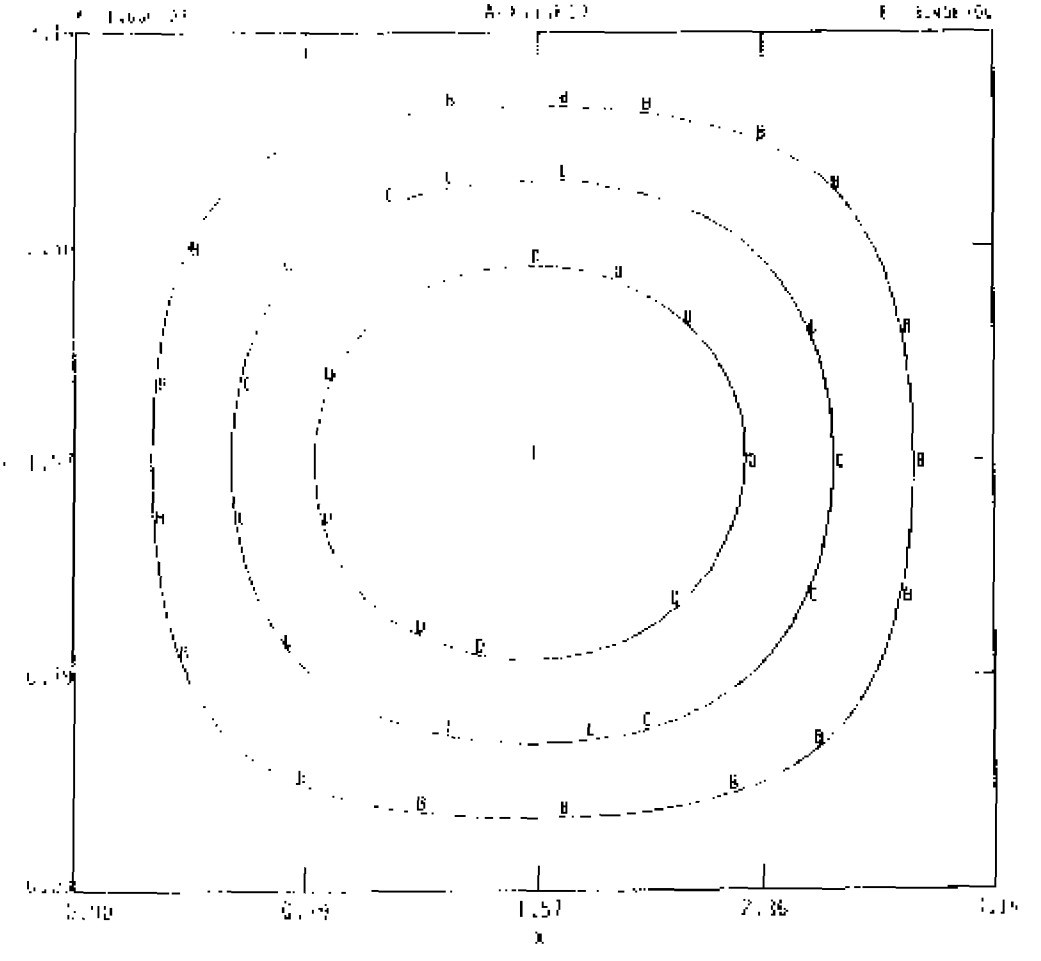

Figure 68. - Contours at t = 26.40, for CASE 4, $\varepsilon_0 = 0.05$, $\nu = 0.0$:
68 (a): contours of A = constant, poloidal cut.

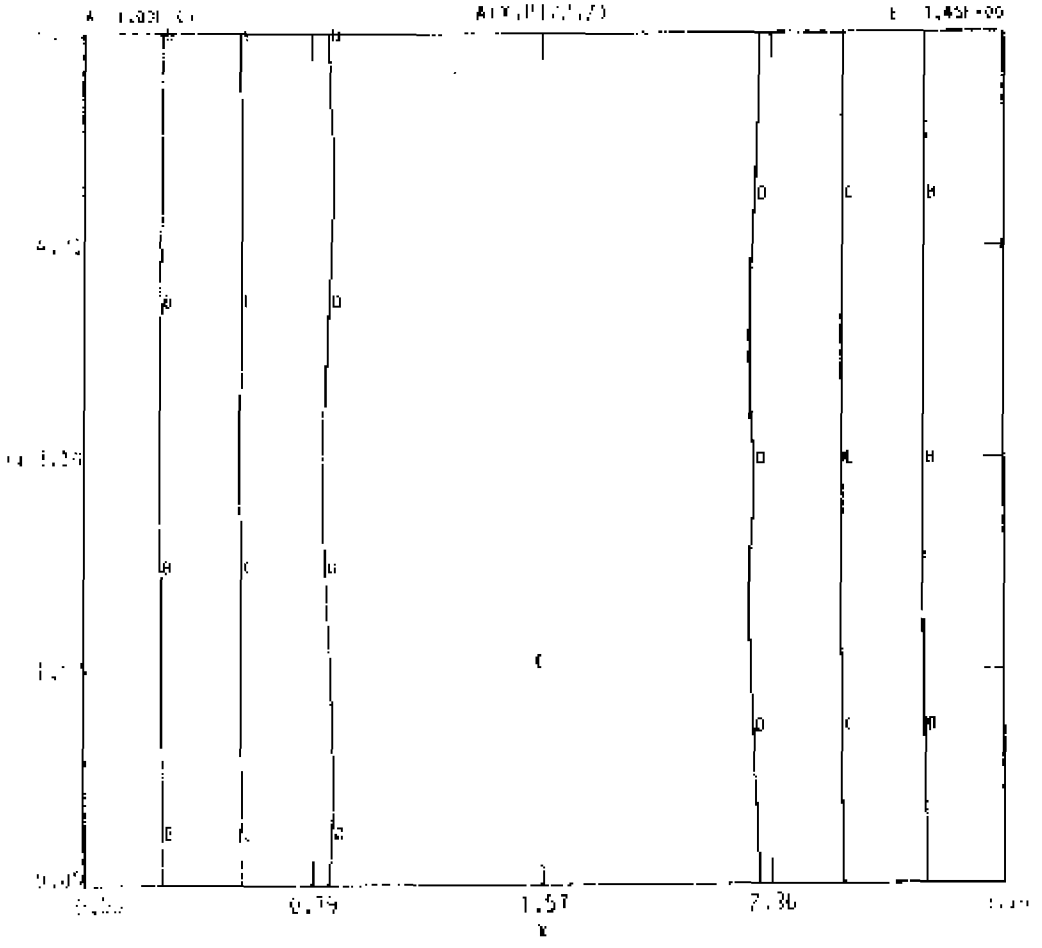

68 (b): contours of A = constant, toroidal cut.

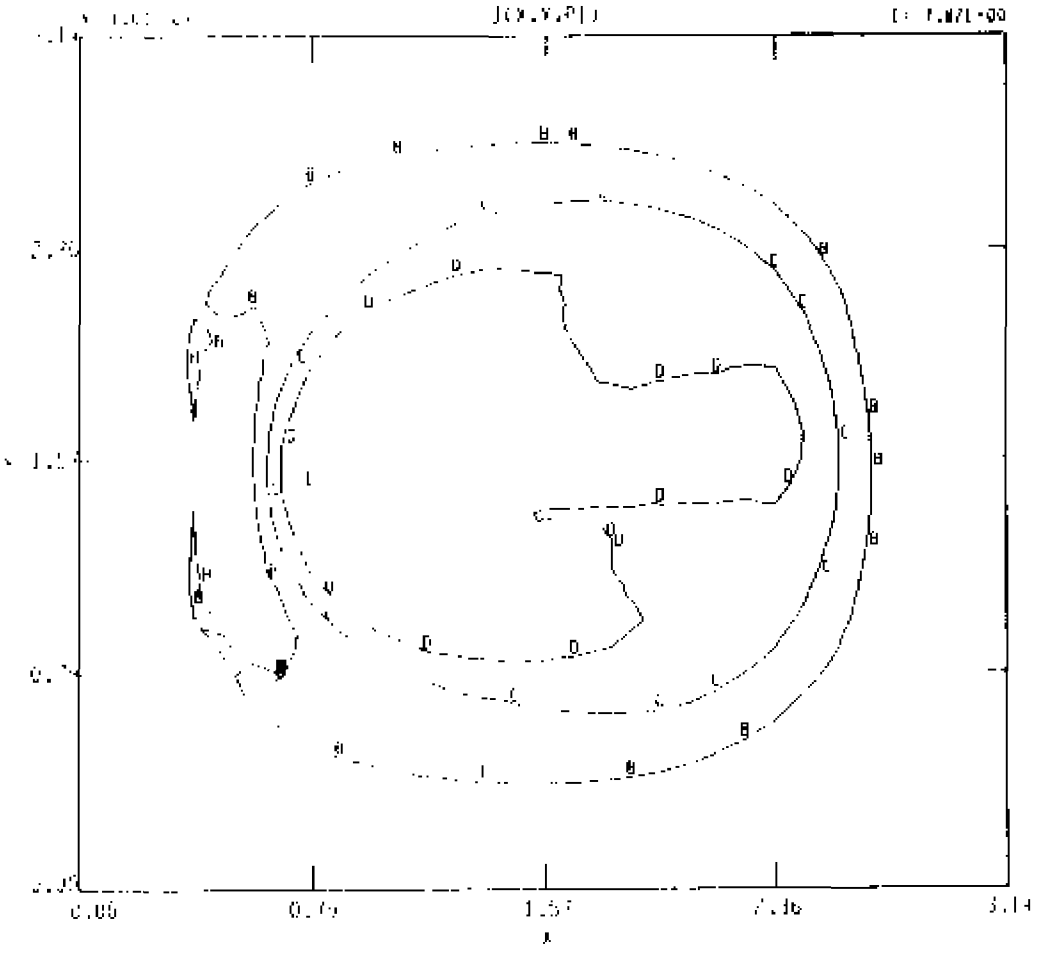

68 (c): contours of j = constant, poloidal cut.

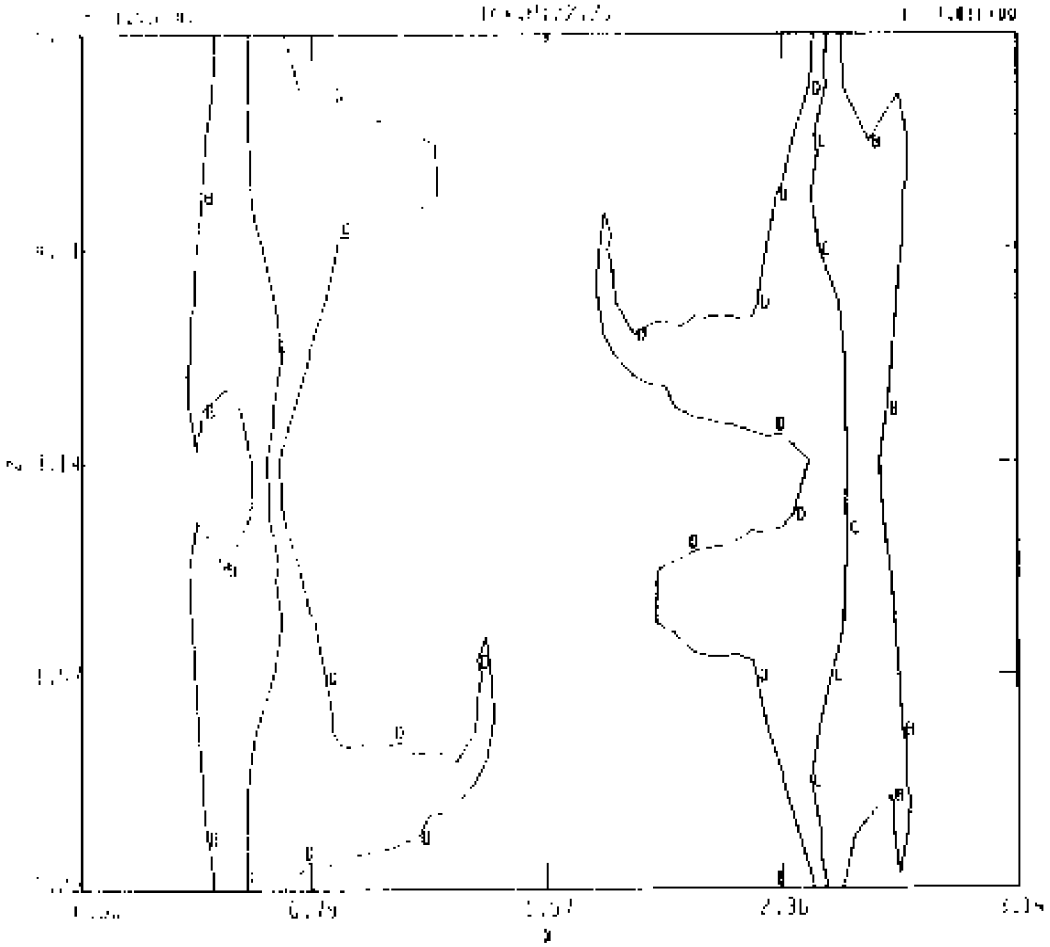

6# (d): contours of j * constant, toroidal cut.

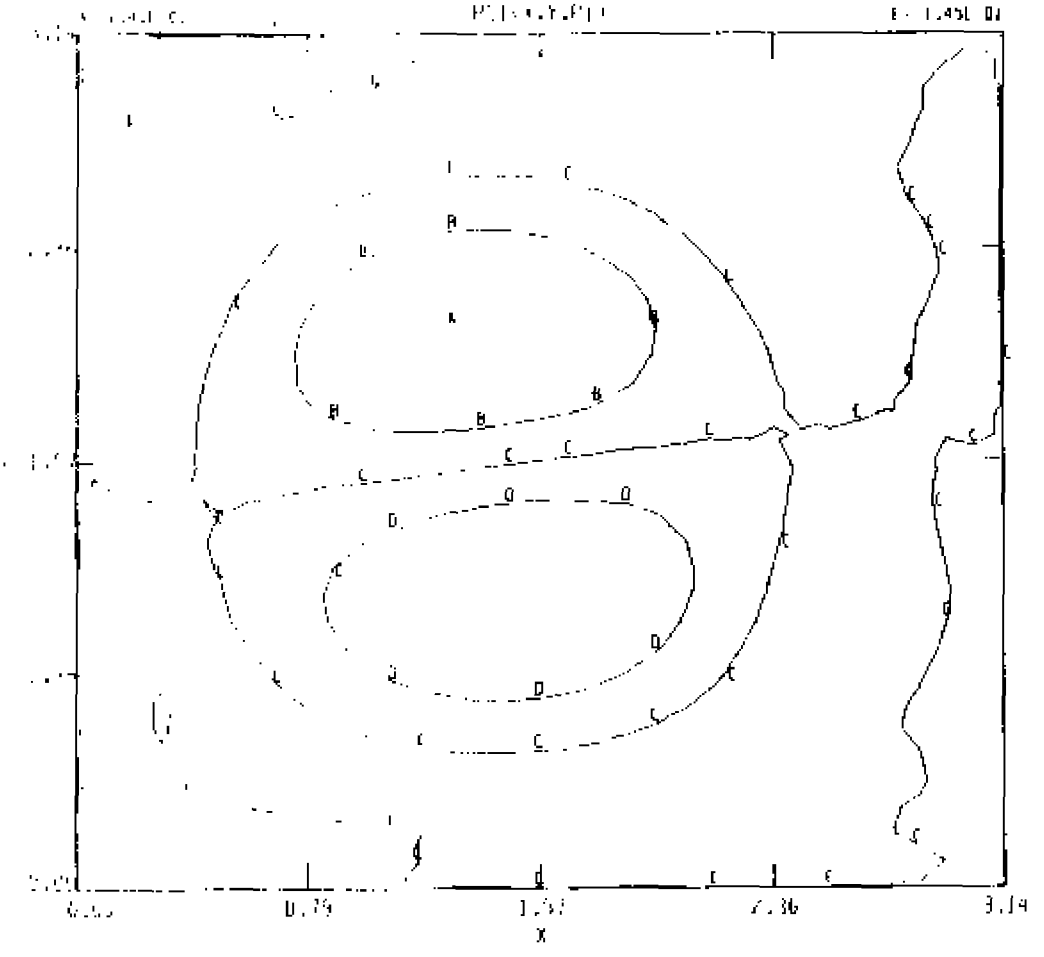

68 (e): contours of Ψ = constant, poloidal cut, and

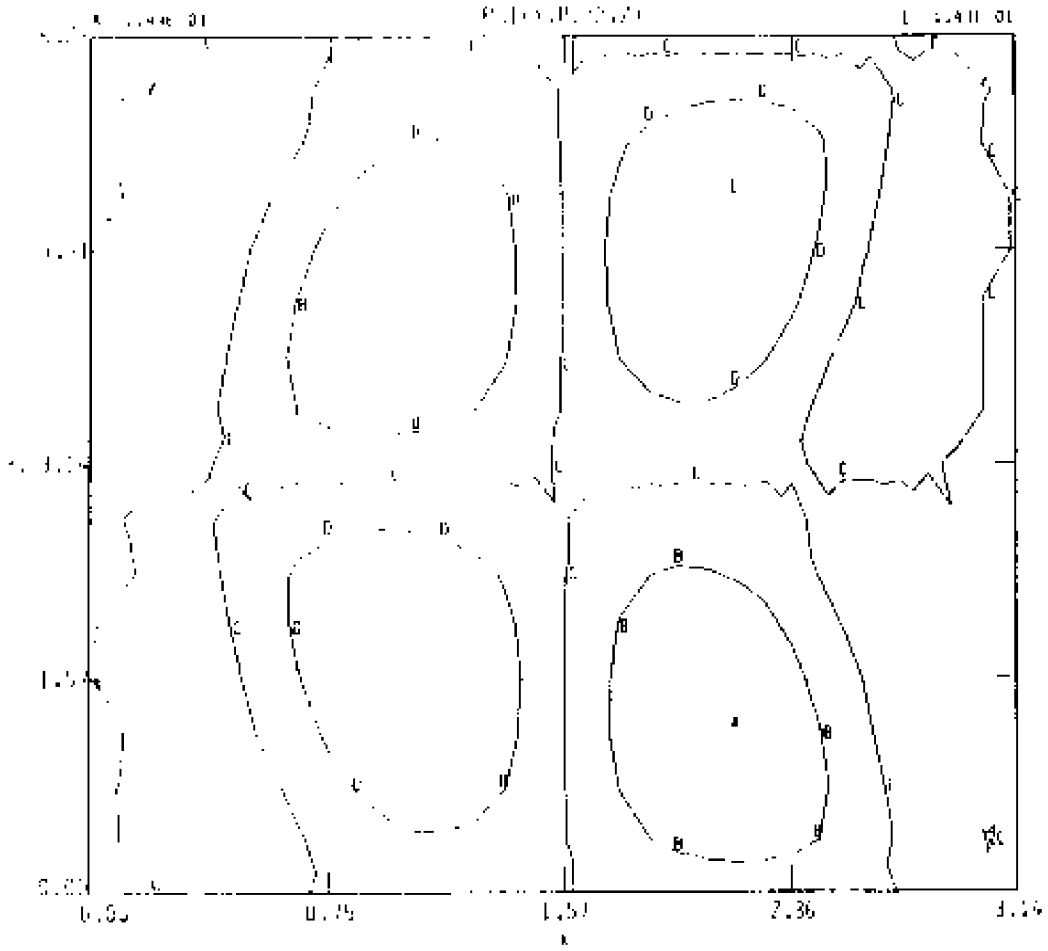

60 (f): contours of Ψ = constant, toroidal cut.

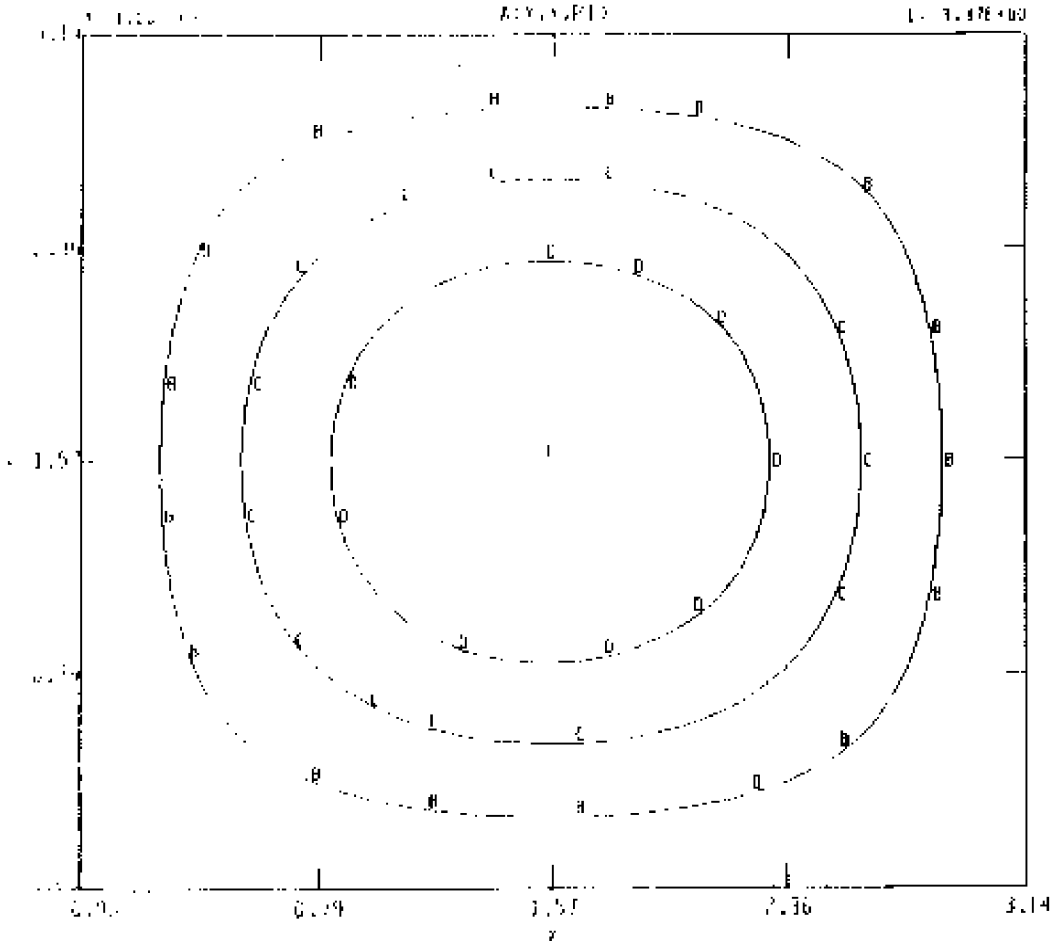

Figure 61. - Contours at t = 36.24, for CASE 4, β_o = 0.05, ν = 0.0
61 (a): contours of A = constant, poloidal cut.

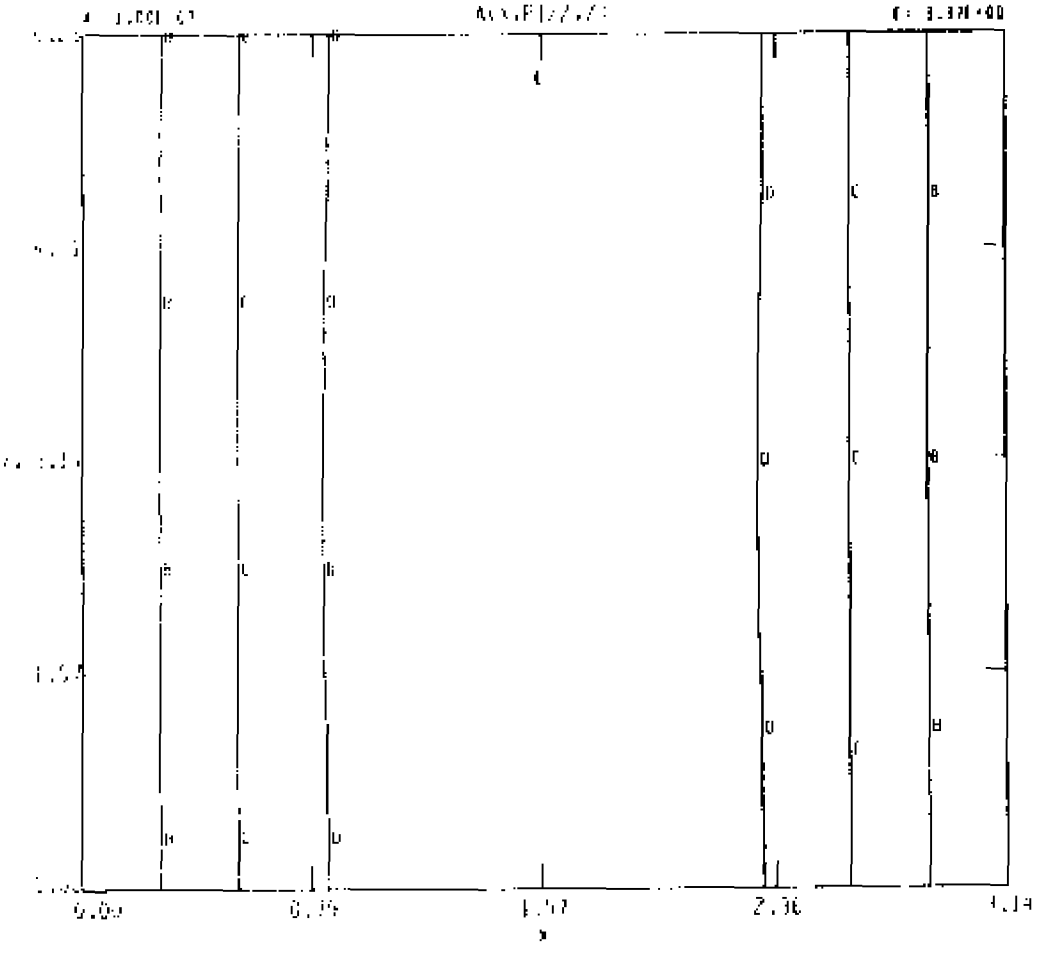

61 (b): contours of A = constant, toroidal cut.

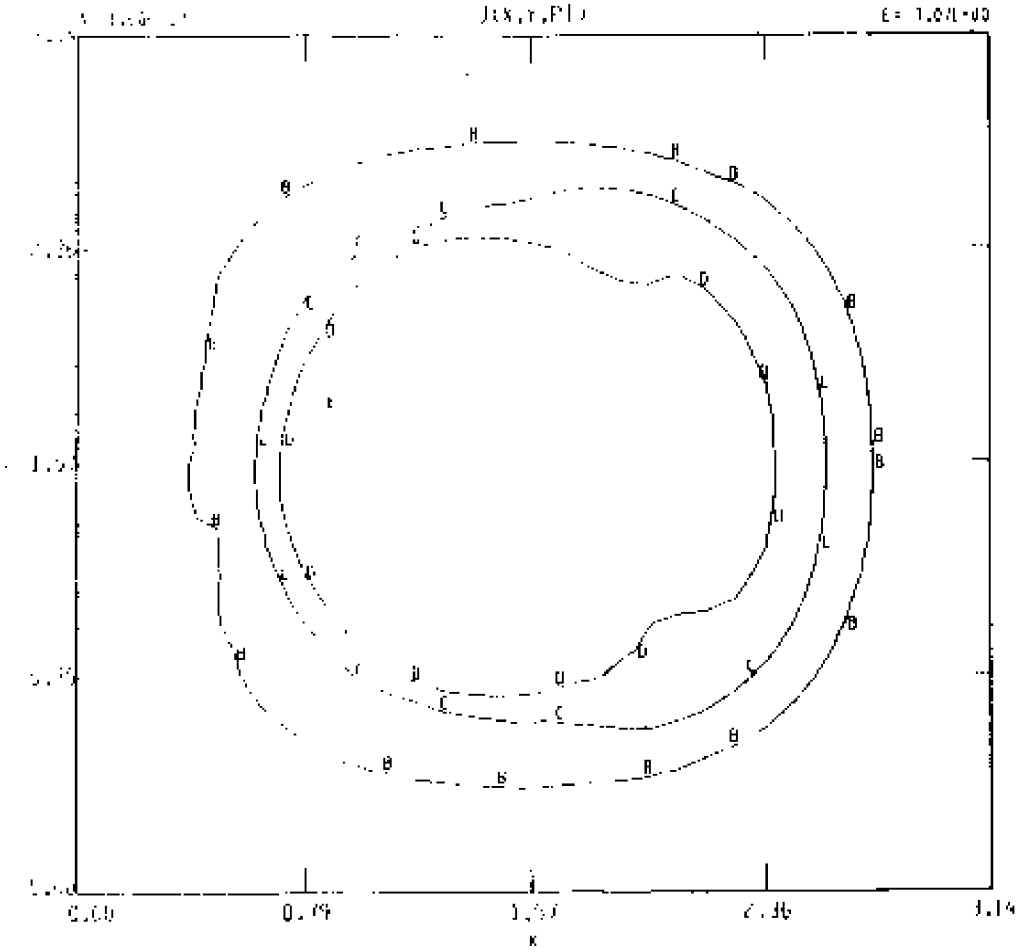

61 (c): contours of j = constant, poloidal cut.

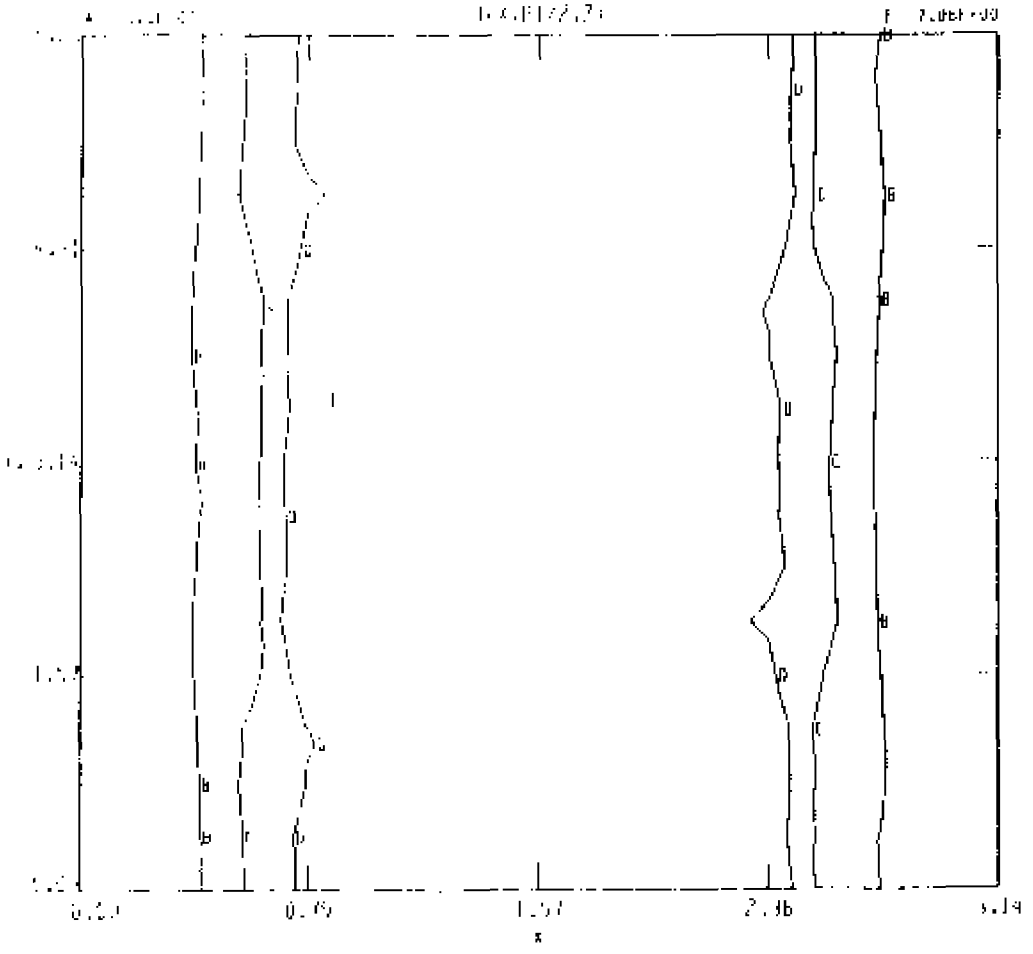

61 (d): contours of j = constant, toroidal cut.

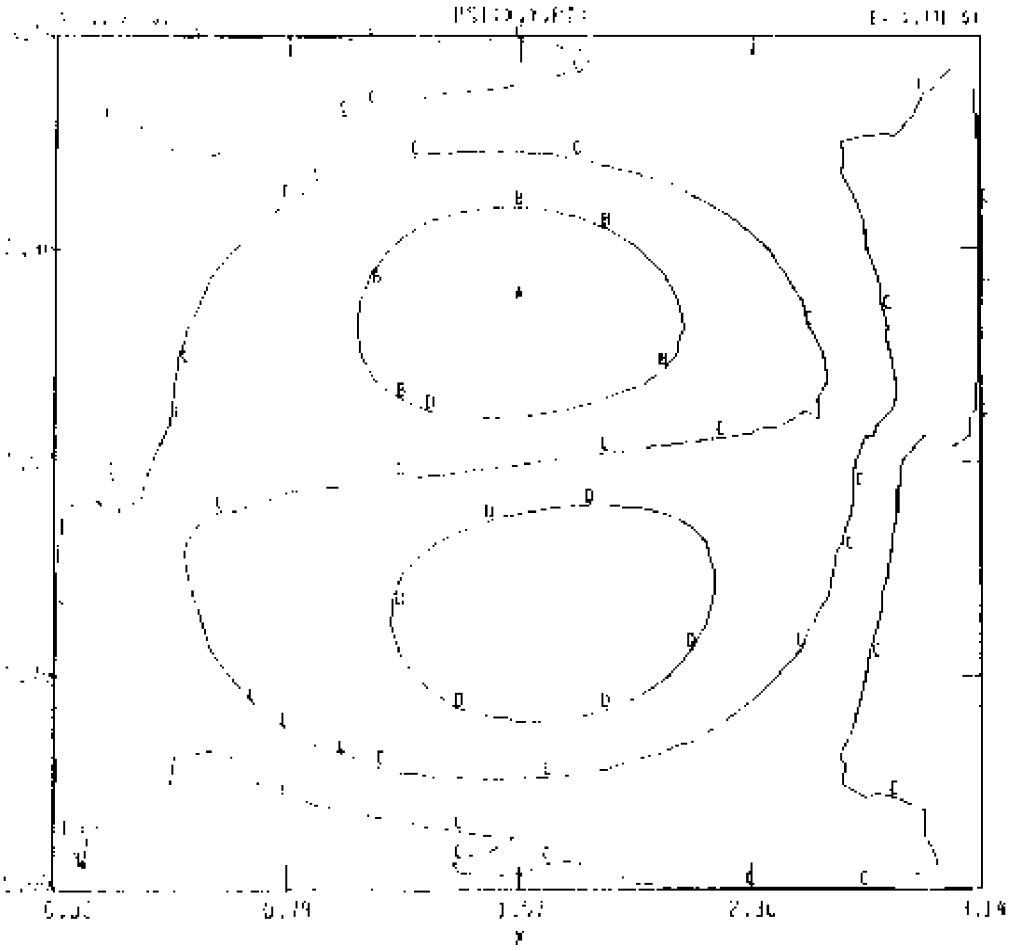

61 (e): contours of Ψ = constant, poloidal cut, and

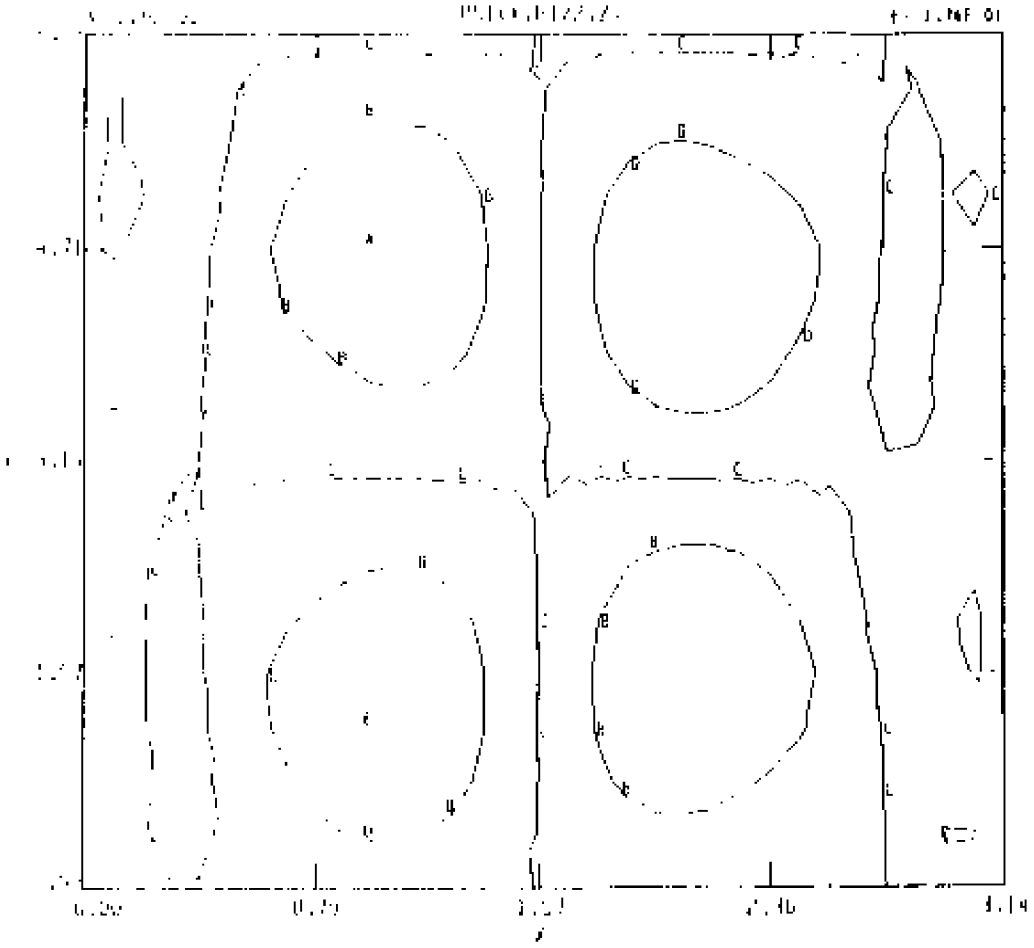

61 (f): contours of Ψ = constant, toroidal cut.

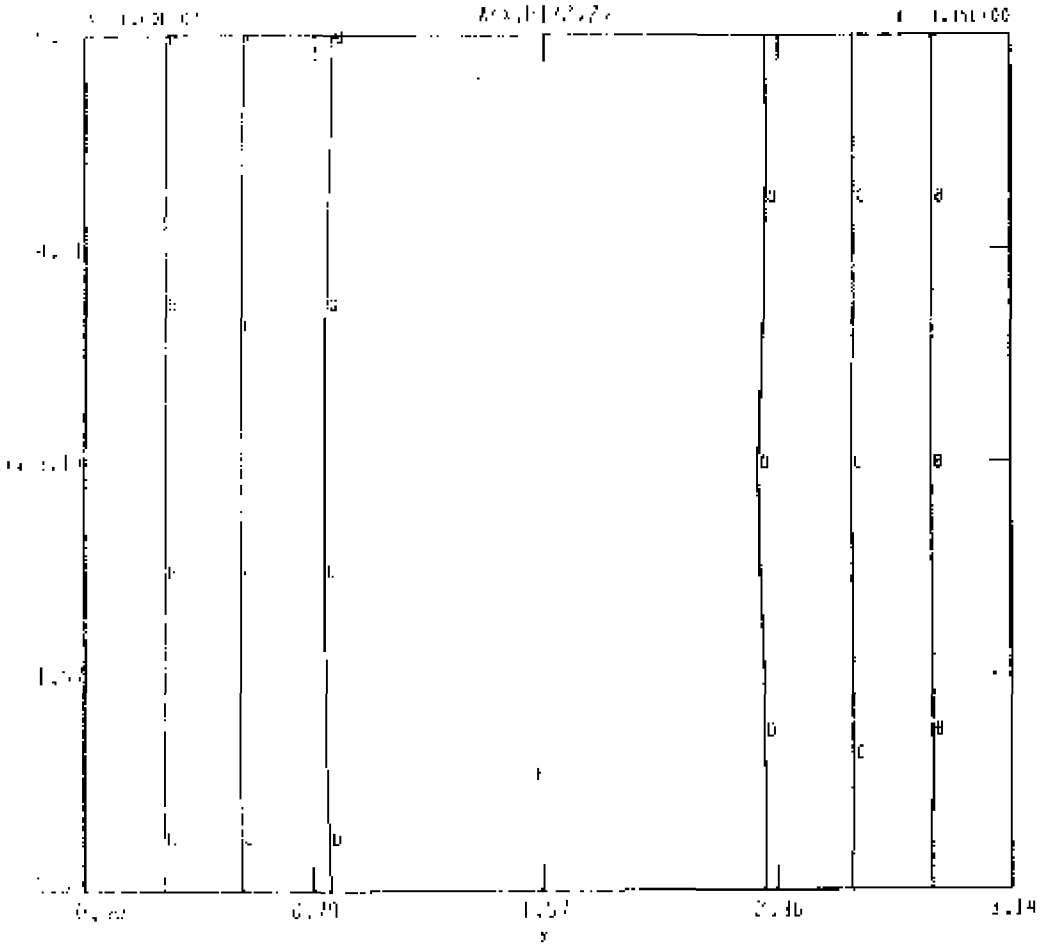

Figure 62. - Contours at t = 42.00, for CASE 4, ε_o = 0.05, ν = 0.0:
62 (a) : contours of A = constant, toroidal cut.

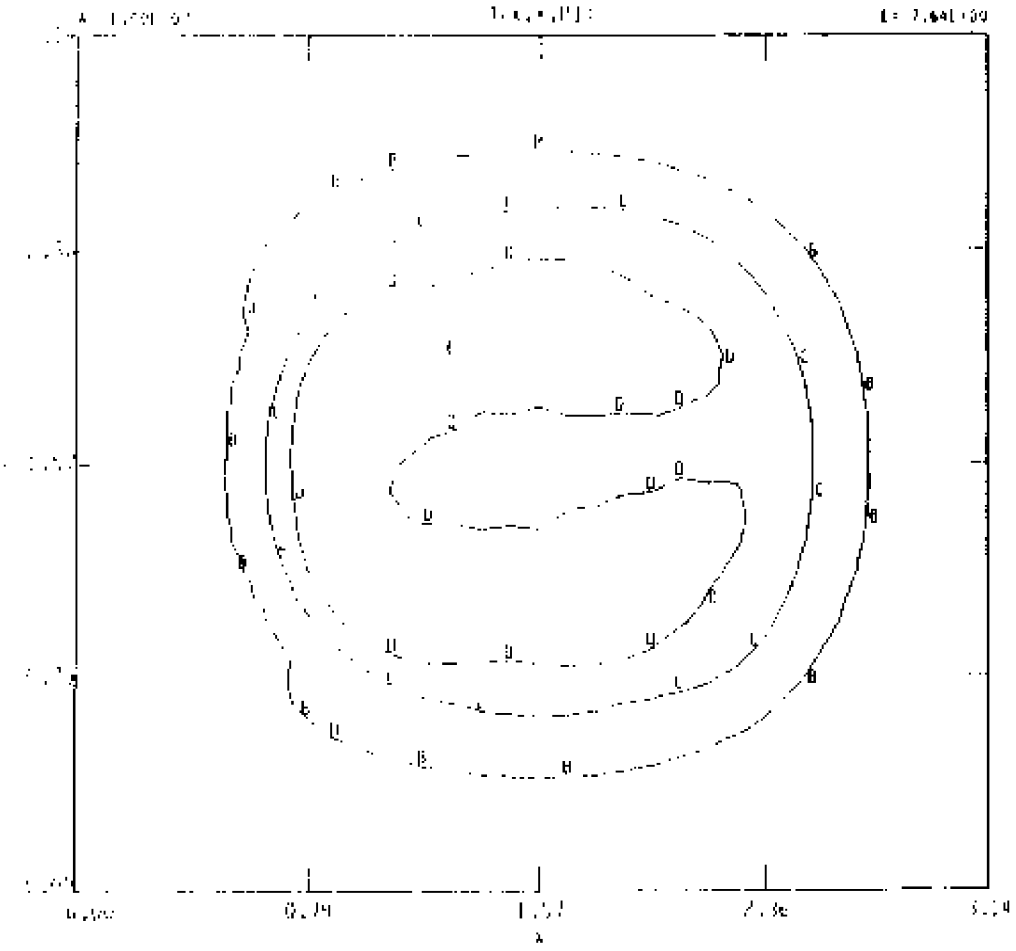

62 (b): contours of $\frac{1}{j}$ = constant, poloidal cut,

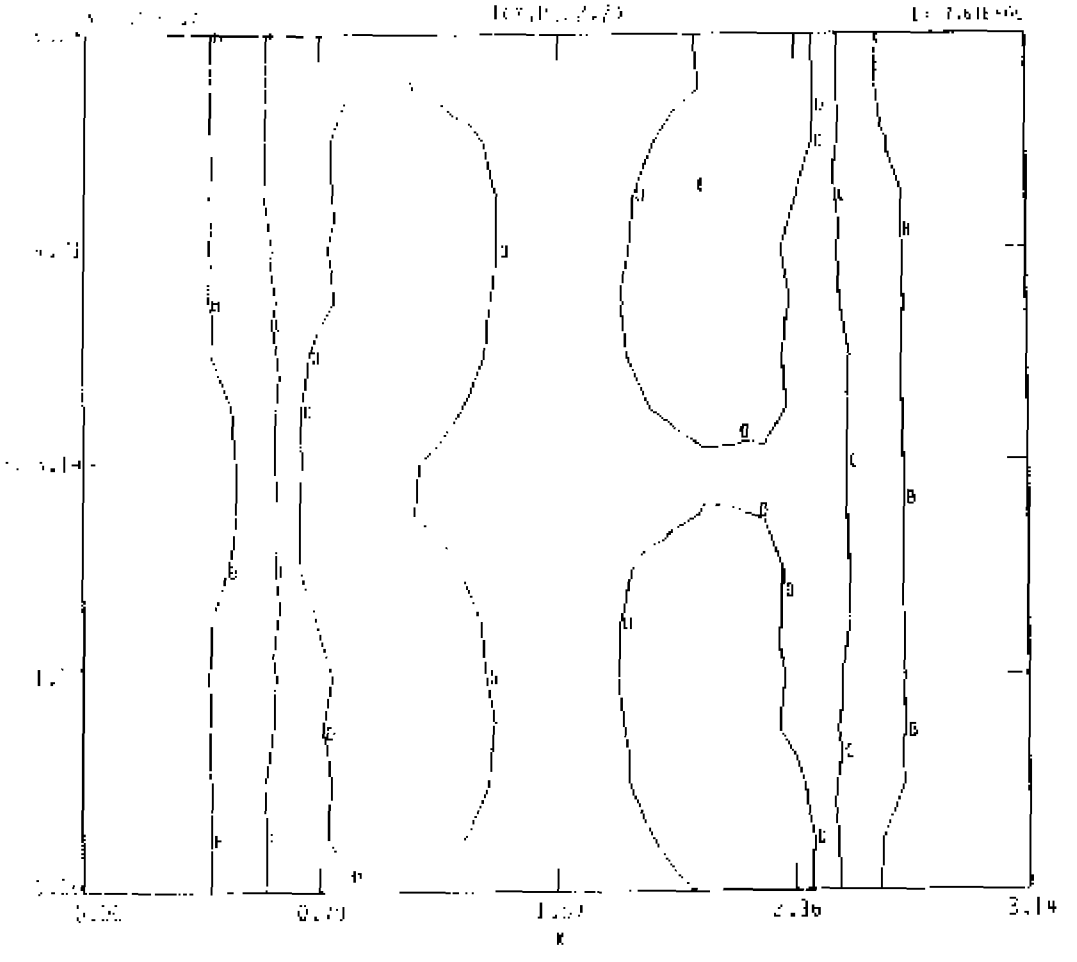

62 (c): contours of j = constant, toroidal cut,

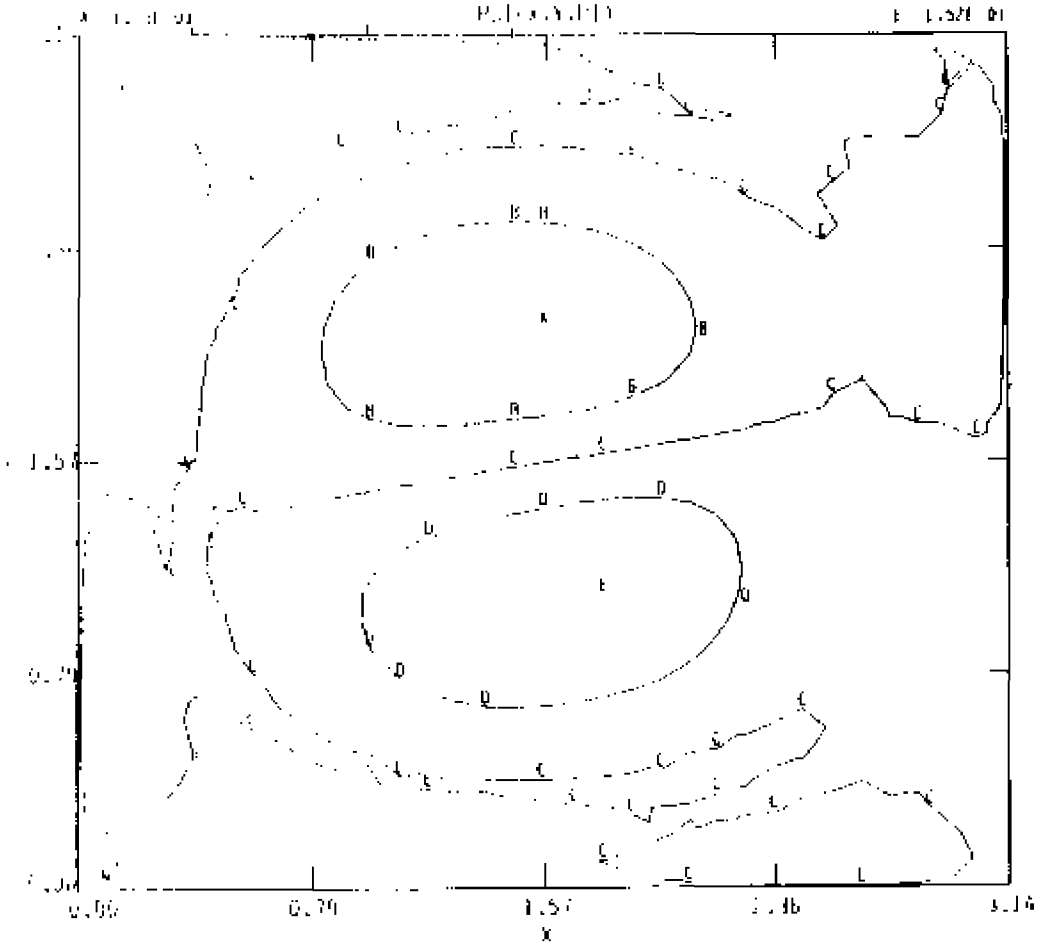

and 62 (d) : contours of Ψ = constant, poloidal cut.

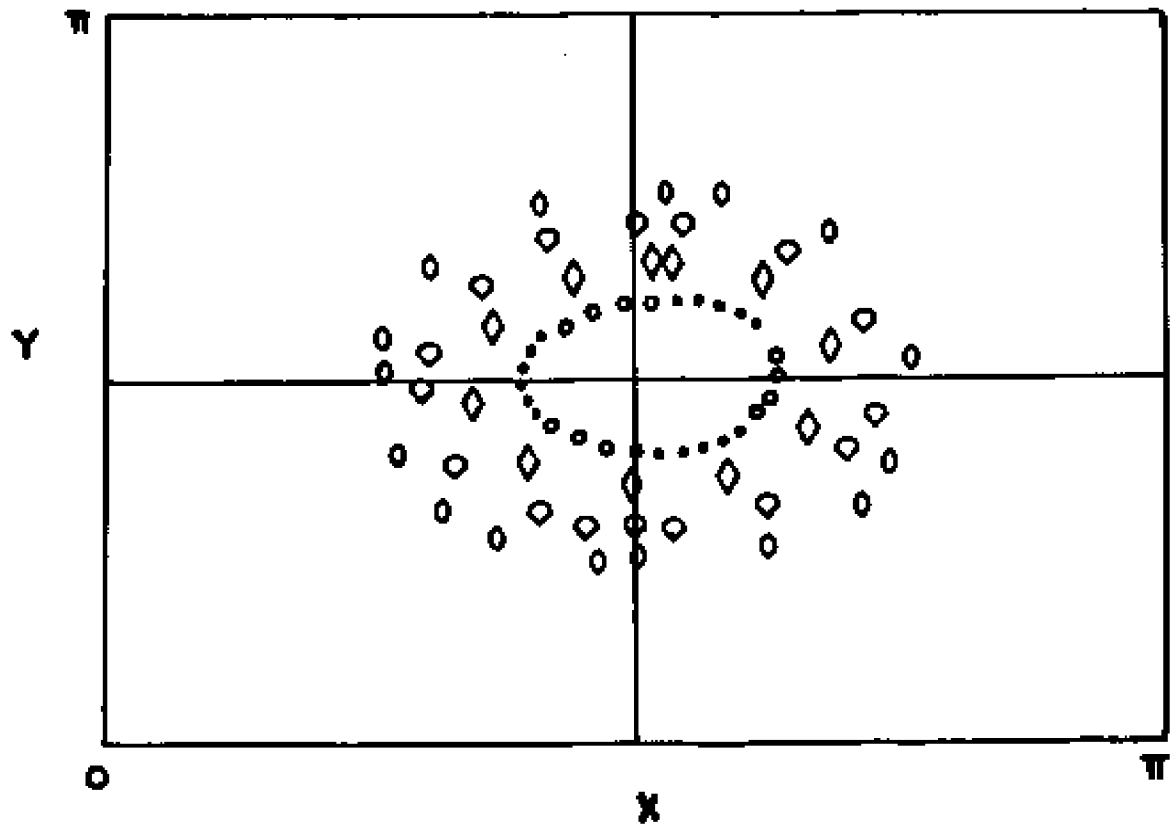

Figure 63. - Poincaré plot, t = 42.00, for CASE 4, ε_0 = 0.05, and ν = 0.0.

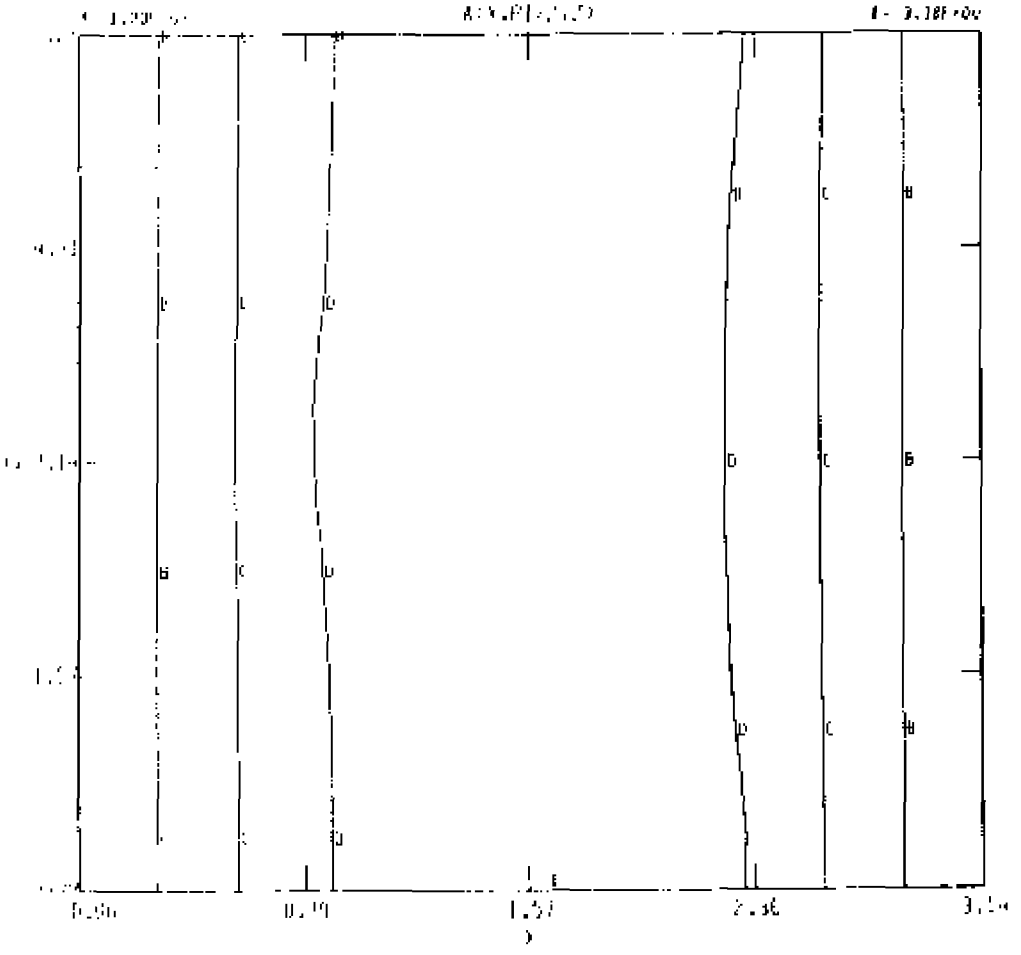

Figure 64. - Contours at t = 109.44, for CASE 4, E_0 = 0.05, ω = 0.0:
64 (a) : contours of A = constant, toroidal cut.

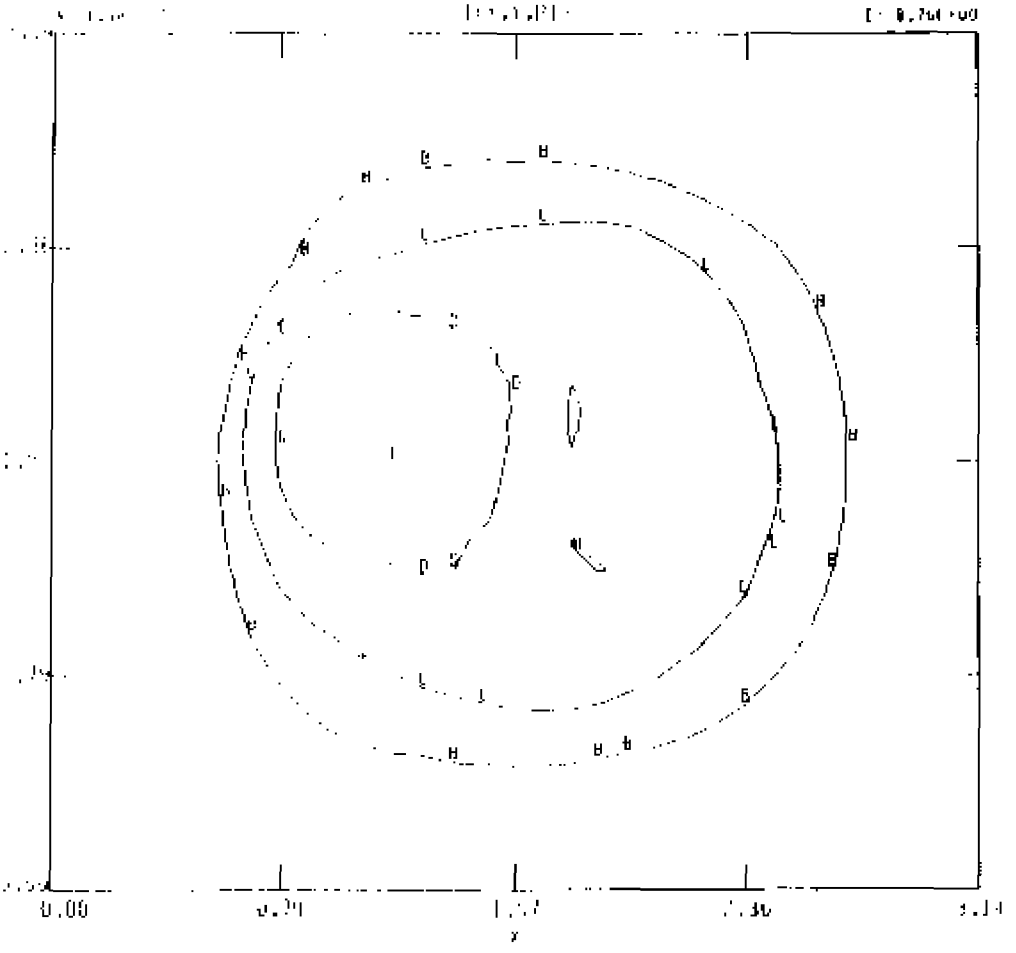

64 (b): contours of j = constant, poloidal cut.

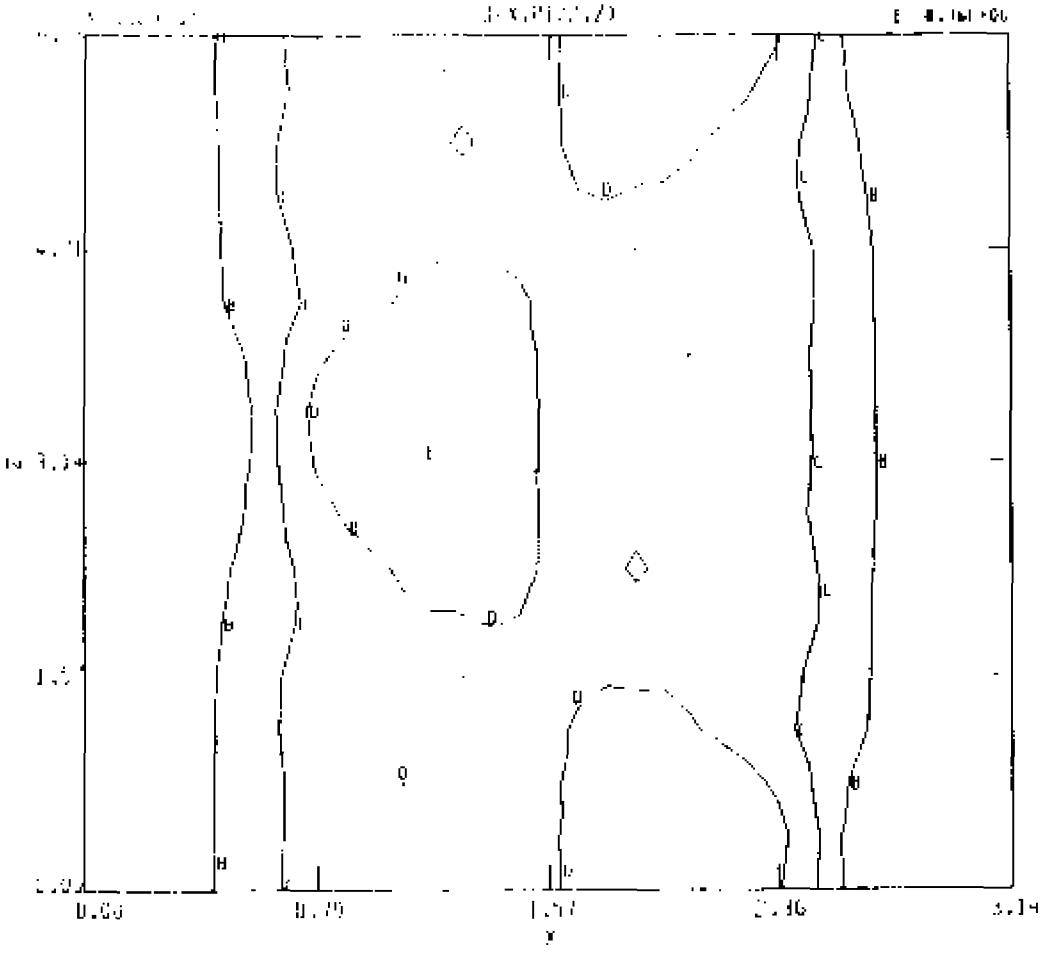

64 (c): contours of j = constant, toroidal cut.

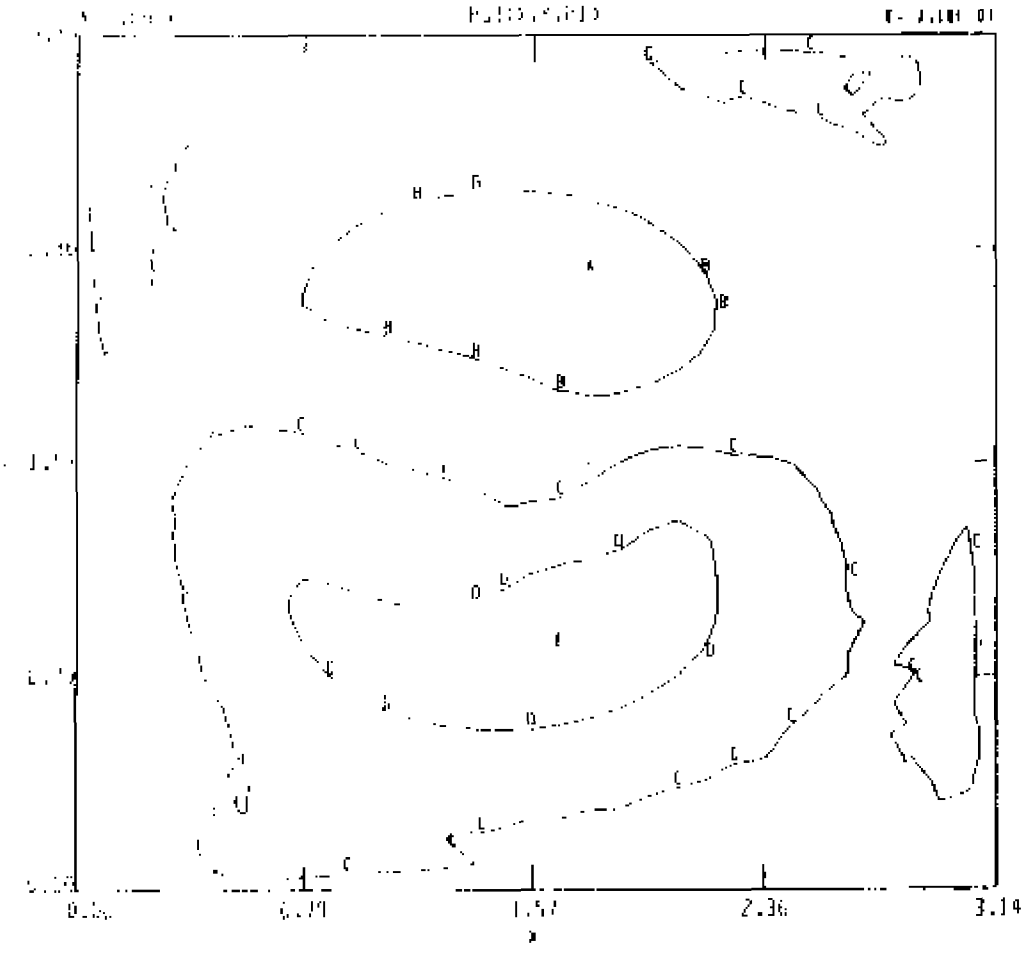

and 64 (d) : contours of Ψ = constant, poloidal cut.

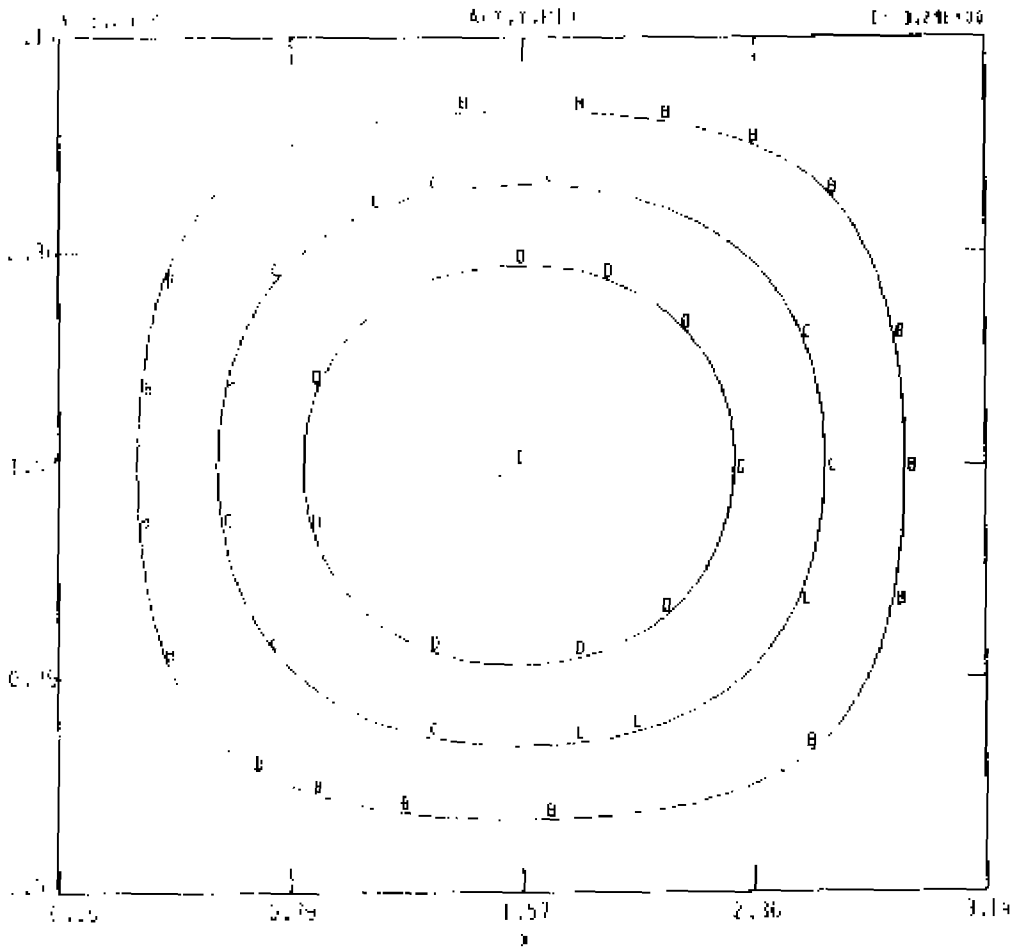

Figure 65. - Contours at t = 157.92, for CASE 4, ε_0 = 0.05, υ = 0.0: 65 (a): contours of A = constant, poloidal cut.

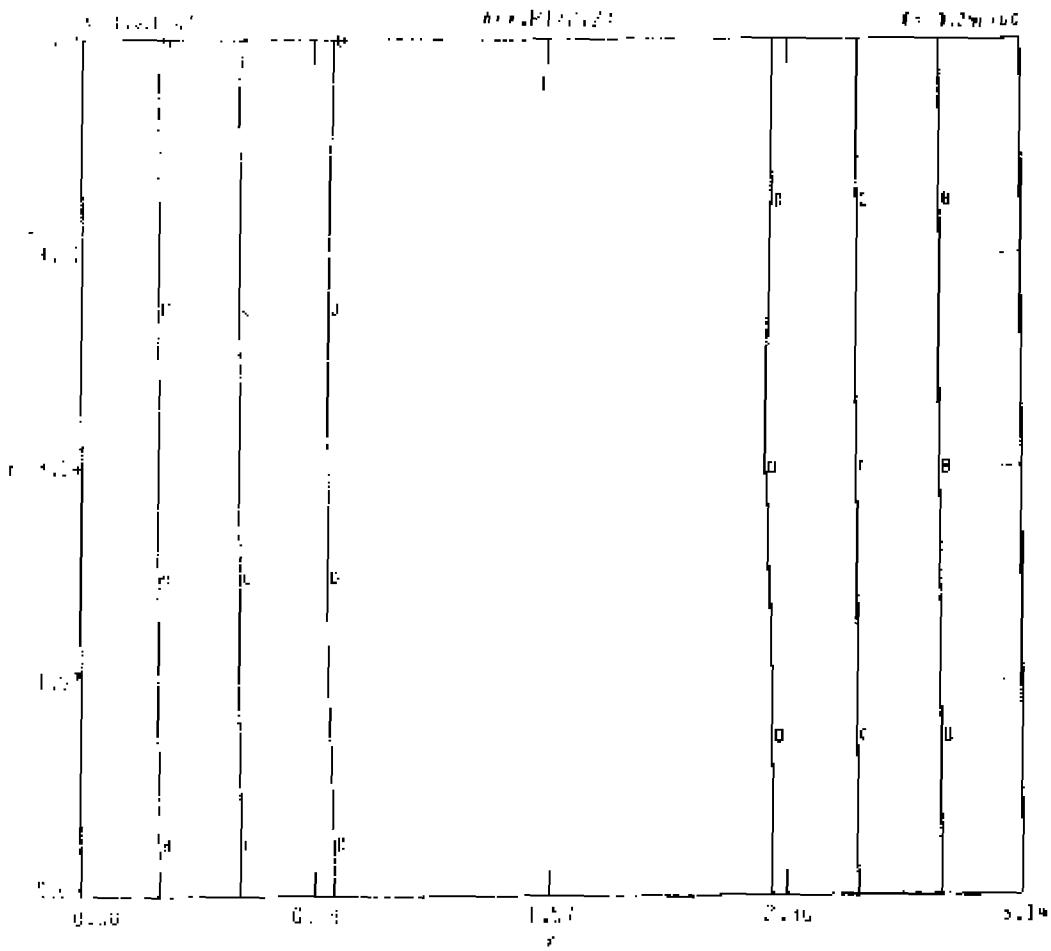

65 (b): contours of A = constant, toroidal cut.

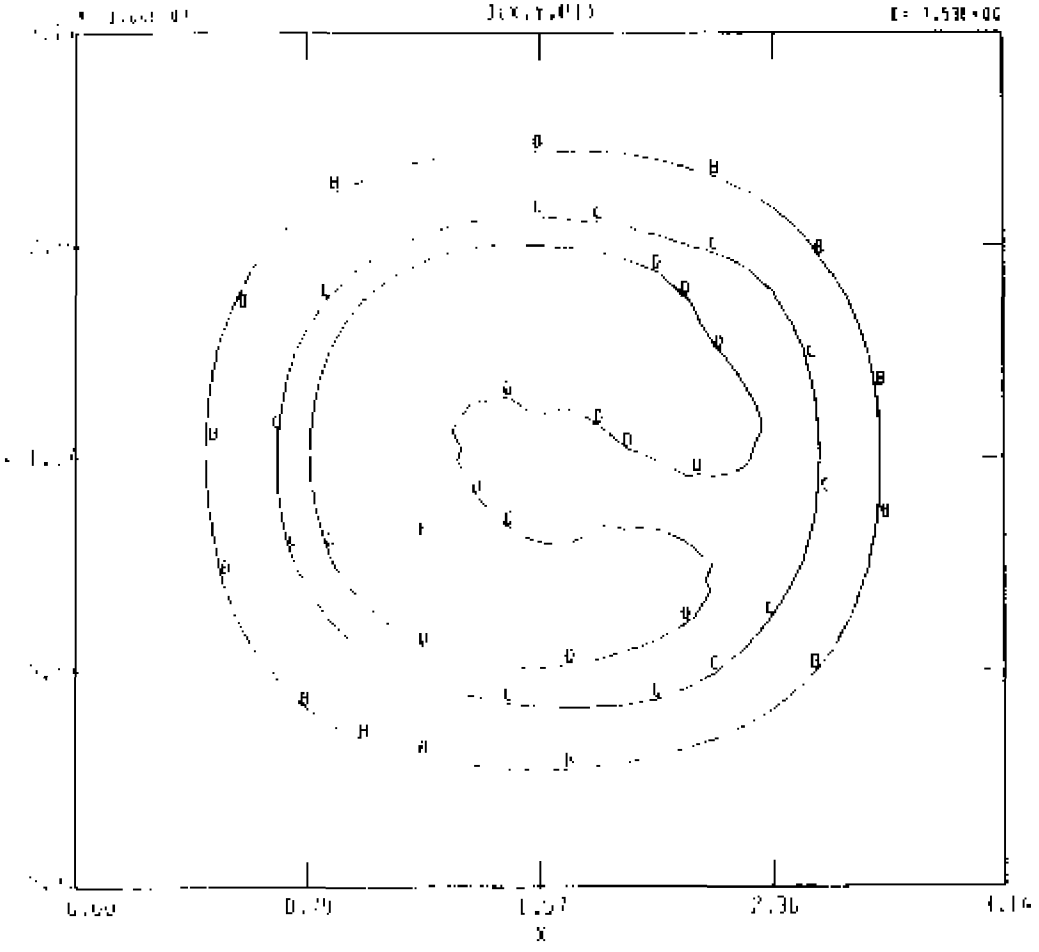

65 (c): contours of j = constant, poloidal cut.

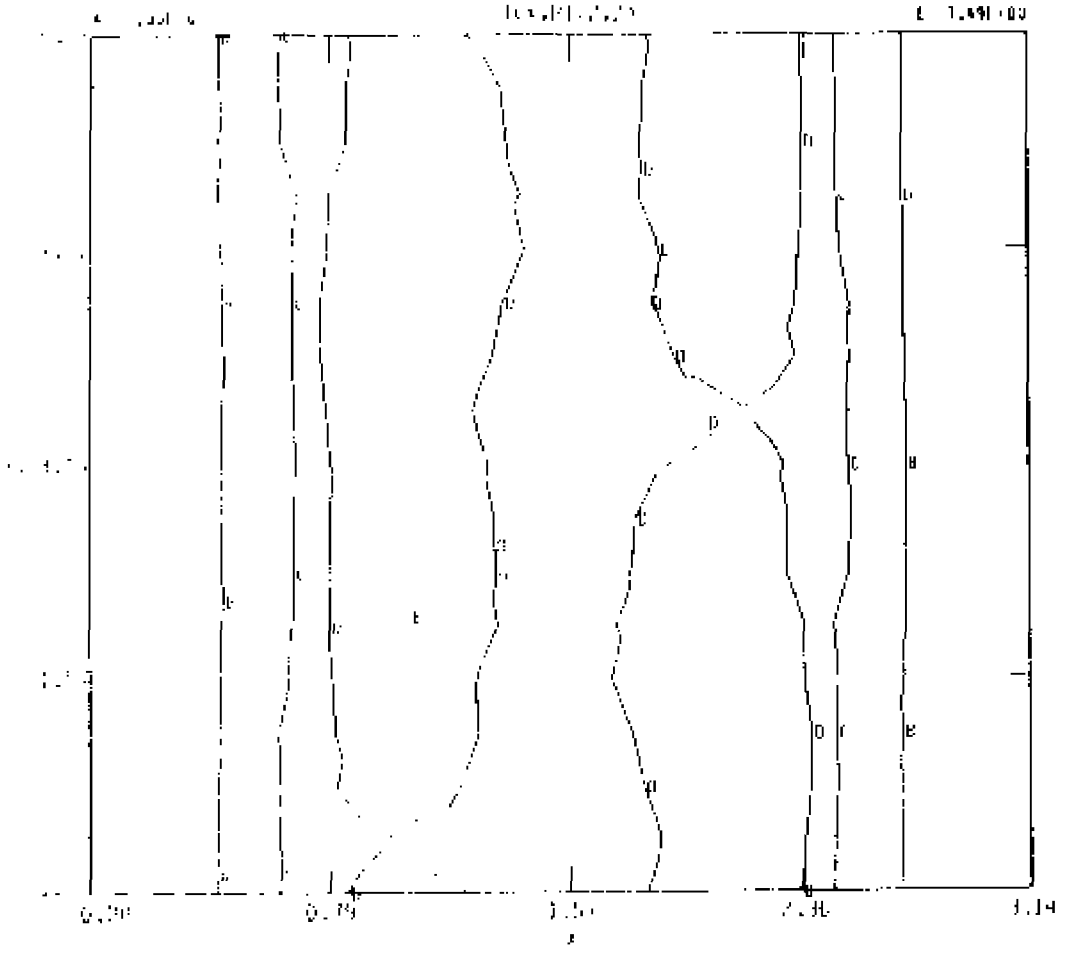

65 (d): contours of j * constant, toroidal cut.

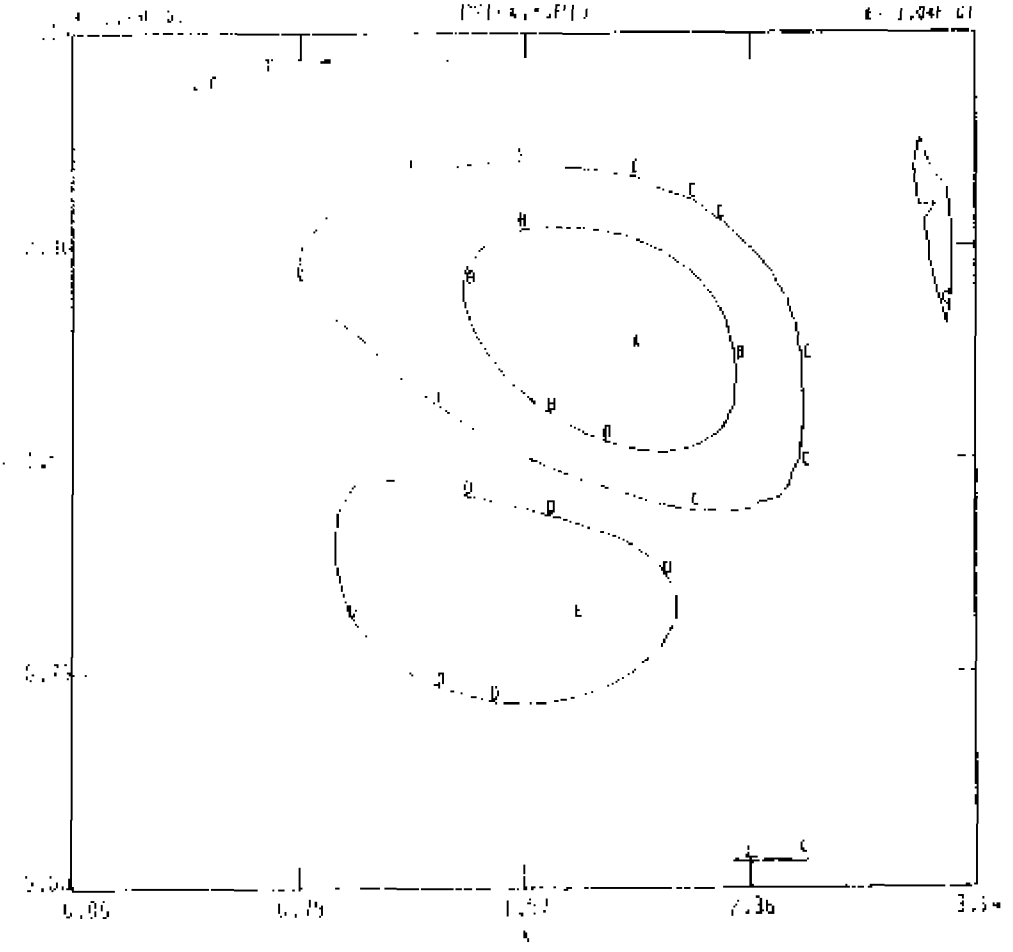

65 (e): contours of Ψ = constant, poloidal cut, and

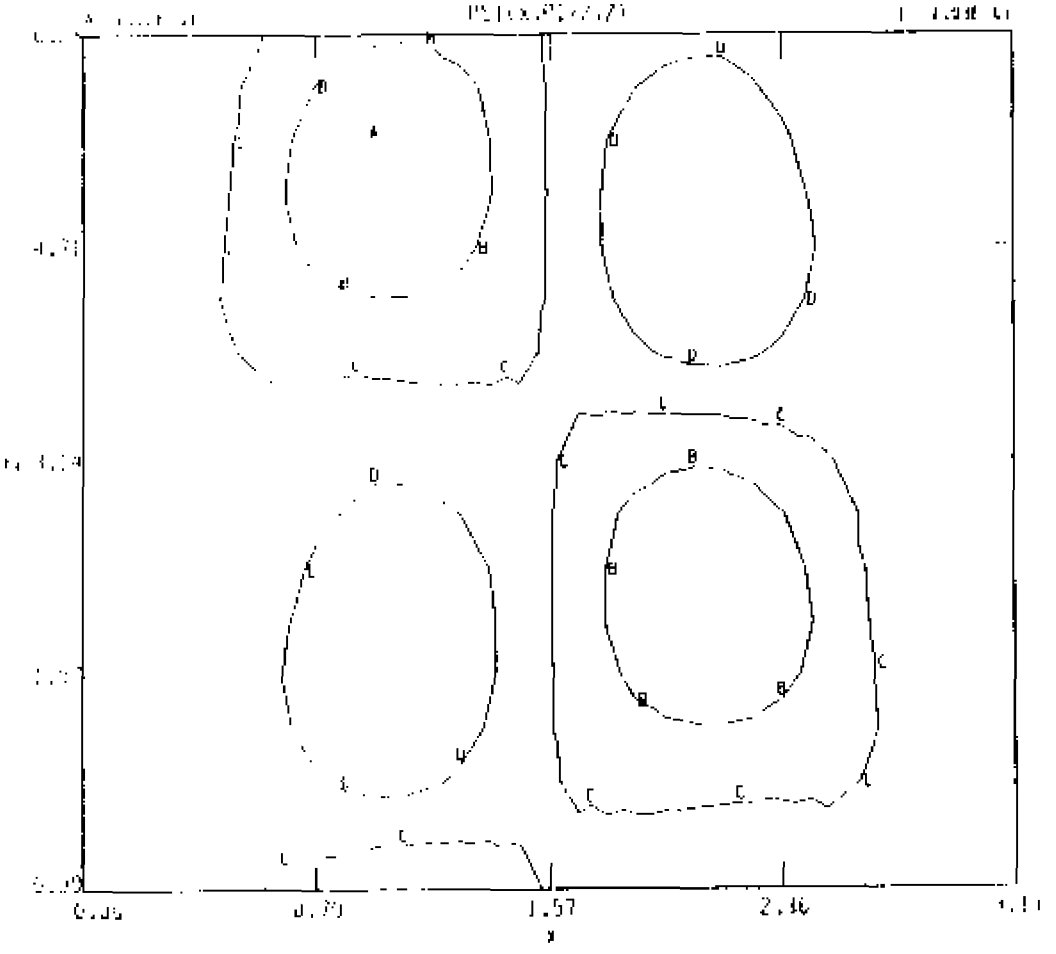

65 (f): contours of Ψ = constant, toroidal cut.

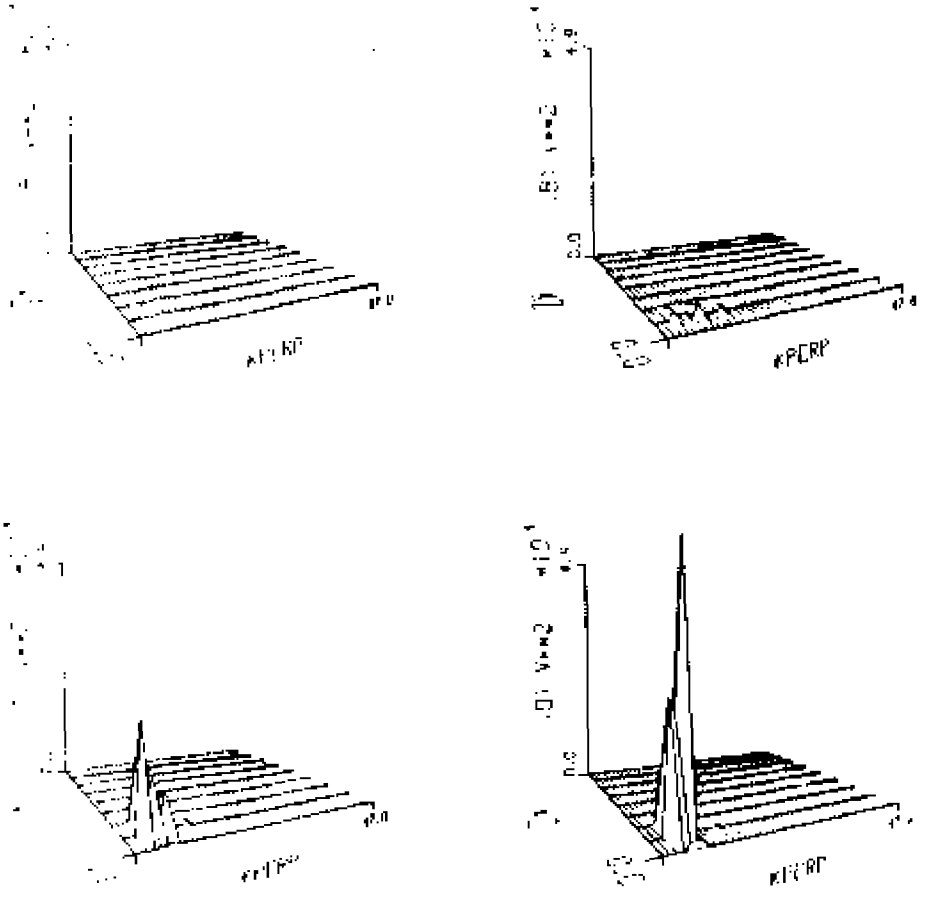

Figure 66. - Spectra, CASE 4, with E_o = 0.05, V_o = 0.00,
66(a): t = 0.00,

66(b): t = 101.76,

66(c): t = 109.44,

66(d): t = 117.12.

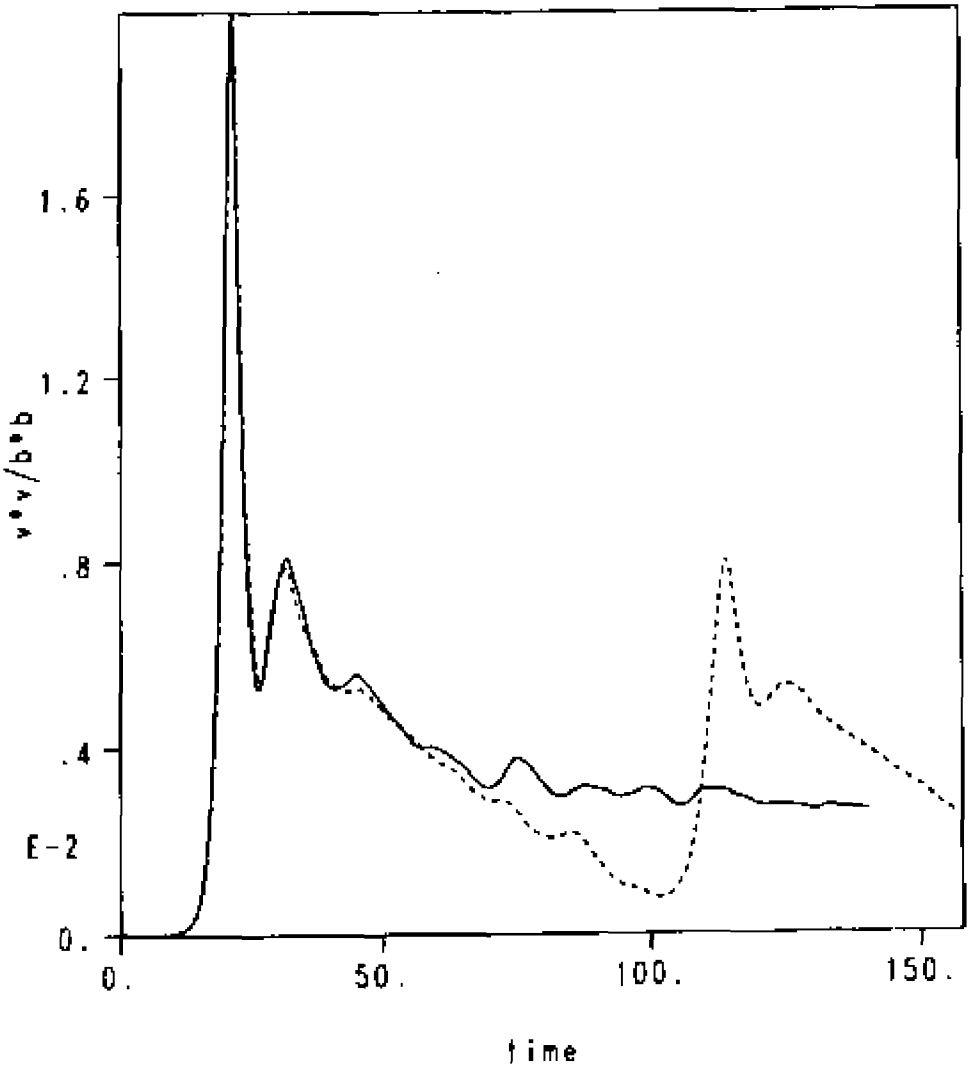

Figure 67. - Ratio of kinetic to magnetic energies for CASE 4, E_p = 0.05, ν = 0.0,
Dashed line: 32 * 32 * 16 grid.
Solid line: 16 * 16 * 16 grid.

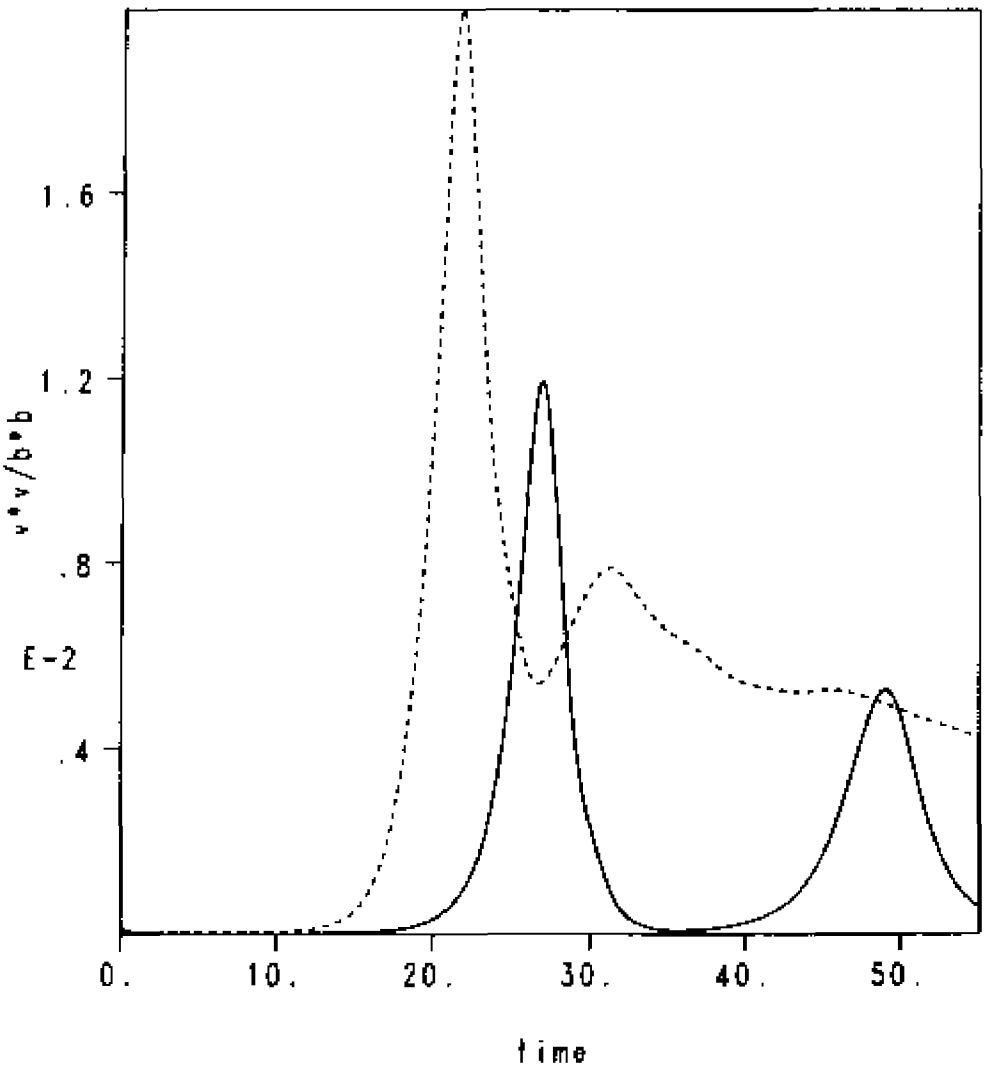

Figure 68. - Global quantities, CASE 4, E_o = 0.05,
Dashed line: ν = 0.00,
Solid line: ν = 0.01,
68(a): ratio of kinetic to magnetic energies as a function of time.

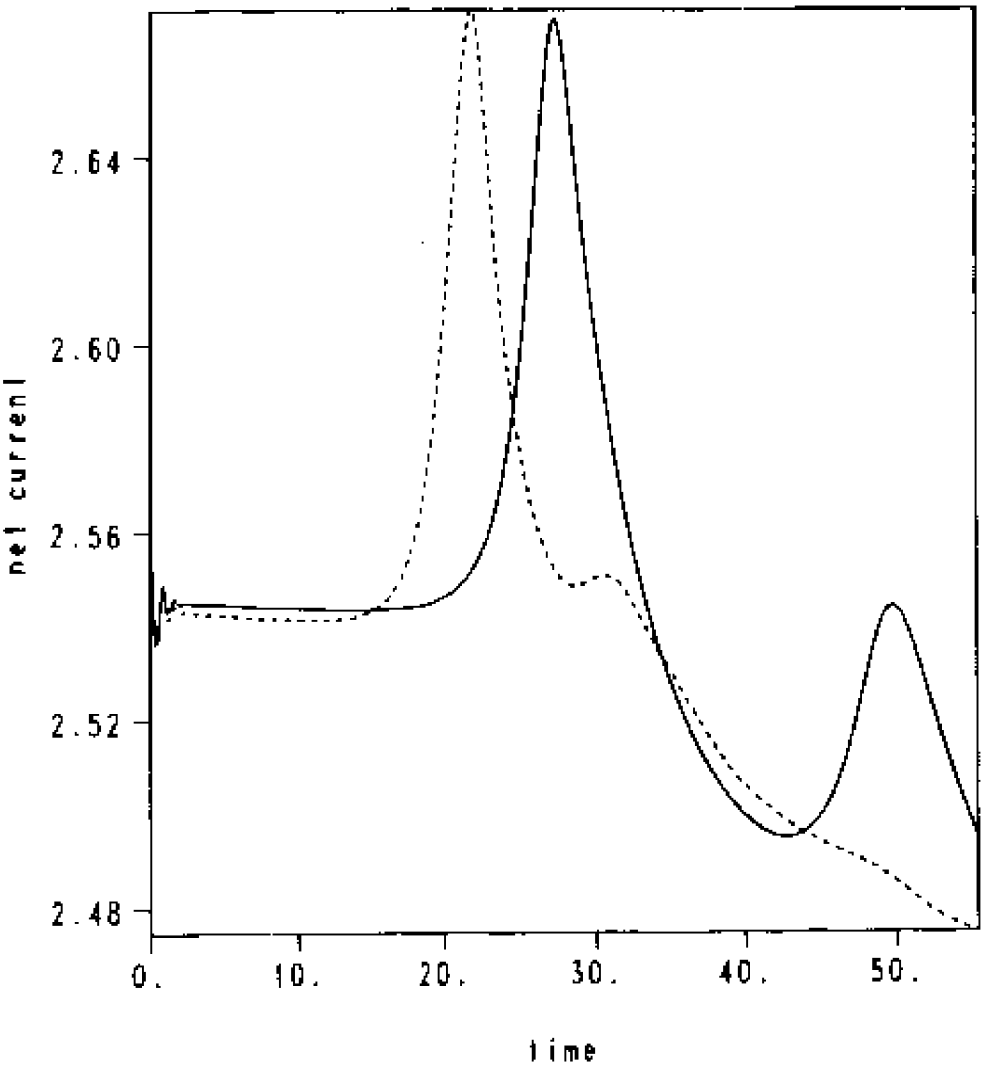

68(b): total integrated current as a function of time.

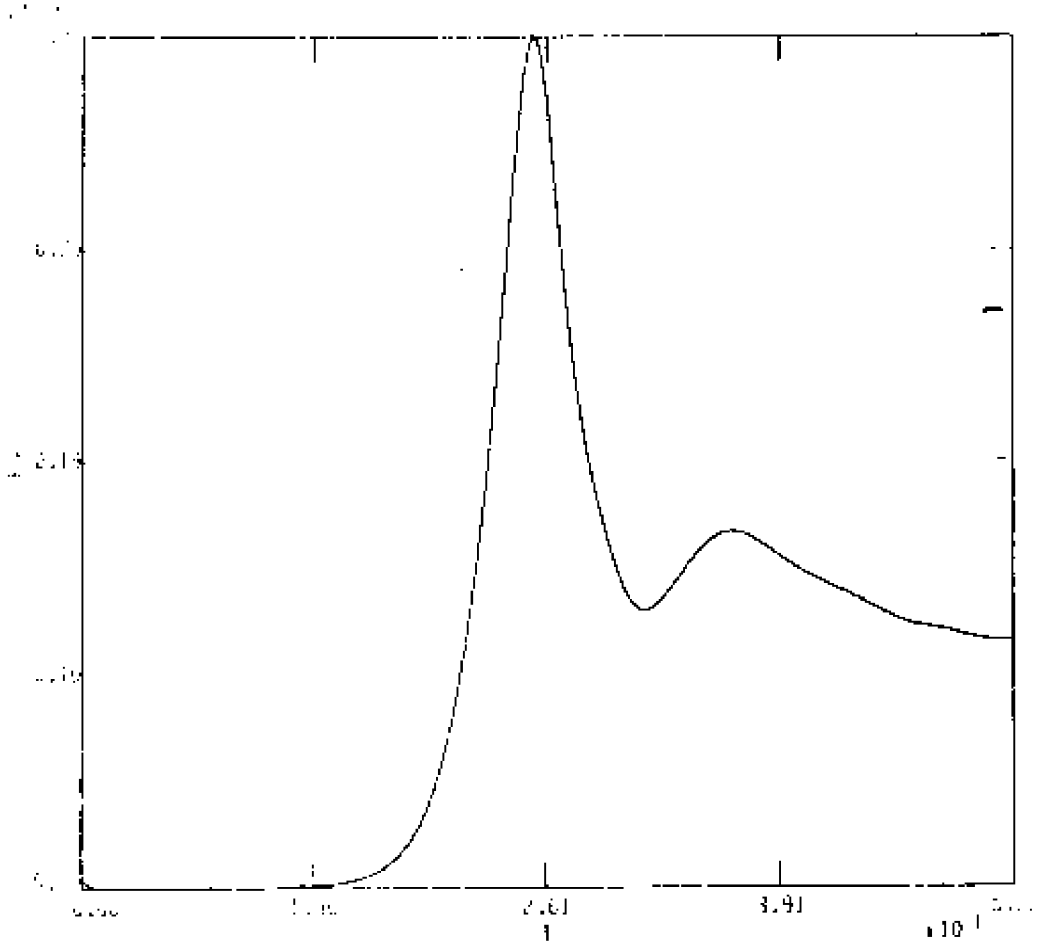

Figure 69. - Globals for CASE 5, E_p = 0/200, ν = 0.0:
69(a): kinetic energy as a function of time.

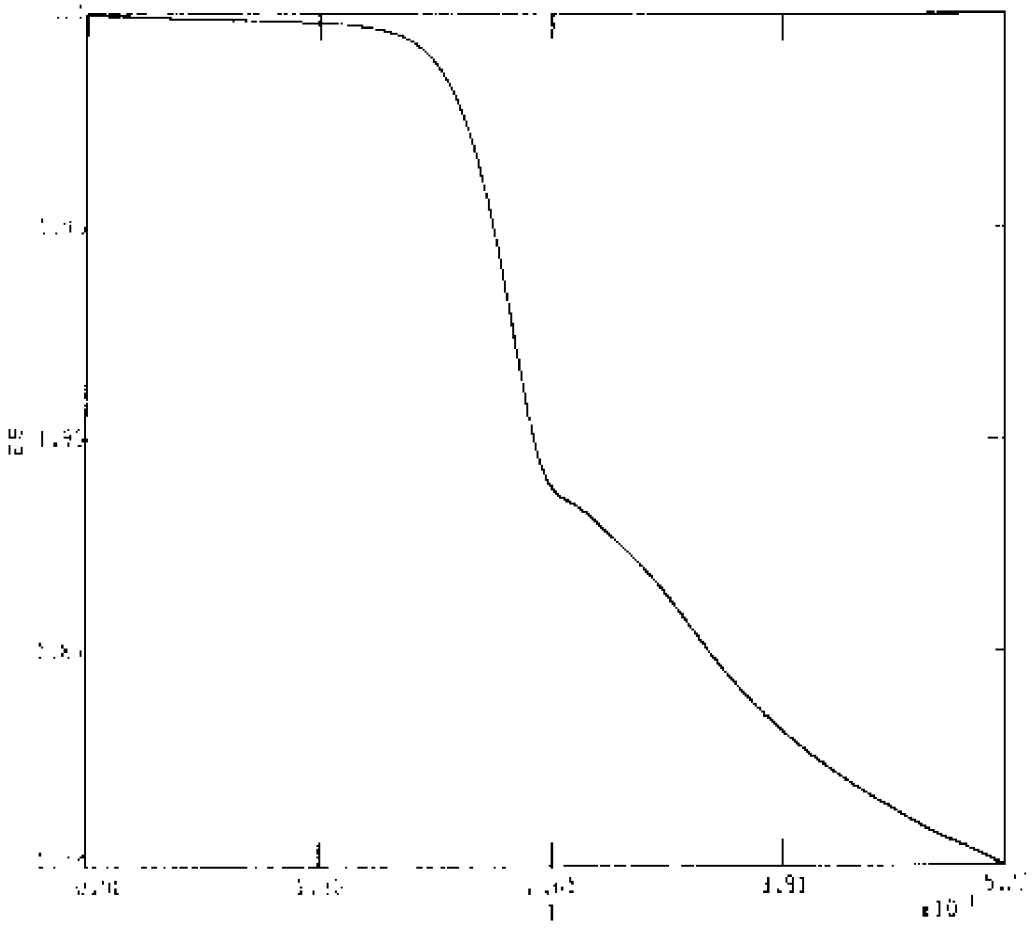

69(b): magnetic energy as a function of time, and

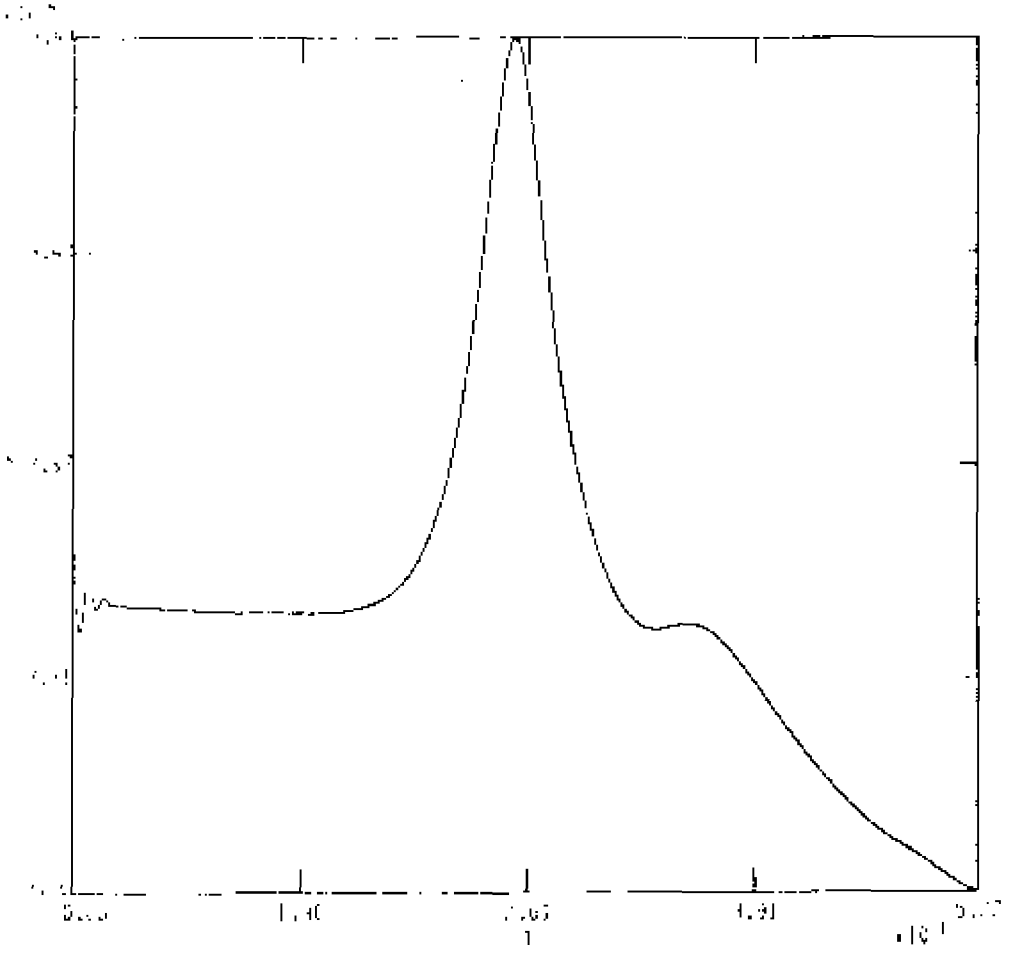

69(c): total integrated current as a function of time.

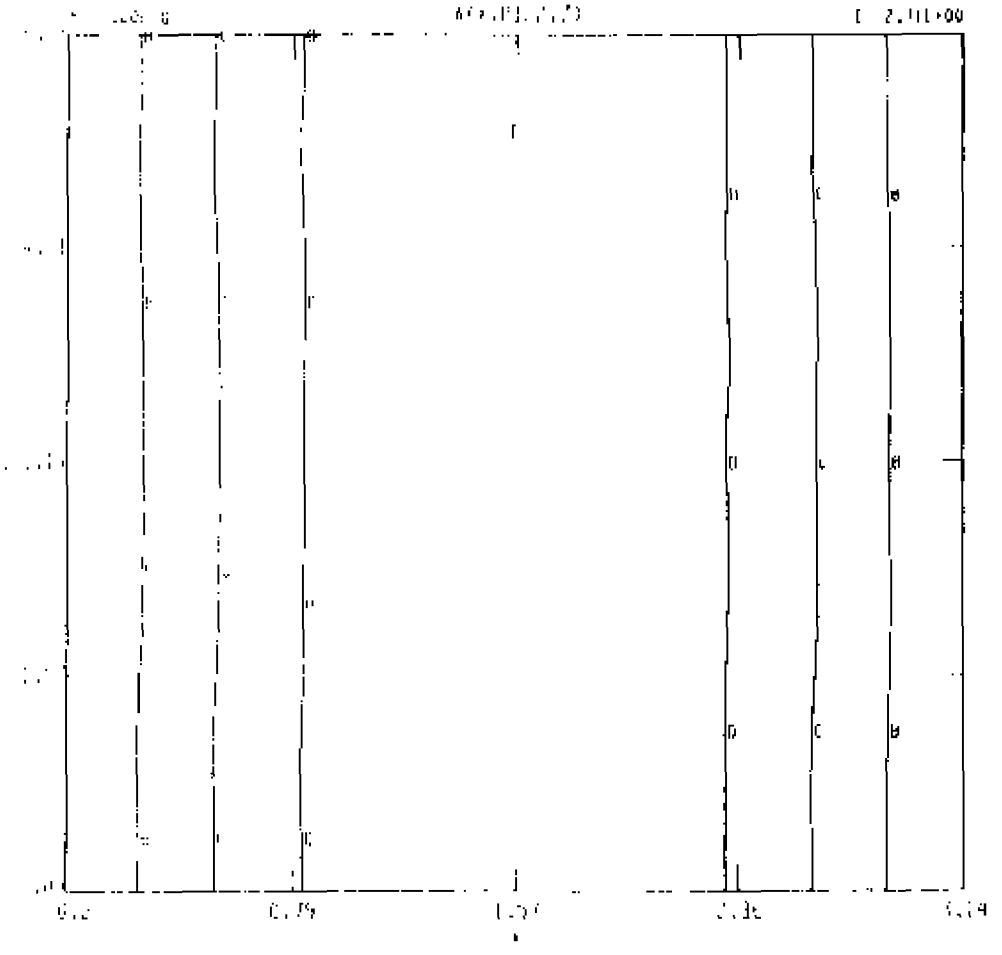

Figure 70. - Contours at t = 26.76, for CASE 5, E_o = 0/200, ψ = 0.0:
70 (a) : contours of A = constant, toroidal cut,

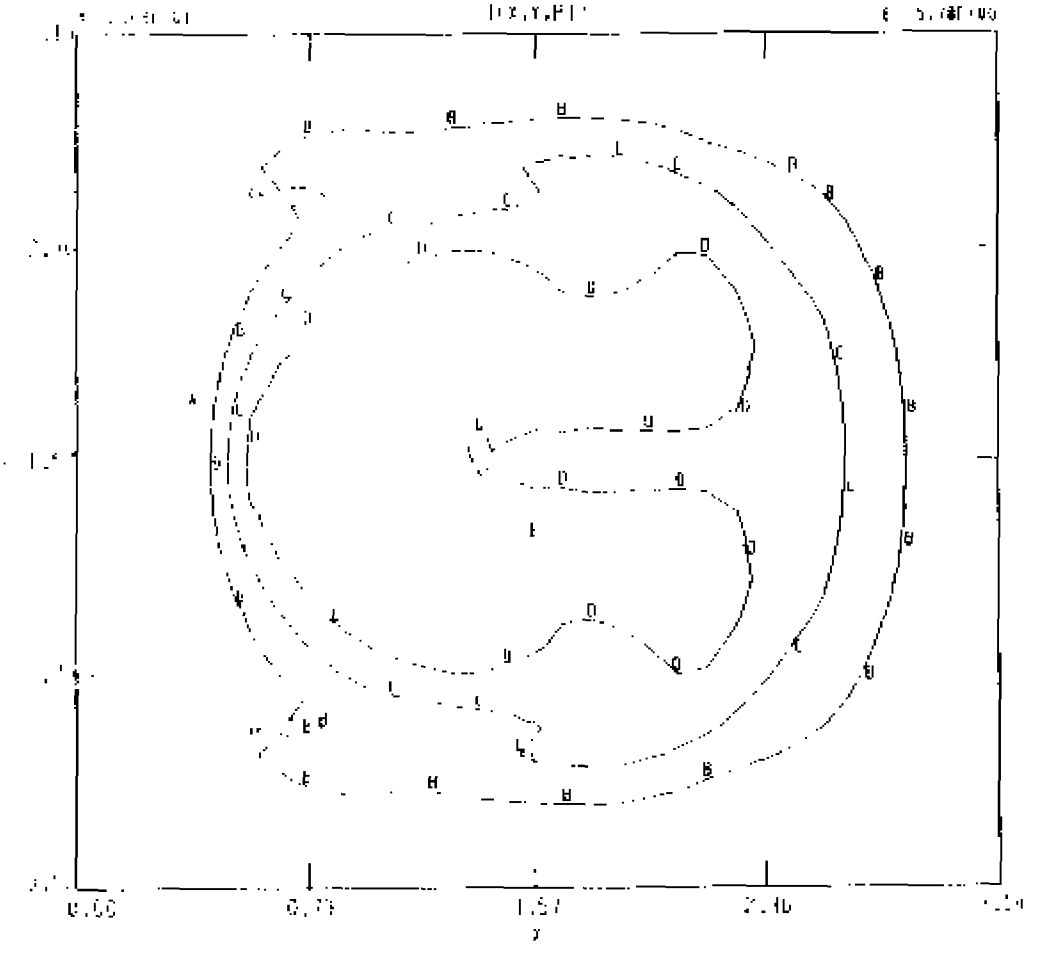

70 (b): contours of j = constant, poloidal cut,

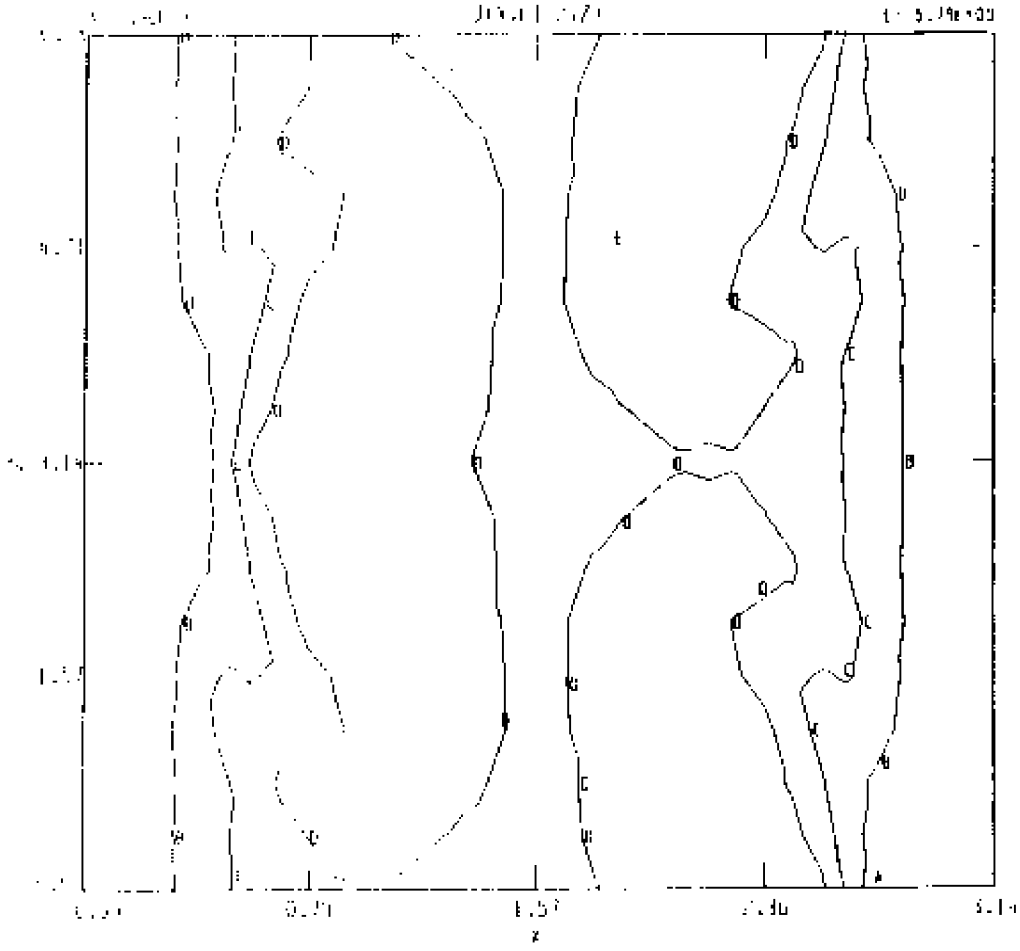

78 (c): contours of j * constant, poloidal cut,

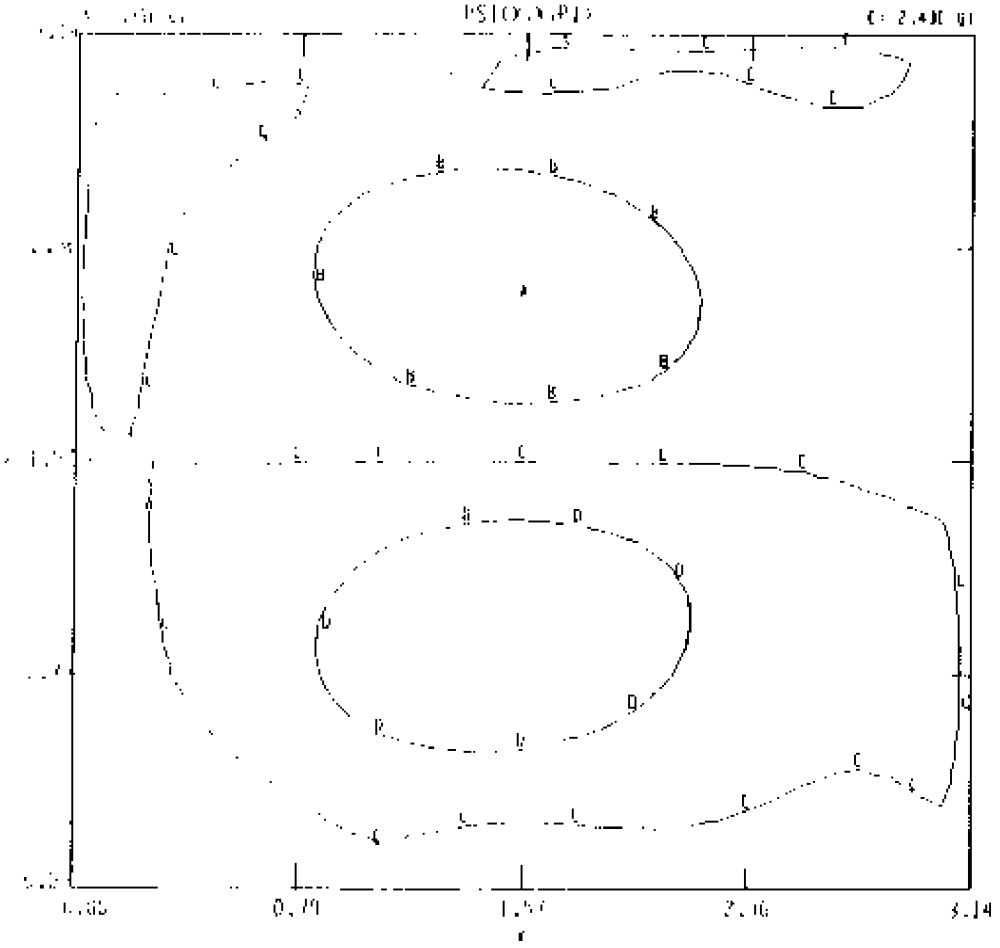

7 (d) : contours of Ψ = constant, poloidal cut.

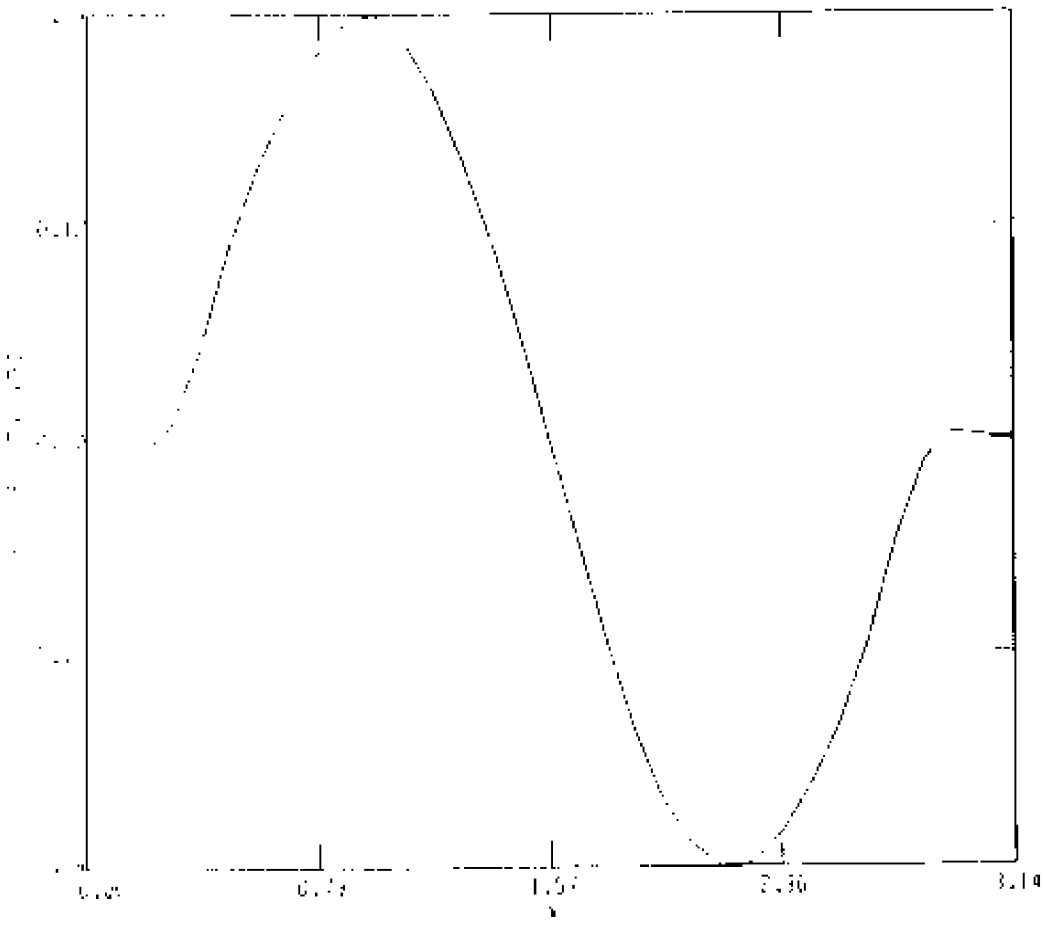

78 (e) : slice of $\Psi(x = \pi/2, y, z = \pi)$, and

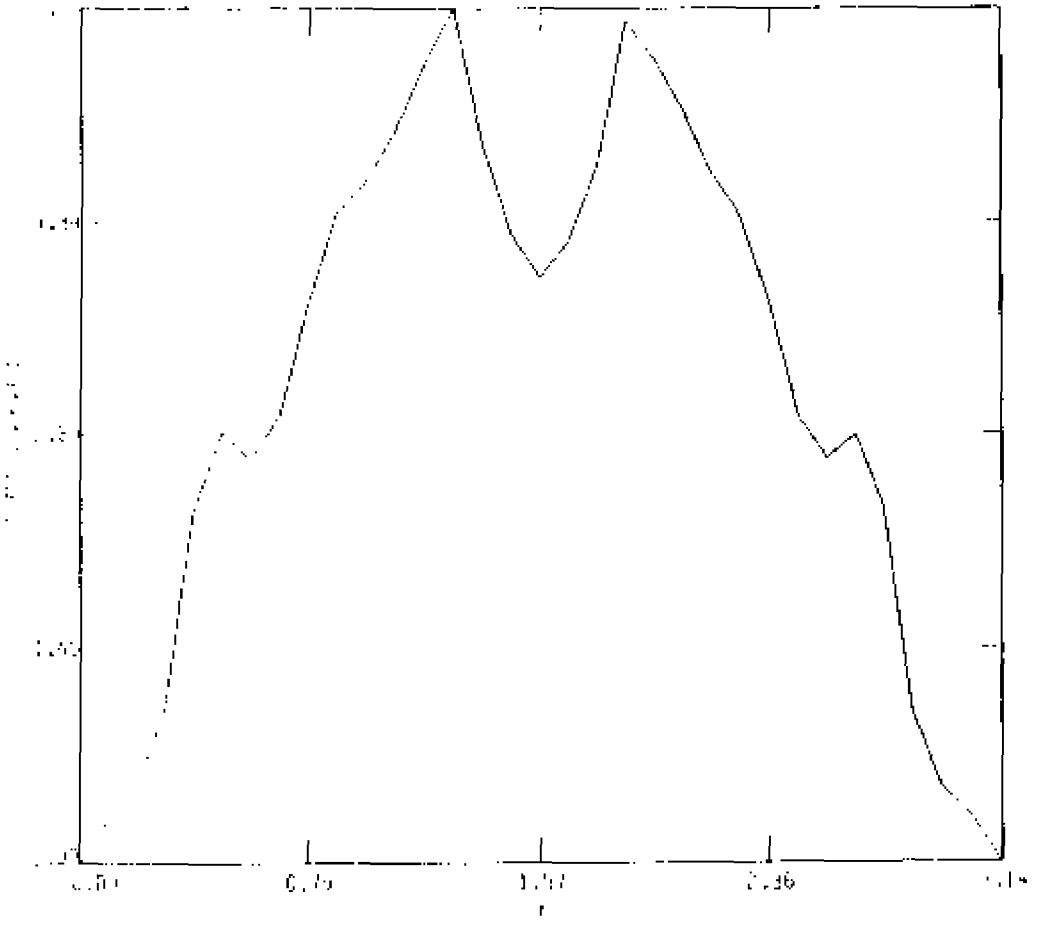

78 (f) : slice of j (x = π/ 2, y, z = π).

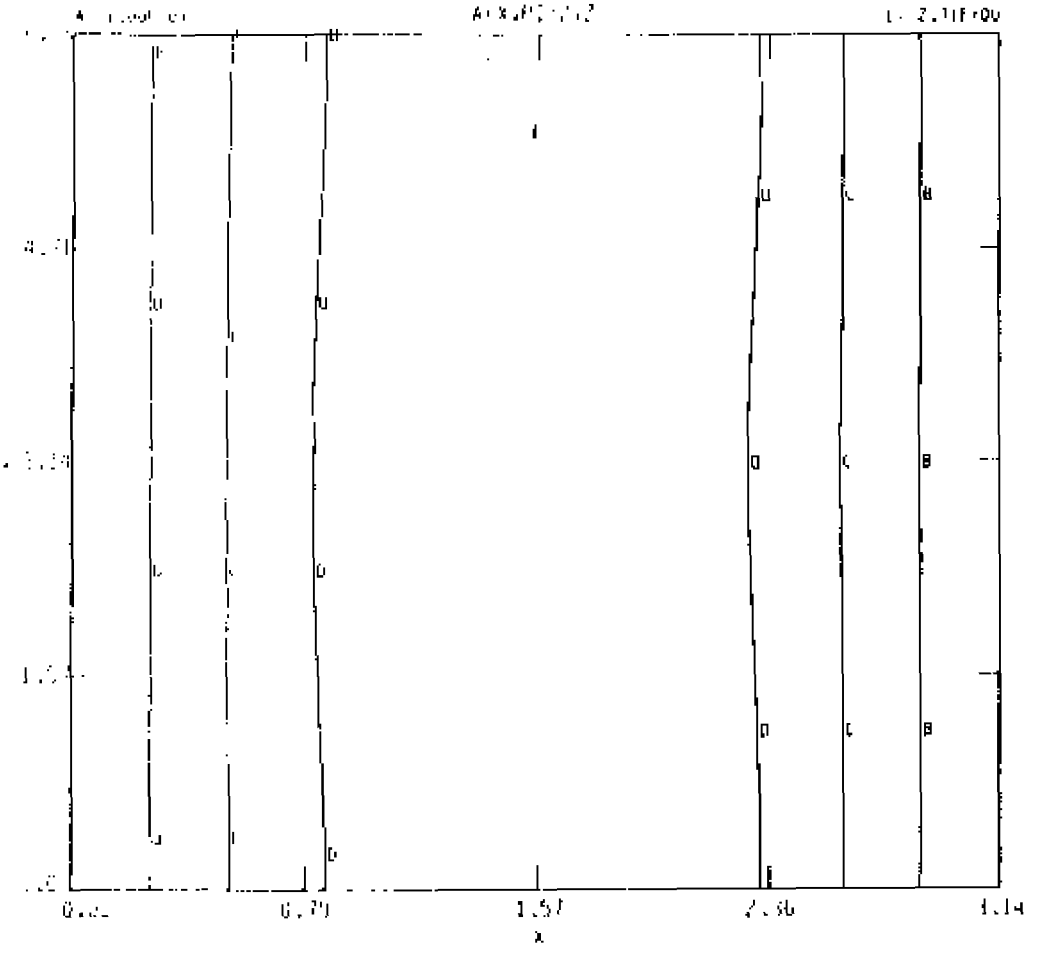

Figure 71. - Contours at t = 35.84, for CASE 5, E_0 = 0/200, υ = 0.9:
71 (a) : contours of A = constant, toroidal cut.

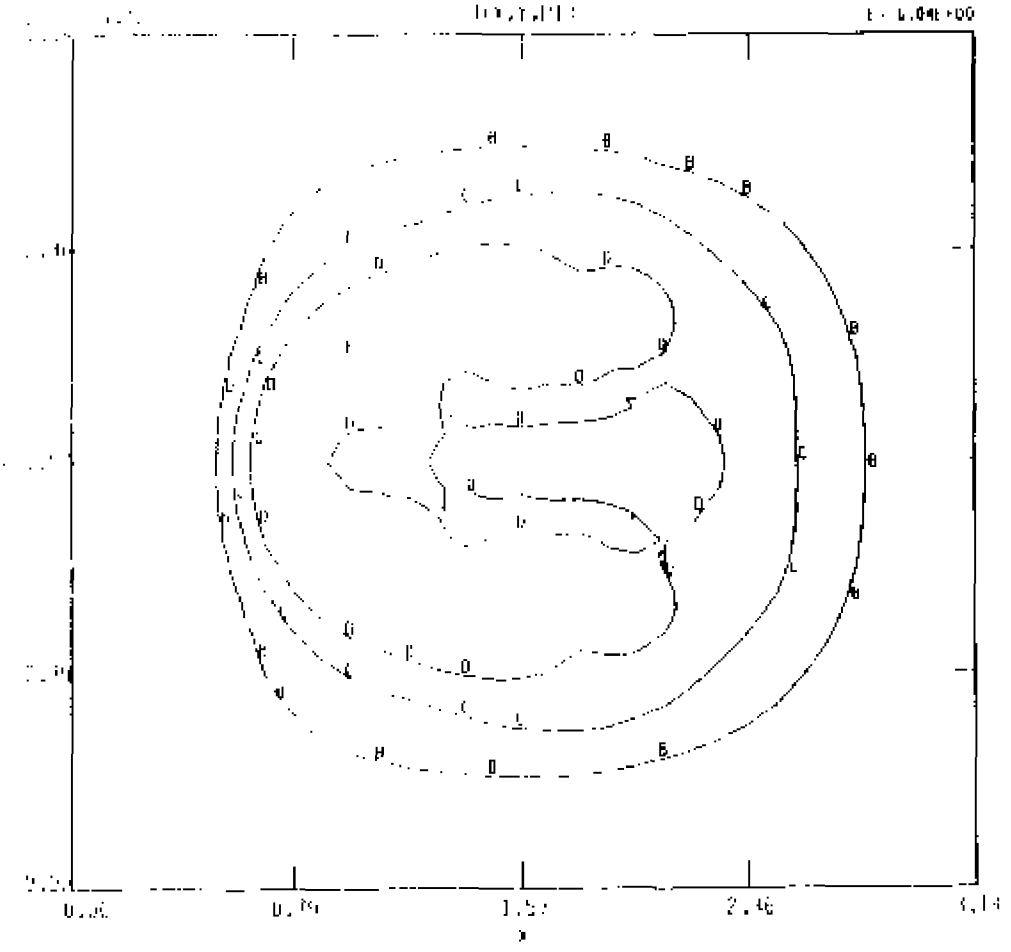

71 (b): contours of j = constant, poloidal cut.

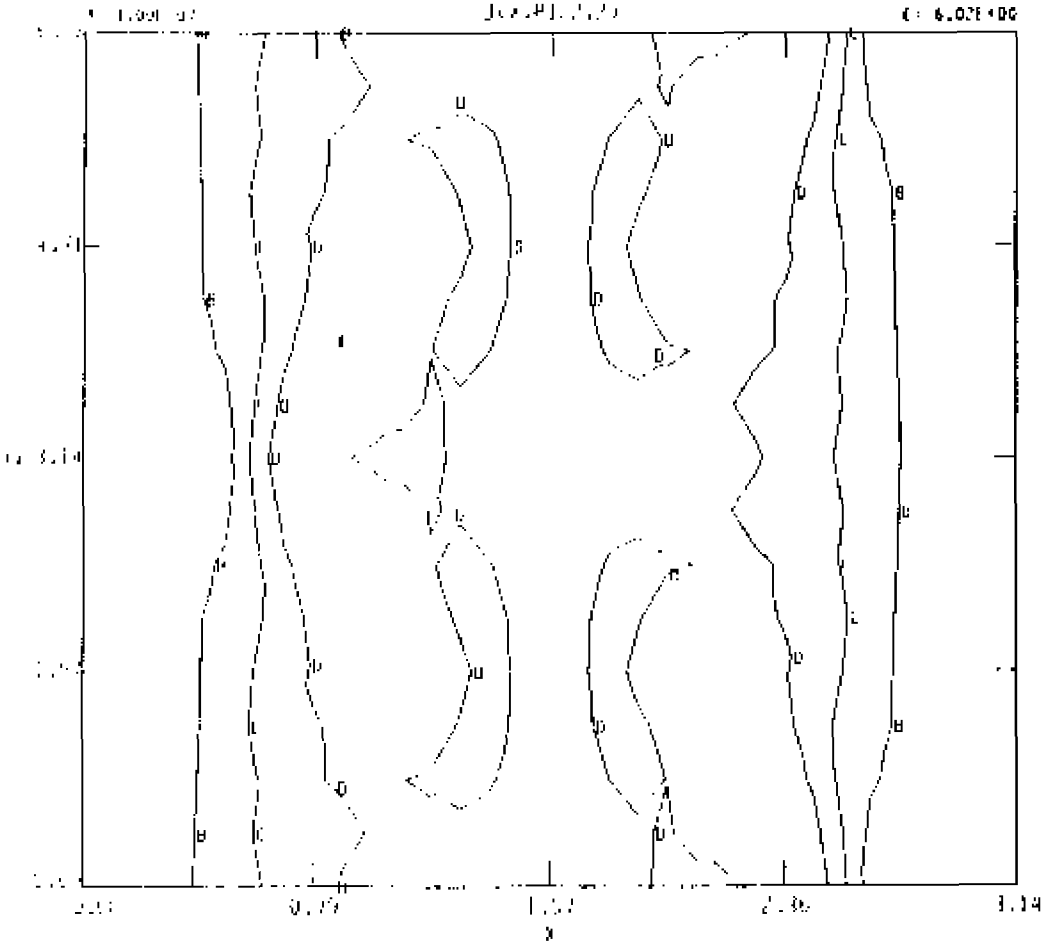

71 (c): contours of j = constant, toroidal cut.

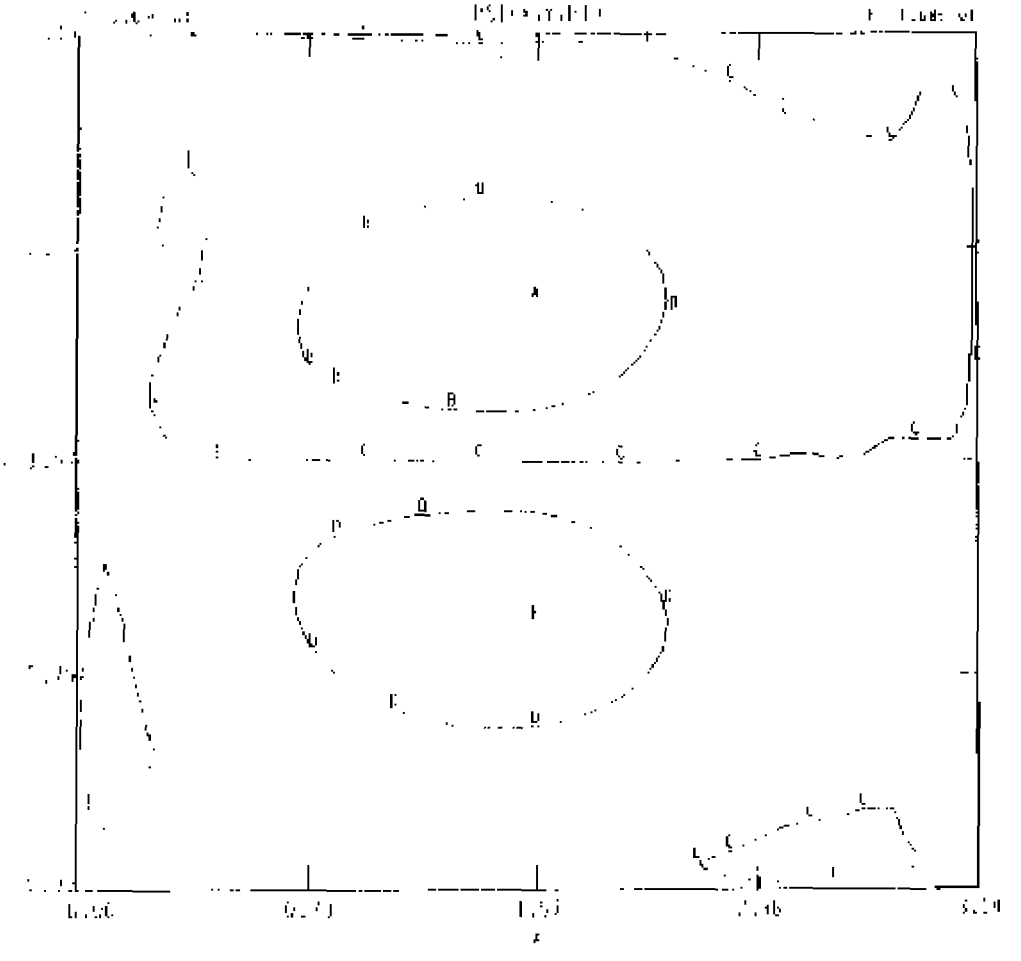

71 (d) : contours of Ψ= constant, poloidal cut.

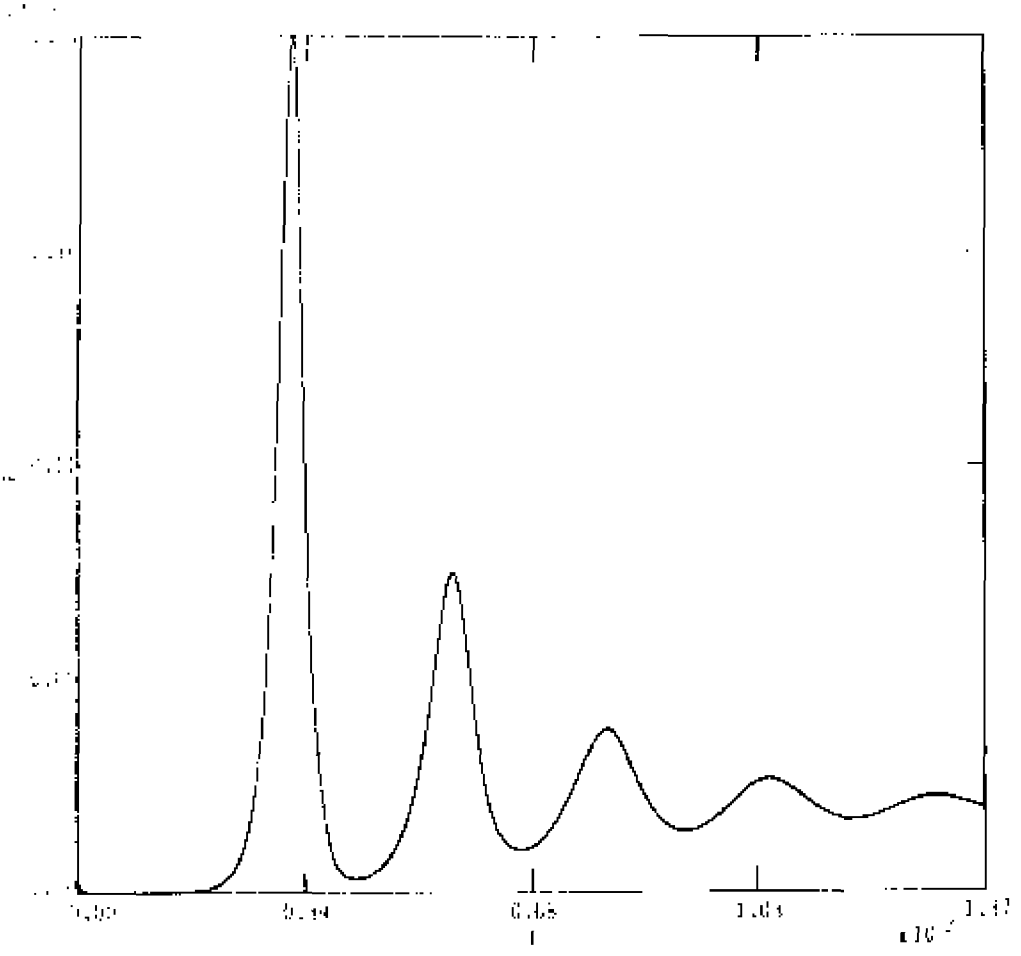

Figure 72. - Globals, CASE 5, with E_o = 0/200, υ = 0.01, 72(a): kinetic energy as a function of time.

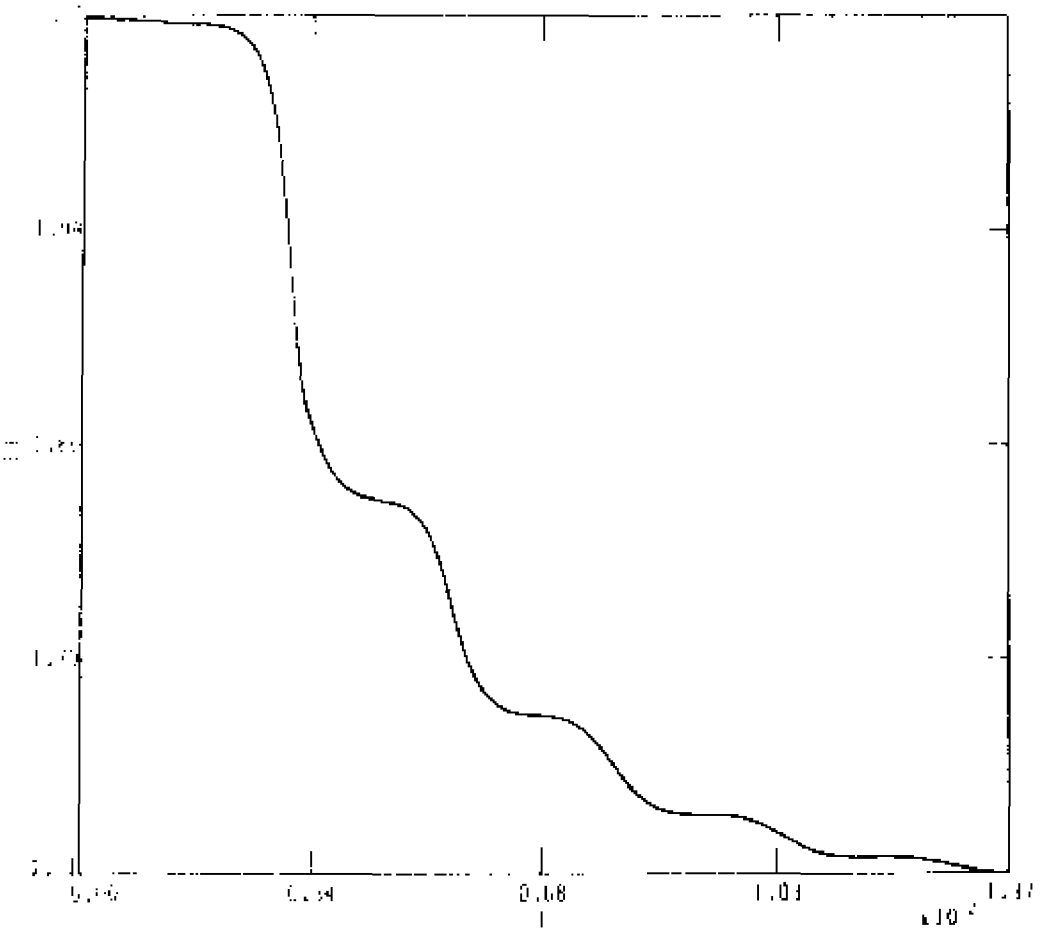

72(b): magnetic energy as a function of time.

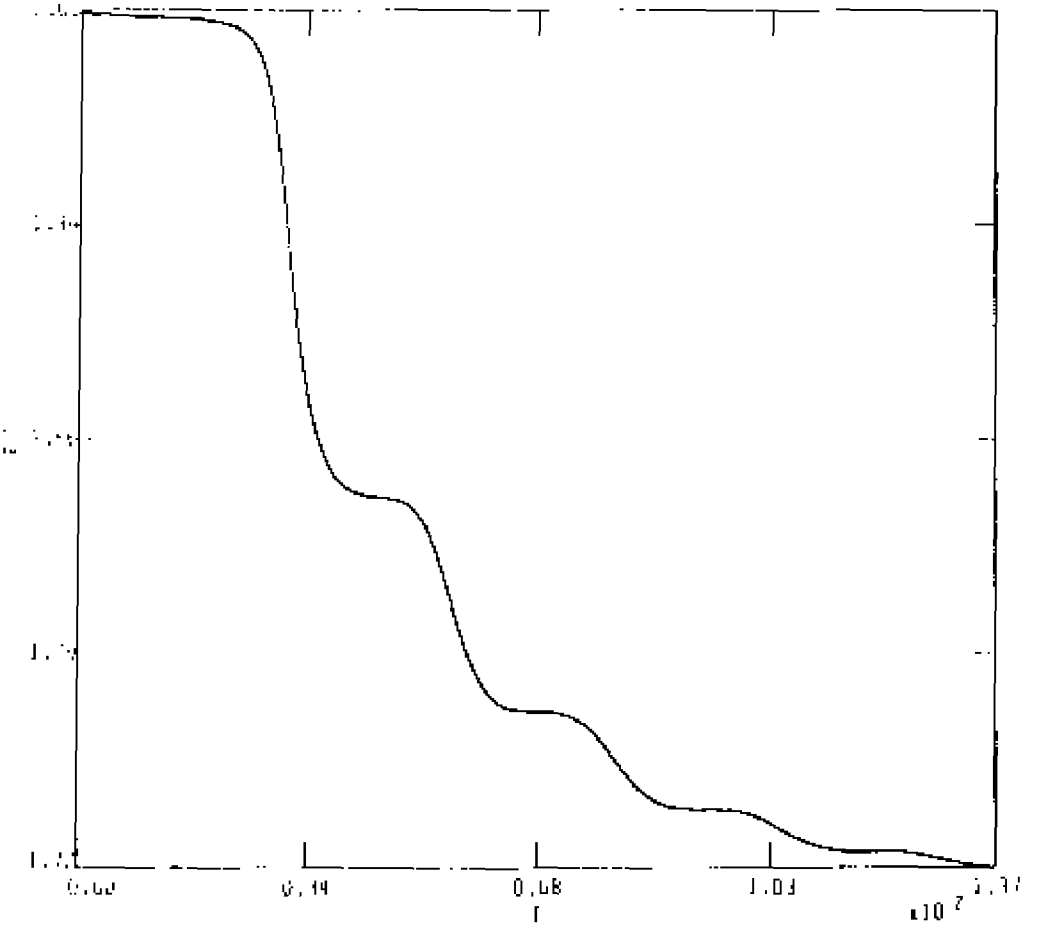

72(c): total energy as a function of time.

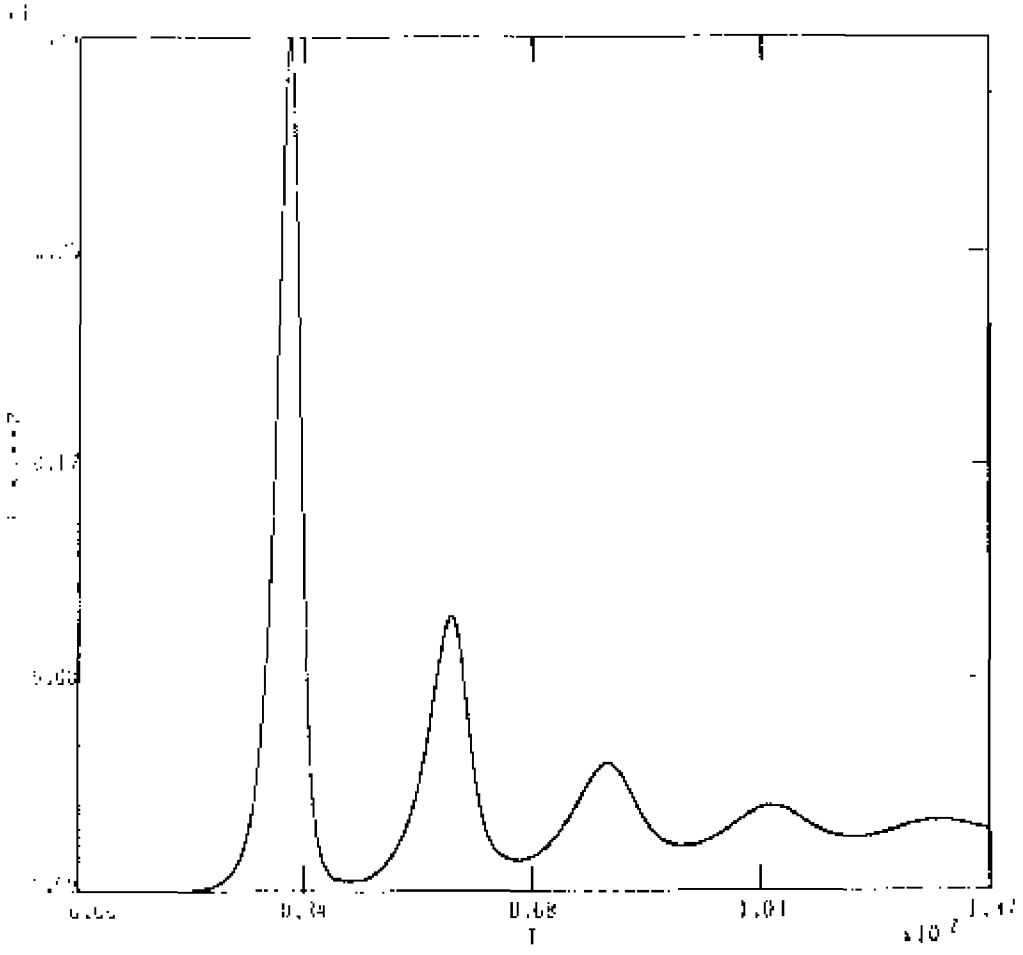

72(d): half the mean square stream function as a function of time,

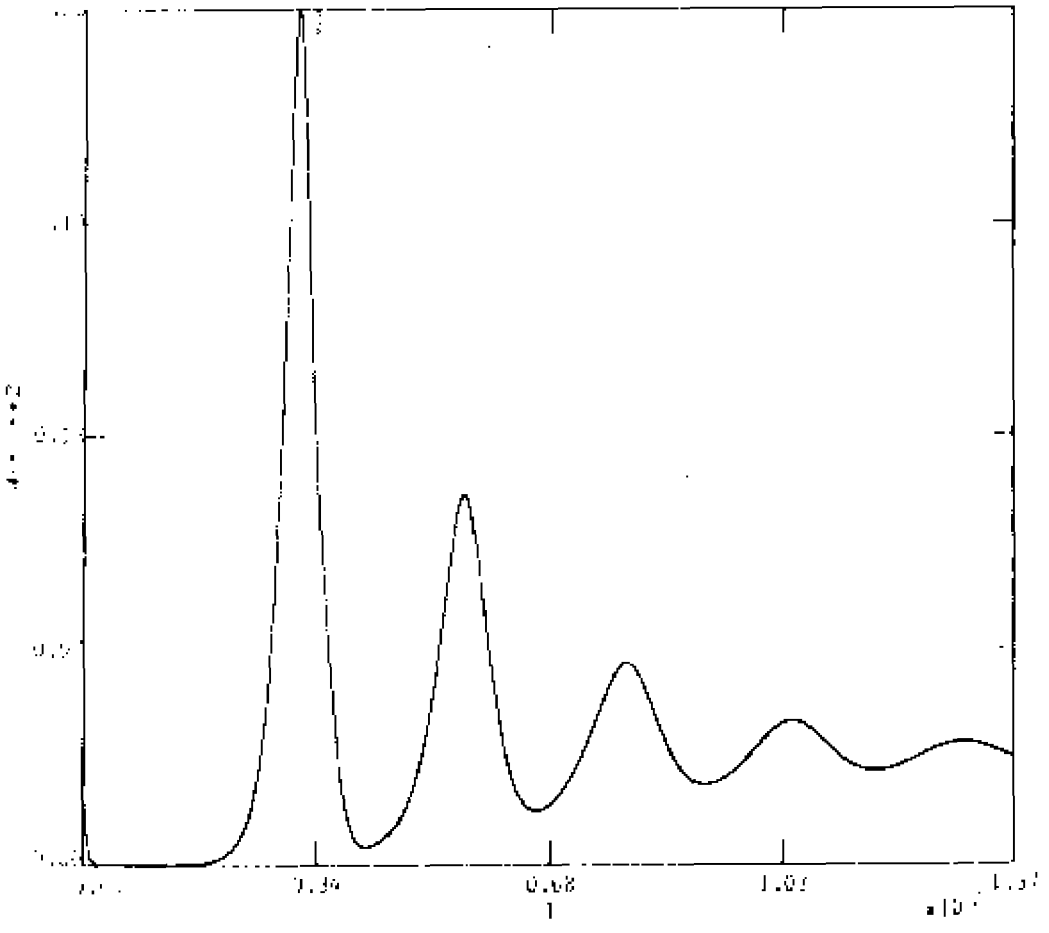

72(e): half the mean square vorticity as a function of time.

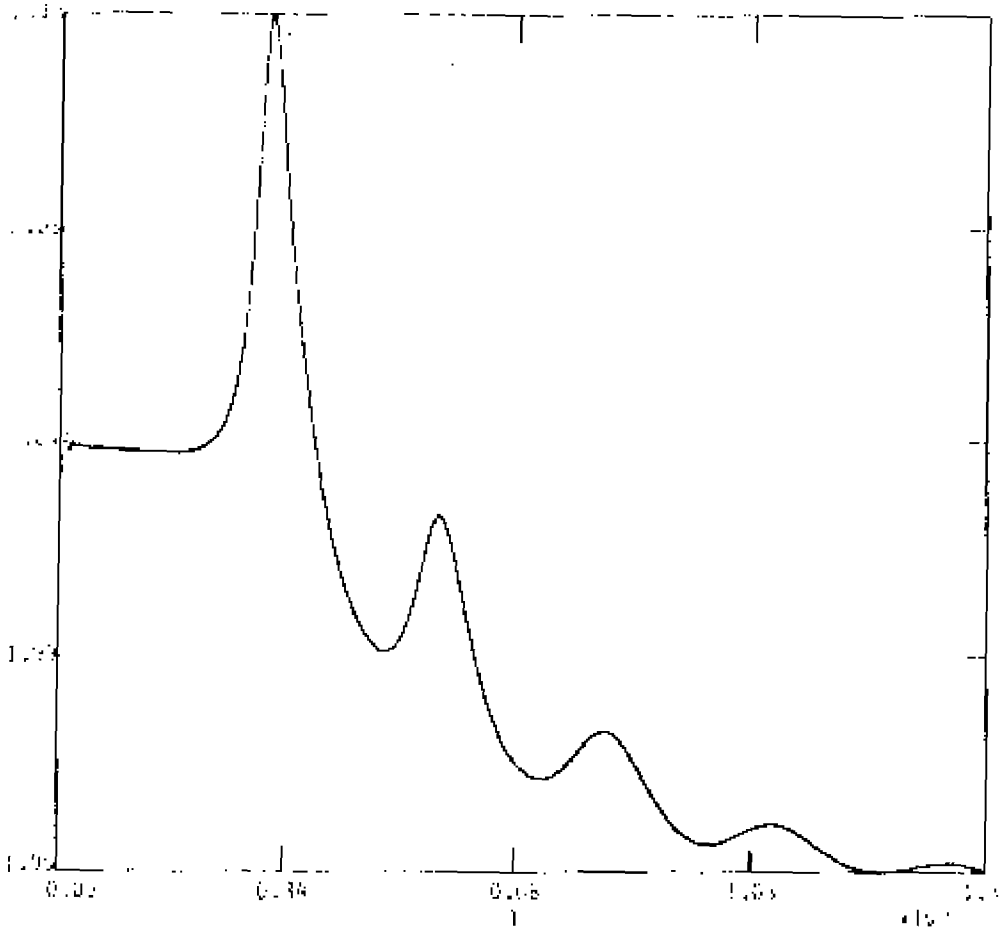

72(f): total integrated current as a function of time.

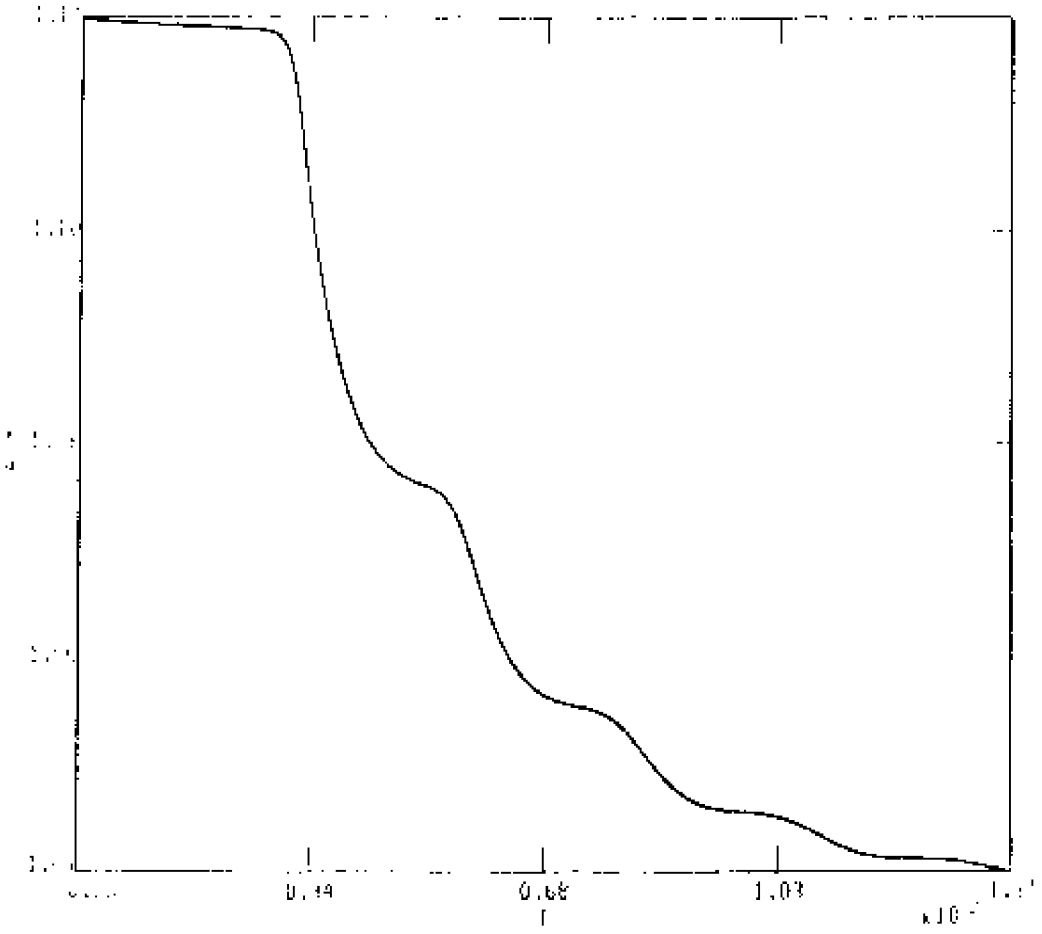

72(g): total integrated vector potential as a function of time.

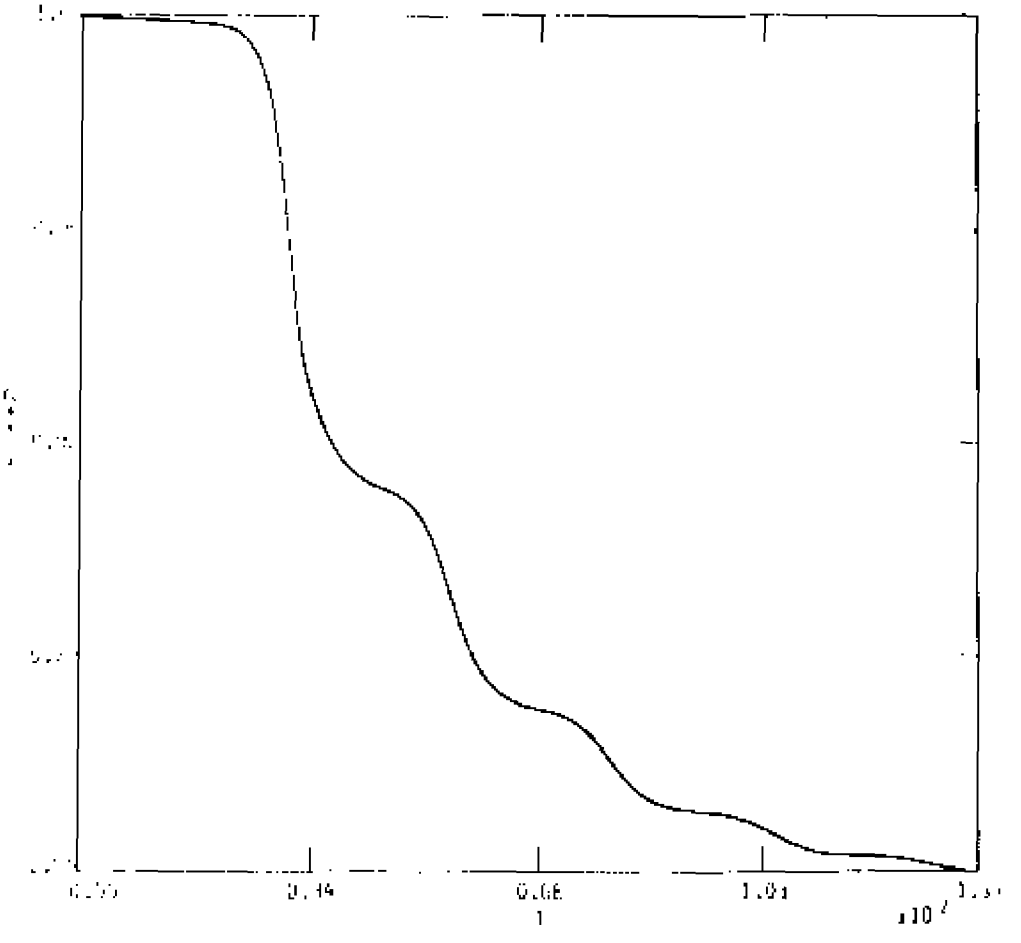

72(h): half the mean square vector potential as a function of time, and

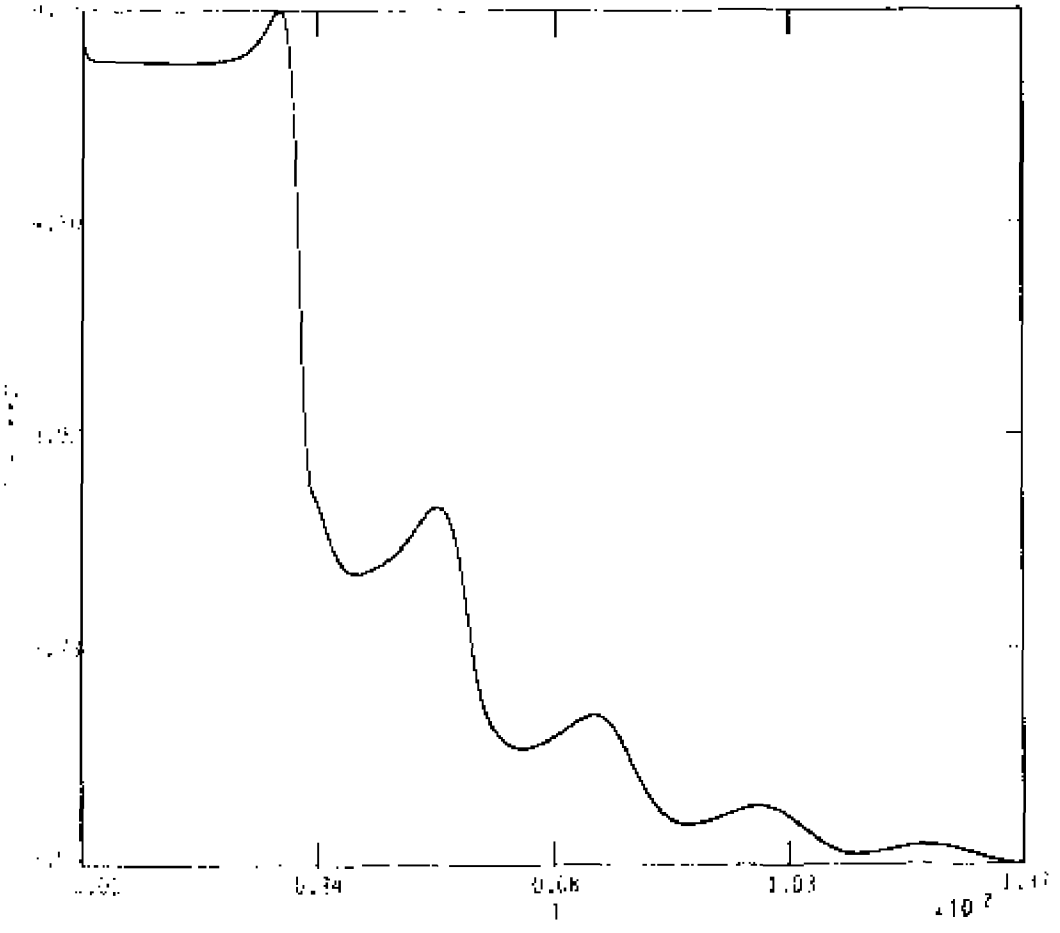

72(i): half the mean square current as a function of time.

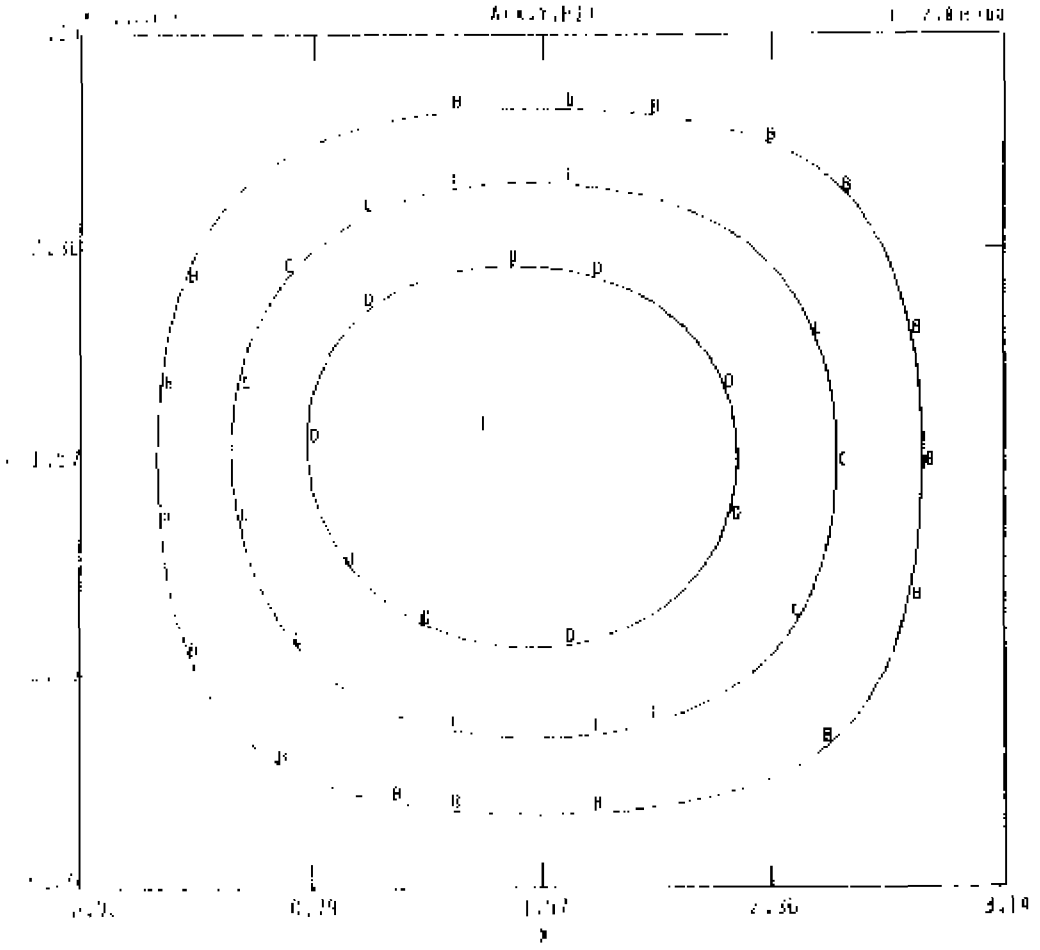

Figure 73. - Contours at t = 29.28, for CASE 5, E_0 = 0/200, $\mathcal{V}$= 0.01:
73 (a): contours of A = constant, poloidal cut.

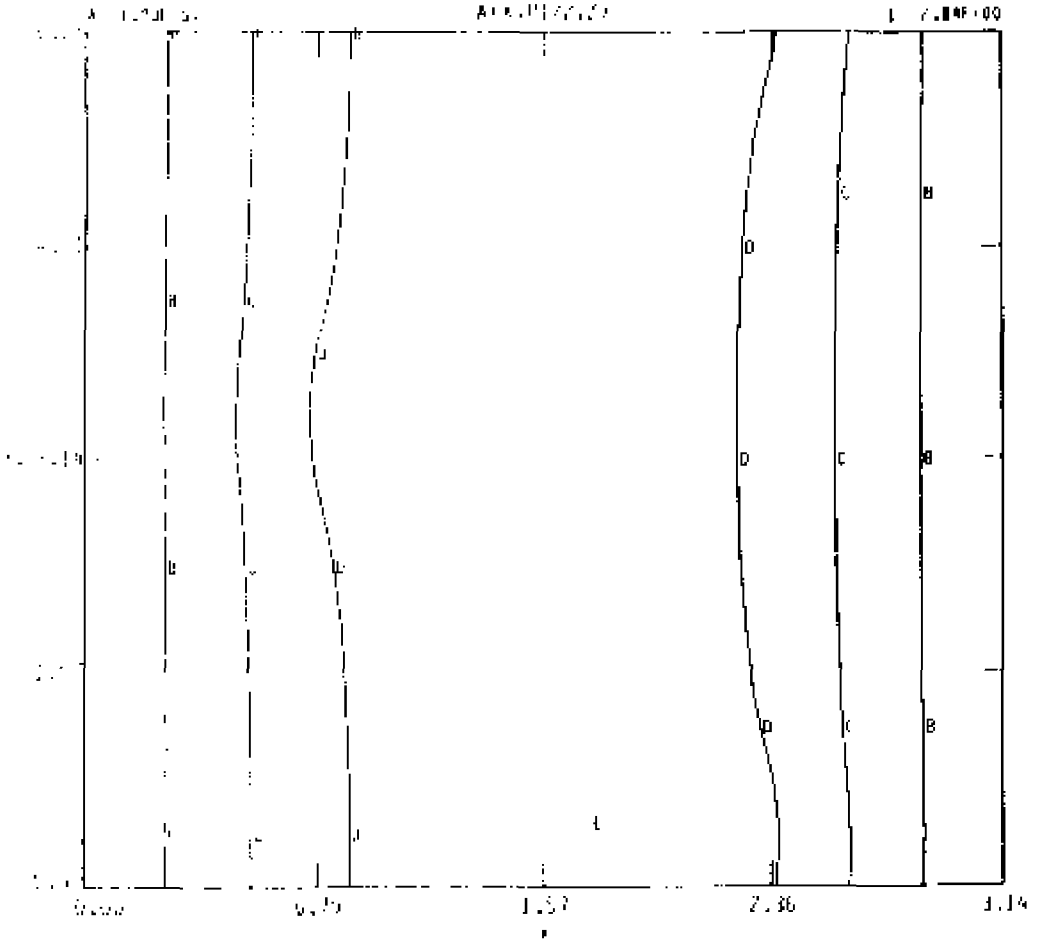

73 (b): contours of A = constant, toroidal cut.

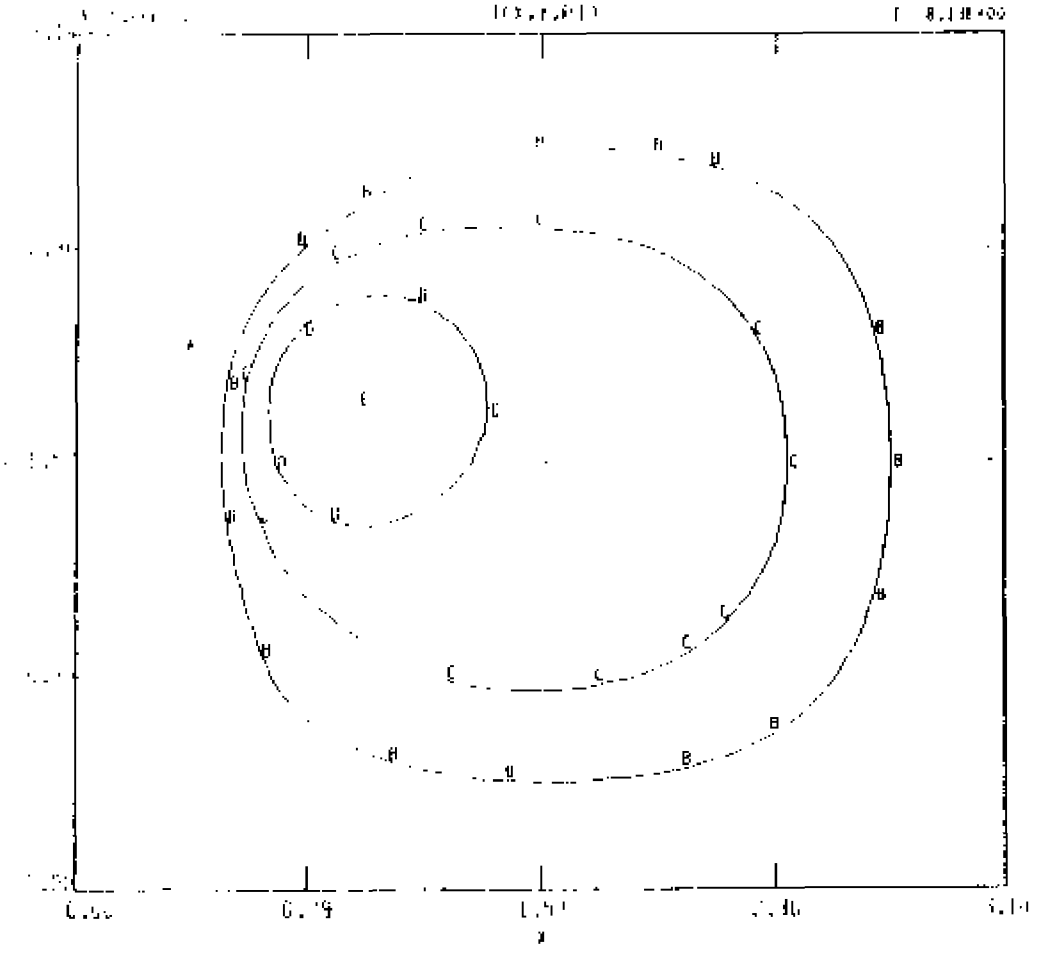

73 (c): contours of j = constant, poloidal cut.

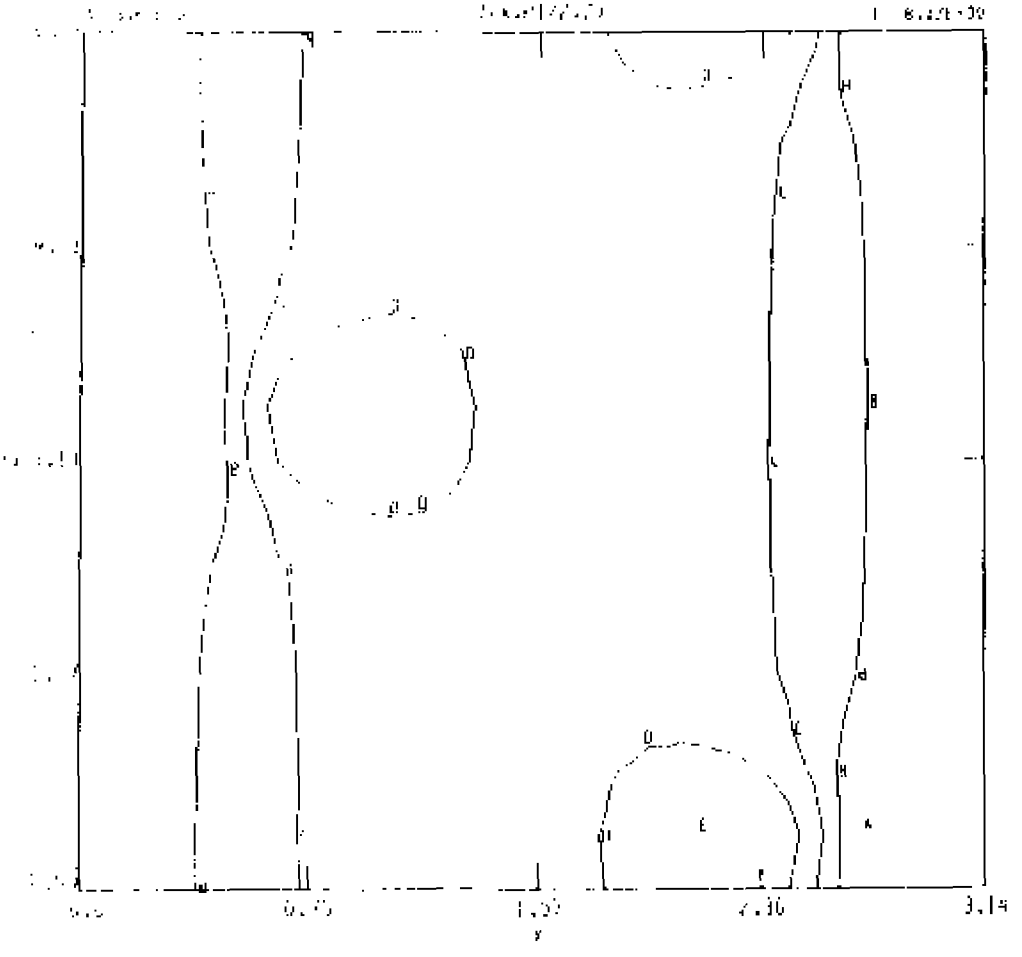

73 (d): contours of j = constant, toroidal cut.

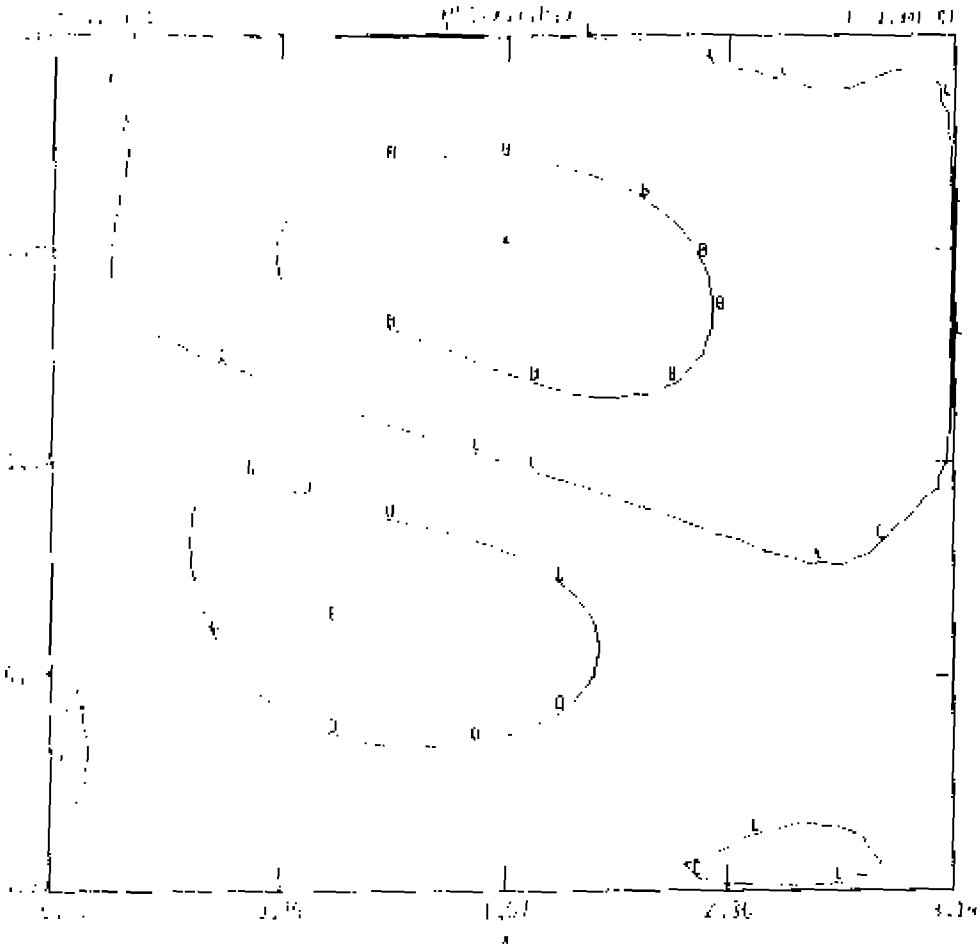

73 (e): contours of Ψ = constant, poloidal cut.

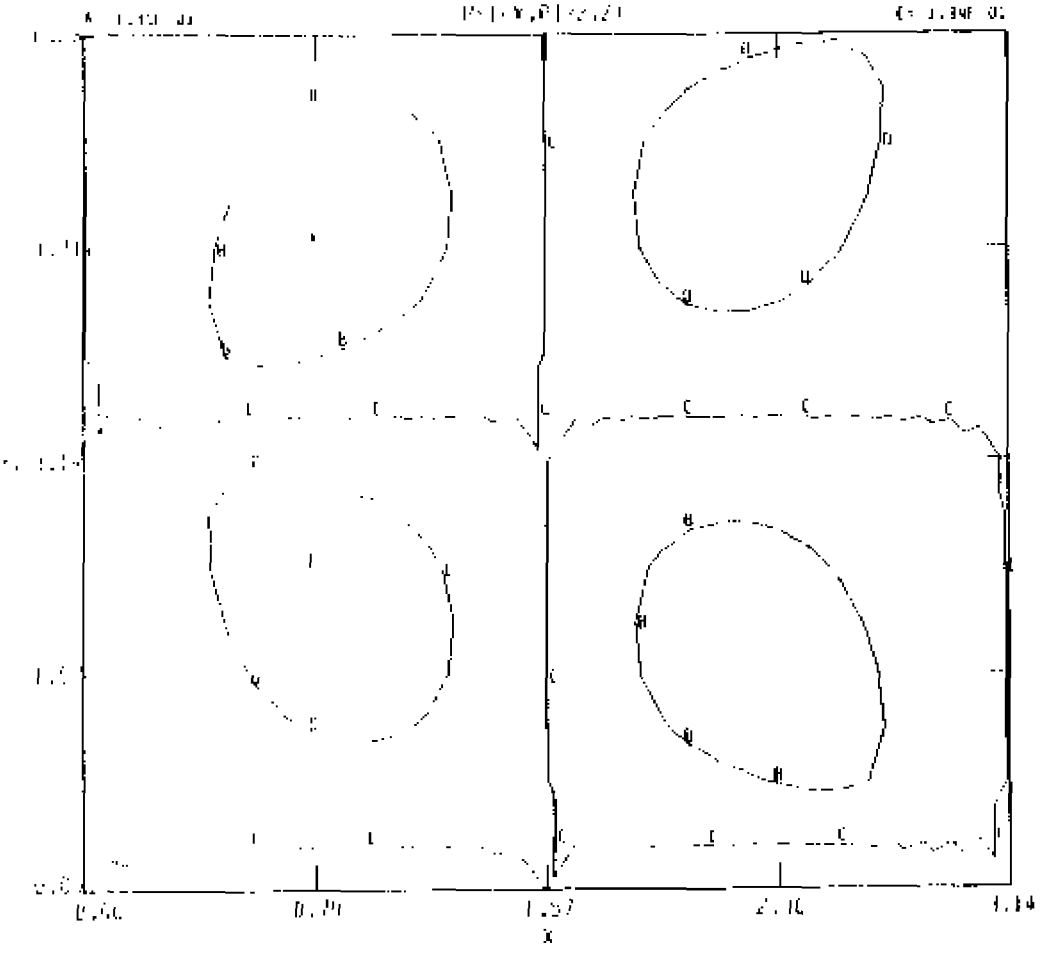

73 (f): contours of Ψ = constant, toroidal cut.

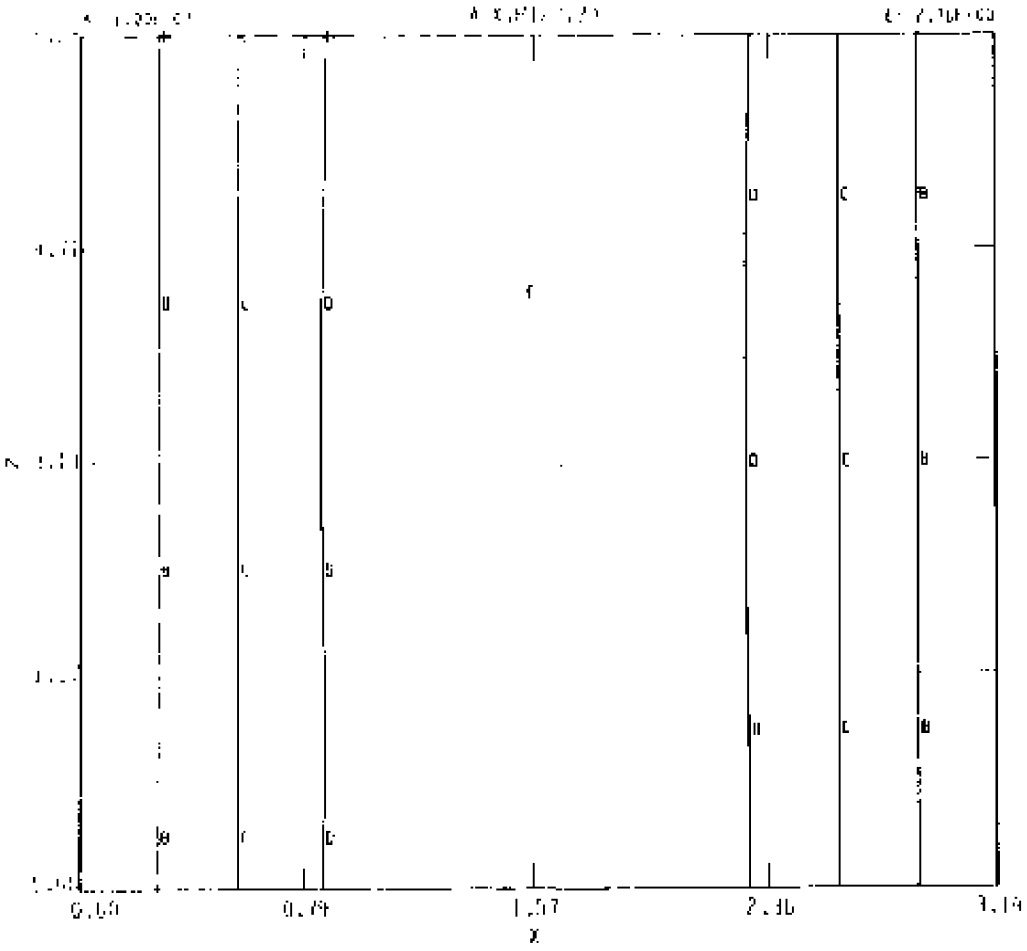

Figure 74. - Contours at t = 39.36, for CASE 5, B_0 = 8/200, υ = 0.01:
74 (a) : contours of A = constant, toroidal cut.

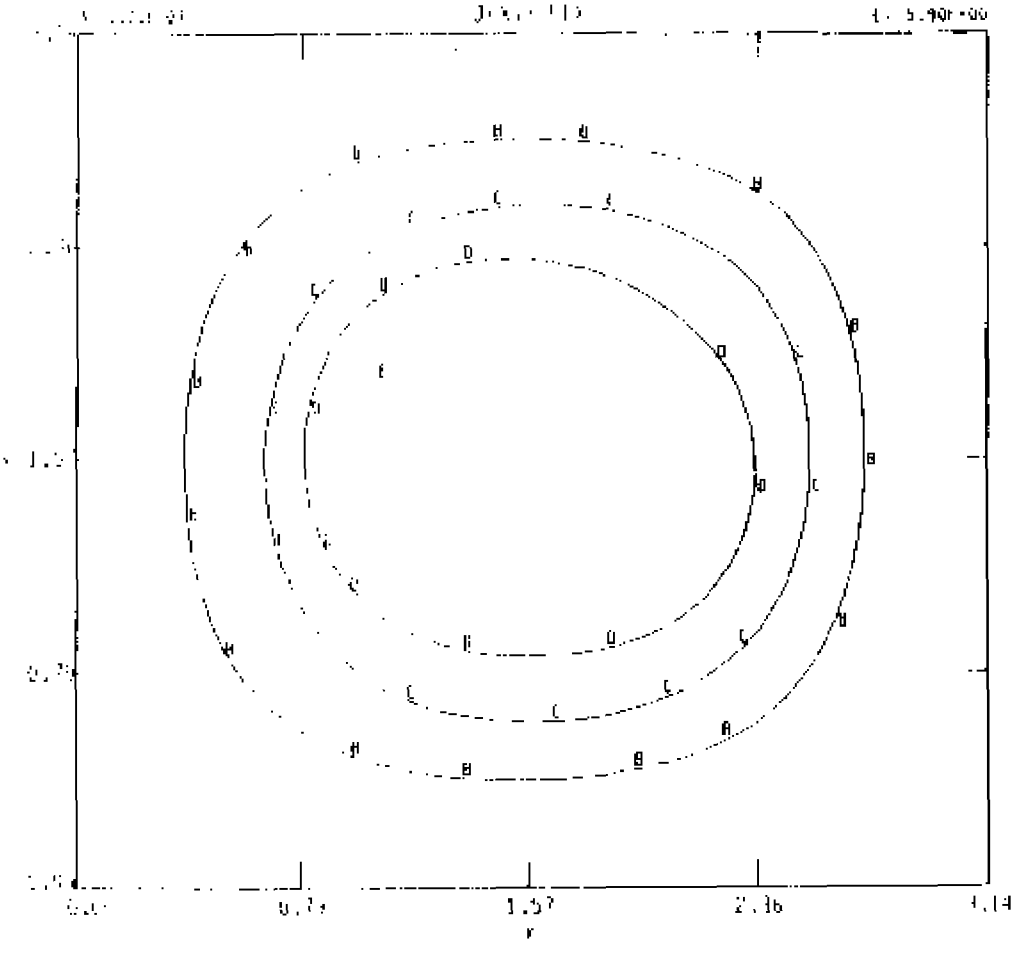

74 (b): contours of j = constant, poloidal cut.

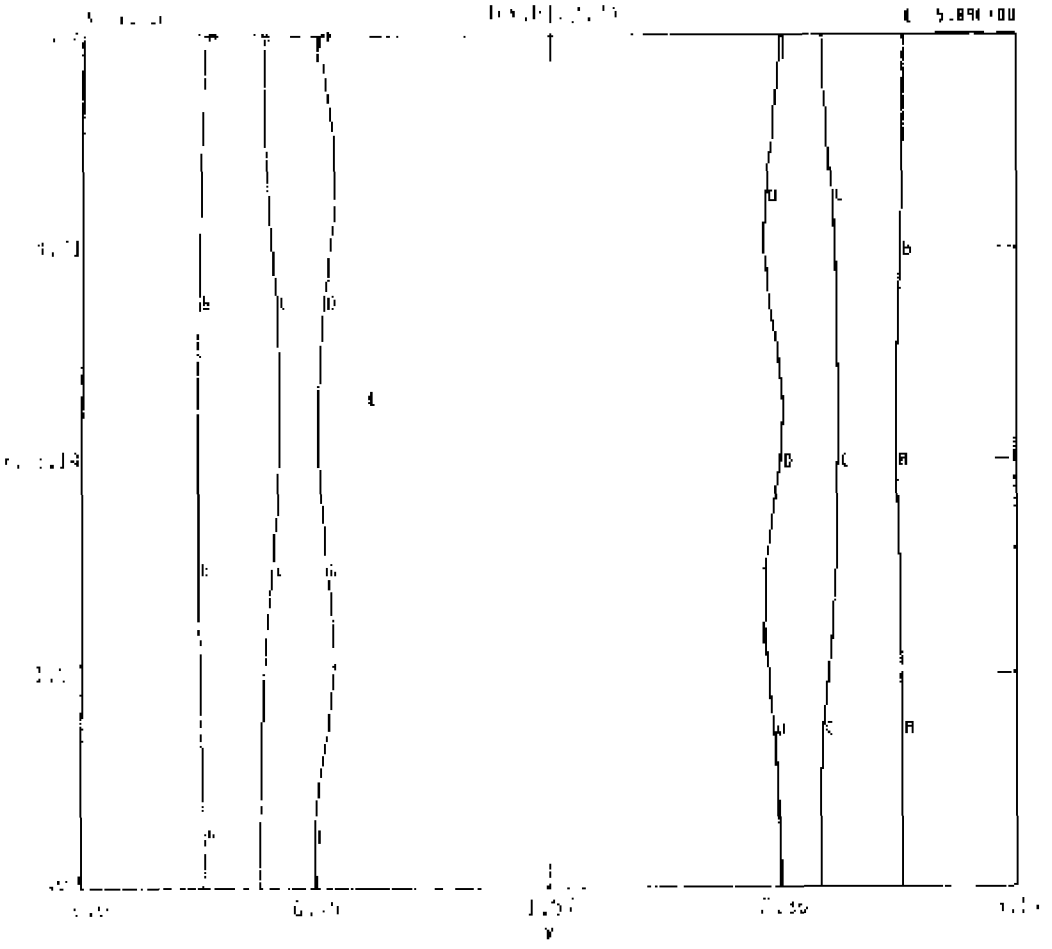

74 (c): contours of j = constant, toroidal cut, and

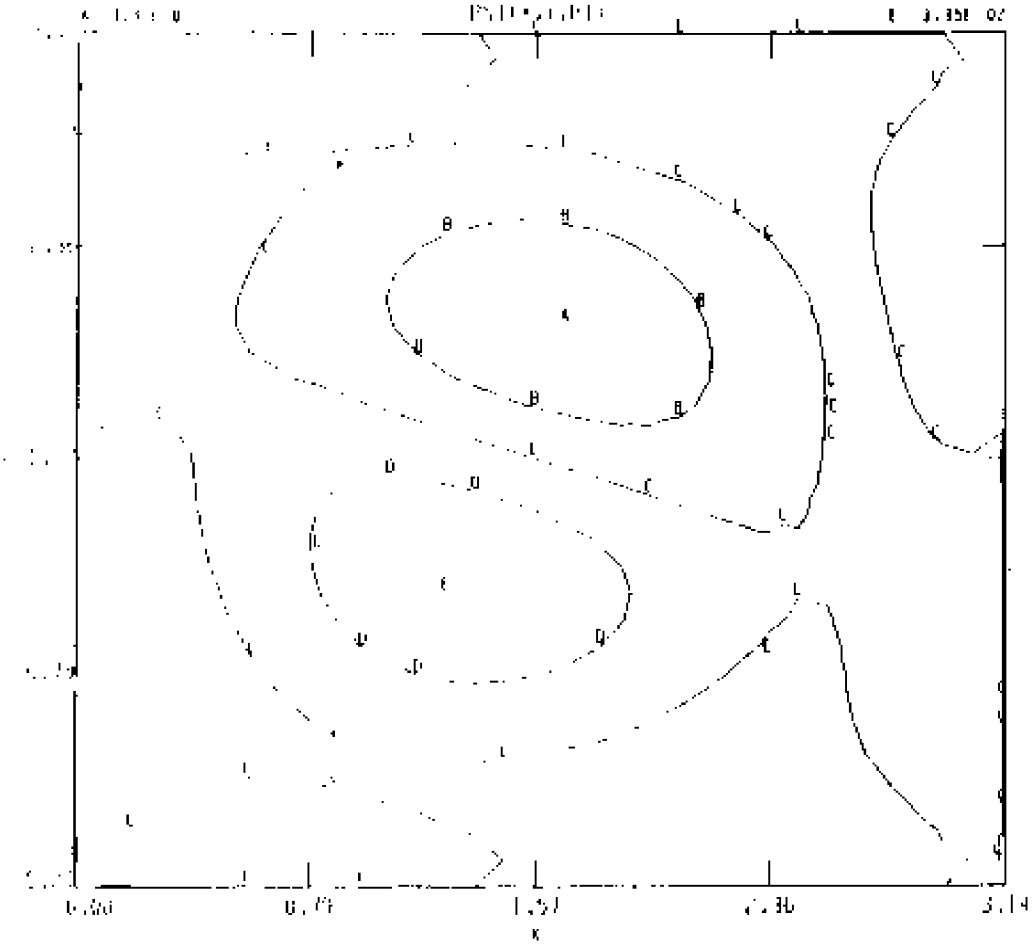

74 (d) : contours of Ψ = constant, poloidal cut.

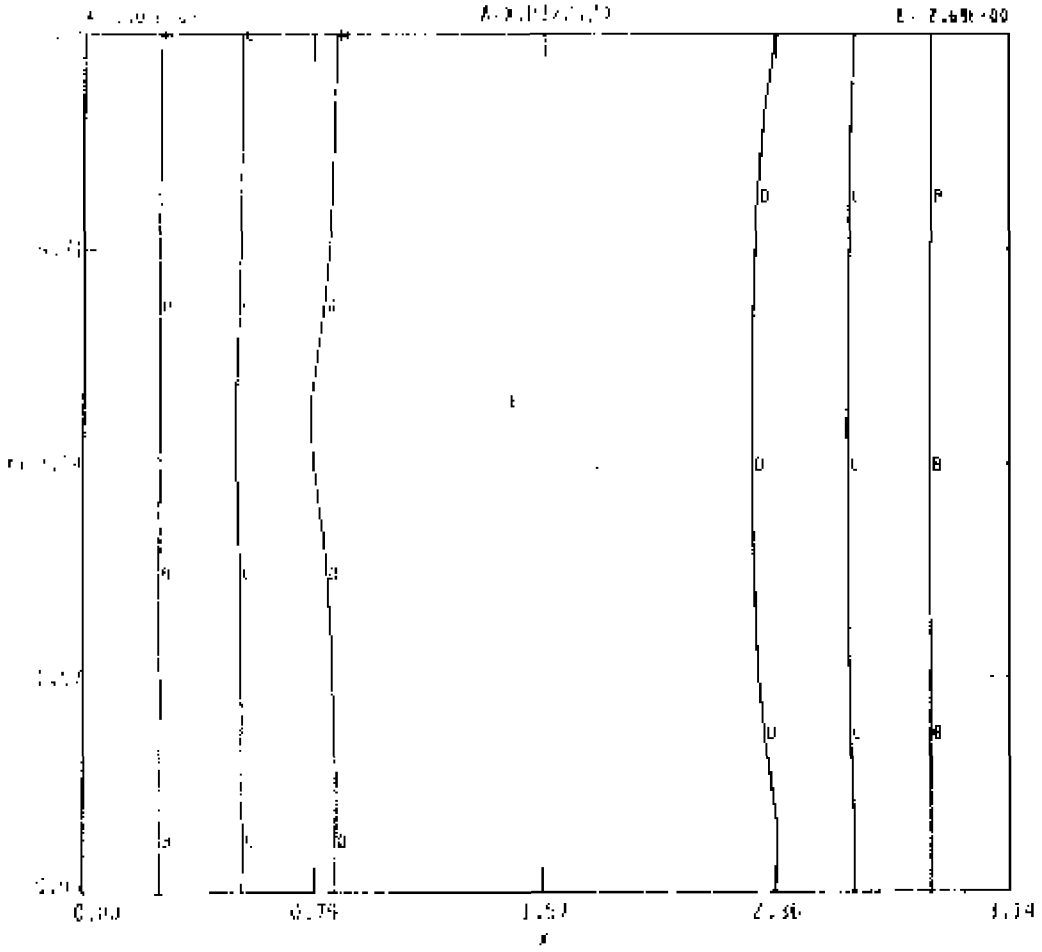

Figure 75. - Contours at t = 54.72, for CASE 5, E_o = 8/200, ν = 0.01:
75 (a) : contours of A = constant, toroidal cut.

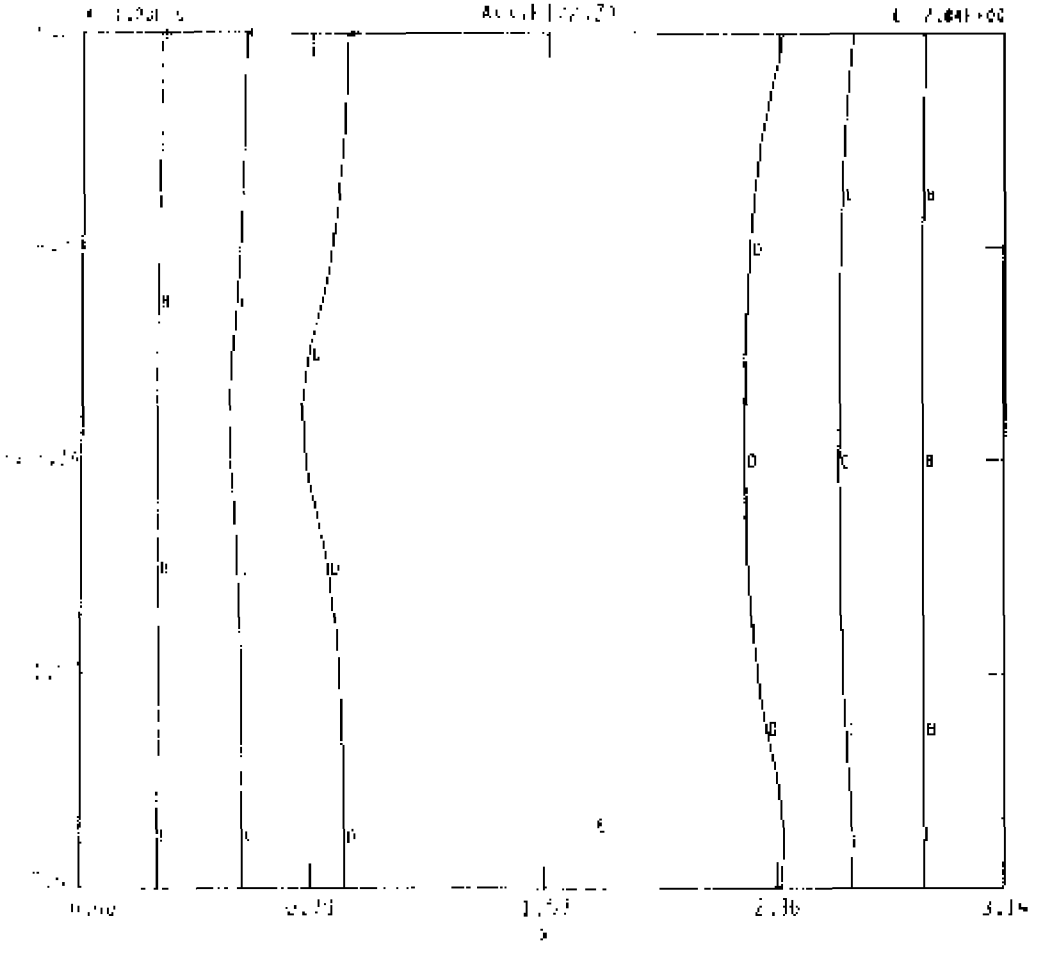

73 (b): contours of A = constant, toroidal cut.

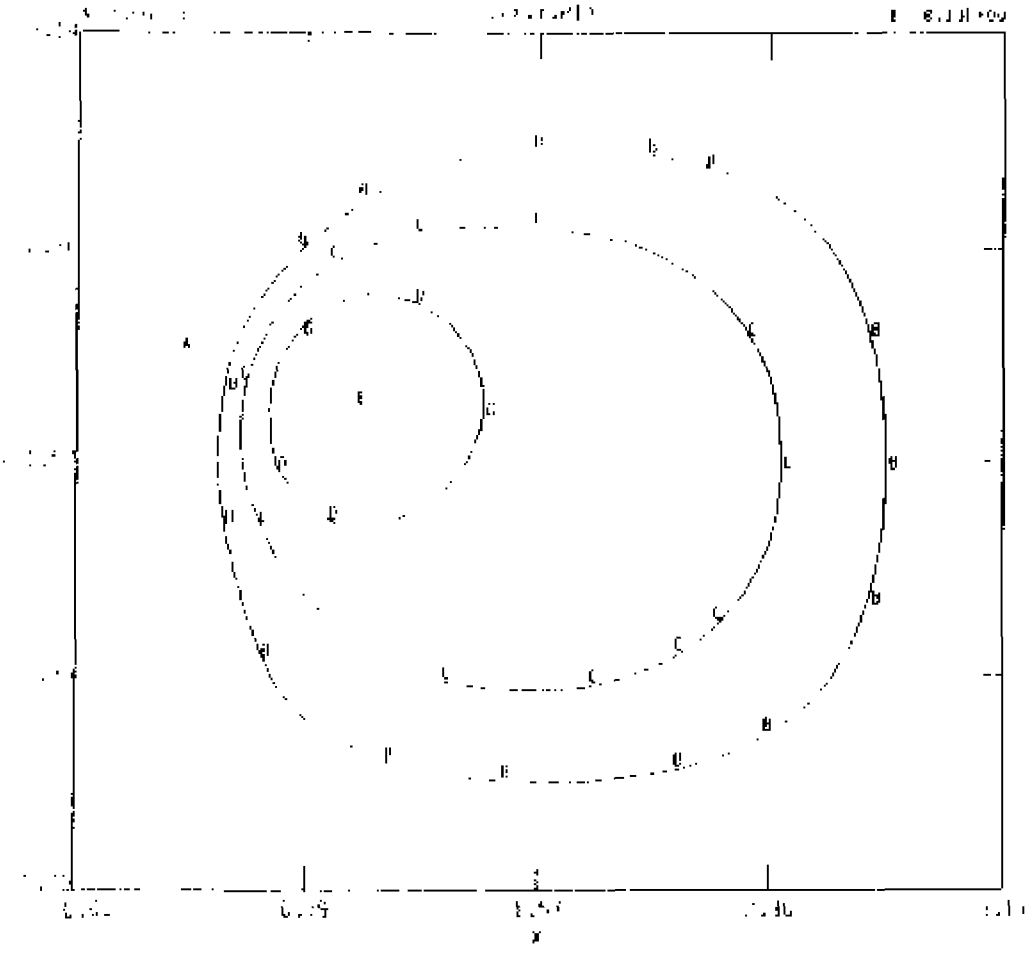

73 (c): contours of j = constant, poloidal cut.

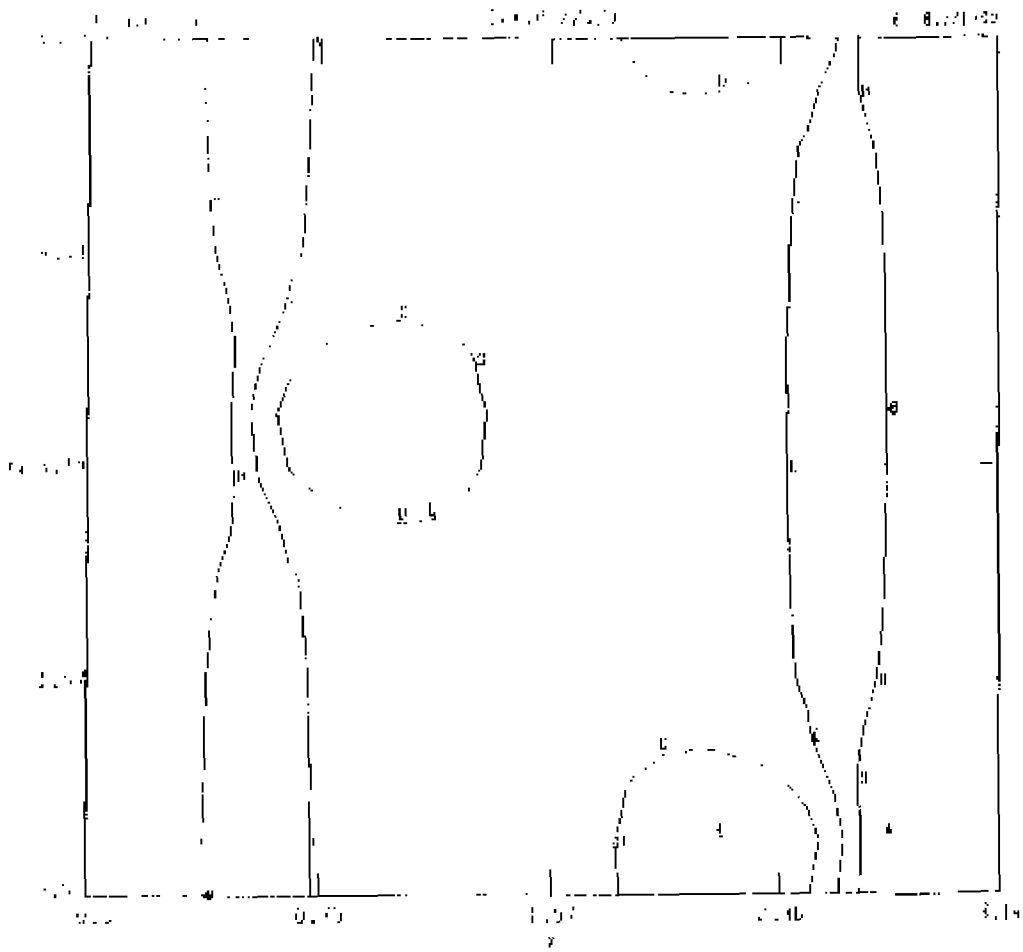

73 (d): contours of j = constant, toroidal cut.

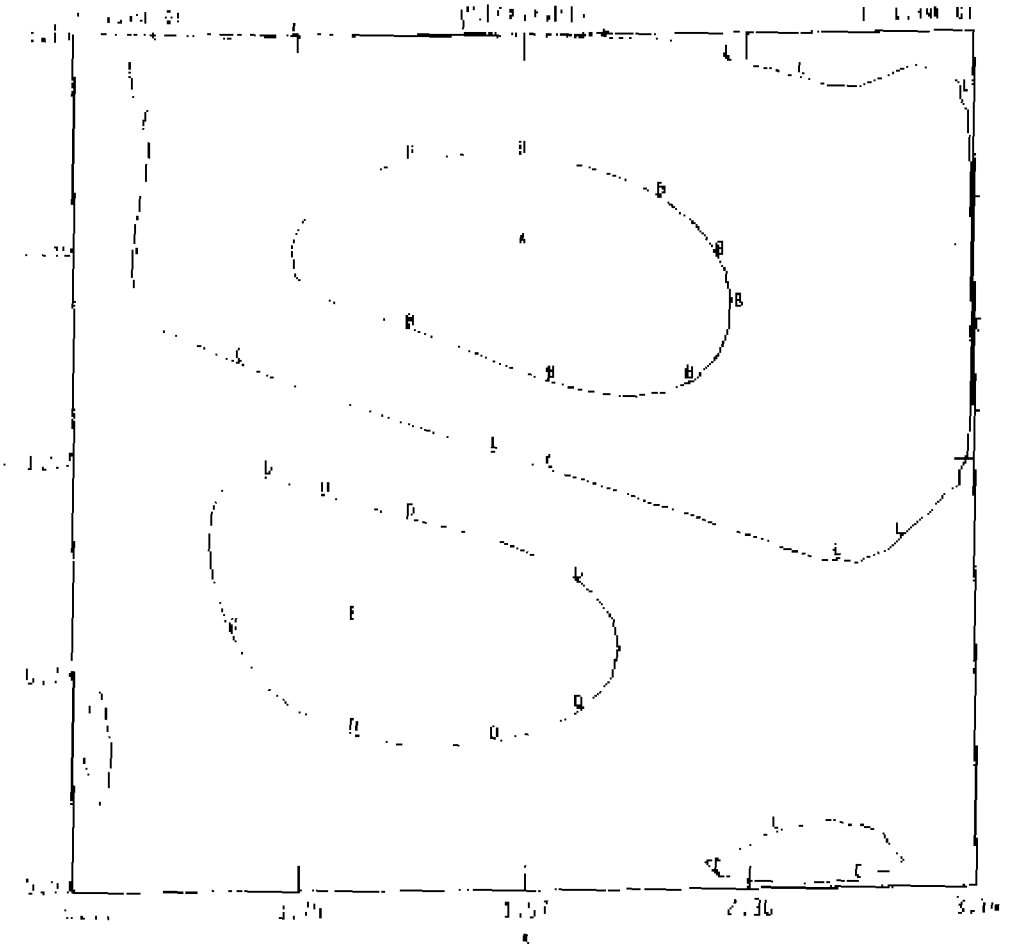

73 (e): contours of Ψ = constant, poloidal cut.

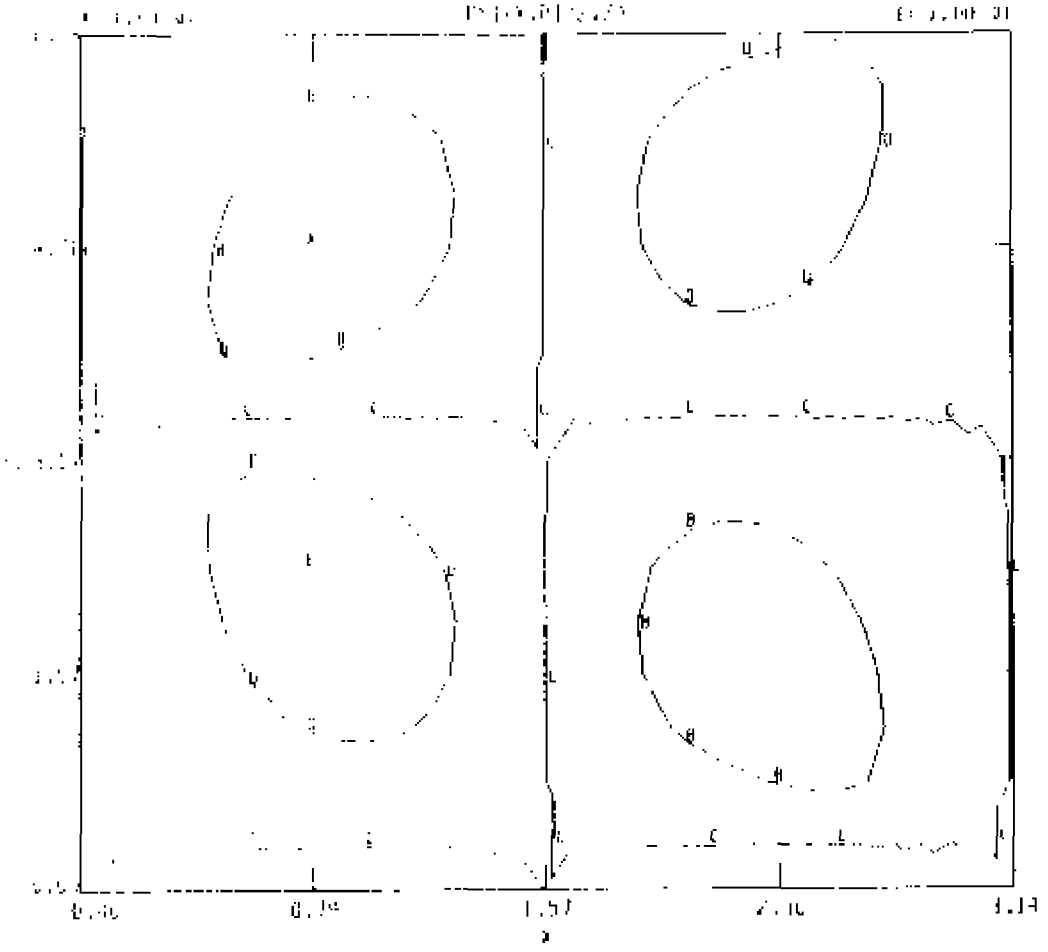

73 (f): contours of Ψ = constant, toroidal cut.

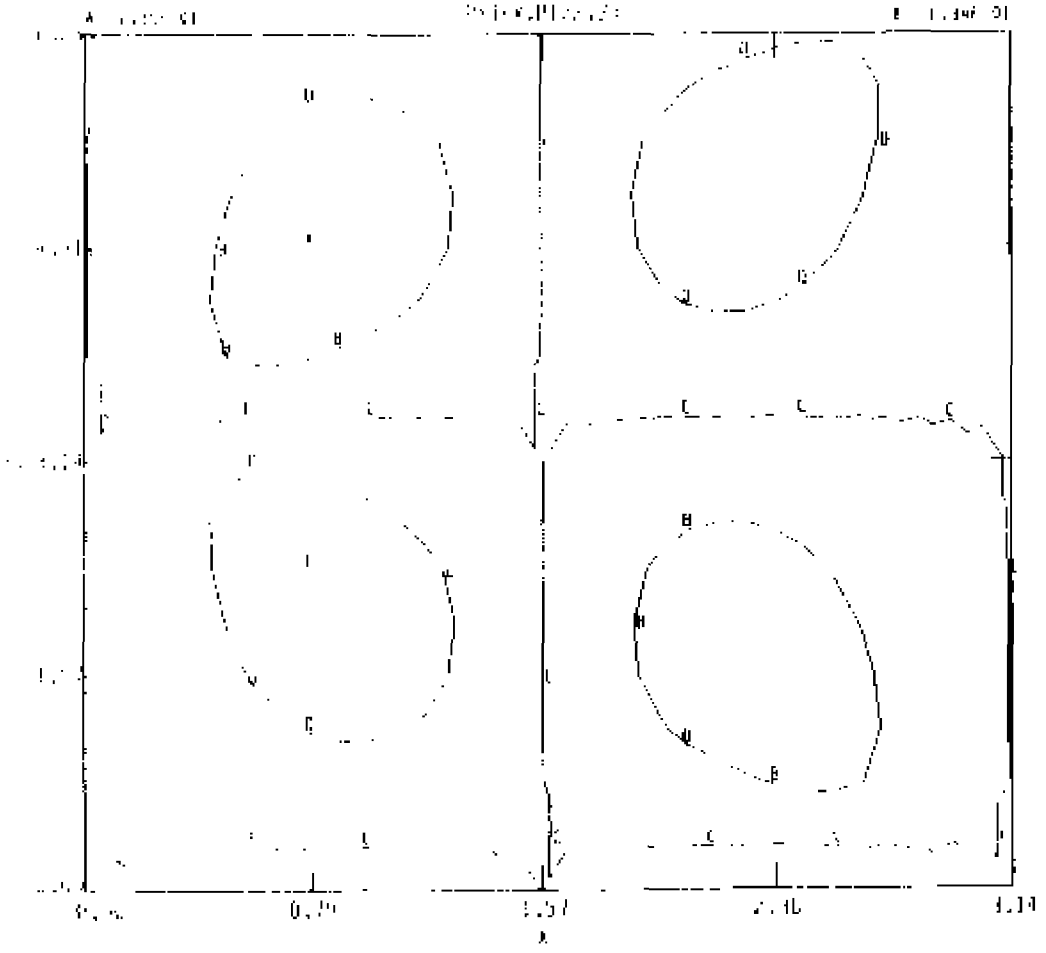

73 (f): contours of Ψ = constant, toroidal cut.

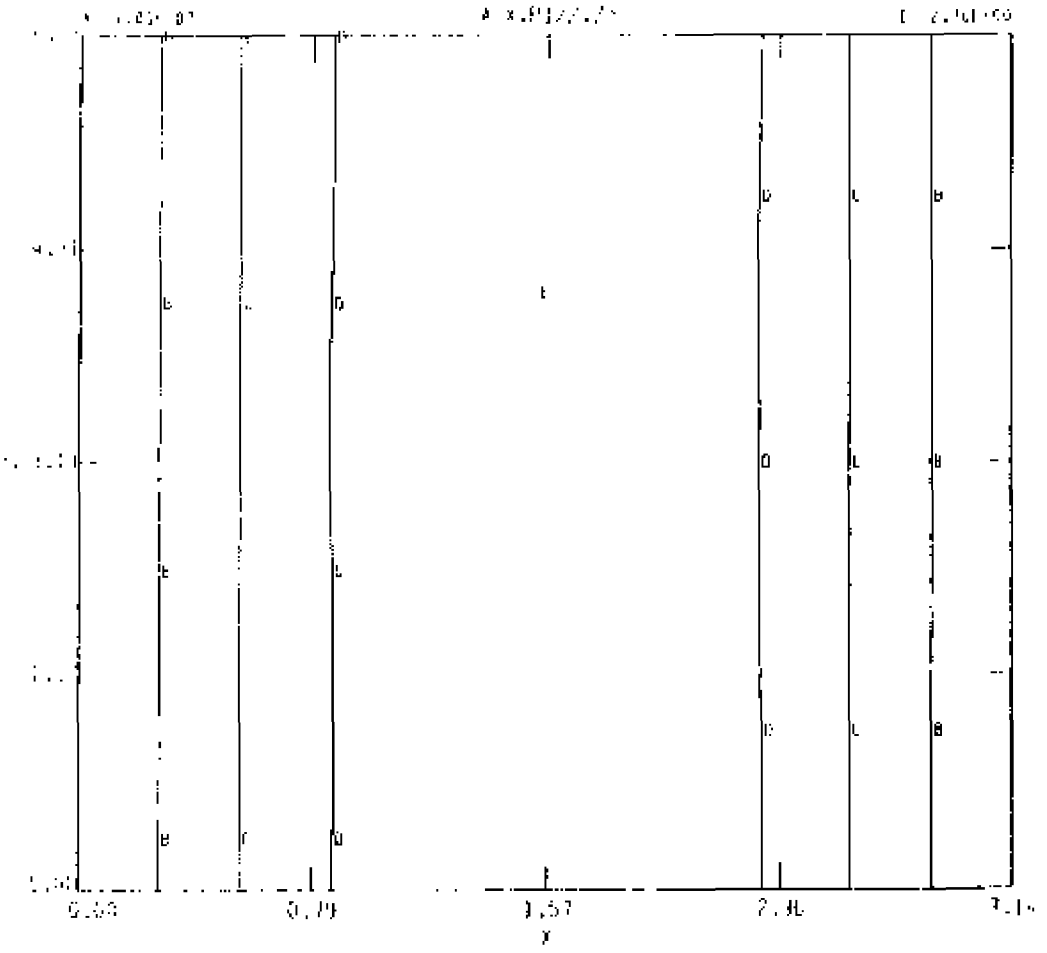

Figure 74. - Contours at t = 39.36, for CASE 5, E_o = 8/200, υ = 0.01:
74 (a) ; contours of A = constant, toroidal cut,

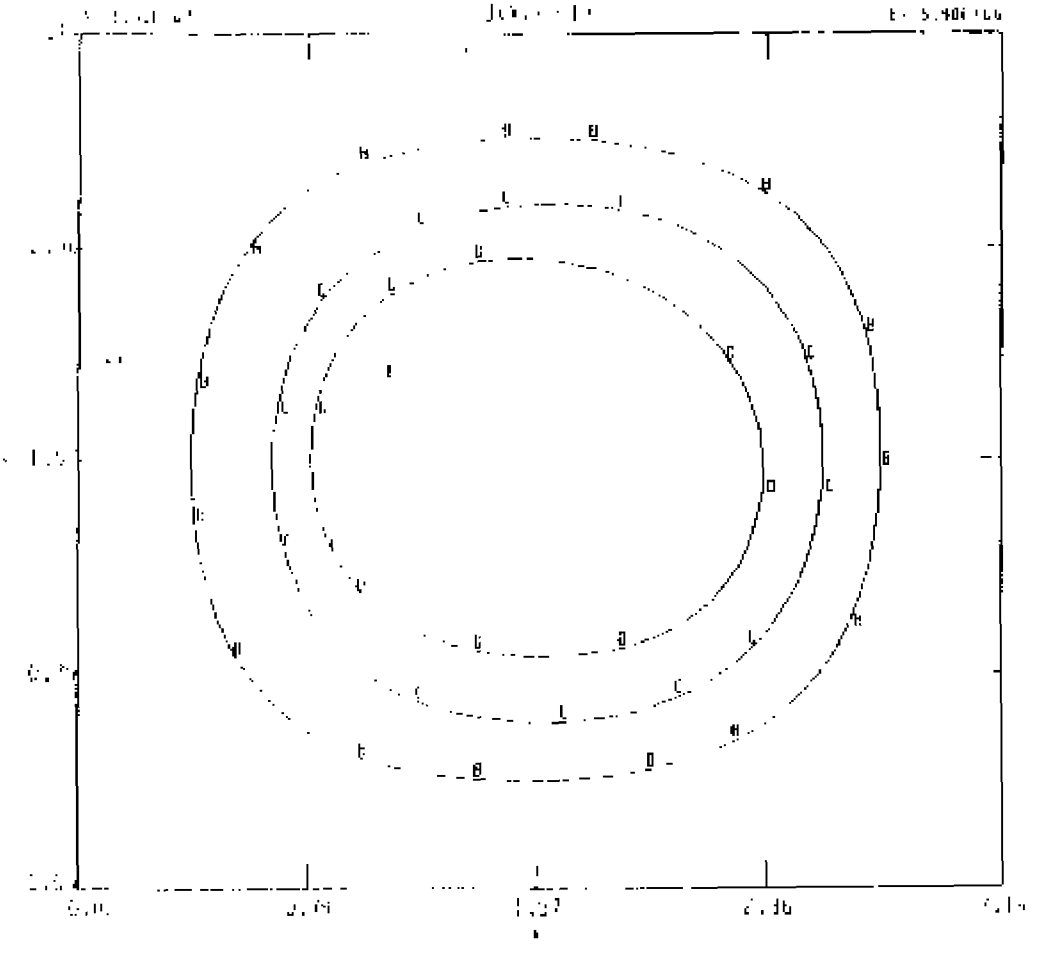

74 (b): contours of j = constant, poloidal cut.

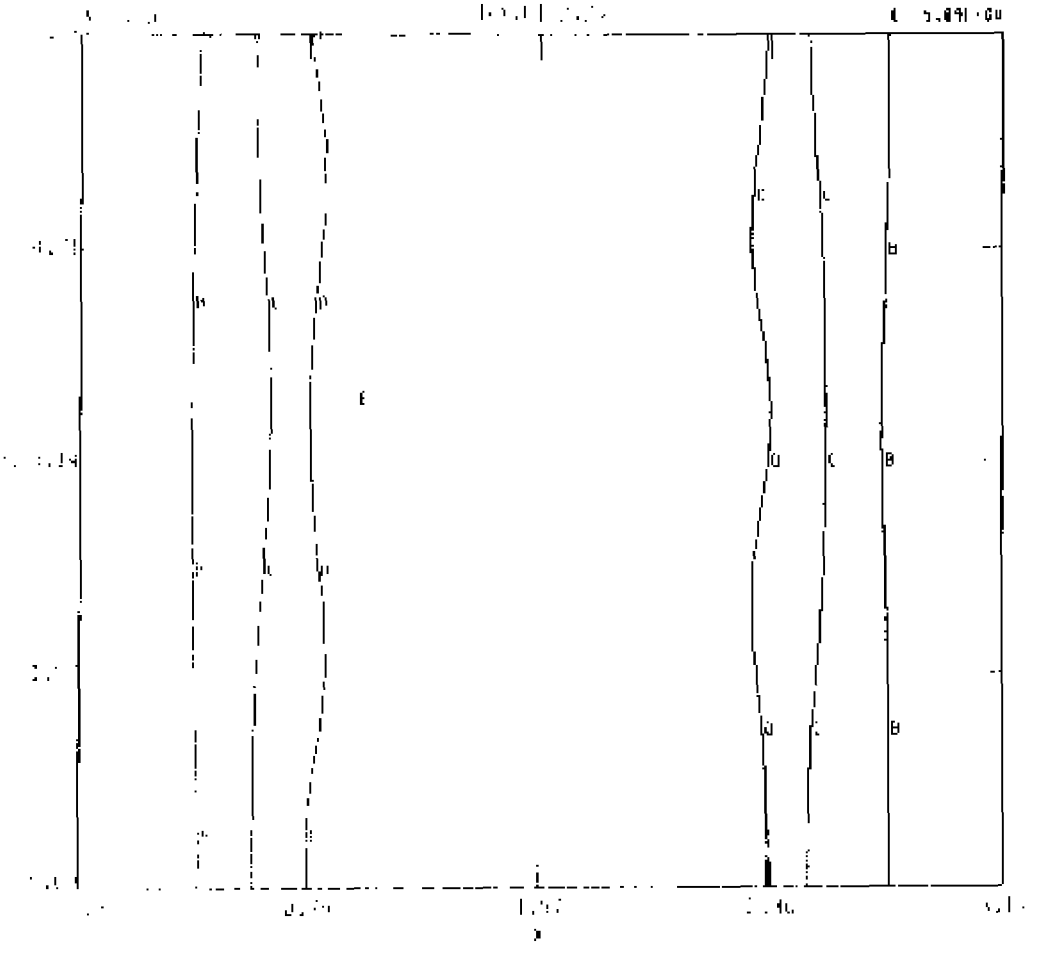

74 (c): contours of j = constant, toroidal cut, and

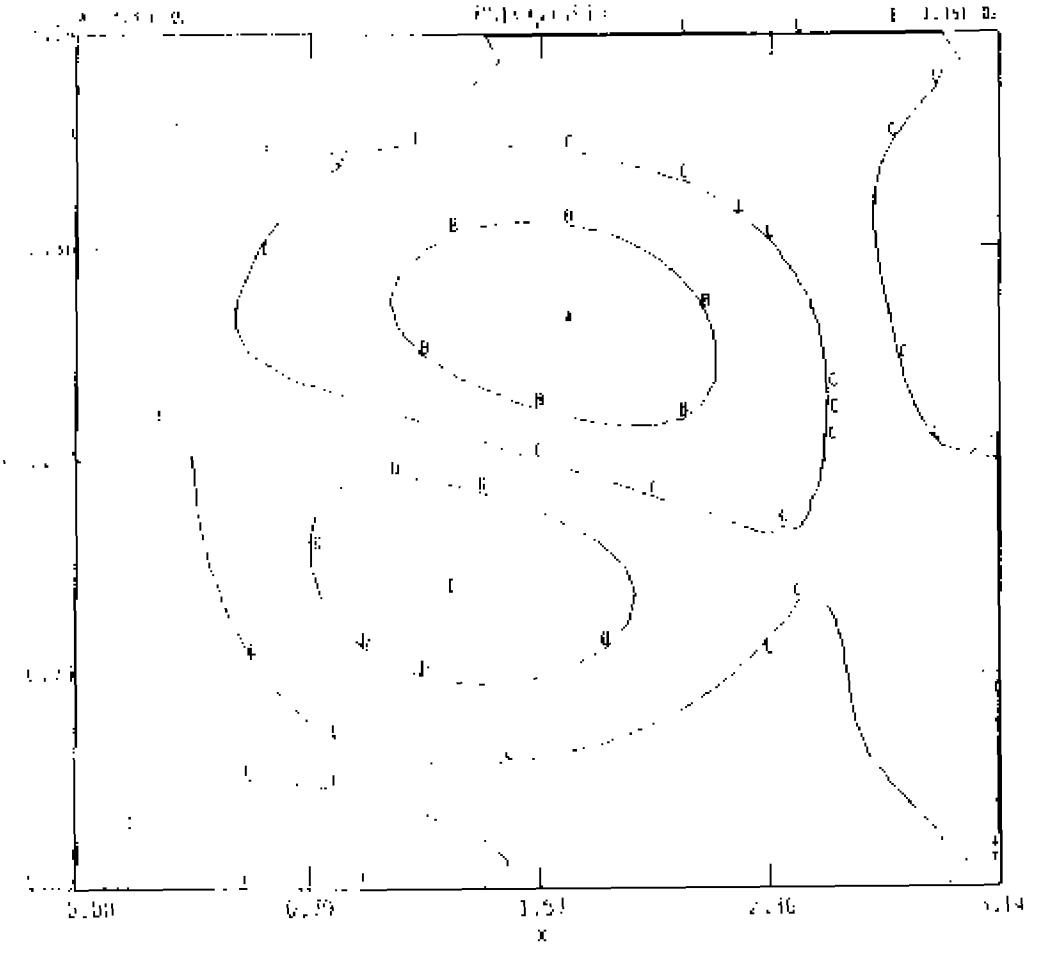

74 (d) : contours of ψ= constant, poloidal cut.

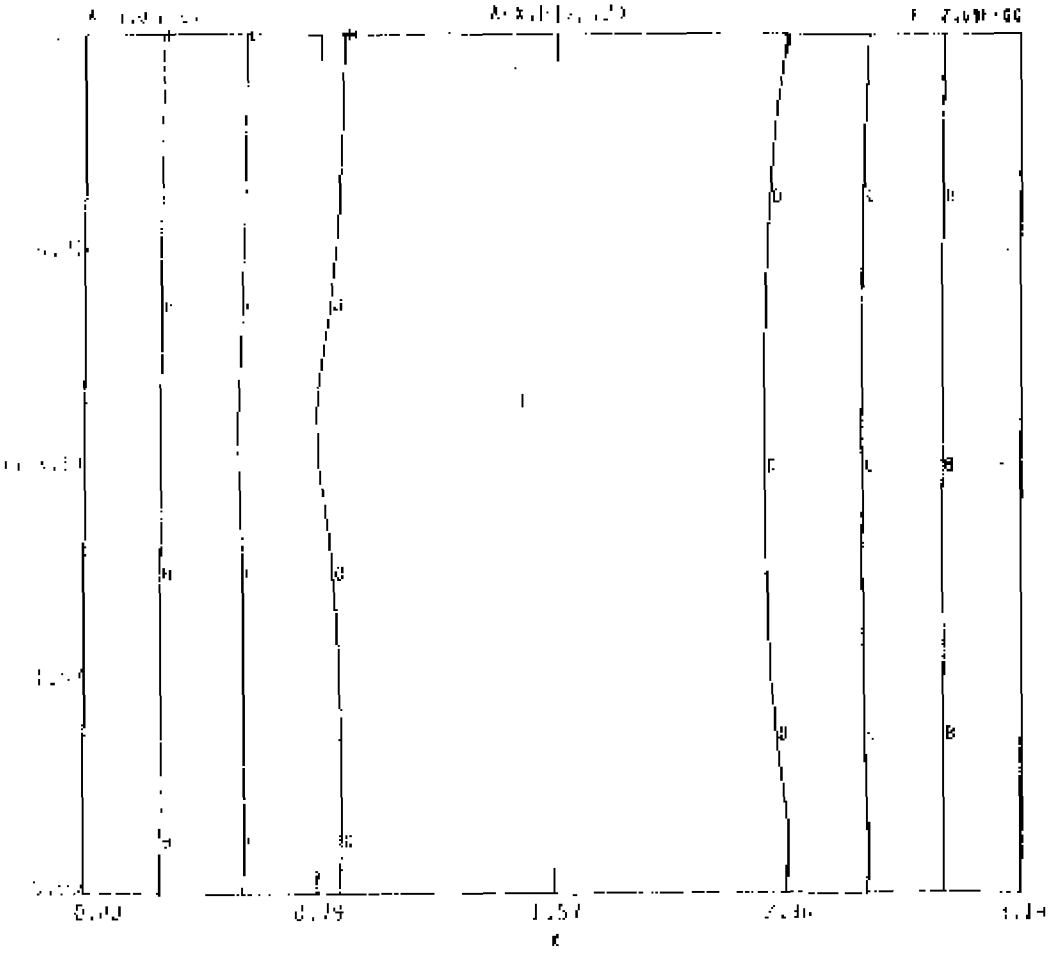

Figure 75. - Contours at t = 54.72, for CASE 5, E_ϕ = 0/200, ν = 0.01:
75 (a) : contours of A = constant, toroidal cut.

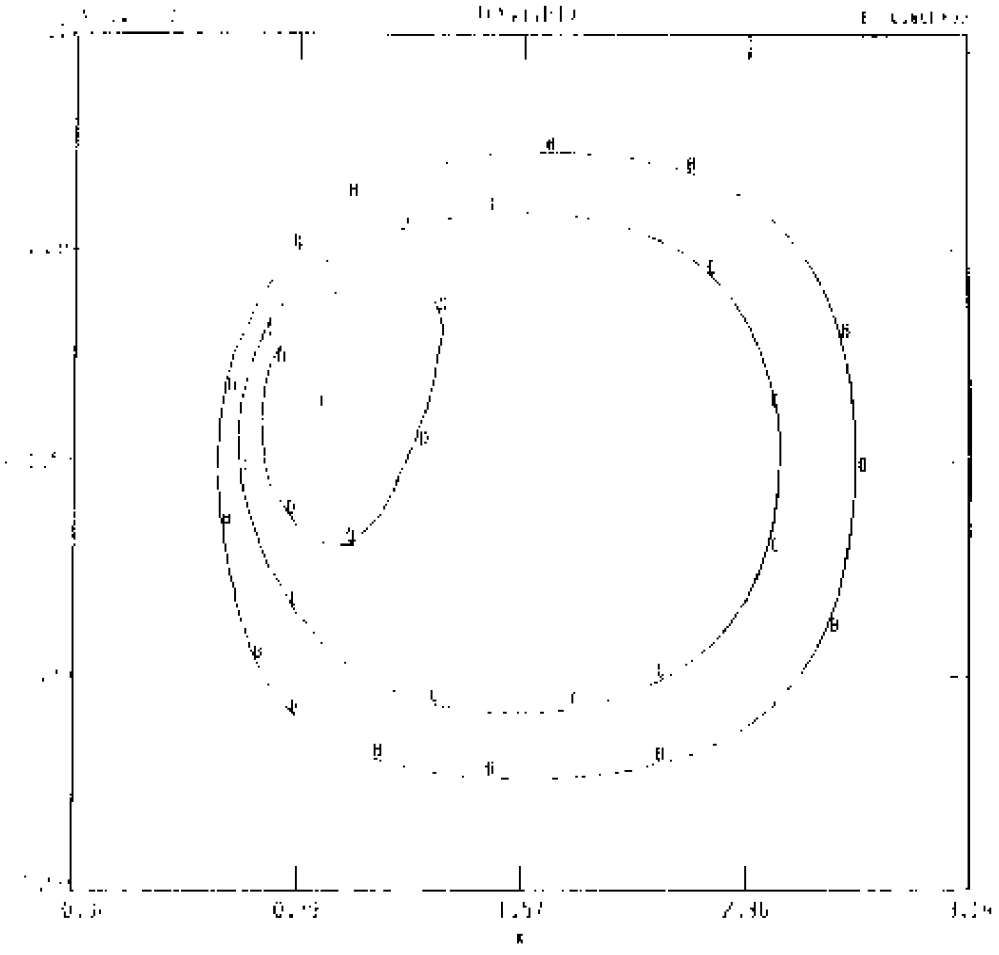

75 (b): contours of j = constant, poloidal / toroidal cut.

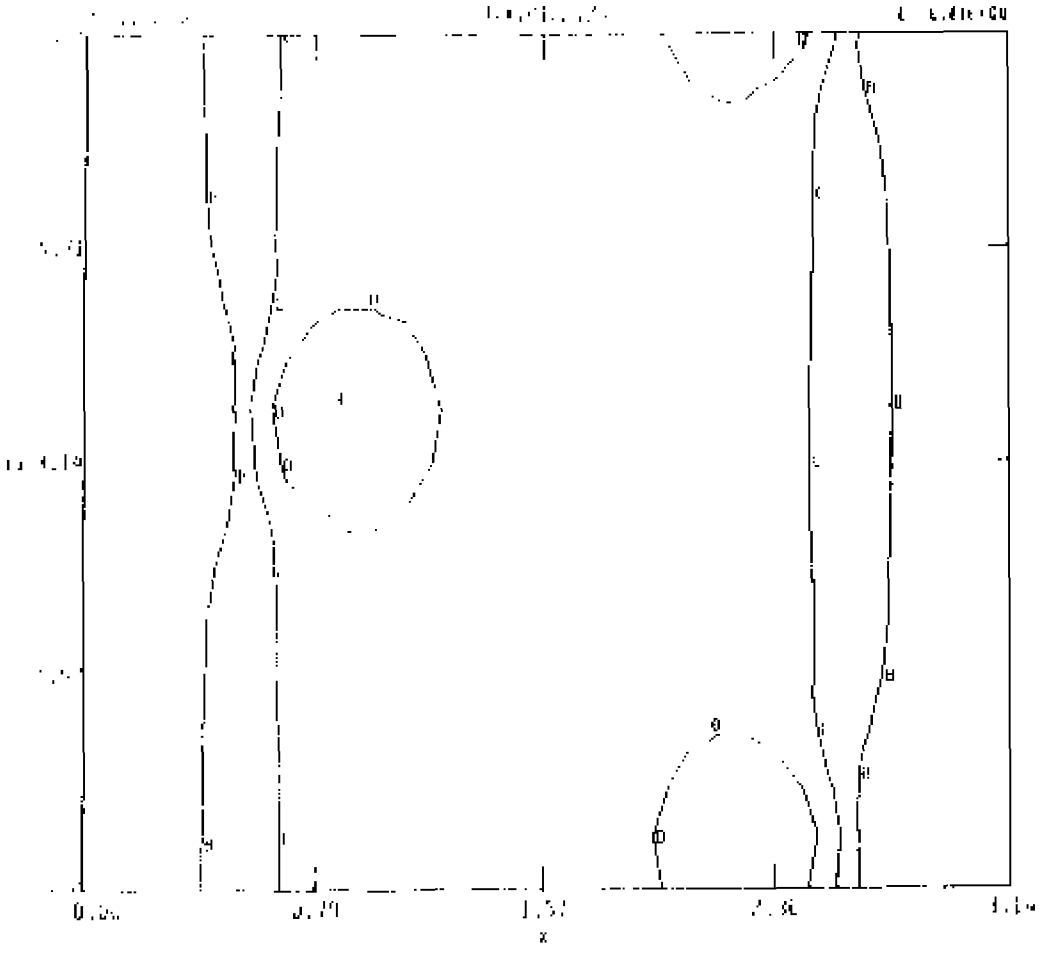

75 (c): contours of j = constant, toroidal cut, and

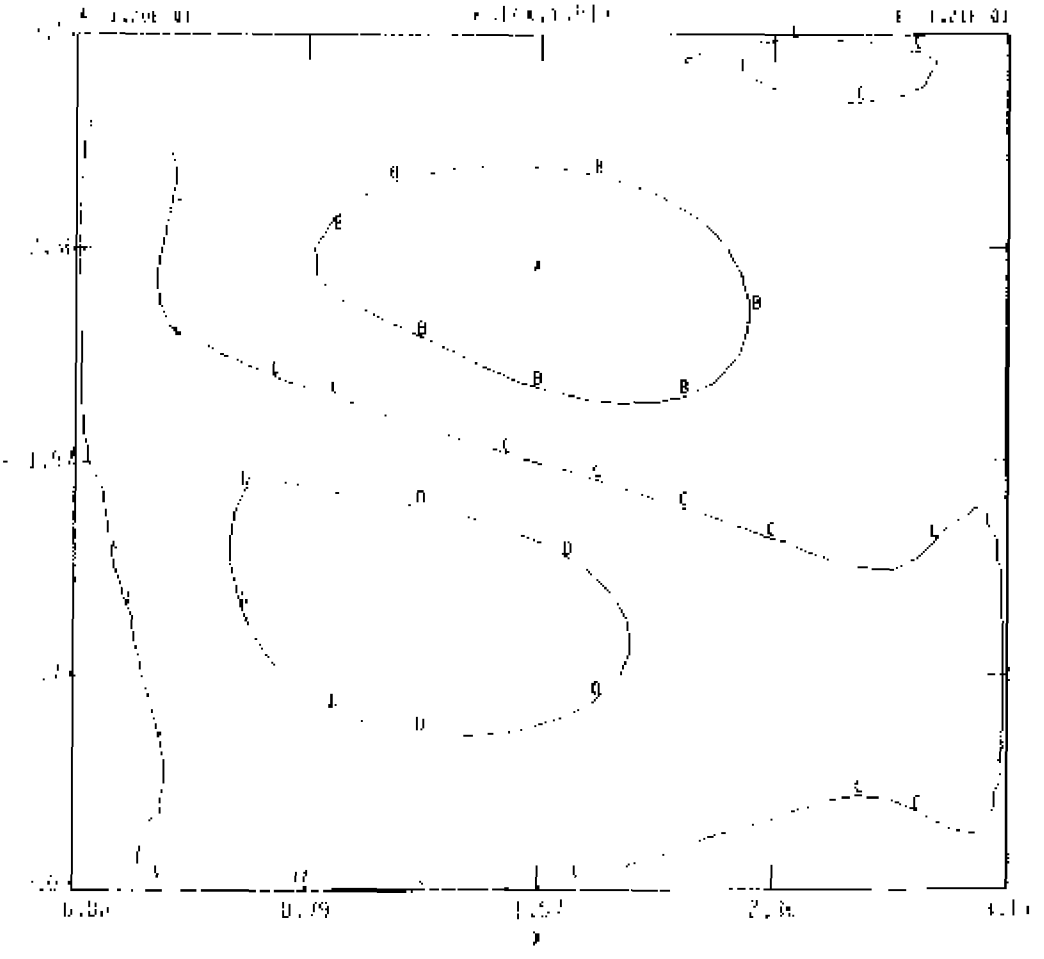

75 (d) : contours of Ψ = constant, poloidal cut.

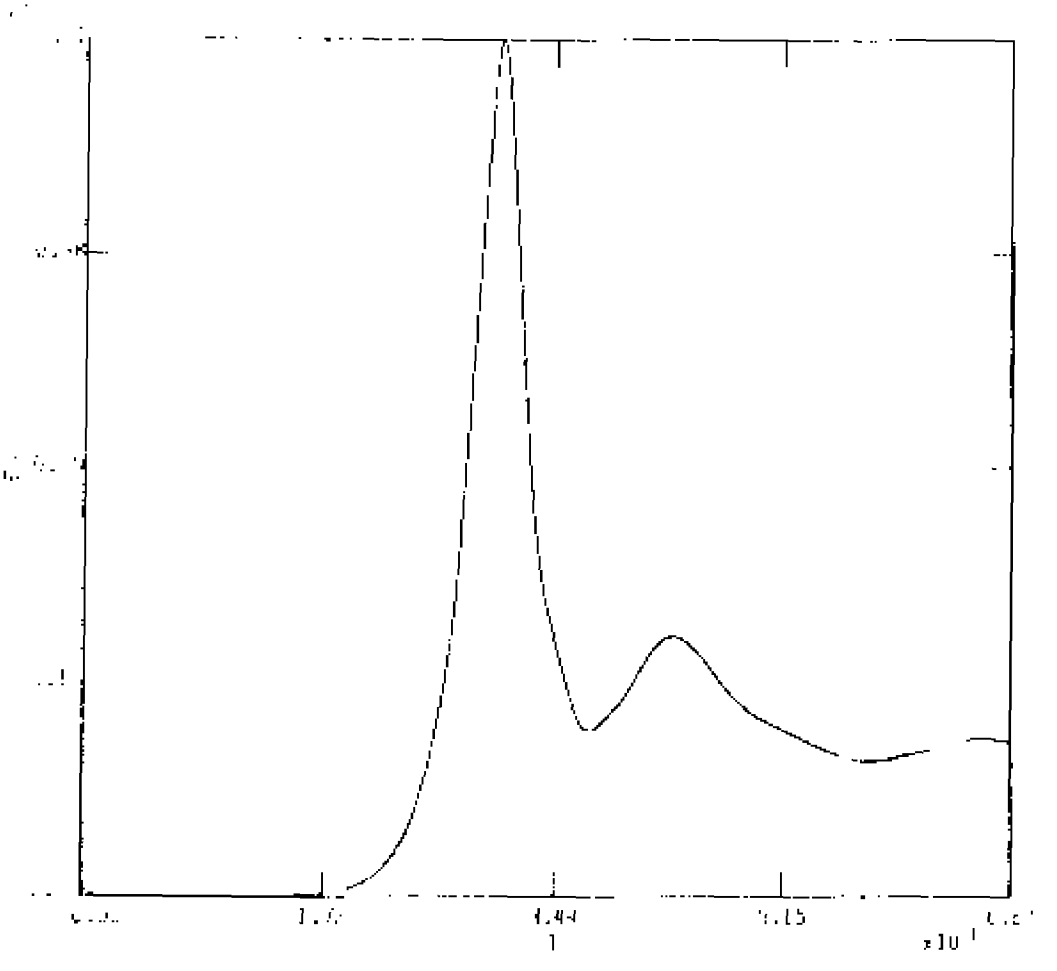

Figure 76. - Globals, CASE 6, E_o = 0/350, ν = 0.00:
76(a): kinetic energy as a function of time.

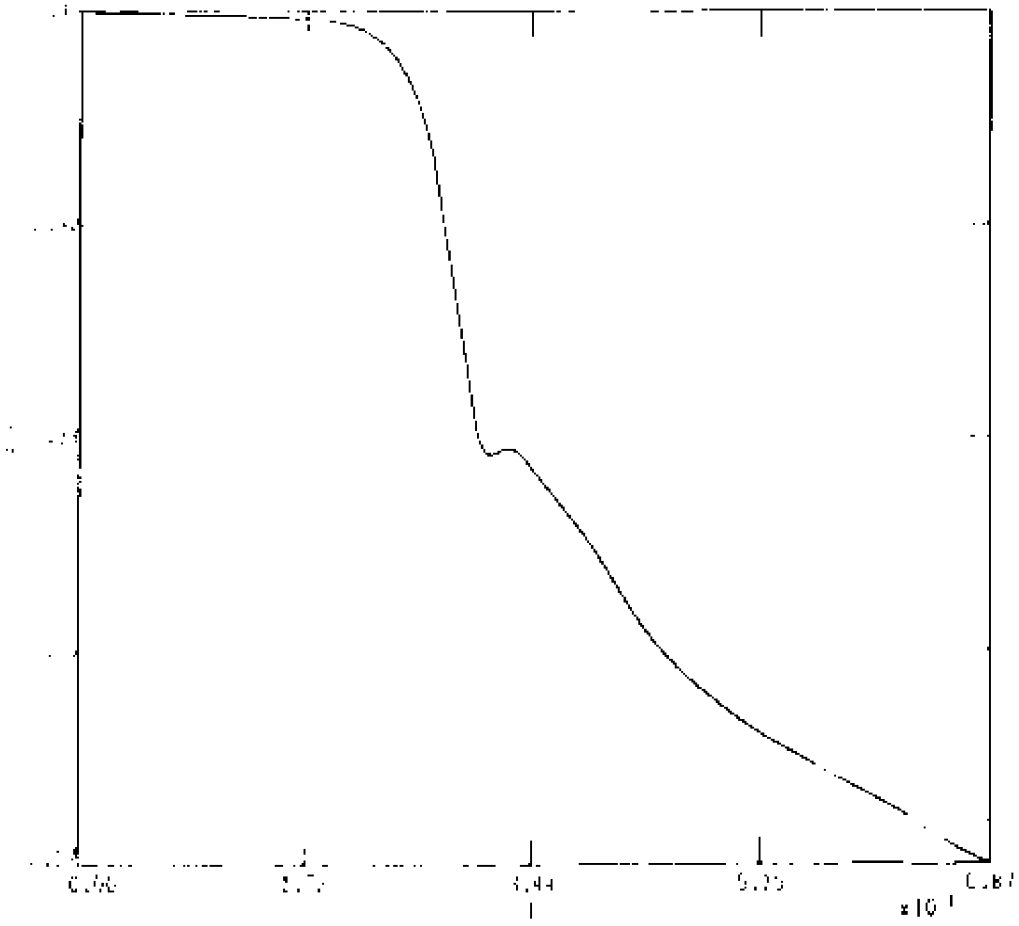

76(b): magnetic energy as a function of time, and

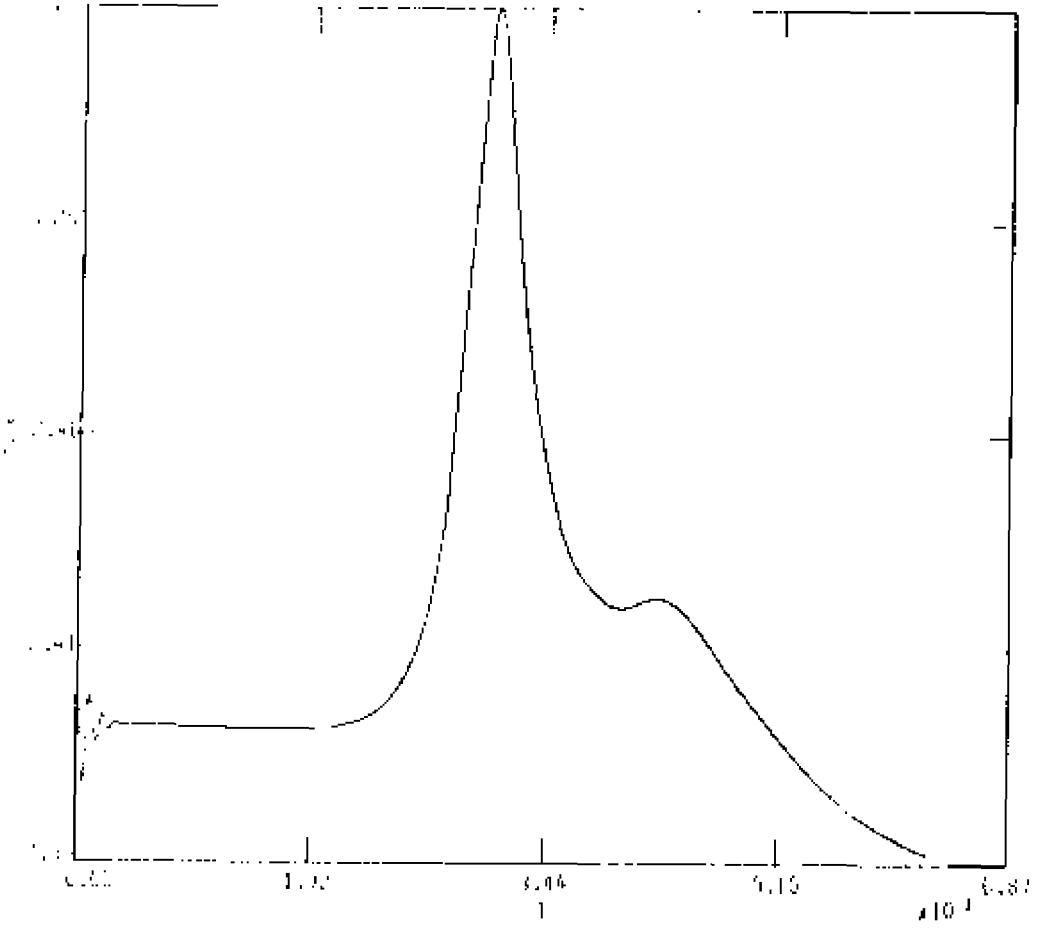

76(c): total integrated current as a function of time.

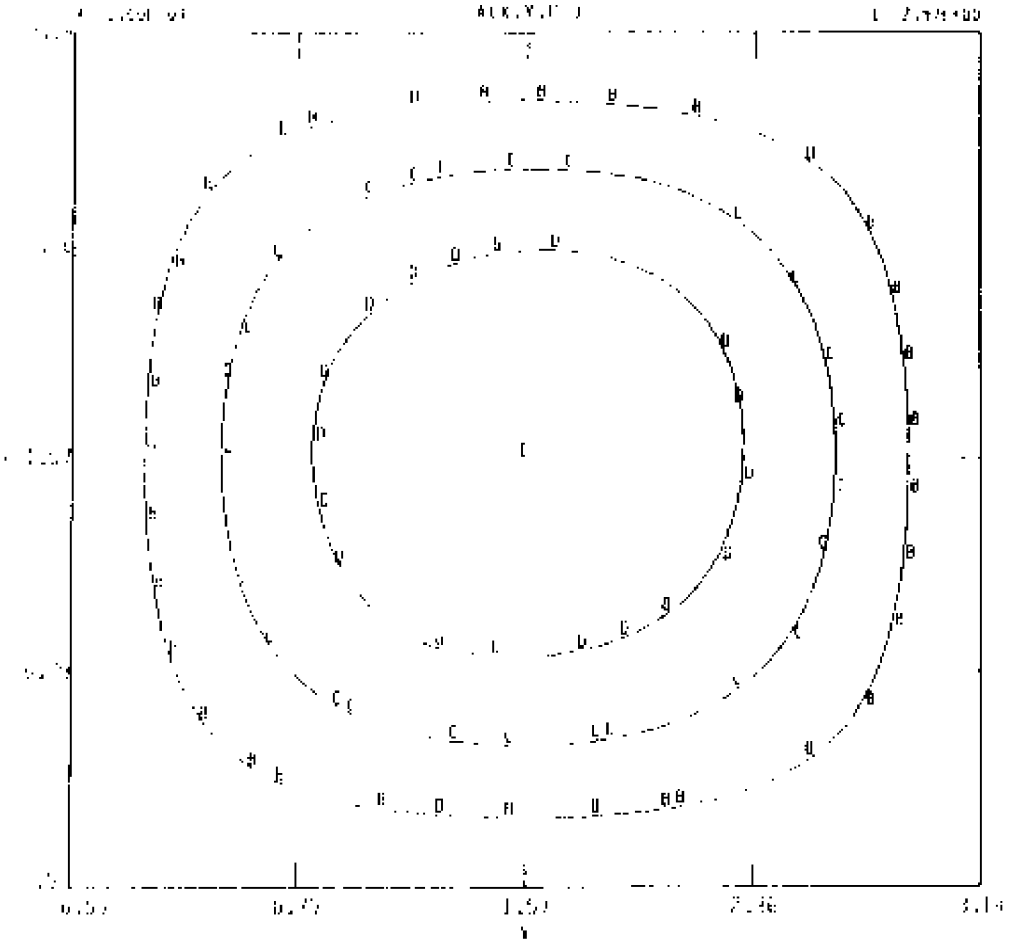

Figure 77. - Contours at t = 39.24, for CASE 6, E_o = 0/350, ν = 0.00. 77 (a): contours of A = constant, poloidal cut.

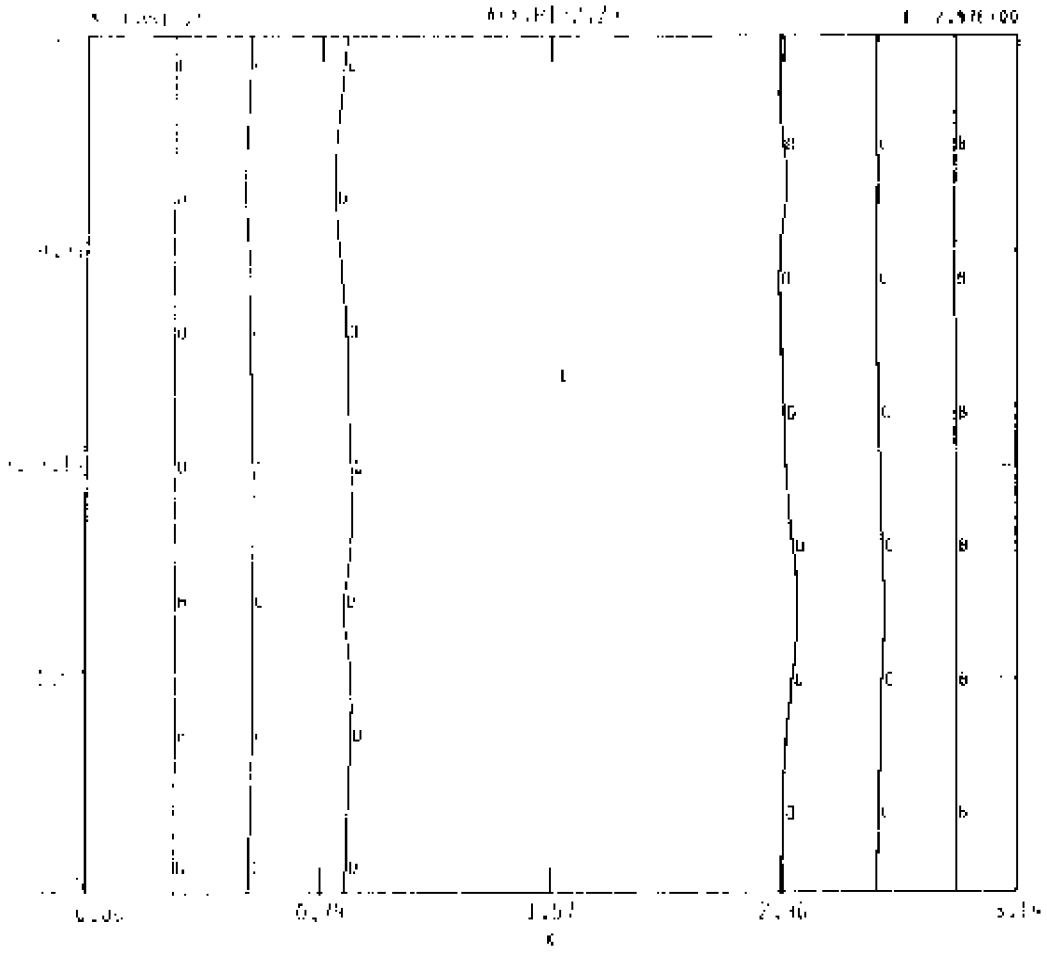

77 (b): contours of A = constant, toroidal cut.

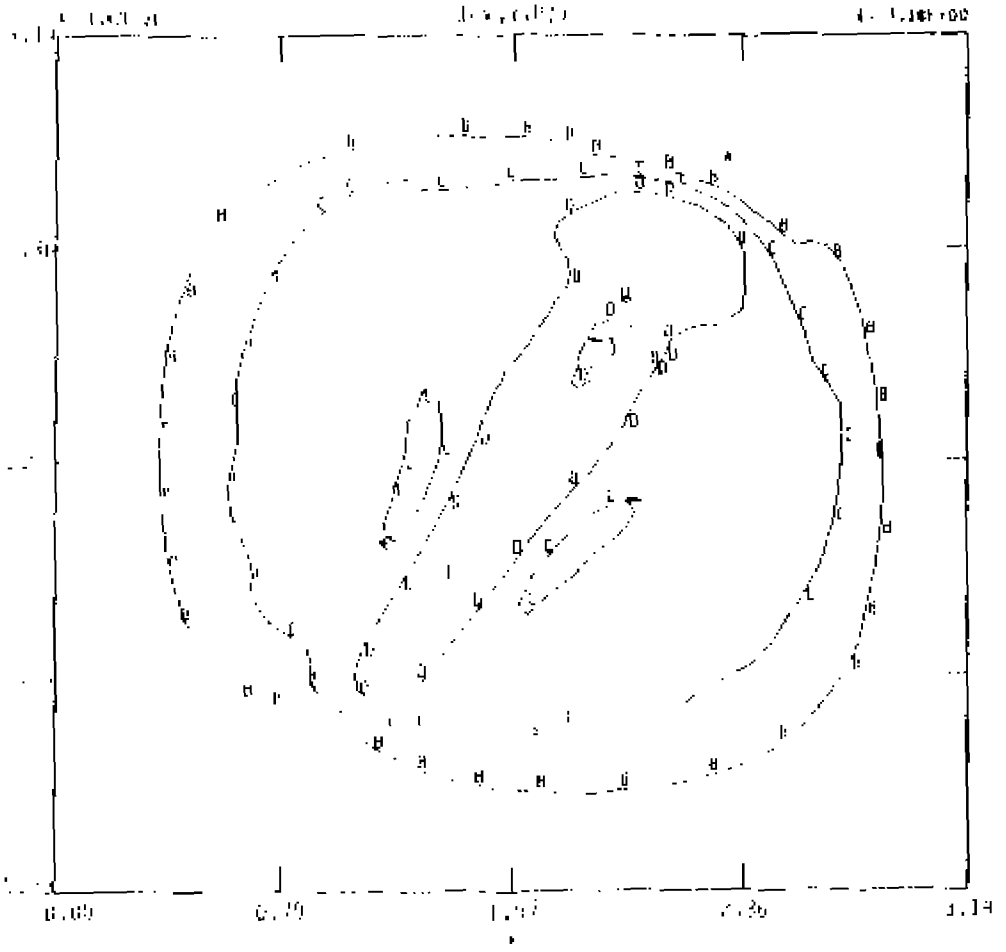

77 (c): contours of j = constant, poloidal cut.

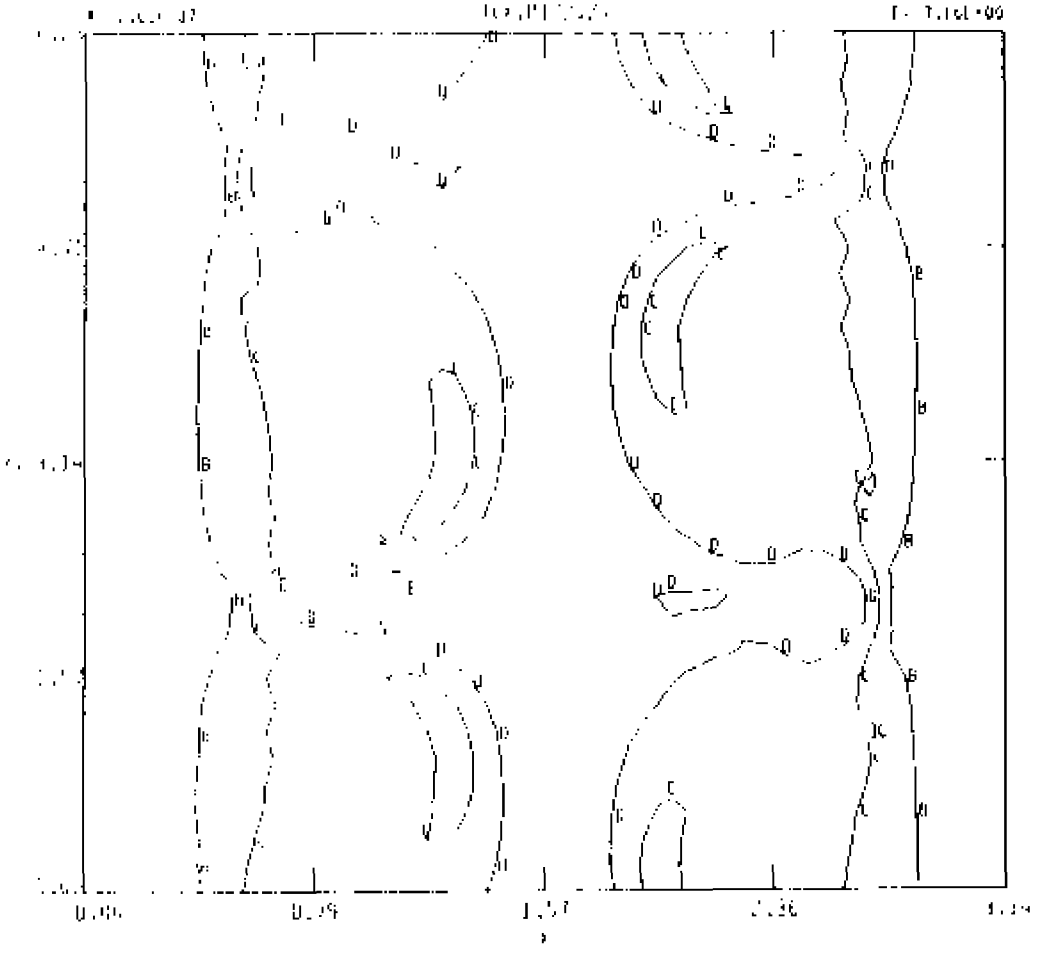

77 (d): contours of j = constant, toroidal cut.

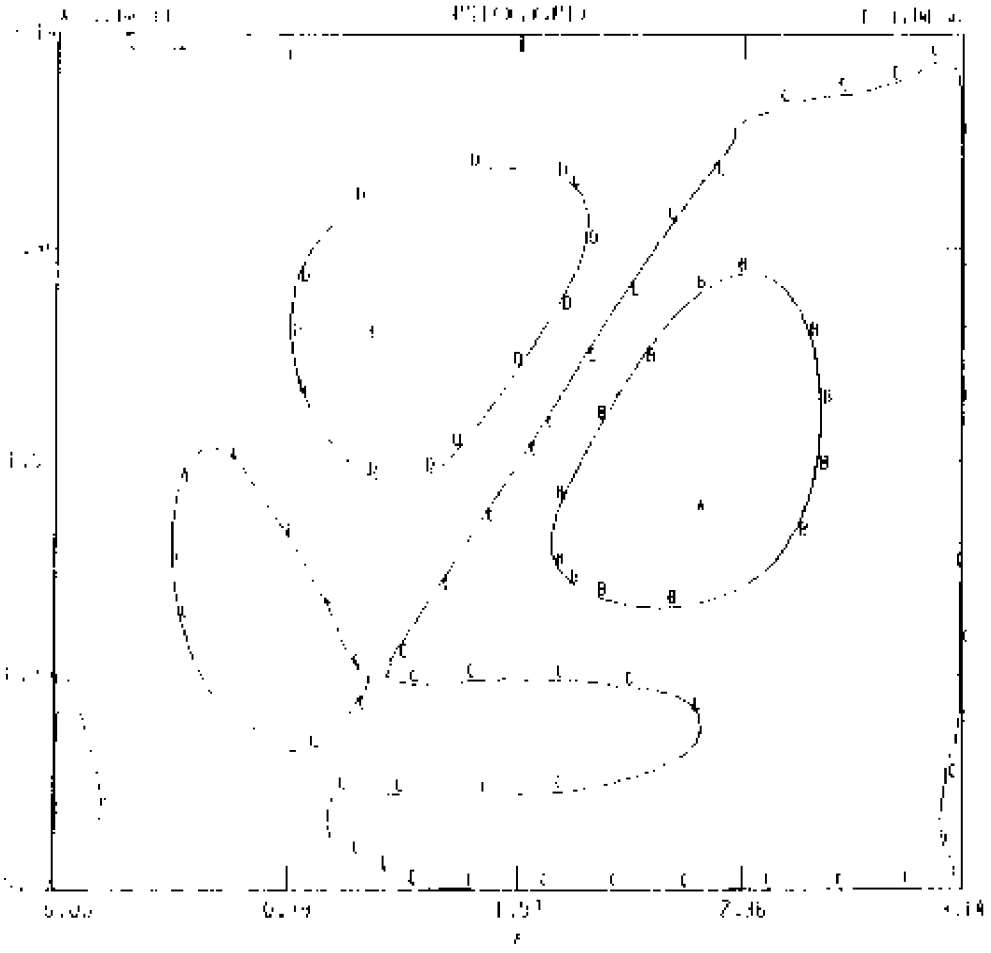

77 (e): contours of Ψ= constant, poloidal cut.

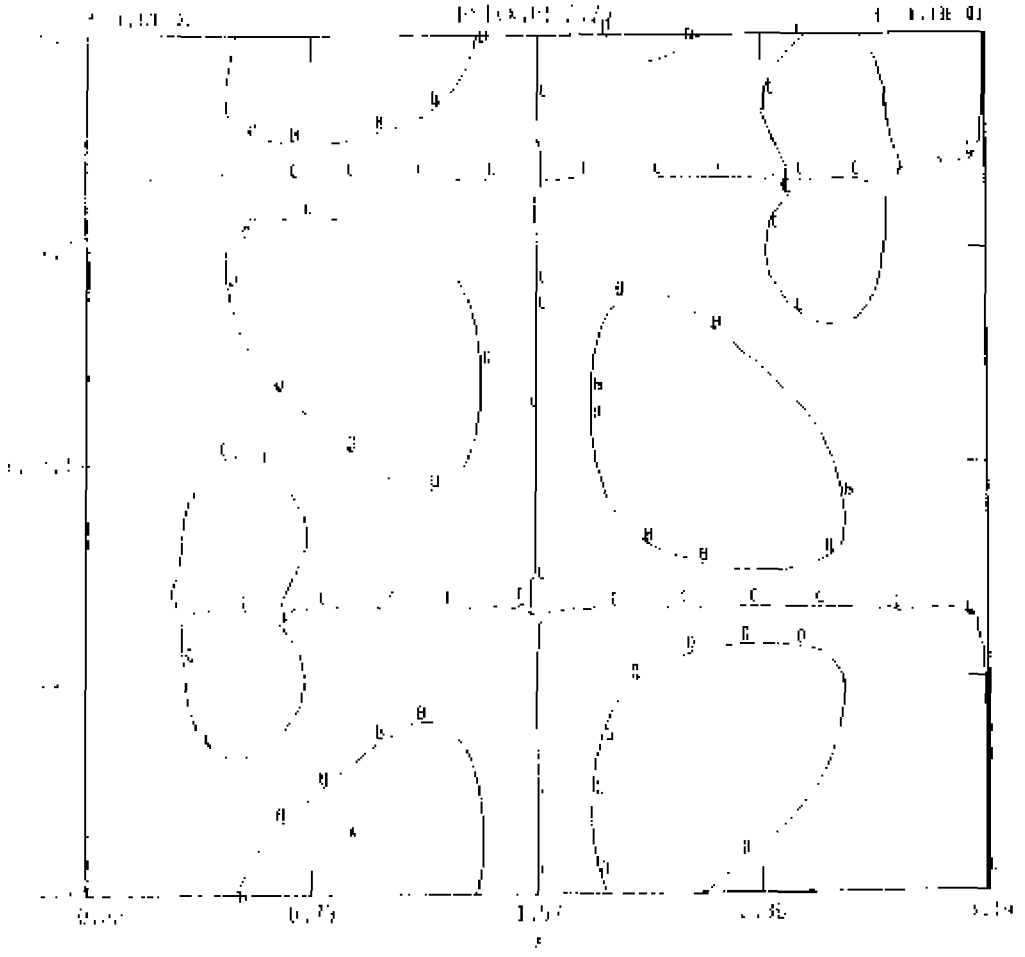

77 (f): contours of Ψ= constant, toroidal cut.

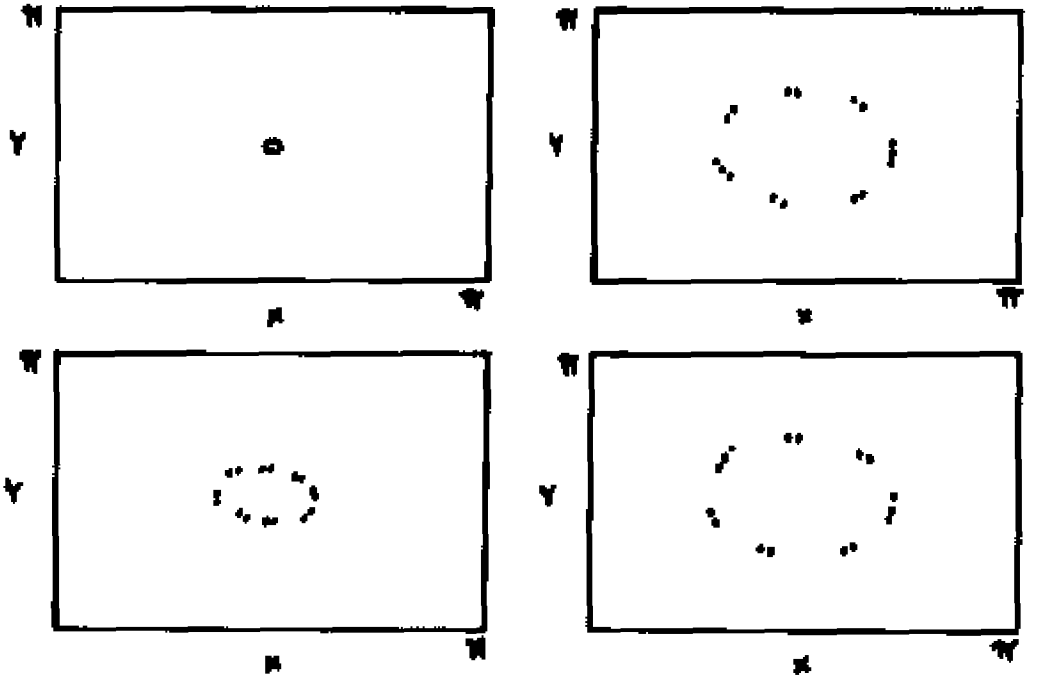

Figure 78. - Poincaré plots, CASE 6, t = 39.24.

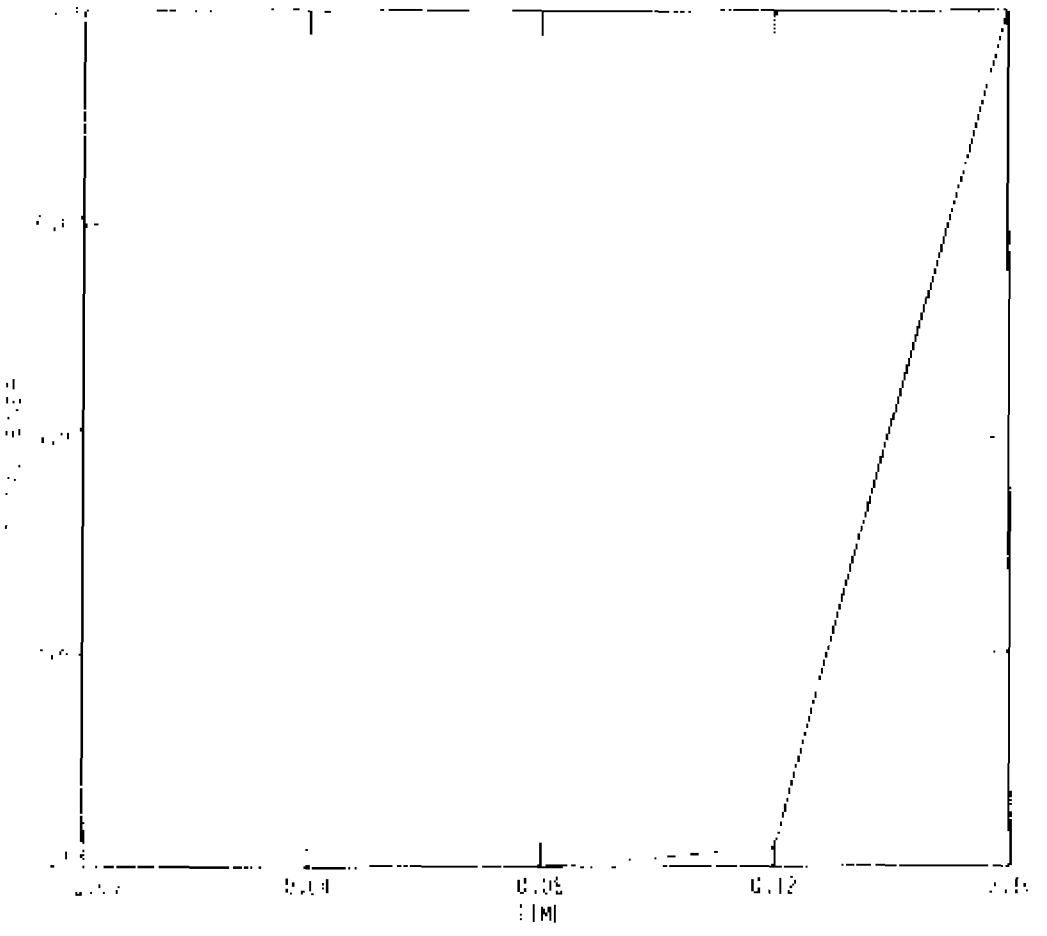

Figure A1. - Total energy versus time for RUN A1.

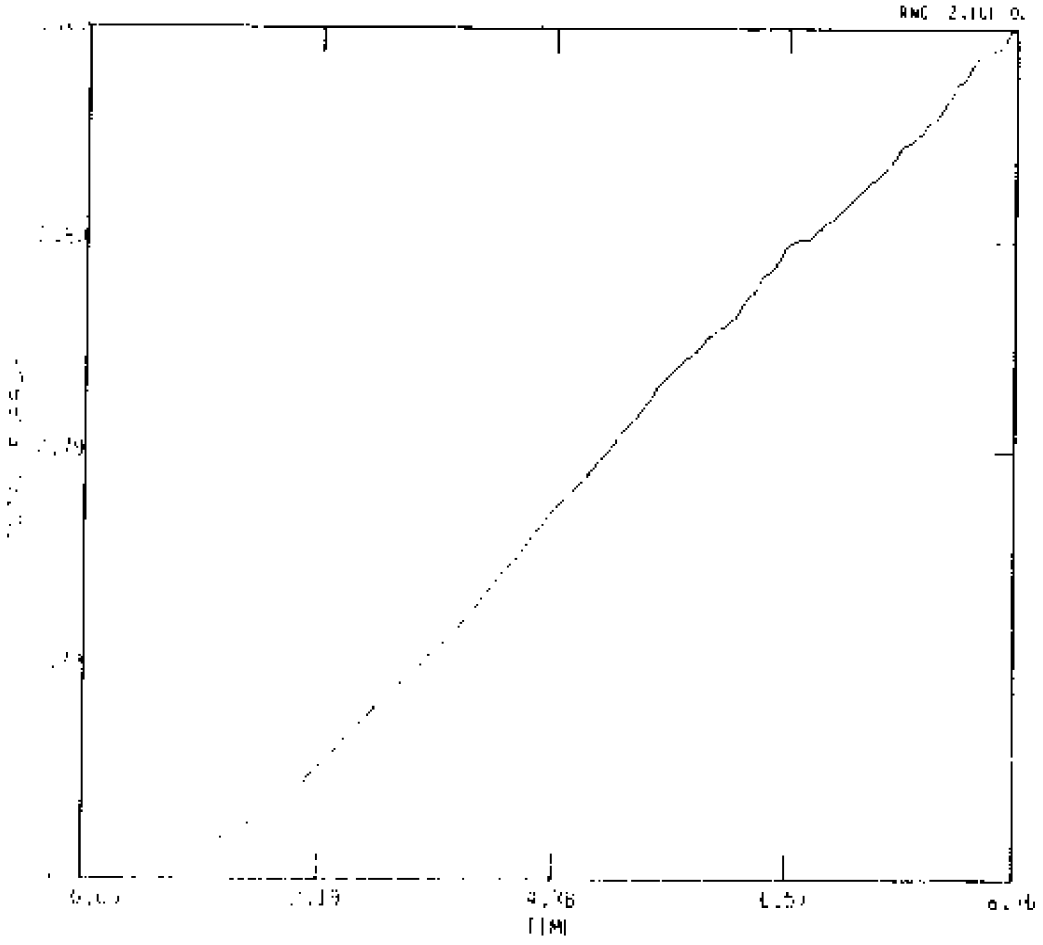

Figure A2. - RUN A2:
A2 (a): E_T as f(t),

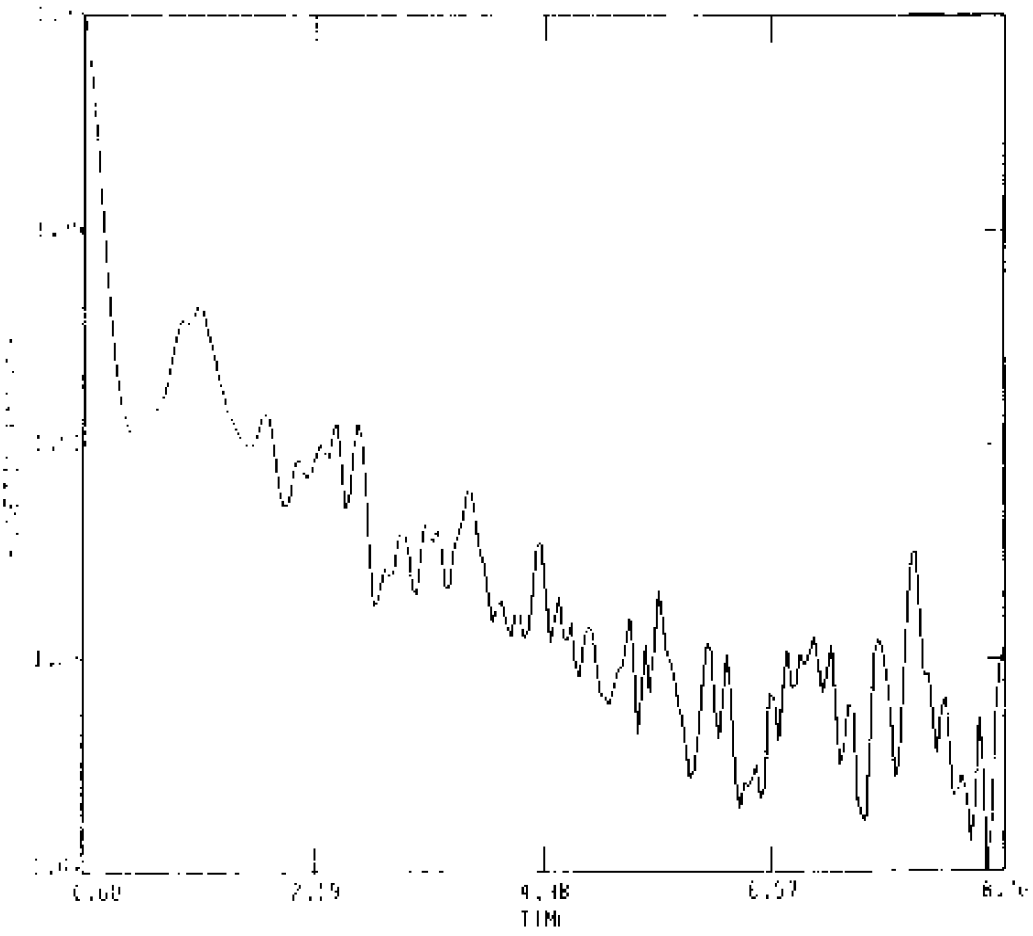

A2 (b): E_v as f(t).

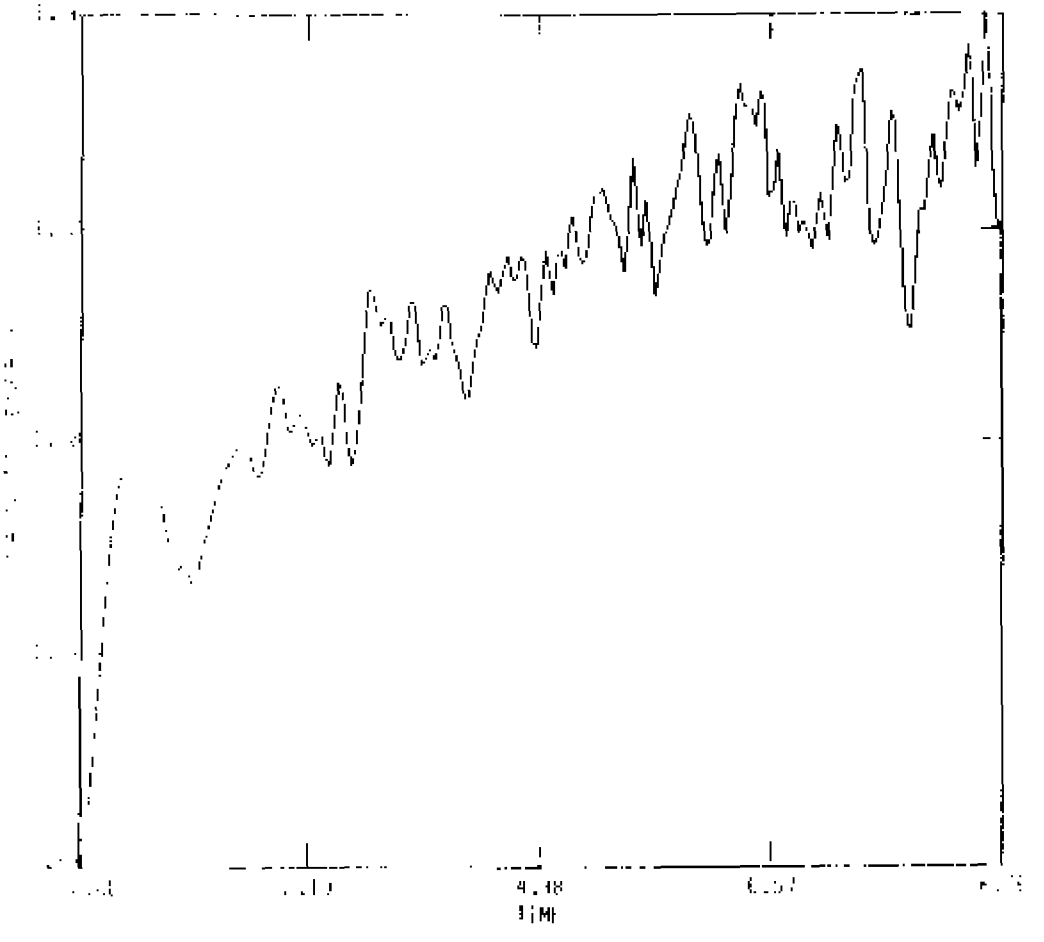

A2 (c): E_B as f(t).

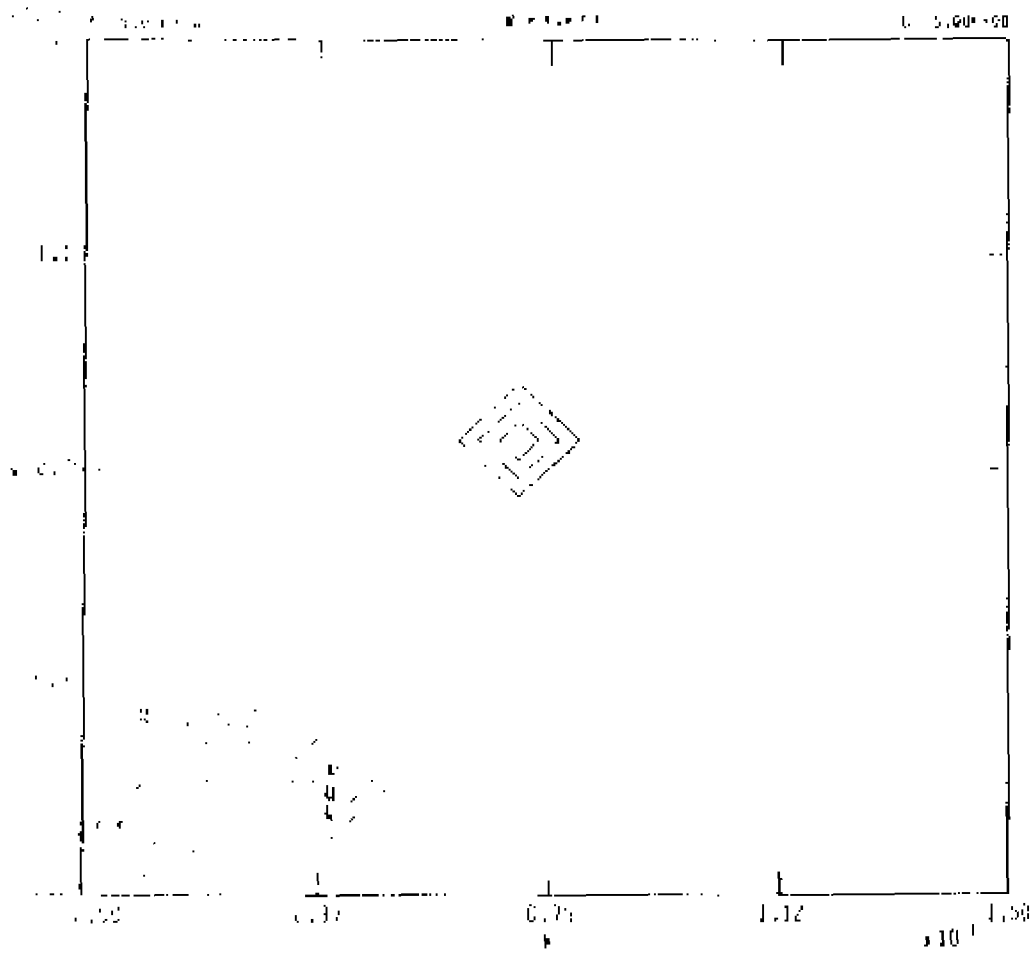

A2 (d): Fourier space contour plots, t = 0.00, of $\widetilde{\omega}$.

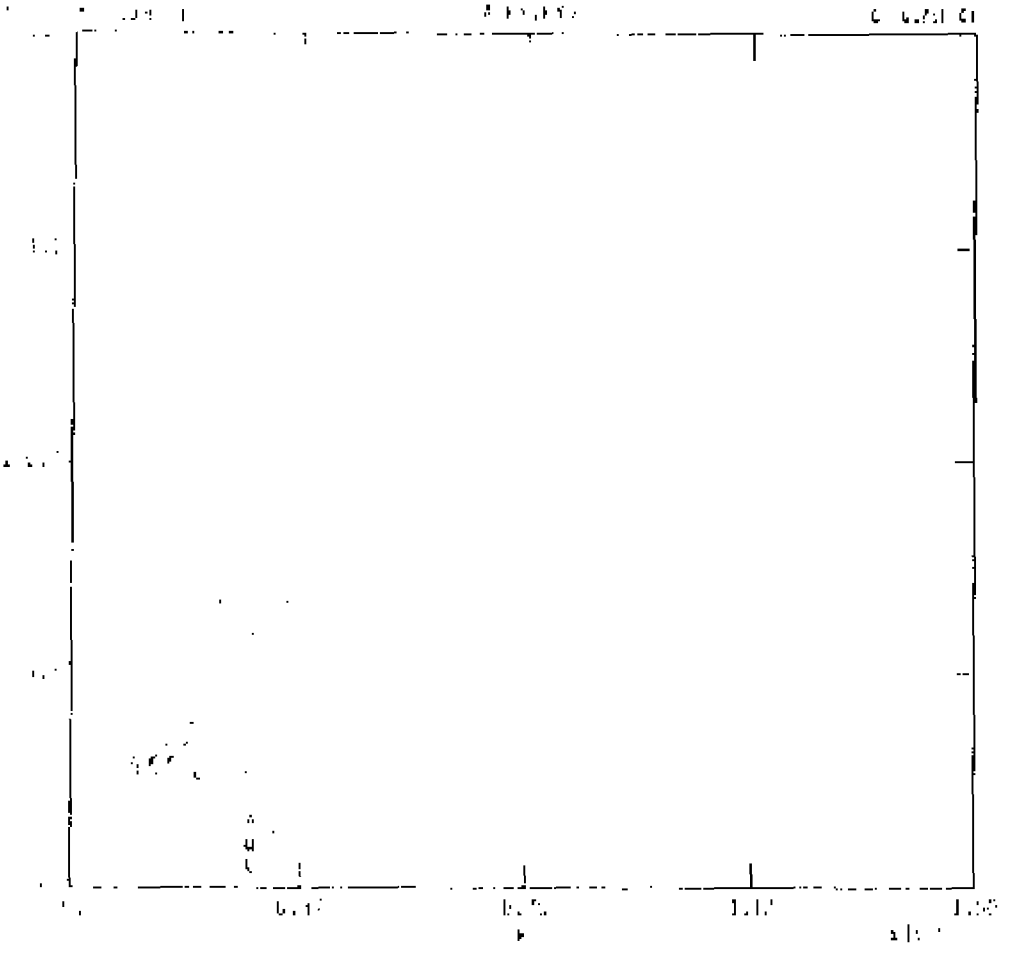

A2 (e): Fourier space contour plots, t = 0.89, of $\widetilde{A}$.

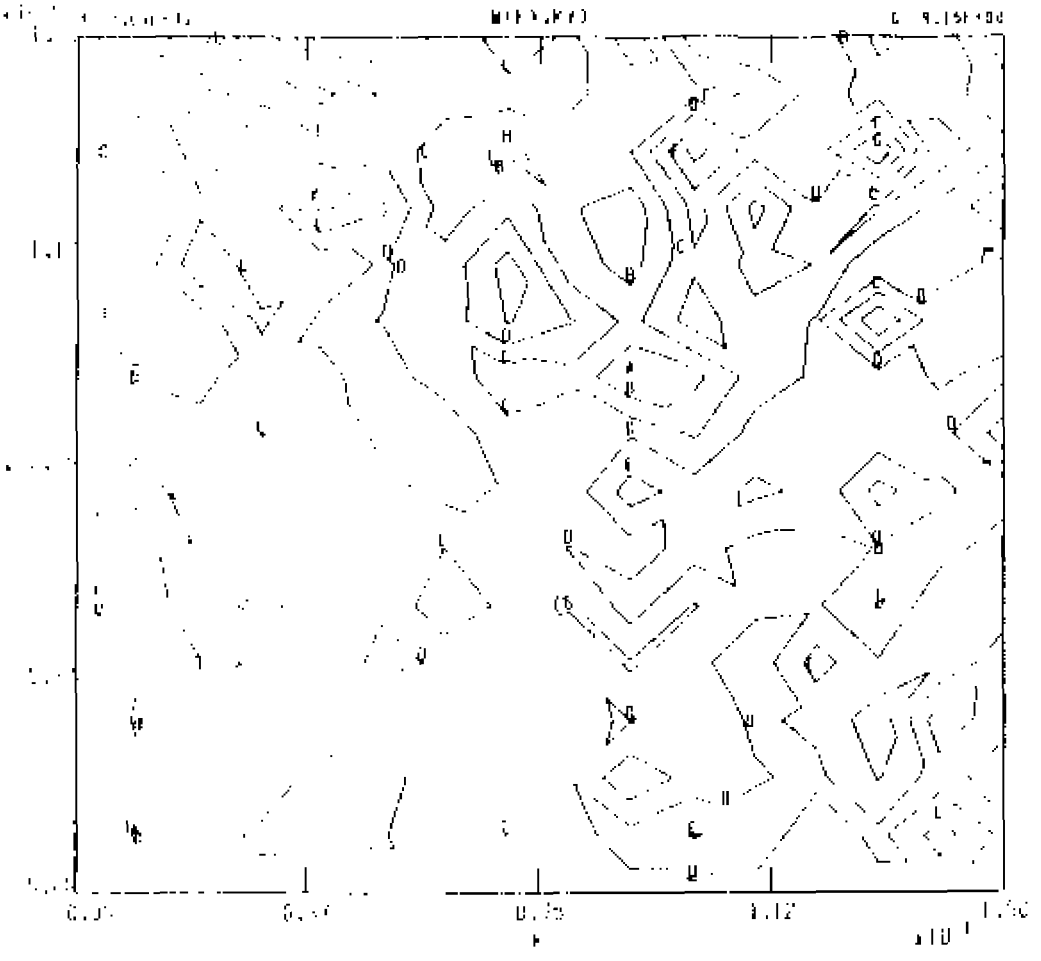

A2 (f): Fourier space contour plots, t = 8.76, of $\bar{\omega}$.

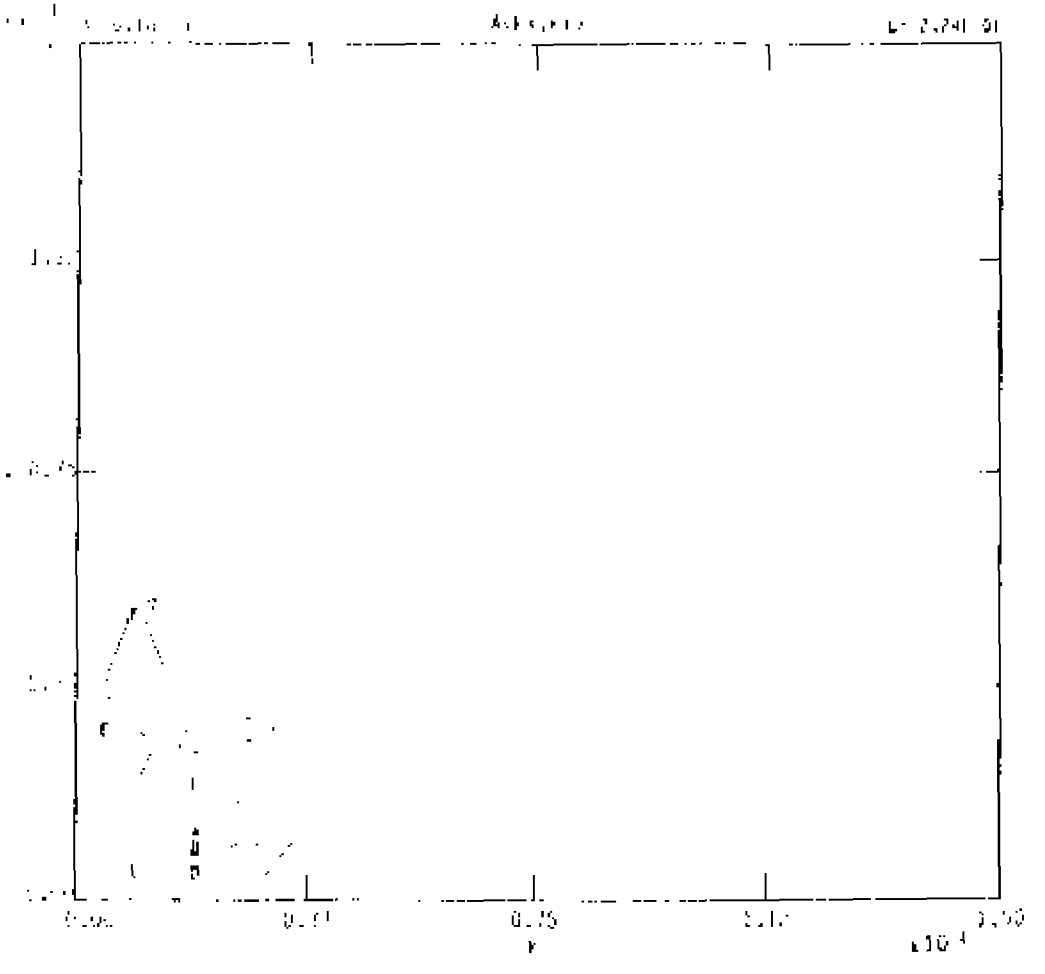

and A2 (g): Fourier space contour plots, t = 8.76, of $\tilde{A}$.

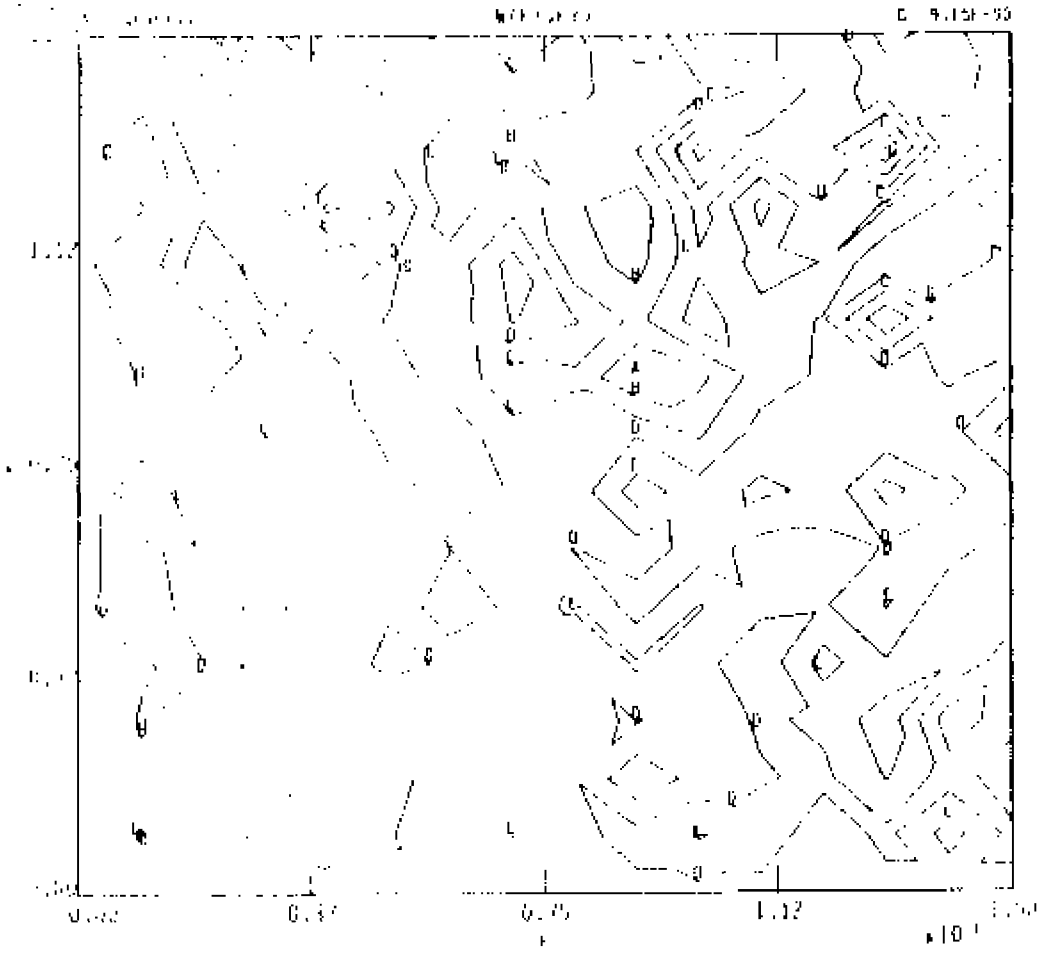

Figure A3. - RUN A3:
A3 (a): Fourier space contour plots, t = 8.76, of $\tilde{\omega}$.

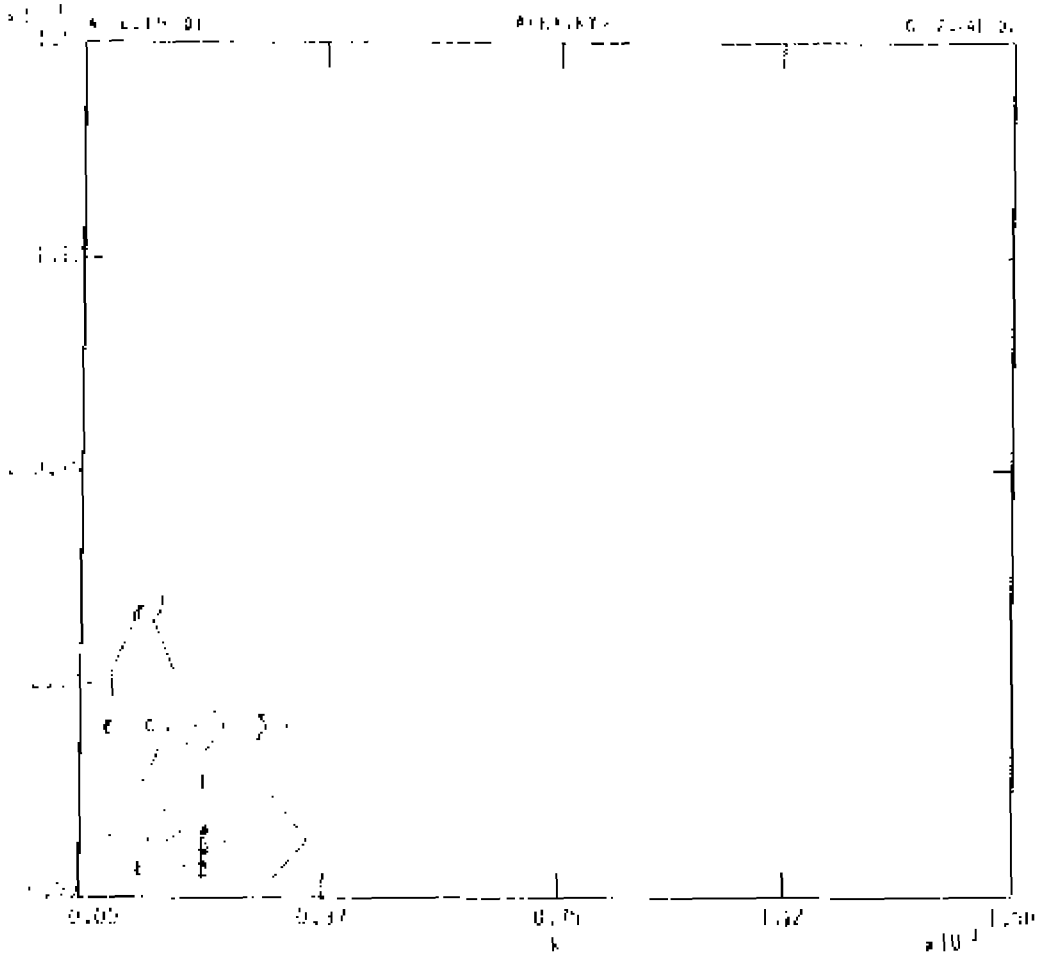

A3 (b): Fourier space contour plots, t = 8.76, of $\tilde{A}$.

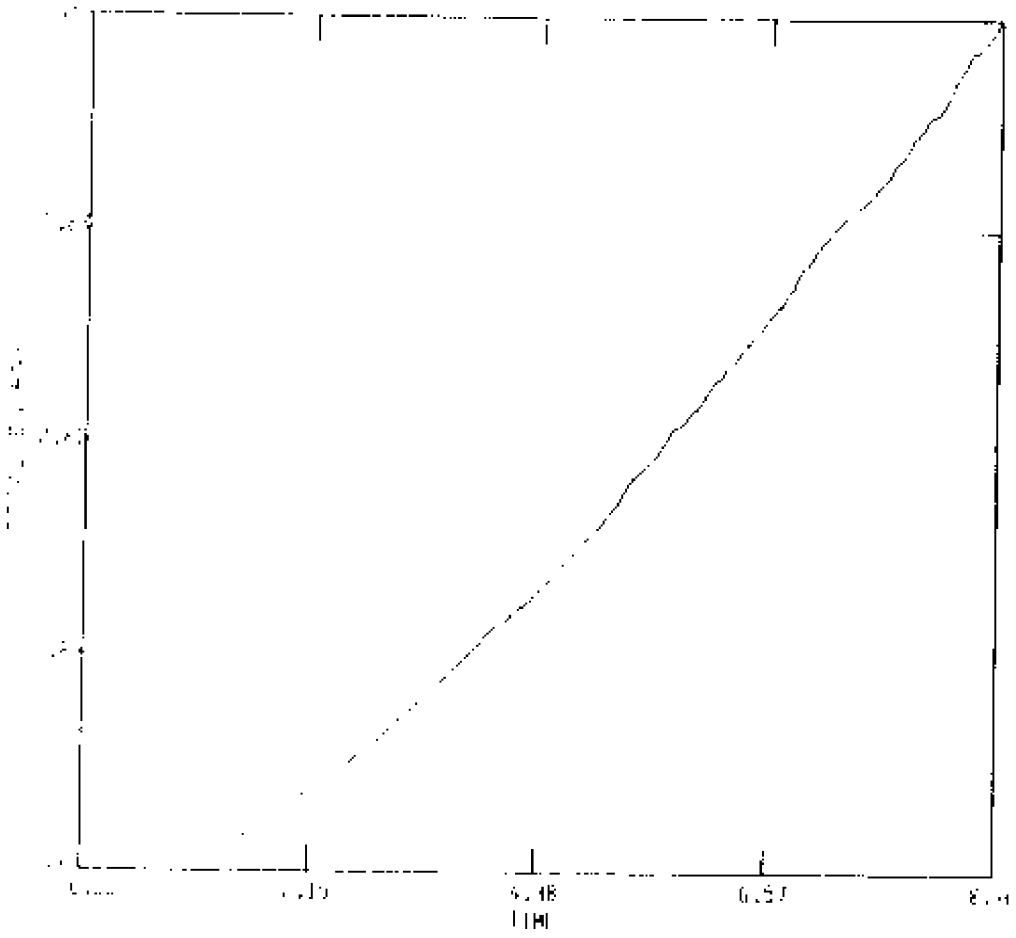

Figure A4. - RUN A4:
A4 (a): E_T as f(t).

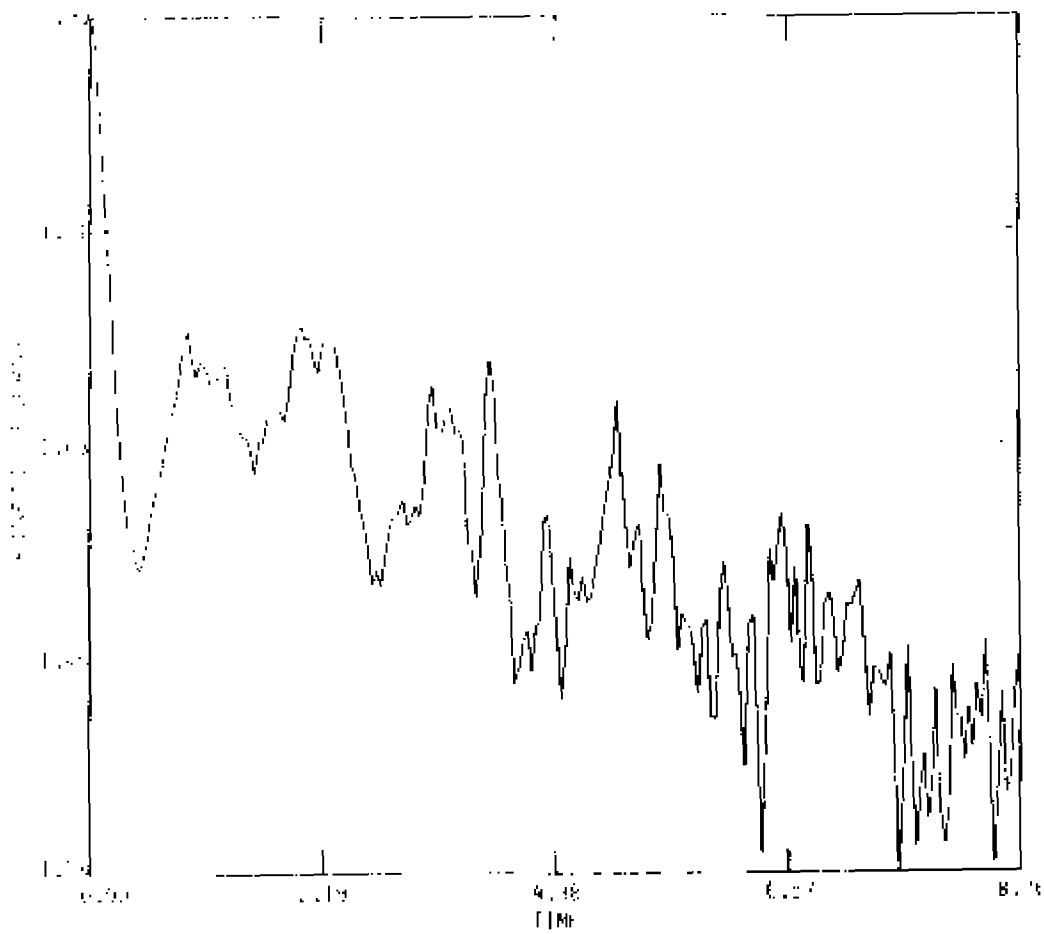

A4 (b): E_v as f(t).

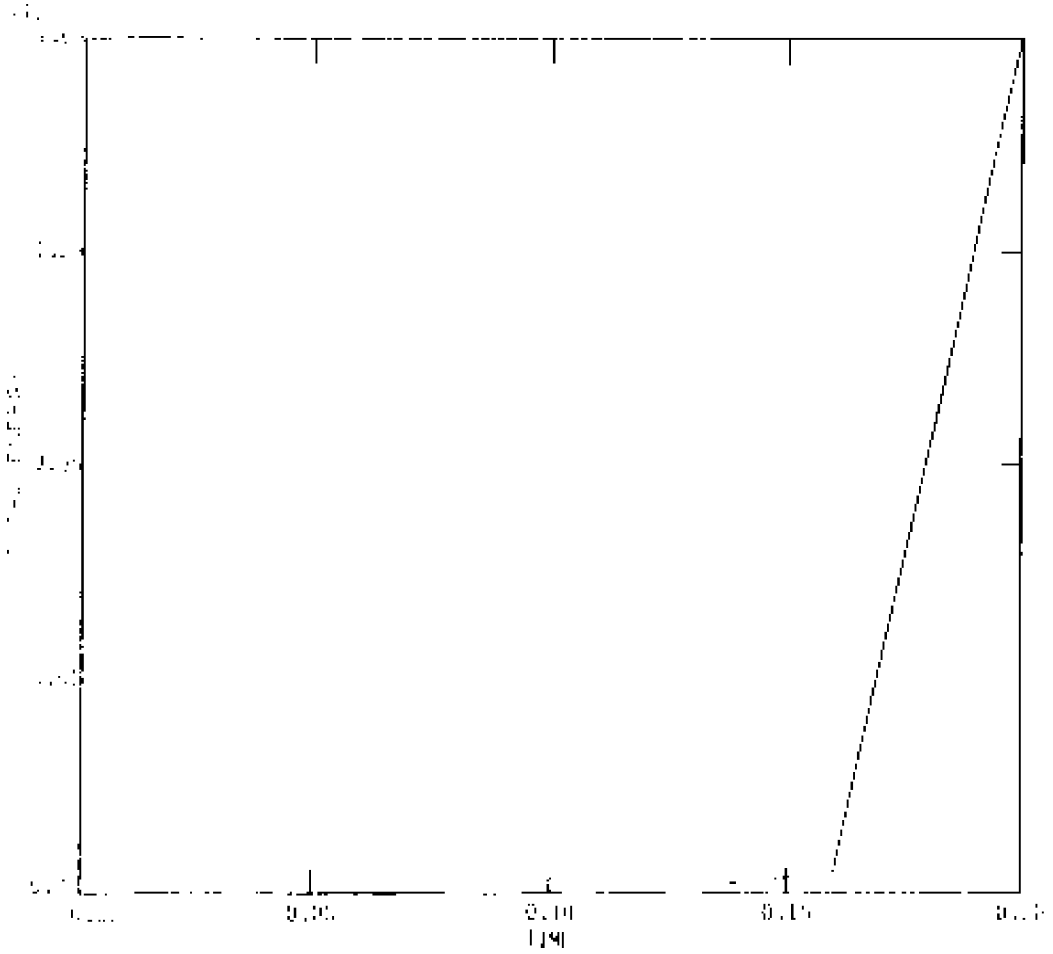

Figure A5. - RUN A5:
A5 (a): E_T as f(t).

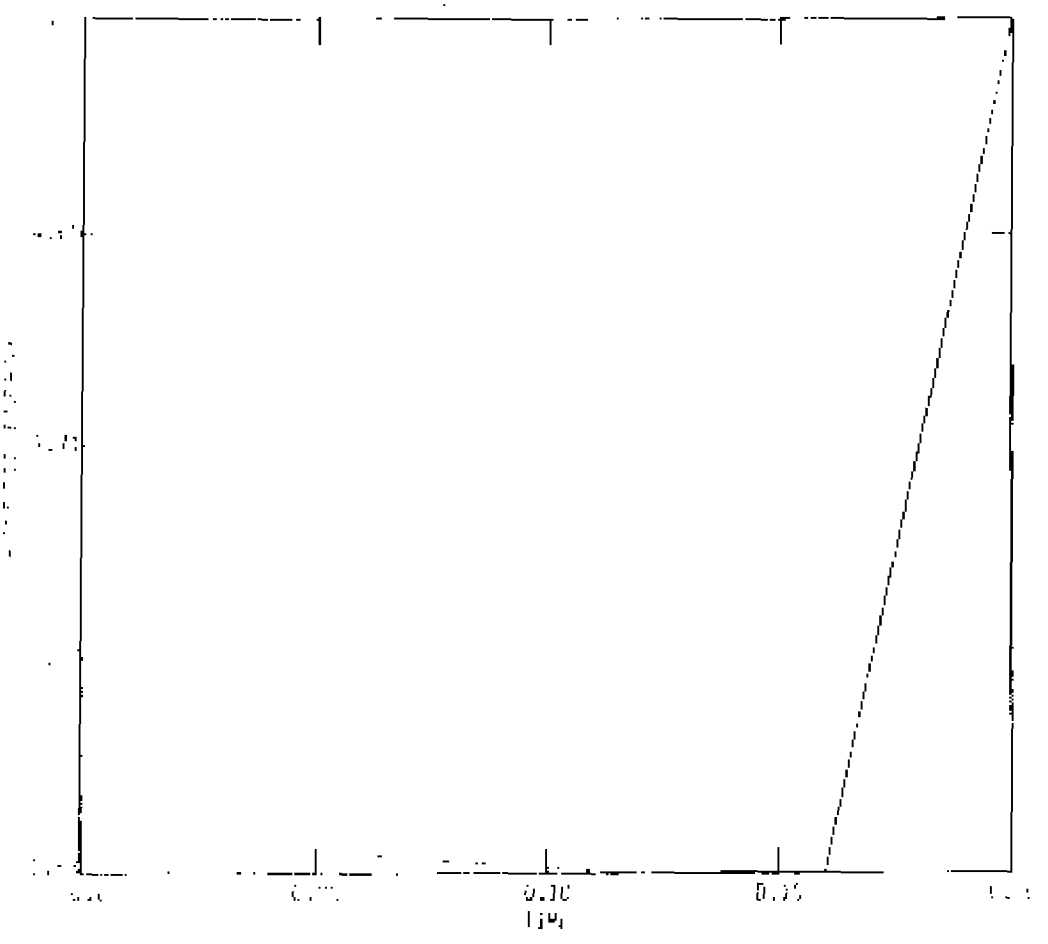

A5 (b): E_v as f(t).

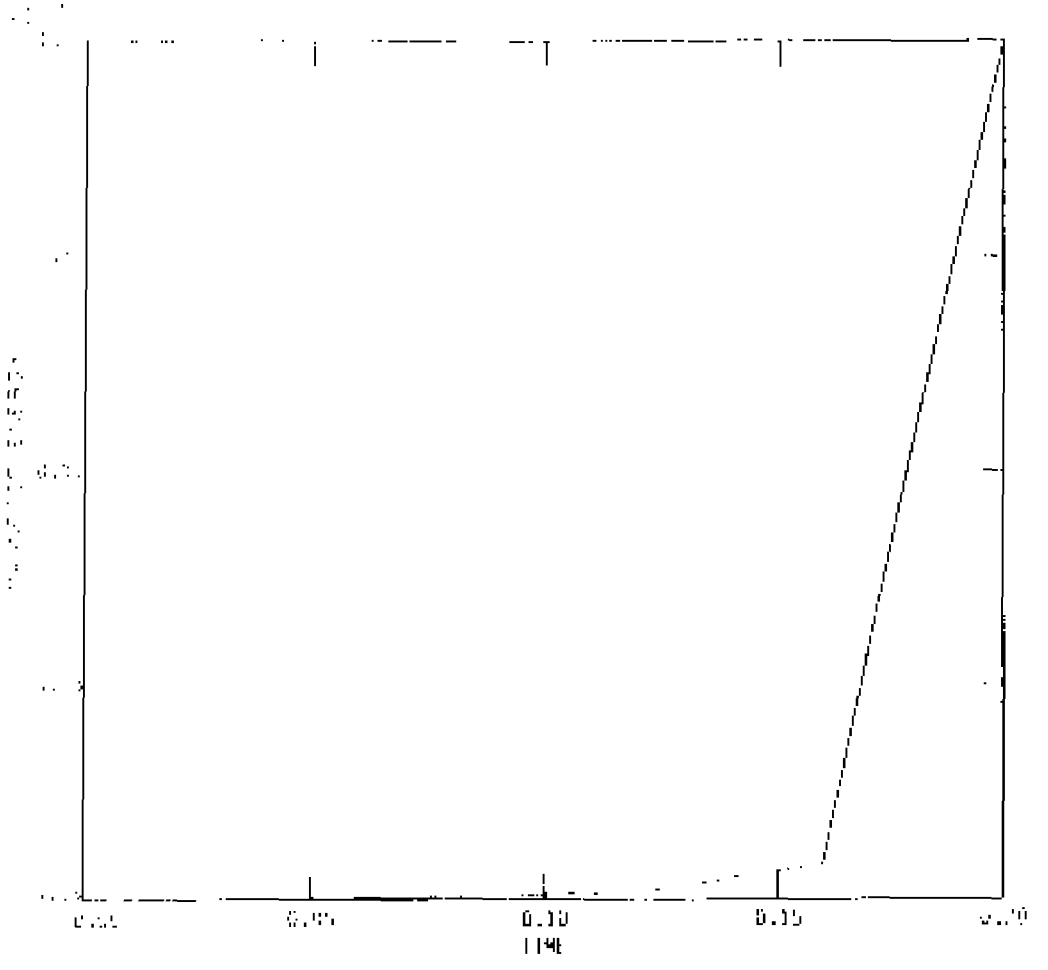

A5 (c): Σ_B as f(t).

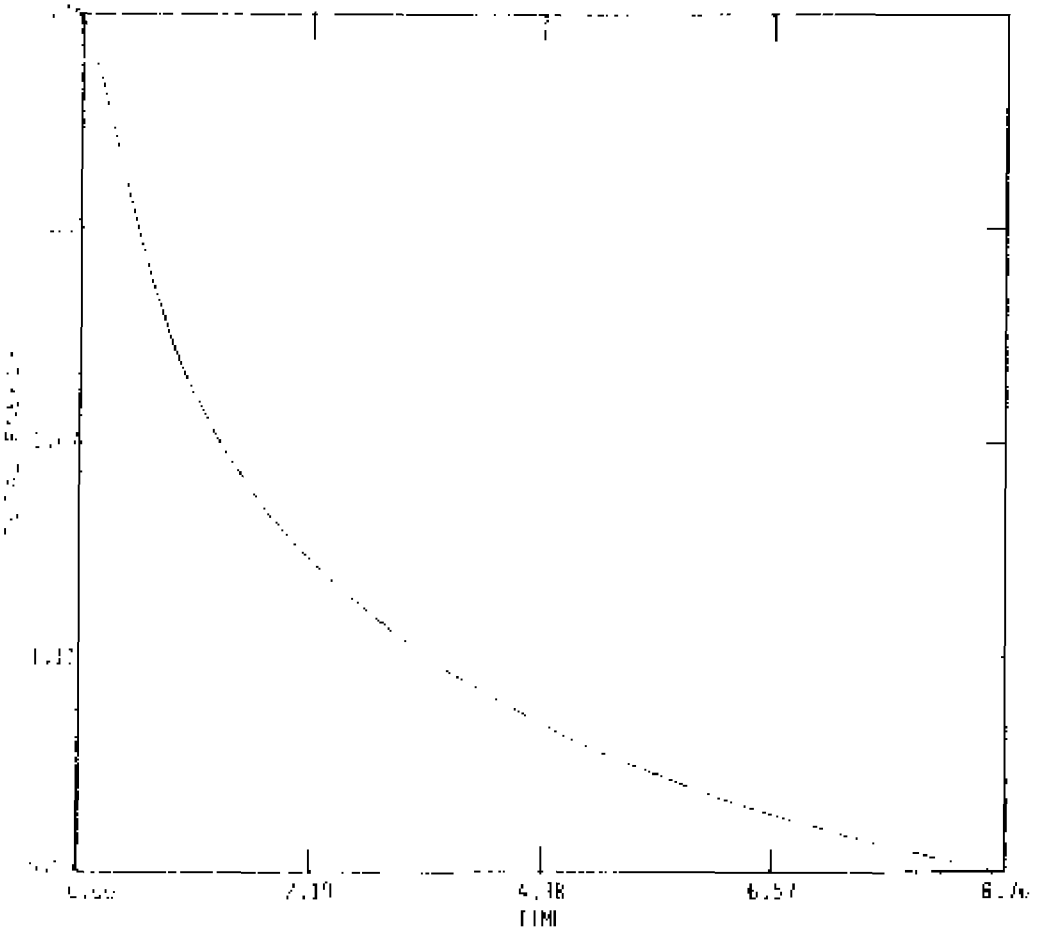

Figure A6. - RUN A6:
A6 (a): E_T as f(t).

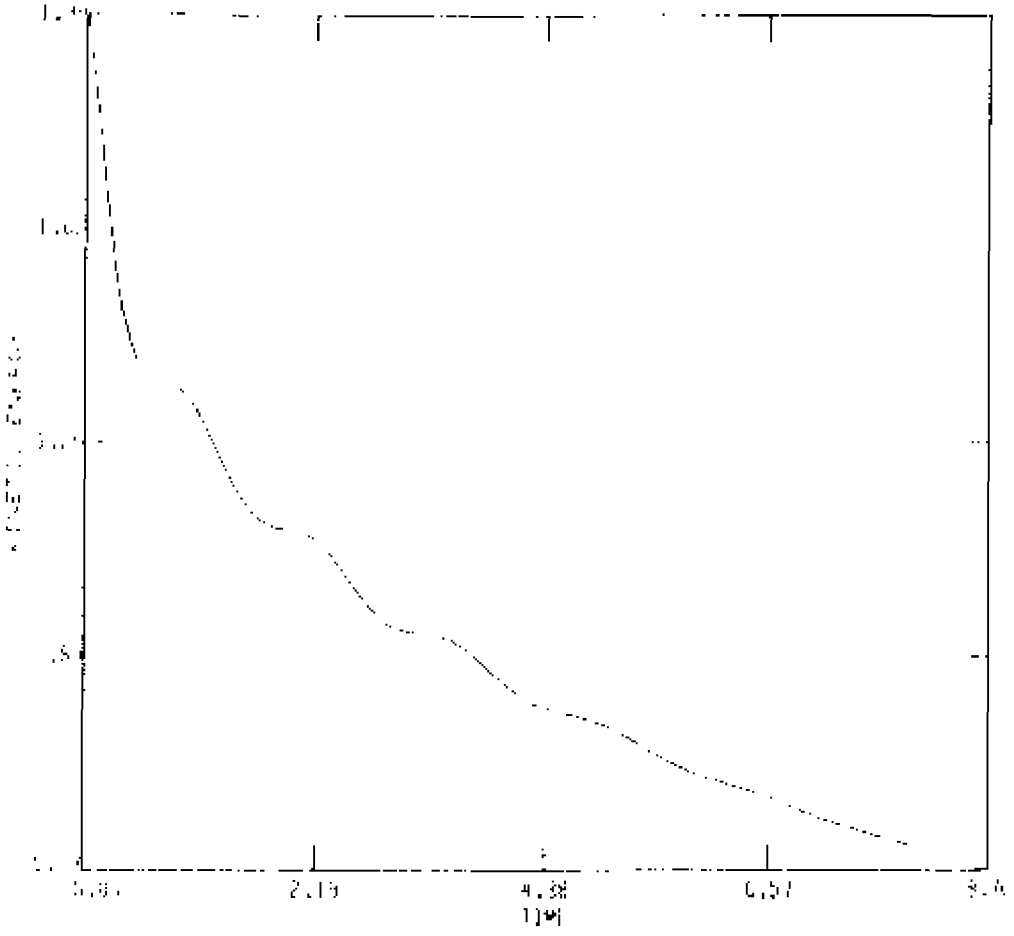

A6 (b): E_v as f(t).

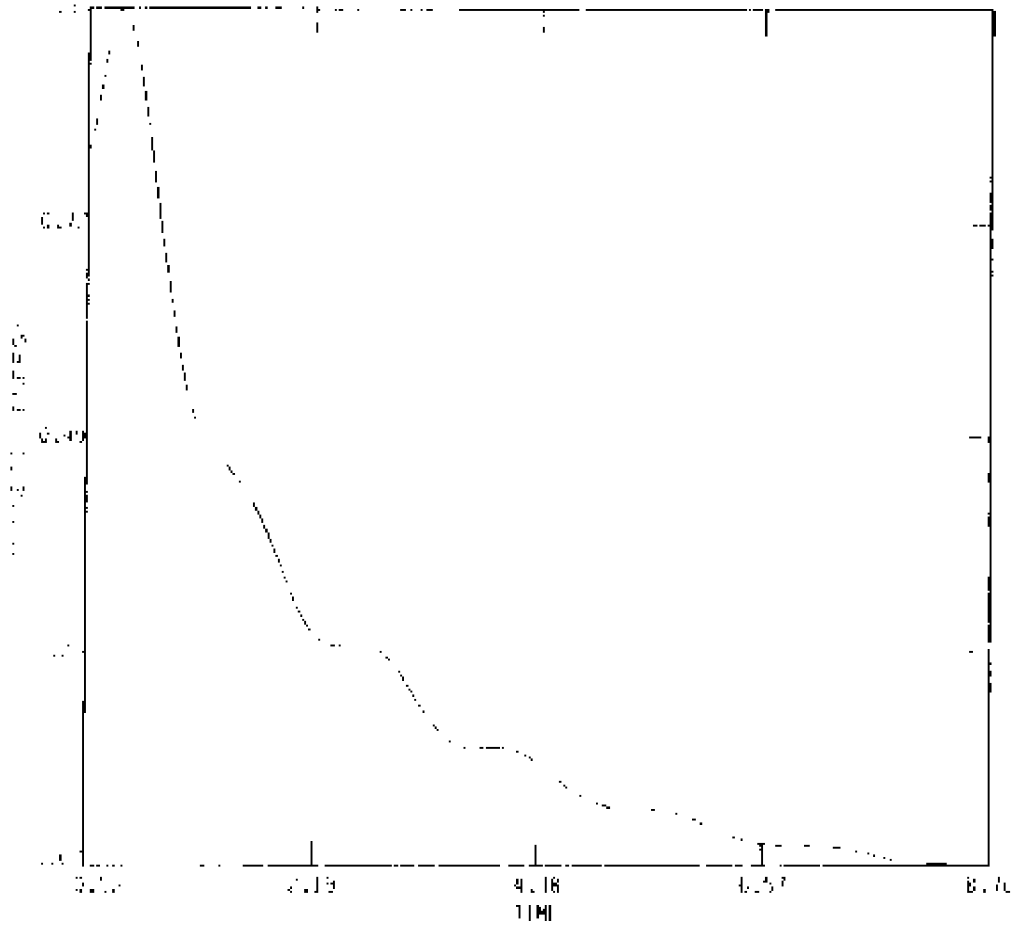

A6 (c): E_B as f(t).

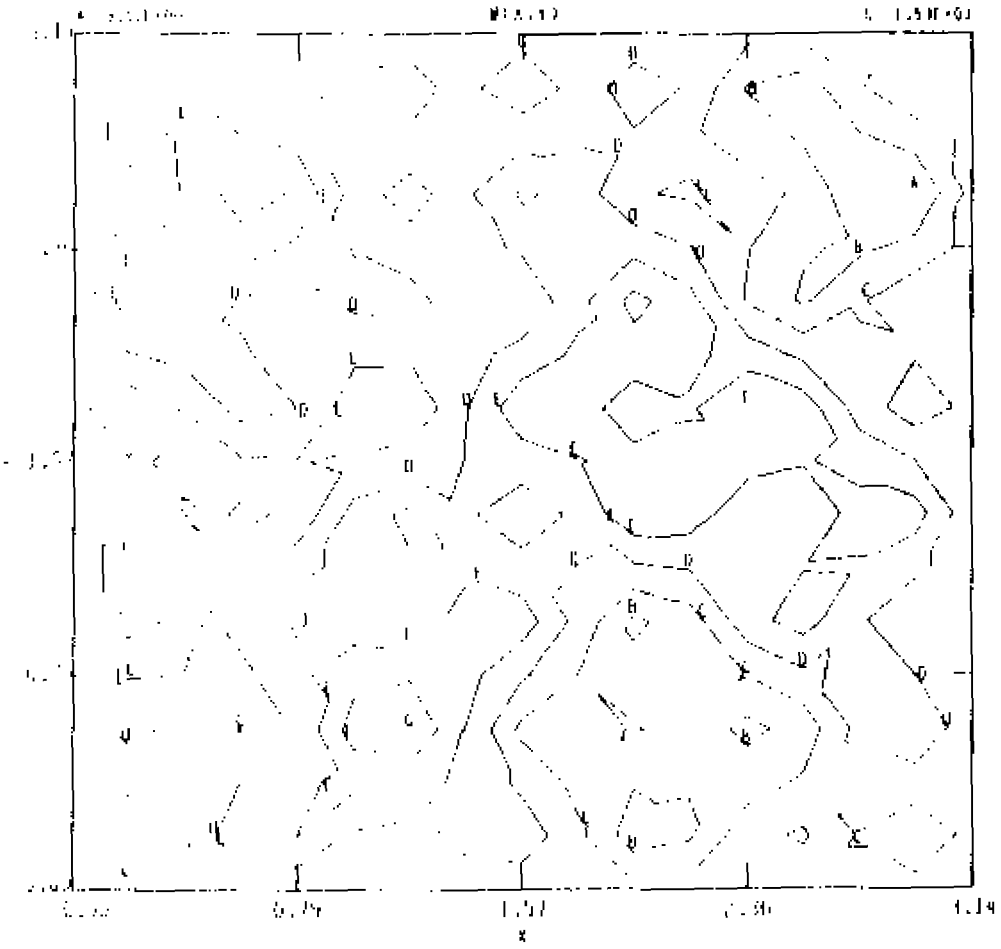

A6 (d): physical space contour plots, t = 0.00, of ω.

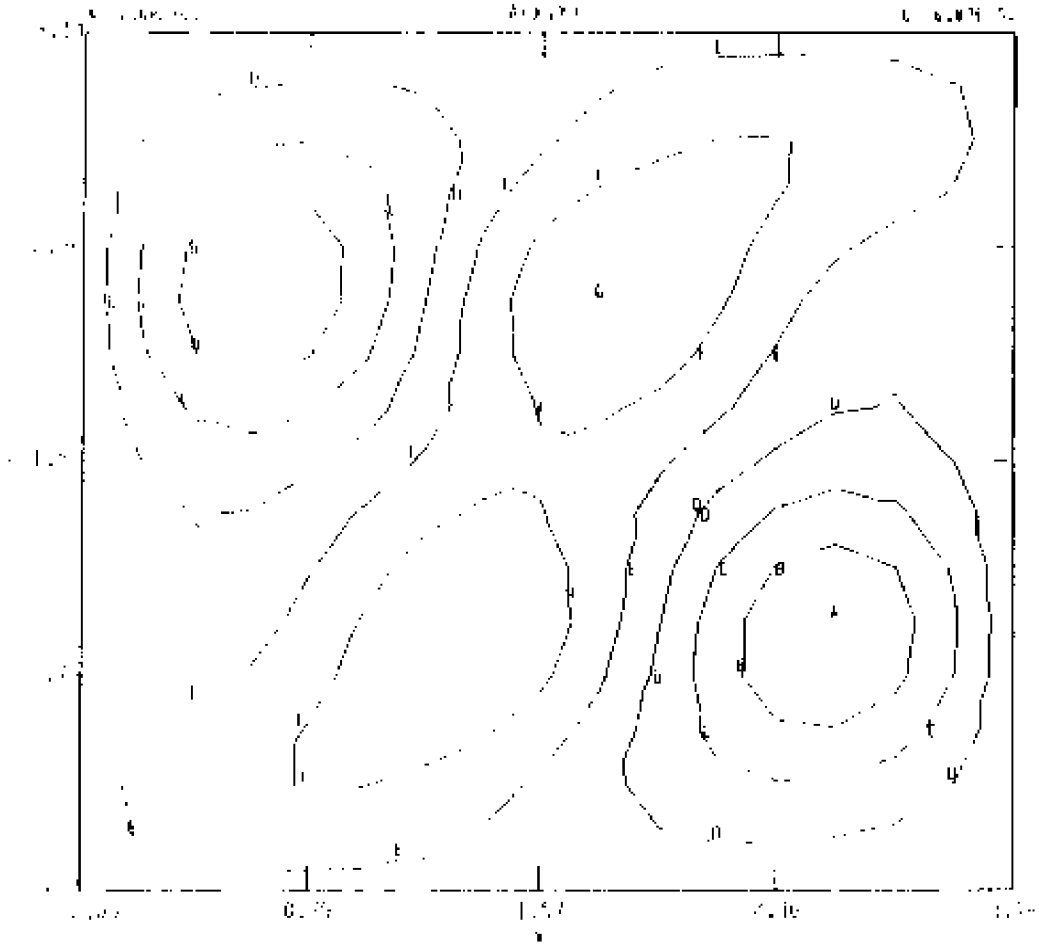

A6 (e): physical space contour plots, t = 0.60, of A.

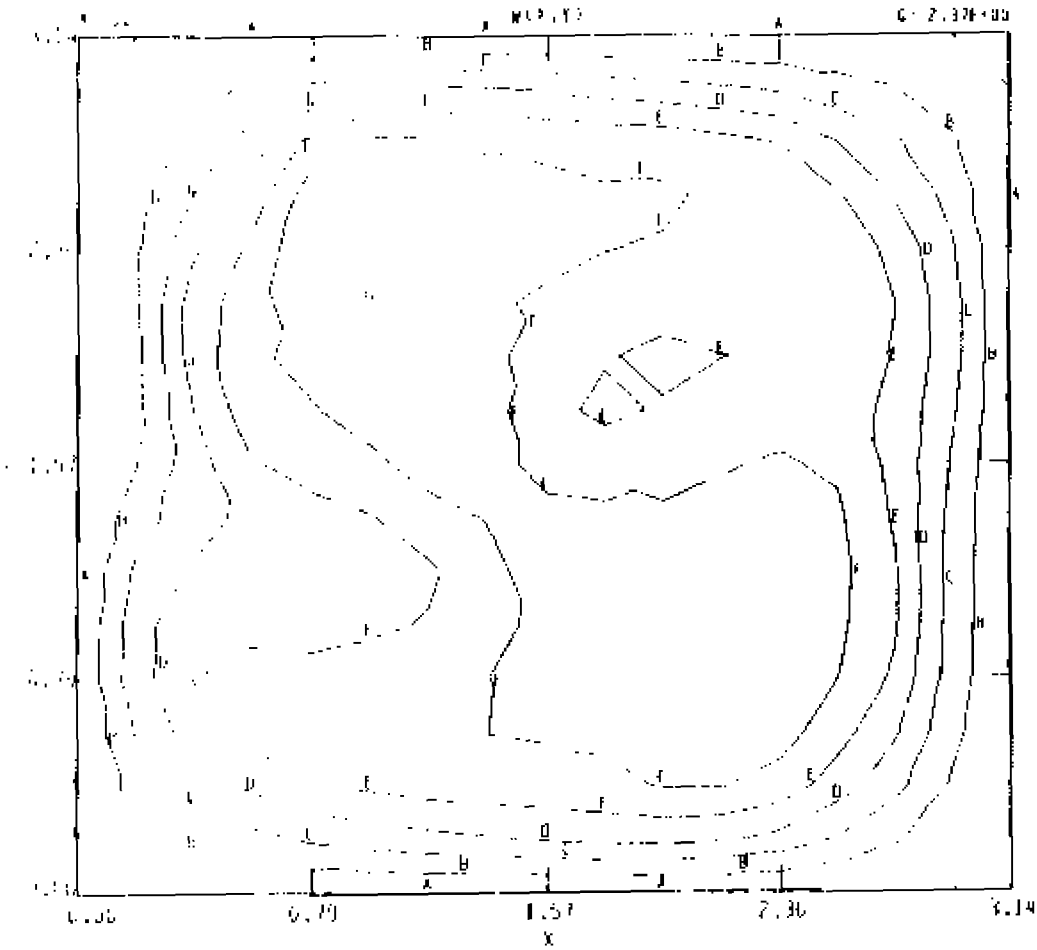

A6 (f): physical space contour plots, t = 8.76, of ω.

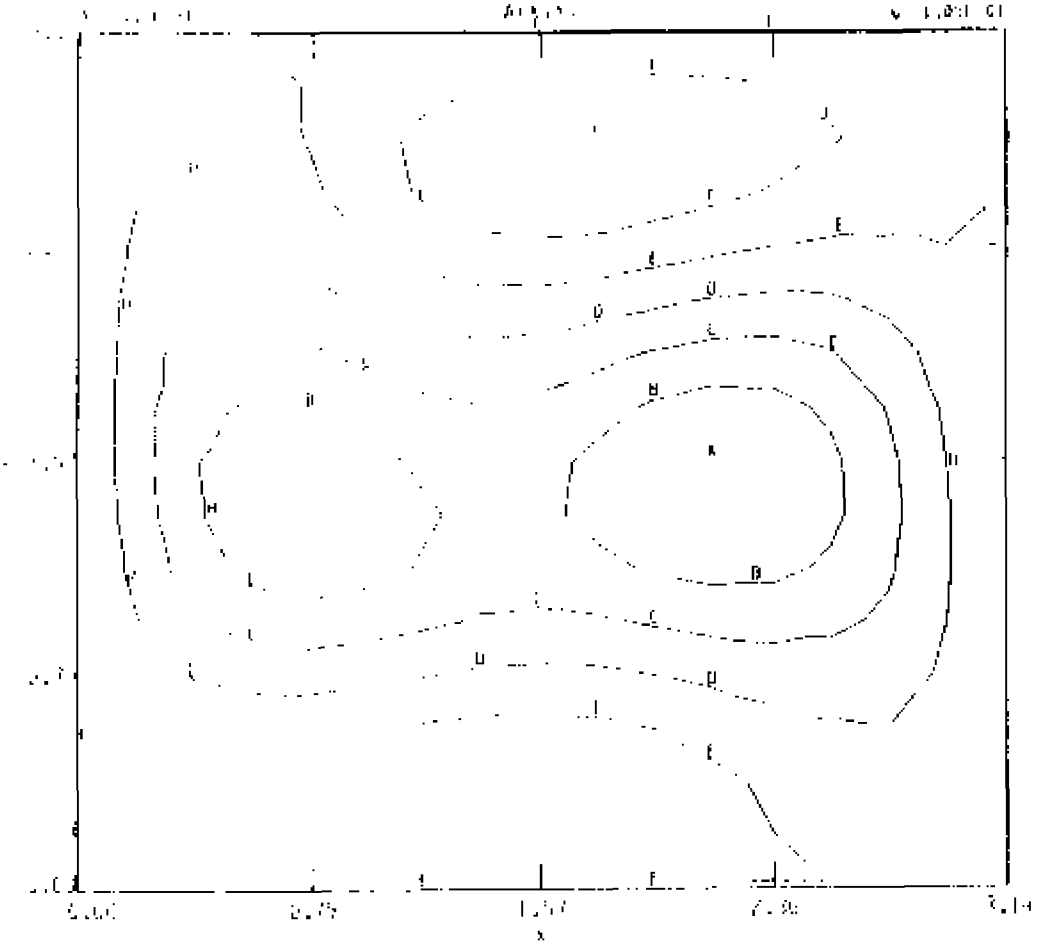

and A6 (g): physical space contour plots, t = 8.76, of A.

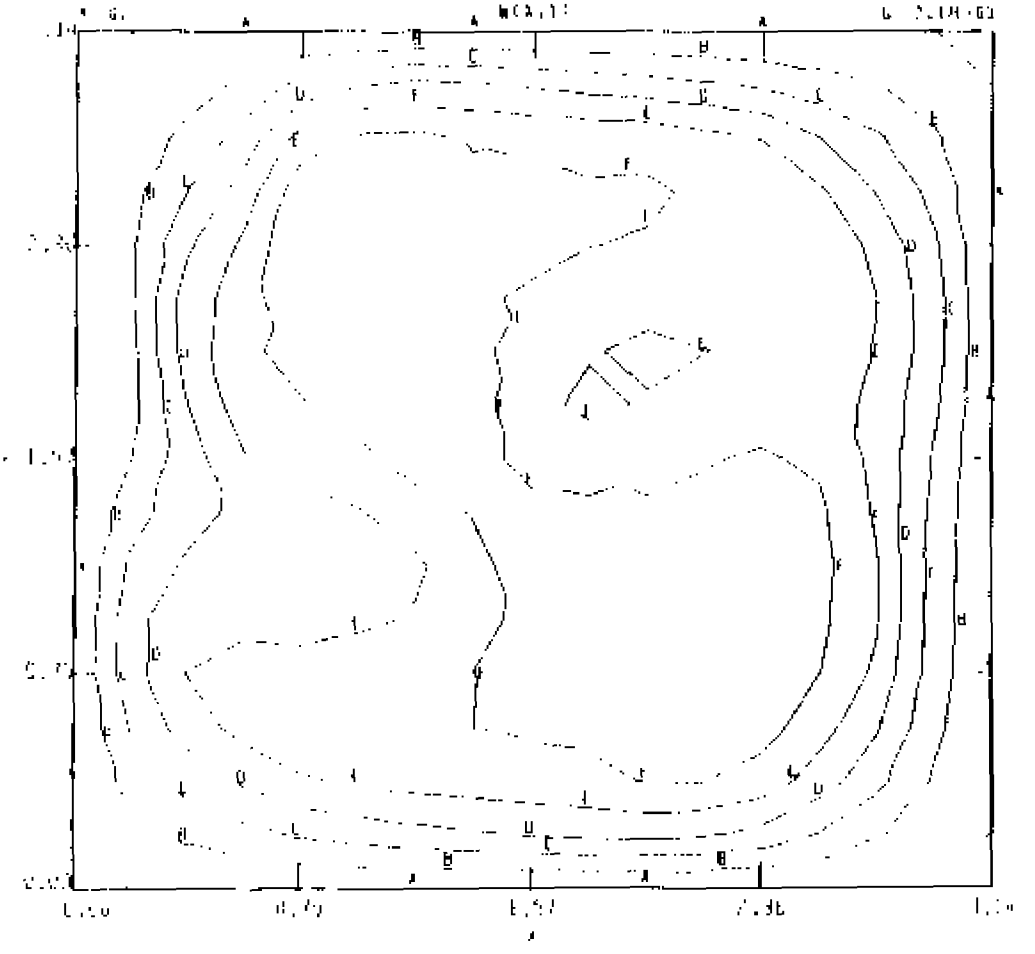

Figure A7. - RUN A7:
A7 (a): physical space contour plots, t = 8.76, of ω.

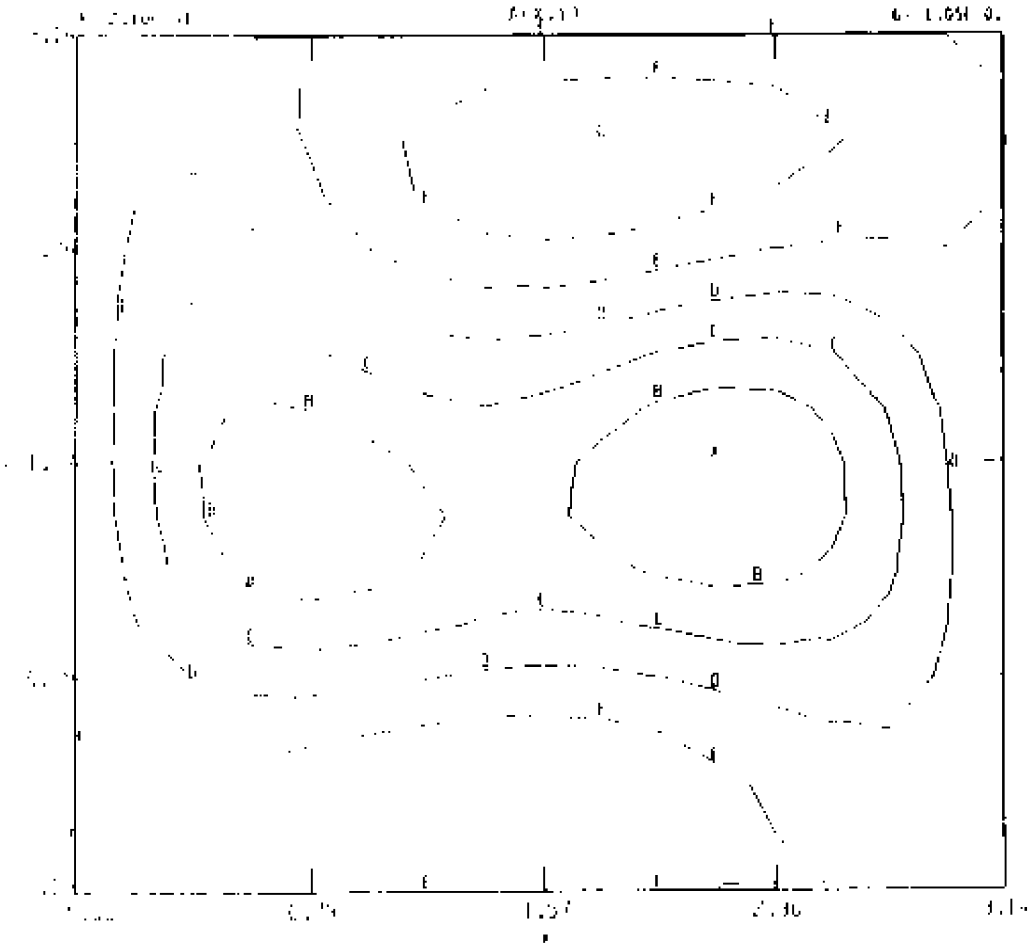

A7 (b): physical space contour plots, t = 8.76, of A.

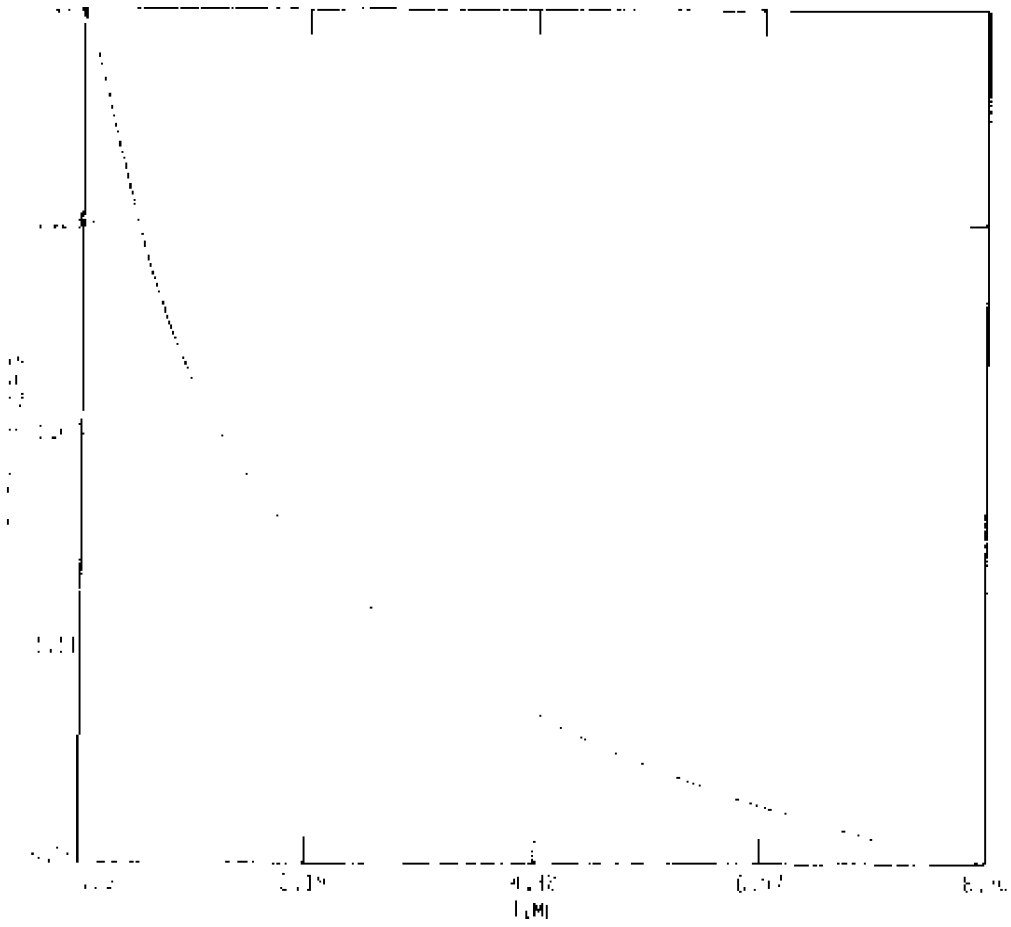

Figure A8. - RUN A8:
A8 (a): E_T as f(t).

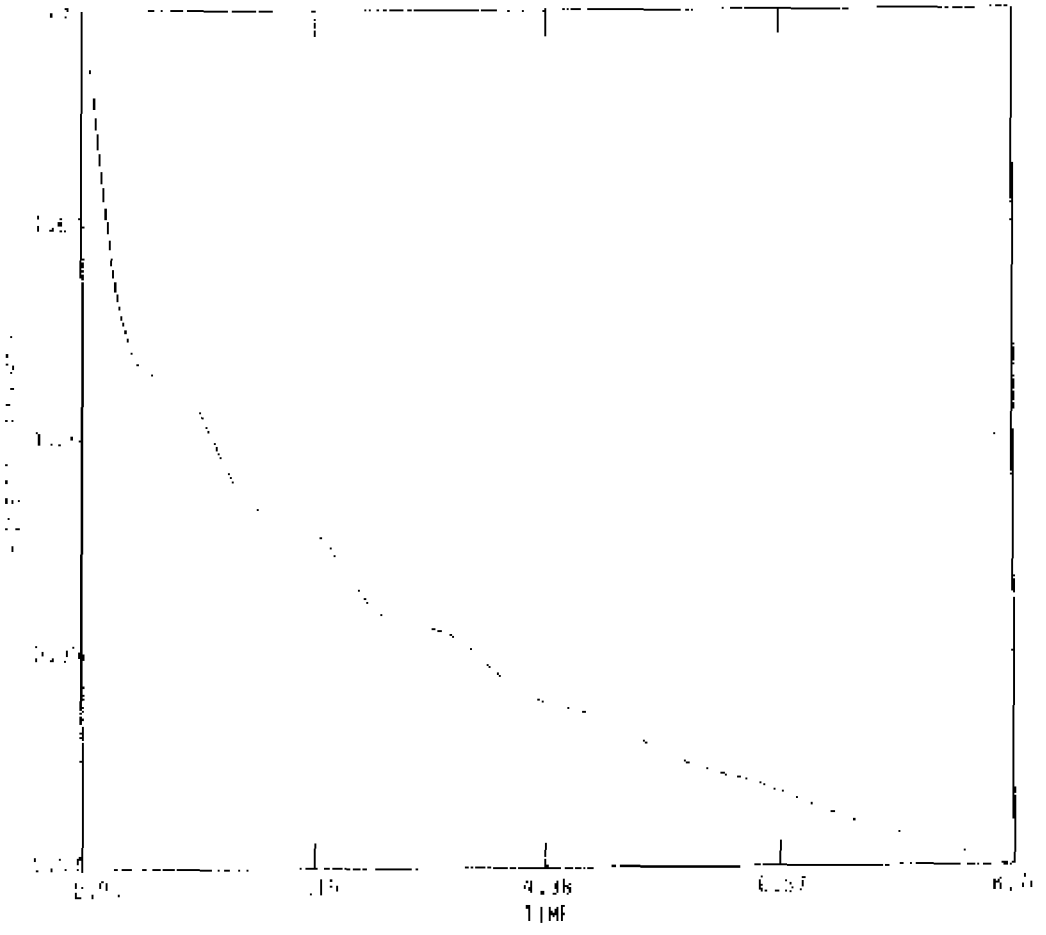

AB (b): E_v as f(t).

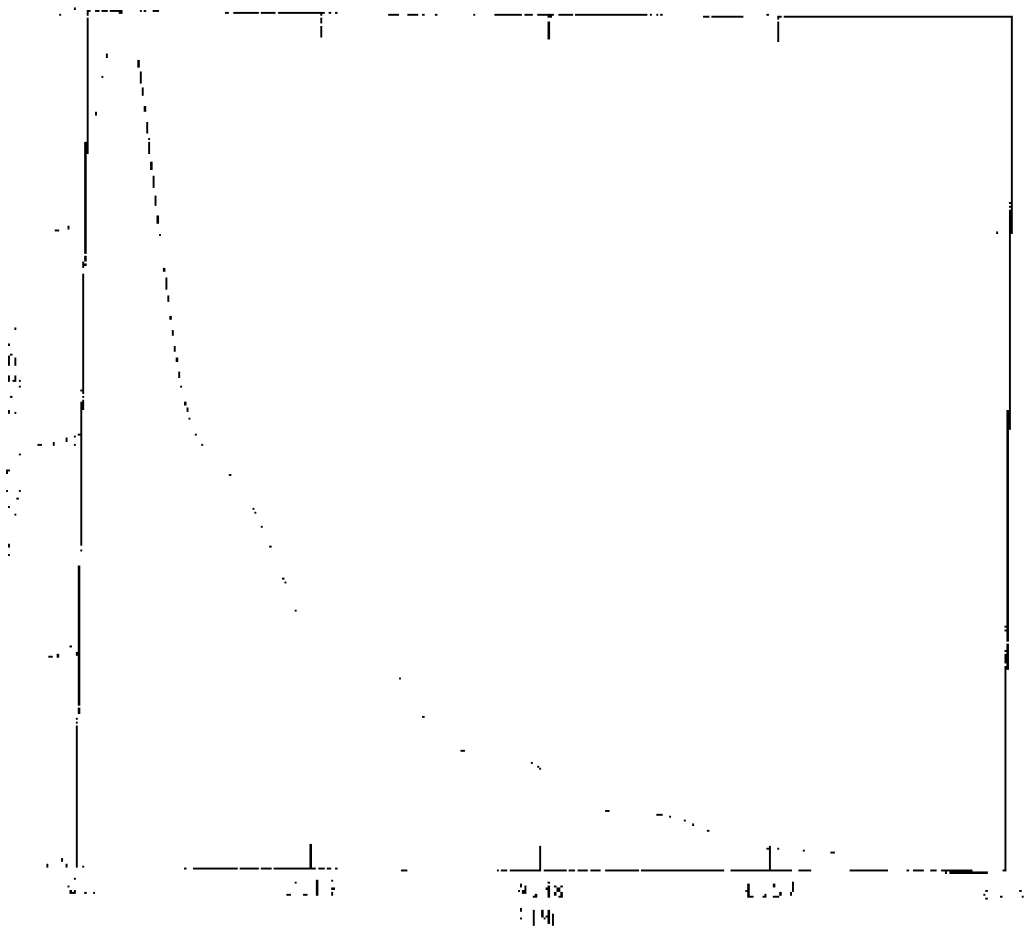

Ab (c): E_B as f(t).

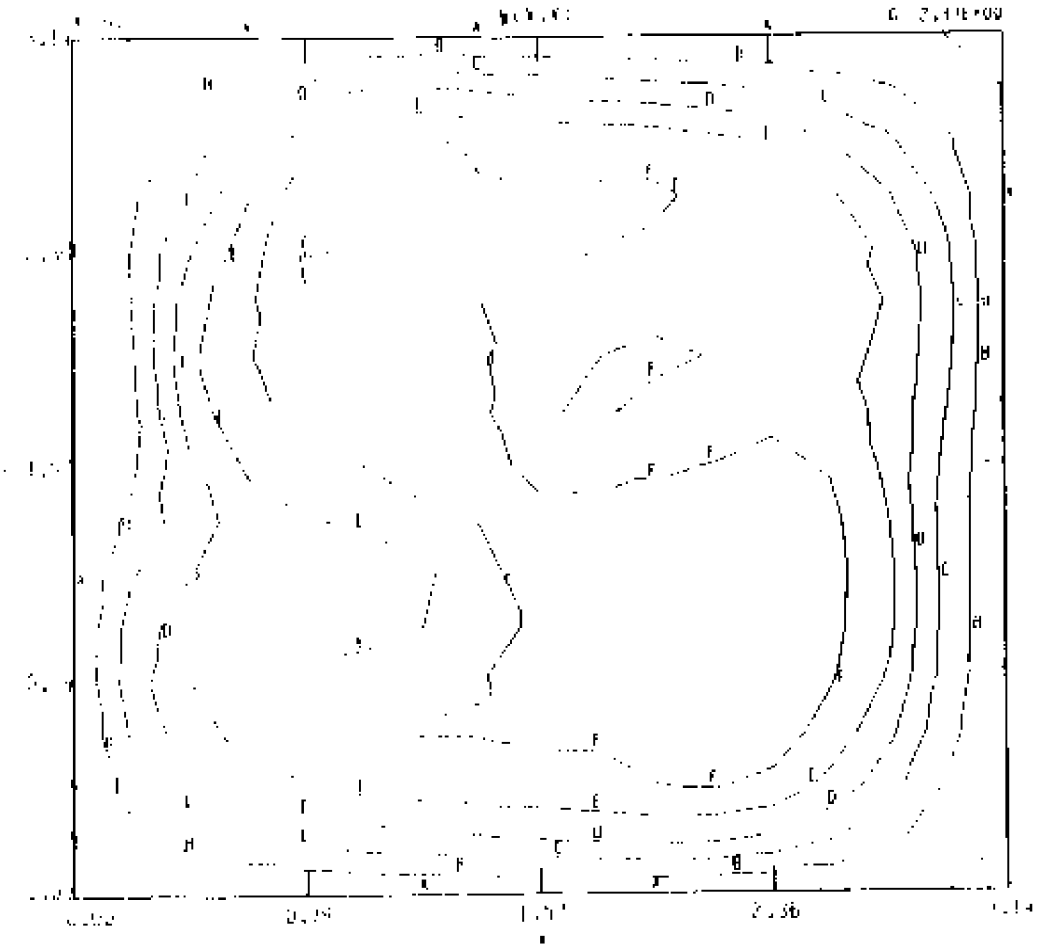

A8 (d): physical space contour plots, $t = 0.76$, of ω.

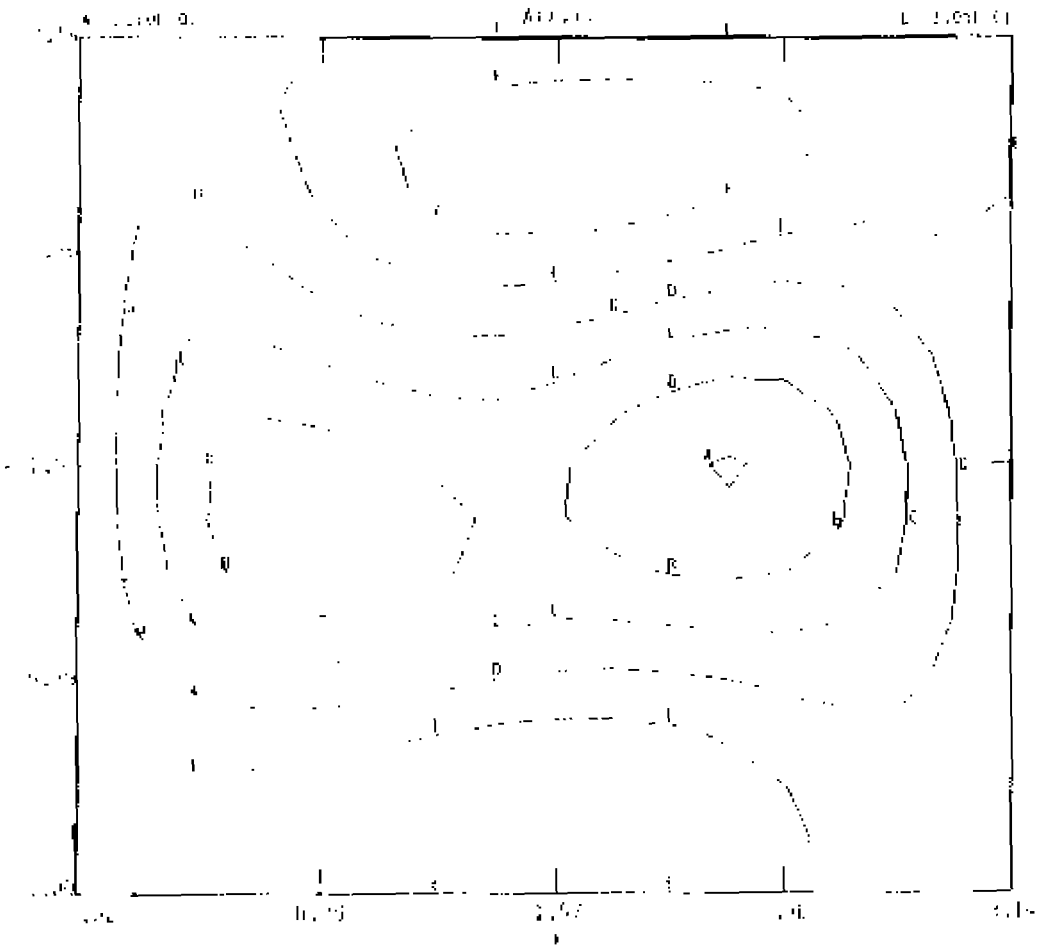

and A8 (e): physical space contour plots, t = 8.76, of A.

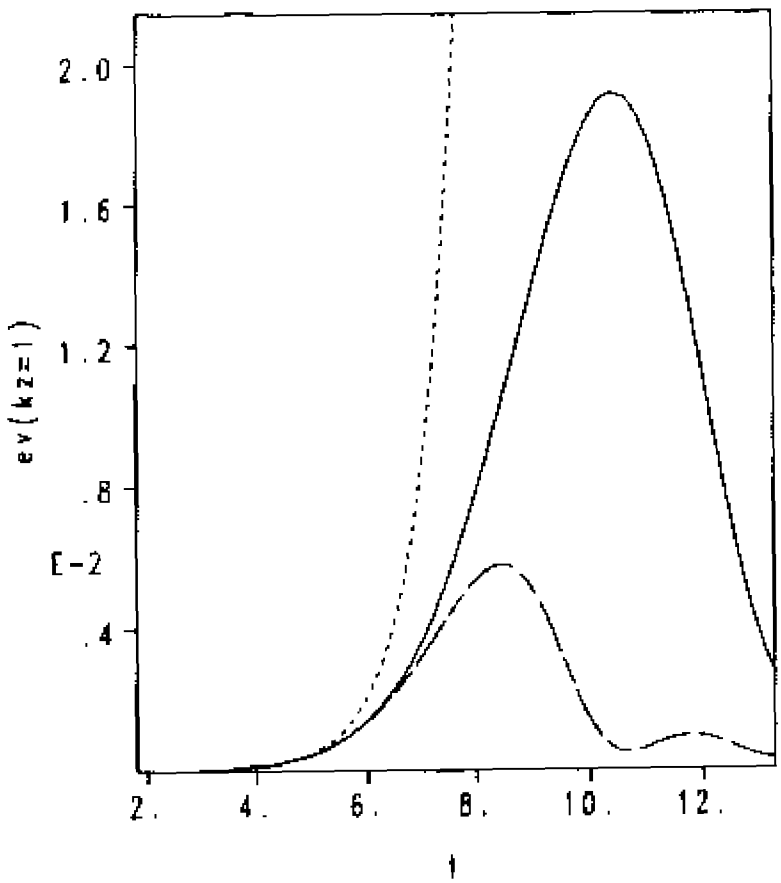

Figure B1. - CASE 2:
B1 (a): kinetic energy ($k_z = 1,t$) for runs:
FROZEN (short dashed line),
THAWED (solid line),
NONLINEAR (long dashed line), and

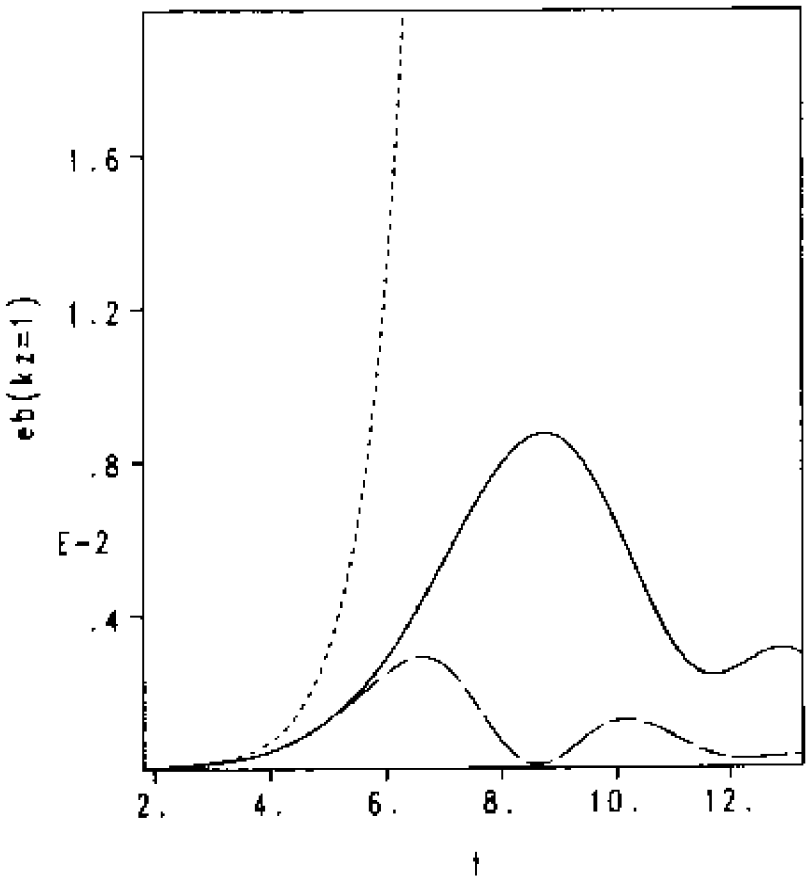

B1 (b): magnetic energy (k_z = 1,t) for runs:
FROZEN (short dashed line),
THAWED (solid line),
NONLINEAR (long dashed line).

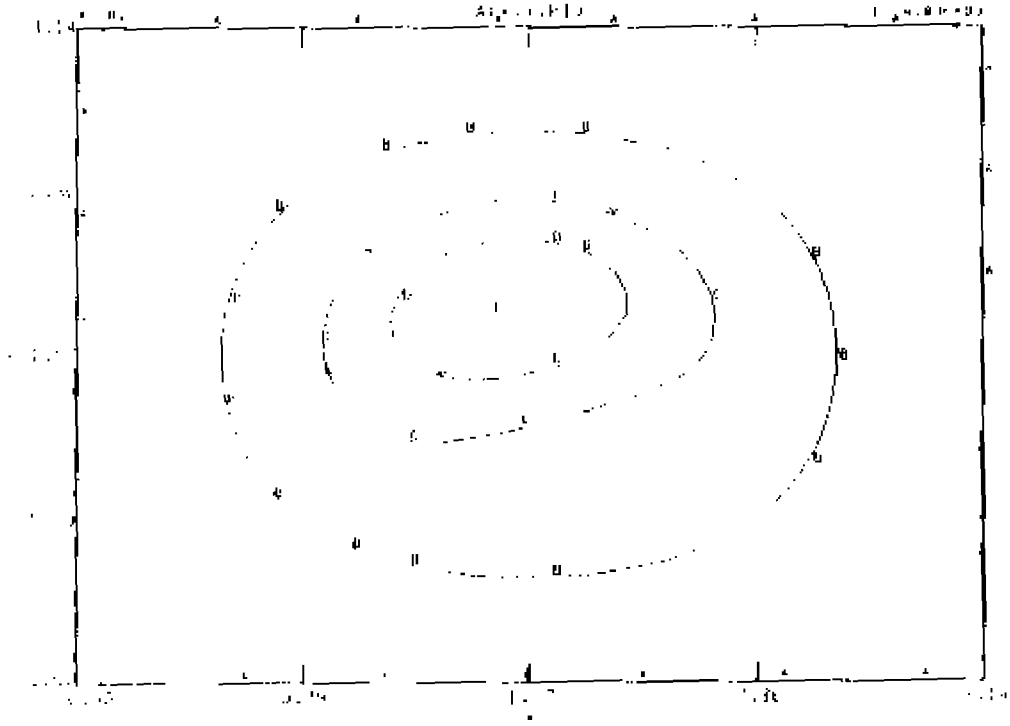

Figure B2. - CASE 2, t = 8.82:
B2 (a): contours of A = constant from FROZEN run.

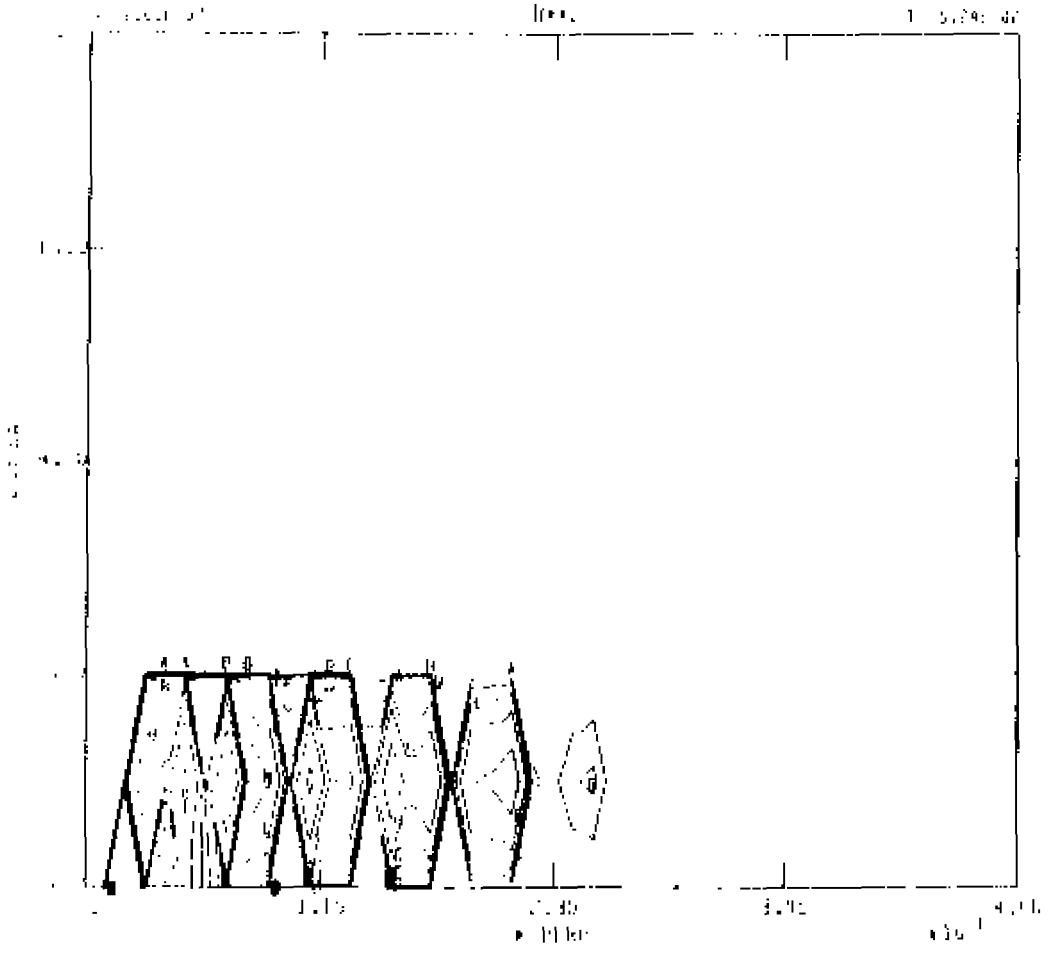

B2 (b): spectra of modal magnetic energy from FROZEN run.

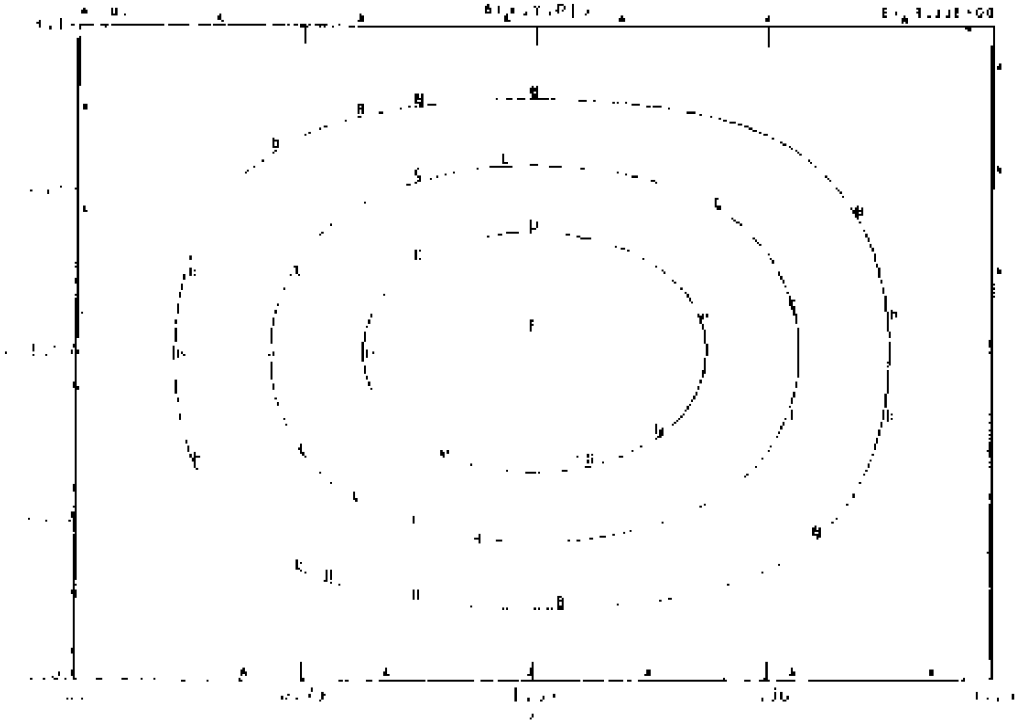

B2 (c): contours of A = constant from THAWED run.

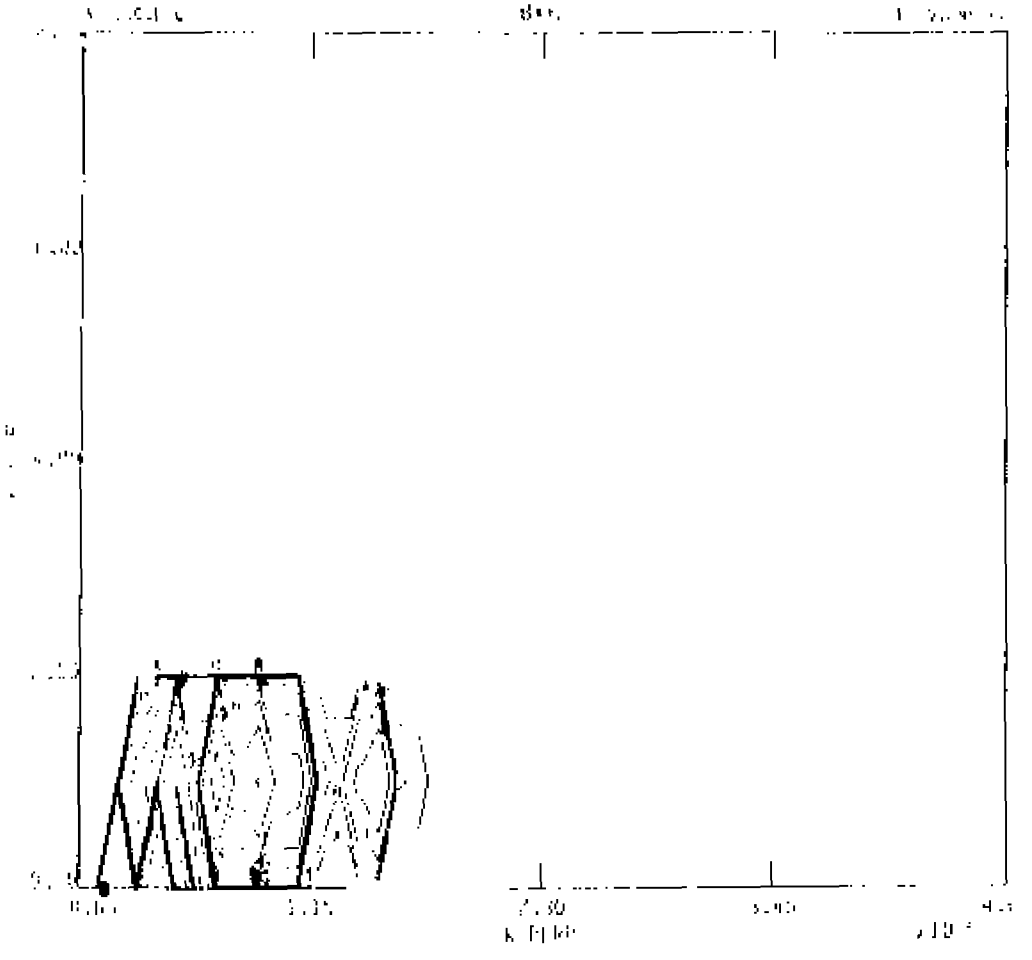

B2 (d): spectra of modal magnetic energy from THAWED run.

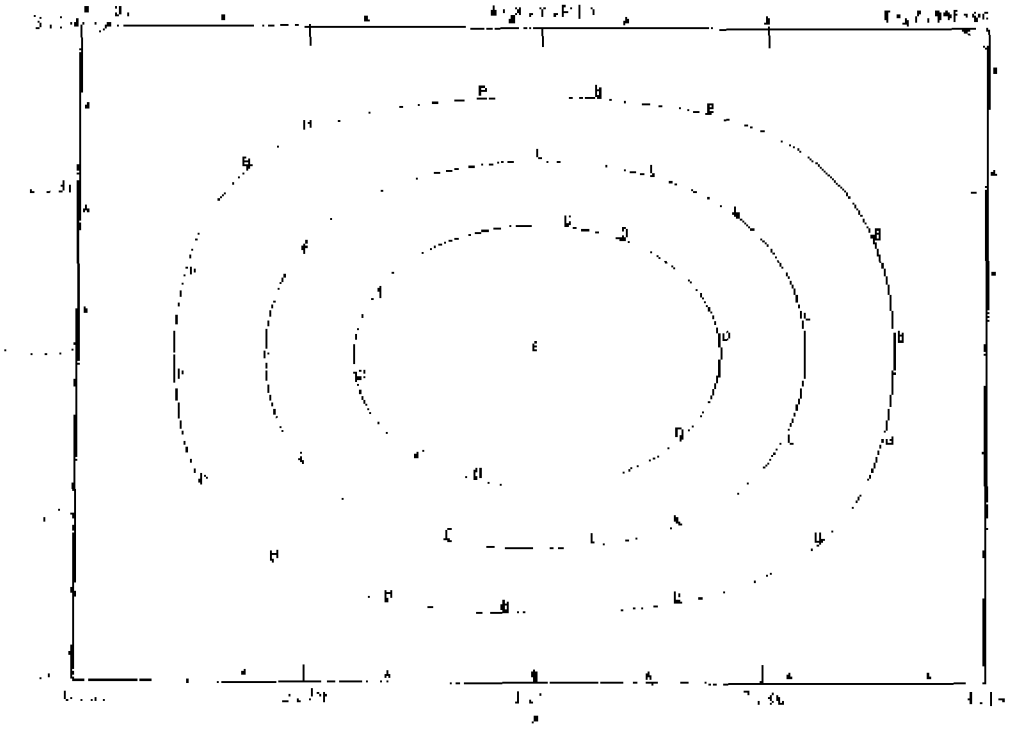

B2 (e): contours of A = constant from NONLINEAR run.

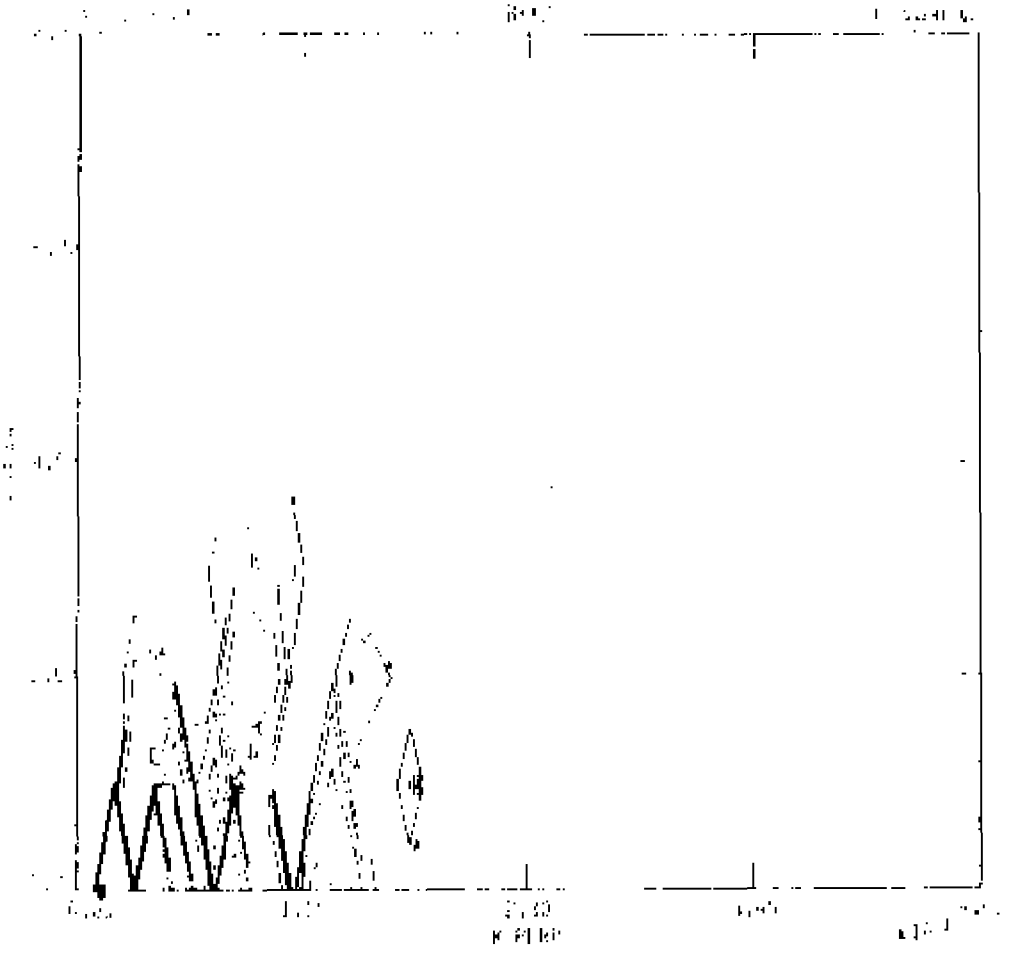

B2 (f): spectra of modal magnetic energy from NONLINEAR run.

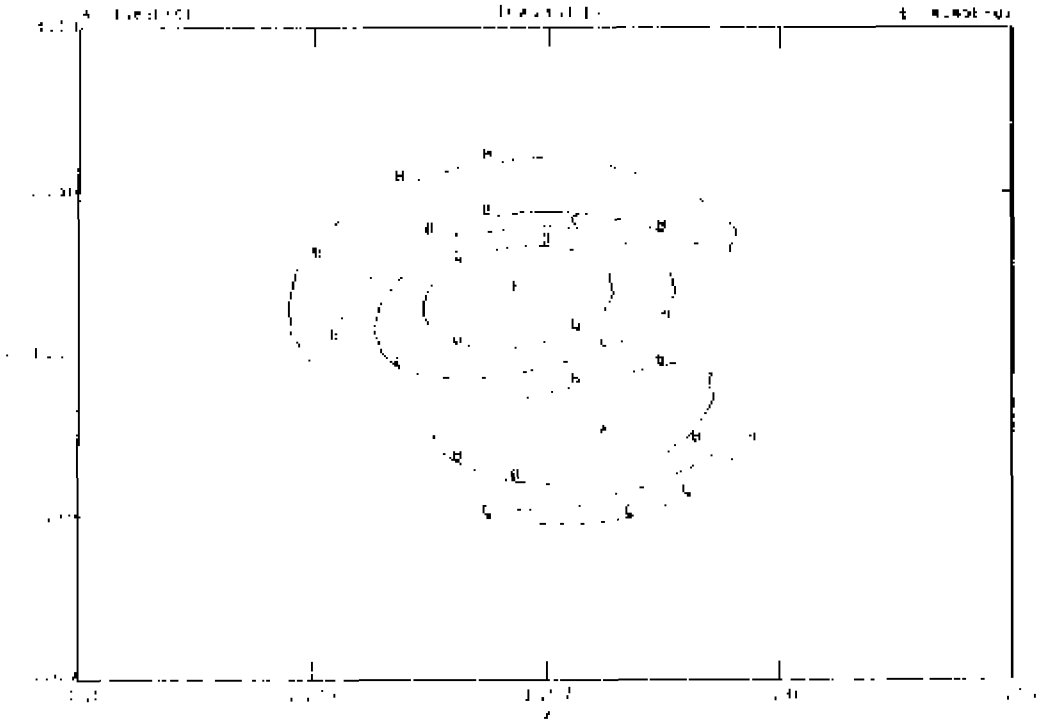

Figure B3. - CASE 2, contours of constant current, t = 8.82.
B3 (a): poloidal cut from FROZEN run.

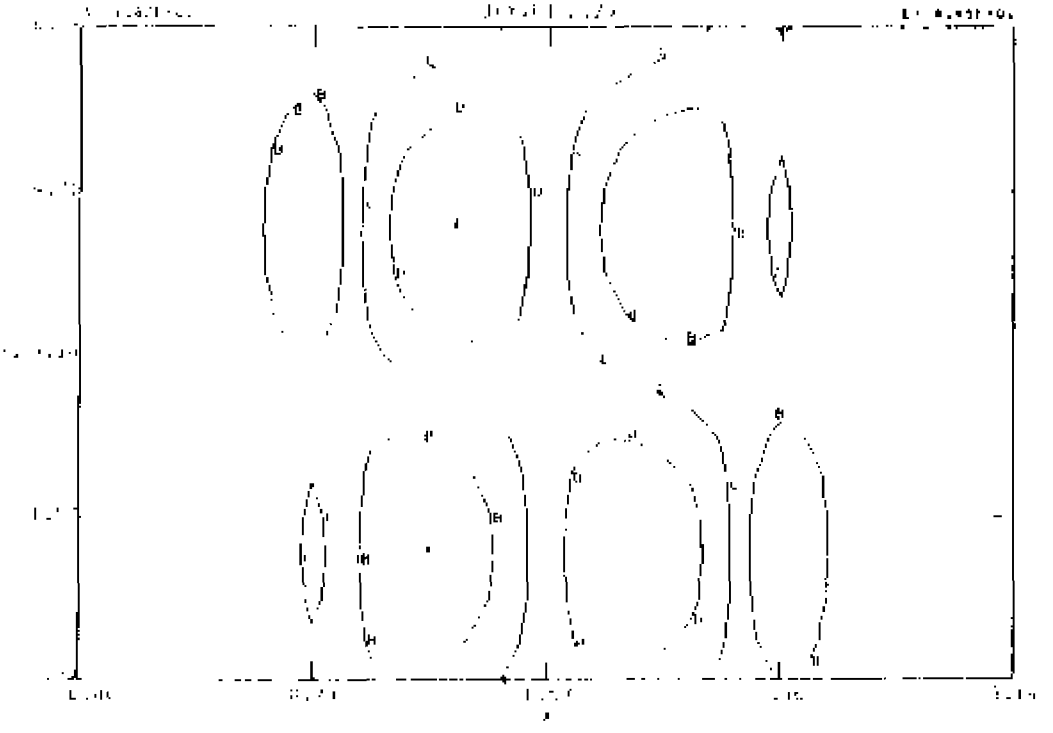

B3 (b): toroidal cut from FROZEN run.

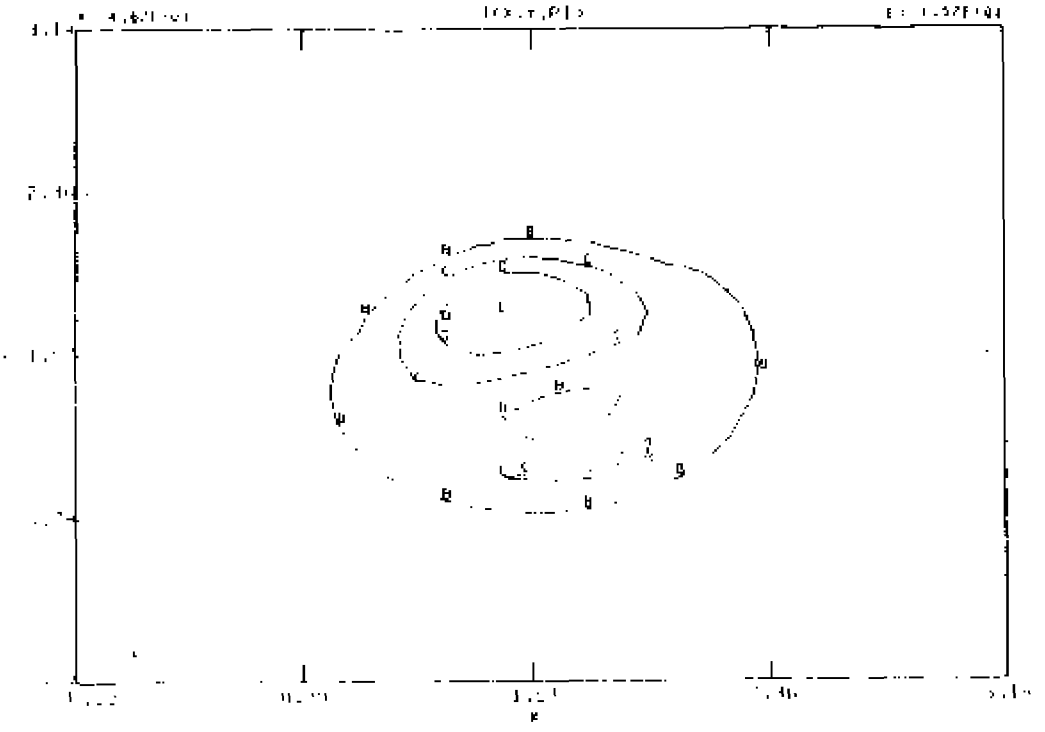

B3 (c): poloidal cut from THAWED run.

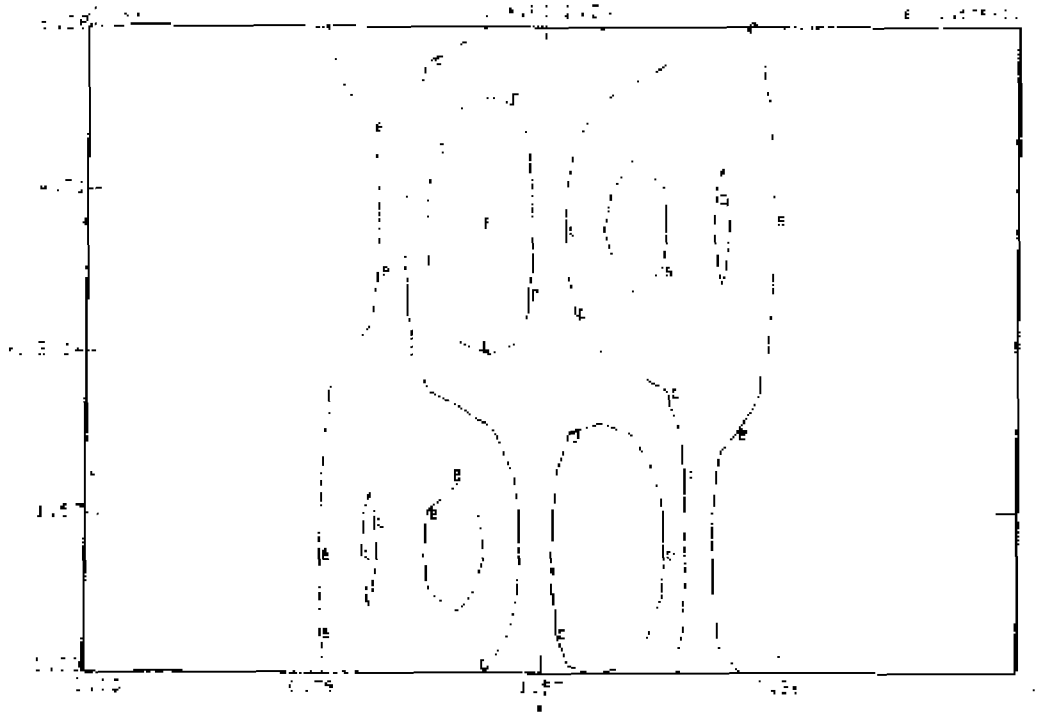

B3 (d): toroidal cut from THAWED run.

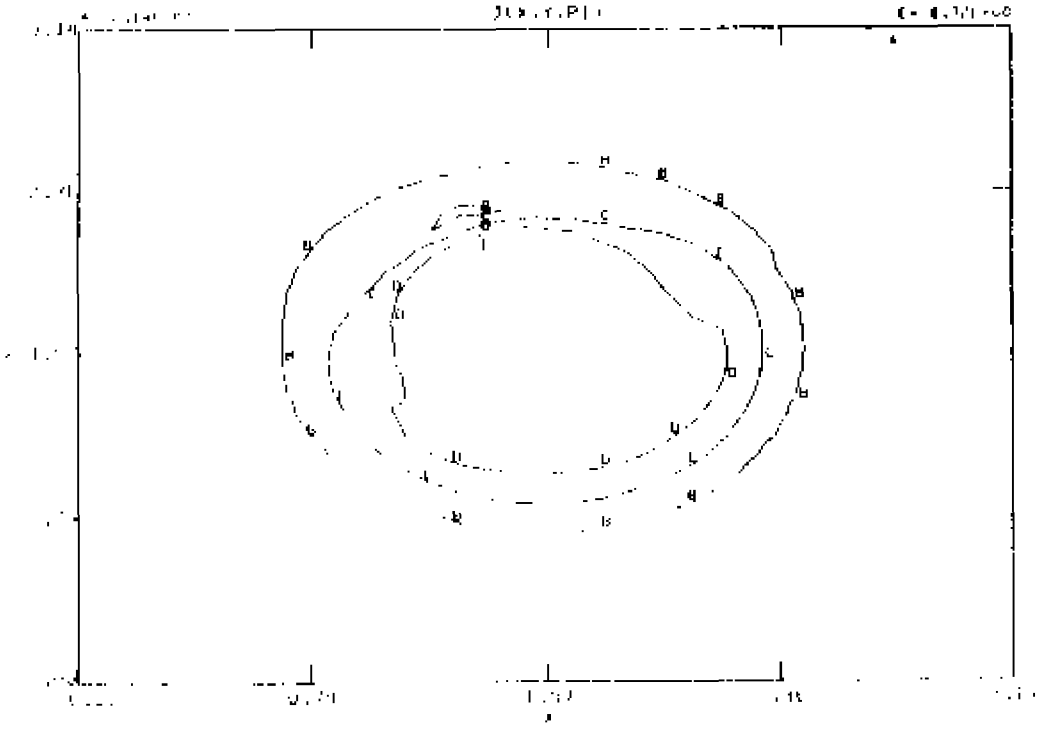

B3 (e): poloidal cut from NONLINEAR run, and

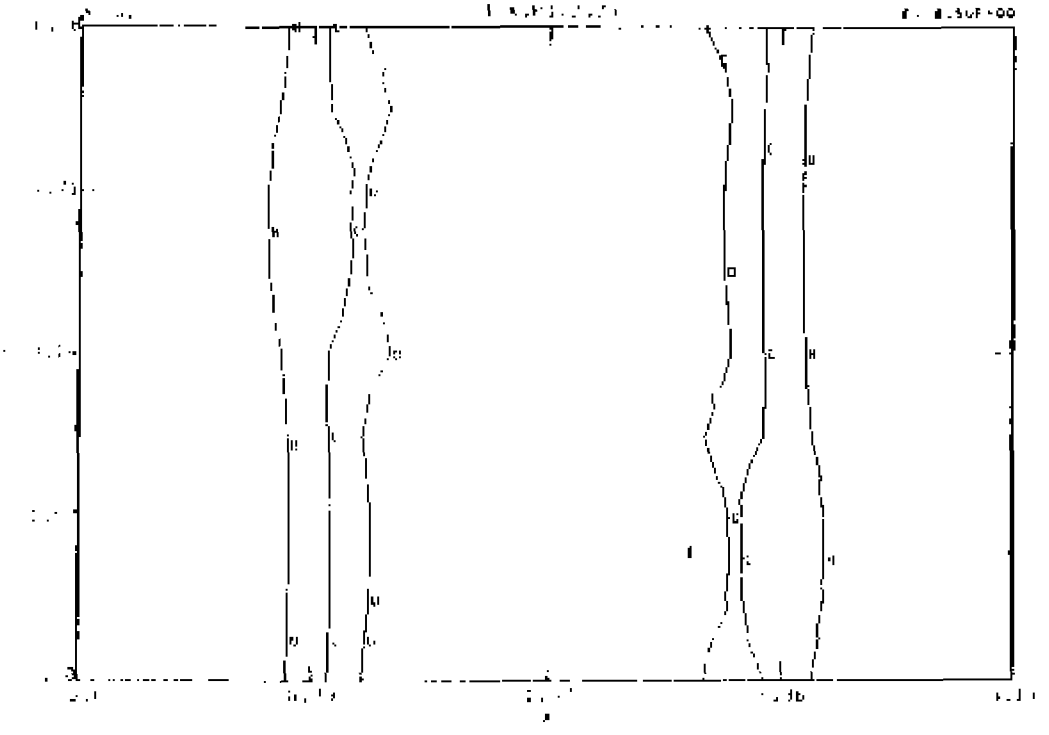

B3 (f): toroidal cut from NONLINEAR run.

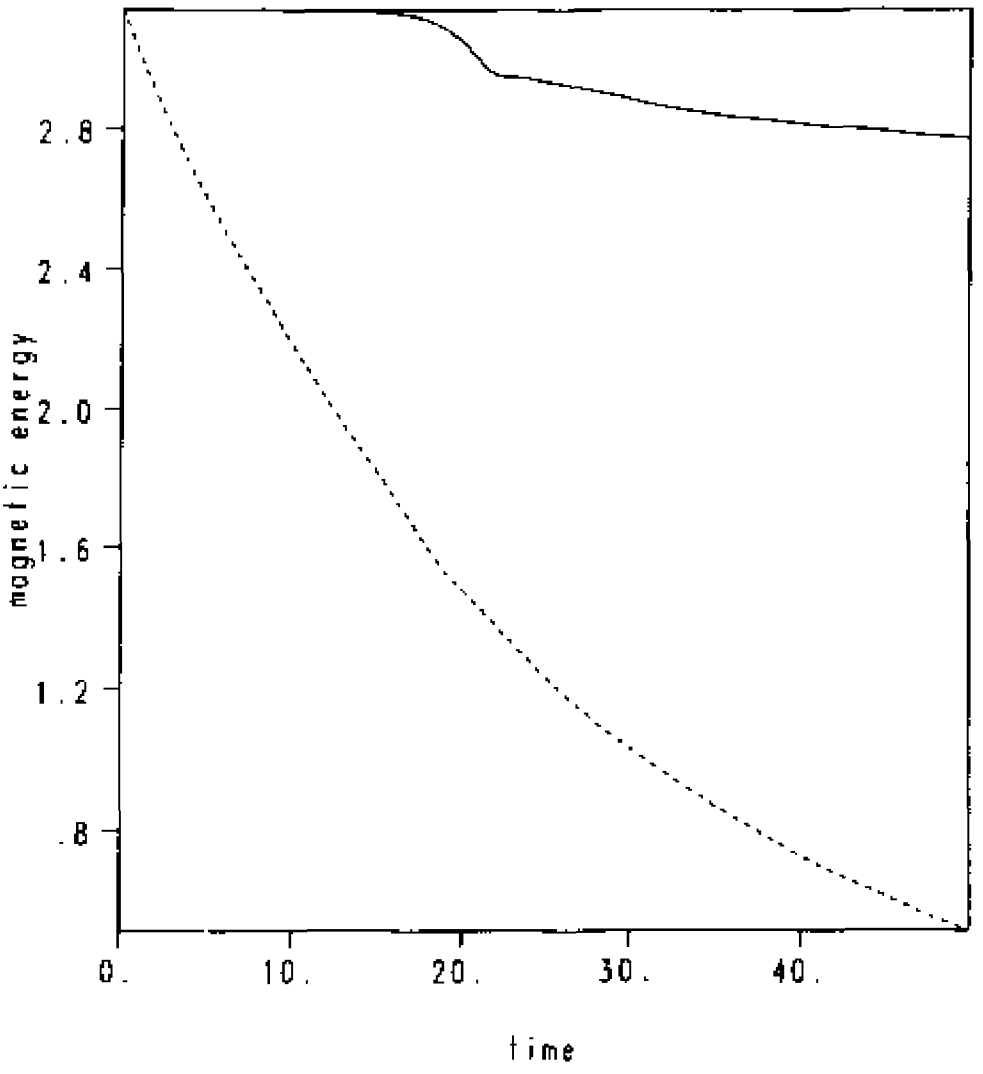

Figure C1. - Comparison globals for CASE 4, $\nu = 0.0$:
C1 (a): magnetic energy as a function of time,
where dashed line: $E_o = 0$,
and solid line: $E_o = 0.05$, and

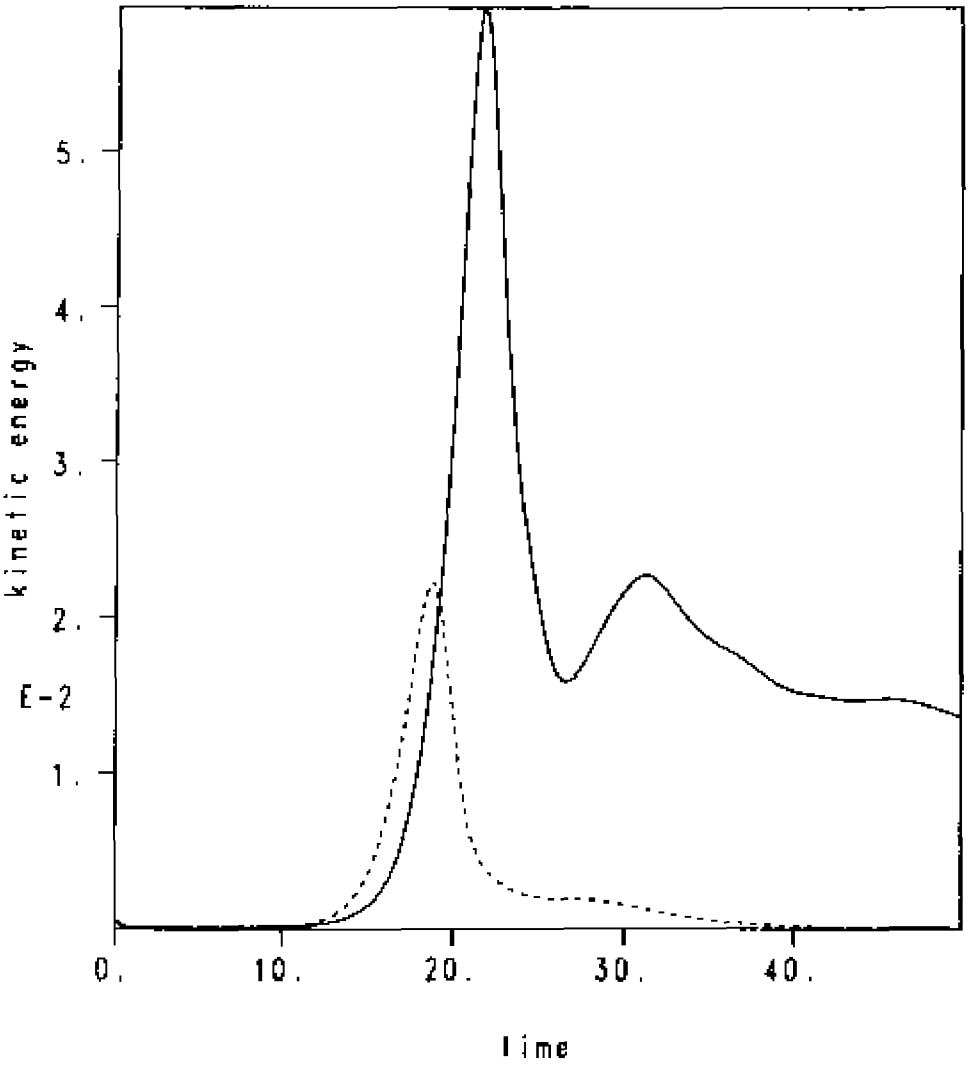

Cl (b): kinetic energy as a function of time,
where dashed line: $E_o = 0$,
and solid line: $E_o = 0.05$.

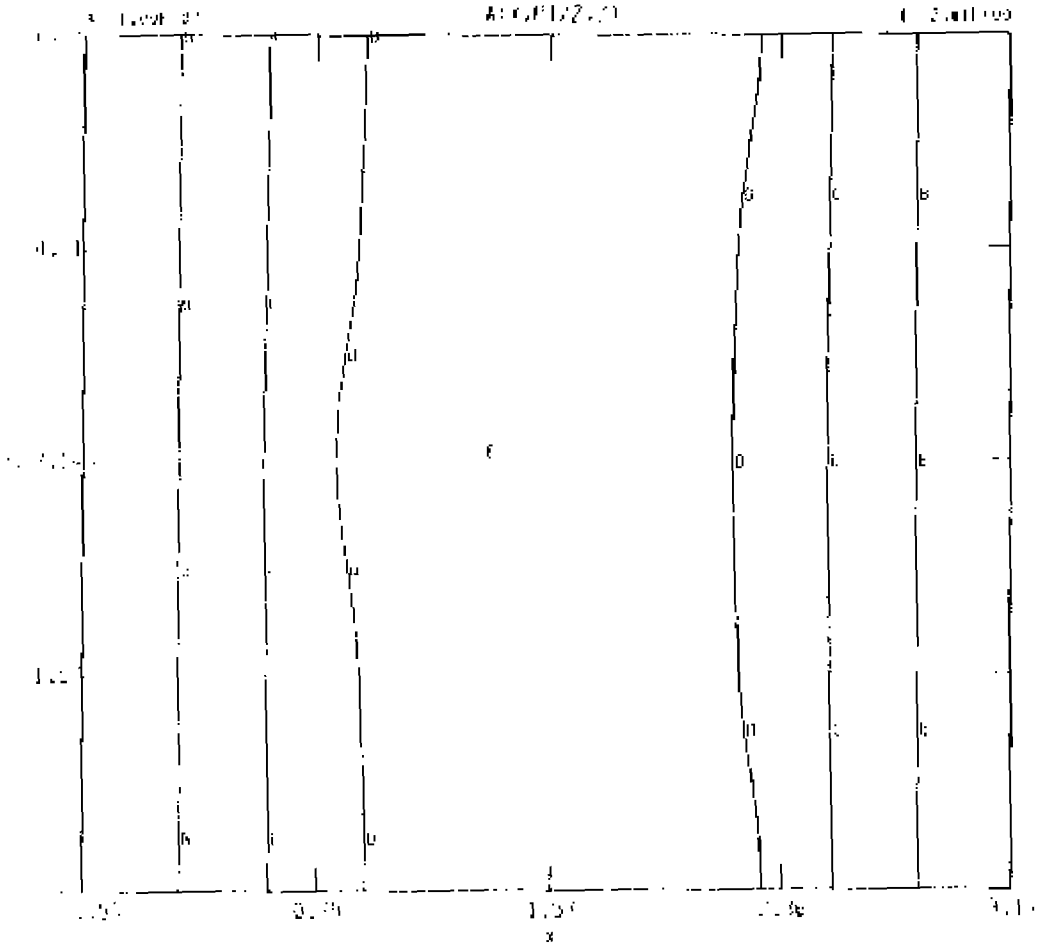

Figure C2. - Contours at t = 16.56, for CASE 4, E_o = 0.0, ν = 0.0:
C2 (a) : contours of A = constant, toroidal cut,

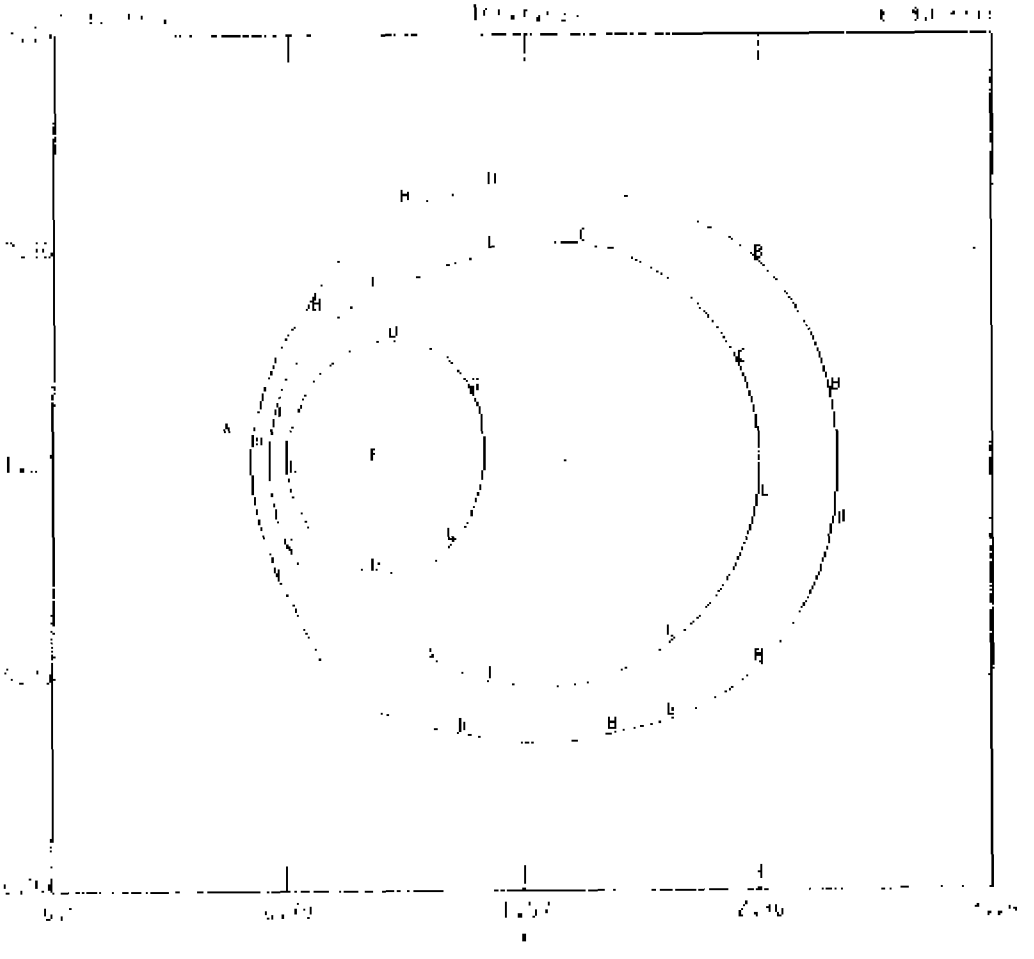

C2 (b): contours of j = constant, poloidal cut.

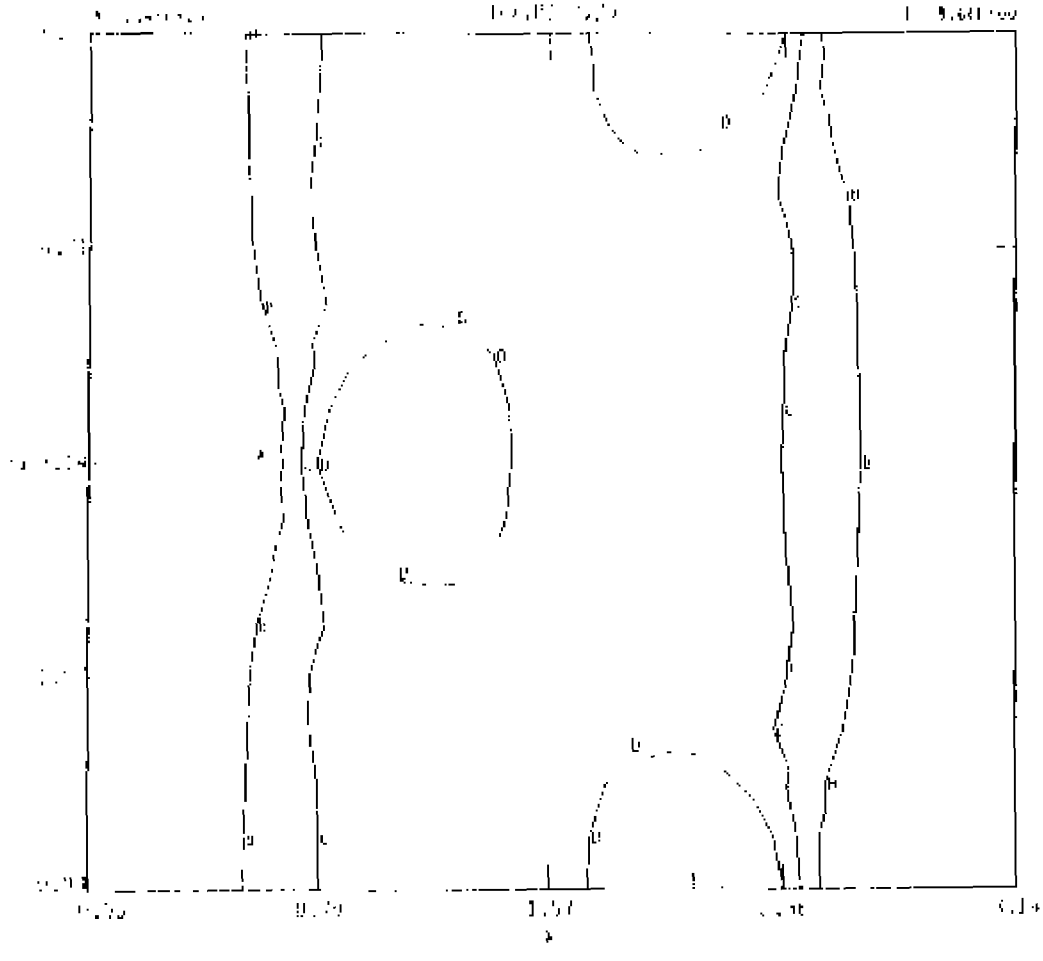

C2 (c): contours of j = constant, toroidal cut, and

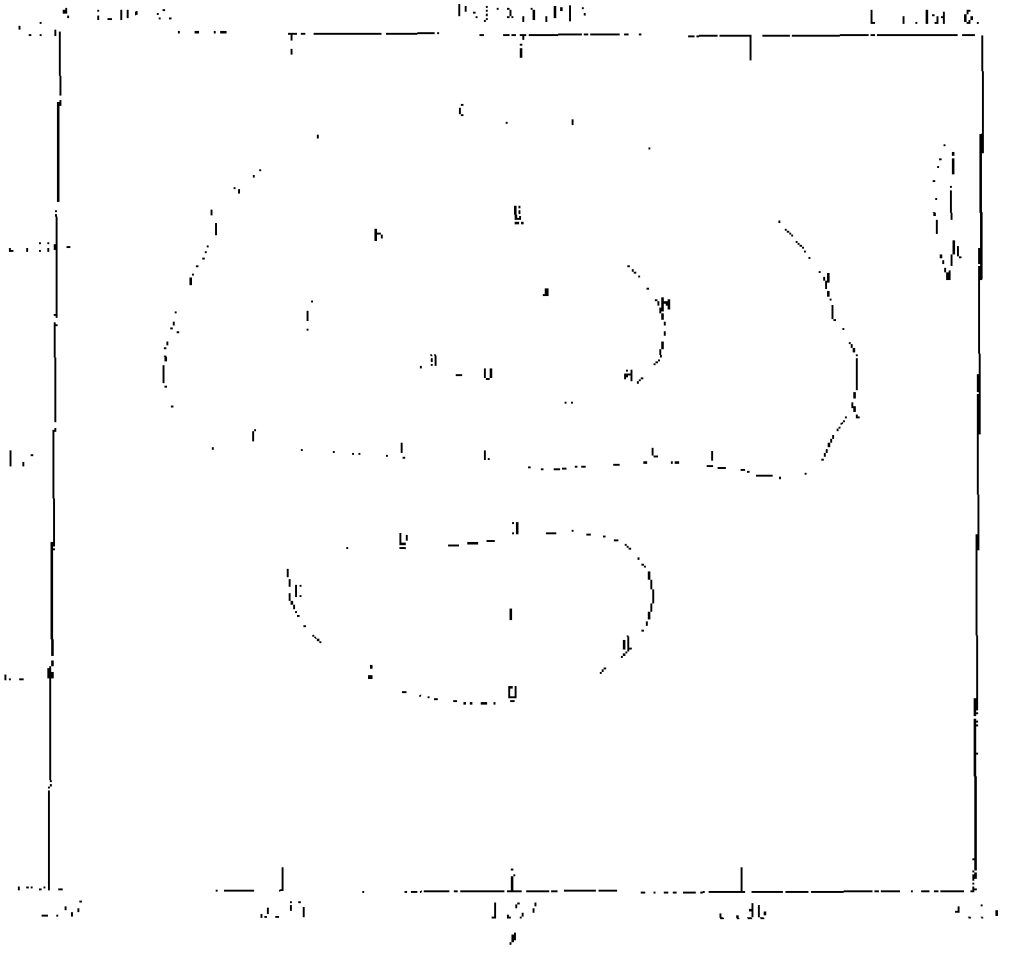

C2 (d) : contours of Ψ^* constant, poloidal cut.

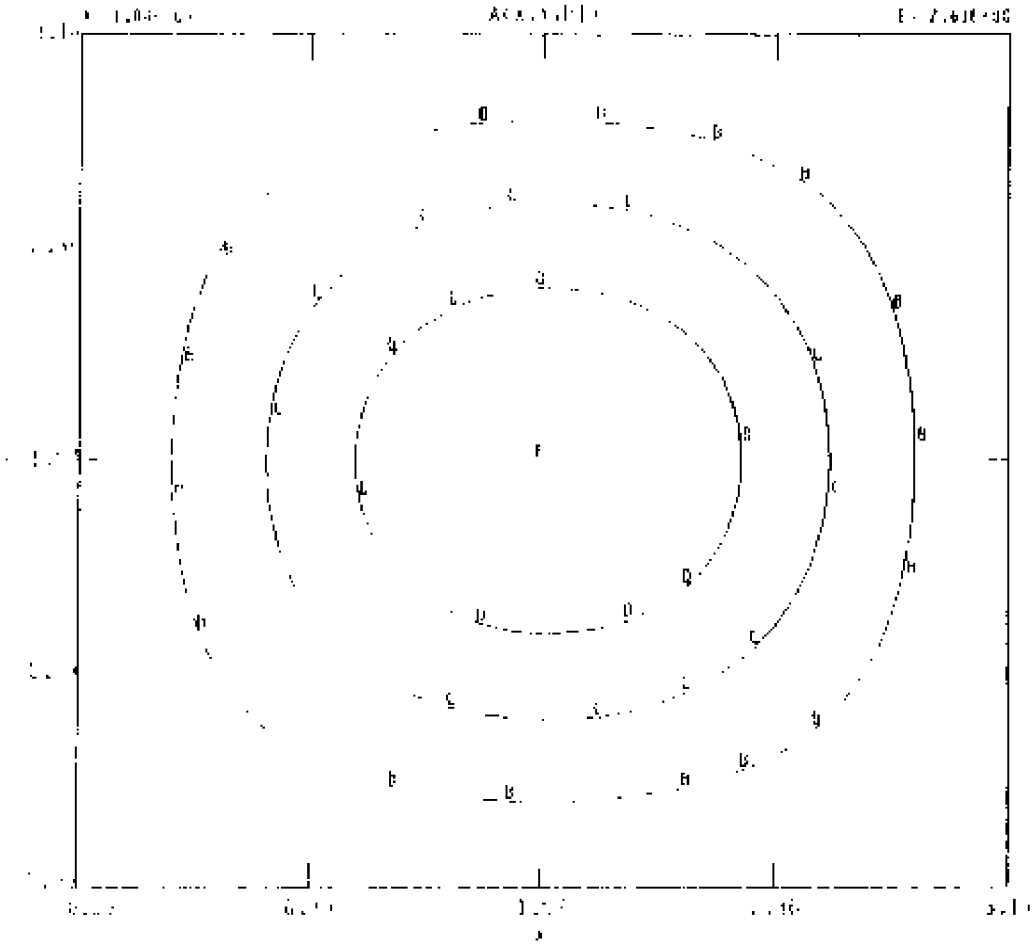

Figure C3. - Contours at t = 20.64, for CASE 4, E_0 = 0.0, $\mathcal{V}$ = 0.0:
C3 (a): contours of A = constant, poloidal cut.

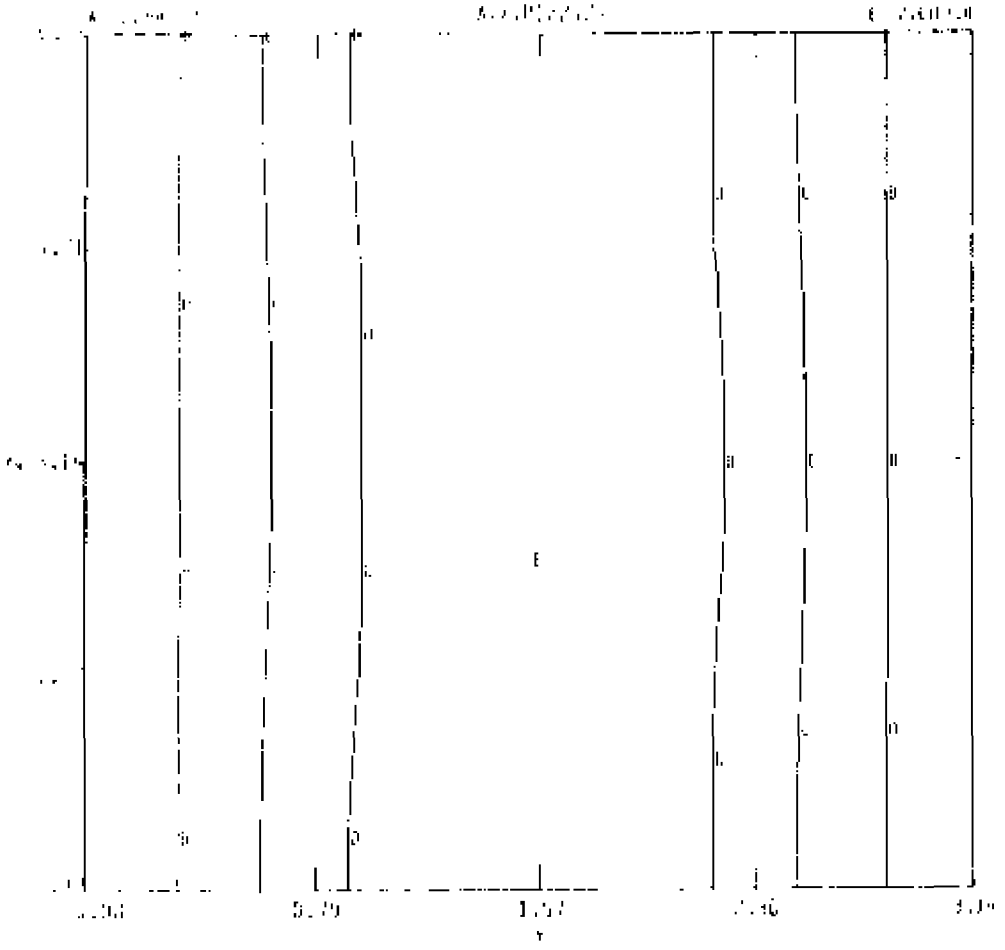

C3 (b): contours of A = constant, toroidal cut,

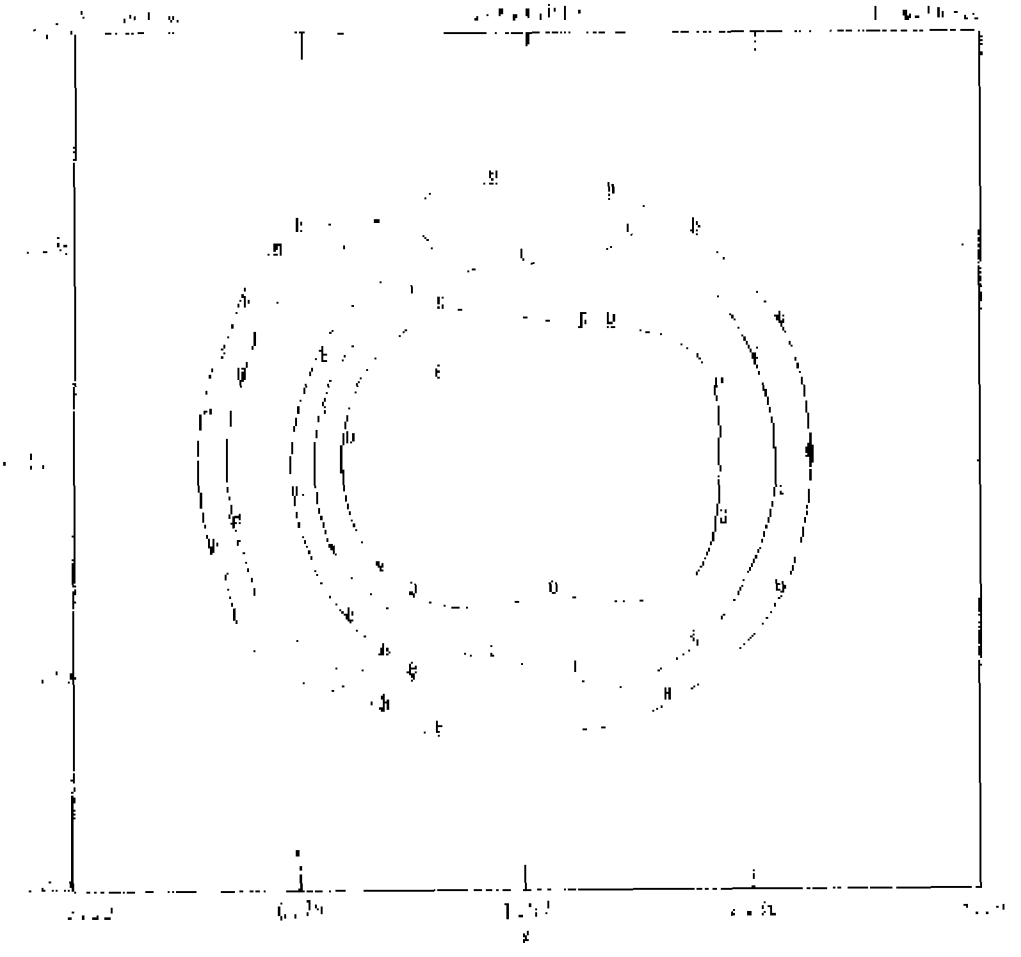

C3 (c): contours of j = constant, poloidal cut,

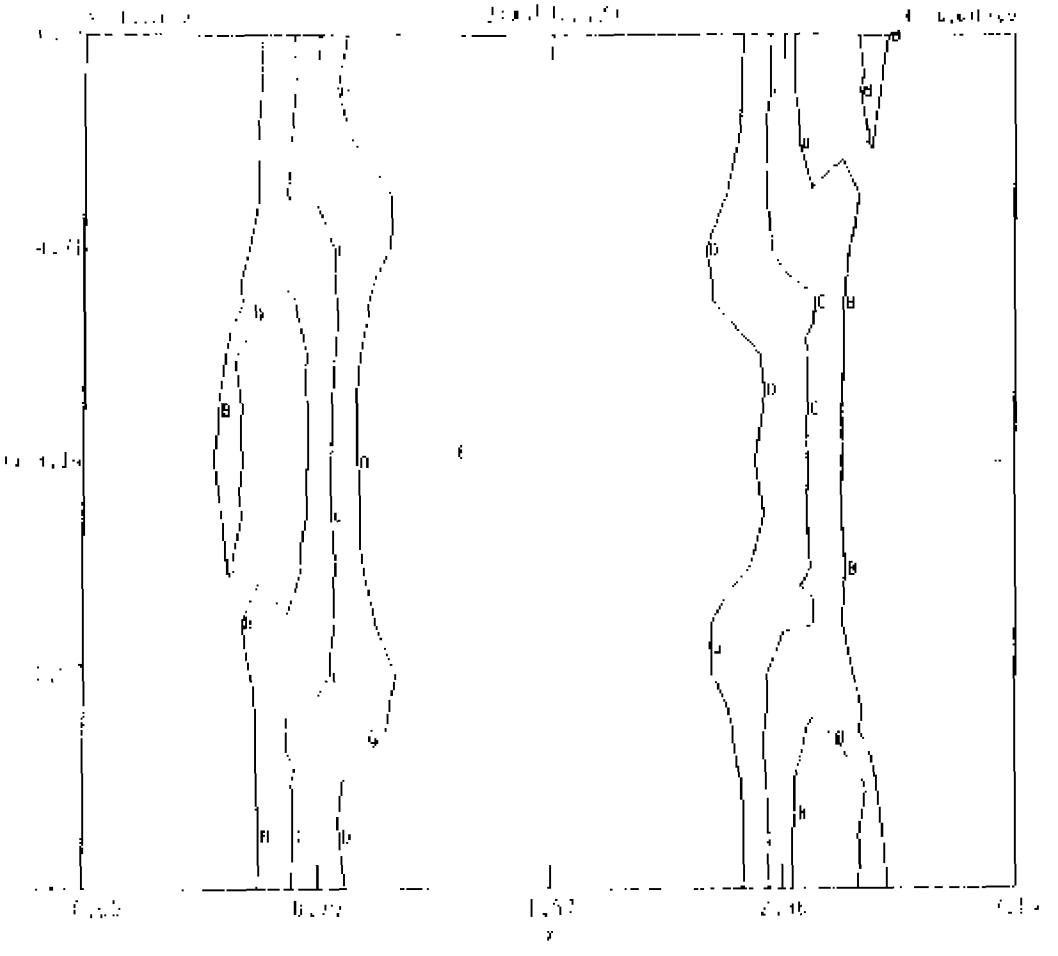

C3 (d): contours of j = constant, toroidal cut.

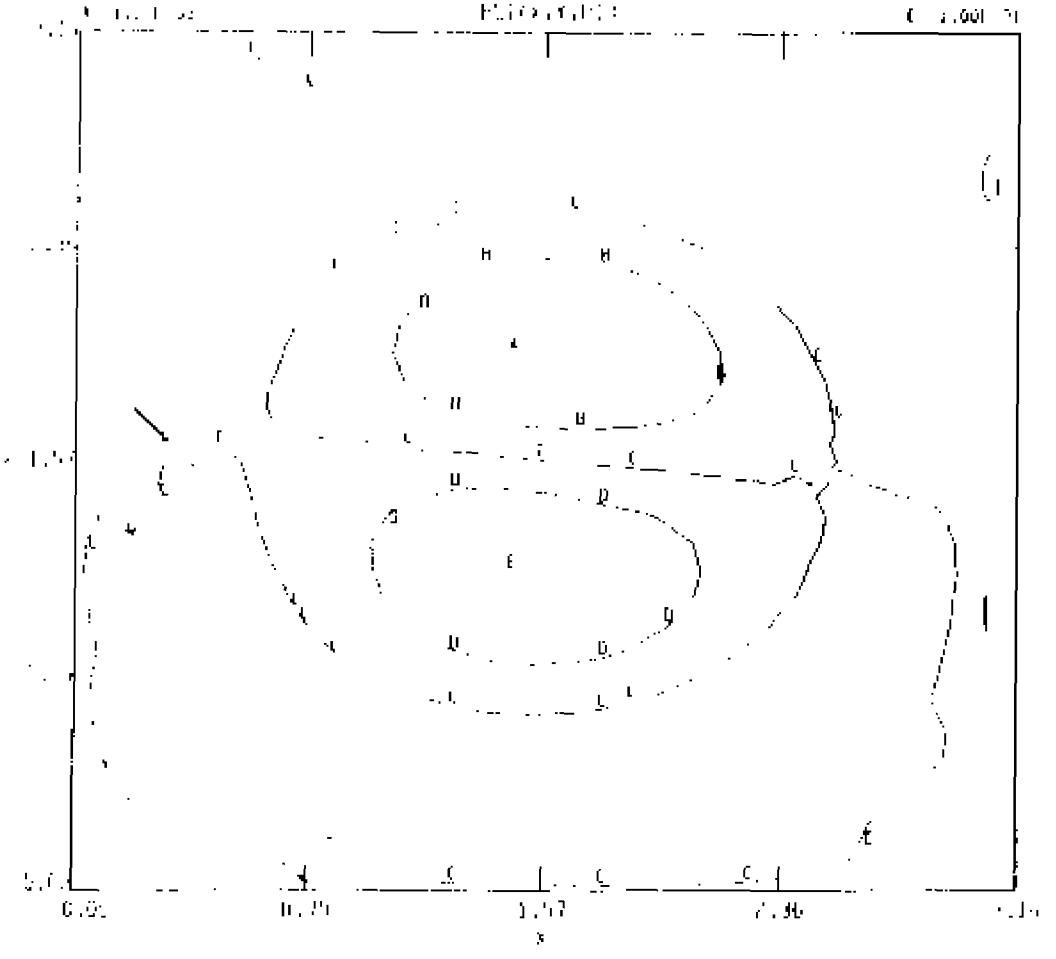

C3 (e): contours of Ψ = constant, poloidal cut, and

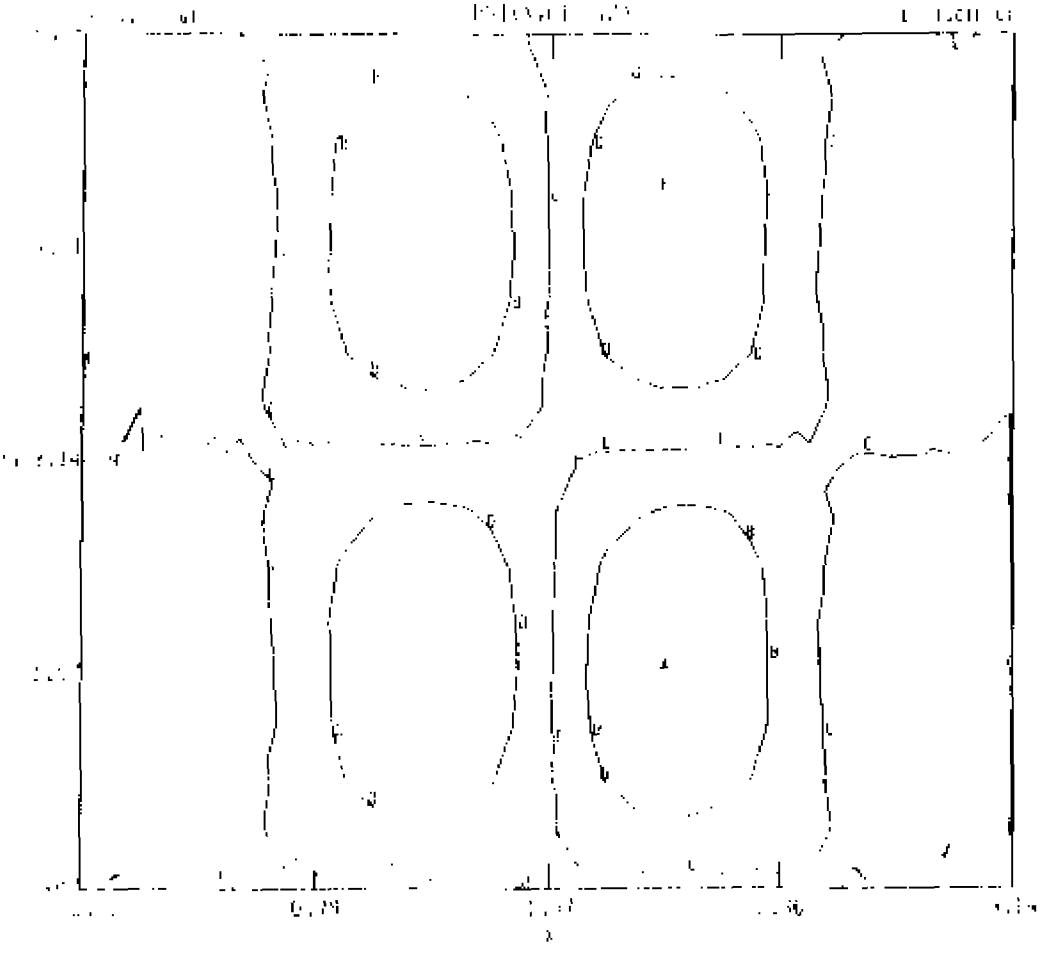

C3 (f): contours of Ψ = constant, toroidal cut.

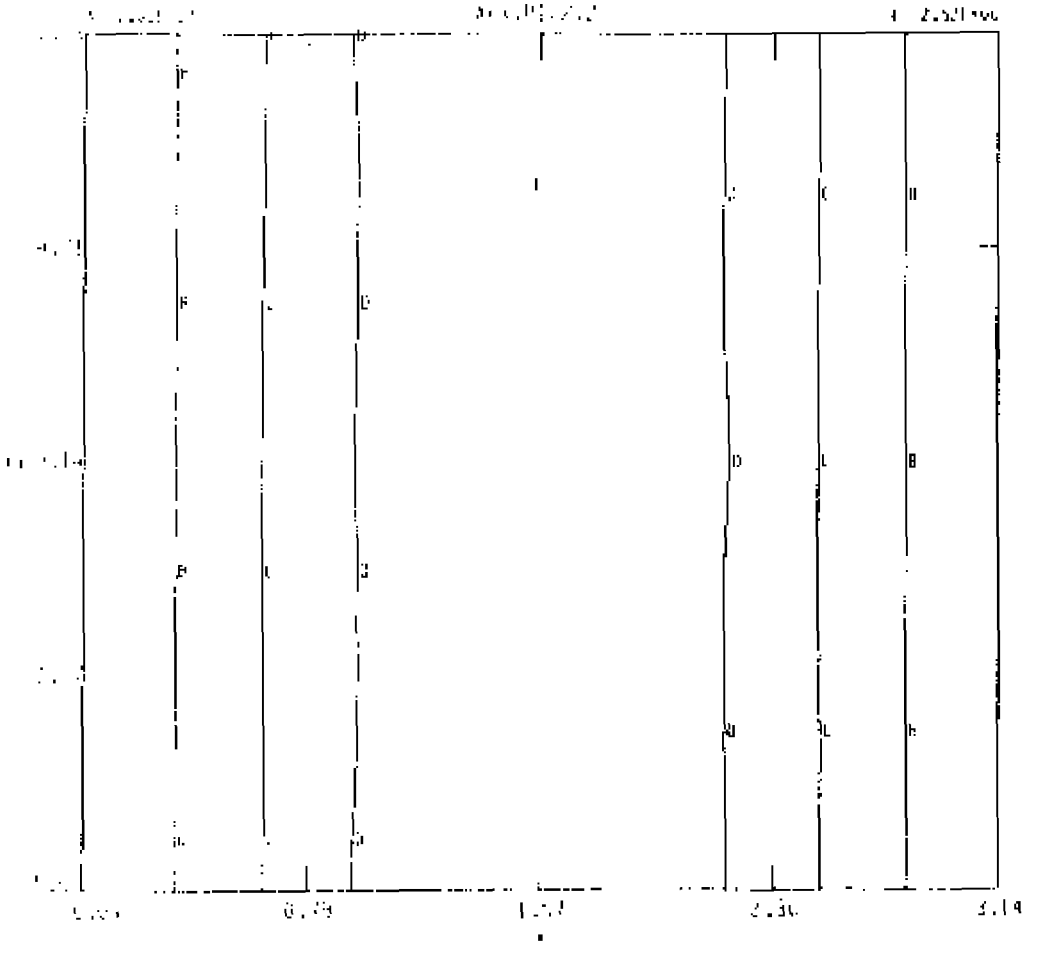

Figure C4. - Contours at t = 23.52, for CASE 4, E_o = 0.5, ν = 0.0;
C4 (a) : contours of A = constant, toroidal cut.

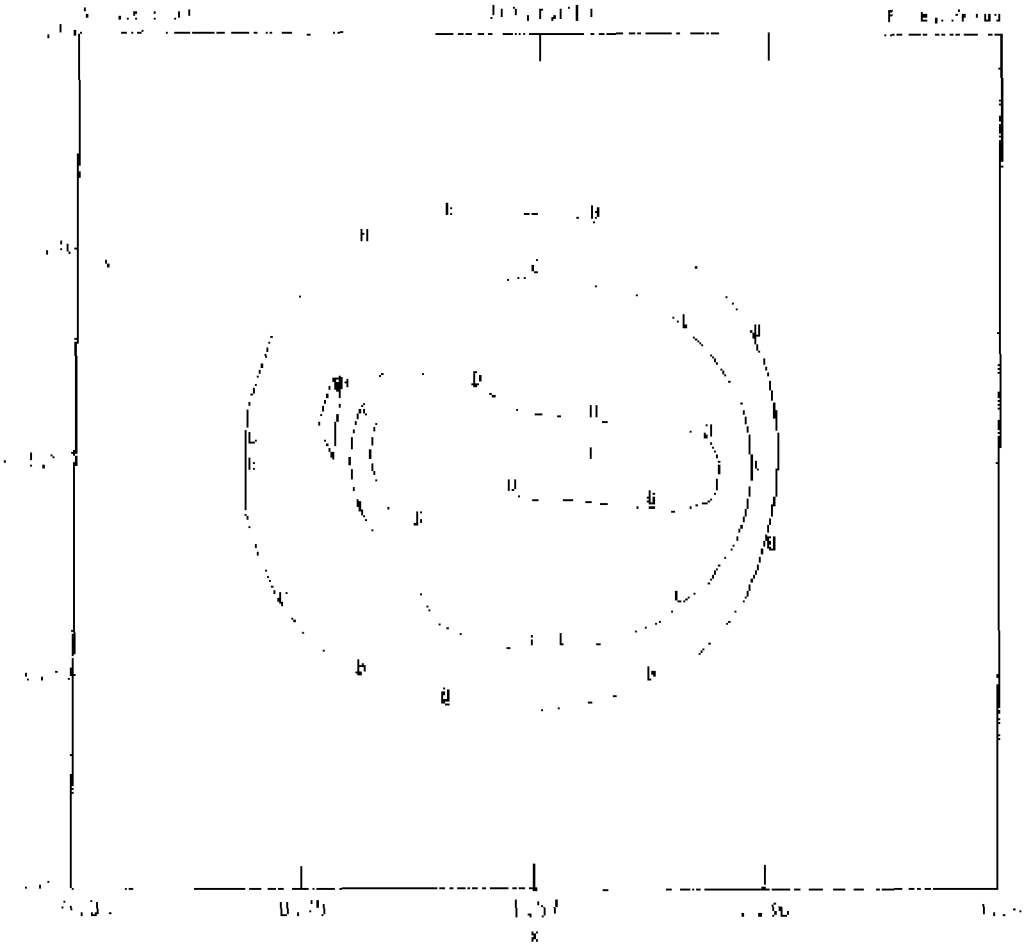

C4 (b): contours of ψ = constant, poloidal cut.

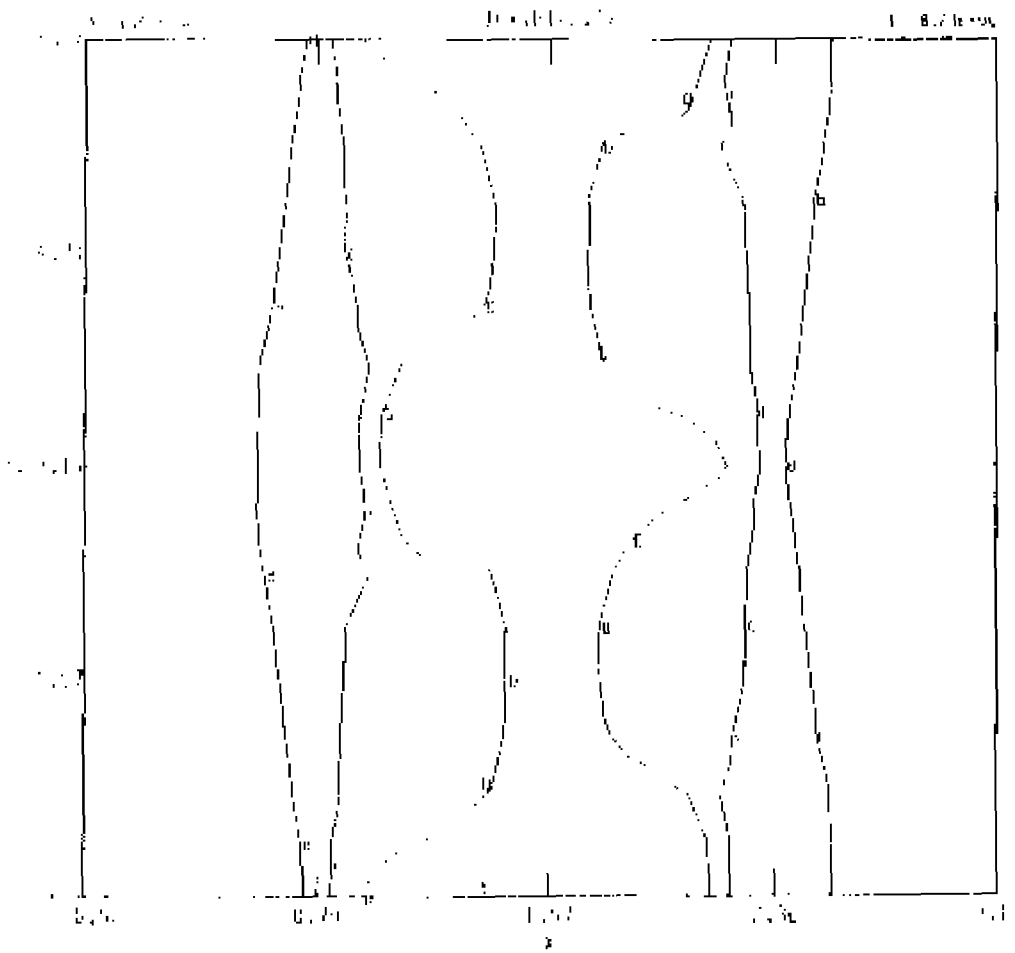

C4 (c): contours of j = constant, toroidal cut, and

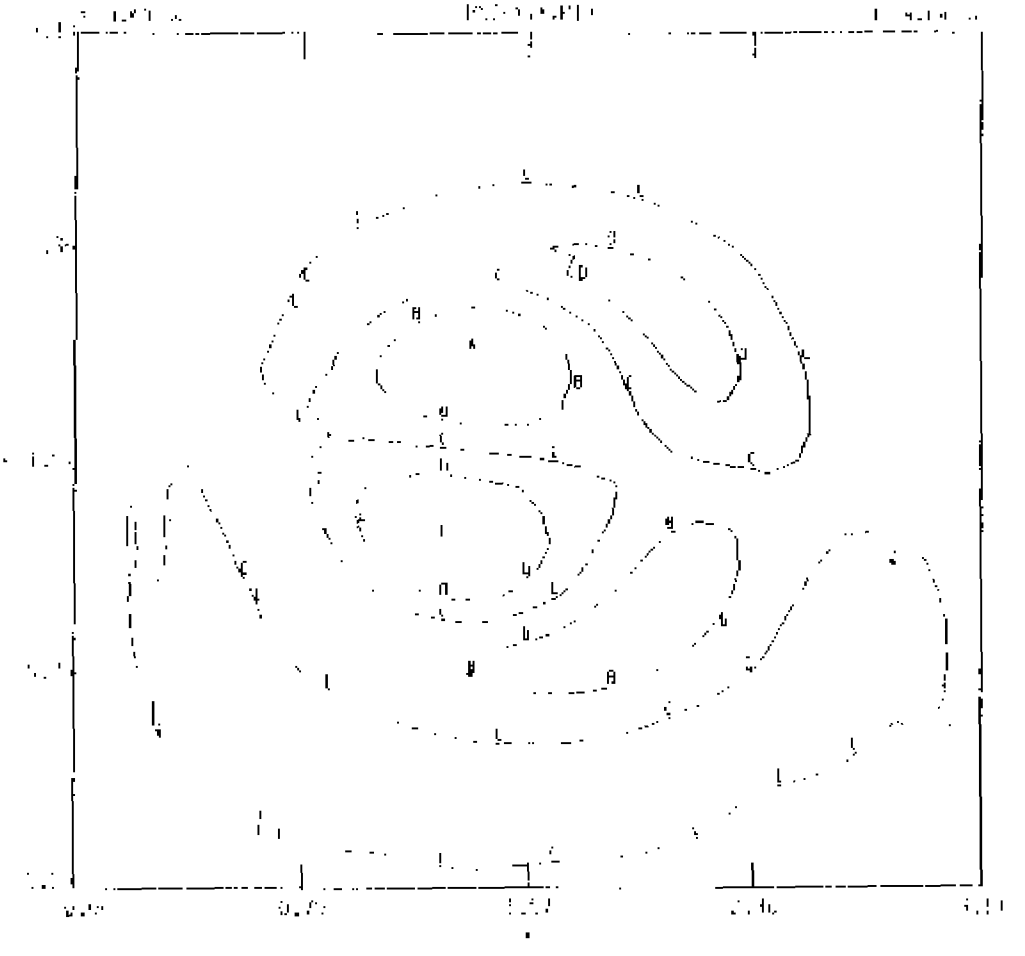

C4 (d) : contours of Ψ = constant, poloidal cut.

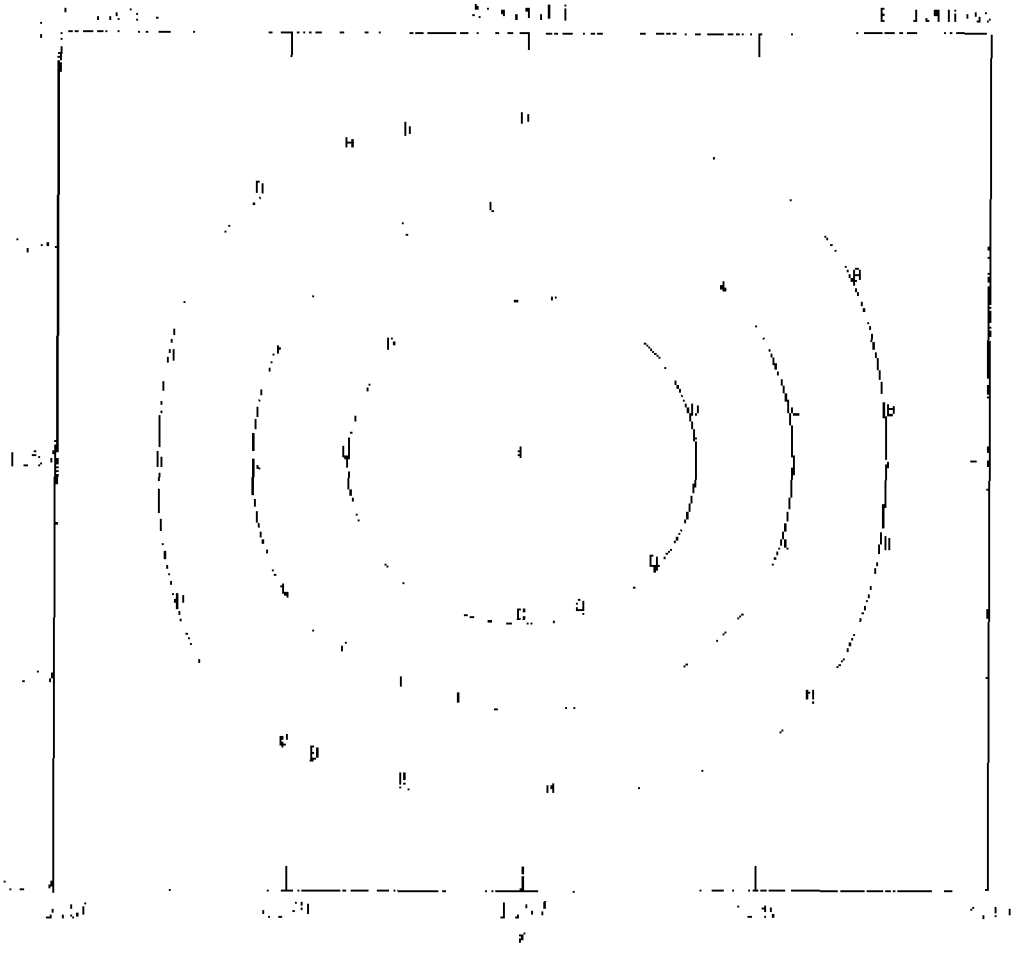

Figure C5. - Contours at t = 40.00, for CASE 4, E_o = 0.0, ∇ = 0.0:
C5 (a): contours of A = constant, poloidal cut,

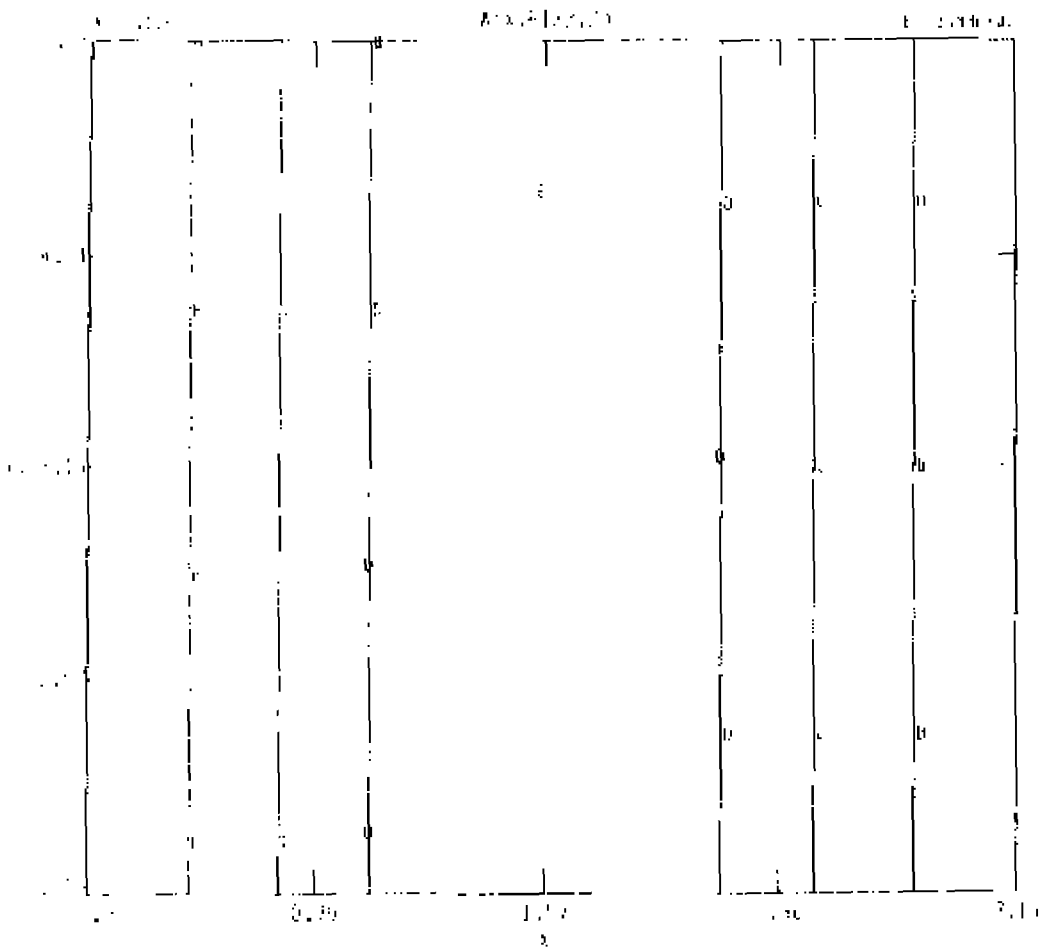

C5 (b): contours of A = constant, toroidal cut.

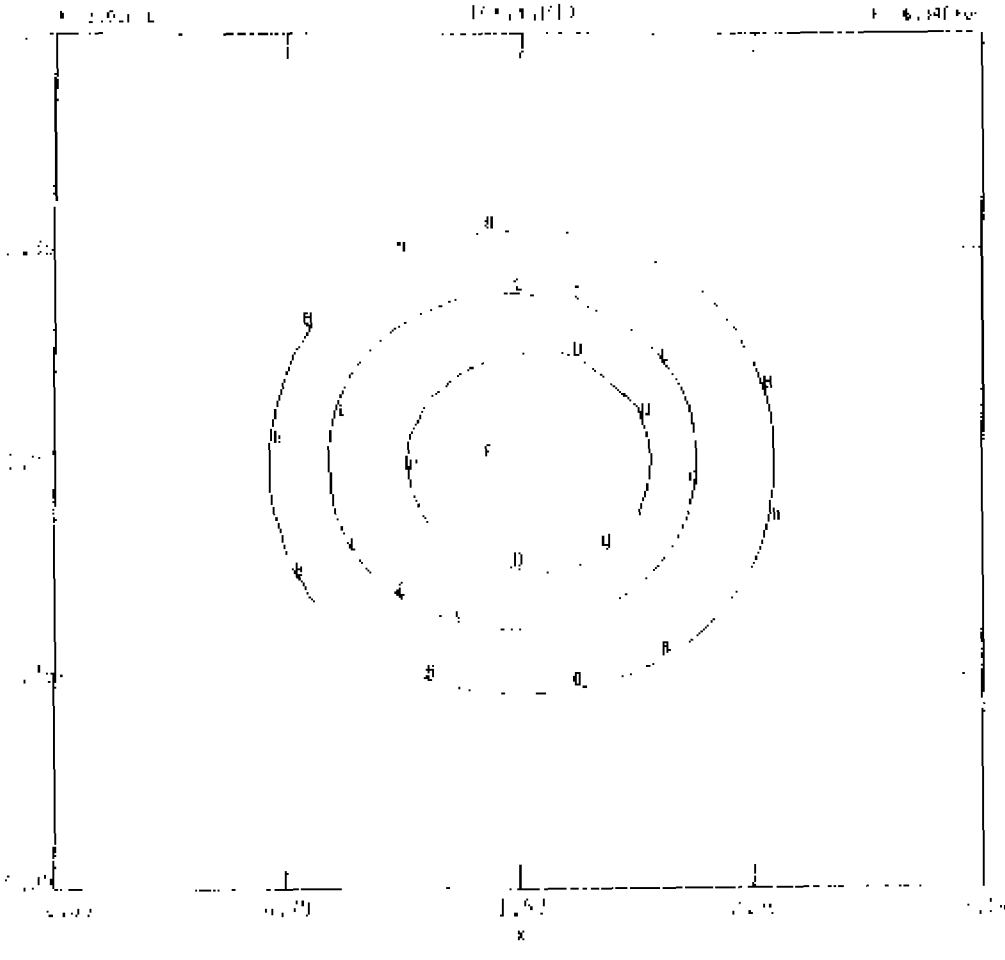

C5 (c): contours of j = constant, poloidal cut,

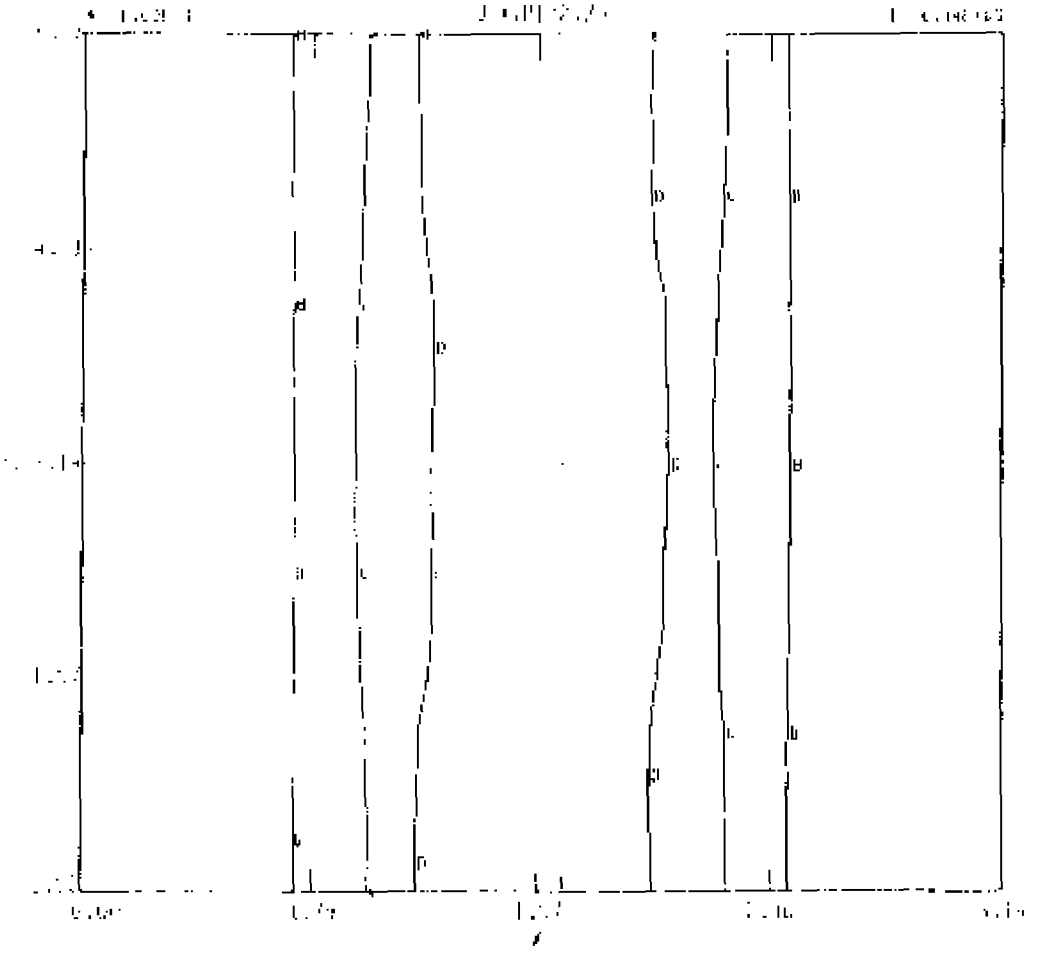

C5 (d): contours of j = constant, toroidal cut.

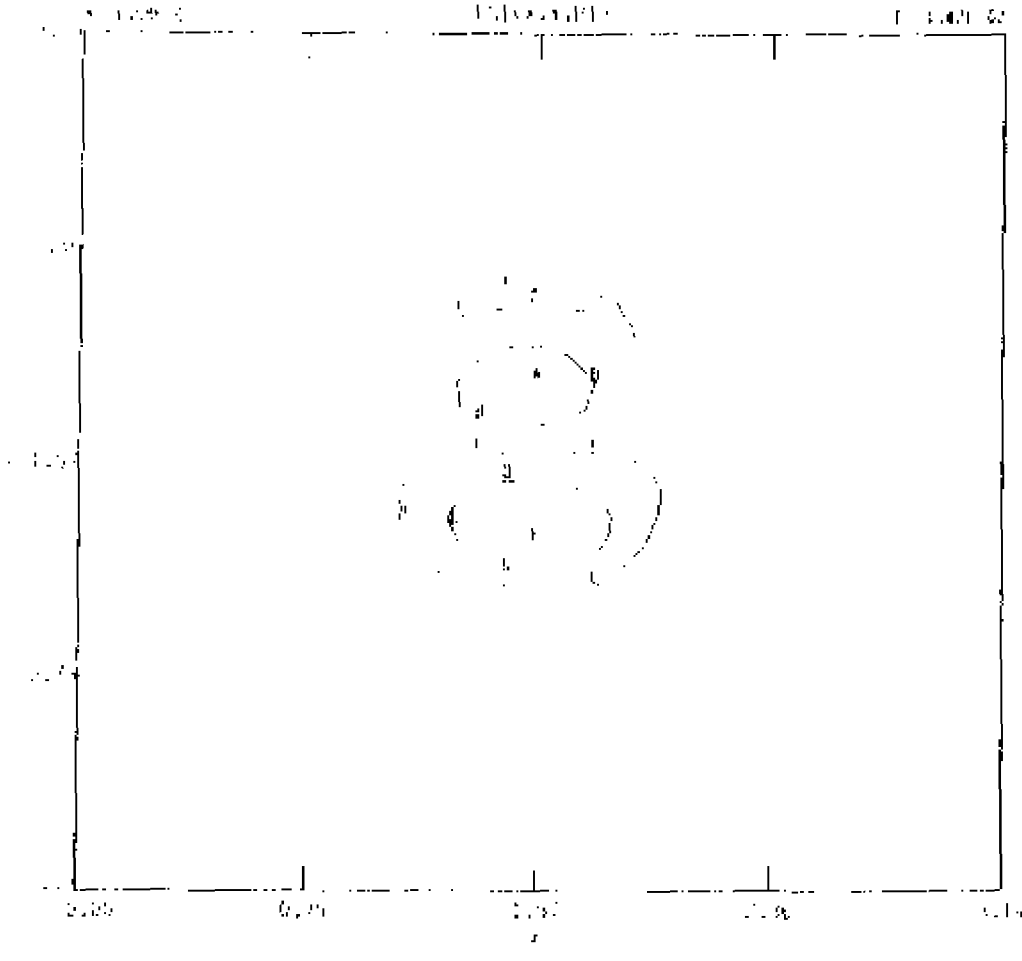

C5 (e): contours of Ψ = constant, poloidal cut, and

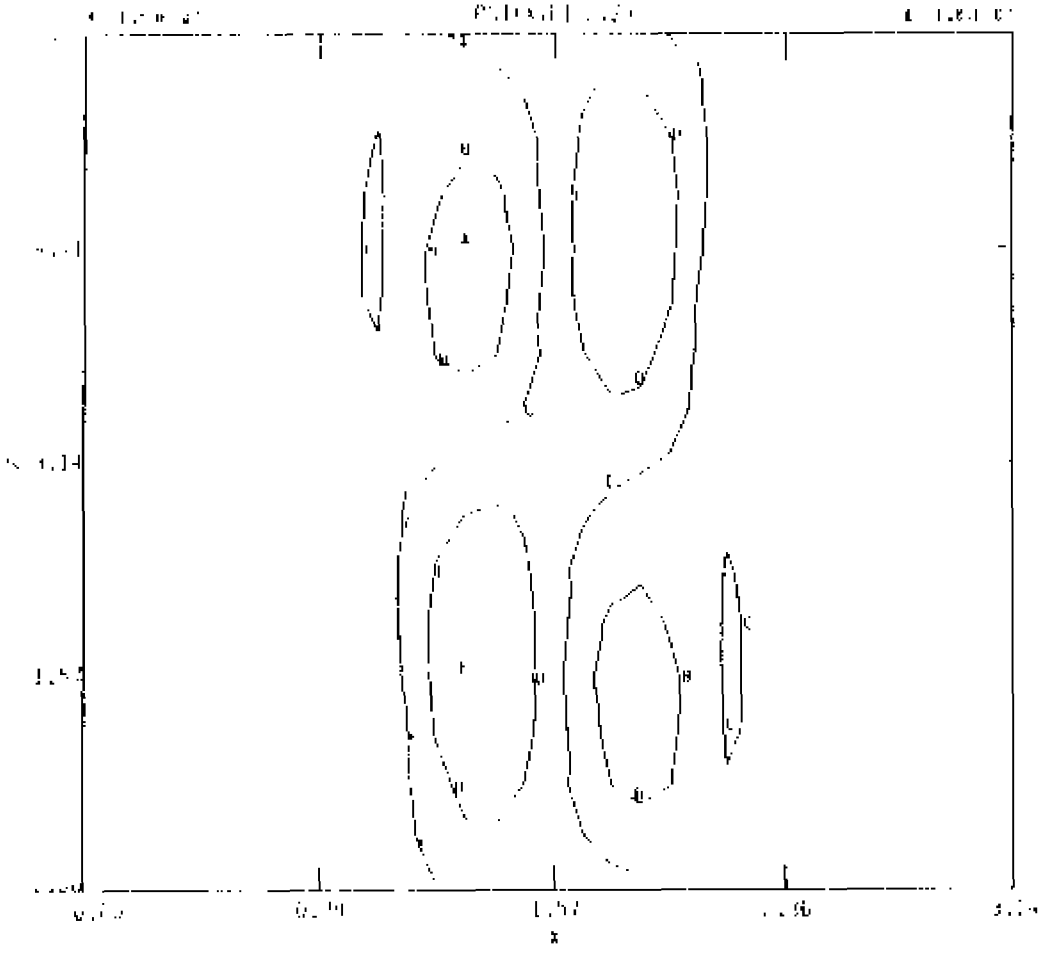

C5 (f): contours of Ψ = constant, toroidal cut.

VITA

Jill Potkalitsky Dahlburg

Born in Chambersburg, Pennsylvania, June 21, 1956. She graduated from Chambersburg Area Senior High School in that town, June, 1974. She attended St. John's College in Annapolis, Maryland in 1974 and graduated in May, 1978, with a Batchelor of Arts degree, with concentration in liberal arts.

In June, 1978, the author entered the College of William and Mary as a graduate assistant in the Department of Physics.